LIÈGE université
Sciences Appliquées

Contribution to the improvement of scroll compressors operating under two-phase conditions

A thesis submitted in partial fulfillment of the requirements
for the degree of Doctor of Philosophy (PhD) in Engineering Science

by
Nicolas Leclercq

Supervisor: Pr. Vincent Lemort

Doctoral College in Aerospace and Mechanics

June 2026

Thermodynamics Laboratory
Aerospace and Mechanical Engineering Department
Faculty of Applied Sciences
University of Liège

Doctoral Thesis

Contribution to the improvement of scroll compressors operating under two-phase conditions

by
Nicolas Leclercq[1]

Supervisor	Pr. Dr. Vincent Lemort Thermodynamics Laboratory University of Liège
President	Dr. Samuel Gendebien Thermodynamics Laboratory University of Liège
Jury member	Pr. Dr. Pierre Dewallef Thermodynamics Laboratory University of Liège
Jury member	Pr. Dr. Steven Lecompte Department of Electromechanical, Systems and Metal Engineering Ghent University
Jury member	Pr. Dr. Andreas Brümmer Chair of Fluidics Dortmund University of Technology
Jury member	Pr. Dr. Christiane Thomas Schaufler Chair of Refrigeration, Cryogenics and Compressor Technology Dresden University of Technology
Jury member	Dr. Eric Winandy OEM Solutions Development and Sales Copeland
Jury member	Dr. Ian Bell Commonwealth Fusion Systems

[1]Email: nleclercq2711@gmail.com
Phone: +32 499 61 44 03

Abstract

Contribution to the improvement of scroll compressors operating under two-phase conditions

by Nicolas LECLERCQ

Supplying a scroll compressor with a two-phase oil-refrigerant mixture can, under certain circumstances, improve both machine and cycle performance. For instance, simulations of a heat pump operating with two-phase conditions at the compressor inlet indicate that supplying the compressor with a vapor quality of 40% can increase the coefficient of performance by 20%, assuming a compressor isentropic efficiency of 70%, due to a better matching of the temperature profiles within the condenser. These results, along with promising findings reported in the literature, motivate research on two-phase compression, in this case, using scroll compressors.

To better understand the behavior of scroll compressors operating under two-phase conditions, numerical and experimental investigations are required. First, a modeling methodology for two-phase oil-refrigerant mixtures is required to describe their behavior during compression. Several mixture property models are proposed and validated against experimental data. These property models are applied to formulate the "desolubilization" assumption, which eliminates the dependence among pressure, temperature, and vapor quality when oil is present in the mixture and consequently simplifies the subsequent numerical calculations.

Experimental investigations are carried out using a test bench dedicated to measuring the performance of compressors under controlled two-phase operating conditions. Four experimental campaigns are performed using a retrofitted compressor and a lab-scale prototype designed for two-phase applications. This lab-scale prototype includes an integrated dynamic pressure sensor, enabling partial acquisition of the pressure-volume diagram and improved validation of the model. The results are analyzed with respect to five operating variables: inlet pressure and vapor quality, pressure ratio, compressor speed, and oil circulation ratio. The results show a significant decrease in compressor performance with decreasing vapor quality.

Finally, a deterministic compressor model incorporating several physics-based features is developed and validated against experimental measurements of power consumption, mass flow rate, and pressure evolution (for the prototype). The model shows good agreement with experiments, with average relative deviations below 3.2% for the prototype and 4.45% for the retrofitted compressor. Performance analyses are then carried out to eventually propose an optimized scroll compressor geometry featuring improved sealing, reduced friction, a larger discharge port and a larger compressor size. Simulations indicate that this design can achieve an isentropic efficiency close to 70% at a vapor quality of 50%, compared to 53% for the prototype under similar conditions.

Keywords: two-phase compression, scroll compressor, experimental testing, deterministic modeling, oil-refrigerant mixture

Résumé

Contribution à l'amélioration des compresseurs scroll fonctionnant en conditions diphasiques

par Nicolas LECLERCQ

Alimenter un compresseur scroll avec un mélange diphasique d'huile et de réfrigérant peut, dans certaines conditions, améliorer les performances de la machine ainsi que celles du cycle dans lequel il est intégré. Par exemple, dans le cadre de simulations réalisées sur une pompe à chaleur fonctionnant avec des conditions diphasiques à l'entrée du compresseur, on observe qu'un titre vapeur de 40% peut augmenter le coefficient de performance de 20%, en faisant l'hypothèse d'une efficacité isentropique du compresseur fixée à 70%. Cette amélioration est notamment liée à une meilleure correspondance des profils de température dans le condenseur de la pompe à chaleur. Ces résultats, ainsi que quelques travaux intéressants publiés dans la littérature, motivent l'étude de la compression diphasique, réalisée ici sur des compresseurs scroll.

Afin d'améliorer la compréhension du comportement des compresseurs scroll en régime diphasique, des investigations numériques et expérimentales sont menées. Une approche de modélisation des mélanges diphasiques huile-réfrigérant est tout d'abord développée afin de décrire leur comportement au cours de la compression. Plusieurs modèles de propriétés du mélange sont proposés et validés à l'aide de données expérimentales. Ces modèles permettent notamment de formuler l'hypothèse de « désolubilisation », qui élimine la dépendance entre pression, température et qualité de vapeur lors de la présence d'huile dans le mélange, simplifiant ainsi les calculs numériques ultérieurs.

Des essais expérimentaux sont ensuite réalisés à l'aide d'un banc d'essai dédié à l'étude des performances de compresseurs, tout en contrôlant les conditions diphasiques auxquelles ils sont soumis. Quatre campagnes expérimentales sont menées sur un compresseur commercial et un prototype spécifiquement conçu pour fonctionner en régime diphasique. Ce prototype est équippé d'un capteur de pression dynamique permettant l'acquisition partielle du diagramme pression-volume ainsi qu'une validation plus précise du modèle. Les résultats sont analysés en fonction des cinq variables de fonctionnement : la pression et la qualité de vapeur à l'entrée, le rapport de pression, la vitesse du compresseur et le taux de circulation d'huile. Les résultats montrent une diminution significative des performances lorsque le titre vapeur diminue.

Pour terminer, un modèle déterministe du compresseur intégrant un grand nombre de contributions physiques liées au régime diphasique est développé et validé à partir de mesures expérimentales de puissance à l'arbre, de débit massique et d'évolution de la pression (pour le prototype). Les prédictions du modèle sont en accord avec les mesures expérimentales, avec des erreurs relatives moyennes inférieures à 3.2% pour le prototype et à 4.45% pour le compresseur commercial. Des analyses des performances sont ensuite réalisées, pour finalement proposer une géométrie optimisée de compresseur scroll, caractérisée par une meilleure étanchéité, une réduction des frottements, un orifice de refoulement plus grand et une taille de compresseur plus importante. Les simulations indiquent que cette conception pourrait atteindre un rendement isentropique proche de 70% pour un titre vapeur de 50%, contre 53% pour le prototype dans des conditions similaires.

Mots clés : compression diphasique, compresseur scroll, essais expérimentaux, modélisation déterministe, mélange huile-réfrigérant

Acknowledgments

Personal acknowledgments

I would like to express my deepest gratitude to Professor Vincent Lemort for his trust since the very beginning of this thesis, his continuous support, and his dedication to always finding solutions to problems related to research, management and funding. His impact on my journey has been truly significant and I cannot thank him enough for that.

I would also like to thank the wonderful team of the Thermodynamics Laboratory. Honestly, I think it is impossible to find better colleagues anywhere else. Of course, I would like to thank them not only for the work-related aspects, but also for the many enjoyable moments shared during everyday lab life, lunches, afterworks, conferences, and beyond. Special thanks to Sam Gendebien, José Concha, Monsieur Bernard and last but not least, Richard Labenda, for their significant contributions to my work during these years.

I am also thankful to the people outside the laboratory who contributed to this work. First, the members of the committee who guided me throughout these years. Then, Benedikt Bederna and Christiane Thomas for the opportunity to work in their laboratory at TU Dresden. Lastly, thanks should also go to Yacine Brahami for his valuable advice and support.

Words cannot express my gratitude to my family for their support all along my studies. Special thanks to my mother for her tireless devotion and constant encouragement. Finally, I am deeply grateful to my love, Marie, for her unconditional support and patience during this last year.

Use of Artificial Intelligence Tools

This thesis was carried out with the assistance of an artificial intelligence tool (ChatGPT, OpenAI) for language editing, sentence reformulation, and minor programming assistance. All scientific content, analyses, and conclusions remain the sole responsibility of the author. Furthermore, the only figure generated using an artificial intelligence tool is the cover image of this thesis.

Funding

The project source of the results presented in this thesis, known as REGEN-BY-2, has received funding from the European Union's Horizon 2020 research and innovation programme under grant agreement No. 851541.

Scope of the thesis

The objective of this doctoral thesis manuscript is twofold: (1) to demonstrate the feasibility and usefulness of two-phase compression in scroll compressors by presenting concrete examples and providing a solid analysis and conclusions regarding the machines' performance under this regime; (2) to provide the reader with accurate modeling tools required to simulate scroll compressors operating with two-phase oil-refrigerant mixtures. This thesis manuscript gathers contributions to the study of two-phase compression (both experimental and numerical), as well as to the study of oil-refrigerant mixtures and heat pump cycle simulations. The presentation of these contributions already requires a considerable amount of space. Therefore, the content of this thesis is limited to these contributions, along with brief state-of-the-art discussions and introductions to the relevant topics. The content is thereby addressed to readers with knowledge of positive-displacement machines, thermodynamic modeling of thermal systems, and thermophysical property modeling. Furthermore, the numerical modeling technique employed and developed to simulate the compressor, namely deterministic modeling, also details only specific contributions and does not provide all the details required for a full implementation of the model. It is therefore recommended to refer to the thesis of Ian Bell (Bell 2011) for a detailed methodology for scroll compressor deterministic modeling. Solving procedures are often required for the systems of equations presented throughout this manuscript. However, in most cases, no details are provided regarding the numerical solution process. Unless otherwise specified, all numerical resolutions are performed using the optimize module of the SciPy library 1.7.3 (Virtanen et al. 2020), with either *fsolve* or *leastsquare*. As a whole, despite the diversity of contributions involved, the thesis follows a clear and coherent progression from the introduction to the conclusion. A glossary can be found in page xxxvii. It is recommended to read it before starting the thesis to facilitate the understanding of some technical terms used throughout the manuscript. Naturally, each term is introduced at least once throughout the manuscript. Two experimental databases have been generated through the experimental investigations, they can be found on Zenodo at the following links: Retrofitted compressor data, Prototype compressor data, for the retrofitted compressor tests and for the prototype tests, respectively. In addition, a custom numerical code was developed specifically for this research to perform the compressor experimental post-processing, modeling, simulation, and analysis tasks described in this manuscript. The source code is available on GitHub at Two-phase compression repository.

Contents

List of Figures

List of Tables

List of Abbreviations

A	**A**nnular
AAD	**A**verage **A**bsolute **D**ifference
ARD	**A**verage **R**elative **D**eviation
CFD	**C**omputational **F**luid **D**ynamics
Comp	**Comp**ressor or **Comp**onent
Comp$_p$	**Comp**ressor **p**rototype
Comp$_r$	**Comp**ressor **r**etrofitted
Cond	**Cond**enser
COP	**C**oefficient **O**f **P**erformance
CRHPs	**C**ompression-**R**esorption **H**eat **P**umps
CV (stat)	**C**ross-**V**alidation
CV (model)	**C**ontrol **V**olume
EU	**E**uropean **U**nion
Evap	**Evap**orator
G	**G**aseous (vapor) phase
GP	**G**aussian **P**rocess
GPExp	**G**aussian **P**rocess tool
HCFO	**H**ydro**c**hloro**f**luoro**o**lefin
HVAC	**H**eating, **V**entilation and **A**ir **C**onditioning
I	**I**ntermittent
L	**L**iquid phase
Liq. corr.	**Liq**uid-phase **corr**ection
M1	**M**ethodology number **1**
M2	**M**ethodology number **2**
Mixt.	**Mixt**ure
NRTL	**N**on-**R**andom **T**wo-**L**iquid model
OCR	**O**il **C**irculation **R**atio
POE	**P**oly**ol**ester
PR	**P**eng-**R**obinson
PTFE	**P**oly**t**etra**f**luoro**e**thylene
PTV	**P**atel-**T**eja-**V**alderrama
RD	**R**elative **D**eviation
Ref.	**Ref**erence
Res	**Res**idual
RMS	**R**oot **M**ean **S**quare
RPM	**R**evolutions **P**er **M**inute
S	**S**tratified
SC	**S**ub**c**ooling
SH	**S**uper**h**eating
SRK	**S**oave-**R**edlich-**K**wong
SW	**S**tratified-**W**avy
TFC	**T**rilateral **F**lash **C**ycle

ULLN	**U**pper **L**imit **L**og-**N**ormal
V	**V**apor (gaseous) phase
$p-\theta$	**p**ressure-**angle**
$p-V$	**p**ressure-**v**olume
2D	**T**wo-**d**imensional
3D	**T**hree-**d**imensional

List of Symbols

Symbol	Name	Unit
a_i	parameters	multiple
A	area	mm^2
A, B, C	Cubic equation of state coefficient	multiple
AU	thermal conductance	$\mathrm{W\,K^{-1}}$
b_i	parameters	multiple
Bo	Boiling number ($= q/(G\,h_{\mathrm{fg}})$)	-
c	sound velocity in a given medium	$\mathrm{m\,s^{-1}}$
C_{d}	discharge coefficient	-
c_p	specific heat capacity at constant pressure	$\mathrm{J\,kg^{-1}\,K^{-1}}$
c_i	parameters	multiple
COP	coefficient of performance	-
d	diameter	m
D	diameter	m
D_{h}	hydraulic diameter	m
D_{32}	Sauter mean diameter	μm
e	specific exergy (also called exergy)	$\mathrm{J\,kg^{-1}}$
$\dot{E}_{\mathrm{D}}$	exergy destruction rate	W
f	Darcy friction factor	-
$\mathcal{F}$	number of intensive variables defining a system	-
Fr	Froude number ($= U^2/(g\,D)$)	-
G	mass flux	$\mathrm{kg\,s^{-1}\,m^{-2}}$
Gr	Grashof number ($= g\,\beta\,(T_{\mathrm{s}} - T_{\infty})\,L^3/\nu^2$)	-
h	specific enthalpy (also called enthalpy)	$\mathrm{J\,kg^{-1}}$
h	heat transfer coefficient	$\mathrm{W\,m^{-2}\,K^{-1}}$
H	height	mm
h_{s}	scroll height	mm
k	index	-
K	effective entrainment slip ratio	-
k_{l}	liquid-thickness correction coefficient	-
k_{ij}	van der Waals mixing parameter	-
K_0	entrainment slip ratio	-
l	length	mm
L	length	mm
m	mass	kg
$\dot{m}$	mass flow rate	$\mathrm{kg\,s^{-1}}$
M	molar mass	$\mathrm{g\,mol^{-1}}$
m_i	measured value	multiple
N	rotating speed	$\mathrm{min^{-1}}$
N	number of discretization elements	-
$\mathcal{N}$	number of components in a system	-
Nu	Nusselt number ($= h\,L/k$)	-

$n_{\mu,k}$	empirical parameters	multiple
p	pressure	bar
$\bar{p}$	mean pressure at the sensor level	bar
P	perimeter	m
$\mathcal{P}$	Poynting correction factor	-
Pr	Prandtl number ($= c_p\,\mu/\lambda$)	-
q	specific heat transfer	$\mathrm{J\,kg^{-1}}$
Q	vapor quality (mass fraction)	-
$\dot{Q}$	heat transfer rate	W
Q_m, d_m, q_m, m_m	mixture equation of state constants	multiple
Q_r	refrigerant-only vapor quality (mass fraction)	-
Q_t	thermal non-equilibrium vapor quality (mass fraction)	-
r	radius	mm
r_h	liquid height ratio	-
$r_\mathrm{v,in}$	built-in volume ratio	-
r_p	compression ratio	-
r_v	volume ratio	-
$\mathcal{R}$	number of constraints in a system	-
R	universal gas constant	$\mathrm{J\,mol^{-1}\,K^{-1}}$
R^2	coefficient of determination	-
Ra	Rayleigh number ($= Gr\,Pr$)	-
RD	relative deviation	-
Re	Reynolds number ($= \rho\,U\,D/\mu$)	-
s	specific entropy (also called entropy)	$\mathrm{J\,kg^{-1}\,K^{-1}}$
s	specific gravity	-
S	sensitivity coefficient	-
SC	supercooling	K
SH	superheating	K
T	temperature	K, °C
t	thickness	mm
t	angle	rad
u	specific internal energy (also called internal energy)	$\mathrm{J\,kg^{-1}}$
u	velocity	$\mathrm{m\,s^{-1}}$
U	speed	$\mathrm{m\,s^{-1}}$
v	specific volume	$\mathrm{m^3\,kg^{-1}}$
V	volume	$\mathrm{cm^3}$
w	specific work	$\mathrm{J\,kg^{-1}}$
W	width	mm
$\dot{W}$	power	W
We	Weber number ($= \rho\,U^2\,D/\sigma$)	-
x	liquid phase composition (mass fraction)	-
$\tilde{x}$	liquid phase composition (mole fraction)	-
x	position in x	m
X	Lockhart-Martinelli parameter	-
X	variable	multiple
y	vapor phase composition (mass fraction)	-
$\tilde{y}$	vapor phase composition (mole fraction)	-
y	position in y	m
z	global mass fraction (mass fraction)	-
Z	compressibility factor	-

α	void fraction (volume fraction)	-
α	friction proportionality coefficient	-
α	parameter	-
β	parameter	-
δ	leakage gap	μm
$\dot{\Phi}$	energy transfer rate	W
γ	activity coefficient	-
κ	isentropic expansion coefficient	-
λ	thermal conductivity	$\mathrm{W\,m^{-1}\,K^{-1}}$
μ	dynamic viscosity	mPa s
ν	kinematic viscosity	$\mathrm{m^2\,s^{-1}}$
μ_M	absolute uncertainty of variable M	multiple
ω	angular speed	$\mathrm{rad\,s^{-1}}$
ω	acentric factor	-
Ω_a, Ω_b, Ω_c	equation of state constants	multiple
ϕ	fugacity coefficient	-
ϕ	involute angle	rad
Φ	energy transfer	J
ϕ^2_{lo}	two-phase multiplier	-
ϕ_{p}	number of phases in a system	-
ψ	entrainment ratio	-
ρ	density	$\mathrm{kg\,m^{-3}}$
σ	surface tension	$\mathrm{N\,m^{-1}}$
σ	area ratio	-
τ_{f}	friction torque	N m
θ	angle	rad
θ_{w}	wet angle	rad
ε	efficiency	-

List of Subscripts and Superscripts

0	reference or initial
A	component A
amb	ambient
B	component B
b	base
c	critical or compression or cross-sectional
cd	condenser
ch	chamber index
cond	condensation
cp	compressor
CV	control volume
d	discharge or droplet
D	dimensionless
dd	discharge
ddd	discharge
dis	discharge
disp	displacement
E	excess
e	effective
ev	evaporator
ex	exhaust (outlet)
exp	experimental
f	final or friction or film or fixed
fit	model fitting
fg	latent
fl	flank
fric	friction
g	gas (vapor)
G	gas (vapor) phase
gl	vapor to liquid
i	component i or initial or chamber index
ie	inner-end
in	internal or indicated
is	isentropic or inner-start
k	angle index
l	liquid
L	liquid phase
lg	liquid to vapor
lim	limit
lk	leakage-related
lump	lump mass
m	mixture or mean or mechanical

M1	methodology number 1
M2	methodology number 2
max	maximum
min	minimum
mix	mixing
ML	mechanical losses
mom	momentum
mot	motor
o	oil or orbiting or outer
oe	outer-end
os	outer-start
p	prototype
PT	pressure drop and heat transfer-related
r	refrigerant or retrofitted or radial
R	residual
red	reduced
ref	reference
res	residual
rev	revolution
s	suction
sa	suction-admission
SC	subcooling
SH	superheating
SP	single-phase
su	supply (inlet)
th	theoretical
tot	total
TP	two-phase
up	upstream
v	volumetric
V	vapor
w	water
wg	wall to vapor
wl	wall to liquid
γ	phase (l or g) index
ϕ	component (r,l, r,g or o) index
σ	saturation
$\star$	target or gross or cumulated

Glossary

Positive-displacement compressor
A compressor in which compression is achieved by reducing the volume of a trapped fluid. Main kinds are screw, scroll, reciprocating and rotary (rolling-piston or vane). Characterized by a built-in volume ratio and a displacement volume.

Isentropic (adiabatic) efficiency
Performance indicator used to characterize positive-displacement compressors. It compares the actual power consumption (mechanical or electrical) with the ideal power consumption corresponding to an adiabatic (no external heat exchange) and reversible (no entropy generation) compression, also referred to as the isentropic power consumption.

Volumetric efficiency
Performance indicator used to characterize positive-displacement compressors. It compares the actual mass flow rate delivered by the compressor with the theoretical mass flow rate determined from the compressor displacement volume, rotational speed, and inlet density.

Ideal-compression
Operating condition of a positive-displacement compressor in which the pressure reached at the end of the volume-reduction phase is equal to the exhaust pressure. This represents the most efficient scenario for a positive-displacement compressor.

Overcompression
Operating condition of a positive-displacement compressor in which the pressure reached at the end of the volume-reduction phase is higher than the exhaust pressure. Additional work is therefore required compared to the ideal-compression condition, resulting in a decrease in isentropic efficiency.

Undercompression
Operating condition of a positive-displacement compressor in which the pressure reached at the end of the volume-reduction phase is lower than the exhaust pressure. This is the most commonly encountered operating condition in positive-displacement compressors. Additional work is therefore required compared to the ideal-compression condition, resulting in a decrease in isentropic efficiency.

Deterministic modeling
Modeling technique based solely on physical principles. It therefore relies on fewer parameters than semi-empirical or empirical modeling approaches. Moreover, the use of physical laws allows for a better interpretation and understanding of the results.

Two-phase compression or **Liquid-flooded compression** or **Wet compression**
Compression process in which liquid is intentionally supplied at the compressor inlet. The two phases can be constituted by the same fluid or by two different fluids (e.g., oil-refrigerant or air-water mixtures).

Liquid injection
Technique used in positive-displacement compressors in which a liquid is intentionally injected into the compressor. The liquid is usually injected in the compression chamber, however, in some cases, liquid-injection can be done upstream of the compressor, which is equivalent to performing a two-phase compression.

Liquid slugging
Phenomenon that can occur in a positive-displacement compressor in which a pure liquid becomes trapped in the compression chamber and is volumetrically compressed, often leading to mechanical damage to the compressor.

Vapor quality
In a closed volume, ratio of the vapor mass to the total fluid mass. In a flow, ratio of the vapor mass flow rate to the total mass flow rate.

Void fraction
In a closed volume, ratio of the vapor volume to the total volume. In a flow, several definitions can be used, the most commonly employed being the ratio between the vapor cross-sectional area and the total cross-sectional area.

Mechanical equilibrium
State in which, within a closed volume, the pressure is assumed to be uniform everywhere.

Thermal equilibrium
State in which, within a closed volume, the temperatures of the liquid and vapor phases are the same.

Hydraulic losses
Losses generated in screw compressors by the presence of liquid that must be accelerated continuously due to friction and momentum losses. These effects are well known in screw compressors and are also investigated in this thesis for scroll compressors in the context of two-phase compression.

Solubility
Ability of one component of a mixture to dissolve in another and form a homogeneous phase. In an oil-refrigerant mixture, the solubility represents the equilibrium amount of refrigerant that can dissolve in the oil at given temperature and pressure conditions. A vapor-liquid equilibrium must be established to reach this solubility. A high solubility for an oil-refrigerant mixture means that a large amount of refrigerant is dissolved in the oil under given conditions.

Miscibility
Ability of two or more liquids to dissolve into a single homogeneous liquid phase. When the liquids do not mix homogeneously, they are said to be immiscible.

Zeotropic mixture
Mixture whose vapor and liquid phase compositions change during evaporation and condensation, i.e., the components of the mixture evaporate and condense at different rates. This behavior leads to a temperature glide during phase change. In contrast, in an oil-refrigerant mixture, the composition of the vapor phase does not change during evaporation or condensation; therefore, such mixtures do not strictly exhibit zeotropic behavior, despite the temperature glide observed during phase change.

Desolubilization
Concept introduced in this thesis to simplify thermodynamic calculations involving oil-refrigerant mixture. In this concept, two states are defined: the "mixed state" where the solubility equations govern, and the "split state" where the solubility is neglected and the refrigerant behaves like a pure fluid, despite the presence of oil. Desolubilizing a mixture consists of calculating its temperature, pressure, and vapor quality while satisfying the energy and mass balances as well as the solubility relation. The mixed state becomes a split state after desolubilization.

Mixed state
State of a mixture in which the solubility relation governs the relationship between temperature, pressure, and vapor quality. This state is easily measurable experimentally, as it corresponds to the natural state of an oil-refrigerant mixture.

Split state
State of a mixture that has been desolubilized, so that the solubility relation no longer governs the relationship between temperature, pressure, and vapor quality. This state is fictitious, however, it could in principle be measured experimentally. It corresponds to the state that would be obtained in a given volume if a fictitious barrier separated the oil and the refrigerant (which may be superheated or two-phase). In this state, the pressure is a function of temperature only if the refrigerant is at saturation, or of both temperature and vapor density if the refrigerant is superheated.

Chapter 1

Introduction

Chapter Abstract

The introduction of this thesis begins with a fundamental premise: reducing overall energy consumption is essential to achieving a more sustainable way of living. This includes refrigeration and heat pump technologies, which are widely used throughout the world. The use of two-phase compression in such refrigeration cycles could improve performance, although the topic has not yet been thoroughly investigated. A state-of-the-art review of liquid-flooded compressors, first focusing on screw compressors and then converging to scroll compressors, is presented to assess the potential improvements in compressor performance. Limitations are illustrated with a simple application example. Then, the potential applications of two-phase compression in thermodynamic cycles is discussed, beginning with a state-of-the-art review of technologies that already employ two-phase compression. Once again, the potential of two-phase compression integrated into a heat pump is illustrated through an application example. This investigation is based on a conference paper from the author (Leclercq et al. 2023). Key findings of the literature review are then outlined, followed by the potential research gap motivating this work. Finally, the main objectives of the thesis are addressed, followed by a presentation of its division into the different chapters. The content of each chapter is briefly overviewed.

1.1 Energy context

Heating and cooling are the dominant end-uses of energy worldwide. Together, they represent around half of the European Union's (EU) total final energy consumption (European Commission 2016). Within this thermal demand, space and water heating in households accounts for more than 64%, while industrial heat represents a major share of thermal demand in manufacturing processes (31%), as represented in Figure 1.1. Space cooling in households and industrial cooling only account for less than 5% of the total demand for heating and cooling in Europe in 2012. Most cooling services in Europe rely on the vapor-compression refrigeration cycle, which is also the fundamental technology behind electric heat pumps. However, while cooling is almost entirely electricity-driven through vapor-compression systems, only a minority of residential heating in Europe is currently provided by heat pumps, with the majority still supplied by combustion-based technologies. In 2020, the EU share of heat pumps for heating demand in residential buildings was 10% (European Commission 2022), which is a five-fold increase since 2009. According to the International Energy Agency (2022), in order to meet the goal of net-zero emissions by 2050, 55% of all heating systems worldwide should be equipped with heat pumps. Because vapor-compression systems consume a large share of the electricity used for cooling and an increasing share for residential heating through heat pumps, even small improvements in their efficiency can translate into substantial energy savings.

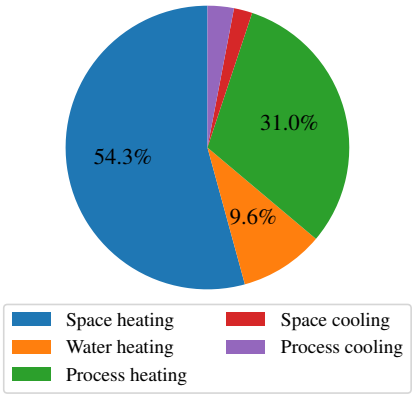

Figure 1.1: Share of the total final energy demand for heating and cooling in Europe in 2012 (Fleiter et al. 2017).

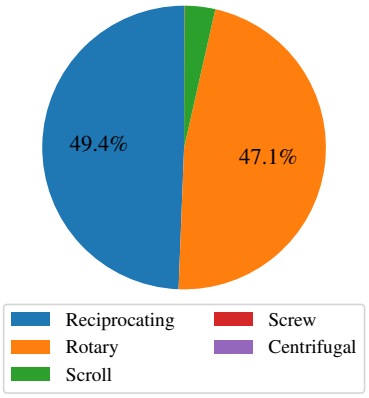

Figure 1.2: Worldwide market share (in sales) of compressors in vapor compression cycles in 2023 (International Institute of Refrigeration 2024).

Improving the efficiency, or coefficient of performance (COP) of vapor-compression cycles can be approached from multiple angles. On the refrigerant side, fluid selection with favorable thermodynamic properties under environmental and safety constraints can optimize the performance under specific working conditions in heat pumps and refrigeration cycles. System-level strategies include optimizing heat-exchanger performance and reducing pressure drops under variable operating conditions. Optimization of heat exchanger performance includes better matching of the temperature profiles between the primary and secondary fluids, which can be achieved using two-phase compression, as detailed later in this introduction chapter. Control-oriented measures such as inverter-driven compressors, smart expansion-valve regulation, and adaptive defrosting further enhance seasonal efficiency. Finally, compressor-focused improvements, such as better internal leakage management, minimized mechanical losses, optimization of the geometry, improved operation under off-design, directly raise the COP of vapor-compression cycles by improving the compressor efficiency or, at least, reducing its power consumption. Compressor performance improvement can be achieved via liquid-flooding or two-phase compression, which is also detailed in a subsequent section of the introduction chapter.

In vapor-compression refrigeration and heat-pump systems, the most widely used compressors are positive-displacement machines. The most common types are reciprocating, scroll, rotary (rolling-piston or vane), and screw compressors, with shares presented in Figure 1.2. Reciprocating compressors have traditionally been used due to their simplicity and robustness, though their use is gradually declining in favor of scroll and rotary units for smaller systems. Scroll compressors have become the industry standard for residential and commercial heating, ventilation and air conditioning (HVAC) because of their high efficiency, low vibration and compactness. Rotary compressors are extensively used in room air-conditioners and small heat pumps thanks to their low cost and good performance at small capacities. For larger commercial and industrial installations, twin-screw compressors are preferred because they offer high reliability, smooth operation, and strong performance over a wide load range.

1.2 Two-phase in positive-displacement compressors

1.2.1 State of the art

Two-phase compression, also referred to as liquid-flooded compression, is defined as a compression process in which liquid is intentionally supplied at the compressor inlet. It can be

categorized into two parts: on the one hand, two different fluids can be used (e.g., air-water mixture or oil-refrigerant mixture), on the other hand, the state of one single fluid can be located under the saturation dome, resulting in the presence of a liquid phase and a vapor phase. In some particular cases, a two- or three-component zeotropic mixture can be used, where each component can be found in both liquid and vapor phases with different mass or molar fractions. In the former case, experimental studies started in the nineteen fifties, where the use of oil to lubricate air screw compressors was necessary to expand machines' lifetime and improve machines' performance of the Lysholm turbine, which was using timing gears and running at high speeds to achieve decent volumetric efficiencies (Taft 1972). Flooding the compressor with oil provided both cooling, allowing higher pressure ratios without associated thermal stress, and the elimination of timing gears. Water-flooding allows to avoid oil contamination of the air but required more expensive materials (corrosion-resistant) and more accurate manufacturing (Zimmern 1984; Nikolov et al. 2014). Research on oil- and water-flooding in screw compressors is still ongoing to improve machine efficiency. For instance, Yusha et al. (2018) studied different methods of oil injection into the working chamber of a screw compressor. In He et al. (2018), an experimental study of an oil-flooded twin-screw compressor is presented, demonstrating increases in volumetric and adiabatic efficiencies[1] at high speeds and a reduction in discharge temperature. The increase in adiabatic efficiency reaches a maximum with speed; as heat transfer between the oil and air decreases, the reduction in discharge temperature becomes limited. Similarly, C. Wang et al. (2018) presented an experimental study on a water-flooded air screw compressor, showing the same overall trends. Moreover, a higher water injection flow rate requires additional power, thereby limiting efficiency beyond a certain point. The first compression of a pure refrigerant in the two-phase region was experimentally investigated in a single-screw compressor around 1969 (Zimmern 1984). The idea was, like for the water flooding for air, to have the same fluid in the liquid phase and the vapor phase (in the form of humidity for air). Moreover, oil-flooding screw compressors required to reach better manufacturing anyway, allowing low-viscosity liquid (relative to pure oil) to provide sufficient sealing effects, as the refrigerant solved in the oil was reducing the viscosity of the liquid phase. The authors could achieve 70% of isentropic efficiency with a 30 kW compressor using R22 as the working fluid. More recently, it has been numerically shown that the compression of wet refrigerant can achieve high isentropic efficiencies (up to 89%) and a significant discharge temperature reduction, within a twin-screw compressor (Ferreira et al. 2006a).

Liquid-flooded compression in scroll machines, like in screw machines, has many advantages, in addition to the sealing effects brought by the liquid blocking the gap between two working chambers, it also enables to get closer to an isothermal process (Li et al. 1992). Nevertheless, some drawbacks can also be identified. First, the increase of the pressure losses in suction/discharge ports due to either the reduction of the speed of sound or the increase of the fluid density (Leclercq et al. 2022). Then, higher mechanical losses, referred to as "hydraulic losses" observed in screw machines, could also decrease the isentropic efficiency (Zaytsev et al. 2000). Moreover, the mechanical reliability of the machine is questioned due to the presence of liquid during the compression. In fact, the well-known liquid slugging phenomenon, in which a pure liquid is volumetrically compressed, is still being investigated to prevent damage to positive-displacement compressors. Liquid slugging occurs when saturated or subcooled liquid is pumped into the compressor, or when the liquid mass fraction is increased throughout the compression process until reaching a pure liquid. This pure-liquid compression results in a rise in pressure that can lead to mechanical failure. Liu et al. (1995) investigated liquid slugging in positive-displacement compressors and concluded that scroll

[1]The volumetric and adiabatic (also referred to as isentropic) efficiencies are performance indicators related to, respectively, the delivered mass flow rate and power consumption of a compressor. Precise definitions are provided in Section 3.3.3 of Chapter 3.

compressors, which have the smallest built-in volume ratio, are less likely to experience liquid slugging. Prasad (2002) numerically investigated the effects of liquid presence in reciprocating compressors and found that filling half of the clearance volume with liquid results in four to five times higher pressure within the cylinder. Lin et al. (2022) and Guo et al. (2024) studied the effect of liquid slugging in rotary compressors with a deterministic model and a computational fluid dynamics (CFD) model, respectively. Both found that the high pressures generated by the liquid compression cause irreversible damage to the crankshaft and other components of the compressor. The scroll pump designed by J. Wang et al. (2015), intended to be used in the petroleum industry, is a scroll compressor with an interesting geometry: the scroll wraps are designed to maintain a high flank clearance between the compression and discharge chambers, thereby preventing liquid slugging. Liquid-flooded scroll compressors were already being experimented with before 1988, when the scroll technology was still viewed as an interesting technology with limited potential by engineers. According to Bush et al. (1988), scroll compressors' tolerance to liquid refrigerant flooding is unlimited, as demonstrated by minimal scroll reaction to cold start-up and heat pump defrosting. However, this tolerance is justified by the slow compression process, providing ample time for leakages, especially when a compliant design is used. The literature does not unanimously agree on the high tolerance of scroll compressors to liquid flooding, as research is still ongoing on how to study and prevent it. In Li et al. (1992), the authors experimentally studied oil injection in scroll machines in order to avoid the costly tip-seal placement. They observed an improvement in the volumetric efficiency by 4.3% despite the heating effect of the injected oil. In Sakuda et al. (2001), an experimental investigation of an oil-flooded compressor for performance improvement is performed. The results show that the cycle efficiency always decreases with increasing oil rates. Hiwata et al. 2002 investigated oil-injection into a CO_2 scroll compressor, where the axial compliance had been reinforced by controlling the thrust force of the orbiting scroll. The results showed the existence of an optimal oil flooding rate ranging between 6 and 15% in mass. More recently, Bell et al. (2012a) investigated the performance of an oil-flooded off-the-shelf open-drive scroll compressor with large amounts of oil that showed no significant decrease in performance. Similarly, Zhao et al. (2005) investigated water flooding in an air scroll compressor, achieving high indicated isothermal efficiency despite a slight increase in power consumption caused by the water injection.

Liquid-refrigerant injection also proved to enhance the performance of scroll compressors. Afjei et al. (1992) numerically investigated the injection of liquid refrigerant upstream of the compressor. They reported an increase in mass flow rate and a decrease in discharge temperature. Nevertheless, they also noted a reduction in volumetric efficiency, likely caused by variations in leakage gaps or by vapor flashing in the suction chambers resulting from liquid leakage, which reduced the usable volume. Dutta et al. (2001) experimentally investigated liquid-refrigerant injection within the compression chambers of a hermetic compressor. An improvement of the adiabatic efficiency was observed when not controlling the oil casing temperature. In the same order of ideas, Cho et al. (2003), experimentally tested a variable-speed hermetic scroll compressor with liquid injection in the suction and compression chambers, varying the injection angle. Some disadvantages were found at low frequency with respect to the compressor power, capacity and adiabatic efficiency due to high leakages. Nevertheless, an improvement in performance and reliability of the compressor was observed at high frequency. Eventually, B. Wang et al. (2008) numerically and experimentally investigated liquid injection and validated their model using dynamic pressure sensors within the compression chambers. They concluded that accurate modeling of liquid injection is essential, as the injection position, angle, and timing must be optimized to achieve performance benefits. Similar conclusions were reported by Xu et al. (2011). Moreover, the authors also stated that the scroll compressor is the most favorable option for liquid-refrigerant injection among the four main types of compressors used in residential and industrial applications (i.e., screw, scroll,

reciprocating and rotary).

Liquid-flooded or two-phase or wet compression is, in some applications, undesirable and may occur during an unconventional operation of a refrigeration cycle. Refrigerant, in the form of liquid, can arrive upstream of a compressor caused by an insufficient superheat at the evaporator outlet. This incomplete evaporation can happen due to a change in operating conditions (defrost of an evaporator) or during the start-up of a refrigeration cycle. Therefore, on the one hand, some authors are studying liquid flooding in compressors during cold start-up or defrosting operation of heat pumps to prevent compressor damage. On the other hand, some authors are studying the benefits of flooding/liquid-injection. Although only a few experimental studies on two-phase refrigerant compression in scroll compressors could be found at the time of the present work, the literature on liquid-flooded screw compressors, using a liquid-phase refrigerant, is substantial. Therefore, the following questions arise: what are the practical differences between applications in which two-phase compression offers advantages and those in which it should be avoided, and what distinguishes the various types of positive-displacement compressors that lead some researchers to seek the benefits of two-phase compression while others aim to avoid it entirely? Possible answers to these questions are discussed in the following subsections.

1.2.2 Practical example of two-phase compression

When referring to "liquid-flooded" or "two-phase" compression, it is often assumed that a significant amount of liquid enters the compressor. However, two-phase compression conditions can vary and are often misunderstood in practice. It is therefore essential to define these two-phase conditions to better understand what the compressor endures during two-phase compressions. A well-known variable used to define a two-phase state is the vapor quality Q. This vapor quality is typically expressed as a molar or mass fraction, representing the proportion of vapor relative to the total quantity of fluid. When expressed in terms of flow, the vapor quality can be defined as the vapor mass flow rate divided by the total mass flow rate. This vapor quality is particularly useful when defining, for instance, the specific enthalpy or density of the fluid. Nevertheless, volumetric machines are characterized by a displacement volume that will be filled with both the liquid and the vapor phases. To clearly determine which portion of this volume is occupied by liquid and vapor, the vapor quality cannot be used directly but rather indirectly, by calculating the vapor volume fraction, also referred to as the "void fraction". When assuming a homogeneous two-phase flow (no speed difference between the phases), the void fraction α can easily be linked with the vapor quality:

$$\alpha(Q) = \frac{Q\, v_{\mathrm{g}}^{\sigma}}{Q\, v_{\mathrm{g}}^{\sigma} + (1-Q)\, v_{\mathrm{l}}^{\sigma}} \tag{1.1}$$

where v is the specific volume, g and l denote the vapor and liquid phases, respectively and σ represents the saturation property. Expressing the conditions in terms of void fraction rather than vapor quality provides a clearer understanding of what the compressor experiences during two-phase compression.

When looking at the temperature-entropy diagram of pure R1233zd(E) refrigerant, two zones can be distinguished: the "danger" zone and the "safe" zone, as represented in Figure 1.3. The "danger" zone is the area under the saturation bell located on the left-hand side of the critical point. Compressing in this zone involves the risk of ending the compression on the liquid saturation curve. Conversely, compressing in the "safe" zone, located on the right-hand side of the critical point, could never end with saturated liquid.

Two examples of isentropic two-phase compression are shown in Figure 1.3, one in the "danger" zone (left side of the critical point) and the other in the "safe" zone (right side of the critical point). Isentropic two-phase compression implies thermal equilibrium between the

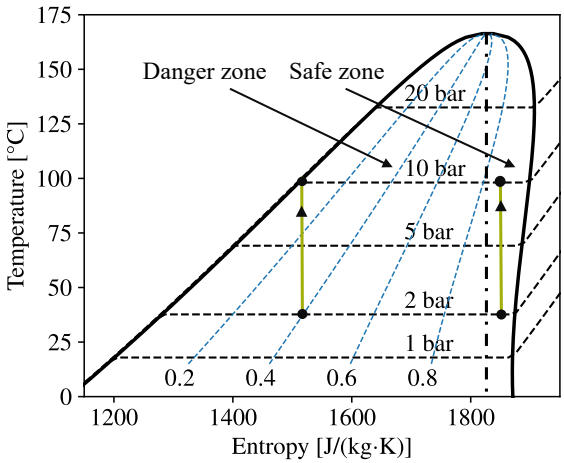

Figure 1.3: Example of isentropic two-phase compression on a temperature-entropy diagram of R1233zd(E).

phases throughout the compression, which must be adiabatic, as will be detailed in the next chapters. Both compressions represented in Figure 1.3 start at a pressure level of 2 bar and end after a compression ratio of 5.2, i.e., at 10.4 bar. The compression represented in the "danger" zone starts at a vapor quality of 0.4. The evolution of the vapor quality and void fraction throughout the compression can be found in Figure 1.4. The first significant observation is the relationship between the vapor quality and the void fraction: despite the relatively low vapor quality, the void fraction is nearly one; that is, the volume is approximately 99% filled with vapor. This high difference between the vapor quality and the volume fraction can be explained by the significant difference in densities between the vapor and the liquid phases. Throughout the compression, the vapor quality progressively decreases down to zero and so does the void fraction, i.e., saturated liquid is eventually reached. Such low vapor quality is obviously undesirable in the compressor; therefore, the pressure ratio should be reduced or the initial vapor quality increased. The compression represented in the "safe" zone starts at a vapor quality of 0.95. The evolution of the vapor quality and void fraction throughout the compression can be found in Figure 1.5. For the same pressure ratio, the vapor quality decrease is lower, and the void fraction change is unnoticeable. The void fraction is higher than 99% at both the start and the end of the compression process. A two-phase-designed scroll compressor could easily withstand such a quantity of liquid.

Therefore, from the two compression examples presented, it seems that, by controlling the conditions, namely, the pressure ratio and the inlet vapor quality, it would be possible to maintain the void fraction within a relatively high range, thereby avoiding the compression of excessive liquid. The problem still lies in defining this "relatively high range" of void fraction that the compressor can sustain. The pressure ratio, despite being indirectly induced by the compressor, comes from the operating conditions of the cycle, and cannot be controlled directly by the compressor. A volumetric compressor increases the pressure through the progressive reduction of the working chamber volume, which compresses the trapped fluid until the final volume is reached, and a certain pressure is achieved. This ratio between the initial volume and the final volume is referred to as the built-in volume ratio ($r_{v,in}$). Ideally, the internal pressure achieved from this built-in volume ratio matches the exhaust pressure level, and a reed valve or electronic valve opens to the exhaust line, allowing the pressurized fluid to leave the compressor. However, if the internal pressure at the end of volume reduction is lower than the discharge pressure, undercompression occurs, leading to a sudden pressure rise associated with efficiency losses. In scroll compressors, a mechanical valve, such as a reed

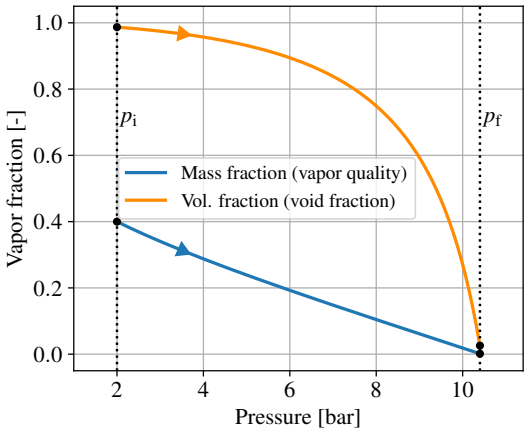

Figure 1.4: Volume and mass vapor fraction evolution for an isentropic two-phase compression, with an initial vapor quality of 0.4.

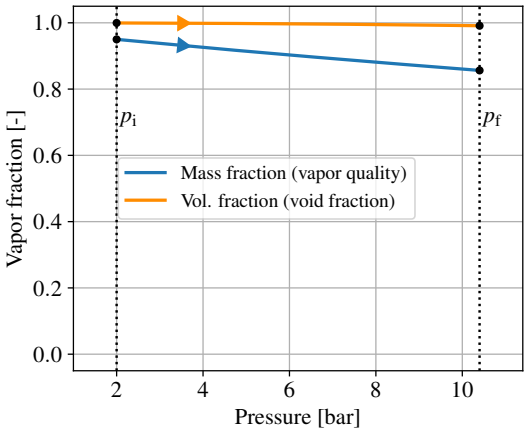

Figure 1.5: Volume and mass vapor fraction evolution for an isentropic two-phase compression, with an initial vapor quality of 0.95.

valve, is often used; therefore, no backflow occurs through the discharge port, which limits the increase of pressure within the discharge chamber. Conversely, if the internal pressure exceeds the discharge pressure before port opening, overcompression takes place, causing unnecessary work and decreased efficiency. The optimal design minimizes both effects by aligning the internal and discharge pressures at the end of the compression process. Optimal designs are, however, difficult to reach when operating in two-phase conditions. Scroll compressors built-in volume ratios typically do not exceed a ratio of 5 (Emhardt et al. 2018). Conditions of the two examples of compressions can be found in Table 1.1. The volume ratios of these compressions, defined as the final density divided by the initial density, are 38.23 for the "danger-zone" compression and 5.68 for the "safe-zone" compression, respectively. Thus, they are both higher than the maximum built-in volume ratio achievable by a scroll compressor, and undercompression losses will most likely occur. As a consequence, the internal compression occurring within a scroll compressor is unlikely to reach the saturated liquid phase, as an excessively high built-in volume ratio would be required to do so. The minimum inlet void fraction required to avoid compressing a saturated liquid phase can be expressed as a function of the built-in volume ratio:

$$\alpha_{\mathrm{su,min}} = 1 - \frac{1}{r_{\mathrm{v,in}}} \tag{1.2}$$

If a built-in volume ratio of 5 is used, the minimum inlet void fraction should be 80%. Depending on the pressure, the corresponding minimum vapor quality can be determined. Taking the example of Figure 1.4, at 7.5 bar, the void fraction of 0.8 corresponds to a minimum vapor quality of 12%. At 1 bar, the same void fraction value would correspond to a minimum vapor quality of 1.8%, which is relatively low. Even if the saturated liquid state is not reached in the compression chamber, i.e., during the volume reduction, damage could still occur due to the high quantity of liquid within the chambers. Nevertheless, this minimum vapor quality constitutes a physical indicator that pure liquid compression is rarely reached during the volume-reduction phase. Even when the saturated-liquid state is not reached during this phase, it can still be reached in the discharge chamber, after the pressure equilibrium due to undercompression has occurred. In this case, the discharge port could open when the exhaust pressure is exceeded, which would occur in the case of saturated liquid compression. However, in practice, the pressure rise induced by saturated-liquid compression would be of such intensity and speed that the reed valve would not have time to move before the pressure increase affects the mechanical design of the machine, potentially leading to compressor

blockage or failure. Therefore, a mechanical failure would most likely result from liquid compression originating from the compressor discharge, not during the volume-reduction phase, with or without reed valve. The design of two-phase scroll compressors should therefore take this aspect into account. An example where a two-phase scroll compressor has been designed specifically for an application is the scroll pump of J. Wang et al. (2015), intended to be used in the petroleum industry: the scroll wraps are designed to maintain a high flank clearance between the compression and discharge chambers, thereby preventing liquid slugging.

Conditions	Danger-zone compression	Safe-zone compression
Initial vapor quality [-]	0.4	0.95
Initial void fraction [-]	0.9869	0.9995
Final vapor quality [-]	0.0014	0.8563
Final void fraction [-]	0.0258	0.9911
Initial density [kg/m^3]	26.79	11.43
Final density [kg/m^3]	1024.35	64.96
Pressure ratio [-]	5.2	5.2
Volume ratio [-]	38.23	5.68

Table 1.1: Comparison of isentropic compression processes starting from different vapor qualities for R1233zd(E), with the danger-zone compression ending in a quasi-liquid state.

Yet, the present analysis considers an extreme case, i.e., a case in which saturated-liquid compression would occur, with an uncontrolled pressure ratio or inlet vapor quality and with a process occurring isentropically, i.e., adiabatically and reversibly. As a matter of fact, a non-isentropic process would increase the final vapor quality of the compression.

1.2.3 Concluding remarks

From the previous analysis and the accompanying literature, it appears that, under controlled conditions, two-phase compression in scroll compressors is physically feasible. This analysis, however, does not apply to reciprocating and rotary compressors, which have have high predefined built-in volume ratios. This limitation may explain why studies on these machines tend to avoid two-phase compression. Scroll compressors, similar to screw compressors, have a predefined built-in volume ratio and are inherently robust due to their geometry, making them good candidates for two-phase compression. Therefore, on the practical aspects, the present analysis explains why screw and scroll compressors can potentially withstand two-phase flows, while other kinds of compressors cannot. Moreover, another major difference between studies involving two-phase compression or liquid injection and studies mentioning the hazardous effects of liquid slugging lies in the controlled nature of the liquid quantity ingested by the machine. On the one hand, liquid-injection or liquid-flooding is tested experimentally under a totally controlled environment. On the other hand, the two-phase conditions occur due to a change in operating conditions (defrost of an evaporator) or during the start-up of a refrigeration cycle, and the accompanying liquid quantity is entirely uncontrolled, making the compressor prone to failure. One final important aspect not considered in the present analysis, but often mentioned in the literature, is the lubrication of the compressor. The presence of liquid refrigerant in the oil decreases the viscosity of the liquid phase. In screw compressors, this problem has been investigated, and improved manufacturing techniques have been developed to mitigate this issue. In scroll compressors, the literature does not yet provide sufficient insight into this effect. Certain orbiting mechanisms may be more capable

of withstanding two-phase compression than others, and only further studies can clarify this issue.

Feeding a scroll compressor with two-phase refrigerant, when optimized, could lead to performance enhancement. For instance, limiting leakage and reducing the discharge temperature have been shown to improve volumetric and isentropic efficiencies. However, the liquid-flooding has only been regarded as a potential improvement of the machine performance, not on the cycle performance. The use of two-phase compression could bring some innovations to conventional thermal systems, as no superheat is met before and after the compressor. Some advantageous applications have already been investigated, while other potential applications remain at an early stage of research. They are presented in the following section.

1.3 Two-phase compression in thermodynamic cycles

1.3.1 State of the art

Studies incorporating two-phase compression in thermodynamic cycles began in the early 1990s, coinciding with the growing interest in two-phase expansion for the Trilateral Flash Cycle (TFC) (Smith et al. 1995). According to Itard (1995), the advantage of a wet compression cycle lies in its ability to achieve the highest possible efficiency for refrigeration cycles operating between two temperatures, with a defined heat source and heat sink. In Vorster et al. (2000), the investigation of two-phase compression in a heat pump is conducted numerically using wet fluids and non-azeotropic mixtures with high vapor qualities, and the results show a better COP when no superheat occurs in the cycle. Conversely, Feng et al. (2009) experimentally tested a heat pump with liquid injection at the inlet of the compressor and pointed out that the system performance decreased with the injection flow rate. Nevertheless, important decreases in discharge temperature were observed. According to Xu et al. (2011), operating compressors at high compression ratios results in high discharge temperature, which can lead to refrigerant/oil degradation and mechanical failure. Two heating applications can benefit from refrigerant injection: low-ambient-temperature heating and heat pump water heating. For instance, injecting liquid into a heat pump compressor operating at low temperatures (around -20°C) allows the system to operate more smoothly. Moreover, the COP of an air-to-water heat pump is improved by injecting liquid into the compressor, resulting in an increased heating capacity with a relatively smaller rise in power consumption. M. Yang et al. (2015) evaluated the performance of an R32 scroll compressor operating with two-phase suction in an air-conditioning thermodynamic cycle, which is equivalent to what is referred to as "two-phase compression" in the context of this thesis. The simulation results indicated that the discharge temperature decreased with decreasing suction vapor quality, and the cooling capacity increased slightly at a suction quality of 0.98, resulting in an optimal COP. At lower vapor qualities, both power consumption and cooling capacity decreased, leading to a lower COP. Seong et al. (2017) experimentally investigated two-phase compression at the compressor inlet, noting that two-phase suction is simpler and less expensive than liquid injection within the compression chamber. The tested vapor qualities ranged from 80% to a superheat of 10 K. The optimal COP values were found to depend on the heat-source water temperature and were observed around a vapor quality of 95%. Optimal isentropic and volumetric efficiencies were also achieved at vapor qualities of 95% and 90%, respectively. Another experimental investigation of a two-phase hermetic scroll compressor for a refrigeration cycle was performed by Sun et al. (2021), aiming to reduce the compressor discharge temperature, as refrigeration compressors tend to stop working under high ambient temperatures due to excessive discharge temperatures. The authors validated a deterministic model and observed a higher COP when no superheat was present at the compressor inlet, however, this also

resulted in a slightly lower cooling capacity. Finally, another experimental investigation on a household air conditioner was conducted by Pan et al. (2024), this time using a rolling piston compressor. The authors observed a slight decrease in COP when the inlet vapor quality was decreased from superheated conditions to 80%. However, this decrease is compensated by the good behavior of the compressor in extreme ambient cold, due to a decreased discharge temperature.

Another well-studied domain in which two-phase compression is applied is that of compression-resorption heat pumps (CRHPs). This promising technology combines the advantages of absorption and vapor compression systems, providing relatively high COP at large temperature lifts (Brunin et al. 1997). A particular characteristic of CRHPs lies in their utilization of desorption and resorption processes that exhibit temperature glide. This behavior arises from the use of a non-azeotropic working fluid mixture (ammonia-water), enabling the temperature profiles of the refrigerant and the heat-transfer fluid at both the source and sink to be closely matched, thereby maximizing the COP (Zamfirescu 2009). The most commonly used mixture in CRHPs is the ammonia-water mixture. A simplified scheme of a CRHP can be found in Figure 1.6. The cycle is composed of 5 components: a resorber, which also serves as a condenser and enriches the solution with ammonia at high pressure; a desorber-evaporator, which weakens the solution; a pump, which circulates the weak solution; a compressor, which compresses the ammonia vapor; and an expansion valve, which expands the rich solution. The weak solution of point $1'$ is commonly separated from the ammonia vapor of point 1 using a liquid-vapor separator.

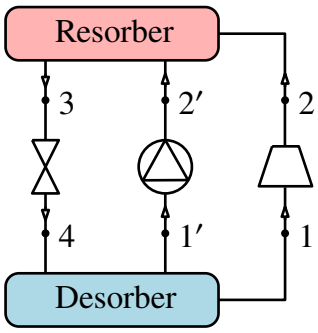

Figure 1.6: CRHP cycle with a dry compression.

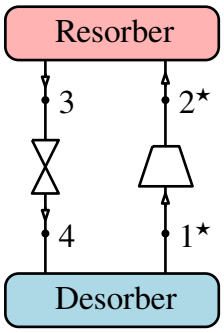

Figure 1.7: CRHP cycle with a wet compression.

CRHPs can also benefit from two-phase compression, by merging the pump of the weak solution with the compressor of the ammonia vapor, avoiding the use of a liquid-vapor separator, as illustrated in Figure 1.7. In this particular technology, higher performance can be achieved (Ferreira et al. 2002). In Ferreira et al. (2006b), an experimental investigation is carried out on an ammonia-water CRHP using an oil-free twin-screw compressor. Liquid-injection ports design and positions are discussed and a maximum compressor isentropic efficiency of 50% could be obtained with the liquid-injection occurring in the compression start phase. In van de Bor et al. (2015), the authors stated that the isentropic efficiency of the two-phase compressor should be at least 70% to be commercially competitive. A more recent study from the same authors (Gudjonsdottir et al. 2019) showed that an isentropic efficiency above 70% could be achieved for a particular design, with inlet vapor qualities ranging from 0.5 to 0.7, without under- and overcompression.

Finally, the innovative cycle currently being developed in the Regen-by-2 European project (Horizon 2020) is also making use of two-phase refrigerant to operate (Briola et al. 2021). This European project is the primary source of funding for this thesis. The Temperature-Entropy diagram of this cycle can be found in Figure 1.9. Regen-by-2 aims to develop a first-of-its-kind lab-scale prototype of a novel thermodynamic cycle and related plant for the revalorisation of renewable thermal energy sources, unlocking their large potential to supply

electric, heating and-or cooling energy vectors. It is constituted by a proper combination of cycles close to the Carnot cycle operating with a two-phase fluid circulating in novel two-phase expanders and two-phase compressors. The loop 1-2-2*-3-4-5-5*-6-7-8-1 found in Figure 1.9 consists in a two-stage vapor expansion cycle, where the high pressure is reached with the help of two compressors and a regenerator in between from point 1 to 3. Likewise, the power is recovered by three expanders, the first two being separated by the same regenerator between the compressors from point 5 to 5*. The low-temperature thermal source, allowing to vaporize the working fluid between points 3 and 4, can come from waste heat recovery or any renewable heat source. Two condensations are then performed in cascade: between points 6 and 7 in order to provide the end-user with heating, and between points 13 and 1 with an air-cooled condenser. Finally, a conventional refrigeration loop is operated between points 1-9-10-11-12-13-1, where an air-cooled condenser allows to reach a saturated liquid state in point 9, before the expansion valve, followed by the end-user cooling between points 10 and 11. The main benefits of this tri-generation lie in its flexibility to adapt to the user demand in heating, cooling and electricity. By controlling only the machine speeds, it is possible to adapt the cycle and reach any required operating point much more easily than when the machine operates under superheated conditions. In this regard, removing the positive superheat constraint upstream of each machine facilitates control of the cycle. The first Regen-by-2 prototype was developed using scroll machines as the compressor and expander, whereas future versions will most likely employ screw machines. In the frame of this innovative cycle, studying and optimizing two-phase machines is essential to achieve maximum efficiency across a wide range of operating conditions and to ensure high cycle performance. In fact, the expander's isentropic efficiency should reach at least 65%, while the compressor's should attain 55% for the cycle to be considered viable (Briola et al. 2021).

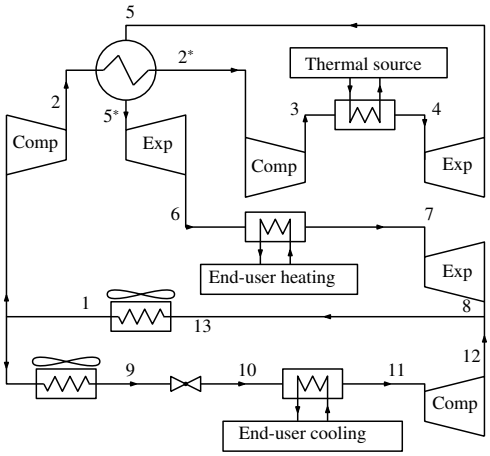

Figure 1.8: Regen-by-2 cycle architecture.

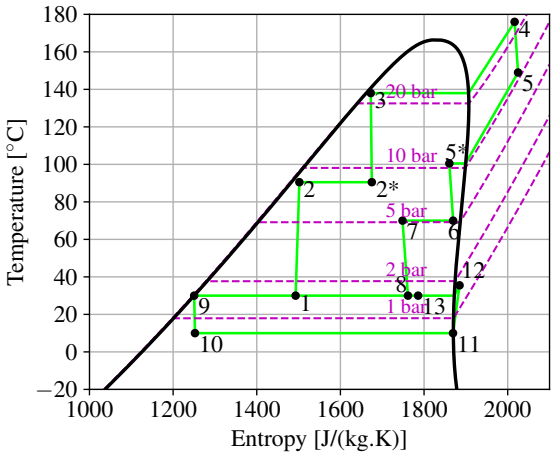

Figure 1.9: Regen-by-2 cycle Temperature-Entropy diagram.

From a general standpoint, the irreversibility creation in vapor compression cycles comes from two sources: the deviation of compression processes from internally reversible processes and the temperature difference between the hot/cold sources/sinks and the working fluid along heat exchanges (external irreversibility). The same principle applies to power production cycles, such as the organic Rankine cycle, where the internal irreversibility comes from the expansion machine and the heat exchangers. Therefore, two-phase refrigerant compression/expansion can be integrated to pursue a beneficial trade-off between internal and external irreversibility, seeking to increase the performance of the cycle by allowing to match as closely as possible the temperature profile of the hot/cold sources/sinks. This is typically what is done in power production cycles such as the TFC (Smith et al. 1995). In most of the

studies where two-phase compression is used, the performances of the cycles are better than in classical cycles where a superheated state is reached before the compression. However, the numerical results obtained strongly rely on the performance of the compression machine used in the cycle. Using internally reversible processes or not taking into account the increase of irreversibilities in the two-phase region is not always a valid assumption. For these reasons, the subsequent study will numerically assess the performance of a heat pump using isentropic-efficiency variation curves as a function of the compressor inlet vapor quality.

1.3.2 Practical example of two-phase compression in cycle

The investigated heat pump[2] is a theoretical water/air-water heat pump providing hot water (50°C) with a heat sink capacity of 5 kW. It uses a high temperature lift (from 15°C to 50°C) from a 15°C heat source and uses the hydrochlorofluoroolefin (HCFO) refrigerant R1233zd(E) as the working fluid. This configuration could for instance be used to simulate a heat-pump water heater when air is used as the heat source. A diagram of the heat pump can be found in Figure 1.10. The evolution of the COP of the heat pump will be investigated with a varying vapor quality up to superheated states. An example of Temperature-Entropy and Pressure-Enthalpy diagrams can be found in Figures 1.11 and 1.12, respectively. The conventional cycle using a superheat (5 K) at the compressor inlet is the cycle 1–2–3–4, while the cycle 1′–2′–3–4 makes use of a medium inlet-quality compression, and the cycle 1″–2″–3–4 uses a low inlet-quality compression.

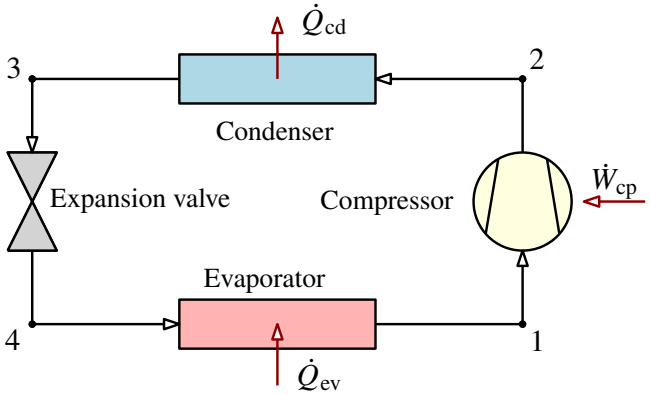

Figure 1.10: Heat pump cycle, showing the condenser and evaporator capacities ($\dot{Q}_{cd}$ and $\dot{Q}_{ev}$) and the compressor power consumption ($\dot{W}_{cp}$).

As already stated, the compressor is modeled using isentropic-efficiency variation curves as a function of the inlet vapor quality. Several laws are used, assuming linear drops in isentropic efficiency with decreasing vapor quality, allowing to consider different scenarios. Moreover, the mass flow rate is calculated proportionally to the compressor speed, given as an input. Furthermore, the heat exchangers are modeled using a moving boundary model inspired from Bell et al. 2015, it has been selected for its ability to get the temperature evolutions of both fluids inside the heat exchangers. It calculates the maximum heat rate that can be transferred based on an internal and an external pinching analysis. Then, the heat exchanger is divided into a given number of cells having a fixed power transferred and two boundaries representing the saturated liquid and vapor points are moving to define cells with subcooled liquid, two-phase fluid and superheated vapor. The log mean temperature difference is then solved on every cell to get the outlet and inlet temperatures on both primary and secondary fluid sides (refrigerant and water). The calculation of the heat transfer coefficients in each cell is different in two-phase regime and single-phase regime. For the two-phase regime, the

[2]We thank Dr. Chris Benson for suggesting to investigate 2-phase compression in heat pump cycles.

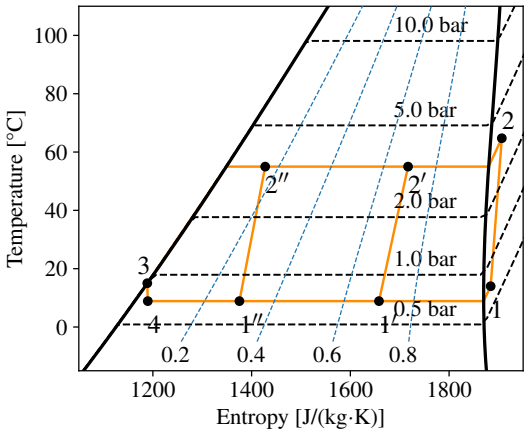

Figure 1.11: Temperature-entropy diagram of the heat pump cycle with different inlet qualities.

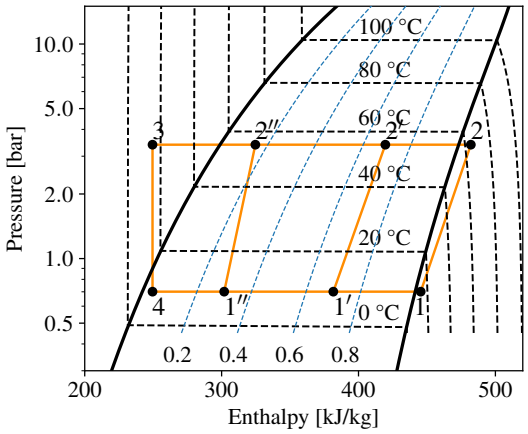

Figure 1.12: Pressure-enthalpy diagram of the heat pump cycle with different inlet qualities.

evaporative and condensation heat transfer coefficients are respectively calculated using the Han boiling and condensing correlations in plate heat exchangers (D.-H. Han et al. 2003a; D.-H. Han et al. 2003b), while for single-phase regimes, the Gnielinski pipe heat transfer correlation is used (Shah 2021). For simplicity, the evaporator will be modeled similarly to the condenser as a plate heat exchanger. Consequently, the heat source is assumed to be water, however, this assumption does not affect the qualitative trends of the results, which remain valid for both air- and water-based sources.

The plate heat exchanger characteristics used can be found in Table 1.2, they are based on a real heat exchanger, oversized with regards to the application.

Parameter	Value	Unit
Surface exchange area	5.04	m^2
Number of plates	88	-
Cross section area	$2.1 \cdot 10^4$	m^2
Dimensions (H×L×W)	524×117×232	mm

Table 1.2: Parameters of the plate heat exchanger used.

The heat pump model consists in the connection between the isentropic efficiency law of the compressor, the two moving boundary models of the heat exchangers, and an isenthalpic valve as presented in Figure 1.13. The isentropic efficiency of the compressor is defined as

$$\varepsilon_{is} = \frac{\dot{m}\left(h_{ex,cp,is} - h_{su,cp}\right)}{\dot{W}_{cp}} \tag{1.3}$$

where $\dot{m}$ is the mass flow rate delivered by the compressor, $h_{su,cp}$ is the inlet enthalpy, $h_{ex,cp,is}$ is the exhaust enthalpy of an isentropic compression and $\dot{W}_{cp}$ is the compressor power consumption.

Therefore, by knowing the compressor inlet state, the exhaust pressure, and its isentropic efficiency, it is possible to determine the exhaust state and the power consumption. Regarding the heat exchangers, by knowing the inlet state of the heat exchanger on the refrigerant side, along with the secondary fluid supply temperature and mass flow rate or exhaust temperature, it is possible to determine the heat exchanger capacity and the exhaust state. As can be seen in Figure 1.13, the inputs of the heat pump model are the condenser inlet/outlet water temperatures $T_{w,su,cd}$ and $T_{w,ex,cd}$ as well as its capacity target $\dot{Q}^{\star}_{cd}$, the inlet vapor quality

or superheating target of the compressor inlet $Q^{\star}_{\text{su,cp}}$ or $SH^{\star}$ and the evaporator water inlet temperature $T_{\text{w,su,ev}}$ and mass flow rate $\dot{m}_{w,ev}$. The solving process is iterative, although some variables can directly be determined from the inputs. For instance, the condensation pressure could physically be fixed by the charge of refrigerant of the cycle, however, due to convergence problems, it has been decided to fix the condensation pressure with the condenser outlet temperature considering a pinch point of 5 K. The condenser water mass flow rate could also directly be fixed by knowing the target capacity $\dot{Q}^{\star}_{\text{cd}}$. Two variables needs to be set using iterative processes: the evaporation pressure and the mass flow rate. The evaporation pressure is set by the compressor inlet vapor quality or superheat target, while the mass flow rate is set by the refrigerant mass flow rate, adjusted by the compressor speed through a proportional law. By decreasing the evaporation pressure, the compressor inlet vapor quality (or superheat) increases, and vice versa. Moreover, when increasing the compressor speed, the condenser capacity increases, and vice versa. Two bisection processes are thus implemented in parallel to obtain the final solution. Eventually, after finding the solution, the compressor power consumption obtained and the condenser capacity can be used to calculate the COP, defined as

$$\text{COP} = \frac{\dot{Q}_{\text{cd}}}{\dot{W}_{\text{cp}}} \tag{1.4}$$

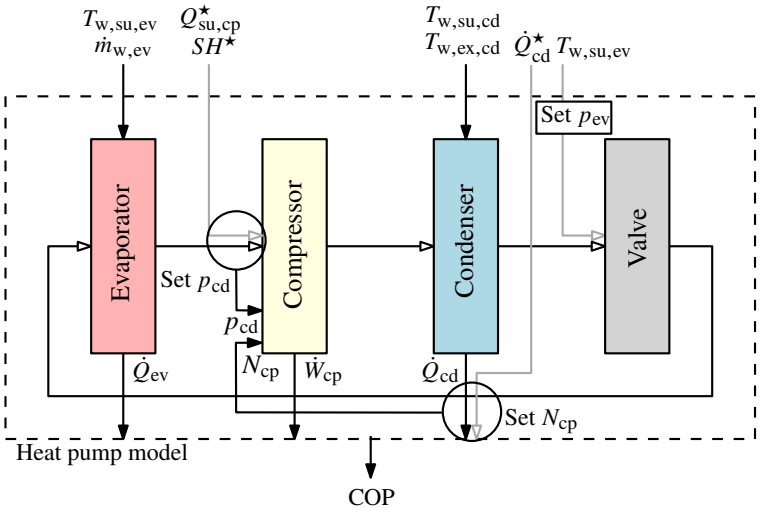

Figure 1.13: Model of the heat pump.

As stated by the second law of thermodynamics, the performance of a heat pump is limited by the efficiency of the reverse Carnot cycle. The performance gap between the ideal heat pump cycle and the real cycle can be evaluated using an exergy analysis, where the heat pump irreversibility creation can be assessed analytically. Exergy can be defined as the maximum work recoverable from a process with regards to a reference temperature and pressure. For reversible processes, the exergy is conserved, while when irreversibilites occur, a part of the exergy is destroyed. The exergy analysis allows to evaluate irreversibility losses in each component of the heat pump, the best performance will therefore correspond to the minimal total exergy destruction. The exergy of a point in the cycle can be seen as a thermodynamic property, defined as

$$e = (h - h_0) - T_0(s - s_0) \tag{1.5}$$

where h_0, T_0 and s_0 are respectively the reference values of enthalpy, temperature and entropy. Similarly to the heat pump exergetic analysis performed in Byrne et al. 2019, the exergy

destruction rate in each component of the cycle can be evaluated using the following equations:

$$\dot{E}_{\mathrm{D,cp}} = \dot{W}_{\mathrm{cp}} - \dot{m}\left[(h_{\mathrm{ex,cp}} - h_{\mathrm{su,cp}}) - T_0(s_{\mathrm{ex,cp}} - s_{\mathrm{su,cp}})\right] = \dot{m}\left[-T_0(s_{\mathrm{su,cp}} - s_{\mathrm{ex,cp}})\right] \tag{1.6}$$

$$\dot{E}_{\mathrm{D,cd}} = \dot{m}\left[(h_{\mathrm{su,cd}} - h_{\mathrm{ex,cd}}) - T_0(s_{\mathrm{su,cd}} - s_{\mathrm{ex,cd}})\right] - \dot{Q}_{\mathrm{cd}}\left(1 - \frac{T_0}{\overline{T}_{\mathrm{w,cd}}}\right) \tag{1.7}$$

$$\dot{E}_{\mathrm{D,valve}} = \dot{m}\left[-T_0(s_{\mathrm{su,valve}} - s_{\mathrm{ex,valve}})\right] \tag{1.8}$$

$$\dot{E}_{\mathrm{D,ev}} = \dot{Q}_{\mathrm{ev}}\left(1 - \frac{T_0}{\overline{T}_{\mathrm{w,ev}}}\right) - \dot{m}\left[(h_{\mathrm{ex,ev}} - h_{\mathrm{su,ev}}) - T_0(s_{\mathrm{ex,ev}} - s_{\mathrm{su,ev}})\right] \tag{1.9}$$

where the temperatures of the heat sink $\overline{T}_{\mathrm{w,cd}}$ and the heat source $\overline{T}_{\mathrm{w,ev}}$ are calculated using a logarithmic mean (isentropic mean):

$$\overline{T} = \frac{T_{\mathrm{w,su}} - T_{\mathrm{w,ex}}}{\ln\left(\frac{T_{\mathrm{w,su}}}{T_{\mathrm{w,ex}}}\right)} \tag{1.10}$$

The irreversibility creation in the compressor is embedded in the isentropic efficiency, i.e., a reduction of isentropic efficiency with the decrease of inlet vapor quality is equivalent to increasing the exergy destruction rate. Regarding the heat exchangers, the irreversibility creation primarily comes from the temperature difference between the refrigerant and the secondary fluid. Pressure losses can also create irreversibilities in the heat exchangers, however, they have not been taken into account in the present analysis. By going from a superheated state to a two-phase state down to a low vapor quality at the compressor inlet, the outlet quality of the compressor is also going to decrease, allowing to better match the temperature profile of the heat sink, which reduces exergy destruction. The objective of the analysis is therefore to determine the optimal compressor inlet vapor quality that minimizes the total exergy destruction rate. By doing so, the trend observed in the heat pump COP reduction can be distributed over the individual components. The simulations are run using three scenarios for the evolution of the compressor isentropic efficiency with vapor quality, starting at 70% for superheated and saturated conditions : a scenario without decrease, another with a slight decrease, and a third with a strong decrease getting down to a 35% isentropic efficiency at a vapor quality of 0.4, as presented in Figure 1.14. Thereby, the isentropic efficiency depends only on the inlet vapor quality and does not consider the pressure ratio or the compressor speed as influencing variables. This assumption can be justified by the unfixed built-in volume ratio of the present compressor, thereby avoiding making the analysis design-oriented. Thus, the compressor design, i.e., the displacement volume and the built-in volume ratio, does not influence the performance of the heat pump.

The evolution of the COP with respect to the compressor inlet conditions is shown in Figure 1.15 for the three scenarios considered. Moreover, the evolution of the pressure ratio, defined as the condensation pressure divided by the evaporation pressure, is also displayed in the same figure. The variation of pressure ratios with vapor quality originates from changes in the evaporation pressure, which is adjusted to achieve the target vapor quality at the compressor inlet. For the worst-efficiency scenario (scenario 3), the maximum of the COP curve is located near the saturated vapor point. When the superheat is reduced until a saturated state is reached, the pressure ratio decreases, thereby reducing the compression work, while the mass flow rate remains nearly unchanged. Therefore, the lower the compressor inlet superheat, the higher the theoretical COP. In this example, the performance improves from a COP of 5.7 at a superheat of 5 K to a value of 6 at saturated conditions. When decreasing the inlet quality, the compressor power consumption increases significantly: this observation is the result of two effects: the work of the compressor is increased due to the low vapor

quality and the mass flow rate is also increased, due to the increase in inlet density. The drawback of a superheated state is that ensuring superheat requires lowering the evaporation pressure, which results in an increase in compressor power; consequently, a superheated inlet state never corresponds to the highest COP. As a consequence, the COP drops from a value of 6 at a saturated state, to value of 4.5 at a compressor inlet vapor quality of 0.4. In the two more favorable efficiency-variation scenarios, the compression work is reduced, but the mass flow rate still increases as the vapor quality decreases, resulting in an increase in COP from the same maximum of 6 to 7 for scenario 1 and a slight decrease to 5.5 for scenario 2.

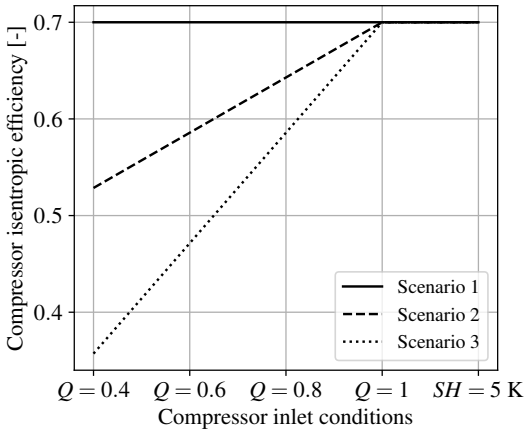

Figure 1.14: Three scenarios of compressor isentropic efficiency evolution with inlet vapor quality.

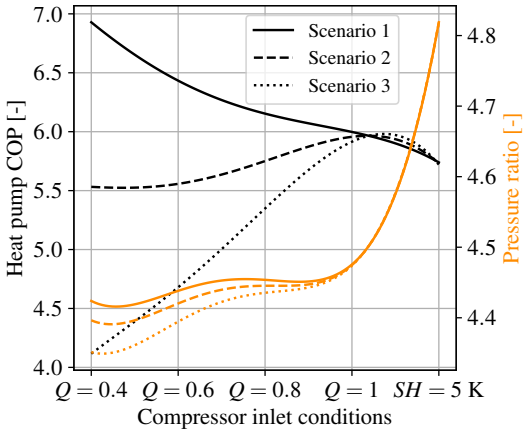

Figure 1.15: Heat pump COP for varying compressor inlet conditions under three different isentropic efficiency scenarios.

The exergy destruction rate of each component for scenario 1 and 3 can respectively be found in Figures 1.16 and 1.17. In both cases, the exergy destruction of the evaporator and the valve are negligible, and the trade-off is mainly between the compressor and the condenser. For scenario 3 (Figure 1.17), the highest compressor exergy destruction occurs at a vapor quality of 0.4, while a minimum is reached at a vapor quality of 1, before increasing again under superheated inlet conditions. For scenario 1 (Figure 1.16), interestingly, the exergy destruction of the compressor decreases continuously with decreasing vapor quality, despite the constant isentropic efficiency, which proves that the entropy generation is not only a function of the isentropic efficiency. Regarding the condenser curves, the exergy destruction is significantly lower at low vapor qualities due to a better match with the condenser water temperature profile, and it increases as the vapor quality increases. For both scenarios, the total exergy destruction is perfectly matching the trend of the COP in Figure 1.15, the COP maximum corresponds to the total exergy destruction minimum. Furthermore, Figures 1.18 and 1.19 show the evolutions of the water temperature inside the condenser and the evaporator, respectively for a 0.4 quality and a 5 K superheated inlet point. The temperature difference inside the evaporator can clearly justify the low exergy destruction rate in this heat exchanger. The same conclusion can be drawn on the condenser, where the exergy destruction rate is lower for the low quality compressor inlet condition due to the proximity between the temperature curves. The present analysis is therefore very sensitive to the compressor performance. If the decrease in compressor isentropic efficiency with decreasing inlet vapor quality is significant, the application of two-phase compression in heat pumps is not attractive from a performance standpoint. Nevertheless, if the decrease in isentropic efficiency can be limited as the vapor quality decreases, the performance of the heat pump can significantly be improved.

In the present practical example of two-phase compression applied to thermodynamic cycles, a strong assumption is made: the isentropic efficiency follows a law that is a function of the inlet vapor quality only. This assumption allows avoiding the fixation of a compressor

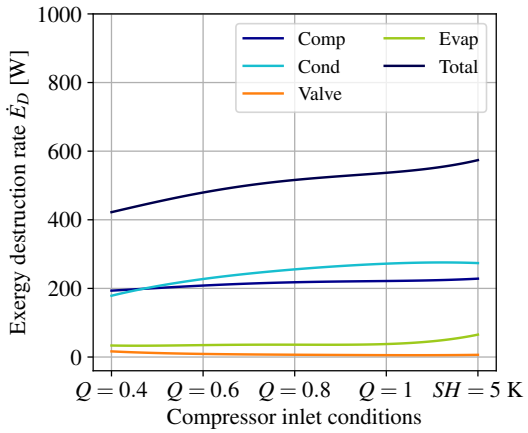

Figure 1.16: Exergy destruction rate of each heat pump component under isentropic efficiency scenario 1.

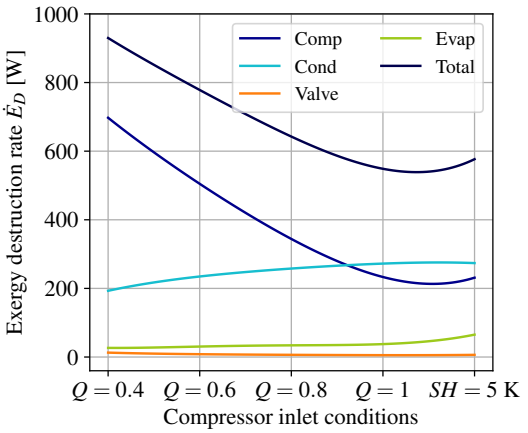

Figure 1.17: Exergy destruction rate of each heat pump component under isentropic efficiency scenario 3.

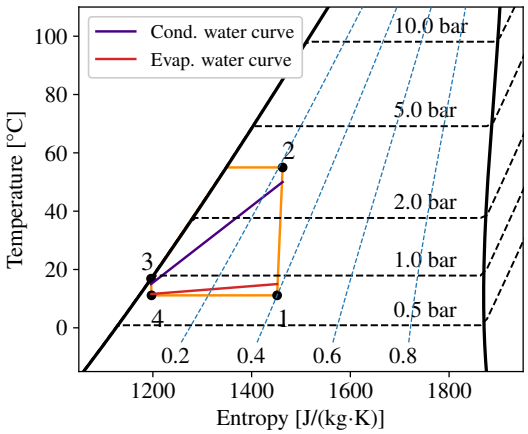

Figure 1.18: Temperature-entropy diagram of the heat pump for a compressor inlet quality of 0.4, including heat exchangers temperature curves.

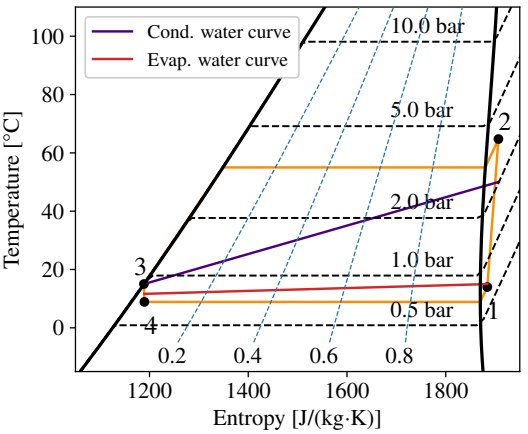

Figure 1.19: Temperature-entropy diagram of the heat pump for a compressor superheat of 5 K, including heat exchangers temperature curves.

design, which could be optimal only under certain conditions and thus influence the results of the analysis. Moreover, it also allows verification of whether, theoretically, two-phase compression could be beneficial for a heat pump cycle, and the results support this conclusion. In this case, the power consumption of the machine is a direct function of the fixed isentropic efficiency, while the delivered mass flow rate is proportional to the speed (constant volumetric efficiency). In reality, the isentropic efficiency of a compressor is also influenced by the pressure ratio, the speed, the inlet pressure, and the oil circulation ratio (OCR), as is the volumetric efficiency. Moreover, at the present stage of the thesis, the trend of isentropic efficiency variation with inlet vapor quality is not well known, despite the studies reported in the literature, which do not investigate such low inlet vapor qualities. It should also be noted that the compressor design also has a strong influence on the results, as two positive-displacement compressors may not behave similarly under the same conditions and even two different scroll compressors may behave differently. Finally, the oil was not considered in the study, which could results in reduced heat exchangers capacities, due to lower heat exchanger coefficient and partial evaporation of the delivered flow rate. On the compressor side, circulating oil is often essential to ensure the robustness of the machine; however, for a given inlet vapor quality (including the liquid oil) and speed, the compressor power consumption would remain constant for a lower delivered refrigerant mass flow rate.

The following conclusions can be drawn from this practical example. First, investigating the isentropic efficiency behavior of positive-displacement compressors, in particular scroll compressors, is very useful for quantifying the drop or gain in the performance of thermodynamic cycles. To this end, experimental investigations are needed to gain insight into the compressor behavior under two-phase operating conditions. Second, accurate modeling of the compressor, validated using prior experimental data, can be used to adapt the geometry and develop a more suitable compressor design for operation under two-phase conditions. Third, this same validated model can be used to investigate the optimal operating point of the thermodynamic cycle under consideration. Finally, optimal thermodynamic performance alone is insufficient; the design must also demonstrate optimal thermo-economic performance to be considered viable. Naturally, the application example investigated here, which could for instance be used in a heat pump water heater, is only one application among others. Other applications may also benefit from two-phase compression. Nonetheless, no further applications are investigated in this thesis, as this would deviate from its scope.

1.3.3 Concluding remarks

From the previous state of the art, it has been seen that the use of two-phase compression has attracted interest in several types of refrigeration and heat pump cycles for various reasons. The first studies investigate numerically the use of two-phase compression in refrigeration cycles, assuming constant or slightly lower compressor isentropic efficiencies, showing benefits in terms of cycle performance when the compressor is fed without superheat/with low vapor qualities. Then, the use of liquid injection, directly within the scroll compressor compression chambers, is experimentally investigated to reduce the discharge temperature, allowing domestic air conditioning and heat pumps to work in extreme temperature conditions. Some of these studies have shown significant reductions in temperature, but slight overall performance increases, or even performance decreases. Two-phase suction, also referred to as "two-phase compression", consisting in injecting the liquid upstream of the compressor, has shown slightly poorer performance, although it offers the benefit of requiring minimal modification to the scroll compressor design. Some experimental studies have shown peak refrigeration cycle performance with inlet vapor qualities around 95%, along with a slight decrease in cooling/heating capacity. Moreover, the application of CRHP, already investigated both numerically and experimentally, has demonstrated interest in two-phase compression, although at a higher power scale than that of scroll compressors. Results suggest that CRHPs may be commercially competitive only if high compressor isentropic efficiencies can be achieved. Furthermore, the Regen-by-2 cycle, employing scroll machines in its first version, requires high machine performance to be competitive (isentropic efficiency 65% for the expander and 55% for the compressor). Eventually, a practical example of a two-phase application, using compressor isentropic efficiency variation scenarios with inlet vapor quality, has shown that a heat pump cycle could achieve better performance without compressor inlet superheat, with the COP increasing from 5.7 to 6 when removing the 5 K superheat and targeting saturated conditions. In addition, when the vapor quality decreases, in the scenario where the isentropic efficiency remains constant, the COP increases from 6 at saturated conditions to 7 at a vapor quality of 0.4. An exergetic analysis shows that external irreversibilities in the condenser decrease as the vapor quality decreases, as a consequence of the closer temperature profiles of both fluids within the heat exchanger. The same trend is also observed with two-phase expansion, where cycles, such as the TFC, have shown good performance numerically, assuming constant or slightly decreased isentropic efficiency of the compressor. Nevertheless, the experimental results did not align with the first numerical results and new studies are trying to optimize two-phase expanders to achieve better performance (Kliem 2005; Bianchi et al. 2017; van Heule et al. 2025).

From a general perspective, several applications could achieve higher performance by employing two-phase compression, nevertheless, the overall cycle performance strongly depends on the machine's efficiency. It is therefore essential to focus on the performance of scroll compressors under two-phase conditions, similar to the investigations already conducted on screw compressors and expanders. As can be seen, the literature reporting experimental studies on two-phase scroll compressors is limited, and considerable uncertainty remains regarding their reliability under two-phase operating conditions.

1.4 Thesis objectives and overview

This thesis began with a state of the art of the interest of two-phase compression from the machine perspective. From the proposed literature review arose the questions of why some compressors can handle two-phase compression better than others, and why some researchers study two-phase compression with interest, while others study it to avoid it. These first questions raised in the thesis could be answered using elements provided by the literature and through the illustration of an example of a two-phase operated positive-displacement compressor with a fixed built-in volume ratio. The difference between scroll and screw compressors from other machines resides in the relatively low built-in volume ratio, making impossible to reach liquid slugging (pure liquid compression) within the working (or compression) chamber. By contrast, in reciprocating or rotary compressors, higher built-in volume ratio are possible due to their mechanisms, making it possible to reach liquid slugging. Moreover, the difference between studies seeking benefits in two-phase compression and studies avoiding it lies in the controllability of the two-phase conditions (vapor quality). Test benches employed to study the performance behavior of compressors are well instrumented and controlled, whereas in a heat pump switching to defrosting mode, the flooding of the compressor with a large quantity of liquid is totally uncontrolled.

Then, two-phase compression integrated into refrigerant/heat pump cycles is discussed, in terms of cycle performance. A state-of-the-art suggests that isentropic efficiency assumptions should not be made when conducting numerical studies involving two-phase compression. Nevertheless, experimental studies found interest in two-phase compression due to its reduction of compressor discharge temperature. This reduction allows heat pump or refrigeration cycles for air conditioning to perform under extreme temperature conditions. Moreover, experimental studies have also observed enhanced performance of the refrigeration cycle without superheat at the inlet of the compressor, although it is often accompanied by a reduction in cooling capacity. Furthermore, other applications, such as CRHPs or the Regen-by-2 cycle, find benefit in two-phase compression when the isentropic efficiency of the compressor remains high enough. If good isentropic efficiencies can be achieved at low vapor qualities, the gain in coefficient of performance of the proposed heat pump application is promising.

The main objective of this thesis is therefore to study deeply two-phase compression using scroll compressors in order to identify possible optimizations in the compressor design. It therefore tries to answer the following key question: how can two-phase compression be made efficient enough to be of practical interest? Scroll compressors have already been experimentally tested under two-phase operating conditions, for instance, during liquid flooding or suction liquid injection. Results analysis provides trends and identifies possible explanations for the observed performance. Nevertheless, most of the employed models used to reproduce the behavior of the machine rely on simple assumptions, which may be valid only under certain operating conditions. For instance, it is often assumed that leakages are fully liquid when operating in two-phase mode and that thermal equilibrium is ensured throughout compression. Also, the effect of oil presence on vapor–liquid equilibrium is barely mentioned, although it plays a significant role in defining the vapor quality. Moreover, a lack of model

validation procedures is often observed, as validated results are sometimes presented without context, and no details are given regarding the fitted parameters. Therefore, no studies have managed to truly explain the causes of the variations in both volumetric and isentropic efficiencies generated by two-phase compression. Without these explanations, it is impossible to consider design enhancements to achieve higher performance.

Thus, the major contribution of this thesis lies in the understanding of the diverse phenomena occurring within the compressor when subjected to two-phase flow. Identifying, analyzing, and quantifying the consequences of the phenomena involved within the compressor help identify possible design improvement solutions. To this aim, both numerical and experimental investigations are required. Furthermore, the oil-related phenomena require the thermophysical properties of the oil-refrigerant mixture to be known and accurate. Eventually, validation of the numerical model employed is necessary to perform sensitivity analyses on the calibrated models. Thereby, the aforementioned research work forms the core content of this thesis. The thesis is divided into four main parts, presented hereunder: oil-refrigerant mixture modeling, experimental investigations, numerical modeling, and model validation and performance analysis. Minor contributions can also be found in each chapter; they are described in what follows. Therefore, the thesis objective focuses on the compressor itself and does not consider its integration into a thermodynamic cycle, although some key elements in this regard have already been presented in the introduction.

The thesis is composed of the following 6 chapters, outlined hereunder:

- **Chapter 1. Introduction**
  This chapter, presented above, introduces the motivations of this research. Two-phase compression within scroll compressors, regarding both machine performance and cycle performance, has been investigated numerically since the 1990s and experimentally since the 2000s. However, the lack of understanding of performance sensitivity to two-phase conditions requires a deeper study of scroll compressors operating with two-phase refrigerant flow, which is the major objective of this thesis.

- **Chapter 2. Oil-Refrigerant Mixture Modeling**
  Before diving into two-phase compression experimental and numerical investigations, it is necessary to understand precisely key concepts regarding two-phase oil-refrigerant mixtures. Therefore, the objective of this chapter is to provide the reader with the necessary tools to understand numerical and experimental challenges regarding fluid properties addressed in the following chapters. This chapter first comprises the numerical and experimental investigations on the characterization of two-phase oil-refrigerant mixtures. Then, examples of applications of two-phase oil-refrigerant mixture, namely, two-phase compression definition, two-phase heat transfer, are introduced. Moreover, an important assumption regarding oil solubility, which consequently simplifies the subsequent numerical calculations, is introduced. Therefore, this chapter constitutes a pillar to understand the developments and results of the following chapters.

- **Chapter 3. Two-phase Compression: Experimental Investigations**
  Prior to any modeling attempts, experimental investigations of two-phase compression allow to gain insight into the compressor's behavior. These insights drive the modeling approach employed in the following chapter. The experimental investigations include the testing of two scroll compressors under two-phase regimes. To this aim, a test bench dedicated to controlling the inlet conditions of the compressors was developed. The test bench layout, instrumentation, and post-processing methodology are discussed. The results are presented using a Gaussian process interpolation tool, and isentropic and volumetric efficiency variations with the inlet conditions are discussed. Furthermore, a dynamic pressure sensor integrated into the second compressor allows the recording of

pressure within the compression and discharge chambers of the compressor, explaining some of the trends observed in the isentropic efficiency behavior.

– **Chapter 4. Two-phase Compression: Numerical Modeling**
This chapter presents the modeling approach employed to predict the compressor performance under two-phase flow. This approach, referred to as deterministic modeling, accounts for the various phenomena occurring within the compressor when subjected to two-phase flow. It uses geometrical data to predict the volume variations of the different chambers created by the superposition of the fixed and orbiting scrolls, and a core model to predict the corresponding pressure and temperature variations by applying mass and energy conservation. The introduced model takes into account oil presence, thermal non-equilibrium between the liquid and vapor phases (different temperatures), inlet flow pattern, intermediate discharge valve, heat transfer, two-phase leakage, and mechanical losses. Thus, this chapter constitutes a presentation of the deterministic model and the various submodels employed; the validation process and results analysis are addressed in the next chapter.

– **Chapter 5. Two-phase Compression: Model Validation and Performance Analysis**
In this chapter can first be found the calibration methodology employed to fit the model parameters with the data set coming from the experimental investigations. The validation results of the models for both machines are then presented and analyzed. Then, the validated pressure–volume diagrams facilitate the analysis of volumetric and isentropic efficiencies, which can be decomposed into several factors affecting performance, such as the indicated work derived from the diagrams. Finally, a sensitivity analysis is conducted on the calibrated models, where the different sources of efficiency losses are quantified for varying inlet vapor qualities and pressure ratios. Therefore, this chapter provides both a qualitative and quantitative understanding of the impact of two-phase flow on scroll compressor performance, thereby addressing the primary research question raised in the introduction.

– **Chapter 6. Conclusions and perspectives**
This final chapter concludes with the main outcomes and results of this research work. The overall trends observed from the experimental and simulation results are summarized in the conclusion. Based on that, answers to the introduction question "how can two-phase compression be made efficient enough to be of practical interest?" are given, applied to scroll compressors. An optimized design of scroll compressor geometry is proposed and simulated using the deterministic model. Perspectives of the work are eventually provided.

Finally, the thesis also comprises three appendix chapters: one for the oil-refrigerant mixture modeling, one for the experimental investigations, and the last for the numerical investigations. These appendix chapters aim to detail the modeling techniques employed and provide results that lie outside the scope of the main thesis body.

References

Leclercq, Nicolas, Vega, Javier, and Lemort, Vincent (2023). “Investigations on a Heat Pump Using Two-Phase Refrigerant Compressions”. In: *36th International Conference on Efficiency, Cost, Optimization, Simulation and Environmental Impact of Energy Systems (ECOS 2023)*. ECOS 2023, pp. 804–814. ISBN: 978-1-7138-7492-8. DOI: 10.52202/069564-0073.

European Commission (2016). *An EU Strategy on Heating and Cooling*.

European Commission (2022). *Clean Energy Technology Observatory, Heat Pumps in the European Union: Status Report on Technology Development, Trends, Value Chains and Markets : 2022*. (Visited on 11/27/2025).

International Energy Agency (2022). *Annual Report 2022: Heat Pumping Technologies*. Tech. rep.

Fleiter, Tobias, Steinbach, Jan, and Ragwitz, Mario (2017). *Mapping and Analyses of the Current and Future (2020 - 2030) Heating/Cooling Fuel Deployment (Fossil/Renewables)*. Tech. rep.

International Institute of Refrigeration (2024). *A Strong Global Compressor Market*.

Taft, G L (1972). "Selection and Application of Industrial Screw Compressors". In: International Compressor Engineering Conference.

Zimmern, B (1984). "From Water to Refrigerant: Twenty Years to Develop the Oil Injection-Free Single Screw Compressor". In: International Compressor Engineering Conference.

Nikolov, Alexander and Brümmer, Andreas (2014). "Influence of Water Injection on the Operating Behaviour of Screw Machines". In: 9th International Conference on Screw Machines.

Yusha, V L, Chernov, G I, and Fedorova, M A (Nov. 2018). "Mathematical Modeling of Working Processes of Variable Frequency Screw Compressor with Differentiated Oil Supply into the Working Chamber". In: *IOP Conference Series: Materials Science and Engineering* 425, p. 012003. ISSN: 1757-899X. DOI: 10.1088/1757-899X/425/1/012003. (Visited on 09/09/2025).

He, Zhilong et al. (May 2018). "Experimental Investigation into the Effect of Oil Injection on the Performance of a Variable Speed Twin-Screw Compressor". In: *Energies* 11.6, p. 1342. ISSN: 1996-1073. DOI: 10.3390/en11061342. (Visited on 09/10/2025).

Wang, Chuang et al. (Oct. 2018). "Development of an Oil Free Water-Lubricated Twin-Screw Air Compressor". In: *Applied Thermal Engineering* 143, pp. 396–402. ISSN: 13594311. DOI: 10.1016/j.applthermaleng.2018.07.119. (Visited on 09/10/2025).

Ferreira, C. A. Infante, Zaytsev, D., and Zamfirescu, C. (2006a). "Wet Compression of Pure Refrigerants". In: International Compressor Engineering Conference.

Li, H et al. (1992). "Research of Oil-Injected Scroll Compressor Working Process". In: *Proceedings of the International Compressor Engineering Conference*. Purdue University.

Leclercq, Nicolas and Lemort, Vincent (2022). "Modeling and Simulation of a Two-Phase Scroll Compressor". In: *International Compressor Engineering Conference*. Purdue University.

Zaytsev, D. and Ferreira, C. A. Infante (2000). "Aspects of Two-Phase Flow Screw Compressor Modelling Part I: Leakage Flow and Rotor Tip Friction". In: *Proceeding of the International Compressor Engineering Conference*. Purdue University.

Liu, Zheji and Soedel, Werner (1995). "A Mathematical Model for Simulating Liquid and Vapor Two-Phase Compression Processes and Investigating Slugging Problems in Compressors". In: *HVAC and R Research* 1.2, pp. 99–109. ISSN: 10789669. DOI: 10.1080/10789669.1995.10391312.

Prasad, B. G. Shiva (Sept. 2002). "Effect of Liquid on a Reciprocating Compressor". In: *Journal of Energy Resources Technology* 124.3, pp. 187–190. ISSN: 0195-0738, 1528-8994. DOI: 10.1115/1.1491981. (Visited on 10/23/2025).

Lin, Jie et al. (July 2022). "Simulation of Single and Two-Phase Refrigerant Compression in Rotary Compressors". In: *Applied Thermal Engineering* 211. ISSN: 13594311. DOI: 10.1016/j.applthermaleng.2022.118465.

Guo, Nini, Lin, Jie, and Wu, Jianhua (Dec. 2024). "Simulation on Two-Phase Refrigerant Compression in the Cylinder of Rotary Compressors Using CFD Method". In: *Scientific Reports* 14.1. ISSN: 20452322. DOI: 10.1038/s41598-024-56856-y.

Wang, Jun et al. (Dec. 2015). "Analysis and Numerical Simulation of a Novel Gas–Liquid Multiphase Scroll Pump". In: *International Journal of Heat and Mass Transfer* 91, pp. 27–36. ISSN: 00179310. DOI: 10.1016/j.ijheatmasstransfer.2015.07.086. (Visited on 09/09/2025).

Bush, James W and Elson, John P (1988). "Scroll Compressor Design Criteria for Residential Air Conditioning and Heat Pump Applications, Part I: Mechanics". In: International Compressor Engineering Conference.

Sakuda, A et al. (2001). "Performance Improvement of Scroll Compressor with New Sealing-Oil Supply Mechanism". In: International Conference on Compressors and their Systems. DOI: C591/019/2001.

Hiwata, A et al. (2002). "Performance Investigation with Oil-Injection to Compression Chambers on CO2-scroll Compressor". In: *International Compressor Engineering Conference*. Purdue University.

Bell, Ian H. et al. (Nov. 2012a). "Liquid Flooded Compression and Expansion in Scroll Machines - Part II: Experimental Testing and Model Validation". In: *International Journal of Refrigeration* 35.7, pp. 1890–1900. ISSN: 01407007. DOI: 10.1016/j.ijrefrig.2012.07.008.

Zhao, Yuanyang et al. (June 2005). "Theoretical and Experimental Studies of Water Injection Scroll Compressor in Automotive Fuel Cell Systems". In: *Energy Conversion and Management* 46.9-10, pp. 1379–1392. ISSN: 01968904. DOI: 10.1016/j.enconman.2004.08.006. (Visited on 11/05/2025).

Afjei, Th., Suter, P., and Favrat, D. (1992). "Experimental Analysis of an Inverter-Driven Scroll Compressor with Liquid Injection". In: *International Compressor Engineering Conference*. Purdue University.

Dutta, Asit K., Yanagisawa, Tadashi, and Fukuta, Mitsuhiro (Sept. 2001). "An Investigation of the Performance of a Scroll Compressor under Liquid Refrigerant Injection". In: *International Journal of Refrigeration* 24.6, pp. 577–587. ISSN: 01407007. DOI: 10.1016/S0140-7007(00)00041-4. (Visited on 09/09/2025).

Cho, Honghyun, Chung, Jin Taek, and Kim, Yongchan (Jan. 2003). "Influence of Liquid Refrigerant Injection on the Performance of an Inverter-Driven Scroll Compressor". In: *International Journal of Refrigeration* 26.1, pp. 87–94. ISSN: 01407007. DOI: 10.1016/S0140-7007(02)00017-8. (Visited on 10/23/2025).

Wang, Baolong et al. (Apr. 2008). "Numerical Research on the Scroll Compressor with Refrigeration Injection". In: *Applied Thermal Engineering* 28.5-6, pp. 440–449. ISSN: 13594311. DOI: 10.1016/j.applthermaleng.2007.05.012. (Visited on 09/10/2025).

Xu, Xing, Hwang, Yunho, and Radermacher, Reinhard (Mar. 2011). "Refrigerant Injection for Heat Pumping/Air Conditioning Systems: Literature Review and Challenges Discussions". In: *International Journal of Refrigeration* 34.2, pp. 402–415. ISSN: 01407007. DOI: 10.1016/j.ijrefrig.2010.09.015. (Visited on 09/09/2025).

Emhardt, Simon, Tian, Guohong, and Chew, John (Aug. 2018). "A Review of Scroll Expander Geometries and Their Performance". In: *Applied Thermal Engineering* 141, pp. 1020–1034. ISSN: 13594311. DOI: 10.1016/j.applthermaleng.2018.06.045. (Visited on 09/09/2025).

Smith, Ian, Stosic, Nikola, and Aldis, Colin (1995). "Trilateral Flash Cycle System: A High Effiency Power Plant For Liquid Resources". In: *Proceedings World Geothermal Congress*.

Itard, L.C.M (Sept. 1995). "Wet Compression versus Dry Compression in Heat Pumps Working with Pure Refrigerants or Non-Azeotropic Mixtures". In: *International Journal of Refrigeration* 18.7, pp. 495–504. ISSN: 01407007. DOI: 10.1016/0140-7007(95)93788-L. (Visited on 11/05/2025).

Vorster, P.P.J and Meyer, J.P (June 2000). "Wet Compression versus Dry Compression in Heat Pumps Working with Pure Refrigerants or Non-Azeotropic Binary Mixtures for Different Heating Applications". In: *International Journal of Refrigeration* 23.4, pp. 292–311. ISSN: 01407007. DOI: 10.1016/S0140-7007(99)00050-X.

Feng, Cao et al. (Oct. 2009). "Study on Performance of a Heat Pump Water Heater Using Suction Stream Liquid Injection". In: *Applied Thermal Engineering* 29.14-15, pp. 2942–2948. ISSN: 13594311. DOI: 10.1016/j.applthermaleng.2009.03.001. (Visited on 11/05/2025).

Yang, Minghong et al. (Nov. 2015). "Evaluation of Two-Phase Suction, Liquid Injection and Two-Phase Injection for Decreasing the Discharge Temperature of the R32 Scroll Compressor". In: *International Journal of Refrigeration* 59, pp. 269–280. ISSN: 01407007. DOI: 10.1016/j.ijrefrig.2015.08.004. (Visited on 11/05/2025).

Seong, Kyoungjin, Lee, Daehui, and Lee, Jinho (Mar. 2017). "The Effects of Wet Compression by the Electronic Expansion Valve Opening on the Performance of a Heat Pump System". In: *Applied Sciences* 7.3, p. 248. ISSN: 2076-3417. DOI: 10.3390/app7030248. (Visited on 10/22/2025).

Sun, Shuaihui et al. (Dec. 2021). "Influence of Two-Phase Suction Injection on Performances of the Scroll Refrigeration Compressor with a High-Temperature Shell". In: *Proceedings of the Institution of Mechanical Engineers, Part E: Journal of Process Mechanical Engineering* 235.6, pp. 2059–2072. ISSN: 0954-4089, 2041-3009. DOI: 10.1177/09544089211030216. (Visited on 10/22/2025).

Pan, Xi et al. (Dec. 2024). "Investigation on Saturated Vapor and Two-Phase Refrigerant Injection in the Rotary Compressor for the Extreme Hot and Cold Conditions". In: *Applied Thermal Engineering* 257, p. 124210. ISSN: 13594311. DOI: 10.1016/j.applthermaleng.2024.124210. (Visited on 11/05/2025).

Brunin, O, Feidt, M, and Hivet, B (Aug. 1997). "Comparison of the Working Domains of Some Compression Heat Pumps and a Compression-Absorption Heat Pump". In: *International Journal of Refrigeration* 20.5, pp. 308–318. ISSN: 01407007. DOI: 10.1016/S0140-7007(97)00025-X. (Visited on 11/07/2025).

Zamfirescu, Calin (Mar. 2009). "Modeling And Optimization of an Ammonia-Water Compression-Resorption Heat Pumps With Wet Compression". In: *Transactions of the Canadian Society for Mechanical Engineering* 33.1, pp. 75–88. ISSN: 0315-8977, 2816-5691. DOI: 10.1139/tcsme-2009-0008. (Visited on 10/23/2025).

Ferreira, C. A. Infante and Zaytsev, Dmytro (2002). "Experimental Compression - Resorption Heat Pump for Industrial Applications". In: International Compressor Engineering Conference.

Ferreira, C. A. Infante, Zamfirescu, C., and Zaytsev, D. (June 2006b). "Twin Screw Oil-Free Wet Compressor for Compression-Absorption Cycle". In: *International Journal of Refrigeration* 29.4, pp. 556–565. ISSN: 01407007. DOI: 10.1016/j.ijrefrig.2005.10.006.

van de Bor, D.M., Infante Ferreira, C.A., and Kiss, Anton A. (Sept. 2015). "Low Grade Waste Heat Recovery Using Heat Pumps and Power Cycles". In: *Energy* 89, pp. 864–873. ISSN: 03605442. DOI: 10.1016/j.energy.2015.06.030. (Visited on 11/07/2025).

Gudjonsdottir, V., Ferreira, C. A. Infante, and Goethals, A. (Feb. 2019). "Wet Compression Model for Entropy Production Minimization". In: *Applied Thermal Engineering* 149, pp. 439–447. ISSN: 13594311. DOI: 10.1016/j.applthermaleng.2018.12.065.

Briola, Stefano et al. (July 2021). "Thermo-Economic Analysis of a Novel Trigeneration Cycle Enabled by Two-Phase Machines". In: *Energy* 227. ISSN: 03605442. DOI: 10.1016/j.energy.2021.120453.

Bell, Ian H. et al. (Mar. 2015). "A Generalized Moving-Boundary Algorithm to Predict the Heat Transfer Rate of Counterflow Heat Exchangers for Any Phase Configuration".

In: *Applied Thermal Engineering* 79, pp. 192–201. ISSN: 13594311. DOI: 10.1016/j.applthermaleng.2014.12.028. (Visited on 01/09/2026).

Han, Dong-Hyouck, Lee, Kyu-Jung, and Kim, Yoon-Ho (July 2003a). "Experiments on the Characteristics of Evaporation of R410A in Brazed Plate Heat Exchangers with Different Geometric Configurations". In: *Applied Thermal Engineering* 23.10, pp. 1209–1225. ISSN: 13594311. DOI: 10.1016/S1359-4311(03)00061-9. (Visited on 01/09/2026).

Han, Dong-Hyouck, Lee, K S, and Kim, Yoon-Ho (July 2003b). "The Characteristics of Condensation in Brazed Plate Heat Exchangers with Different Chevron Angles". In: *Journal of the Korean Physical Society*, pp. 66–73.

Shah, Mizra Mohammad (Feb. 2021). *Two-Phase Heat Transfer*. 1st ed. Wiley. ISBN: 978-1-119-61865-2. DOI: 10.1002/9781119618652. (Visited on 09/10/2025).

Byrne, Paul and Ghoubali, Redouane (Feb. 2019). "Exergy Analysis of Heat Pumps for Simultaneous Heating and Cooling". In: *Applied Thermal Engineering* 149, pp. 414–424. ISSN: 13594311. DOI: 10.1016/j.applthermaleng.2018.12.069. (Visited on 01/09/2026).

Kliem, Bernhard Paul (2005). "Grundlagen Des Zweiphasen-Schraubenmotors". PhD thesis. Universität Dortmund.

Bianchi, Giuseppe et al. (Dec. 2017). "Development and Analysis of a Packaged Trilateral Flash Cycle System for Low Grade Heat to Power Conversion Applications". In: *Thermal Science and Engineering Progress* 4, pp. 113–121. ISSN: 24519049. DOI: 10.1016/j.tsep.2017.09.009. (Visited on 10/23/2025).

van Heule, Xander et al. (Oct. 2025). "Sensitivity Study of a Partially Evaporating Organic Rankine Cycle Model with Non-Equilibrium Expansion". In: *Applied Thermal Engineering* 276, p. 126682. ISSN: 13594311. DOI: 10.1016/j.applthermaleng.2025.126682. (Visited on 11/05/2025).

Chapter 2

Oil-Refrigerant Mixture Modeling

Chapter Abstract

The objective of this chapter is to provide the reader with the necessary tools to understand numerical and experimental challenges addressed in the following chapters. Compression, whether single-phase or two-phase, is typically associated with compressors. However, the purpose of positive displacement compressors is solely to impose a volume reduction on the fluid. In essence, it is a mechanical device that dynamically and continuously reduces the volume of defined control volumes; the resulting pressure increase in the fluid depends on its thermophysical properties. It is therefore crucial to understand the behavior of such fluids under the constraints imposed by the compressor. In this chapter, experimental measurements performed on the oil-refrigerant mixture are used to model the oil-refrigerant mixtures employed in the framework of the thesis. These measurements were carried out during an internship at the Schaufler Chair of Refrigeration, Cryogenics, and Compressor Technology at Technische Universität Dresden. The refrigerant studied is the R1233zd(E) and it has been combined with the Polyolester (POE) oil Emkarate RL32 MAF and an oil mixture (RL32 + Petronas POE40). These experimental results allow the validation of the thermophysical property models employed in the two-phase compressor model described in Chapter 4. This experimental validation part is an extension of the work presented at the Herrick conference 2024, in Leclercq et al. (2024a). Finally, the introduced mixture property models are applied to formulate the "desolubilization" assumption, which eliminates the dependence among pressure, temperature, and vapor quality when oil is present in the mixture and consequently simplifies the subsequent numerical calculations.

2.1 Introduction

In vapor compression refrigeration and heat pump systems with positive displacement compressors, oil is necessary to ensure good lubrication of the compressor. The presence of this oil is required to avoid premature wear between moving parts by creating a thin film, avoiding direct contact between metallic surfaces. Moreover, the oil can act as a sealant in the leakage gaps and allows to reduce the discharge temperature, thereby minimizing mechanical stress induced by large temperature differences (Bell 2011). Nevertheless, the presence of oil in thermodynamic cycles also presents some drawbacks (Youbi-Idrissi et al. 2008). First of all, it reduces the heat transfer coefficient in the heat exchangers, especially in the two-phase region, implying the use of bigger heat exchangers. Moreover, it reduces the cooling capacity of refrigeration cycles by not allowing a full evaporation of the refrigerant, as a part of this refrigerant that is solved in the oil stays in the liquid phase. More pressure losses are also faced in micro-channel heat exchangers due to the high oil viscosity. Finally, it modifies the thermodynamic properties of the refrigerant (enthalpies, densities, vapor-liquid equilibria, etc.), making the evaluation of cycle performance more difficult, especially when high oil

mass fractions are used. Accurate knowledge of mixture behavior enables better prediction of phase equilibrium, energy balances, and oil circulation throughout the system. Without considering the impact of oil, models can significantly deviate from reality, misleading the interpretation of results.

In the frame of an oil-refrigerant two-phase mixtures with variable vapor qualities, the accurate knowledge of the properties is even more important. For instance, in liquid-rich mixtures (low vapor qualities), the viscosity and density are strongly dependent on the liquid composition (H. Li et al. 2013), while for a vapor-rich mixture (high vapor quality), the liquid phase is mainly composed of oil and the vapor phase of refrigerant. For the same reason, enthalpy and entropy are also significantly impacted. This problem has been mainly studied for cycle design, as the cooling capacity of a refrigeration cycle is directly influenced by the oil concentration (Youbi-Idrissi et al. 2004; Barbosa 2001; X. Yang et al. 2024; Neto et al. 2011; Ossorio et al. 2022).

Within the framework of two-phase compression of an oil-refrigerant mixture, these properties are required for several purposes:

- several energy balances are used in the experimental setup, requiring an accurate enthalpy calculation technique;
- the deterministic model of the scroll compressor accounts for the oil circulation ratio and therefore requires knowledge of the thermodynamic, thermal, physical and transport properties of the mixture, also known as thermophysical properties;
- the experimental relationship between compressor inlet superheat and vapor quality helps improve the accuracy of the results and requires precise knowledge of the mixture's solubility.
- to simplify the modeling of the compressor, a metholodogy allowing to "desolubize" the oil refrigerant mixture is presented. This methodology also requires precise knowledge of the mixture's solubility.

Fortunately or not, most oil-refrigerant mixtures behave differently, which keeps research in this field ongoing as current refrigerants are gradually phased out and replaced by new ones. Numerous measurements and modeling techniques can therefore be found in the literature.

The chapter starts with the definition of a binary mixture and its thermodynamic behavior. Then, the experimental measurements performed on the oil-refrigerant mixture are described. The refrigerant studied is the hydrochlorofluoroolefin (HCFO) R1233zd(E) and it has been combined with the POE oil Emkarate RL32 MAF and an oil mixture (RL32 + Petronas POE40). The measurement setups are presented along with the uncertainties of the sensors used to measure the required properties. Subsequently, thermophysical properties modeling techniques are introduced, applied and compared in terms of accuracy and simplicity. Finally, the concept of "desolublization" of an oil-refrigerant mixture is introduced. In this concept, two states are defined: the "mixed state" where the solubility equations govern, and the "split state" where the solubility is neglected and the refrigerant behaves like a pure fluid, despite the presence of oil. This methodology allows the simplification of calculations involving the presence of oil and is applied in specific cases to illustrate key principles using two-phase oil-refrigerant mixtures, such as isentropic compression and heat transfer.

2.2 Definition of a binary mixture

Before diving into the thermophysical property measurements and modeling of the oil–refrigerant mixtures studied in the frame of this thesis, it is important to first present the basic theory of binary mixtures and their behavior. First, the composition of a mixture is thoroughly defined, in order to derive the equation allowing to calculate the vapor quality from the pressure,

temperature and global composition. Subsequently, the derived equations are applied to the oil-refrigerant mixture studied in the context of this thesis.

2.2.1 Composition of a binary mixture

A binary mixture is a mixture composed of two components (fluids), e.g., the two-phase mixture that can be found in Figure 2.1. For a two-phase mixture, each component may be present in both the vapor and liquid phases, with the phase compositions governed by the mixture's vapor–liquid equilibrium (VLE).

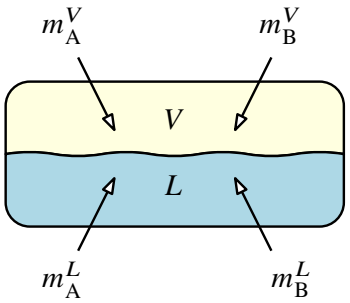

Figure 2.1: Definition of a binary mixture.

Therefore, a mixture is defined by the distribution of the masses of both components between the vapor and/or liquid phases. Furthermore, by normalizing these masses with respect to the total mass, the compositions can be expressed in terms of mass fractions, as shown in Figure 2.2. For instance, z_A^V is the mass fraction of component A in vapor phase. The mass fraction of vapor can be obtained by adding the mass fractions of component A and component B in the vapor phase, thereby defining the mass-based vapor quality Q. By adding the vapor and liquid mass fractions of component A, the global mass fraction of component A is obtained, i.e., z_A. Thereby, some equalities can be derived from Figure 2.2 with first the system written in terms of masses (2.1) followed by the system written in terms of mass fractions (2.2).

	Comp. A	Comp. B	
Vapor	m_A^V	m_B^V	m^V
Liquid	m_A^L	m_B^L	m^L
	m_A	m_B	m_{tot}

$\cdot/m_{tot}$

	Comp. A	Comp. B	
Vapor	z_A^V	z_B^V	Q
Liquid	z_A^L	z_B^L	$1-Q$
	z_A	z_B	1

Figure 2.2: Composition of a binary mixture.

$$\begin{cases} m_A^V + m_A^L + m_B^V + m_B^L = m_{tot} \\ m_A^V + m_A^L = m_A \\ \dfrac{m_B^L}{m^L} m_A^L - \dfrac{m_A^L}{m^L} m_B^L = 0 \\ \dfrac{m_B^V}{m^V} m_A^V - \dfrac{m_A^V}{m^V} m_B^V = 0 \end{cases} \tag{2.1}$$

$$\Longleftrightarrow \begin{cases} z_A^V + z_A^L + z_B^V + z_B^L = 1 \\ z_A^V + z_A^L = z_A \\ (1 - x_A) z_A^L - x_A z_B^L = 0 \\ (1 - y_A) z_A^V - y_A z_B^V = 0 \end{cases} \tag{2.2}$$

Two variables have been defined in the system of equations 2.2: the mass fraction of component A in the liquid phase $x_A = m_A^L / m^L = 1 - x_B$ and the mass fraction of component A in the vapor phase $y_A = m_A^V / m^V = 1 - y_B$, also called liquid and vapor phases compositions, respectively. Those two newly defined variables are intensive variables of the system. Gibb's phase rule allows to define the number of intensive properties required for a system to be fully determined[1] (de Hemptinne 2012). This number is given by

$$\mathcal{F} = \mathcal{N} - \phi_p + \mathbf{2} - \mathcal{R} \tag{2.3}$$

where $\mathcal{N}$ defines the number of components in the system, ϕ_p, the number of phases and $\mathcal{R}$ the number of constraints (critical point, azeotropy). For a single-phase binary mixture, this number ($\mathcal{F}$) is equal to three, while in two-phase, it reduces to two. Consequently, the newly defined intensive properties x_A and y_A can be obtained based on the pressure and temperature only in two-phase, while, in single-phase, they are independent of the temperature and pressure and the global composition z_A is required to fully determine the system. At a given temperature, varying x_A would thereby define the bubble pressure curve, whereas varying y_A defines the dew pressure curve, as can be seen in Figure 2.3. The bubble curve, where evaporation initiates and vapor quality begins to rise, can thus be distinguished from the dew point curve, which corresponds to the complete evaporation of the mixture, typically achieved through an increase in temperature or a reduction in pressure. The properties of the phases within the region between the dew and bubble curves (the L+V zone) can thus be determined using two intensive variables, while a third intensive variable, such as the overall composition z_A, is required in the pure liquid (L) or vapor (V) zones.

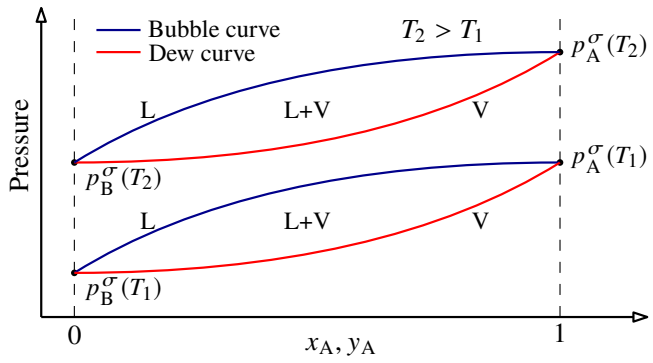

Figure 2.3: $p - x - T$ diagram of a conventional binary mixture.

To fully determine the state of the mixture (i.e., the distribution of both components in the phases), the system of equations 2.3 can be solved for z_A^V, z_A^L, z_B^V and z_B^L, as z_A, x_A and y_A are known. The results can be found in Equations 2.4. The vapor quality Q can finally be derived with Equation 2.5, also known as the lever rule, that can be applied on a $p - x - T$ or

[1] With Gibb's phase rule, the phases of a system can be fully determined in terms of thermophysical properties, however, the mass distribution among the phases requires knowledge of a global property of the mixture, such as the vapor quality.

$T - x - p$ diagram. This relation explicitly shows the dependence of the vapor quality of a binary mixture on the temperature, the pressure and the global mass fraction.

$$\begin{cases} z_{\mathrm{A}}^{V} = \dfrac{x_{\mathrm{A}} y_{\mathrm{A}} - y_{\mathrm{A}} z_{\mathrm{A}}}{x_{\mathrm{A}} - y_{\mathrm{A}}} \\ z_{\mathrm{A}}^{L} = \dfrac{-x_{\mathrm{A}} y_{\mathrm{A}} + x_{\mathrm{A}} z_{\mathrm{A}}}{x_{\mathrm{A}} - y_{\mathrm{A}}} \\ z_{\mathrm{B}}^{V} = \dfrac{-x_{\mathrm{A}} y_{\mathrm{A}} + x_{\mathrm{A}} + y_{\mathrm{A}} z_{\mathrm{A}} - z_{\mathrm{A}}}{x_{\mathrm{A}} - y_{\mathrm{A}}} \\ z_{\mathrm{B}}^{L} = \dfrac{x_{\mathrm{A}} y_{\mathrm{A}} - x_{\mathrm{A}} z_{\mathrm{A}} - y_{\mathrm{A}} + z_{\mathrm{A}}}{x_{\mathrm{A}} - y_{\mathrm{A}}} \end{cases} \tag{2.4}$$

$$Q = \frac{m^{V}}{m_{\mathrm{tot}}} = z_{\mathrm{A}}^{V} + z_{\mathrm{B}}^{V} = \frac{x_{\mathrm{A}} - z_{\mathrm{A}}}{x_{\mathrm{A}} - y_{\mathrm{A}}} = f(z_{\mathrm{A}}, p, T) \tag{2.5}$$

A binary mixture typically exhibits zeotropic behavior, meaning that the compositions of the vapor and liquid phases change during evaporation and condensation, i.e., the two components evaporate and condense at different rates. Usually, for asymmetric mixtures (different molecule sizes or asymmetric in energy), the more volatile component (lower molecule size) tends to evaporate faster than the heavier component. Moreover, this kind of mixture also exhibits temperature glide, i.e., the phase change occurs along with a temperature change.

2.2.2 Case of an oil-refrigerant mixture

An oil-refrigerant mixture is a binary mixture where component A is refrigerant, represented by the subscript r, and component B is oil, represented by o. In oil-refrigerant mixtures, the dew curve is usually not reachable, as the high temperature required would imply oil degradation. In fact, the saturation pressure at room temperature of an oil is extremely low (Scialdone et al. 1996), which explains the need for very high temperatures to vaporize this oil. Therefore, the dew curve does not exist ($y_r = 1$ and $y_o = 0$), and only the bubble curve is usually represented on diagrams. As a consequence, only the refrigerant is assumed to be found in the vapor phase, and the oil never evaporates. This kind of mixture, where a high difference in molecule size is met, is classified as a type III system according to the classification of van Konynenburg et al. (1980). This behavior cannot be classified as a zeotropic behavior, as only the refrigerant evaporates. However, the presence of oil introduces a temperature glide during the phase change. For example, the higher the vapor quality, the greater the difference between the evaporation temperature and the saturation temperature of the pure refrigerant at the given bubble pressure. An apparent refrigerant superheat is therefore created. An example of $p - x - T$ diagram of one of the oil-refrigerant mixtures studied in the context of this thesis can be found in Figure 2.4. As can be seen, all the iso-temperature curves seems to start from a zero pressure to reach the saturation pressure at $x_{\mathrm{r}} = 1$ (no oil at all). When the pressure and the temperature of the diagram are fixed and if the state is two-phase, x_{r} can be determined from the bubble curve, if the state is liquid, then x_{r} is equal to the global composition z_{r}. Applying Equation 2.5 to get the global vapor quality of the oil-refrigerant mixture gives

$$Q = \frac{x_{\mathrm{r}} - z_{\mathrm{r}}}{x_{\mathrm{r}} - 1} < z_{\mathrm{r}} = 1 - z_{\mathrm{o}} \tag{2.6}$$

The vapor quality will always be lower than the overall refrigerant mass fraction, since the oil remains entirely in the liquid phase (Thome 1995). A refrigerant-only vapor quality Q_{r}, ranging between 0 and 1, can be defined as (referring to Figure 2.2 and Equation 2.4)

$$Q_{\mathrm{r}} = \frac{m_{\mathrm{r}}^V}{m_{\mathrm{r}}} = \frac{m^V}{m_{\mathrm{r}}} = \frac{z_{\mathrm{r}}^V + z_{\mathrm{o}}^V}{z_{\mathrm{r}}} = \frac{Q}{z_{\mathrm{r}}} \tag{2.7}$$

which results in the global vapor quality divided by the refrigerant mass fraction. The maximum value of this refrigerant-only vapor quality is theoretically 1, however, this would imply an infinitely high temperature or a pressure approaching zero.

As already mentioned, the liquid mass fraction of refrigerant is a function of the pressure and the temperature (see Figure 2.4), a direct link between the global vapor quality and the apparent superheat (defined as $SH = T - T_{\mathrm{r}}^{\sigma}(p)$) can therefore be made as follows (Dickes 2019)

$$Q(p, T, z_{\mathrm{r}}) = \frac{x_{\mathrm{r}}(p, T) - z_{\mathrm{r}}}{x_{\mathrm{r}}(p, T) - 1} = \frac{x_{\mathrm{r}}(p, SH) - z_{\mathrm{r}}}{x_{\mathrm{r}}(p, SH) - 1} = Q(p, SH, z_{\mathrm{r}}) \tag{2.8}$$

The vapor quality can thus be determined as a function of the apparent superheat at a fixed pressure for different refrigerant mass fractions, as illustrated in Figure 2.5. Experimentally, this means that the vapor quality can be determined from temperature and pressure measurements alone, provided that the oil mass fraction is known. Moreover, the higher the oil mass fraction, the higher the dependence between the vapor quality and the superheat. At low oil mass fractions, the sensitivity of the vapor quality to the apparent superheat is huge, implying that a small error in the apparent superheat measurement would totally over- or under-predict the vapor quality. Finally, this relation will be used in the following chapters to help improve the accuracy of the experimental data obtained on two-phase compression. An interesting point to highlight is that, as can be observed at the bottom of Figure 2.5, a minimum apparent superheat is required to obtain a non-zero vapor quality. In other words, even in the presence of an apparent superheat, the mixture can still be entirely liquid.

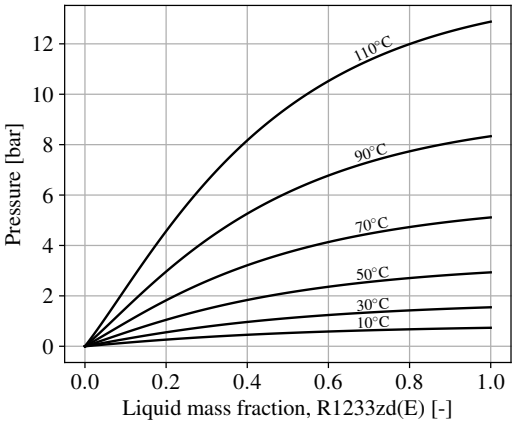

Figure 2.4: $p-x-T$ diagram of an oil-refrigerant mixture.

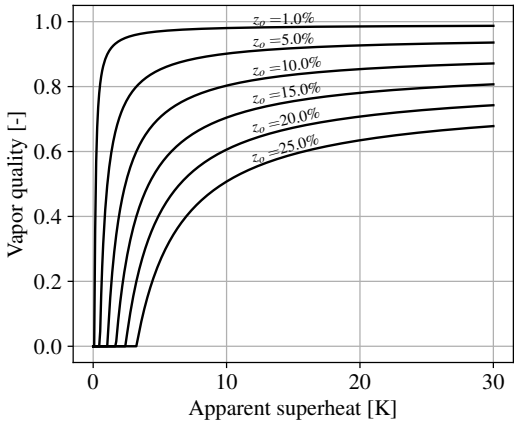

Figure 2.5: Q-SH-z diagram of an oil-refrigerant mixture at 1.5 bar (T_{r}^{σ} = 29.1°C).

2.2.3 Liquid viscosity of an oil-refrigerant mixture

In lubricated compressors, the viscosity of the liquid phase plays an important role in determining the longevity and efficiency of the machine. The lubricating oil must have the right viscosity to form a stable film between moving parts, reducing wear and preventing metal-to-metal contact. At the same time, it should flow well enough to carry heat away from bearings, pistons, or rotors and ensure proper circulation. Usually, when an oil-refrigerant mixture exhibits high solubility behaviors, or equivalently, when the presence of refrigerant in the liquid phase is important and it decreases its viscosity, higher-viscosity-grade oils are

employed (Ossorio et al. 2021). The liquid-phase viscosity of a two-phase oil-refrigerant mixture must therefore be analyzed to ensure proper lubrication of the machine.

As stated in Section 2.2.2, the vapor quality can be expressed as a function of the liquid phase composition, dependent on the temperature and the pressure, and the oil mass fraction. Conversely, the refrigerant liquid phase composition can be expressed as a function of the oil mass fraction and the vapor quality. Converting Equation 2.8 gives

$$x_{\mathrm{r}} = \frac{1 - z_{\mathrm{o}} - Q}{1 - Q} \tag{2.9}$$

This equation is illustrated in Figure 2.6. As can be expected, at higher oil mass fractions, the refrigerant liquid composition decreases. At the minimum oil mass fraction of 1%, the liquid phase is composed almost exclusively of refrigerant over the entire vapor quality range. Therefore, increasing the oil mass fraction allows to increase the oil mass fraction in the liquid phase. This effect could be justified by the increase of maximum vapor quality, as the higher the oil mass fraction, the lower the maximum vapor quality reachable. However, even when expressed as a function of the refrigerant-only vapor quality (Q_{r}), the effect is still observed, as represented in Figure 2.7. At constant refrigerant vapor quality, increasing the global oil mass fraction consequently increases the oil composition in the liquid phase, which is required to increase the liquid-phase viscosity.

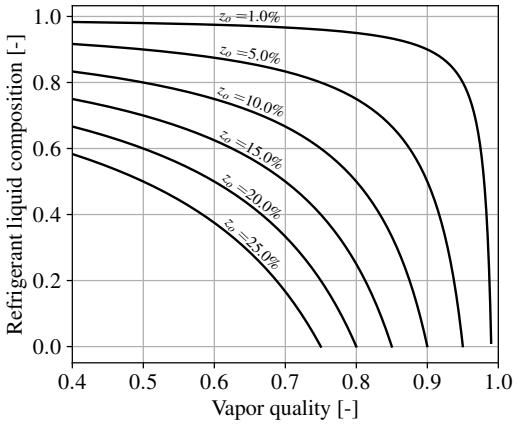

Figure 2.6: Refrigerant liquid phase composition as a function of the vapor quality at different oil mass fractions.

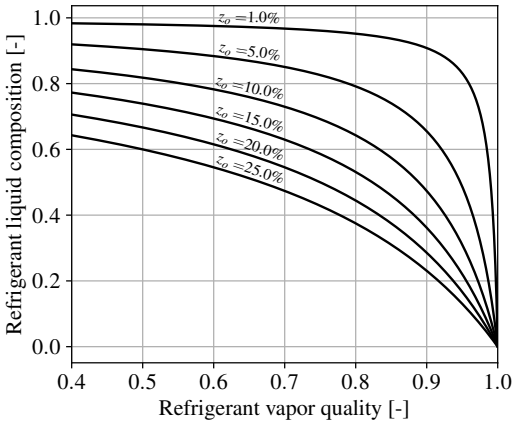

Figure 2.7: Refrigerant liquid phase composition as a function of the refrigerant vapor quality at different oil mass fractions.

The liquid phase viscosity of the first studied oil-refrigerant mixture can be found in Figure 2.8 and 2.9, respectively expressed as a function of the global and refrigerant vapor qualities. The modeling technique employed to determine the viscosity is presented in the next section. As expected, the liquid-phase viscosity is strongly impacted by the vapor quality of the mixture. Despite the oil mass fraction decreasing reasonably with the decrease in refrigerant vapor quality, the viscosity drop is important. Below the refrigerant vapor quality of 0.8, the liquid-phase viscosity remains under 5 mPa·s and appears to reach a plateau, where the refrigerant viscosity predominates. At a vapor quality of 0.5, the viscosity stands between 0.5 and 2 mPa·s, according to the literature, such low viscosity could be harmful for the machine. Moreover, viscosity tends to drop with the increase in temperature brought by the compression. Therefore, it is clear that, even by increasing the oil mass fraction, the viscosity does not reach typical values experienced in compressors. However, the higher quantity of liquid circulating in the machine could help in bringing a sealing and cooling effect. The experimental response of the machine under these conditions will be discussed in the following chapter.

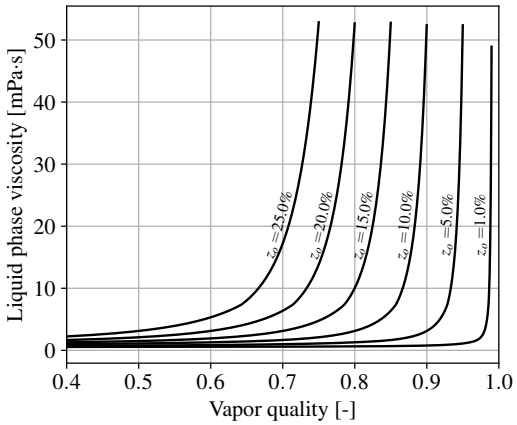

Figure 2.8: Liquid phase viscosity composition as a function of the vapor quality for a temperature of 20°C at different oil mass fractions.

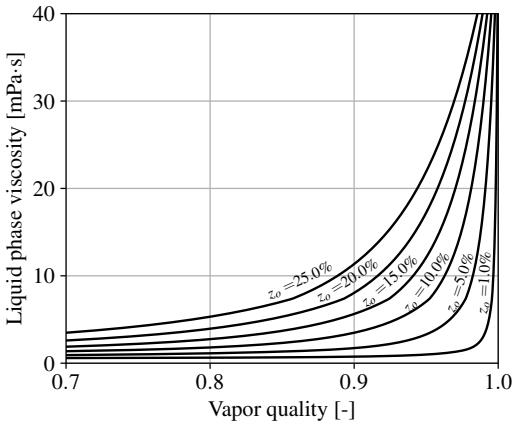

Figure 2.9: Liquid phase viscosity composition as a function of the refrigerant vapor quality for a temperature of 20°C at different oil mass fractions.

2.3 Thermophysical properties modeling

The binary mixture previously defined allowed to understand the behavior of an oil-refrigerant mixture. Based on this understanding, the thermophysical properties of the studied oil-refrigerant mixtures can now be established. Therefore, this section constitutes the core of the chapter, as the calculation of mixture properties represents a key element for the subsequent modeling work. It first presents the experimental investigations performed on the two oil-refrigerant mixtures employed, i.e., the refrigerant HCFO R1233zd(E) mixed with the oil Emkarate RL32 MAF and the oil mixture 39% of Emkarate MAF with 61% of Petronas POE40, in mass. Then, a subsection is dedicated to the modeling of the mixture solubility or VLE, followed by density, viscosity and other transport properties. Afterwards, the presented models are validated and compared. Finally, the enthalpy and entropy of the mixture are determined, and pressure-enthalpy as well as temperature-entropy diagrams are derived.

The solubility of a mixture is the equilibrium mass fraction of refrigerant dissolved in the liquid phase. It is strongly dependent on the temperature and the pressure of the mixture (at VLE). On the other hand, the mixture miscibility is defined as the ability of two or more liquids to dissolve into a single homogeneous liquid phase (Albatati 2015). If, under some conditions of temperature and pressure, two fluids are partially miscible, two liquid phases will form, resulting in a vapor-liquid-liquid-equilibrium (VLLE) and the composition of the two liquid phases can vary with the temperature and pressure. Miscibility will not be studied in the frame of this thesis, as the studied oil-refrigerant mixture did not exhibit this behavior; it has been checked visually.

The calculation of mixture properties usually requires pure fluid properties. The pure refrigerant thermophysical properties are computed using the abstract state class from CoolProp 6.4.3 (Bell et al. 2014), while pure oil thermophysical properties are calculated using the equations of Appendix A.2.

Some of the formulas presented in the subsequent sections use the liquid composition $\tilde{x}$, which is a mole fraction, while some others use the mass fraction liquid composition x. The conversion from one to another can be done with the following conversion equations introducing the molar mass of the mixture M_m:

$$M_\mathrm{m} = \frac{1}{\dfrac{x_\mathrm{r}}{M_\mathrm{r}} + \dfrac{(1 - x_\mathrm{r})}{M_\mathrm{o}}} \tag{2.10}$$

$$\tilde{x}_{\mathrm{r}} = x_{\mathrm{r}} \cdot \frac{M_{\mathrm{m}}}{M_{\mathrm{r}}} \tag{2.11}$$

where the molar mass of the oil has been assumed to be 300 g/mol for both mixtures studied. In Bruno et al. (2019), the molar mass of some POE ranges between 500 and 700 g/mol, however, in the model proposed by X. Yang et al. (2023), a value of 200 g/mol is proposed for a POE, according to the authors, this value does not impact the results of the models employed.

2.3.1 Experimental measurements

The experimental data used for this work have been collected using experimental setups from the Schaufler Chair of Refrigeration, Cryogenics and Compressor Technology of the Technische Universität Dresden. Two setups have been used: one for conducting vapor-liquid equilibrium measurements, i.e., for determining the bubble pressure of the mixture as a function of the liquid phase composition (x_{r}), and another for determining density and viscosity of the mixture in the liquid phase.

Vapor-liquid equilibrium

The liquid-vapor equilibrium experimental setup consists in some hand-made iso-volume units using glass tubes. The glass allows to measure the liquid height, and thus to deduce the volume taken by the vapor and to detect potential miscibility gaps. The objective is, for several oil-refrigerant liquid compositions, to measure the bubble point pressures as a function of the temperature. More information regarding this setup can be found in Stöckel et al. (2023). Four tubes filled with the mixture (known global composition) are placed inside a climate chamber allowing temperature regulation, as shown in Figure 2.10. Each tube is composed of a valve allowing the filling, and of two sensors to get the temperature and the pressure, as can be seen in Figure 2.11. The tubes need to be shaken every 5 minutes to reach a stable pressure equilibrium, using a shaft connecting them and providing access outside the chamber. Two to three hours are required to get 4 measurement points (from the four tubes) for a single temperature. The volumes of each four units are initially measured using pressurized nitrogen (the length of the pipe can vary from one another), however, the mass of the injected nitrogen being very low, a lot of uncertainty is faced as can be seen in Figure 2.12. Nevertheless, as this uncertainty only impacts the volume taken by the vapor phase (the liquid volume is directly measured through the glass), which has a negligible mass in comparison to the liquid, it does not consequently impact the final refrigerant liquid mass fraction determined.

The objective of this setup is therefore to link the liquid phase composition (x_{r}) with the measured pressure, for different global compositions (z_{r}) and different temperatures, to obtain a similar plot as Figure 2.4. The pressure is directly obtained from the sensor measurement, however, the composition of the liquid phase requires some calculations. First, the height of the liquid in the transparent tube can be visually obtained, allowing to figure out the liquid volume. The total volume of the unit being known, the vapor volume can be deduced. The vapor phase being only composed of refrigerant, the vapor density and thereby mass can be known from the temperature and pressure measurements. Given that the total refrigerant mass injected into the unit is known from using a mass scale, the mass of refrigerant present in the liquid phase can then be determined. The sensors used in this setup, along with their ranges and uncertainties, can be found in Table 2.1.

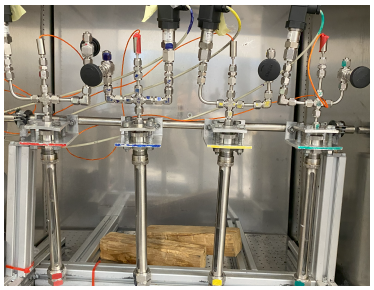

Figure 2.10: Tubes inside the climate chamber.

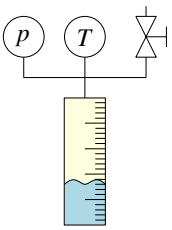

Figure 2.11: Representation of an isovolume unit.

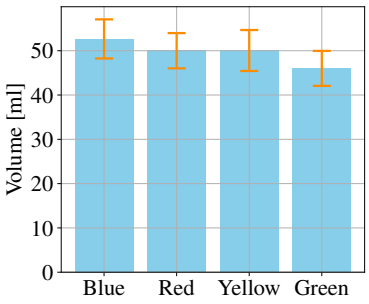

Figure 2.12: Volumes of the four units with uncertainties

Density and viscosity

The density-viscosity setup consists in a cycle placed inside a climate chamber using a pump to circulate the mixture. The cycle diagram can be found in Figure 2.13. The objective of this setup is to measure the liquid phase mixture properties (speed of sound, density, viscosity) for different temperatures set by the climate chamber. To vary the composition of the mixture, some oil or refrigerant can be added to the cycle until the maximum volume is reached. To obtain low refrigerant mass fractions, the setup was first filled with oil, and refrigerant was added little by little with a known mass in order to know the refrigerant mass fraction. On the contrary, for high refrigerant mass fractions, the refrigerant is added first, and the oil is added little by little, until reaching the maximum volume of the unit. Once again, the properties can directly be measured by the sensors of the setup, but the liquid phase composition has to be determined. In this case, however, no visual deduction can be made, but the liquid density is measured. Thereby, by knowing the total volume and mass of the setup and by knowing the densities of both phases, it is possible to deduce the liquid phase composition. The sensors used in this setup, along with their ranges and uncertainties, can be found in Table 2.1. The speed of sound meter details are not given here, as this property is not investigated.

1. Gear pump
2. Cambridge viscometers
3. Anton Paar densimeter
4. Anton Paar sound velocity meter
5. Pressure tank
6. 70 bar overpressure valve
7. Sight glass
8. Needle valve
9. High-pressure plug valve
10. Plug valve
11. Keller 50 bar pressure sensor
12. Temperature sensor Pt100
13. Climate chamber

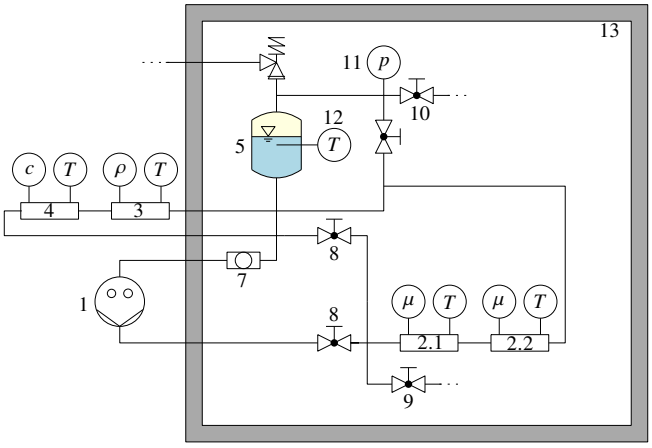

Figure 2.13: Diagram of the viscosity-density measurement setup

2.3.2 Mixture solubility modeling

Solubility models can be classified into two categories: empirical and thermodynamic approaches (Youbi-Idrissi 2003). Solubility models usually link the bubble pressure with the

Sensor	Equipment - Working principle	Range	Uncertainty
Scale	Kern PFB	0 - 3000 [g]	0.05 [g]
Temperature LV	PT100	-75 - 250 [°C]	0.5 [K]
Pressure LV	Keller PA-21y - Piezoresistive	0 - 25 [bara]	0.125 [bar]
Viscometer 1	Cambridge ViscoPRO 2100 - Piston	2.5 - 50 [mPa·s]	0.5 [mPa·s]
Viscometer 2	Cambridge ViscoPRO 2100 - Volumetric flask	0.25 - 5 [mPa·s]	0.05 [mPa·s]
Densimeter	Anton Paar L-DENS 7400 - Resonance frequency	0 - 3000 [kg/m^3]	0.1 [kg/m^3]

Table 2.1: Sensors used, range and standard uncertainties.

temperature and liquid phase composition, such as

$$p = f(x_r, T) \tag{2.12}$$

Empirical models are easy to use as they only require fitting empirical parameters to predict the pressure, without any pre-modeling. They can be reliable, although they are not based on any physical principle. Several equation shapes can be found (Mermond et al. 1999), from the Antoine Equation with variable coefficients A and B to modifications of Raoult's law, such as the Cavestri equation. Conversely, thermodynamic models are based on the equality of fugacity in the liquid and vapor phases for both components, which expresses the equality of the chemical potential and corresponds to the minimum Gibbs energy:

$$f_i^V = f_i^L \tag{2.13}$$

The vapor phase fugacity is usually calculated using a residual approach, using an equation of state. It is given by

$$f_i^V = \tilde{y}_i \phi_i^V p \tag{2.14}$$

where ϕ_i^V is the fugacity coefficient of the vapor phase for component i, calculated via the EoS. It is important to note the tilde on the vapor phase composition (y_i), indicating that it is a mole fraction and not a mass fraction as previously defined. The liquid phase fugacity can be calculated in two different ways. Using a residual approach, i.e., with an equation of state, the same expression as for the vapor phase can be written:

$$f_i^L = \tilde{x}_i \phi_i^L p \tag{2.15}$$

Using an equation of state to calculate the liquid-phase fugacity of an oil–refrigerant mixture can be challenging and may introduce inaccuracies (X. H. Han et al. 2010). In fact, equations of state are usually imprecise when used with macromolecular compounds and polar molecules. Moreover, the challenge resides in the need for detailed thermophysical data of the oil (critical pressure, temperature, acentric factor), which are difficult to obtain. Therefore, another approach is often used to calculate the liquid phase: the excess approach, also called the excess Gibbs energy approach. The expression of the fugacity thereby becomes

$$f_i^L = \gamma_i \tilde{x}_i \phi_i^\sigma p_i^\sigma \mathcal{P}_i \tag{2.16}$$

where γ_i is the activity coefficient, ϕ_i^σ the fugacity coefficient of component i at saturation and $\mathcal{P}$ is the Poynting correction.

Complete thermodynamic models take into account three kinds of non-idealities (Martz et al. 1994): vapor phase, liquid phase and mixture non-idealities. Vapor phase non-idealities are taken into account with a residual approach using the vapor fugacity coefficient (ϕ_i^V). This fugacity coefficient is usually determined through an equation of state. The liquid phase

non-ideality is also taken into account via a fugacity coefficient, but at saturation conditions (ϕ_i^σ). The Poynting correction ($\mathcal{P}_i$) accounts for the difference between the system pressure and the saturation pressure. It is calculated as

$$\mathcal{P}_i = \exp\left(\frac{1}{RT}\int_{p_i^\sigma}^{p} v_i^L \, dp\right) \approx \exp\left(\frac{v_i^L\left(p - p_i^\sigma\right)}{RT}\right) \tag{2.17}$$

where v_i^L is the liquid specific volume of component i at the temperature p in single-phase conditions.

Finally, the mixture non-ideality is expressed through the activity coefficient γ_i. When γ_i, ϕ_i^V, ϕ_i^σ and $\mathcal{P}_i$ are equal to unity, Equation 2.13, combined with Equations 2.14 and 2.16, reflects the behavior of an ideal solution of ideal gases. This equation, known as Raoult's law, is written as follows

$$\tilde{y}_i p = \tilde{x}_i p_i^\sigma \tag{2.18}$$

An ideal solution of real gases would take into account the gases and liquid non-idealities with the fugacity and the Poynting coefficients, Equation 2.13 then reduces to the Lewis-Randall rule, with only the activity coefficient deviating from unity. Finally, a non-unity activity coefficient expresses the non-ideal behavior of the mixture. An activity coefficient greater than unity suggests that intermolecular forces between similar species are stronger than those between dissimilar species; conversely, a coefficient less than unity implies stronger interactions between unlike molecules.

When modeling oil-refrigerant mixtures, three primary approaches are commonly employed: the empirical approach; the residual-residual approach, which uses Equations 2.14 and 2.15 to evaluate the fugacity in the vapor and liquid phases, respectively; and the residual–excess approach, in which Equation 2.16 is used to compute the fugacity of the liquid phase. Solubility modeling approaches of oil-refrigerant mixture from various authors in the literature have been gathered in Table 2.2. The residual approach using an equation of state is commonly employed to calculate the vapor phase fugacity. The Peng-Robinson (PR) equation of state (D.-Y. Peng et al. 1976) is widely used for this purpose, as applied by Youbi-Idrissi (2003), Neto et al. (2010), and Bock (2015) and many other authors in the literature. Among the other equations of state employed can be found the second order Virial development (X. Wang et al. 2021; Caramaschi et al. 2023; Jia et al. 2020), the Soave-Redlich-Kwong (SRK) (Soave 1972), employed by Albatati (2015) and the Patel-Teja-Valderrama (PTV) (Patel et al. 1982) employed by X. Yang et al. (2023). The SRK equation of state is usually employed with a 6-parameter mixing rule from Yokozeki (2007). According to de Hemptinne (2012), at a pressure under 5 bar, an ideal vapor phase behavior can be assumed ($\phi_i^V = 1$), this assumption was also made by X. H. Han et al. (2010). Comprehensive information on the application of cubic equations of state-such as the PR, SRK, and PTV models-can be found in Appendix A.1.

Regarding the excess approach, several activity coefficient models are usually employed, the most famous one is the Wilson model (Wilson 1964), which was later on modified to create the non-random two-liquid (NRTL) model (Renon et al. 1968), commonly used in oil-refrigerant mixture modeling. The latter has, for instance, been used by the following authors: Youbi-Idrissi (2003), X. Wang et al. (2021), X. H. Han et al. (2010), Caramaschi et al. (2023), Neto et al. (2008), Bock (2015), and Jia et al. (2020). A model combining the features of the Wilson and NRTL models has been proposed by Heil et al. (1966). This model has proven to be more accurate than other models for oil-refrigerant mixtures modeling, as can be seen in Table 2.2. The more rarely used Flory-Huggins (FH) (Tesser et al. 1999) is the only model that outperformed the Heil model, as shown by Neto et al. (2008). Another model, called

UNIQUAC, which requires knowledge of the structural characteristics of the oil molecules, was employed by Bock (2015), but it did not outperform the other models investigated. It is interesting to note that only a few studies considered the liquid-phase correction (Liq. corr. in Table 2.2) using the Poynting correcting factor.

Among the empirical approaches, lots of correlations can be found. For instance, a model with one single empirical parameter, based on Raoult's law, is proposed by Dawo et al. 2021. The Cavestri equation has been employed by Youbi-Idrissi (2003) and Stöckel et al. (2023) while other authors preferred to create their own correlations (Caramaschi et al. 2023; Zhelezny et al. 2007).

Regarding the solubility modeling precision in Table 2.2, it has been compared in terms of average relative deviation (ARD). The precision ranges from 0.4% to 15.27%; however, no clear correlation was observed between the models employed and the accuracy achieved. Moreover, no particular oil-refrigerant pair appears to align better with one model over another. Finally, the precision of the experimental data also plays its role in the reported accuracies, which does not simplify the analysis. Overall, it seems that most of the proposed approaches respond well to the solubility modeling of oil-refrigerant mixtures.

In this thesis, two of the proposed approaches will be applied to model the behavior of the oil-refrigerant mixtures used. First, the Cavestri equation (Cavestri 1995) will be applied and calibrated to the experimental dataset. This equation constitutes a modified Raoult's law, where 6 empirical parameters (a_1 to a_6) need to be fitted. Such an equation usually requires a lot of data to be accurate over a wide range of temperatures and refrigerant liquid molar fractions. The Cavestri equation can be found in Equation 2.19, where p_r^σ stands for the saturation pressure of the pure refrigerant at the given temperature. It is important to note that the refrigerant liquid fraction $\tilde{x}_r$ is a molar fraction. The bubble pressure from the Cavestri equation is given by

$$p(\tilde{x}_r, T) = \tilde{x}_r p_r^\sigma(T) + \tilde{x}_r \cdot (1 - \tilde{x}_r) \cdot (a_1 + a_2 T + a_3 T^2 + a_4 + a_5 \tilde{x}_r T + a_6 \tilde{x}_r T^2) \tag{2.19}$$

A thermodynamic model is also going to be employed and its results will be compared with the results of the Cavestri equation mentioned earlier. The approach is based on the methodology proposed by X. Yang et al. (2023), where the thermophysical properties of lubricants, considered as "pure entities" and their mixtures with refrigerants, are modeled. This model makes use of a small amount of experimental data (density, viscosity, thermal conductivity and heat capacity) of the "pure" lubricant to obtain the fluid constants (e.g., critical temperature) required in the PTV cubic equation of state (Patel et al. 1982; Valderrama 1990) and residual entropy scaling approaches (X. Yang et al. 2022; X. Yang et al. 2023). This approach is therefore allowing not only to get vapor-liquid equilibrium points, but to get a complete set of thermophysical properties and transport properties, and will therefore be used to predict the density and the viscosity as well. Details regarding the PTV equation of state, including the procedure for computing fugacities, are provided in the Appendix A.1.

2.3.3 Mixture density

Density is an intensive thermodynamic property defined as the mass of a given volume divided by this volume. For convenience in calculations, it is often preferable to use specific volume-the reciprocal of density-because its unit places kilograms in the denominator, making it easier to work with mass fractions when multiplying it. The specific volume of a two-phase oil-refrigerant mixture is calculated as a weighted sum of the vapor and liquid specific volumes. It is thus given by (Hughes et al. 1982)

Author	Approach(es)	Model(s) name(s)	Liq. corr.	Best results	Studied mixture(s)	Precision (ARD)
Youbi 2003	Correlation Res-Excess	Cavestri PR - Wilson, Heil, NRTL	Yes	Heil	R134a/POE R32/POE R125/POE	12.4% 6.6% 3.4%
Wang 2021	Res-Excess	Virial - NRTL	No		R290/3GS R290/4GS	1.93% 1.79%
Han 2010	Ideal-Excess	Ideal - NRTL, Wilson	No	NRTL	HFC-161/POE	2.5%
Brocus 2022	Res-Res	SRK - SRK	No		R32/POE80 R290/4GS R134a/POE80 R1336mzz(Z)/SE220 R1233zd(E)/SE220	2.5% 6.5% 1.9% 0.4% 0.88%
Caramaschi 2023	Correlation Res-Excess	Own Virial - NRTL	No	Correl.	Propylene/PAG DME/PAG	1.3% 4.3%
Stöckel 2023	Correlation	Cavestri	No		R152a/POE R744/POE R290/POE DME/POE	3.34% 15.27% 5.85% 4.10%
Neto 2008	Res-Res Res-Excess	PR - PR, Heil, F-H	Yes	F-H	R600a/POE	4.48%
Neto 2010	Res-Res	PR - PR	No		R600a/AB	8.01%
Neto 2014	Raoult, Res-Res	PR - PR	No	PR	R134a/POE R1234yf/POE	3.22% 3.53%
Bock 2015	Raoult, Res-Excess	PR - Wilson, Heil, NRTL, UNIQUAC	Yes	Heil	R1234ze(E)/POE	1.96%
Dawo 2021	Extended Raoult	Own	No		R245fa/POE R1233zd(E)/POE R1224yd(Z)/POE R1336mzz(Z)/POE	NA
Zhelezny 2007	Correlation	Own	No		R245fa/POE	[0.3-2.7]%
Albatati 2015	Res-Res	SRK - SRK	No		R744/POE	NA
Jia 2020	Res-Excess	Virial - NRTL	No		R1234yf/POE R1234ze(E)/POE	[0-4]%
Yang 2023	Res-Res	PTV - PTV	No		R290/PAG68	1.6%

Table 2.2: Solubility models of oil-refrigerant mixtures used in the literature. The approaches pattern is given by "vapor phase approach - liquid phase approach".

$$v_{\mathrm{m}} = Q \cdot v_{\mathrm{m}}^{V} + (1 - Q) \cdot v_{\mathrm{m}}^{L} \tag{2.20}$$

where the vapor phase specific volume v_{m}^{V} is taken as that of pure refrigerant vapor, while the liquid phase specific volume is calculated based on oil-refrigerant solution. To model this solution, an excess approach is generally used, as molecular interactions are strong in liquids. The specific volume can be calculated as

$$v_{\mathrm{m}}^{L} = (1 - x_{\mathrm{r}}) v_{\mathrm{o}}^{L} + x_{\mathrm{r}} v_{\mathrm{r}}^{L} + v^{E} \tag{2.21}$$

where v^{E} is the excess specific volume representing the deviation of the liquid volume from the ideal volume calculated as a weighted sum of the refrigerant and oil volumes. According to Wei et al. (2008), when the refrigerant density is bigger than the oil density, the excess volume can be neglected with reasonable deviations (3.8% of ARD for a R410a/POE mixture), this assumption has also been used by Mermond et al. (1999). Three main approaches are generally used in the literature to model the mixture density: application of an equation of state with a mixing rule (with or without correction) (Neto et al. 2008; X. Yang et al. 2023), use of Equation 2.21 and calculation of the excess volume (Neto et al. 2008) and empirical correlations (Zhelezny et al. 2007; Conde 1996; Medvedev et al. 2004; Barbosa et al. 2004).

Once again, the thermodynamic approach developed in X. Yang et al. (2023) will be applied to determine the density of the mixture, directly as an output of the PTV equation of state applied to the mixture. Moreover, Henderson (1994) proposes two correlations for both viscosity and density, for low ($< 30\%$) and high ($> 70\%$) refrigerant mass fractions and each of them uses 9 empirical parameters (from a_1 to a_9). In between 30% and 70%, a weighted average of the densities coming from both formulations can be applied. These correlations are also going to be calibrated in the frame of this thesis, and the results of both approaches will be compared. The two equations, respectively for low and high refrigerant liquid compositions, can be written as follows

$$\rho(x_{\mathrm{r}}, T) = [a_1 + a_2 T + a_3 T^2] + x_{\mathrm{r}}[a_4 + a_5 T + a_6 T^2] + x_{\mathrm{r}}^2 [a_7 + a_8 T + a_9 T^2] \tag{2.22}$$

$$\rho(x_{\mathrm{r}}, T) = [a_1 + a_2 T_{\mathrm{red}} + a_3 T_{\mathrm{red}}^2] + x_{\mathrm{r}}[a_4 + a_5 T_{\mathrm{red}} + a_6 T_{\mathrm{red}}^2] + x_{\mathrm{r}}^2 [a_7 + a_8 T_{\mathrm{red}} + a_9 T_{\mathrm{red}}^2] \tag{2.23}$$

where T_{red} is a reduced temperature defined as $T_{\mathrm{red}} = 1 - T/T_{\mathrm{r,c}}$.

2.3.4 Mixture viscosity

According to the literature, all the equations proposed to estimate the viscosity (dynamic or kinematic) of oil-refrigerant solution give unsatisfactory results (Conde 1996). The equation giving the least deviation is the following:

$$\ln \mu_{\mathrm{m}}^{L} = (1 - x_{\mathrm{r}}) \ln \mu_{\mathrm{o}}^{L} + x_{\mathrm{r}} \ln \mu_{\mathrm{r}}^{L} + \ln \mu^{E} \tag{2.24}$$

where the excess viscosity μ^{E} is often neglected (Mermond et al. 1999; Conde 1996). Neto et al. (2008) calculated the excess viscosity in two ways, showing acceptable accuracy (ARD $\approx 15\%$ for a R600a/POE mixture). Correlations can also be used to estimate the mixture viscosity; this has been done by numerous authors (Wei et al. 2008; Barbosa et al. 2004) with an R-square value higher than 0.9. Quiñones-Cisneros et al. (2005) use an interesting approach called the "f-theory", where the PR equation of state repulsive and attractive terms are calculated separately. These terms are used in a correlation using a mixing rule to obtain the parameters. Unfortunately, no information about the accuracy is given. X. Yang et al. (2022) use a residual entropy scaling (RES) technique to estimate the viscosity of mixtures,

where 3 or 4 parameters need to be fitted, linking the residual entropy of the mixture to its residual viscosity. However, while the RES technique is proving to be accurate for pure fluids, it still shows high relative errors (up to 300%) for a R290/POE mixture studied in X. Yang et al. (2023). Similarly to what is done for the mixture density, the thermodynamic approach developed in X. Yang et al. (2023) will be applied to determine the viscosity of the mixture. The methodology applied can be found in Appendix A.4. Moreover, Henderson (1994) empirical correlations is also applied, for low (< 30%) and high (> 70%) refrigerant liquid compositions, respectively:

$$\begin{aligned}\log_{10}(\log_{10}(\mu(x_\mathrm{r},T)+0.7)) = {} & [a_1 + a_2\log_{10}(T) + a_3\log_{10}^2(T)] \\ & + x_\mathrm{r}[a_4 + a_5\log_{10}(T) + a_6\log_{10}^2(T)] + x_\mathrm{r}^2[a_7 + a_8\log_{10}(T) + a_9\log_{10}^2(T)]\end{aligned} \tag{2.25}$$

$$\log_{10}(\mu(x_\mathrm{r},T)) = [a_1+a_2/T+a_3/T^2]+x_\mathrm{r}[a_4+a_5/T+a_6/T^2]+x_\mathrm{r}^2[a_7+a_8/T+a_9/T^2] \tag{2.26}$$

with T expressed in K and μ in mPa·s. In between liquid compositions of 30% and 70%, a weighted sum of both right-hand sides of Equations 2.25 and 2.26 is used, where the 0.7 term in Equation 2.25 is adjusted according to the liquid composition.

2.3.5 Other transport properties

In this subsection, other transport properties equations commonly used for oil-refrigerant mixtures are presented, i.e., the heat capacity, the thermal conductivity and the surface tension. Nevertheless, for those properties, no experimental validation is provided.

The specific heat capacity of the oil-refrigerant solution can be estimated using a simple weighted sum of the specific heat capacities from the pure fluids (Mermond et al. 1999)

$$c_{p,\mathrm{m}}^L = (1-x_\mathrm{r})c_{p,\mathrm{o}}^L + x_\mathrm{r}c_{p,\mathrm{r}}^L \tag{2.27}$$

In the vapor phase, the heat capacity is assumed to be that of the pure refrigerant.

Regarding the liquid thermal conductivity, Mermond et al. (1999), Conde (1996), and Wei et al. (2008) use the following equation:

$$\lambda_\mathrm{m}^L = (1-x_\mathrm{r})\lambda_\mathrm{o}^L + x_\mathrm{r}\lambda_\mathrm{r}^L - 0.72(\lambda_\mathrm{o}^L - \lambda_\mathrm{r}^L)(1-x_\mathrm{r})x_\mathrm{r} \tag{2.28}$$

Finally, the mixture surface tension is given by (Wei et al. 2008)

$$\sigma_\mathrm{m}^L = \sigma_\mathrm{r}^L + (\sigma_\mathrm{o}^L - \sigma_\mathrm{r}^L)x_\mathrm{r}^{0.51} \tag{2.29}$$

As already stated, the pure oil properties are calculated with the equations provided in Appendix A.2 and the pure refrigerant properties are retrieved from CoolProp 6.4.3 (Bell et al. 2014), except for the properties of R1233zd(E) that are not available in CoolProp 6.4.3 (i.e., thermal conductivity and surface tension), for which the calculations can be found in Appendix A.3.

2.3.6 Models validation

When modeling the thermophysical properties of oil-refrigerant mixtures, validation is essential to ensure accuracy. Two of the modeling approaches are therefore applied to the studied mixture: the thermodynamic modeling approach proposed by X. Yang et al. (2023) and empirical correlations proposed by Cavestri (1995) for the solubility, and by Henderson (1994)

for the viscosity and the density. Those two modeling approaches are compared based on several criteria: the accuracy, the number of experimental data required, the ability to predict other properties and the physical sense of the calibrated parameters. The comparison is based on the mixture of R1233zd(E) with the oil Emkarate RL32 only, but calibrated parameters are also provided for the other mixture in Appendix A.5.

Approach of X. Yang et al. (2023) (Thermodynamic model)

In the modeling approach proposed by X. Yang et al. (2023), the oil must be characterized as a pure fluid using the PTV equation of state and a residual entropy scaling approach for the viscosity (see Appendix A.4). Thereby, the following steps must be carried out:

- Get an estimation of the molar mass of the oil. No experimental data allowing to get the molar mass are available, the rough estimation $M_o = 300$ g·mol^{-1} will therefore be used.
- The critical compression factor must be fixed as usually, no good estimation can be obtained from experimental data. The recommended value is $Z_c = 0.2563$.
- The critical temperature and density must be determined using a modified Rackett equation (Equation 2.30). Two experimental density points of the pure oil can be used for that, if the temperature difference between the two points is large enough, which is the case. Then, the critical pressure can be deduced using the critical compression factor.

$$\rho = \rho_c Z_c^{-(1-\frac{T}{T_c})^{\frac{2}{7}}} \tag{2.30}$$

- One of the previously used density measurements can be reused in the PTV equation of state (see Appendix A.1) to get an estimation of the acentric factor ω.
- No experimental point allows to get the isobaric heat capacity. The density being known, it can be estimated using equation A.20.
- The estimation of the viscosity requires 4 pure oil viscosity data points. The four parameters used by the residual entropy scaling relation are therefore determined ($n_{\mu,k,o}$) for the pure oil.
- No thermal conductivity data has been collected, no fitting of the residual entropy scaling relation for the thermal conductivity can therefore be carried out.
- Finally, the interaction parameter (k_{ij}) used in the van der Waals mixing rule for the PTV equation of state can be determined using one or more mixture bubble point pressures of the oil and the refrigerant R1233zd(E).

After this procedure has been followed, the parameters of the pure oil are determined and can be found in Table 2.3. With those parameters, the PTV equation of state could be used to estimate the densities at the same temperatures as the collected experimental data. The relative deviation of the fitting can be found in Figure 2.14 for the density and in Figure 2.15 for the viscosity, where a good fitting is observed (relative deviation less than 2% for both the density and the viscosity).

As mentioned previously, the fitting of the binary interaction parameter only relies on the bubble point pressure data. By definition, this parameter can also influence the density computed with the equation of state. Nevertheless, as can be understood from Figure 2.16, the sensitivity of the density is relatively small compared to the viscosity, moreover, the diagram justifies the value of the binary interaction parameter, minimizing the Root Mean Square (RMS) of the relative error with the experimental data.

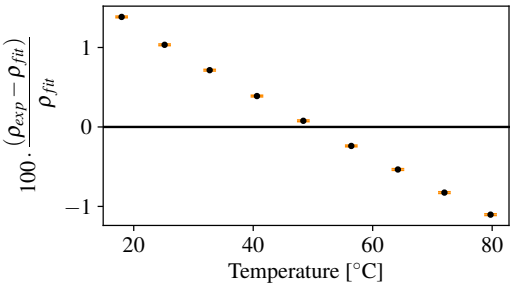

Figure 2.14: Relative error of experimental densities of POE RL32 from predictions of the model set with experimental uncertainties (orange bars).

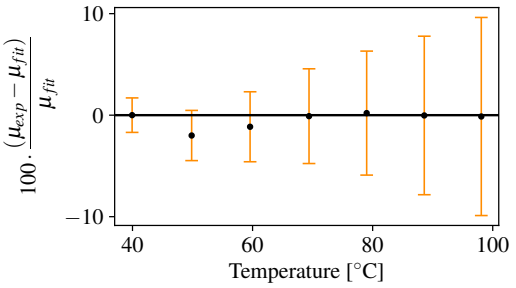

Figure 2.15: Relative error of experimental dynamic viscosities of POE RL32 from predictions of the model set with experimental uncertainties (orange bars).

M [g/mol]	T_c [K]	ρ_c [kg/m^3]	Z_c [-]	P_c [bar]	ω [-]	k_{ij}	$n_{\mu,1,o}$	$n_{\mu,2,o}$	$n_{\mu,3,o}$	$n_{\mu,4,o}$
300	733.29	304.56	0.2563	23.8	0.8033	0.008	0.2649	-0.1055	0.0217	0.0000

Table 2.3: Estimated parameters for the pure oil.

Empirical correlations

The fitting of each empirical correlation has been done by minimizing the sum of the absolute errors between the predictions and the experimental data. The parameters of the five equations 2.19, 2.22, 2.23, 2.25 and 2.26 have therefore been obtained. All the fitted parameter values can be found in Table 2.4. Furthermore, the empirical laws have been plotted in Figures 2.17, 2.18 and 2.19. These diagrams, in addition to showing the good fitting between the experimental data and the correlation predictions, allow to see the whole experimental data set collected. Regarding the bubble point pressure data, the range comprises temperatures from 10°C to 110°C with refrigerant liquid mass fraction from 15% to 95%. Regarding density and viscosity, fewer datapoints could be obtained. On the one hand, the range from 0% to 24.6% liquid refrigerant mass fraction could be covered by increasing the refrigerant mass little by little in the density-viscosity setup. On the other hand, the range from 100% to 94.2% liquid refrigerant mass fraction could be obtained by increasing the oil content. Unfortunately, no other valid data has been obtained with high refrigerant mass fractions due to a measurement problem.

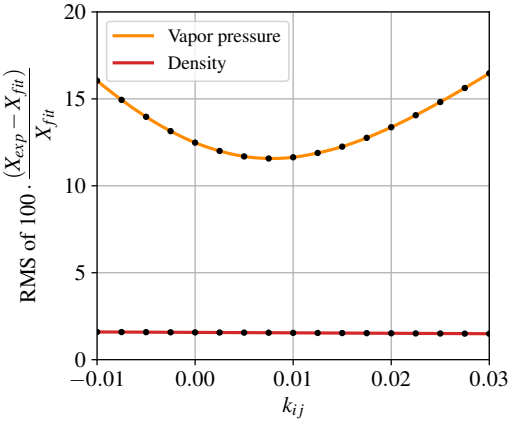

Figure 2.16: Sensitivity of the calculated density and bubble-point pressure with the binary interaction parameter k_{ij}.

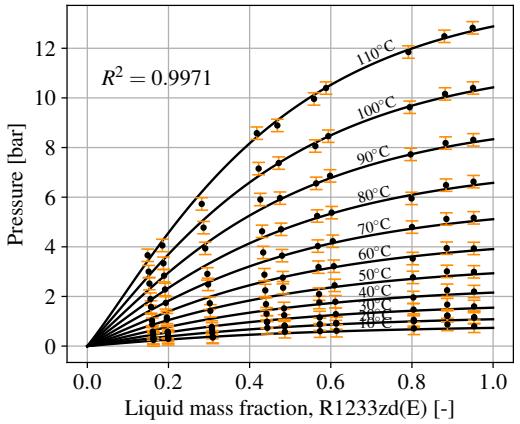

Figure 2.17: Vapor pressure predicted by the Cavestri equation and experimental data with uncertainties (orange bars).

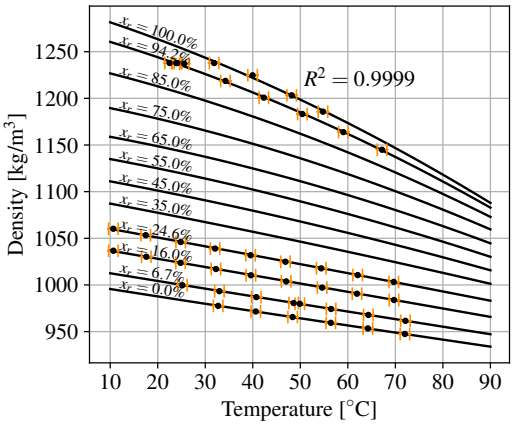

Figure 2.18: Mixture liquid phase density predicted by Henderson's equations and experimental data with uncertainties (orange bars).

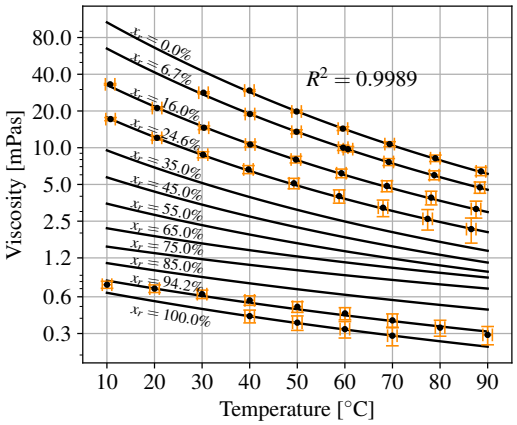

Figure 2.19: Mixture liquid phase dynamic viscosity predicted by Henderson's equations and experimental data with uncertainties (orange bars).

	Cavestri Vapor pressure	Henderson - ρ Low ref. frac.	Henderson - ρ High ref. frac.	Henderson - μ Low ref. frac.	Henderson - μ High ref. frac.
a_1	$-4.81 \cdot 10^{-12}$	$1.25 \cdot 10^{3}$	$-1.14 \cdot 10^{3}$	$-2.51 \cdot 10$	$-1.94 \cdot 10^{-1}$
a_2	$-3.36 \cdot 10^{-9}$	$-9.70 \cdot 10^{-1}$	$5.79 \cdot 10^{3}$	$2.37 \cdot 10$	$2.00 \cdot 10^{2}$
a_3	$-2.04 \cdot 10^{-6}$	$3.07 \cdot 10^{-4}$	$2.90 \cdot 10^{3}$	-5.45	1.25
a_4	$4.18 \cdot 10^{-11}$	$1.73 \cdot 10^{2}$	$3.76 \cdot 10^{2}$	-4.14	$-2.83 \cdot 10^{-1}$
a_5	$1.42 \cdot 10^{-8}$	$9.63 \cdot 10^{-1}$	$3.01 \cdot 10^{2}$	4.75	$1.89 \cdot 10^{2}$
a_6	$4.74 \cdot 10^{-6}$	$-2.46 \cdot 10^{-3}$	$-6.39 \cdot 10^{2}$	-1.36	1.18
a_7	/	$3.13 \cdot 10^{1}$	$1.83 \cdot 10^{3}$	$2.79 \cdot 10^{-1}$	-1.7167
a_8	/	$6.36 \cdot 10^{-1}$	$-4.96 \cdot 10^{3}$	2.20	$1.79 \cdot 10^{2}$
a_9	/	$-1.93 \cdot 10^{-3}$	$-4.09 \cdot 10^{3}$	-1.05	1.12

Table 2.4: Empirical parameters of the Cavestri/Henderson equations.

Comparison between the two models

In this section, the accuracy of both models is going to be compared. Graphs of relative errors and R^2 fitting indicators resulting from the thermodynamic approach of X. Yang et al. (2023) and from the empirical correlations are used to compare both modeling techniques. Moreover, experimental uncertainties are added to the relative error calculations in order to check if these deviations can be explained by sensors inaccuracy or by the models themselves.

First, the vapor pressure relative deviations of both models can be found in Figures 2.20 and 2.21, and, as can be observed, the graphs are very similar and the same goes for the R^2 indicators. An increase of the relative error is noticeable for low temperatures (i.e., < 50°C), where the pressures are low (< 2.5 bar according to Figure 2.17), moreover, the uncertainty also increases for low temperatures due to this low pressures as the absolute uncertainty of the pressure sensors is getting closer to the measured values. Therefore, the high relative errors of both models' predictions could probably come from inaccurate measurements of the bubble point pressures.

Second, as can be seen in Figures 2.22 and 2.23, the density predictions of the thermodynamic model are good, with less than 3.5% of relative deviation, while the empirical model predicts the densities with an almost perfect fitting (R^2 = 0.9999). The measurement uncertainties do not influence the relative deviations in this case. Although a noticeable difference in accuracy can be observed between both models, it is important to keep in mind

that the density prediction of the thermodynamic model only relies on a few pure oil fitted semi-empirical parameters, while the empirical correlations of Henderson, rely on 18 purely empirical parameters to be fitted in total (9 parameters for both low and high refrigerant liquid compositions).

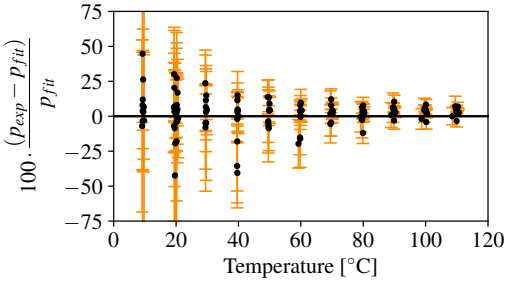

Figure 2.20: Relative error of the vapor pressure prediction from the PTV equation of state with experimental uncertainties (orange bars) (R^2 = 0.9944).

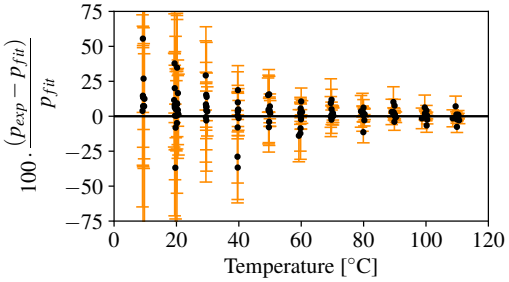

Figure 2.21: Relative error of the vapor pressure prediction from the Cavestri equation with experimental uncertainties (orange bars) (R^2 = 0.9971).

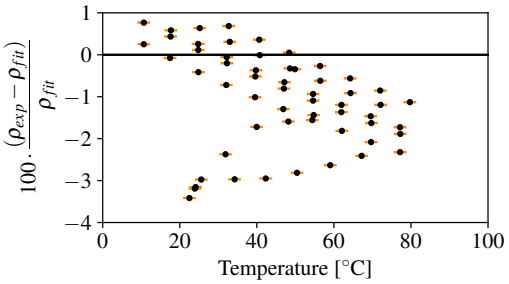

Figure 2.22: Relative error of the density prediction from the PTV equation of state with experimental uncertainties (orange bars) (R^2 = 0.9617).

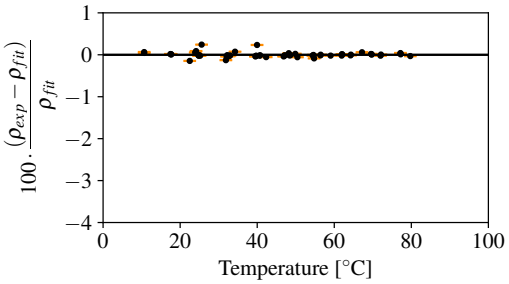

Figure 2.23: Relative error of the density prediction from the Henderson equation with experimental uncertainties (orange bars) (R^2 = 0.9999).

Finally, the relative deviations of the viscosity can be found in Figures 2.24 and 2.25. As can be observed, the predictions of the thermodynamic model are very bad (more than 50% of relative deviation for some points), while those of the Henderson empirical equations are good (less than 5%). High measurement uncertainties are faced for the viscosity, however, seeing the low relative deviations of the empirical correlation and the uncertainty ranges, which are far from the zero line for the thermodynamic model, the uncertainty is certainly not the cause of those high relative deviations. Moreover, as stated in X. Yang et al. (2023), viscosity prediction does not work well for strongly asymmetric mixtures, i.e., when the molecule sizes of the two components are very different, which is usually the case for oil-refrigerant mixtures.

In general, the comparison between both models clearly shows the superior performance of the empirical modeling techniques in terms of accuracy, setting aside the possibility of overfitting. However, it is important to highlight other aspects of the modeling techniques, as in some cases, accuracy is not always what matters the most. Firstly, in this specific scenario, a large amount of experimental data was collected, which allowed a very precise calibration of the empirical equations employed. With less data, such good calibration would not have been possible, whereas the fitting of the thermodynamic model would have been similar, as it mainly relies on pure fluid properties and can provide good fitting with a low number of experimental data. Secondly, except for the viscosity, the prediction of the thermodynamic

model remains accurate. The accuracy is relative to what the predictions are needed for. Obtaining perfect predictions of thermodynamic properties is sometimes unnecessary when it is combined with other sources of uncertainties that propagate in the final results obtained. The most important and final argument towards thermodynamic modeling techniques is the sense of physics behind those models. In particular, the parameters fitted for the pure oil have a physical sense. For instance, the critical point coordinates do have a meaning, even though it is not possible to measure them due to oil degradation with the high temperatures involved. The thermodynamic model, moreover, allows to predict many different properties with one single model using correlated mechanisms, such as the residual entropy scaling technique for viscosity.

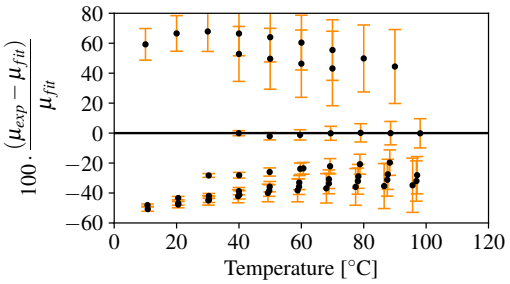

Figure 2.24: Relative error of the dynamic viscosity prediction from the RES with experimental uncertainties (orange bars) ($R^2 = 0.1910$).

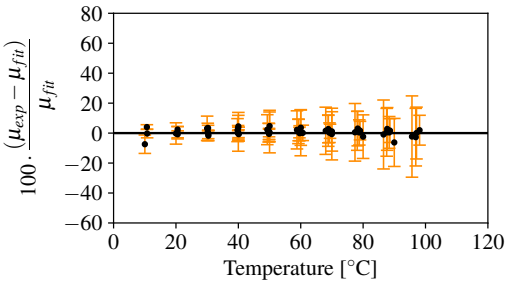

Figure 2.25: Relative error of the dynamic viscosity prediction from the Henderson equation with experimental uncertainties (orange bars) ($R^2 = 0.9989$).

2.3.7 Mixture enthalpy and entropy

When in a two-phase state, oil-refrigerant mixtures' specific enthalpies and entropies are calculated with a vapor quality weighted sum of the phases' properties. For instance, the specific enthalpy is written as (Hughes et al. 1982)

$$h_{\mathrm{m}} = Q \cdot h_{\mathrm{m}}^{V} + (1 - Q) \cdot h_{\mathrm{m}}^{L} \tag{2.31}$$

Once again, the vapor phase specific enthalpy is assumed to be that of pure refrigerant, while the liquid phase enthalpy is that of an oil-refrigerant solution, calculated as

$$h_{\mathrm{m}}^{L} = x_{\mathrm{r}} \cdot h_{\mathrm{r}}^{L} + (1 - x_{\mathrm{r}}) \cdot h_{\mathrm{o}}^{L} + h^{E} \tag{2.32}$$

where h^E is the excess enthalpy of the solution. Medvedev et al. (2004) has calculated this excess enthalpy for an R134a/Arctic22(oil) mixture and has found a maximum absolute value reaching 0.9 kJ/kg, which is negligible compared to an average vaporization enthalpy of 150 kJ/kg. According to Youbi-Idrissi et al. (2003), the enthalpies of refrigerant for both the vapor and the liquid phases should be taken at saturation. However, if an apparent superheat is met, for instance, when having a non-negligible oil mass fraction and a high vapor quality, the vapor phase enthalpy should be calculated at the vapor conditions, i.e., at the mixture pressure and temperature. Eventually, the two-phase mixture enthalpy can be calculated as

$$h_{\mathrm{m}}(p,T) = Q h_{\mathrm{r}}^{V}(p,T) + z_{\mathrm{o}} h_{\mathrm{o}}(T) + (1 - Q - z_{\mathrm{o}}) h_{\mathrm{r}}^{L,\sigma}(T) \tag{2.33}$$

where the liquid refrigerant is always taken at saturation conditions, as indicated by the σ symbol. Calculating the mixture enthalpy thereby requires knowing the pressure, the temperature, which can be used to calculate the vapor quality using Equation 2.8, while the oil mass fraction is supposed to be known. The same procedure can be used to calculate the

entropy of the mixture. When combining property models from different sources, reference-state consistency is required to obtain a valid mixture property model. In the case where only energy balance are applied, the reference state consistency does not matter, even when the composition of the mixture changes.

Temperature-entropy and pressure-enthalpy diagrams can finally be plotted. To compare both diagrams with that of the pure refrigerant, only the refrigerant enthalpies will be plotted. Therefore, on the one hand, pure-refrigerant properties are plotted; on the other hand, refrigerant-only properties within the mixture are plotted. Adding the oil contribution to the mixture's specific enthalpy/entropy does not actually bring much information to the plot. The difference between the pure refrigerant and the mixture specific enthalpy/entropy is going to increase with the increase of vapor quality because the oil does not evaporate, resulting in an overall lower mixture specific enthalpy/entropy as can be observed in p-h diagrams of X. Wang et al. (2021) and Youbi-Idrissi et al. (2003). Moreover, plotting the mixture specific enthalpy/entropy on the diagrams requires an adjustment of the reference enthalpy for the oil to get the best comparison possible. The reference enthalpy/entropy of the oil will therefore be set at the same value as the refrigerant (R1233zd(E)) in CoolProp (Bell et al. 2014), at the reference pressure and temperature. The following equation is used, with the enthalpy as an example, to compute the refrigerant enthalpy within the mixture:

$$h_r = Q_r h_r^V + (1 - Q_r) h_r^L \tag{2.34}$$

$$= \frac{Q}{1 - z_o} h_r^V + \left(1 - \frac{Q}{1 - z_o}\right) h_r^L \tag{2.35}$$

$$= \frac{Q}{1 - z_o} h_r^V + \frac{1 - Q - z_o}{1 - z_o} h_r^L \tag{2.36}$$

$$= \frac{h_m - z_o h_o}{1 - z_o} \tag{2.37}$$

In Equation 2.34, the refrigerant enthalpy is expressed as a function of the pure-refrigerant vapor quality, previously defined in Equation 2.7. Finally, the pure-refrigerant enthalpy can be expressed as a function of the mixture enthalpy and oil mass fraction only. Representing the refrigerant enthalpy contribution in the mixture is useful in order to verify coherence with a pure refrigerant when the mixture is liquid or highly superheated, i.e., if the refrigerant is in the vapor phase only. Equation 2.37 can also be applied to the refrigerant entropy to derive the Temperature-entropy diagram.

Temperature-entropy and pressure-enthalpy diagrams with an oil mass fraction of 10% can be found in Figures 2.26 and 2.27. A first observation to be made is the fact that the bubble point curves seem to be the same for the mixture refrigerant as for the pure refrigerant. It is actually not the case; a slight deviation can be seen, for instance, on the p-h diagram on the 20°C iso-T line that starts at a lower pressure than the pure-refrigerant iso-T. Regarding the dew line, it does not exist for the mixture, as the oil theoretically never evaporates. The maximum vapor quality that can be reached by the mixture is therefore 0.9, which would result in a liquid phase full of oil and a vapor phase containing all the refrigerant, nonetheless, those conditions can be approached only at a high temperature or a low pressure. Thus, when an iso-p line/iso-T line is followed at a high temperature/pressure, the vapor quality converges towards the maximum vapor quality reachable, i.e., 0.9. In that case, the pure-refrigerant and the mixture refrigerant curves start to overlap, which can be explained by the pure-refrigerant vapor quality reaching one, i.e., the vapor phase contains all the refrigerant. When following an increase in vapor quality, the detachment point between the pure-refrigerant and the mixture refrigerant iso-property lines is a function of the oil global mass fraction. Having a 10% oil mass fraction is uncommon in refrigeration systems; the behavior presented here is therefore

not typical. At lower oil mass fractions, the detachment point would occur closer to the dew point line of the pure refrigerant, resulting in a more complete evaporation at constant temperature and pressure before detachment. Finally, these kinds of diagrams, and especially the definition of the mixture enthalpy and entropy, will help to understand principles regarding two-phase compression and therefore provide a basis for the understanding of the upcoming chapters.

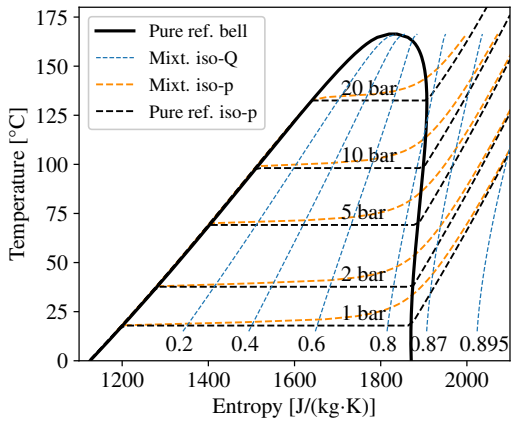

Figure 2.26: R1233zd(E)/RL32 temperature-entropy diagram with an oil mass fraction of 10%.

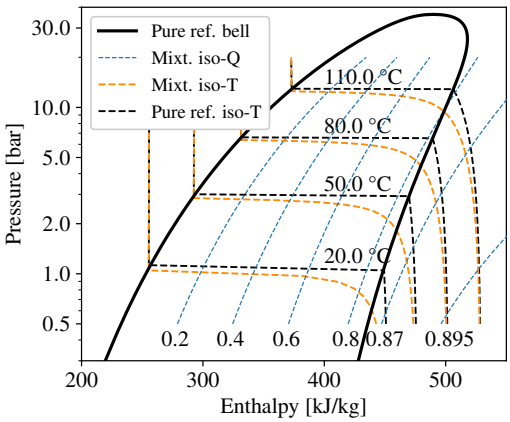

Figure 2.27: R1233zd(E)/RL32 pressure-enthalpy diagram with an oil mass fraction of 10% (enthalpy from Equation 2.37).

2.4 Model applications

To conclude this chapter, some applications of the oil-refrigerant mixture properties model previously defined are given in the following subsections. Among these applications can be found an assumption regarding the oil-refrigerant solubility used in the two-phase compression model, an application of ideal two-phase compressions and heat transfer and the definition of the mixture compression efficiency. From now on and until the rest of the thesis, the vapor phase, or gaseous phase, will be referred to as "g" for "gas", to avoid any confusion with the specific volume v or the absolute volume V that are used more often in what follows.

2.4.1 Desolubilization of the oil-refrigerant mixture

The assumption introduced here is used to simplify the computational complexity of two-phase compression calculations. Let's imagine a two-phase oil-refrigerant mixture is placed into a fixed volume at a given pressure p_1 and given temperature T_1, as represented in Figure 2.28. The vapor phase is only composed of refrigerant while the liquid phase is an oil-refrigerant solution. The oil mass fraction is known and equal to $z_{o,1}$. As explained in section 2.2, by knowing the pressure, temperature and oil mass fraction, the vapor quality can be determined (see Equation 2.8). From there, the specific volume can also be known using Equation 2.20. The following relation can thereby be written as

$$v_{m,1} = f(p_1, T_1, z_o) \tag{2.38}$$

Before reaching the state of the oil-refrigerant mixture presented in Figure 2.28, a question to be asked is: what could be the state of the refrigerant (temperature, pressure, vapor quality) and the oil (temperature, pressure) to be mixed together to obtain the state of setup 1? Let's imagine that the control volume of Figure 2.28 is divided into two parts by a fictitious barrier,

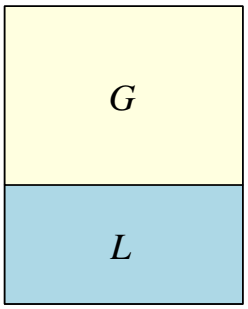

Figure 2.28: Oil-refrigerant mixture with a homogeneous liquid phase (setup 1: mixed state).

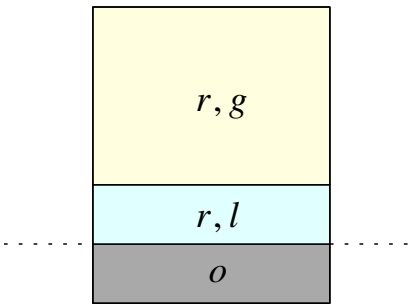

Figure 2.29: Oil-refrigerant mixture with a split liquid phase by a fictitious barrier (setup 2: split state).

like in Figure 2.29. At the bottom part, only oil is present, while in the upper part, two-phase (or superheated) refrigerant can be found. This control volume is also in thermal and mechanical equilibrium (same temperature and pressure on the two sides) and has the same volume as the control volume of setup 1. If the fictitious barrier is removed, the state of setup 2 converges towards the state of setup 1 adiabatically, but not isentropically, resulting in a new pressure, temperature and vapor quality. State of setup 1 can be referred to as the "mixed state" while state of setup 2 can be referred to as the "split state". To switch from one state to another, energy and mass conservation can be applied, while the third equation to be added is the link between the pressure and the temperature. Therefore, to switch from the mixed state (1) to the split state (2), the following system can be solved for T_2, p_2 and Q_2:

$$\begin{cases} u_{\mathrm{m},2}(p_2, T_2, Q_2, z_\mathrm{o}) = u_{\mathrm{m},1} \\ v_{\mathrm{m},2}(p_2, T_2, Q_2, z_\mathrm{o}) = v_{\mathrm{m},1} \\ T_2 = f(p_2) \end{cases} \tag{2.39}$$

where the last equation simply translates the dependency between the temperature and pressure at saturation for the refrigerant. To switch from the split state (2) to the mixed state (1), the following system can be solved, this time for T_1, p_1 and Q_1:

$$\begin{cases} u_{\mathrm{m},1}(p_1, T_1, Q_1, z_\mathrm{o}) = u_{\mathrm{m},2} \\ v_{\mathrm{m},1}(p_1, T_1, Q_1, z_\mathrm{o}) = v_{\mathrm{m},2} \\ T_1 = f(p_1, Q_1, z_\mathrm{o}) \end{cases} \tag{2.40}$$

where the last equation expresses the solubility of the mixture (Equation 2.8). The conversion from a mixed state to a split state is thereby going to change the pressure, the temperature and the vapor quality of the system. Moreover, in some cases, the split state results in an oil liquid phase mixed with superheated vapor only, without refrigerant in the liquid phase. This can be visually represented by plotting the superheat before and after conversion, as represented in Figure 2.30. As can be observed, there is an initial mixed vapor quality for which a superheat appears in the split state, followed by an increase in the superheat reaching high values when approaching the limit in vapor quality $(1 - z_\mathrm{o})$. The value of this mixed state vapor quality threshold can be figured out by fixing the vapor quality of the split state at the maximum vapor quality of $(1 - z_\mathrm{o})$. This value does not really matter, as the plot uses the mixed state vapor quality for both curves to check the consistency in the conversion: the curves should overlap when the superheat is increased, i.e., when the liquid phase is only constituted by oil. Switching from a mixed state to a split state changes the pressure, the temperature as well as the vapor quality, but the change in vapor quality is not represented. Regarding the changes in pressure and temperature, they can be found in Figure 2.31. The

conversion into a split state is accompanied by an increase in pressure, which can be explained by more mass in the vapor phase (no liquid refrigerant is solved in the oil), increasing the vapor phase density and then the pressure. A decrease in temperature is also observed, result of the energy required to vaporize a part of the liquid refrigerant. Considering the inverse scenario, it would mean that the temperature of oil and refrigerant is increasing when mixing them, as the condensation of the refrigerant releases heat while decreasing the pressure. For both pressure and temperature, a change in sign of the slope is noticeable at the transition point between two-phase and superheated refrigerant and both pressure and temperature differences converge towards zero, as at the maximum vapor quality (0.9), the mixed and split states are equivalent (no liquid solved in the oil). Overall, the superheat of the mixed state increases regardless of the initial vapor quality of the split state, and the same goes for the vapor quality, until the maximum is reached.

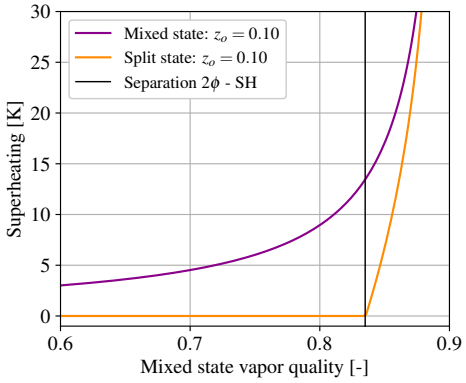

Figure 2.30: Comparison of superheat between a mixed state and a split state (p_1 = 1 bar)

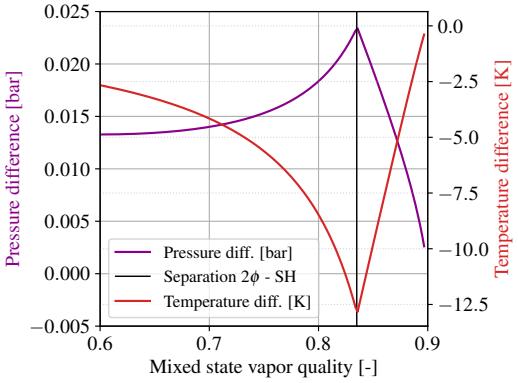

Figure 2.31: Difference in pressure and temperature between a mixed state and a split state for an oil mass fraction of 10%.

The exclusive dependency between the pressure and the temperature coming from the saturated state of the refrigerant enables simplifying calculations from operations such as heat transfer, compression, as illustrated in Figure 2.32. The split state therefore sees the oil as a liquid phase releasing or absorbing the heat from the two-phase (or superheated) refrigerant. The mixed state is therefore converted into a split state to get this exclusive dependency between the pressure and the temperature. This dependency allows, for instance, to keep a constant temperature when heat transfer occurs in an open system, only the vapor quality is going to change up to its maximum value, despite the presence of oil. Moreover, it simplifies calculations of volume reduction or expansion. Examples of applications are provided in the next subsection. Furthermore, this conversion also simplifies the calculations when thermal equilibrium is no longer assumed, and distinct temperatures are considered for the liquid and vapor phases, as shown in the next chapters. After performing the operations, the split state is converted back into a mixed state, finalizing the calculation process illustrated in Figure 2.32. The operations (heat or work transfer) could also be directly applied to the mixed state, however, this adds complexity in the solving process as will be shown in the subsequent sections.

Therefore, the split state is not a fictitious state created to simplify calculations: it has a physical meaning. When preparing containers of oil and refrigerant before mixing, both substances are in a split state. Let's consider the case where the refrigerant and the oil are contained in fixed volumes. If we merge these containers and keep the sum of both volumes, the resulting solution converges towards a mixed state. However, it takes time to reach the final equilibrium of the solution (the mixed state): the solution therefore stands between split and mixed states properties until the mixed state is reached. The convergences towards a

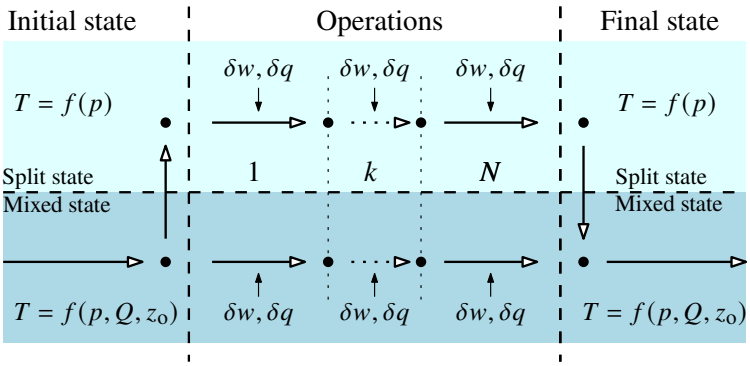

Figure 2.32: Desolubilization process of the oil-refrigerant mixture.

mixed state can thus be measured experimentally to check the rate of conversion to reach the final solubility state, and the data to be measured can either be the temperature or the pressure, ensuring no heat transfer with the environment. In the frame of this thesis, the split state is only used as a reasonable assumption to simplify calculations. Taking into account thermal non-equilibrium (different temperatures of the vapor and liquid phases) in two-phase compression already complicates the equations and the resulting analyses. It is therefore simpler to assume a split state which directly correlates the phase equilibrium between the refrigerant vapor and liquid without considering the oil. The real state during the compression would possibly stand between the split and the mixed state, the compressor dynamics being quite fast compared to the solution dynamics.

2.4.2 Compression process

Let's assume thermal and mechanical equilibrium are ensured, meaning, respectively, that the temperature and pressure of both phases are always the same. Consequently, if heat is added to the control volume (CV), or if its volume is reduced (work added to the CV), the state i is converging into a new state f, with a new pressure p_1^f, a new temperature T_1^f and a new vapor quality Q_1^f. A reduction of volume of a given volume ratio r_v will be applied to the control volume of the mixed state (setup 1) presented in Figure 2.28. Assuming an adiabatic and reversible compression with no mass transfer, the new state can be determined only through the knowledge of r_v, the following system of equations must be solved:

$$\begin{cases} s_{\mathrm{m},1}^f(p_1^f, T_1^f, Q_1^f, z_o) = s_{\mathrm{m},1}^i \\ v_{\mathrm{m},1}^f(p_1^f, T_1^f, Q_1^f, z_o) = v_{\mathrm{m},1}^i / r_v \\ T_1^f = f(p_1^f, Q_1^f, z_o) \end{cases} \tag{2.41}$$

which translates the isentropic compression of a two-phase oil-refrigerant mixture of a given volume ratio through a system of three equations and three unknowns p_1^f, T_1^f, and Q_1^f. Moreover, performing a volume reduction (isentropic compression) of ratio r_v to the split state instead of the mixed state, the following system must be solved for T_2^f, P_2^f and Q_2^f:

$$\begin{cases} s_{\mathrm{m},2}^f(p_2^f, T_2^f, Q_2^f, z_o) = s_{\mathrm{m},2}^i \\ v_{\mathrm{m},1}^f(p_2^f, T_2^f, Q_2^f, z_o) = v_{\mathrm{m},2}^i / r_v \\ T_2^f = f(p_2^f) \end{cases} \tag{2.42}$$

which allows to solve an easier system than the system of Equations 2.41 by adding the exclusive dependency between the pressure and the temperature from the saturation state of the refrigerant. As a matter of fact, the third equation can directly be substituted in the first two equations, reducing the system complexity from three strongly coupled non-linear

equations to essentially two. The final pressure achieved by performing the volume reduction can be found in Figure 2.33. As can be seen, by decreasing the vapor quality, the final pressure achieved decreases. As the liquid phase only sees its temperature increasing by heat transfer with the vapor phase, more condensation of vapor at saturation is required to increase the temperature of the liquid phase for low vapor qualities, which results in a lower vapor phase density and therefore a lower pressure. More explanations about this phenomenon are provided in the next chapters, as it is not the focus of the current section. As illustrated in Figure 2.32, two resolution schemes of the compression can be followed, either directly compressing the mixed state, or first converting the mixed state into a split state, performing the compression and then converting back the split state into a mixed state. The difference in enthalpy between the followed schemes can be found in Figure 2.34 at the four given initial vapor qualities and with a varying volume ratio. This difference is divided by the compression work for the sake of comparison, as a simple relative deviation would strongly depends on the reference state chosen for enthalpy. The difference reaches less than 0.5% at the given conditions, which confirms that both resolution schemes are valid.

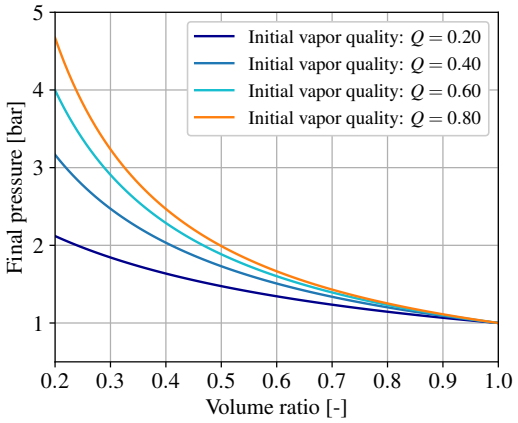

Figure 2.33: Evolution of the final pressure as a function of the volume ratio for an oil mass fraction of 10% (obtained from a split state).

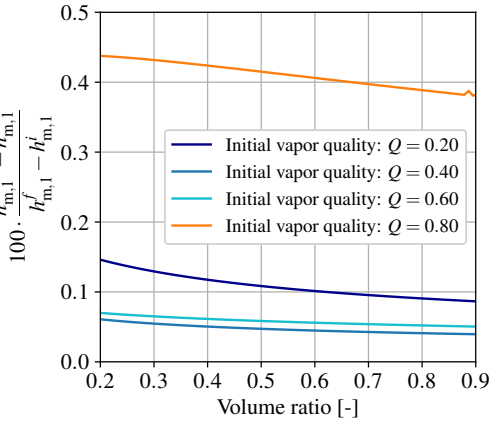

Figure 2.34: Difference in final enthalpies obtained from split and mixed states solving processes divided by the compression work for an oil mass fraction of 10%.

The difference in enthalpy obtained between the two resolution schemes arises from the difference in pressure when performing the compression from a split state or from a mixed state. Indeed, the work required to compress the mixture depends on the initial pressure and on the pressure evolution throughout the volume reduction, which translates into a different area under the pressure–volume curve. Therefore, the larger the pressure difference between a split state and a mixed state, the greater the enthalpy difference between the two resolution schemes. According to Figure 2.31, for an oil mass fraction of 10%, the maximum pressure difference between the two states occurs at a vapor quality of approximately 0.835. To confirm the origin of the enthalpy deviation, Figure 2.34 can be recreated for a narrower vapor-quality range, from 0.8 to 0.9, thereby allowing the influence of the pressure difference to be observed more clearly. Figure 2.35 shows that the maximum error occurs at vapor qualities of 0.82 and 0.85, whereas at a vapor quality of 0.88, the deviation is reduced because the pressure difference is also smaller.

2.4.3 Heat transfer process

Heat transfer processes computation is also simplified using the split state method. Let's imagine a heated pipe crossed by a two-phase oil-refrigerant mixture flow at thermal equilibrium, with a heat flow rate $\dot{Q}$, as represented in Figure 2.36. The mass flow rate is given by

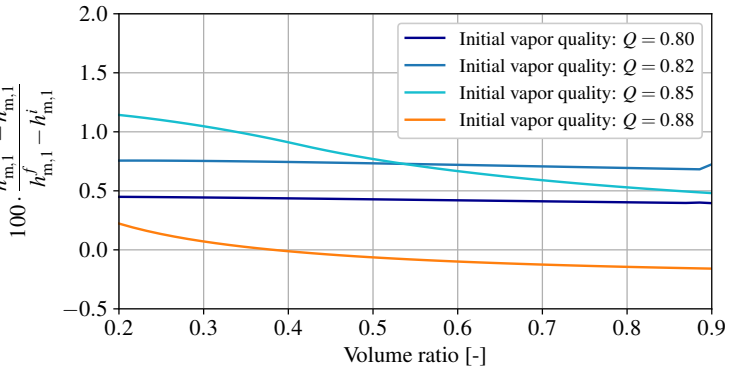

Figure 2.35: Difference in final enthalpies obtained from split and mixed states solving processes divided by the compression work for an oil mass fraction of 10% and a narrower range of vapor quality.

$\dot{m}$ and the initial enthalpy by h_{m}^{i}. The final enthalpy h_{m}^{f} can be calculated with the following formula:

$$h_{\mathrm{m}}^{f} = h_{\mathrm{m}}^{i} + \frac{\dot{Q}}{\dot{m}} \tag{2.43}$$

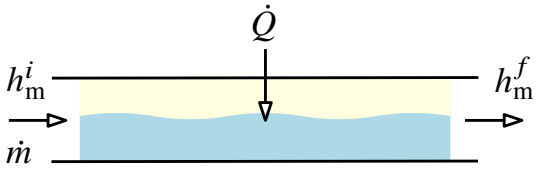

Figure 2.36: Heat transfer in a two-phase flow.

Heat transfer in an open system can be considered an isobaric transformation. Again assuming a thermal equilibrium, the two unknowns of the system are the final temperature T^f and vapor quality Q^f. The methodologies found in Table 2.5 can be solved for both the mixed and the split state, knowing that $p^f = p^i$, with the unknowns colored in gray. The introduced limit enthalpy $h_{\mathrm{m},2}^{f,\mathrm{lim}}$ is enthalpy from a split state, calculated with saturated refrigerant at the maximum value of the vapor quality of $1 - z_{\mathrm{o}}$:

$$h_{\mathrm{m},2}^{f,\mathrm{lim}} = f(Q_2^{f,\mathrm{max}}, p_2^f, T_2^{f,\sigma}, z_{\mathrm{o}}) \tag{2.44}$$

Beyond this enthalpy, the refrigerant becomes superheated and the vapor quality is fixed while the temperature can vary. Directly applying the equations of the mixed state, or converting to a split state, applying the equations, and converting back, yields exactly the same results. Nevertheless, the resolution process of the split state is much simpler, removing one unknown of the problem. Overall, applying both conversions and performing the calculations could be computationally more expensive than directly applying the solving process to the mixed state; however, simpler operations could be applied before converting back, offering a major benefit to this approach. Nevertheless, an important assumption stands by the illustrated example: the heat flow rate $\dot{Q}$ is considered constant. When a split state is used, the temperature of the two-phase mixture is modified, implying changes in the heat flow rate. Applying the split state to heat transfer therefore propagates errors. Nevertheless, even the mixed state would not accurately represent reality, as the solubility equilibrium may vary during heat transfer. Moreover, the high uncertainties associated with heat transfer coefficient calculations makes the use of a split state assumption acceptable.

Mixed state	**Split state**
$\begin{cases} h^f_{\mathrm{m},1} = f(Q^f_1, p^f_1, T^f_1, z_\mathrm{o}) \\ T^f_1 = f(Q^f_1, p^f_1, z_\mathrm{o}) \end{cases}$	`if` $h^f_{\mathrm{m},2} > h^{f,\mathrm{lim}}_{\mathrm{m},2}$`:` *(superheated case)* $h^f_{\mathrm{m},2} = f(Q^{f,\mathrm{max}}_2, p^f_2, T^f_2, z_\mathrm{o})$ `else:` *(two-phase case)* $h^f_{\mathrm{m},2} = f(Q^f_2, T^i_2, z_\mathrm{o})$

Table 2.5: Mixed state and split state heat transfer solving processes.

2.4.4 Compression efficiency definition

In the deterministic modeling of compressors, the initialization process requires guess values for properties such as temperature, pressure, density and vapor quality. The closer those guess values to the final solution, the faster the solving process. The guess values along a compression process can be estimated assuming an isentropic efficiency and a thermal equilibrium. Two situations are faced in the model: either the final pressure is known, and the temperature, vapor quality, and density need to be computed, or the density ratio is known, in which case the pressure, temperature, and vapor quality need to be determined.

The isentropic efficiency was already defined for a compressor in Chapter 1, Equation 1.3. The isentropic efficiency of a compression process compares its ideal power consumption with its real power consumption and can be obtained from

$$\varepsilon_\mathrm{is} = \frac{h^f_{\mathrm{m,is}} - h^i_\mathrm{m}}{h^f_\mathrm{m} - h^i_\mathrm{m}} \tag{2.45}$$

with $h^f_{\mathrm{m,is}}$ the outlet enthalpy following an isentropic (adiabatic and reversible) compression. This isentropic enthalpy can be computed using the mixed state or the split state. The calculation of isentropic efficiency using the mixed state is detailed in the next chapter. For the estimation of initial guess values, the isentropic enthalpy is computed using the split state approach.

Reformulating Equation 2.45, the final enthalpy of a compression process can be calculated using:

$$h^f_\mathrm{m} = h^i_\mathrm{m} + \frac{(h^f_{\mathrm{m,is}} - h^i_\mathrm{m})}{\varepsilon_\mathrm{is}} \tag{2.46}$$

The computation of $h^f_{\mathrm{m,is}}$ and estimation of the isentropic efficiency ε_is therefore allows to determine the final enthalpy of the process. From this enthalpy, it is possible to compute the temperature, pressure or density of the final state, depending on the given inputs. Three cases of two-phase compression can be met using the split state, as illustrated in Figures 2.37 and 2.38. The isentropic final enthalpy can end up in the two-phase region or in the superheated zone. If it ends up in the superheated zone, the final enthalpy also ends up superheated (case 1). If it ends up in the two-phase region, the final enthalpy can still end up in the superheated zone (case 2) or in the two-phase zone (case 3). The details of the calculations are given in the following subsections.

Pressure as an input

When the pressure is given as an input, the final state of the compression can easily be determined using temperature-entropy diagrams with the isobaric lines, as depicted in Figure 2.37. This scenario is usually faced when computing the outlet state of the compressor model,

as the outlet pressure is usually an input. Similarly to what has been done with enthalpy in the heat transfer calculations in Table 2.5, a limit entropy can be defined and, when exceeded, the final state of the isentropic enthalpy becomes superheated:

$$s_{\mathrm{m}}^{f,\mathrm{lim}} = f(Q^{f,\mathrm{max}}, p^f, T^{f,\sigma}, z_{\mathrm{o}}) \tag{2.47}$$

A limit enthalpy is also required to be compared with the final enthalpy h_{m}^f, computed with Equation 2.46:

$$h_{\mathrm{m}}^{f,\mathrm{lim}} = f(Q^{f,\mathrm{max}}, p^f, T^{f,\sigma}, z_{\mathrm{o}}) \tag{2.48}$$

The resolution processes of the three cases from a given pressure can be found in Table 2.6. First, comparing the initial entropy $s_{\mathrm{m}}^i = s_{\mathrm{m,is}}^f$ to this limit entropy allows to determine if case 1 (superheated isentropic state) is met. In this case, the isentropic unknown is the temperature and the vapor quality is set to the maximum value. The unknowns are highlighted in gray when they are still unsolved, and become black when determined. Equation 2.46 is then applied and the temperature is the only unknown left to determine (as the isentropic efficiency normally does not exceed 100%, except if the process is cooled). In the other case, the isentropic unknown is the vapor quality. The final enthalpy is compared to the limit enthalpy to see if the final state is in the two-phase region (case 3) or superheated (case 2). The remaining unknown (Q^f or T^f) is calculated accordingly.

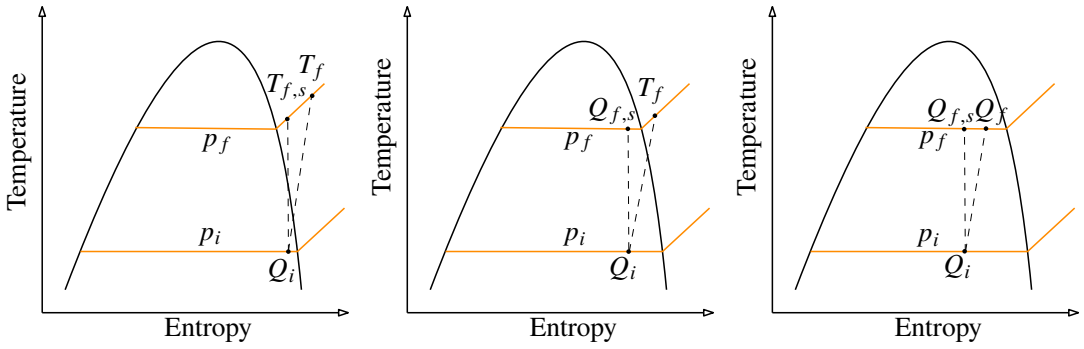

(a) Case 1 (b) Case 2 (c) Case 3

Figure 2.37: Final state definition from a given pressure.

Density as an input

The computation of the final state from the density as an input is more difficult than from the pressure, as the density is not directly involved in the equations of the enthalpy and the entropy, unlike the pressure. The density can be given as an input in a scenario where the state needs to be computed from the built-in volume ratio. In that case, the pressure becomes a new unknown of the problem. Temperature-entropy diagram, along with iso-density lines, illustrates the problem in Figure 2.38. Again, limit entropy and enthalpy need to be defined, this time, from the final density ρ_{m}^f that is known. They can be determined by solving the following system:

$$\begin{cases} \rho_{\mathrm{m}}^f = f(Q^{f,\mathrm{max}}, p^{f,\mathrm{lim}}, T^{f,\sigma}, z_{\mathrm{o}}) \\ s_{\mathrm{m}}^{f,\mathrm{lim}} = f(Q^{f,\mathrm{max}}, p^{f,\mathrm{lim}}, T^{f,\sigma}, z_{\mathrm{o}}) \\ h_{\mathrm{m}}^{f,\mathrm{lim}} = f(Q^{f,\mathrm{max}}, p^{f,\mathrm{lim}}, T^{f,\sigma}, z_{\mathrm{o}}) \end{cases} \tag{2.49}$$

The resolution processes of the three cases from a given density can also be found in Table 2.6. As for the pressure input, the initial entropy $s_{\mathrm{m}}^i = s_{\mathrm{m,is}}^f$ is compared to the limit entropy to

check if the isentropic state is superheated (case 1). In this case, the isentropic unknowns are the temperature and the pressure; they can be determined by adding the density equation. As a reminder, the unknowns are highlighted in gray when they are still unsolved, and become black when determined. The final enthalpy is determined in the same way as in the pressure input scenario. Finally, the two unknowns, the final pressure and temperature (p^f and T_f) can be determined using the density equation again. In the case of a two-phase isentropic state, the isentropic enthalpy needs to be computed using the vapor quality and the pressure as unknowns, and then converted into the final enthalpy. This final enthalpy is compared to the limit enthalpy to check if the final state is superheated (case 2) or two-phase (case 3). The two remaining unknowns are calculated accordingly.

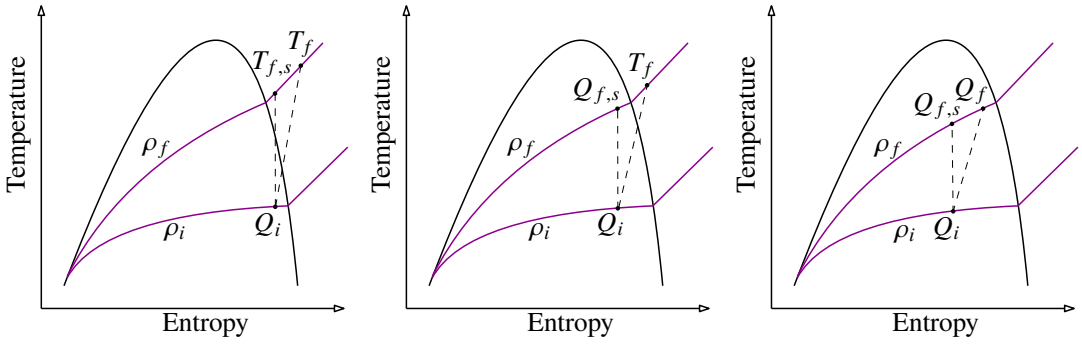

(a) Case 1 (b) Case 2 (c) Case 3

Figure 2.38: Final state definition from a given density.

Pressure input

if $s^f_{\text{m,is}} > s^{f,\text{lim}}_{\text{m}}$: *(case 1)*

$$\begin{cases} s^f_{\text{m,is}} = f(Q^{f,\max}, p^f, T^f_{\text{is}}, z_{\text{o}}) \\ h^f_{\text{m,is}} = f(Q^{f,\max}, p^f, T^f_{\text{is}}, z_{\text{o}}) \\ h^f_{\text{m}} = f(h^f_{\text{m,is}}) \\ h^f_{\text{m}} = f(Q^{f,\max}, p^f, T^f, z_{\text{o}}) \end{cases}$$

else: *(case 2 or 3)*

$$\begin{cases} s^f_{\text{m,is}} = f(Q^f_{\text{is}}, p^f, T^{f,\sigma}, z_{\text{o}}) \\ h^f_{\text{m,is}} = f(Q^f_{\text{is}}, p^f, T^{f,\sigma}, z_{\text{o}}) \\ h^f_{\text{m}} = f(h^f_{\text{m,is}}) \end{cases}$$

if $h^f_{\text{m}} > h^{f,\text{lim}}_{\text{m}}$: *(case 2)*

$$h^f_{\text{m}} = f(Q^{f,\max}, p^f, T^f, z_{\text{o}})$$

else: *(case 3)*

$$h^f_{\text{m}} = f(Q^f, p^f, T^{f,\sigma}, z_{\text{o}})$$

Density input

if $s^f_{\text{m,is}} > s^{f,\text{lim}}_{\text{m}}$: *(case 1)*

$$\begin{cases} \rho^f_{\text{m}} = f(Q^{f,\max}, p^f_{\text{is}}, T^f_{\text{is}}, z_{\text{o}}) \\ s^f_{\text{m,is}} = f(Q^{f,\max}, p^f_{\text{is}}, T^f_{\text{is}}, z_{\text{o}}) \\ h^f_{\text{m,is}} = f(Q^{f,\max}, p^f_{\text{is}}, T^f_{\text{is}}, z_{\text{o}}) \\ h^f_{\text{m}} = f(h^f_{\text{m,is}}) \\ \rho^f_{\text{m}} = f(Q^{f,\max}, p^f, T^f, z_{\text{o}}) \\ h^f_{\text{m}} = f(Q^{f,\max}, p^f, T^f, z_{\text{o}}) \end{cases}$$

else: *(case 2 or 3)*

$$\begin{cases} \rho^f_{\text{m}} = f(Q^f_{\text{is}}, p^f_{\text{is}}, T^{f,\sigma}, z_{\text{o}}) \\ s^f_{\text{m,is}} = f(Q^f_{\text{is}}, p^f_{\text{is}}, T^{f,\sigma}, z_{\text{o}}) \\ h^f_{\text{m,is}} = f(Q^f_{\text{is}}, p^f_{\text{is}}, T^{f,\sigma}, z_{\text{o}}) \\ h^f_{\text{m}} = f(h^f_{\text{m,is}}) \end{cases}$$

if $h^f_{\text{m}} > h^{f,\text{lim}}_{\text{m}}$: *(case 2)*

$$\begin{cases} \rho^f_{\text{m}} = f(Q^{f,\max}, p^f, T^f, z_{\text{o}}) \\ h^f_{\text{m}} = f(Q^{f,\max}, p^f, T^f, z_{\text{o}}) \end{cases}$$

else: *(case 3)*

$$\begin{cases} \rho^f_{\text{m}} = f(Q^f, p^f, T^{f,\sigma}, z_{\text{o}}) \\ h^f_{\text{m}} = f(Q^f, p^f, T^{f,\sigma}, z_{\text{o}}) \end{cases}$$

Table 2.6: Resolution process of a compression from a split state given an isentropic efficiency with a final pressure output or final density output.

2.5 Summary and conclusion

This chapter aimed to provide a strong basis for the understanding of oil-refrigerant mixture behavior. Oil-refrigerant mixture thermophysical properties are, in essence, the pillar to understand how two-phase compression works. Positive displacement compressors are only mechanical devices trying to impose a volume reduction to a mixture as efficiently as possible, however, it is the response of the mixture that matters the most. To understand this response, accurate modeling of mixture properties is required. Therefore, this chapter is useful for someone who already has thermodynamic knowledge, but does not understand precisely how an oil-refrigerant mixture behaves: it starts with the basics and progressively provides the essentials required to understand the next chapters. Despite the considerable literature that can be found on oil-refrigerant mixture modeling, this chapter tends to be concise and to provide elements that seemed primordial only. Moreover, to conclude the chapter, applications of the derived equations are proposed. Naturally, the chapter contains novel contributions to the literature, which help clarify certain principles of two-phase mixture, a topic that remains poorly understood. The main outcomes of this chapter can be summarized as follows:

- A new approach to the modeling of binary mixture is proposed, where the mixture mass is distributed in four parts, i.e., divided by two components and divided by two phases. Basic equations are derived from this point of view and the solubility and vapor quality are introduced. The concept is then applied to an oil–refrigerant mixture, showing that pressure and superheat can be used to determine the vapor quality of the mixture, provided the oil mass fraction is known.
- Experimental setups used to measure properties of two oil-refrigerant mixtures employed in this work are presented. These setups are the property of the Schaufler Chair of Refrigeration, Cryogenics and Compressor Technology of the Technische Universität Dresden. Details are given on how the desired properties (i.e., vapor pressure, liquid phase viscosity and density) are measured, and how the inputs to get those properties are derived.
- The modeling of thermophysical properties of oil-refrigerant mixtures is presented, providing a state of the art for each of them. Interesting methodologies are selected, validated with experimental data and compared. Some properties, however, are not validated with experimental data: the specific heat capacity, the thermal conductivity and the surface tension.
- The enthalpy and entropy calculations are described in detail, as they are extensively used throughout the remainder of the thesis. Pressure-enthalpy as well as temperature-entropy diagrams of the mixture are presented and commented on. The method of deriving these diagrams is, to the author's knowledge, completely novel in representing only the refrigerant contribution in the mixture to ensure consistency with the pure refrigerant curves.
- Applications of the oil-refrigerant properties allow to understand the basic concept of two-phase compression and why the definition of mixture properties is of such importance. The concept of "desolubilization", allowing to simplify calculations of compression and heat transfer, is introduced. In this concept, two states are defined: the "mixed state" where the solubility equations govern, and the "split state" where the solubility is neglected and the refrigerant behaves like a pure fluid, despite the presence of oil. Eventually, a two-phase compression definition from given isentropic efficiencies is provided, where the input can either be the final pressure or the final density.

This chapter thereby constitutes a key to the understanding of the post-processing required to analyze the data from the experimental investigations conducted on the compressors. Moreover, the defined thermophysical properties are even more extensively used in the numerical

modeling of these compressors. These experimental and numerical aspects are, respectively, matters of the next two chapters.

References

Bell, Ian H. (2011). "Theoretical and Experimental Analysis of Liquid Flooded Compression in Scroll Compressors". PhD thesis. Purdue University.

Leclercq, Nicolas et al. (2024a). "Modeling and Experimental Validation of the Thermophysical Properties of a POE+R1233zd(E) Mixture". In: *Proceeding of the International Compressor Engineering Conference*. Purdue University.

Youbi-Idrissi, M. and Bonjour, Jocelyn (Mar. 2008). *The Effect of Oil in Refrigeration: Current Research Issues and Critical Review of Thermodynamic Aspects*. DOI: 10.1016/j.ijrefrig.2007.09.006.

Li, H. and Hrnjak, Predrag (2013). "Effect of Lubricant on Two-phase Refrigerant Distribution in Microchannel Evaporator". In: *International Journal of Materials and Manufacturing* 6.3, pp. 567–575. DOI: 10.2307/26268552. JSTOR: 10.2307/26268552.

Youbi-Idrissi, M. et al. (May 2004). "Oil Presence in an Evapoator: Experimental Validation of a Refrigerant/Oil Mixture Enthalpy Calculation Model". In: *International Journal of Refrigeration*. Vol. 27, pp. 215–224. DOI: 10.1016/j.ijrefrig.2003.11.001.

Barbosa, J.R. (2001). "Phase Change of Single Component Fluids and Mixtures in Annular Flow". PhD thesis. University of London & Imperial College of Science, Technology and Medicine.

Yang, Xiaoxian and Richter, Markus (2024). "Thermophysical Property Model of Lubricant Oils and Their Mixtures with Refrigerants". In: *Proceedings of the International Compressor Engineering Conference*. Ray W. Herrick Laboratories, Purdue University.

Neto, Moisés A. Marcelino and Barbosa, Jader R. (2011). "Modeling the Thermodynamic Properties of Refrigerant–Oil Mixtures and the Effect of the Oil Circulation Ratio on the Performance of Vapor Compression Systems". In: *Proceedings of the VI Congresso Brasileiro de Termodinâmica Aplicada*. CBTermo Organizing Committee.

Ossorio, Ruben et al. (2022). "Impact of Lubricant in the Evaporator as a Function of Oil Circulation Rate in Variable Speed Heat Pumps Working with R290". In: *Proceedings of the International Refrigeration and Air Conditioning Conference*. Purdue University.

de Hemptinne, Jean-Charles (2012). *Select Thermodynamic Models for Process Simulation : A Practical Guide Using a Three Steps Methodology*. Editions Technip. ISBN: 978-2-7108-0949-4.

Scialdone, John J., Miller, Michael K., and Montoya, Alex F. (1996). *Methods of Measuring Vapor Pressures of Lubricants With Their Additives Using TGA and/or Microbalances*. Tech. rep. NASA.

van Konynenburg, P. H. and Scott, R. L. (Dec. 1980). "Critical Lines and Phase Equilibria in Binary van Der Waals Mixtures". In: *Philosophical Transactions of the Royal Society of London. Series A, Mathematical and Physical Sciences* 298.1442, pp. 495–540. ISSN: 0080-4614. DOI: 10.1098/rsta.1980.0266.

Thome, John R. (1995). "Comprehensive Thermodynamic Approach to Modeling Refrigerant-Lubricating Oil Mixtures". In: *HVAC and R Research* 1.2, pp. 110–125. ISSN: 10789669. DOI: 10.1080/10789669.1995.10391313.

Dickes, Rémi (2019). "Charge-Sensitive Methods for the off-Design Performance Characterization of Organic Rankine Cycle (ORC) Power Systems". PhD thesis. University of Liège.

Ossorio, Ruben and Navarro-Peris, Emilio (Mar. 2021). "Study of Oil Circulation Rate in Variable Speed Scroll Compressor Working with Propane". In: *International Journal of*

Refrigeration 123, pp. 63–71. ISSN: 01407007. DOI: 10.1016/j.ijrefrig.2020.12.002. (Visited on 09/09/2025).

Albatati, Faisal Ali S. (2015). "Investigation of Environmentally Friendly Power Generation Systems for Low-Grade Waste Heat Recovery". PhD thesis. University of Nottingham.

Bell, Ian H. et al. (Feb. 2014). "Pure and Pseudo-Pure Fluid Thermophysical Property Evaluation and the Open-Source Thermophysical Property Library Coolprop". In: *Industrial and Engineering Chemistry Research* 53.6, pp. 2498–2508. ISSN: 08885885. DOI: 10.1021/ie4033999.

Bruno, Thomas J et al. (Aug. 2019). *Thermophysical Properties of Polyol Ester Lubricants*. Tech. rep. NIST IR 8263. Gaithersburg, MD: National Institute of Standards and Technology, NIST IR 8263. DOI: 10.6028/NIST.IR.8263. (Visited on 09/24/2025).

Yang, Xiaoxian et al. (Nov. 2023). "Thermophysical Property Modeling of Lubricant Oils and Their Mixtures with Refrigerants Using a Minimal Set of Experimental Data". In: *Industrial and Engineering Chemistry Research* 62.44, pp. 18736–18749. ISSN: 15205045. DOI: 10.1021/acs.iecr.3c02474.

Stöckel, Katharina et al. (Aug. 2023). "Measurement of Vapour Pressure, Miscibility and Thermal Conductivity for Binary and Ternary Refrigerant Lubricant Mixtures in the Context of Heat Pump Tumble Dryers". In: *International Journal of Refrigeration* 152, pp. 223–233. ISSN: 01407007. DOI: 10.1016/j.ijrefrig.2023.04.016.

Youbi-Idrissi, M. (2003). "Impact de l'huile de Lubrification Sur Les Performances Thermodynamiques Des Pompes à Chaleur Réversibles". PhD thesis. Conservatoire national des arts et métiers (CNAM).

Mermond, Y., Feidt, M., and Marvillet, C. (Nov. 1999). "Propriétés Thermodynamiques et Physiques Des Mélanges de Fluides Frigorigènes et d'huiles". In: *International Journal of Refrigeration* 22.7, pp. 569–579. ISSN: 01407007. DOI: 10.1016/S0140-7007(99)00015-8.

Han, Xiao Hong et al. (Sept. 2010). "Solubility and Miscibility for the Mixture of (Ethyl Fluoride + Polyol Ester Oil)". In: *Journal of Chemical and Engineering Data* 55.9, pp. 3200–3207. ISSN: 00219568. DOI: 10.1021/je1000507.

Martz, W. L. and Jacobi, A. M. (1994). *Refrigerant-Oil Mixtures and Local Composition Modeling*. Tech. rep. Air Conditioning and Refrigeration Center, University of Illinois.

Peng, Ding-Yu and Robinson, Donald B. (Feb. 1976). "A New Two-Constant Equation of State". In: *Industrial & Engineering Chemistry Fundamentals* 15.1, pp. 59–64. ISSN: 0196-4313. DOI: 10.1021/i160057a011.

Neto, Moisés A. Marcelino and Barbosa, Jader R. (May 2010). "Solubility, Density and Viscosity of Mixtures of Isobutane (R-600a) and a Linear Alkylbenzene Lubricant Oil". In: *Fluid Phase Equilibria* 292.1-2, pp. 7–12. ISSN: 03783812. DOI: 10.1016/j.fluid.2009.12.029.

Bock, Jessica (2015). "Vapor-Liquid Equilibria of a Low Gwp Refrigerant, R-1234ZE(E), Mixed with a POE Lubricant". PhD thesis. University of Illinois at Urbana-Champaign.

Wang, Xiaopo, Jia, Xiucan, and Wang, Dongbo (Apr. 2021). "Experimental Investigation on the Solubility of R290 in Two Mineral Oils". In: *International Journal of Refrigeration* 124, pp. 13–19. ISSN: 01407007. DOI: 10.1016/j.ijrefrig.2020.12.021.

Caramaschi, Matteo et al. (2023). "Experimental Investigations and Modeling of Propylene and DME Solubility in PAG Oil". In: *Proceedings of the International Congress of Refrigeration*. International Institute of Refrigeration. DOI: DOI:10.18462/iir.icr.2023.0412.

Jia, Xiucan et al. (June 2020). "Phase Equilibrium of R1234yf and R1234ze(E) with POE Lubricant and Thermodynamic Performance on the Evaporator". In: *Fluid Phase Equilibria* 514. ISSN: 03783812. DOI: 10.1016/j.fluid.2020.112562.

Soave, Giorgio (June 1972). "Equilibrium Constants from a Modified Redlich-Kwong Equation of State". In: *Chemical Engineering Science* 27.6, pp. 1197–1203. ISSN: 00092509. DOI: 10.1016/0009-2509(72)80096-4.

Patel, Navin C. and Teja, Amyn S. (1982). "A New Cubic Equation of State for Fluids and Fluid Mixtures". In: *Chemical Engineering Science* 37.3, pp. 463–473. ISSN: 00092509. DOI: 10.1016/0009-2509(82)80099-7.

Yokozeki, A. (Feb. 2007). "Solubility Correlation and Phase Behaviors of Carbon Dioxide and Lubricant Oil Mixtures". In: *Applied Energy* 84.2, pp. 159–175. ISSN: 0306-2619. DOI: 10.1016/j.apenergy.2006.05.003. (Visited on 07/22/2025).

Wilson, Grant M. (Jan. 1964). "Vapor-Liquid Equilibrium. XI. A New Expression for the Excess Free Energy of Mixing". In: *Journal of the American Chemical Society* 86.2, pp. 127–130. ISSN: 0002-7863. DOI: 10.1021/ja01056a002.

Renon, Henri and Prausnitz, J. M. (Jan. 1968). "Local Compositions in Thermodynamic Excess Functions for Liquid Mixtures". In: *AIChE Journal* 14.1, pp. 135–144. ISSN: 0001-1541. DOI: 10.1002/aic.690140124.

Neto, Moisés A. Marcelino and Barbosa, Jader R. (Jan. 2008). "Solubility, Density and Viscosity of a Mixture of R-600a and Polyol Ester Oil". In: *International Journal of Refrigeration* 31.1, pp. 34–44. ISSN: 01407007. DOI: 10.1016/j.ijrefrig.2007.08.004.

Heil, J. F. and Prausnitz, J. M. (July 1966). "Phase Equilibria in Polymer Solutions". In: *AIChE Journal* 12.4, pp. 678–685. ISSN: 0001-1541. DOI: 10.1002/aic.690120412.

Tesser, R. et al. (Oct. 1999). "Description of the Vapor–Liquid Equilibrium in Binary Refrigerant/Lubricating Oil Systems by Means of an Extended Flory–Huggins Model". In: *Journal of Fluorine Chemistry* 99.1, pp. 29–36. ISSN: 00221139. DOI: 10.1016/S0022-1139(99)00119-0.

Dawo, Fabian et al. (Apr. 2021). "R1224yd(Z), R1233zd(E) and R1336mzz(Z) as Replacements for R245fa: Experimental Performance, Interaction with Lubricants and Environmental Impact". In: *Applied Energy* 288. ISSN: 03062619. DOI: 10.1016/j.apenergy.2021.116661.

Zhelezny, V. P. et al. (Sept. 2007). "An Experimental Investigation and Modelling of the Solubility, Density and Surface Tension of 1,1,1,3,3-Pentafluoropropane (R-245fa)/Synthetic Polyolester Compressor Oil Solutions". In: *Journal of Fluorine Chemistry* 128.9, pp. 1029–1038. ISSN: 00221139. DOI: 10.1016/j.jfluchem.2007.05.011.

Brocus, Julien et al. (Feb. 2022). "Solubility Measurements of Refrigerants in Polyolesters Lubricants at Temperature from 323.K to 383.K". In: *International Journal of Refrigeration* 134, pp. 278–292. ISSN: 01407007. DOI: 10.1016/j.ijrefrig.2021.09.025.

Neto, Moisés A. Marcelino, França, Rafael M., and Barbosa, J.R. (2014). "Convection-Driven Absorption of R-1234yf in Lubricating Oil". In: *International Journal of Refrigeration* 44, pp. 151–160. ISSN: 01407007. DOI: 10.1016/j.ijrefrig.2014.05.008.

Cavestri, Richard C. (1995). *Measurement of Viscosity, Density, and Gas Solubility of Refrigerant Blends in Selected Synthetic Lubricants*. Tech. rep. Imagination Resources, Inc.

Valderrama, José O. (1990). "A Generalized Patel-Teja Equation of State for Polar and Nonpolar Fluids and Their Mixtures." In: *JOURNAL OF CHEMICAL ENGINEERING OF JAPAN* 23.1, pp. 87–91. ISSN: 0021-9592. DOI: 10.1252/jcej.23.87.

Yang, Xiaoxian et al. (Dec. 2022). "Linking Viscosity to Equations of State Using Residual Entropy Scaling Theory". In: *International Journal of Thermophysics* 43.12. ISSN: 15729567. DOI: 10.1007/s10765-022-03096-9.

Hughes, D. W., Mcmullan, J. T., and Morgan, R. (1982). "Determination of the Thermodynamic Properties of Refrigerant-Oil Mixtures". In: *Proceedings of the International Compressor Engineering Conference*. Ray W. Herrick Laboratories, Purdue University.

Wei, Wenjian et al. (June 2008). "Models of Thermodynamic and Transport Properties of POE VG68 and R410A/POE VG68 Mixture". In: *Frontiers of Energy and Power Engineering in China* 2.2, pp. 227–234. ISSN: 16737393. DOI: 10.1007/s11708-008-0020-7.

Conde, Manuel R. (Jan. 1996). "Estimation of Thermophysical Properties of Lubricating Oils and Their Solutions with Refrigerants: An Appraisal of Existing Methods". In: *Applied Thermal Engineering* 16.1, pp. 51–61. ISSN: 13594311. DOI: 10.1016/1359-4311(95)00011-2.

Medvedev, Oleg O., Zhelezny, Petr V., and Zhelezny, Vitaly P. (Jan. 2004). "Prediction of Phase Equilibria and Thermodynamic Properties of Refrigerant/Oil Solutions". In: *Fluid Phase Equilibria* 215.1, pp. 29–38. ISSN: 03783812. DOI: 10.1016/j.fluid.2003.06.006.

Barbosa, J.R., Lacerda, V.T., and Prata, A.T. (Mar. 2004). "Prediction of Pressure Drop in Refrigerant–Lubricant Oil Flows with High Contents of Oil and Refrigerant Outgassing in Small Diameter Tubes". In: *International Journal of Refrigeration* 27.2, pp. 129–139. ISSN: 0140-7007. DOI: 10.1016/j.ijrefrig.2003.08.004. (Visited on 07/22/2025).

Henderson, David R. (1994). *Solubility, Viscosity and Density of Refrigerant/Lubricant Mixtures*. Tech. rep. Spauschus Associates.

Quiñones-Cisneros, S. E. et al. (Aug. 2005). "Phase and Viscosity Behaviour of Refrigerant-Lubricant Mixtures". In: *International Journal of Refrigeration* 28.5, pp. 714–724. ISSN: 01407007. DOI: 10.1016/j.ijrefrig.2004.12.004.

Youbi-Idrissi, M. et al. (May 2003). "Impact of Refrigerant–Oil Solubility on an Evaporator Performances Working with R-407C". In: *International Journal of Refrigeration* 26.3, pp. 284–292. ISSN: 01407007. DOI: 10.1016/S0140-7007(02)00129-9.

Chapter 3

Two-phase Compression: Experimental Investigations

Chapter Abstract

The objective of this chapter is to present the experimental investigations performed during the course of the thesis. These investigations include the testing of two scroll compressors under two-phase regimes: a retrofitted compressor and a lab-scale prototype. A test bench dedicated to controlling the inlet conditions of the compressor was developed for this purpose. The objective of this test bench is to assess the performance of the compressor working with the two-phase refrigerant-oil mixtures studied in Chapter 2 under varying conditions such as inlet pressures, inlet vapor qualities, oil circulation ratios, pressure ratios and speeds. The methodology to obtain the compressor inlet vapor quality is detailed, and the related assumptions are developed. A first methodology not considering the refrigerant solved in the oil was performed in Leclercq et al. (2024b), while another methodology was proposed in Leclercq et al. (2025), showing more accuracy in the post-processing. A total of four experimental campaigns were conducted: three with a retrofitted compressor and one with a lab-scale prototype developed for two-phase applications. Of the first three campaigns, two were conducted to compare the oils, while the last was performed without oil. The results of this comparison are presented in Leclercq et al. (2025) and are not included in this thesis. The results of the campaign conducted on the lab-scale prototype had not been published at the time of writing (November 2025) and are discussed in a subsequent section. This lab-scale prototype is equipped with an integrated dynamic pressure sensor, enabling partial acquisition of the pressure–volume diagram. The performance results of both machines are discussed in detail, with the dynamic pressure measurements helping to justify the observed trends. Two experimental databases have been generated through the experimental investigations, they can be found on Zenodo at the following links: Retrofitted compressor data, Prototype compressor data, for the retrofitted compressor tests and for the prototype tests, respectively.

3.1 Introduction

Understanding the behavior of two-phase compression with precision would not be possible without proper experimental data. Experimenting on a topic is required, especially when existing literature on the topic is limited, to validate numerical models that can describe the physical phenomena involved. Experimentation on two-phase refrigerant compression using scroll compressors is, from the author's knowledge, an emerging area of research and therefore not yet extensively studied. The results and conclusions presented in this thesis strongly rely on those experimental investigations, and without their support, the further numerical investigations would lack credibility. Consequently, this chapter is dedicated to a complete

description of the experimental investigations conducted within the scope of this thesis. First, a test bench dedicated to the two-phase scroll compressors testing is described. This test bench is specifically designed to deliver two-phase oil-refrigerant flows to compressors and to evaluate their performance. Its configuration, as well as the actuators used to control the compressor operating conditions are presented. The sensors employed are discussed, and their operating ranges and uncertainty are given. Furthermore, details are given about the test bench materials, and its layout is justified. In a second step, the post-processing methodology, to figure out the vapor quality as well as the compressor performance indicators, i.e., volumetric and isentropic efficiencies, is introduced. This post-processing methodology requires some calibration techniques to achieve good result accuracy. Results interpretation is enabled by the use of a Gaussian prediction tool called GPExp, which allows to perform interpolation and extrapolation, with some limitations. Two machines have been tested: a retrofitted compressor as well as a lab-scale prototype specifically developed for the two-phase application. The latter is equipped with an integrated dynamic pressure sensor, allowing partial acquisition of the pressure-volume diagram. The results are eventually presented and discussed, and conclusions are drawn.

3.2 Test bench description

3.2.1 Test bench conception

The layout of the test bench is inspired by a heat pump and can be found in Figure 3.2. It has a similar layout as the heat pump test bench proposed by Sun et al. (2021), intended to decrease the compressor discharge temperature when high pressure ratio are encountered. This test bench is dedicated to characterizing compressor performances, namely, to measure their power consumption and delivered flow to derive their volumetric and isentropic efficiencies over a wide range of operating conditions (inlet pressure, pressure ratios, oil circulation ratio, vapor quality, and speed). Two different compressors have been tested: a retrofitted compressor and a lab-scale prototype specifically developed for the two-phase application; their characteristics are provided in the next subsection. They are powered by electric motors and a torquemeter is used to measure their power consumption. Regarding lubrication, it is ensured by an independent oil loop allowing to regulate the oil circulation ratio (OCR) using the valve V3. To separate the oil from the refrigerant, the two-phase oil-refrigerant mixture, coming from the outlet of the compressor, is heated up by a resistor to vaporize as much refrigerant as possible, the oil is then recovered by an oil separator. After separation, the oil is cooled and redirected to the inlet line of the compressor, referred to as the "mixing line". Regarding the superheated vapor recovered from the separator, a part of it is directly redirected towards the mixing line while the remaining part is condensed and subcooled. By varying the opening of the three controlled discharge valves (V1, V2, V3) and the water mass flow rate in the heat exchangers using the manual control valves (V4, V5, V6), a wide range of conditions can be met, allowing to test different pressure ratios, inlet pressures, inlet vapor qualities and OCR. Furthermore, the compressor speed can also be controlled using a variable-frequency drive. A temperature-entropy diagram, along with a pressure-enthalpy diagram of an operating point can be found in Appendix B.2.1. A test bench schematic representing the temperatures, pressures, mass flow rates and compressor conditions of this operating point is also represented.

The test bench 3D representation can be found in Figure 3.1, it uses the same legend as in Figure 3.2. Some pictures of the test bench are also available in the Appendix B.1.1. As can be observed, the compressor has been placed vertically to avoid liquid accumulation in the discharge chamber. The liquid, present in the discharge chamber, will therefore naturally flow toward the discharge port reed valve and be ejected from the compressor. In the case of a

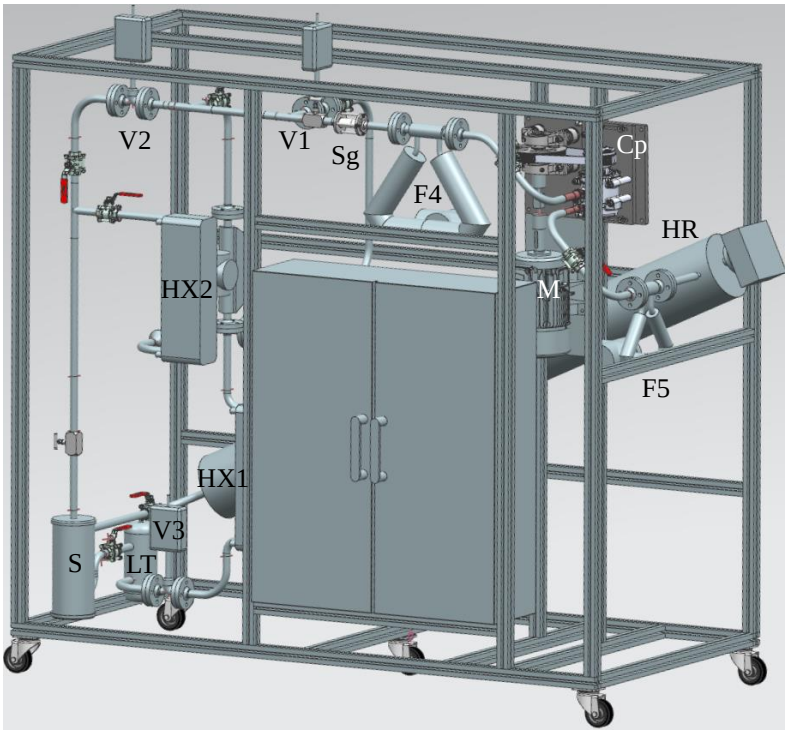

Figure 3.1: Test bench 3D representation.

liquid accumulation leading to a pure-liquid compression, a torque limiter has been placed on the shaft coupling, disengaging when excessive torque is encountered. The latter mechanism allows to protect both the compressor and the torquemeter. Regarding the heating resistor, it has been designed to provide a surface power exchange of 1.9 W/cm^2 to avoid oil degradation due to too high temperatures. Its maximum power rating is 30 kW and it reaches a length of 2.4 meters. As can be observed, it is placed diagonally, to facilitate the entrainment of the oil with the gravity, as the speed of the refrigerant is not high enough to carry the oil within this cross-sectional area. A total of 20 kg of refrigerant (HCFO R1233zd(E)) has been filled in the test bench. The lubricating oil is either the Emkarate RL32 MAF or a mixture of the RL32 and a POE40 from Petronas depending on the test campaign. A total of 3 kg of oil is filled in the test bench. Regarding sealing joints, the compatibility between the refrigerant and plastic/elastomers has been investigated, as bad experiences from the past have already occurred with this kind of fluid. According to Honeywell International Inc. (2018), Viton is suitable for use as its volume only increases between the flanges, with an 8.6% volume expansion observed after two weeks of immersion. Nevertheless, it appears that sealing joint degradation has been observed anyway, as illustrated in Appendix B.1.3, requiring the flanges to be regularly tightened to prevent leakages.

3.2.2 Tested compressors

Two scroll compressors have been tested in the frame of this thesis. The first is a retrofitted compressor from Sanden; the purpose of those tests was to see if a commercial retrofitted compressor could withstand two-phase compression with low vapor qualities. It also helped in designing the second compressor: a lab-scale prototype specifically made for the two-phase application. This lab-scale prototype is the third version; two failures were encountered while testing the earlier versions, and small modifications were therefore introduced. Both tested compressors' characteristics are summarized in Table 3.1. The retrofitted compressor is an open-drive automotive scroll compressor, the model is the TGVE08 from Sanden. It has a

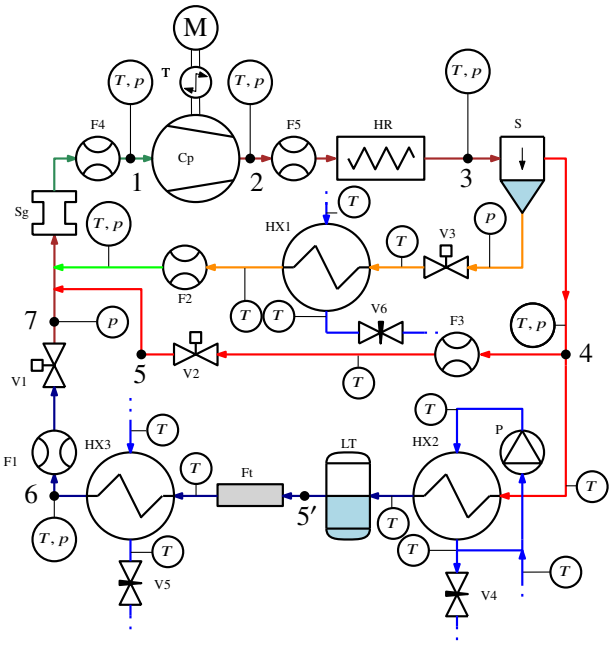

* HX1 – Oil cooler
* HX2 – Condenser
* HX3 – Subcooler
* Cp – Compressor
* HR – Heating Resistor
* S – Oil separator
* Sg – Sight Glass
* Ft – Filter
* LT – Liquid Tank
* T – Torquemeter
* F1 – Liquid Coriolis Flowmeter
* F2 – Oil Coriolis Flowmeter
* F3 – Vapor Rotameter
* F4 – Compressor inlet Coriolis Flowmeter
* F5 – Compressor outlet Coriolis Flowmeter
* V1 – Liquid Control Valve
* V2 – Vapor Control Valve
* V3 – Oil Control Valve
* P – Circulation Pump
* T – Temperature sensor
* p – Pressure sensor
* M – Electric Motor
* Refrigerant Liquid Line
* Refrigerant Vapor Line
* Compressor Supply Line
* Compressor Discharge Line
* Oil line
* Water Line

Figure 3.2: Test bench layout.

displacement volume of 86 cm^3 and a built-in volume ratio of 2.3. This compressor operates with a fixed orbiting scroll trajectory, always keeping the same radial and axial gaps at rest. This orbiting motion is driven by a crank pin inserted into the orbiting scroll bearing. Metallic balls are trapped between the orbiting scroll and a cage connected to the casing, allowing relative movement between the scroll without rotation, as depicted in Appendix B.1.3. This orbiting mechanism has been patented by Sanden (Sugimoto et al. 1985). Those metallic balls also allow to keep the axial and radial gaps constant, even when an overturning moment is generated by the chambers' pressure. No axial nor radial compliance mechanism is used. Tip seals are used to ensure axial sealing and the high pressure ensures contact between the tip seals and baseplates of the opposing scrolls (Carrier Corporation 2004). A reed valve is placed on the discharge port, avoiding backflow inside the discharge chamber. Intermediate discharge valves are located within the compression chambers of this compressor. Regarding the lab-scale prototype, it has a larger displacement volume (200 cm^3) and built-in volume ratio (3). The orbiting movement of the orbiting scroll is ensured by an Oldham ring. It uses a balancing counterweight placed with an angular offset (15°) from the drive angle, allowing to always keep the scroll in contact with a net force averaging 150 N between the two scrolls. A radial compliance is therefore ensured when compression from full liquid occurs. Like the retrofitted compressor, no axial compliance mechanism is used and carbon-filled polytetrafluoroethylene (PTFE) tip seals ensure proper sealing. Intermediate discharge valves can also be found in the compression chambers of the lab-scale prototype, as well as a reed valve. As a result of the significant differences in displacement volumes from the retrofitted compressor to the prototype, changes in the test bench were necessary to adapt sensor measurement ranges. The vapor rotameter as well as the vapor valves have therefore been replaced to adapt to the higher mass flow rates. Images of the tested compressors can be found in Figures 3.3 and 3.4. As already mentioned, they have been placed vertically to avoid liquid accumulation inside the compressors. Moreover, images of the orbiting scroll of the retrofitted compressor and fixed scroll of the lab-scale prototype can be found in Figures 3.5 and 3.6, respectively. More images can be found in Appendix B.1.3.

The retrofitted compressor was able to withstand two-phase conditions, even without oil. After more than 200 hours of operation, the compressor was visually inspected for damage, and no trace of wear was observed. Regarding the lab-scale prototype, more issues were experienced. This lab-scale prototype is the third version; two failures were encountered while testing the earlier versions, and small modifications were therefore introduced. The compressor handled more than 70 hours of operation and slight damage has been noticed. Despite the testing at very low oil circulation ratios or even without oil at all, lubrication did not seem to be a problem for both compressors. The low viscosity experienced should have led to ultra-thin films separating the surfaces, with a thickness comparable to the surface roughness, which could be detrimental to machine lifespan. Nevertheless, experiments with the R1233zd(E) refrigerant suggest that, even at low OCR, lubrication is still possible in that situation thanks to an adsorbed layer of refrigerant formed on iron oxide surfaces (Tromp 2018). Therefore, the lubrication would not be ensured by the oil, but by the refrigerant itself. Moreover, the lack of a compliance mechanism in both machines prevents metallic surfaces from coming into contact, apart from a radial contact on the lab-scale prototype and contacts originating from the orbiting mechanisms. Finally, despite the low oil mass fraction, the cooling effect is still ensured by the liquid refrigerant, except at superheated points, which were limited in number.

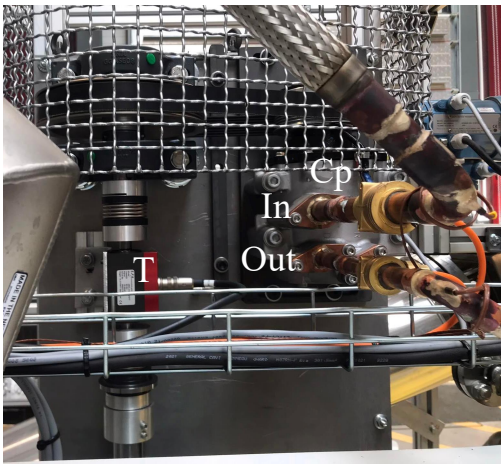

Figure 3.3: Picture of the retrofitted scroll compressor (Cp denotes the compressor, and T the torque meter).

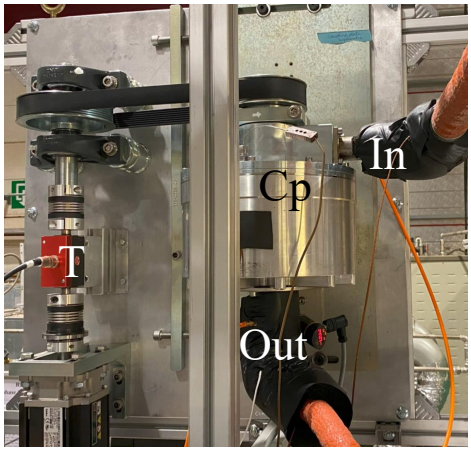

Figure 3.4: Picture of the lab-scale prototype of scroll compressor.

Characteristics	Retrofitted compressor	Lab-scale prototype
Displacement volume [cm^3]	86	200
Built-in volume ratio [-]	2.3	3.0
Orbiting mechanism	Ball mechanism	Oldham ring
Axial compliance	No	No
Radial compliance	No	Yes
Reed valve	Yes	Yes
Int. discharge valves	Yes	Yes
Pulley ratio [-]	1.7	0.77
Motor type	Asynchronous (3 pole pairs)	Synchronous (6 pole pairs)

Table 3.1: Tested compressors' characteristics.

Figure 3.5: Orbiting scroll of the retrofitted compressor.

Figure 3.6: Fixed scroll of the lab-scale prototype.

3.2.3 Measurement techniques/instrumentation equipment

The precise characterization of the compressor's performance requires a complete set of instrumentation equipment. On the one hand, numerous temperature/pressure measurements are taken, mainly to check the energy balances all over the test bench. On the other hand, the mass flow rates of each line (refrigerant vapor, refrigerant liquid and oil) are measured, using Coriolis flowmeters for the oil and the liquid lines and a rotameter for the vapor line. The cooling water mass flow rates are also measured using electromagnetic flowmeters to check energy balances of the three heat exchangers. A cylindrical sight glass has been placed in the mixing line in order to visualize the flow, particularly useful at the test bench start-up, to ensure the operating conditions are optimal before increasing the speed of the compressor (limited presence of liquid). Nevertheless, this sight glass does not allow any image processing to figure out further data regarding the flow. The key issue faced in the design of the test bench is the evaluation of the vapor quality with decent accuracy. No sensor allows measuring the vapor quality directly, as most of the time, the sensors used in the literature measure parameters that can be correlated with vapor quality. A review of the vapor quality assessment has been conducted, showing that most of the sensors are neither reliable nor mature, it can be found in Table 3.2. The two main types that are easily applicable are the capacitive and the Coriolis, allowing measurement of the void fraction. However, this void fraction can not always be easily linked with the vapor quality of the flow, as non-unity slip ratios can appear. Two Coriolis flowmeters from the Emerson's Elite series have been installed on the test bench, before and after the compressor, to measure the density at the compressor inlet/outlet. It however appeared that they only deliver good accuracy when high (> 0.95) or low vapor (< 0.1) qualities are tested. These Coriolis flowmeters were therefore used to calibrate the vapor rotameter with superheated conditions, to match the total mass flow rate obtained with the mass flow rates of each line measured individually ($\dot{m}_{F1} + \dot{m}_{F2} + \dot{m}_{F3} = \dot{m}_{F4} = \dot{m}_{F5}$, in Figure 3.2). Therefore, the vapor is determined using an energy balance on the mixing line (line from which the mixing is done, upstream of the compressor); the details will be shown in the subsequent section. Regarding the compressor power consumption assessment, as already mentioned, a torquemeter is used to measure the torque on the motor shaft, moreover, it also provides speed measurement eventually allowing to obtain the mechanical power developed by the motor. This power, however, is different from the power provided to the compressor, as the power is transmitted via a pulley-belt mechanism inducing power losses. These power

losses have been estimated by unclutching the retrofitted compressor, allowing to measure only losses generated by the pulley-belt mechanism. Unfortunately, even though the exhaust pressure and temperature are measured, as well as the power of the heating resistor, the exhaust vapor quality of the compressor could not be retrieved due to a too high thermal inertia of the heating resistor. Therefore, heat balance could not be applied to the compressor, which could have been used to estimate the ambient heat losses.

Type and studies	Sub-type	Comments
Electric (Billiet 2019; Danel 1978; De Kerpel 2015; Elstroem 2017; Kaya 2021; Pochet 2012; Sakamoto et al. 2019)	Capacitive (Dielectric constant)	Available commercial product; Needs a conductive fluid
	Resistive	Weak to parasite; Needs conductive fluid; Difficult calibration
	Electromagnetic	Not mature
Calorimeter (Dorfman et al. 2006)	Discharging calorimeter	Only theoretical; Influence on process; Only high vapor quality
	Throttling calorimeter	Influence on process; Only high vapor quality
	Separating calorimeter	Only pedagogical; Influence on process; Only high vapor quality
	Electrical calorimeter	Influence on process; Only high vapor quality
Plug flow (Fukuta et al. 2018)	–	Only very low void fraction
Density (Dutton et al. 2006)	Coriolis	Available commercial product
	Vortex	Available commercial product; Low accuracy
Local thermal (Delhaye 1968)	Hot anemometer	Complexity of signal interpretation; Only local
	Micro thermocouple	Complex electronics; Only local
Optical (Danel 1978; Wojtan et al. 2004)	Nearly Infrared	Not mature
	Refraction	
	Flow patterns	Cheap; Not mature
Model based	–	Cheap; Very sensitive to error measurement

Table 3.2: Classification of vapor quality measurement technologies.

Eventually, the models of the sensors employed on the test bench, their operating ranges as well as their uncertainties can be found in Table 3.3. The measurement uncertainties propagation is going to be studied through the post-processing methodology to check its impact on the determined performance indicators. The absolute uncertainty μ_M of a calculated variable M is calculated via

$$\mu_M = \sqrt{\sum_i \left(\frac{\partial M}{\partial m_i} \mu_i \right)^2} \tag{3.1}$$

where μ_i are the standard uncertainties of each measured/used values m_i used to compute M (Bell et al. 2012b).

Sensor	Equipment	Range	Uncertainty
Pressure sensors	Keller PAA21Y	0 - 10 [bara]	0.05 [bar]
Temperature sensors	T-thermocouple	-185 - 300 [°C]	0.5 [K]
Torquemeter	ETH DRV-II-20Nm	0 - 20 [Nm]	0.02 [Nm]
Compressor inlet	Emerson Elite CMF100M	15 - 333 [g/s]	0.25%
Coriolis Flowmeter		0 - 5000 [kg/m^3]	0.5 [kg/m^3]
Compressor outlet	Emerson Elite CMF050M	3 - 333 [g/s]	0.1%
Coriolis Flowmeter		0 - 5000 [kg/m^3]	0.5 [kg/m^3]
Liquid Coriolis Flowmeter	Emerson R025S	2 - 180 [g/s]	0.5%
Oil Coriolis Flowmeter	Bronkhorst Cori-Flow M55	1 - 33 [g/s]	0.2%
Vapor Rotameter 1	Krohne H250 M40	6 - 60 [g/s]	0.9 [g/s]
Vapor Rotameter 2	Krohne H250 M40	15 - 150 [g/s]	2.25 [g/s]

Table 3.3: Sensors used in the compressor test bench, range and standard uncertainties.

3.3 Data post-processing

3.3.1 Tests campaigns

The objective of the test campaigns is to record numerous steady-state operating points, varying the compressor speed, inlet pressure, pressure ratio, OCR as well as the inlet vapor quality, to calculate the isentropic and volumetric efficiencies of the compressor, also called performance indicators. Four test campaigns have been conducted on the test bench. First, a test campaign using the oil Emkarate RL32 MAF as a lubricant allowed to test 142 operating points, with a compressor speed ranging from 1000 RPM to 5000 RPM, and a vapor quality from 0.35 to highly superheated conditions, as represented in Figure 3.7. A second test campaign, where a partial replacement of the oil has been performed, allowed to record 71 points, only at the speed of 2000 RPM. The oil mixture composed of mass fractions of 39% of RL32 and 61% of a POE40 from Petronas was therefore used during this campaign. The two tested oils have dynamic viscosities of 32 mPas and 37 mPas at 40°C, for the pure oil and the oil mixture, respectively, which is not a significant difference. A third test campaign allowed to test the compressor without oil at two speeds (2000 and 3000 RPM), with a total of 72 points recorded, including 23 points with superheated inlet conditions. The last test campaign was conducted on the lab-scale prototype with a total of 97 points recorded with speeds ranging from 1000 RPM to 3250 RPM. Higher speeds could not be tested as the torquemeter's maximum measurable torque was limited to 20 Nm. Although calculations indicated that such torque should not have been reached on average, transient torque peaks within each rotation caused the torque limiter to disengage, preventing further testing. From these 97 points, 23 have been removed because the superheat at the heating resistor outlet was too low (3 K) and the uncertainty regarding the oil circulation ratio was too high. Therefore, only 74 data points could be used. The x-axis in Figure 3.7 represents the difference between the measured inlet temperature and the refrigerant saturation temperature at the measured inlet pressure, called apparent vapor superheat. As can be observed, even when two-phase conditions (vapor quality below 1) are met, a superheat is measured, result of the mixture temperature glide brought by the oil. Only a few points meet this behavior without oil, which could be the result of thermal non-equilibrium between the liquid and the vapor phases, inducing error in the temperature measurement. The inlet vapor quality represented on the plot is the ratio between the vapor mass flow rate and the total mass flow rate at the compressor inlet.

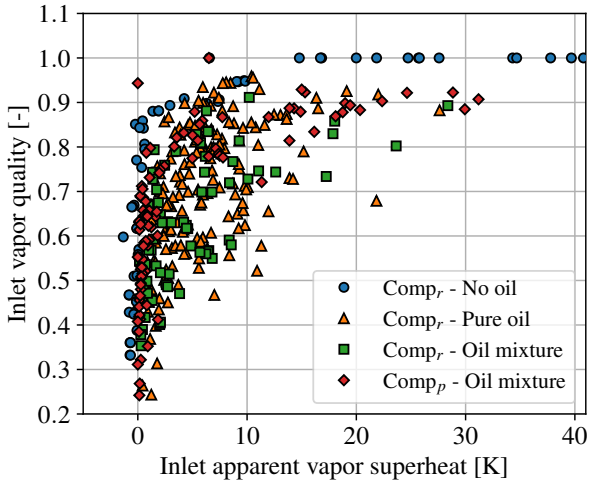

Figure 3.7: Inlet conditions of the data points collected from the four experimental campaigns (Comp$_r$ stands for the retrofitted compressor while Comp$_p$ stands for the prototype).

3.3.2 Vapor quality determination methodology

A vapor quality determination methodology has already been presented by the author in Leclercq et al. (2024b), with some of the same experimental data used in the frame of this thesis. Three assumptions were used to apply an energy balance on the mixing line, allowing the determination of the unknown inlet quality. These assumptions have been improved as follows:

1. In the previous method, it was assumed that no refrigerant is flowing in the oil line after the oil separator, as a minimum apparent superheat is ensured at the outlet of the heating resistor. Nevertheless, oil-refrigerant solubility experimental data support that, even with a high apparent superheat, refrigerant mass fraction in the liquid phase is non-negligible, even when the vapor quality is high. Therefore, oil-refrigerant data measurements were used to estimate the liquid phase composition after phases separation, with the calibrated Cavestri equations of Section 2.3.6. Measurements of the temperature and the pressure at the inlet of the oil separator allow to figure out the liquid phase composition. From this liquid phase composition, the mass flow rate of refrigerant flowing with the oil can easily be figured out. Regarding the oil mass fraction in the vapor phase after separation, it is neglected as the saturation pressure of the oil is extremely low compared with the refrigerant (Scialdone et al. 1996). Therefore, the mass flow rate of vapor is assumed to be only refrigerant.
2. Thermal equilibrium was assumed before the compressor, where the temperature of the mixture is measured. This assumes that the liquid phase and the vapor phase have the same temperature. However, depending on the operating point measured, it may be possible that this equilibrium is not reached, thereby inducing errors in the inlet temperature measurement. Thus, the new methodology proposes to figure out the vapor quality differently. This methodology does not assume thermal equilibrium at the inlet of the compressor as it does not use the inlet temperature measurement. It is based on oil-refrigerant solubility data and therefore assumes a mixture equilibrium (solubility equilibrium reached). A comparison of the two proposed methodologies is presented later.
3. No thermal losses were taken into account in the mixing line, so that the energy balance from the mixing point to the compressor inlet could be respected without heat losses. This assumption was deemed reasonable as the pipe is well insulated, moreover, for most of the

points, the mixture reaches temperatures close to the ambient temperature (≈ 20°C) in the low-pressure side (R1233zd(E) has a boiling point of 19°C). Improvement on this side has been brought using the 23 superheated points without oil, enabling the estimation of the heat losses through temperature and pressure measurements only, as full vapor condition is met at the compressor inlet.

A representation of the mixing line, downstream line of the mixing between flows coming from the superheated vapor line (g), the subcooled liquid line (l) and the oil line (o) can be found in Figure 3.8. As stated in the assumption, the oil line is not only driving oil, but also some liquid refrigerant, and this must be taken into account in the energy balance. The applied energy balance is written as follows:

$$h_{su} = h_{mix} - \frac{\dot{Q}_{amb}}{\dot{m}_{tot}} \tag{3.2}$$

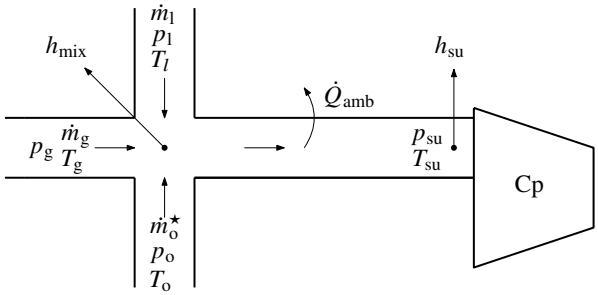

Figure 3.8: Representation of the mixing line.

The total mass flow rate can be calculated simply by adding the measurements from the three lines: $\dot{m}_{tot} = \dot{m}_g + \dot{m}_l + \dot{m}^\star_o$. The enthalpies are calculated using the definition provided in Section 2.3.7 and is thus derived from Equation 2.33. As underlined in the first assumption, the mass fraction of refrigerant solved in the oil ($x_{r,o}$) is taken into account in the calculation. This gives

$$\begin{aligned} h_{mix} = {} & Q_{mix} h_{r,g}(p_g, T_g) + z^\star_o x_{r,o} h_{r,l}(T_o, p_o) \\ & + z^\star_o \left(1 - x_{r,o}\right) h_o(T_o) + \left(1 - Q_{mix} - z^\star_o\right) h_{r,l}(p_l, T_l) \end{aligned} \tag{3.3}$$

$$\begin{aligned} h_{su} = {} & Q_{su}\, h_{r,g}(p_{su}, T_{su}) + z^\star_o\, x_{r,o}\, h^\sigma_{r,l}(T_{su}) \\ & + z^\star_o \left(1 - x_{r,o}\right) h_o(T_{su}) + \left(1 - Q_{su} - z^\star_o\right) h^\sigma_{r,l}(T_{su}) \end{aligned} \tag{3.4}$$

where the conditions (temperatures, pressures and mass flow rates) coming from the three main lines (vapor g, liquid l and oil o) and the supply (su) of the compressor are known. The corrected oil mass fraction, also called oil circulation ratio (OCR) is a function of the gross oil mass fraction $z^\star_o$, based on the measured mass flow rate flowing through the oil line ($z^\star_o = \dot{m}^\star_o / \dot{m}_{tot}$). It is defined as

$$z_o = z^\star_o \left(1 - x_{r,o}\right) \tag{3.5}$$

Moreover, the corrected oil mass flow rate can be defined similarly:

$$\dot{m}_o = \dot{m}^\star_o \left(1 - x_{r,o}\right) \tag{3.6}$$

The mixing quality, defined as the vapor quality before mixing, when no heat exchange has occurred yet, is given by $Q_{mix} = \dot{m}_g / \dot{m}_{tot}$.

The ambient losses in Equation 3.2 are expressed using the following equation:

$$\dot{Q}_{amb} = AU_{amb} \left(T_{su} - T_{amb}\right) \tag{3.7}$$

where the thermal conductance AU_{amb} is determined, as explained in assumption 3, using 23 inlet superheated points without oil circulation. These superheated points allow to calculate h_{mix} and h_{su} from measurements only. The methodology to determine AU_{amb} is therefore written as

$$\begin{aligned} AU_{amb} &= \arg\min \sum_k \left[h^k_{mix} - h^k_{su} + \frac{AU_{amb}}{\dot{m}^k_{tot}} \left(T^k_{su} - T^k_{amb}\right) \right] \\ &= 3.05^{1} \text{ [W/K]} \end{aligned} \tag{3.8}$$

where k is the index used to loop over the superheated points collected.

The previous methodology presented in Leclercq et al. (2024b) to determine the vapor qualities simply applies the energy balance written in Equation 3.2, as all pressures, temperatures and mass flow rates of each line are measured. Therefore, when combining Equations 3.3, 3.4 and 3.2, the only remaining unknown is the inlet vapor quality Q_{su}. This methodology assumes a thermal equilibrium between the two phases at the compressor inlet, as it uses the homogeneous measured temperature T_{su}. Moreover, this previous methodology did not consider the liquid refrigerant flowing in the oil line. In the new proposed methodology, the energy balance in Equation 3.2 is also applied. However, the compressor inlet temperature T_{su} is not going to be taken from the measurements anymore, and will become an unknown of the system. This allows getting rid of the thermal equilibrium assumption. Nevertheless, an additional equation is necessary to obtain a solvable system, which is the solubility equation applied to the two-phase oil-refrigerant mixture (Chapter 2, Equation 2.8). For both oils employed, the Cavestri equation is again used to determine the refrigerant liquid mass fraction at the compressor supply $x_{r,su}$, as a function of the inlet temperature and pressure. The refrigerant mass fraction is simply the difference between unity and the corrected OCR: $z_r = 1 - z_o$. The unknowns of the new system of equations are thereby Q_{su} and T_{su}. The limitation of this new methodology lies in its reliance on a good mixing between the oil and the refrigerant, so that the solubility equation can be applied. The measured temperature T_{su} is going to be replaced by the newly calculated temperature in the calculations of the volumetric and isentropic efficiencies. A comparison of the two aforementioned methodologies is shown in Figure 3.9.

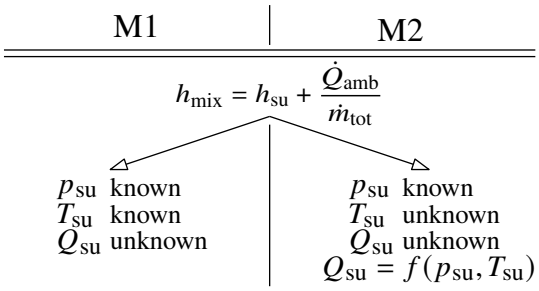

Figure 3.9: Presentation of vapor quality determination methodologies (previous M1, new M2).

The relative deviations between the vapor quality calculations from the previous (M1) and the new (M2) methodologies are represented as a function of the apparent superheat in Figures 3.10 and 3.11, without and with OCR correction, respectively. The uncertainty propagation from the vapor quality determination is also included in the relative error calculation, and

[1] A higher value has been used for the labscale-prototype as 1 meter of pipe length has been added to ensure thermal equilibrium despite the higher volumetric flow rates experienced with this machine.

represented in both figures. The idea behind the representation of the uncertainty is to check if the 0-error axis is crossed by the orange line (uncertainty), in which case the error propagation could explain the deviation between the two methodologies. This is especially true at low superheats, as the uncertainty propagation from the pressure results in more deviation in vapor quality (solubility equation).

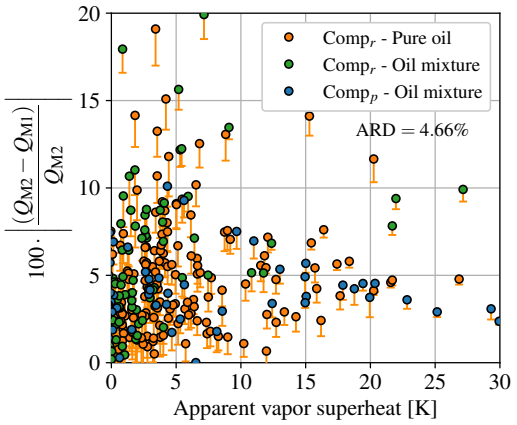

Figure 3.10: Relative deviation between the vapor qualities coming from both methodologies without correction of the OCR.

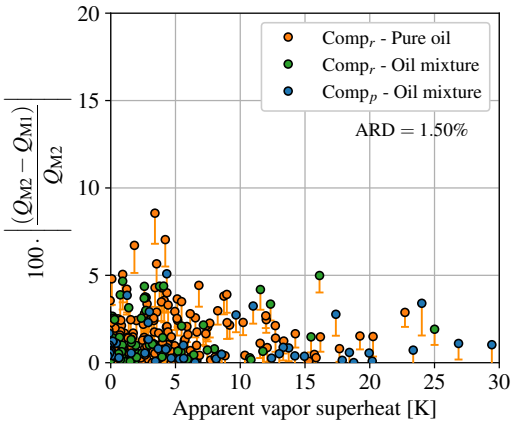

Figure 3.11: Relative deviation between the vapor qualities coming from both methodologies with correction of the OCR.

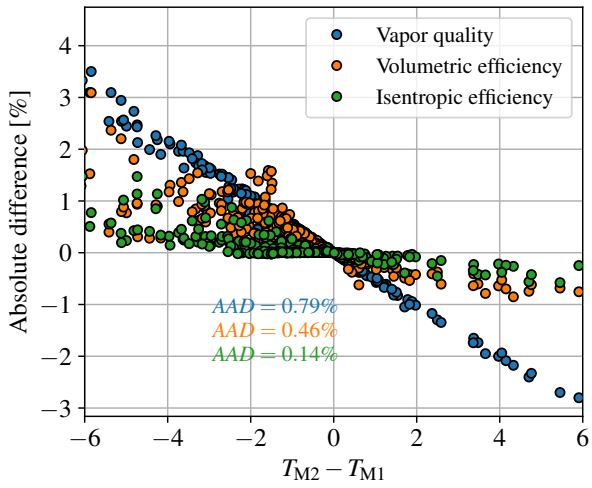

Figure 3.12: Absolute deviation in vapor quality, volumetric and isentropic efficiency as a function of the inlet temperature difference between both methodologies, for the whole dataset.

An important observation derived from the two figures is the clear improvement of the results when the refrigerant solved in the oil line is taken into account. The correction of the OCR allows the average relative deviation (ARD) to decrease from 4.66% to 1.50%, which is non-negligible. This reduction in deviation between the two methodologies does not necessarily indicate better accuracy for either one. However, since both methods predict similar vapor qualities, it is reasonable to conclude that correcting the OCR improves the overall prediction of vapor qualities. Eventually, after correction of the OCR, the comparison between the two methods still presents some points where the uncertainty propagation does not justify the difference. The difference between those specific points comes either from the thermal or the mixing non-equilibrium. Nevertheless, the relative deviation always remains below 10%, providing a good approximation of the vapor quality from both methodologies. The difference between the newly calculated inlet temperature and the measured temperature

is displayed in Figures 3.12 x-axis, while the differences in vapor qualities, volumetric and isentropic efficiencies (defined in the next subsection) are plotted on the y-axis. As can be seen, the average absolute difference (AAD) between the two methodologies is low, especially for the isentropic efficiency computed, from which the AAD stands below 1%, which supports the hypothesis that both methodologies are valid. The remaining results of this chapter are obtained using average values of inlet temperature and vapor qualities from both methodologies.

3.3.3 Volumetric and isentropic efficiencies

The volumetric and isentropic efficiencies of the compressors account for the presence of the liquid phase. In other words, in this section, they serve solely to characterize the machine's performance, without considering its integration into a complete thermodynamic cycle. Under ideal conditions, the values would equal one. For instance, without leakages, nor pressure losses or heat transfer would result in a volumetric efficiency equal to one, while if compression was reversible and adiabatic, the isentropic efficiency would equal one. If the efficiencies were to be investigated for integration into a thermodynamic cycle, the presence of oil would negatively impact the cycle performance; therefore, the definitions of the volumetric and isentropic efficiencies should be modified accordingly. In the present work, the focus is placed solely on the compressor itself, allowing these definitions to be used with the oil contribution included.

The volumetric efficiency of the compressor compares its measured mass flow rate with its theoretical mass flow rate, by multiplying the inlet density (ρ_{su}) by the volumetric flow rate, computed by multiplying the speed of the compressor (N_{cp}) and its displacement volume (V_{disp}). It can be computed using the following equation:

$$\varepsilon_v = \frac{\dot{m}_{tot}}{N_{cp}\, V_{disp}\, \rho_{su}} \tag{3.9}$$

The inlet density can be calculated using

$$\rho_{su}^{-1} = Q_{su}\, \rho_{r,g}^{-1}(p_{su}, T_{su}) + (1 - Q_{su})\, \rho_{l}^{-1}(p_{su}, T_{su}) \tag{3.10}$$

where the liquid density ρ_l can be calculated using the calibrated Henderson equation presented in Section 2.3.3.

The isentropic efficiency compares the ideal power consumption of the compressor with its real power consumption and can be obtained from

$$\varepsilon_{is} = \frac{\dot{m}_{tot}\left(h_{ex,is} - h_{su}\right)}{\dot{W}_{shaft,cp}} \tag{3.11}$$

with $h_{ex,is}$ the outlet enthalpy following an isentropic (adiabatic and reversible) compression and $\dot{W}_{shaft,cp}$, the power consumed at the compressor shaft, defined as

$$\dot{W}_{shaft,cp} = \omega_{mot} \cdot \tau_{shaft,mot} - \dot{W}_{f,belt} \tag{3.12}$$

where $\dot{W}_{f,belt}$ is the power loss from the pulley-belt mechanism, which could be directly measured by disengaging the clutch of the compressor while measuring the torque developed when running the motor at different speeds as represented in Figure 3.14. The values of the calibrated law can be found in Appendix B.2.2.

The definition of the isentropic compression outlet enthalpy of a two-phase oil-refrigerant mixture is inspired by the definition of Ramaraj et al. (2014), where the entropy exchange between the oil and the refrigerant is taken into account. However, the authors did not

consider the part of the refrigerant solved in the oil, as their inlet superheats were high enough to neglect it. A new definition is therefore proposed, where the part of the refrigerant solved in the oil is taken into account. The derivation of the isentropic enthalpy is similar to the developments provided in Section 2.4.4, except that it is here directly defined from the mixed state rather than from the split state. In this definition, two unknowns have to be defined:

- The isentropic temperature T_{is}
- The isentropic vapor quality Q_{is}

These two unknowns will allow to compute the isentropic enthalpy as follows

$$h_{is} = Q_{is}\, h_{r,g}(p_{ex}, T_{is}) + z_o\, h_o(T_{is}) + (1 - Q_{is} - z_o)\, h^{\sigma}_{r,l}(T_{is}) \tag{3.13}$$

Two equations are necessary to solve the system with the two previously defined unknowns: the conservation of entropy along the compression and the oil-refrigerant solubility equation (derived from Equation 2.8). The system to solve is therefore the following, with $s_{su} = s_{ex,is}$:

$$\begin{cases} s_{su} = Q_{su}\, s_{r,g}(p_{su}, T_{su}) + z_o\, s_o(T_{su}) + (1 - Q_{su} - z_o)\, s^{\sigma}_{r,l}(T_{su}) \\ s_{ex,is} = Q_{is}\, s_{r,g}(p_{ex}, T_{is}) + z_o\, s_o(T_{is}) + (1 - Q_{is} - z_o)\, s^{\sigma}_{r,l}(T_{is}) \\ Q_{is}\left[1 - x_{r,is}(p_{ex}, T_{is})\right] = 1 - z_o - x_{r,is}(p_{ex}, T_{is}) \end{cases} \tag{3.14}$$

The isentropic work determination process is illustrated in Figure 3.13. The crossing point between the two temperature lines defines the isentropic quality. It thus finds the temperature and vapor qualities allowing to respect the conservation of entropy and the solubility equation of the mixture. The obtained isentropic vapor quality then allows to get the isentropic work (illustrated by the green arrow).

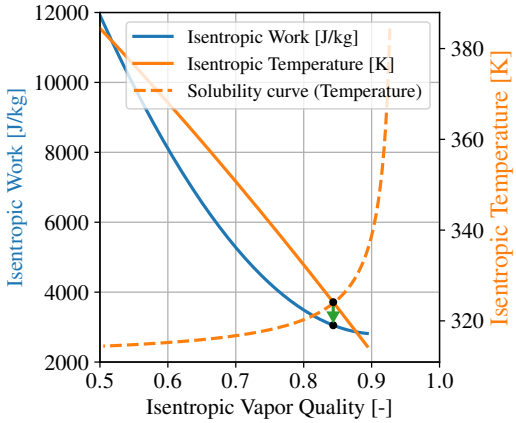

Figure 3.13: Illustration of the isentropic work calculation.

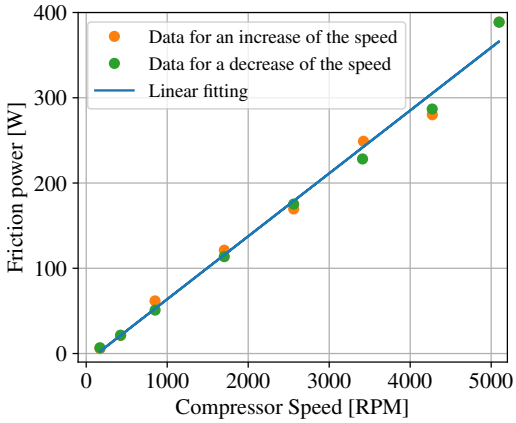

Figure 3.14: Power dissipated by the pulley-belt mechanism without load at different compressor speeds.

3.3.4 Interpolation tool

To remove the dependency of the maximum inlet quality Q^{max}_{su} on z_o (the higher the OCR the lower the maximum vapor quality), all results will be plotted as a function of the refrigerant-only vapor quality (varying between 0 and 1). As a reminder, it was defined in the previous chapter as: $Q_{r,su} = Q_{su}/(1 - z_o)$. This vapor quality could in theory never be equal to one, as it would mean a high enough apparent superheat allowing to have 0% refrigerant solved in the oil. This strategy helps in keeping the same vapor quality ranges whatever the oil circulation, for comparison purposes. The results coming from this refrigerant-only vapor

quality still have some dependency on the OCR, as a division is not a linear operation. For instance, having an OCR of 5% and a vapor quality of 50% would become a refrigerant-only vapor quality of 52.6%, while if the OCR was 10%, the refrigerant-only vapor quality would become 55.6%.

In total, 5 variables can influence the compressor performance:

1. The compressor inlet pressure p_{su}
2. The oil circulation ratio (or oil mass fraction) z_o
3. The compressor speed N_{cp}
4. The inlet vapor quality $Q_{r,su}$
5. The compression ratio r_p

All those variables have varying degrees of impact on both the isentropic and volumetric efficiencies of the compressor. However, it is impossible to get a high number of experimentally tested values for each variable for two reasons. First, the test bench limitations do not allow to test any conditions, for instance, the mass flow rate varies from 4 g/s (high quality with a low speed) to 90 g/s (low quality with a high speed), meaning that the pressure losses in the test bench will only allow to test high compression ratios at high speeds. Then, too many operating points are needed to test each variable with many values; for instance, if 4 fixed values were to be tested for each variable, the total number of operating points would be $4^5 = 1024$, which is impractical.

Therefore, instead of targeting all possible points, a useful predictive tool has been used to interpolate points that were not recorded. The tool is called GPExp (Quoilin et al. 2016) and is a machine learning tool using Gaussian processes to predict data in the 5 dimensions given a set of points. It can get rid of the outliers and perform a cross-validation (CV) with the dataset used, to prevent overfitting/underfitting. The cross-validation consists of removing one or several points from the dataset and then using the Gaussian process model on the remaining points to predict the removed points. This methodology is applied to the whole dataset and if the total error is below a fixed tolerance, the dataset is accepted. If too much error is resulting from the cross-validation, it means that some data are missing to get accurate predictions. This tool is very accurate when points need to be interpolated, but loses its accuracy when extrapolation is performed.

In total, 192 points have been validated by GPExp for the first test campaign (pure oil with the retrofitted compressor), while 106 points have been validated for the second (oil mixture, one tested speed on the retrofitted compressor). Moreover, the two-phase points without oil have been included in both test campaigns. The interpolation tool could not be applied to the third test campaign (retrofitted machine without oil) because only 49 points were recorded in the two-phase region. The data coming from the third test campaign with superheated conditions are only used for sensor calibration. The results from the test campaign on the retrofitted compressor with the oil mixture will not be analyzed, as no conclusion could be taken from the comparison between the two oils, as detailed in Leclercq et al. (2025). The last test campaign performed on the lab-scale prototype counts 74 operating points, including 68 validated by GPExp.

The fitting error as well as the cross-validation error on the volumetric and isentropic efficiency can respectively be seen in Figure 3.15 and Figure 3.16, for both tested machines. The average absolute deviation of the two performance indicators can be found in Table 3.4. On average, the accuracy of the interpolation (based on the cross-validation) can be trusted within a 4% point range for the volumetric efficiency and within a 3% range for the isentropic efficiency. It is essential to emphasize that those AAD do not take into account the mean uncertainty propagation on both volumetric and isentropic efficiency, which are equal to 4.4% and 3.7%, respectively. This is a limitation of the algorithm; the predicted values of isentropic and volumetric efficiencies may be correct on average, but deviations can occur, especially

in the 5D space where the density of recorded points is lower. Therefore, the purpose of the following analyses is only to catch and analyze some trends, not to provide the reader with data on isentropic and volumetric efficiency, as the total uncertainty is consequent. The variables having the most influence on the isentropic efficiency have been identified as being the inlet vapor quality and the pressure ratio. Thereby, 2D color maps have been generated to show the evolution of the isentropic and volumetric efficiencies as a function of these operating variables.

	Predictions		Cross-validation	
	ε_v	ε_{is}	ε_v	ε_{is}
Retrofitted compressor (comp$_r$)	2.62%	1.52%	3.41%	2.56%
Lab-scale prototype (comp$_p$)	2.36%	1.39%	4.77%	3.45%

Table 3.4: Average absolute deviation (AAD) of the prediction and the cross-validation of the efficiencies for both tested machines.

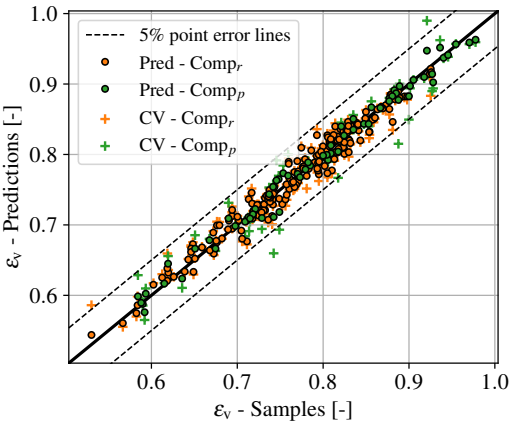

Figure 3.15: Datasets versus predictions (Pred) and cross-validation (CV) for the volumetric efficiency.

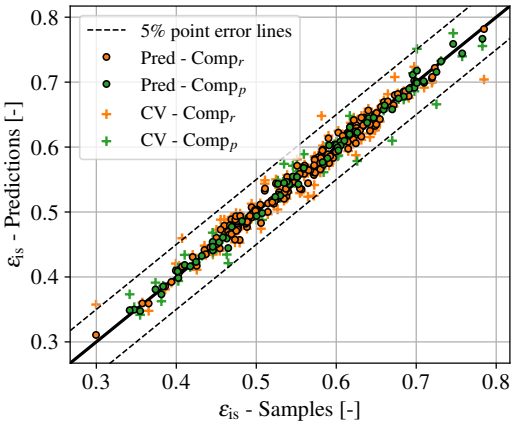

Figure 3.16: Datasets versus predictions (Pred) and cross-validation (CV) for the isentropic efficiency.

3.4 Retrofitted compressor results

A considerable number of operating points have been recorded on the retrofitted compressor. Therefore, results from its test campaign are used to understand the behavior of a compressor under two-phase flow regimes. A reference case is first set up, with fixed inlet pressure, OCR and speed and the resulting 2D colored maps are analyzed. Then, variations of the fixed variables are performed to check the sensitivity of the reference 2D maps. Finally, the case of pure-refrigerant compression is studied, using the limited data available to understand some trends.

3.4.1 Reference case

First, the reference plots of the isentropic and volumetric efficiencies are analyzed (Figures 3.17 and 3.18). Those reference plots will be used as a basis for the following plots (Figures 3.19 to 3.24), displaying only the difference in efficiencies with respect to these references, making the analysis easier. In this reference case, the speed of the compressor is fixed at 2500

RPM, the inlet pressure is set at the average tested pressure, i.e., at 1.5 bar and the OCR is also fixed at its average tested value of 5%. Moreover, tested points are represented on the reference plots, despite the variations with the three remaining operating variables, allowing to envision the whole datasets for the two compared testing campaigns, thereby allowing to see where extrapolation is performed on these two dimensions, as it is less reliable than interpolation. The 2D reference maps of the isentropic and volumetric efficiencies can be found in Figure 3.17 and Figure 3.18. As can be seen, the experimental points almost cover the entire maps, meaning that extrapolation is limited for the two displayed variables. To make the visualization easier, complementary 3D plots of the reference 2D maps can be found in Appendix B.3.

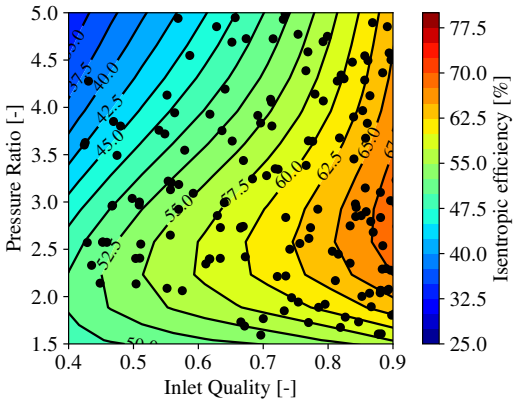

Figure 3.17: Evolution of the isentropic efficiency for the retrofitted compressor, with an inlet pressure of 1.5 bar, an OCR of 5% and a compressor speed of 2500 RPM (reference case).

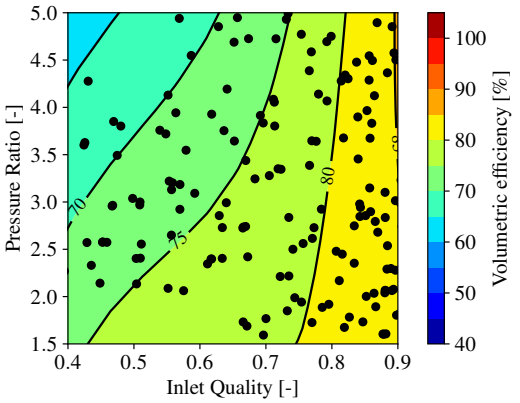

Figure 3.18: Evolution of the volumetric efficiency for the retrofitted compressor, with an inlet pressure of 1.5 bar, an OCR of 5% and a compressor speed of 2500 RPM (reference case).

Analyzing the results with accuracy requires validated numerical models allowing to understand diverse phenomena occurring within the machine. This numerical modeling is part of the next two chapters. Nevertheless, it is already possible to analyze the interpolated maps, resulting from the application of GPExp, and understand some trends without deep analysis. The first trend observed is that the isentropic efficiency decreases as the inlet quality decreases. This undesirable decrease highlights the key question addressed in this thesis: how can two-phase compression be made efficient enough to be of practical interest? The origin of this decrease is twofold. First, it can be justified with the decrease of the volumetric efficiency when the vapor quality decreases (see Figure 3.18), which could be explained by higher volumetric leakages faced by the compressor in the suction chambers. This volume, coming from the upstream compression chambers, reduces the volume that can be sucked by the compressor. The pressure-loss pathway has also been investigated; however, in that case, the volumetric efficiency would not increase with increasing speed. Therefore, the primary origin of the decrease in volumetric efficiency is leakage, and it also impacts the isentropic efficiency. The other origin of the isentropic efficiency decrease is the thermal non-equilibrium brought by the non-compressible liquid phase generating irreversibilities. The lower the vapor quality, the more pronounced this effect.

Another observable trend is the undercompression losses that are emphasized with low vapor qualities, as can be seen from the decreasing slope of the iso-isentropic efficiency curves towards lower vapor qualities. This can be explained by the shift of the ideal pressure ratio towards lower values when lowering the qualities, as the inlet-outlet volume ratio diverges further from the compressor's built-in volume ratio. Therefore, when lowering the vapor quality, undercompression losses are increased and overcompression losses are decreased.

The mechanical losses also affect the isentropic efficiency, nevertheless, they may affect it uniformly. The operating variable that strongly impact the mechanical losses would be the compressor speed, whose effects are studied in the next subsection.

To help understand more deeply some trends, the mass flow rate and the power consumption (at the shaft) have been displayed in Appendix B.3.2. Those mass flow rate and power are directly linked with the efficiencies, however, their behaviors are more straightforward to understand as they do not depend on a formula influenced by several variables, but are directly measured. Interestingly, power consumption is not affected by vapor quality, whereas mass flow rate shows a strong dependency. Furthermore, ideal work of compression and theoretical mass flow rate can also be found in the appendix, enabling a complete comprehension of the factors influencing the isentropic and volumetric efficiencies.

3.4.2 Effect of the speed

Both 2D maps of isentropic and volumetric efficiency difference with the reference case at 2500 RPM, where the speed has been increased to 5000 RPM, can be found in Figure 3.19 and Figure 3.20. The improvement of the volumetric efficiency for an increase in speed can either be explained by a reduction of leakages at low vapor qualities or by the total mass flow rate being higher, minimizing the impact of the leakage. The effect of an increase in speed at high vapor qualities seems to decrease the isentropic efficiency, which could be explained by the increase in mechanical losses inside the compressor, despite the increase in volumetric efficiency. These mechanical losses come from friction in the bearings and between touching parts from the orbiting mechanism, increasing with the increase in speed. Nevertheless, the efficiency at low vapor qualities is enhanced, with an increase of more than 5% point for high compression ratios. The increase in volumetric efficiency is thus able to counterbalance the increase in mechanical losses, resulting in an increase in isentropic efficiency at low vapor quality. Regarding the increase at high pressure ratios, one explanation could be the reduction of the high undercompression losses induced by the low vapor qualities, as for high speeds, the liquid could be preventing an isochoric compression when the compression chamber opens to the discharge chamber. The liquid could somehow increase the built-in volume ratio by shifting the discharge angle. This latter explanation requires numerical validation to be confirmed, which will be included in the next two chapters. An interesting result that can not be seen on the plots regards the position of the no-difference in isentropic efficiency line (0.0 in Figure 3.19). This line shifts progressively to the left (toward lower vapor qualities) as the speed increases, showing that the positive effect of increasing speed on the isentropic efficiency becomes less significant at higher speeds. Friction generation therefore dominates the balance between leakage reduction and friction generation.

As can be understood, the speed significantly affects both volumetric and isentropic efficiencies. Increasing the speed reduces leakage impact but may increase the impact of mechanical losses. Therefore, a trade-off must exist to maximize the isentropic efficiency. In other words, for each vapor quality, pressure ratio, inlet pressure and OCR, an optimal speed maximizes the isentropic efficiency. Variation of isentropic efficiency for several vapor qualities can be found in Figure 3.21. As can be observed, each iso-quality curve seems to reach a maximum, however, the lower the quality, the higher the speed maximizing the efficiency. Consequently, it seems that the reduction of the leakage impact is counterbalanced the increase of friction losses at low vapor qualities, as already observed. A representation of the optimal speed as a function of vapor quality is provided in Figure 3.22. The tendency is clear: the optimal speed increases with the decrease of vapor quality for three (out of four) of the represented pressure ratios, until reaching the maximum speed of 5000 RPM. This figure could be used to design the optimal compressor speed, however, it requires the selection of the right displacement volume prior to the speed optimization, which results in an iterative

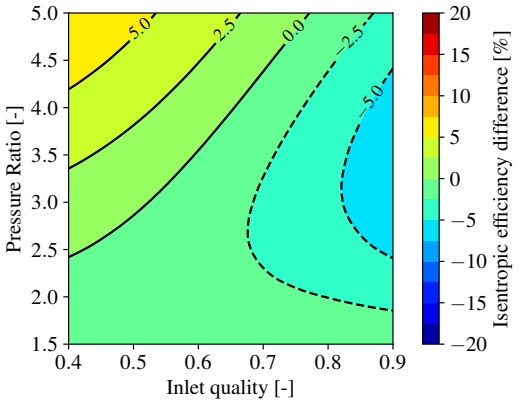

Figure 3.19: Difference in isentropic efficiency from the reference case speed of 2500 RPM to 5000 RPM.

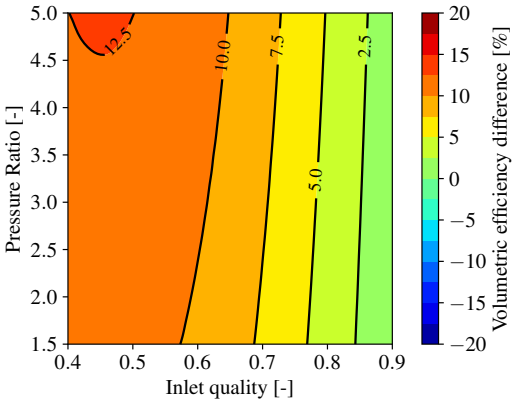

Figure 3.20: Difference in volumetric efficiency from the reference case speed of 2500 RPM to 5000 RPM.

process, given that the performance of the compressor under two-phase conditions is known, or can be estimated.

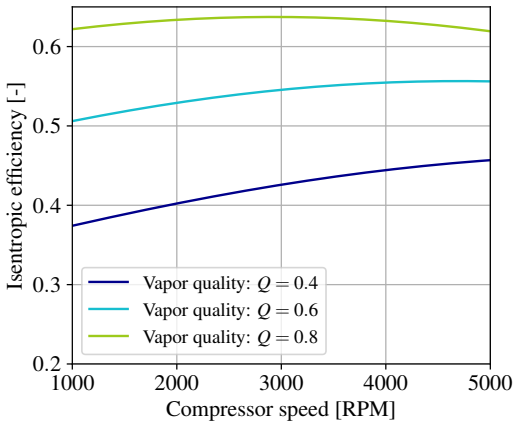

Figure 3.21: Variation of the isentropic efficiency with the compressor speed at different vapor qualities for a compression ratio of 3, an OCR of 5% and an inlet pressure of 1.5 bar (through GPExp).

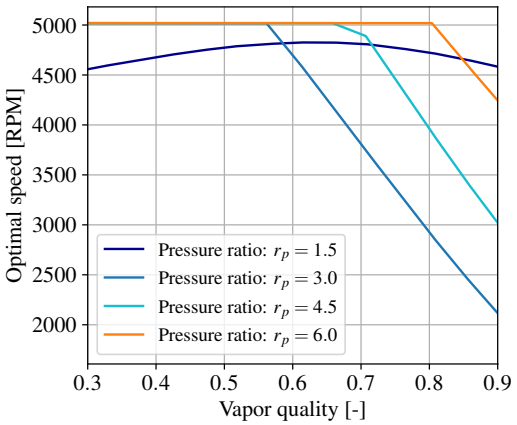

Figure 3.22: Optimal compressor speed as a function of the vapor quality for different pressure ratios at an OCR of 5% and an inlet pressure of 1.5 bar.

3.4.3 Effect of the OCR

Both 2D maps of isentropic and volumetric efficiency difference with the reference case at an OCR of 5%, where the OCR has been increased to 10%, can be found in Figure 3.23 and Figure 3.24. It is important to highlight the slight dependency of the refrigerant-only vapor quality on the OCR, as the higher the OCR, the higher the liquid mass fraction (oil comprised), as for the same quantity of refrigerant in the liquid phase, more oil can be found. Higher OCR would therefore lead to more liquid in the compressor chamber, for the same refrigerant-only vapor quality. Therefore, it is difficult to quantify the impact of the OCR, as a higher OCR affects the overall vapor quality by decreasing the refrigerant liquid mass fraction, while simultaneously affecting the refrigerant-only vapor quality by increasing the overall liquid mass fraction. Consequently, the effects at high and low vapor qualities are expected to differ. When the inlet quality is high, this results in an increase in the volumetric efficiency due to a higher liquid viscosity, potentially creating a sealing effect. This effect is observed in Figure 3.24, while, at low vapor qualities, the effect of the oil on the viscosity is negligible

due to high mass fractions of refrigerant, so that the higher liquid mass fraction induces more leakage, as already observed in the Figure 3.18. This reduction of liquid viscosity is described in Section 2.2.3 of previous chapter. The difference in isentropic efficiency (Figure 3.23) globally follows the trend of the volumetric efficiency (Figure 3.24), however, an important increase can be observed at low pressure ratios. In other words, it seems that overcompression losses are reduced when working at high OCR. The higher global liquid mass fraction at high OCR could reduce the ideal pressure ratio for the given built-in volume ratio, explaining why overcompression is favored while undercompression is penalized. The volumetric and isentropic efficiencies for different OCR have also been plotted at a fixed vapor quality of 50%, varying with the pressure ratio, in Figure 3.25. A vapor quality of 50% has been chosen to avoid any influence of change of viscosity on the results. For high pressure ratios, the OCR of 0% leads to higher volumetric efficiencies. This can again be explained by the low overall liquid mass fraction when the OCR is reduced, resulting in less leakage. At low pressure ratios, this effect is reduced as leakages are overall. Regarding the isentropic efficiency, a clear trend is observed: the higher the OCR, the lower the ideal pressure ratio that maximizes isentropic efficiency, this trend was also observed in Figure 3.23.

Eventually, the effects of inlet pressure variation are also analyzed; however, since the influence is not significant, the results are reported in Appendix B.3.3.

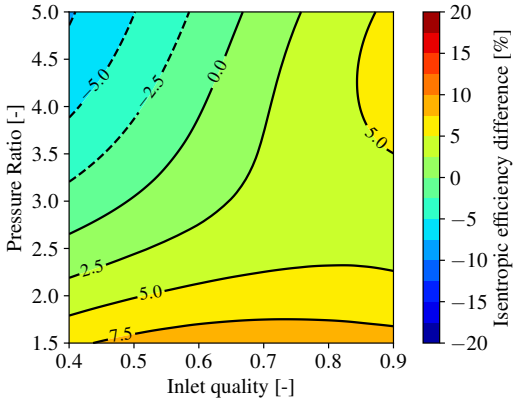

Figure 3.23: Difference in isentropic efficiency from the reference case OCR of 5% to 10%.

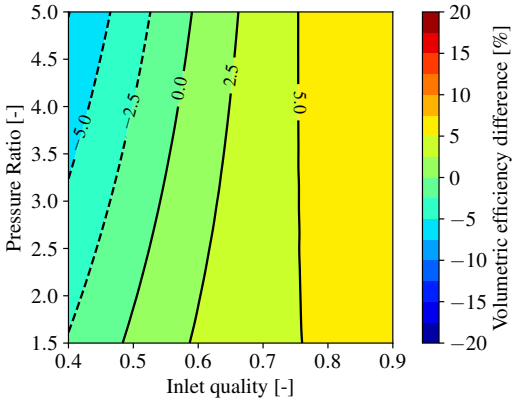

Figure 3.24: Difference in volumetric efficiency from the reference case OCR of 5% to 10%.

3.4.4 Pure refrigerant compression

Some results of the pure-refrigerant (no oil) two-phase compression can be found in Figure 3.26, as well as the associated uncertainties. To get enough data on the plot, experimental points have been selected with some margin on the operating variables, i.e., 1 ± 0.1 bar for the inlet pressure and 2.7 ± 0.25 for the pressure ratio. The speed is fixed at 2000 RPM, while the OCR is zero (no oil) and the vapor quality is varying. The curves have been obtained by using GPExp and fixing the OCR to zero, which does not constitute an extrapolation, as the no-oil experimental points have been included in the dataset. The selected nominal pressure ratio of 2.5 is actually optimal at low vapor qualities (lower than 0.6), thereby achieving relatively high isentropic efficiency (minimum of ±50%), even at low vapor qualities. Regarding volumetric efficiency, it is clear that a reduction in vapor quality induces an increase in leakage, up to a point at which the ratio between the leakage going in the suction chamber and the delivered mass flow rate becomes quasi-constant, resulting in an approximately constant volumetric efficiency. This effect is more deeply analyzed in the numerical part (Chapter 5). A superheat of 20 K has been measured for the point at a 100% vapor quality. This interpolated curve does not reach this point, as data with vapor qualities of one have been excluded from the algorithm

since the superheat would become a new operating variable for those points. Reformulated otherwise, different superheats can lead to different performances for a given quality of 1. Interestingly, this figure also allows to show the good fitting of the algorithm, despite the experimental uncertainties combined with prediction uncertainties from GPExp.

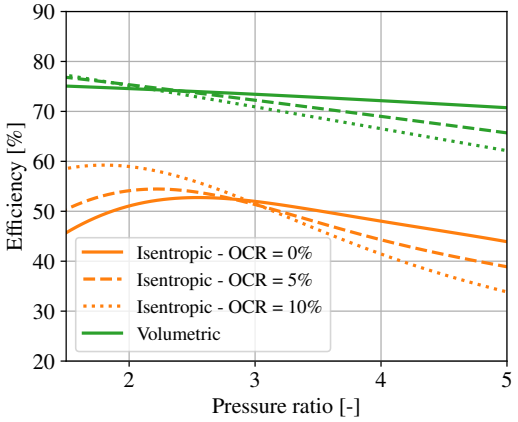

Figure 3.25: Isentropic and volumetric efficiencies for a varying OCR with an inlet pressure of 1.5 bar, a refrigerant vapor quality of 50% and a compressor speed of 2500 RPM.

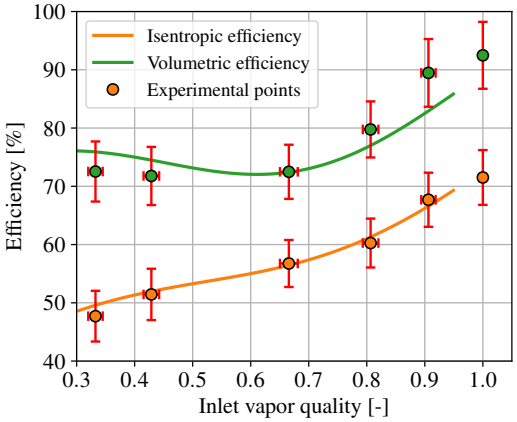

Figure 3.26: Isentropic and volumetric efficiencies varying with the vapor quality without oil, for a speed of 2000 RPM, an inlet pressure of 1 ± 0.1 bar and a pressure ratio of 2.7 ± 0.25.

3.5 Lab-scale prototype results

Despite the lower number of points recorded with the lab-scale prototype (72), the GPExp interpolation algorithm performed quite well, although not as well as for the retrofitted compressor. In this test campaign, the cross-validation absolute deviation increased from 3.41% to 4.77% for the volumetric efficiency and from 2.56% to 3.45% for the isentropic efficiency. Results from the final testing campaign are compared with the retrofitted compressor, based on efficiency differences with the reference maps. Moreover, this compressor has been equipped with a dynamic pressure sensor from Kulite, allowing recording of the internal pressure with a frequency of 25.6 kHz, thereby providing a new reference for model validation.

3.5.1 Comparison with the retrofitted compressor

Difference in isentropic and volumetric efficiencies can be found in Figures 3.27 and 3.28. Surprisingly, the prototype seems to show better volumetric efficiencies. Two phenomena could explain this trend: on the one hand, the greater displacement volume of the machine with similar volumetric leakages in the suction chamber, and on the other hand, the radial compliance mechanism allowing direct radial contact between the scrolls, with a force of 150 N, could decrease the leakages. At high vapor qualities, the minimal difference in volumetric efficiency suggests that the prototype performs as well as the retrofitted compressor with nearly full vapor. Furthermore, the better volumetric efficiency at higher pressure ratios could be the results of the greater number of compression chambers working in parallel for this machine, which limits the impact of the discharge chamber pressure on the suction process. The volumetric efficiency of the lab-scale prototype appears to be independent of the pressure ratio; however, this behavior is not observable in the difference plot. To observe this phenomenon, absolute maps (both 2D and 3D) of the lab-scale prototype isentropic and volumetric efficiencies can be found in Appendix B.4.1. Regarding the isentropic efficiency,

it seems to be lower at high vapor qualities; it could also be explained by the radial compliance mechanism increasing friction losses. This effect could decrease the overall isentropic efficiency across the map, however, the increase in volumetric efficiency, combined with the increase in built-in volume ratio, favors undercompression over overcompression. Therefore, an increase is observed at high pressure ratios while the efficiency is decreasing at low pressure ratios. Finally, increased mechanical losses in the lab-scale prototype could also explain the important decrease in isentropic efficiency at low pressure ratios, as the power loss remains constant but relatively significant in comparison with the lower power consumptions at those ratios.

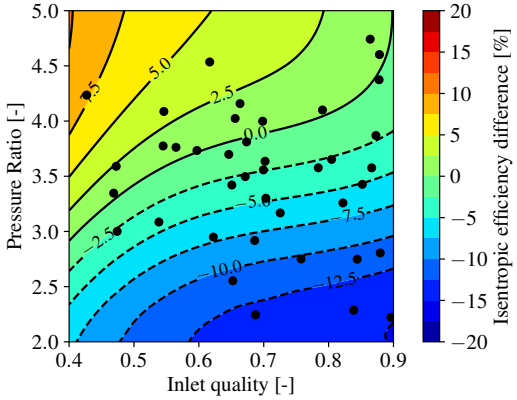

Figure 3.27: Difference in isentropic efficiency from the retrofitted compressor to the lab-scale prototype at the reference conditions.

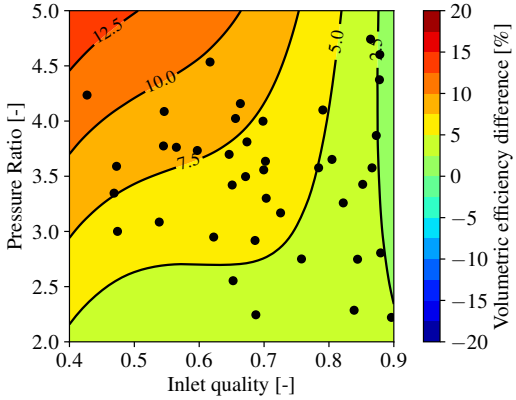

Figure 3.28: Difference in volumetric efficiency from the retrofitted compressor to the lab-scale prototype at the reference conditions.

The power consumption and the mass flow rate, at the reference conditions, are respectively provided in Figures 3.29 and 3.30. Similar trends to those of the retrofitted compressor (Appendix B.3.2) are observed: the compressor power shows low sensitivity to vapor quality, and the mass flow rate shows low sensitivity to the pressure ratio. It seems, however, that the mass flow rate is even less sensitive to the pressure ratio than in the retrofitted compressor (i.e., more vertical iso-mass flow rate lines), suggesting that the prototype experiences less leakage. It also seems that, at constant pressure ratio, power consumption slightly increases as vapor quality decreases (i.e., less horizontal iso-power lines). This could be explained by increasing suction pressure losses at lower vapor qualities; however, only the models would be able to confirm this phenomenon. Overall, power consumption and mass flow rate are higher for the prototype, due to its larger displacement volume.

3.5.2 Dynamic pressure sensor

Literature on pressure measurements within scroll compressors is scarce. Chang et al. (2004) and Mahfouz (2004) used numerous pressure sensors on scroll compressors to validate deterministic models; however, limited information is provided regarding the validation procedure. Picavet et al. (2014) analyzed the pressure-volume ($p-V$) diagram obtained from six pressure sensors to characterize the efficiency losses of a compressor; moreover, they characterized the performance of the intermediate discharge valve at low pressure ratios. B. Wang et al. (2007) used four pressure sensors to validate a deterministic model; moreover, they provided practical information on sensor placement to avoid unwanted pressure distortion caused by the natural frequency of the setup. They advised minimizing the volume between the sensor and the measured pocket and maximizing the measurement port diameter. A dynamic pressure sensor has also been placed on the lab-scale prototype studied in the frame of this thesis, enabling measurement directly inside the compressor chambers. The model used is a Kulite

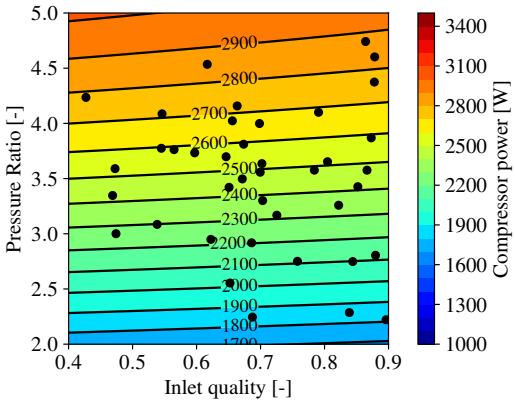

Figure 3.29: Evolution of the power consumption of the lab-scale prototype at the reference conditions.

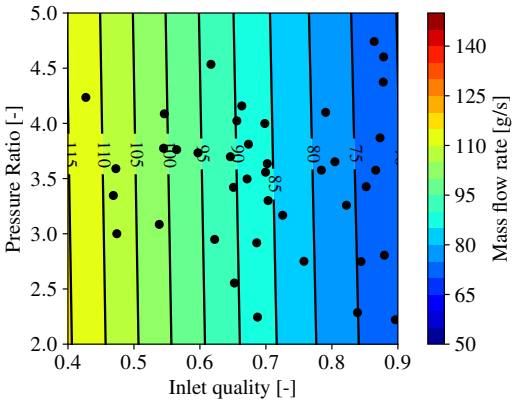

Figure 3.30: Evolution of the mass flow rate of the lab-scale prototype at the reference conditions.

XT-190 (see Figure 3.33), with the acquisition frequency set to 25.6 kHz to ensure sufficient data is captured over a single revolution of the compressor shaft. The disposition of the fixed scroll ports can be found in Figure 3.34. As can be seen in Figure 3.31, the sensor has been integrated from the bottom of the casing and reaches the fixed scroll. The vertical placement of the sensor can be seen in Figure 3.32, a short gap of 8.2 mm separates the surface of the sensor from the base of the fixed scroll and a port diameter of 4.2 mm is used, which respects the placement procedure recommended by B. Wang et al. (2007). However, although the port diameter is similar to the scroll thickness, the tip seal thickness is smaller, making leakage through the port possible.

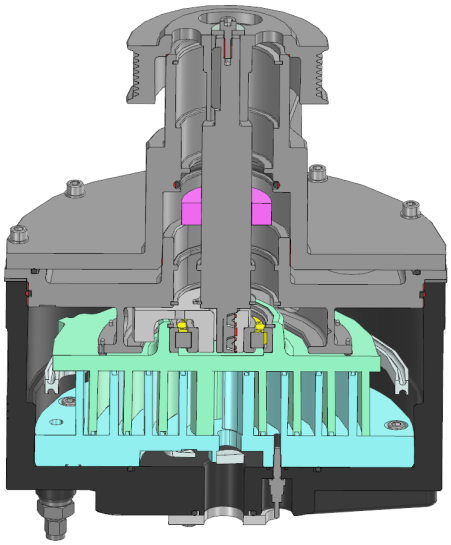

Figure 3.31: Global view of the pressure sensor position.

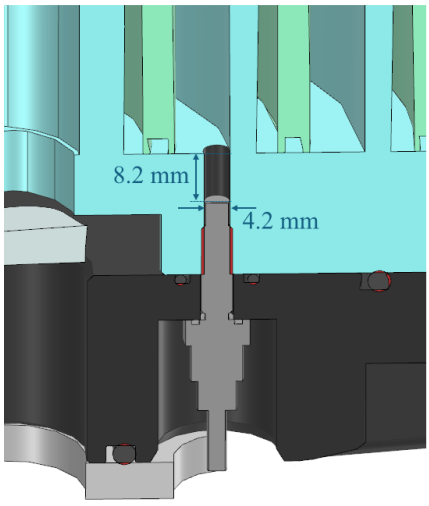

Figure 3.32: Zoomed view of the pressure sensor position.

The sensor allows partial measurement of the compression and discharge chambers' pressure. However, 2.4 revolutions are necessary to compress until the discharge process, which is itself performed along one full rotation. Taking the suction process into account, a total of 4.4 revolutions are necessary for the volume of fluid to travel from the inlet to the outlet without considering leakages. Therefore, the dynamic pressure sensor is only able to measure less than 25% of the angle range of the total pressure evolution throughout

the machine. No other pressure sensors could have been placed on the machine for budget reasons. Nevertheless, the pressure evolution over one full rotation along the compression and the discharge already gives plenty of information regarding the behavior of the machines under two-phase conditions. Phenomena such as under- and overcompression can clearly be caught with the opening of the compression chamber to the discharge chamber. Furthermore, the sensor is close to an intermediate discharge valve, as can be seen in Figure 3.34, the sensor thus allows to directly see the evolution of pressure when the valve opens. Additionally, the first pressure seen by the sensor (when the new compression chamber reaches the sensor) allows linking a partial volume ratio to a pressure ratio, although suction pressure losses influence the final pressure ratio determined. Finally, the pressure variation over a full revolution provides a strong reference for calibrating the deterministic model, allowing the contributions of thermal non-equilibrium and leakage to be distinguished in the pressure evolution. Finally, this evolution allows to validate a part of the pressure-volume diagram that can be obtained from the simulation model.

As can be observed in Figure 3.34, the pressure sensor port is placed next to the fixed scroll. At a certain point of the revolution, the orbiting scroll progressively covers the port until full coverage and, when it moves past it, a new compression chamber becomes measurable by the sensor. The evolution of the sensor port area with the orbiting angle is provided in Figure 3.35, with the initial orbiting angle being defined as the zero-volume suction chamber. As can be seen, an important part of the revolution is partially or fully covered by the orbiting scroll, leading to phenomena difficult to explain and model. Therefore, the analysis is restricted to a window where the validity of the pressure signal is ensured.

Figure 3.33: Kulite pressure sensor.

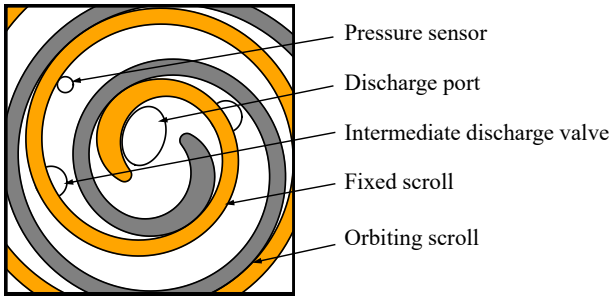

Figure 3.34: Prototype ports configuration.

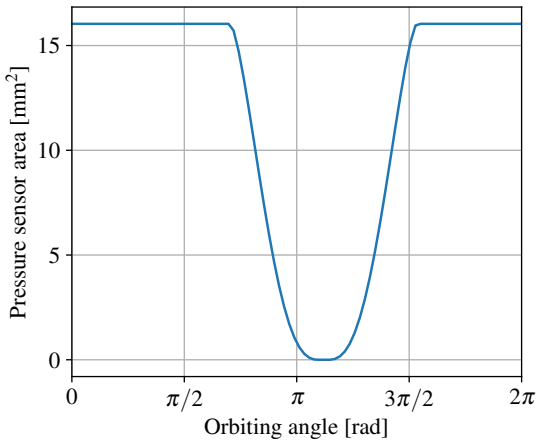

Figure 3.35: Pressure sensor area evolution with the orbiting angle.

Pressure measurement post-treatment

Data obtained by the sensor is a temporal evolution of the pressure; a typical signal recorded can be found in Figure 3.36. From one revolution to the next, the recorded pressure signal varies slightly due to measurement uncertainty and vibration-induced irregularities in the compression process. Therefore, to obtain a cleaner signal, the pressure measurement from each revolution must be aligned and averaged, which requires an accurate speed measurement.

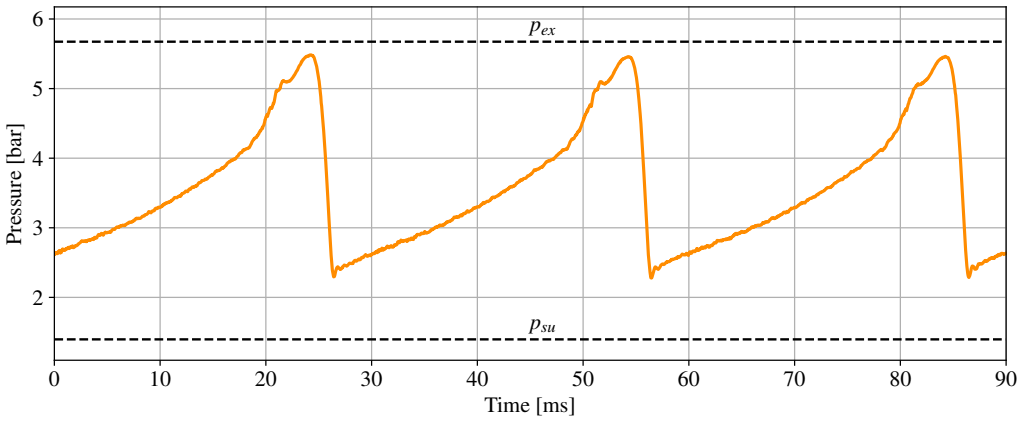

Figure 3.36: Raw pressure measurement as a function of time.

The torquemeter already allowed speed measurement of the motor shaft using an internal optical sensor, the compressor speed is then calculated from the pulley ratio. Even though the accuracy of this measurement technique is quite good (< 0.1% of deviation), belt slippage between the two pulleys creates a slight deviation between the measured and actual speed. This speed deviation is, on average, equal to 0.3%, and does not have a significant impact on the final shaft power determined. Nevertheless, when the average pressure over several revolutions needs to be calculated, no error is permissible, as instantaneous speed deviations accumulate when determining the corresponding angular position. For instance, even the slightest deviation of 0.3% results in a 30% angle deviation after 100 revolutions. Therefore, a more accurate speed measurement is required to average the pressures obtained from each revolution over a time period of up to 5 seconds. Up to 249 revolutions are recorded for the higher speeds. An inductive sensor has therefore been placed on the top of the compressor pulleys; more information regarding the setup and the calculation of the new speed is provided in Appendix B.4.2.

Using the newly calculated speed, or directly using the revolution period, allows to know the exact number of measurements taken in one revolution, provided that the acquisition frequency (25.6 kHz) is accurately known. Accumulating the pressure signals from each revolution finally allows to obtain signals displayed in Figures 3.37 and 3.38, respectively, for high and low vapor qualities. At the high vapor quality point, the signal is easily interpretable and shows a clear undercompression trend that could be obtained from a typical scroll compressor deterministic model. Nonetheless, the low vapor quality point shows a totally different trend: the undercompression behaves differently and the signal exhibits two distinct peaks which are difficult to interpret. The pressure signals still need to be adjusted with respect to the orbiting angle, in order to start where the port can measure the pressure from the new compression chamber, and to place the discharge angle on the plot accordingly. A straightforward approach is to use the minimum recorded value as the reference pressure when the orbiting scroll begins to uncover the port, however, this strategy proved to be unreliable for many points. The new strategy proposed consists in differentiating the measured pressure, filtering the derivative, and identifying the angle of transition between an approximately

flat region and a sudden change caused by the opening of the compression chamber to the discharge chamber. This compression chamber opening starts at an angle defined as the discharge angle, whose position can be determined from the geometry definitions of both orbiting and fixed scroll. This angle defines the exact moment when the two scrolls cease to remain in contact, resulting in a smooth and continuous opening between the compression and the discharge chambers. Nevertheless, changes in pressure cannot be detected right after the discharge angle, but when the opening becomes sufficient to induce a significant mass transfer between the two pockets, itself inducing a sudden pressure variation. The delayed discharge angle is therefore defined and corresponds to the angle where the pressure derivative changes suddenly. This delayed angle is defined as the discharge angle plus 20 degrees as can be seen in Figures 3.41. The 20 degree angle is an estimated angle coming from the model developed in the next chapter.

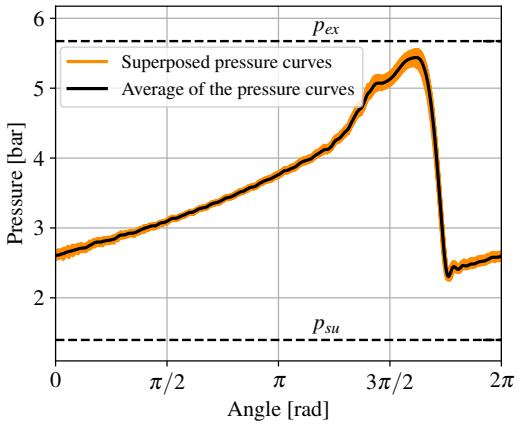

Figure 3.37: Post-treatment of the raw pressure for a high vapor quality (Q = 0.88).

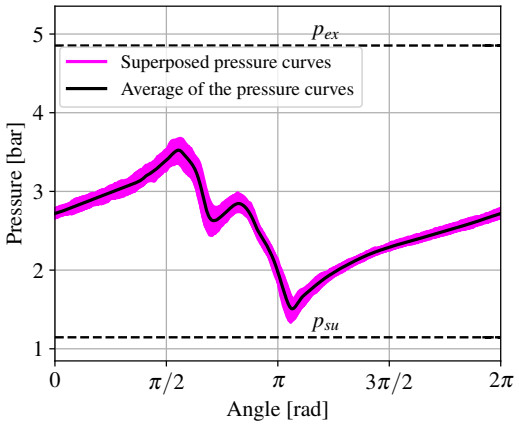

Figure 3.38: Post-treatment of the raw pressure for a low vapor quality (Q = 0.42).

A first example of the angle adjustment has been applied to the same point given the signal displayed in Figure 3.37, i.e., a high vapor quality with an undercompression trend. The results from the derivative can be found in Figure 3.41 and the final post-treated results in Figure 3.42. The starting orbiting angle of the figures is the angle at which the sensor port is fully covered by the mobile scroll. This reference also allows to fix the discharge angle on the plot. For clarity, the port area has been added to the figures. The hatched gray region represents the portion of the port area where the pressure behavior cannot be reliably interpreted, as unwanted effects, such as local pressure fluctuations on the sensor surface, may occur. It is the zone where the sensor port is partially or fully recovered by the scroll. Thereby, the discharge angle plus 20 degrees, corresponding to the angle at which the change in derivative occurs, has been used as a reference to set the angle of the pressure curve. In this specific case, the change is induced by the higher pressure of the discharge chamber, result of the undercompression trend, as can be observed in Figure 3.42, after the discharge angle. This graph also provides evidence that the minimum pressure cannot be associated with the zero port area. The gray zone clearly shows unexpected trends. More specifically, when the right zone is crossed, the pressure rise is interrupted and then resumes until a full rotation is completed. On the contrary, the pressure drop when the port starts to uncover (zero angle) is expected, as the lower pressure from the new compression chamber reaches the sensor.

A second example of the angle adjustment has been applied to the same point given the signal displayed in Figure 3.38, i.e., a low vapor quality with an undercompression trend. The results from the derivative can be found in Figure 3.43 and the final post-treated results in Figure 3.44. In this case, the change of derivative is even clearer than for the high-quality case. Moreover, the position of the pressure signal minimum is even more shifted in this case.

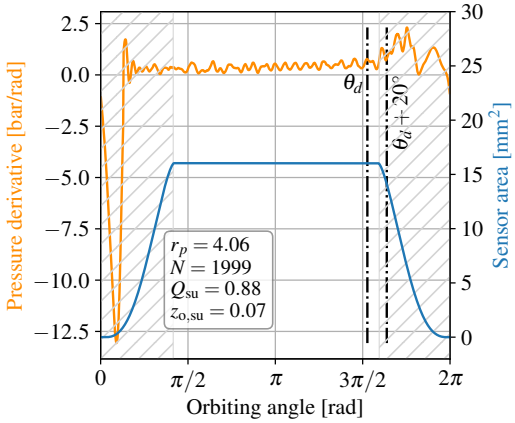

Figure 3.39: Derivative of the pressure signal with a high vapor quality ($Q = 0.88$).

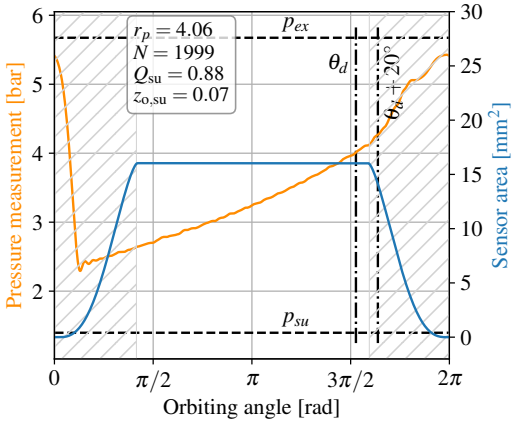

Figure 3.40: Post-treated pressure signal with a high vapor quality ($Q = 0.88$).

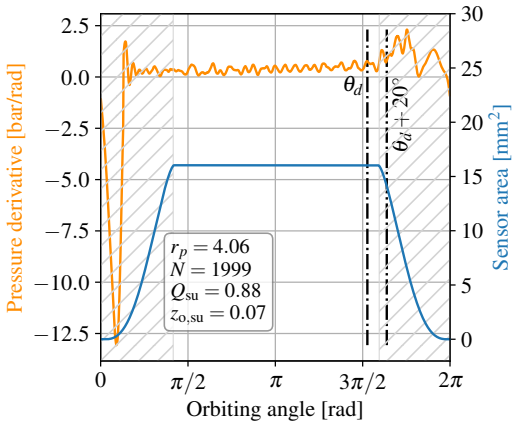

Figure 3.41: Derivative of the pressure signal with a high vapor quality ($Q = 0.88$).

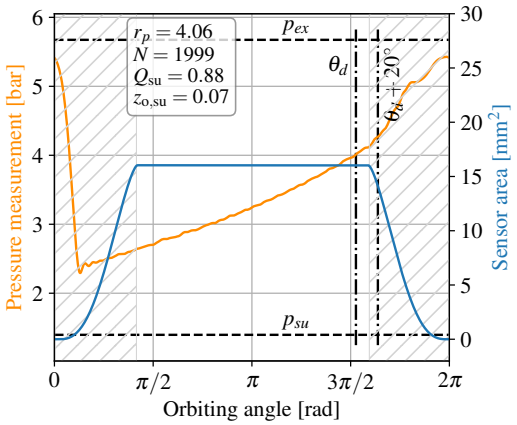

Figure 3.42: Post-treated pressure signal with a high vapor quality ($Q = 0.88$).

Interestingly, despite the undercompression trend, the pressure does not rise as fast as for the high-quality case. Again, the gray zone reveals totally unexpected trends. A sudden drop of pressure is encountered directly after reaching this zone; moreover, after full coverage of the port, a pressure rise is experienced, followed by a sudden drop reaching the new chamber pressure. A possible explanation for this phenomenon could be the increase of leakage gaps due to the presence of liquid, due to scroll deformation, radial compliance mechanism or movement of the tip seal, which could result in such pressure fluctuations from the sensor. Moreover, thermal non-equilibrium may also contribute to this phenomenon. Such trends can only be explained through prediction via an accurate model.

Pressure measurement results

As previously stated, the strategic positioning of the pressure sensor allows to catch the behavior of the pressure when the compression chamber opens to the discharge chamber, opening starting at the discharge angle θ_d. Therefore, it allows comparison of operating points experiencing undercompression, ideal-compression and overcompression, with similar vapor qualities. In other words, three operating points with similar conditions of speed, vapor quality and inlet pressure but different pressure ratios have been selected and compared to each other. This selection process is applied at a high vapor quality ($Q = 0.8 \pm 0.05$ [-]), a medium vapor quality ($Q = 0.6 \pm 0.05$ [-]) and a low vapor quality ($Q = 0.4 \pm 0.05$ [-]). Resulting

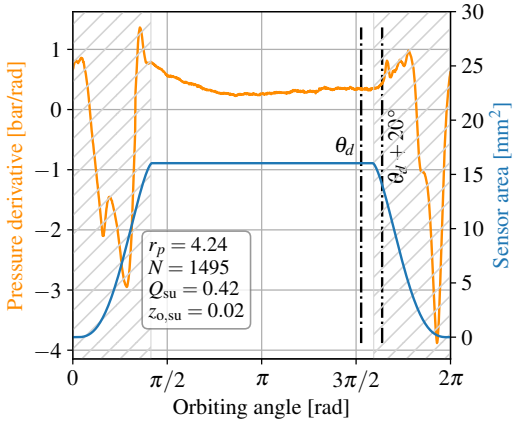

Figure 3.43: Derivative of the pressure signal with a low vapor quality ($Q = 0.42$).

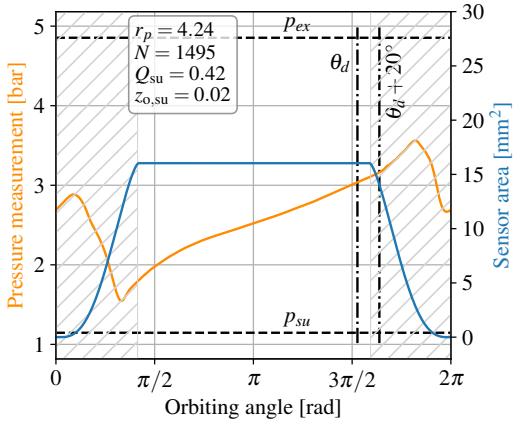

Figure 3.44: Post-treated pressure signal with a low vapor quality ($Q = 0.42$).

pressure measurements are displayed on three distinct plots and can be found in Figure 3.45. At high vapor qualities (Figure 3.45a), the three curves exactly behave as expected. The high pressure ratio results in undercompression, where the discharge pressure is reached after the discharge angle. Pressure losses caused by the reed valve can also be observed on this curve. At the medium pressure ratio, the pressure reaches the discharge pressure approximately at the discharge angle, while at the lowest pressure ratio, the discharge pressure is already reached long before the discharge angle, causing the intermediate discharge valves to open. As can be observed, the intermediate discharge valves, with their small diameter, create more pressure losses than the reed valve. Pressure measurements at a medium vapor quality ($Q = 0.6 \pm 0.05$ [-]) can be found in Figure 3.45c. At a high pressure ratio, the sensor is unable to capture the point at which the discharge pressure is reached. The pressure slope is therefore certainly steeper before reaching the discharge pressure than for a higher vapor quality, causing an increase in the compression work. The medium pressure ratio experiences a similar behavior as for a higher quality, i.e., the discharge pressure is reached at the discharge angle. The difference in slope may simply be a matter of graph scale, which will be verified later. At the lowest pressure ratio, overcompression is encountered, but at an angle closer to the discharge angle.

Finally, pressure measurements at low vapor qualities can be found in Figure 3.45b. The clear trend here is that every operating point experiences undercompression, as the discharge pressure is never reached by the curves. As already observed in the 2D maps analysis, it seems that overcompression is favored while undercompression is penalized when decreasing the vapor quality. All three curves exhibit similar shapes: a drop in pressure is observed at the beginning of the gray zone, followed by a rise after the full coverage of the sensor by the orbiting scroll, before the final drop. No direct analysis of these phenomena can be provided here, as the observed trends are difficult to justify. Moreover, they may not be adequately captured by the model, which does not account for the relative positioning of the pressure sensor port and the orbiting scroll tip seal.

Directly comparing similar pressure ratios and inlet pressure at different qualities allows to highlight the clear difference in behavior when reducing the vapor quality. Figure 3.46 shows three curves at similar inlet pressures (1.25 ± 0.15 bar), pressure ratios (4.0 ± 0.2) and speeds (2000 RPM), but different vapor qualities. The high selected pressure ratio allows to ensure undercompression trends for the three curves. Interestingly, the slopes only slightly differ from each other before reaching the discharge angle. The high vapor quality curve exhibits an early increase in pressure, while the other curves seem to barely react to the opening to the discharge chamber. Moreover, despite the suction pressure being very similar,

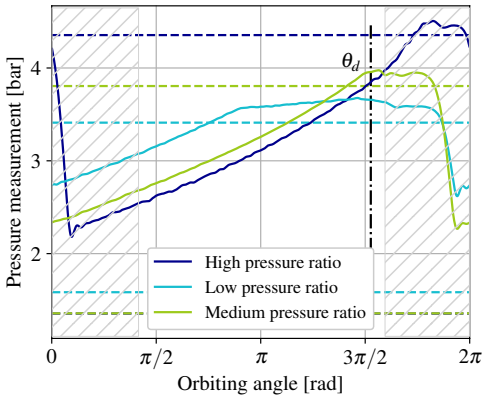

(a) High vapor qualities $Q = 0.8 \pm 0.05$ [-].

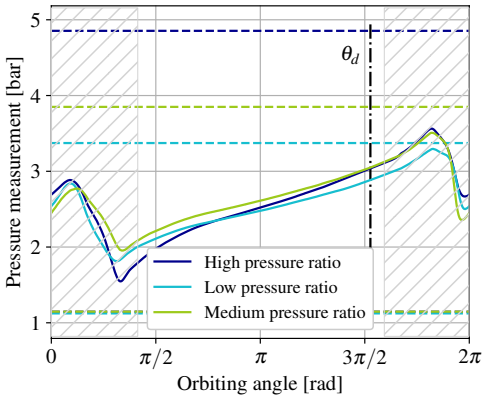

(b) Low vapor qualities $Q = 0.4 \pm 0.05$ [-].

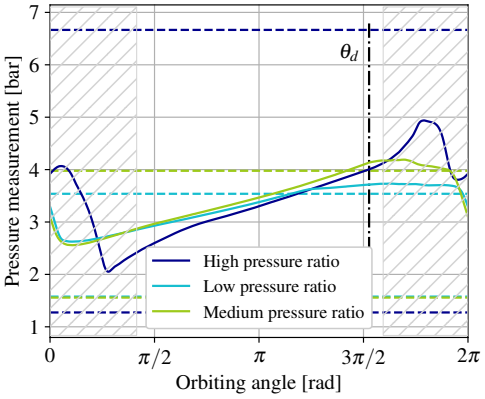

(c) Medium vapor qualities $Q = 0.6 \pm 0.05$ [-].

Figure 3.45: Dynamic pressure measurements comparing different vapor qualities at high, medium and low pressure ratios.

important differences can already be observed when the sensor starts seeing the pressure from the new compression chamber. This phenomenon can more specifically be observed when looking at the minimum of each curve. Unfortunately, the pressure increase from the beginning of the suction process to the compression process, where the sensor measures the pressure, could not be recorded, and interesting leakage phenomena appear to occur in this region. The higher leakages experienced at low vapor quality may take place in this region, explaining the drop in pressure downstream to the instrumented region. Regarding the curve shape, similarities can be observed, with the main difference lying in the intensity of the phenomena occurring. For instance, right after entering the gray zone, even the high vapor quality curve exhibits a sudden change of slope, although this change is not followed by a drop of pressure. The drop appears most pronounced at the lowest vapor quality, although a significant drop is also observed at medium vapor quality. During the uncovering of the sensor port (left-side gray zone), a pressure increase is observed only at the lowest quality, whereas the other two qualities exhibit a pressure decrease. Nevertheless, the slope of the pressure drop appears smaller in absolute value at the medium quality, while a sharp decrease is observed at the highest vapor quality. Finally, the position of the pressure minimum seems to be more and more shifted when decreasing the vapor quality. At the two lowest qualities, the phenomenon seems to occur outside the gray zone, once the sensor is in complete contact with the new chamber. Once again, only accurate modeling of the compressor would enable a better understanding of the observed and unexpected phenomena.

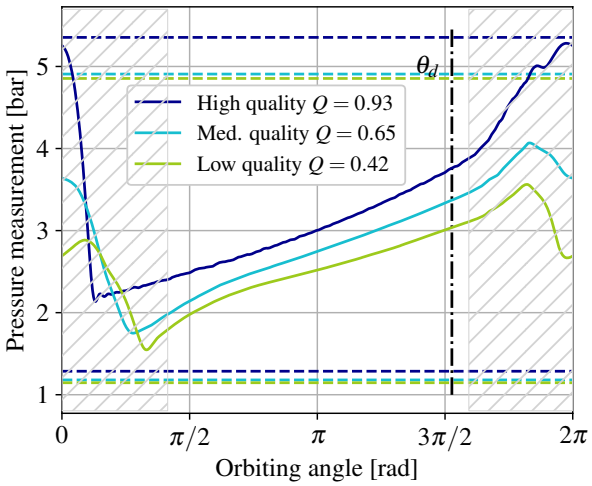

Figure 3.46: Dynamic pressure measurement comparing different vapor qualities at similar inlet pressures (1.25 ± 0.15 bar), pressure ratios (4.0 ± 0.2) and speeds (2000 RPM).

3.6 Summary and conclusions

This chapter presents the experimental investigations performed in the frame of this thesis, focusing on the characterization of scroll compressors' performance under two-phase conditions. To this aim, a test bench dedicated to the testing of compressors with two-phase conditions allowed the testing of two scroll compressors: a retrofitted compressor and a lab-scale prototype developed specifically for the application. The test bench design and architecture are presented, as well as the sensors used to efficiently characterize the performance of the compressors under various operating conditions. The investigated performance indicators are the isentropic and volumetric efficiencies, however, power consumptions and delivered mass flow rates are also analyzed. Furthermore, the lab-scale prototype is equipped with a dynamic pressure sensor, which allows a better understanding of pressure variations from the end of compression to the discharge. Two experimental campaigns are analyzed and the results compared. The first is conducted on the retrofitted compressor, covering as many operating conditions as possible with the oil Emkarate RL32 MAF (142 points). The second is carried out on the lab-scale prototype using an oil mixture (74 points). Moreover, a brief testing campaign without oil was conducted on the retrofitted compressor, and the collected points were included in those of the first campaign (for a total of 192 points). To the author's knowledge, the experimental investigations conducted in the frame of this thesis are the first of their kind. Research on two-phase compression has focused and still focuses primarily on screw compressors. Moreover, little literature is available on the placement of dynamic pressure sensors in scroll compressors. The main outcomes of this chapter can be summarized as follows:

- A test bench dedicated to the testing of compressors with two-phase operating conditions has been presented. By an accurate control, subcooled liquid, superheated vapor and oil can be mixed in the right proportions to reach the desired operating inlet and outlet conditions. Therefore, the test bench allows control of the inlet pressure, pressure ratio, inlet vapor quality, OCR and speed of the compressor. The compressor performance is obtained using mass flow meters and a torque meter placed on the motor shaft.
- An energy balance is applied by measuring the oil-refrigerant mixture before and after mixing to determine the inlet vapor quality. Two strategies have been applied. The first consisted in keeping the inlet temperature measurement and applying the balance

to obtain the vapor quality, thereby assuming a thermal equilibrium at the compressor inlet. The second converted the inlet temperature into an unknown and introduced the solubility equation to the system, thereby assuming a mixture equilibrium. Both strategies proved to be effective, with an average relative deviation of 1.5% and a maximum deviation of 8% between the obtained vapor qualities.

- Definitions of two-phase oil-refrigerant mixture volumetric and isentropic efficiencies have been implemented. By definition, these performance indicators range between 0 and 1.
- A Gaussian prediction algorithm was applied to the results. Using this algorithm, interpolations between the five tested dimensions (inlet pressure, pressure ratio, vapor quality, OCR, and speed) were performed, and 2D color maps were generated to analyze the trends.
- A retrofitted compressor was able to withstand two-phase conditions, even without oil. After more than 200 hours of operation, the compressor was visually inspected for damage, and no trace of wear was observed.
- A lab-scale prototype specifically designed for two-phase operation has proven to be working. This lab-scale prototype is the third version; two failures were encountered while testing the earlier versions, and small modifications were therefore introduced. This prototype proved to be functional, but not necessarily superior to the retrofitted compressor at all points. The higher built-in volume ratio of 3 (compared with 2.3 for the retrofitted compressor) makes it more suitable for operation at higher pressure ratios. The compressor handled more than 70 hours of operation and slight damage has been noticed.
- Eventually, datapoints have been used to generate 2D colored maps, showing the evolution of the efficiencies for varying pressure ratios and inlet qualities. Those maps have been analyzed by checking the influence of the speed and the OCR. The results have shown a decrease in efficiency at low vapor qualities, especially for high pressure ratios, where undercompression is amplified. For instance, a decrease in isentropic efficiency from 65% to 35% is observed at a pressure ratio of 4.5, a speed of 2500 RPM, an OCR of 5% and an inlet pressure of 1.5 bar, when going from an inlet quality of 90% to 50%. Generally, when increasing the speed, both volumetric and isentropic efficiencies are increased at low vapor qualities, while the isentropic efficiency decreases at high vapor qualities, due to increased friction. The general increase in volumetric efficiency with increasing speed could be explained by reduced leakage due to a sealing effect, but also by leakage becoming relatively lower compared to the theoretical mass flow rate of the compressor. Optimal speeds have been found at different vapor qualities and pressure ratios to find the trade-off between irreversibility creation from leakages and friction losses. The results of the pure-refrigerant compression have been analyzed, showing decent isentropic efficiencies with a minimum of 50% obtained for a given optimal pressure ratio of 2.7.
- A dynamic pressure sensor has been placed on the lab-scale prototype, enabling measurement directly inside the compressor chambers. The acquisition frequency was set to 25.6 kHz to ensure sufficient data is captured over a single revolution of the compressor shaft. The sensor allows partial measurement of the compression and discharge chambers' pressure. The results obtained from the pressure measurements confirm the analyses derived from the performance indicators. Nevertheless, unexplained trends are observed at low vapor qualities, particularly when the orbiting scroll covers the sensor port.

Some explanations have been proposed to interpret the results; however, they remain assumptions based on the observable trends. Therefore, a deeper analysis is necessary to confirm the presented assumptions. The validation of an accurate model could help in

confirming the analysis; this numerical modeling is part of the next chapter.

References

Sun, Shuaihui et al. (Dec. 2021). "Influence of Two-Phase Suction Injection on Performances of the Scroll Refrigeration Compressor with a High-Temperature Shell". In: *Proceedings of the Institution of Mechanical Engineers, Part E: Journal of Process Mechanical Engineering* 235.6, pp. 2059–2072. ISSN: 0954-4089, 2041-3009. DOI: 10.1177/09544089211030216. (Visited on 10/22/2025).

Scialdone, John J., Miller, Michael K., and Montoya, Alex F. (1996). *Methods of Measuring Vapor Pressures of Lubricants With Their Additives Using TGA and/or Microbalances*. Tech. rep. NASA.

Leclercq, Nicolas, Bederna, Benedikt G., and Lemort, Vincent (2024b). "Experimental Testing of a Scroll Compressor with Two-Phase Refrigerant Flows". In: *13th International Conference on Compressors and Their Systems*. Springer, pp. 239–250. DOI: 10.1007/978-3-031-42663-6_19.

— (Sept. 2025). "Experimental Study of a Retrofitted Scroll Compressor for Operation with Two-Phase Refrigerant Flows". In: *International Journal of Refrigeration* 177, pp. 219–231. ISSN: 01407007. DOI: 10.1016/j.ijrefrig.2025.05.013. (Visited on 08/15/2025).

Honeywell International Inc. (2018). *A Better Environment with Next-Generation Solstice Zd Refrigerant*.

Sugimoto, Kazuo, Shimizu, Shigemi, and Terauchi, Kiyoshi (1985). "Rotation-Preventing Device for an Orbiting Piston-type Fluid Displacement". US Patent 4545746.

Carrier Corporation (2004). *High Efficiency Compression for Commercial and Industrial Applications*.

Tromp, Stéphane (2018). "Lubrication with a Refrigerant: An Industrial Challenge Investigated through Multiscale Modeling Based on Fluid/Surface Chemistry". PhD thesis. Université de Lyon (INSA).

Billiet, Marijn (2019). "Phase Distribution of a Refrigerant Two-Phase Flow over an Impacting t-Junction". PhD thesis. Universiteit Gent.

Danel, François (1978). "Mesure Locale Dans Les Écoulements Diphasiques: Développements Récents Des Sondes Optiques". In: *La Houille Blanche N°5*.

De Kerpel, Kathleen (2015). "Refrigerant Two-Phase Flow Behaviour and Pressure Drop up- and Downstream of a Sharp Return Bend". PhD thesis. Universiteit Gent.

Elstroem, Michael (2017). "New Refrigerant Quality Measurement and Demand Defrost Methods". In: *IIAR Natural Refrigeration Conference & Heavy Equipment Expo*.

Kaya, Alihan (2021). "Experimental Study of Nucleate and Convective Flow Boiling in a Large Diameter Horizontal Tube". PhD thesis. Universiteit Gent.

Pochet, Steven (2012). "Développement d'un Système Pour La Mesure Du Taux de Vide Dans Un Écoulement Diphasique Par Une Méthode Utilisant Des Micro-Ondes". PhD thesis. Ecole Polytechnique de Montréal.

Sakamoto, Yuki et al. (July 2019). "Investigation of the Void Fraction–Quality Correlations for Two-Phase Hydrogen Flow Based on the Capacitive Void Fraction Measurement". In: *International Journal of Hydrogen Energy* 44.33, pp. 18483–18495. ISSN: 03603199. DOI: 10.1016/j.ijhydene.2019.05.066.

Dorfman, Abram and Fridman, Ella (June 2006). "Vapor Quality Measurement by a Discharging Calorimeter". In: *Fluid Phase Equilibria* 244.1, pp. 46–51. ISSN: 03783812. DOI: 10.1016/j.fluid.2006.03.019.

Fukuta, Mitsuhiro et al. (2018). "Quality Measurement of Two Phase Flow with Plug Flow". In: *International Refrigeration and Air Conditioning Conference*. Purdue University.

Dutton, Robert E. and Mattar, Wade M. (2006). "Two-Phase Steam Measurement System". US Patent 2006/0123923 A1.

Delhaye, Jean-Marc (1968). *Mesure Du Taux de Vide Local En Écoulement Diphasique Eau-Air Par Un Anémomètre à Film Chaud*. Tech. rep. Centre d'Etudes Nucléaires.

Wojtan, Leszek, Ursenbacher, Thierry, and Thome, John R. (2004). "Interfacial Measurements in Stratified Types of Flow. Part II: Measurements for R-22 and r-410A". In: *International Journal of Multiphase Flow* 30.2, pp. 125–137. ISSN: 03019322. DOI: 10.1016/j.ijmultiphaseflow.2003.11.009.

Bell, Ian H. et al. (Nov. 2012b). "Liquid-Flooded Compression and Expansion in Scroll Machines - Part I: Model Development". In: *International Journal of Refrigeration* 35.7, pp. 1878–1889. ISSN: 01407007. DOI: 10.1016/j.ijrefrig.2012.07.010.

Ramaraj, Sugirdhalakshmi et al. (2014). "Experimental Analysis of Oil Flooded R410A Scroll Compressor". In: *International Journal of Refrigeration* 46, pp. 185–195. ISSN: 01407007. DOI: 10.1016/j.ijrefrig.2014.08.006.

Quoilin, Sylvain and Schrouff, Jessica (May 2016). "Assessing Steady-State, Multivariate Experimental Data Using Gaussian Processes: The Gpexp Open-Source Library". In: *Energies* 9.6, p. 423. ISSN: 1996-1073. DOI: 10.3390/en9060423.

Chang, Yu Choung et al. (2004). "Computer Simulation and Experimental Validation of Scroll Compressors". In: *International Compressor Engineering Conference*. Purdue University.

Mahfouz, Hamdy A Gouda (2004). "Analytical and Experimental Study on a Scroll Compressor". In: *International Compressor Engineering Conference*. Purdue University.

Picavet, Alain and Ginies, Pierre (2014). "Experimental Pressure-Volume Diagrams of Scroll Compressors". In: *International Compressor Engineering Conference*. Purdue University.

Wang, Baolong et al. (Jan. 2007). "Design of Experimental Bench and Internal Pressure Measurement of Scroll Compressor with Refrigerant Injection". In: *International Journal of Refrigeration* 30.1, pp. 179–186. ISSN: 01407007. DOI: 10.1016/j.ijrefrig.2006.04.007. (Visited on 10/22/2025).

Chapter 4

Two-phase Compression: Numerical Modeling

Chapter Abstract

The objective of this chapter is to present an approach that physically explains the experimental results obtained in Chapter 3. This approach, referred to as deterministic modeling, accounts for the various phenomena occurring within the scroll compressor when subjected to two-phase flows. A two-phase deterministic model of scroll compressor developed in Python has already been developed by the author in Leclercq et al. (2022), however, this model was considering a thermal equilibrium and no heat transfer model was implemented. Moreover, lubricating oil was not considered in the model and no experimental validation was provided. Therefore, the model introduced in this chapter can be seen as an improvement of the previous version, incorporating all relevant phenomena able to qualitatively and quantitatively explain the decrease in isentropic and volumetric efficiencies observed in Chapter 3 when decreasing the inlet vapor quality of the compressor. The core submodel, which enables the simulation of adiabatic two-phase compression without leakage or oil, was previously introduced in Leclercq et al. (2024c). In its updated version, the oil mass fraction has been incorporated into the resolution process. Thus, this chapter constitutes a presentation of the deterministic model and the various submodels employed; the validation process and results analysis are addressed in the next chapter.

4.1 Introduction

From the experimental results obtained and analyzed in the previous chapter, trends were identified and possible explanations were proposed. Those lines of justification were based on three obtained results: the isentropic and volumetric efficiencies as well as the pressure evolution recorded in the compression/discharge chamber by a dynamic pressure sensor. To efficiently confirm and justify rigorously the trends obtained experimentally, a compressor model, validated with the experimental results, can be used. Therefore, a deterministic model (also referred to as a mechanistic or multi-chamber model) of scroll compressors is presented in this chapter, with corresponding validation provided in the next chapter. This deterministic model takes into account multiple physical phenomena involved in two-phase compression, in order to provide the best explanation for every trend observed in the experimental data analyses. Moreover, it is also capable of predicting the performance of compressors under untested conditions and performing a sensitivity analysis of the compressor geometry to optimize future two-phase compressor designs. From compressor geometrical data, usually obtained from a scan of the orbiting and fixed scroll, the model predicts the variation of volume of each of the chambers formed by the scrolls' superposition with the orbiting angle. From these pressure variations, thermodynamic property evolutions are

derived by applying energy and mass conservation equations. This model is thus globally deterministic, although submodels such as heat transfer, flow or mechanical losses can rely on semi-empirical parameters. Eventually, the power consumption and mass flow rate of the simulated machine are obtained, and performance indicators are calculated, in a similar way to that used for the experimental results. First, the overall model architecture is presented, followed by the developments of each submodel. The output results of each submodel are presented to facilitate understanding. Finally, details regarding the resolution processes are given and conclusions are drawn. Therefore, this chapter only constitutes a presentation of the deterministic model. The model validation as well as a thorough analysis of the compressor performance results are part of the following chapter.

4.2 Overall model architecture

The deterministic model objective is to describe as accurately as possible the physical phenomena involved inside the compressor, when operated with two-phase conditions. If performance predictions under untested operating conditions alone were needed, the interpolation algorithm used in the previous chapter (GPExp) would be sufficient. In addition to the ability of a model to predict performance outside of the tested range, it can also help in understanding the physics behind the results. Semi-empirical modeling techniques are suitable when performance depends on only a few physical phenomena, such as leakage, heat transfer, and mechanical friction. However, they cannot be applied to two-phase compression, where numerous phenomena interact. Such models have, for instance, been applied to a hermetic compressor by Winandy et al. (2002) and to an electric automotive compressor by Cuevas et al. (2012), showing good agreement with experimental data. Deterministic modeling takes into account the precise geometry of the compressor, described by a set of parameters usually obtained from a scan of the orbiting and fixed scrolls. This geometry can then be optimized to improve performance through sensitivity analysis. Globally, the model can be seen as deterministic, however, some submodels rely on parameters (empirical or semi-empirical), and those parameters need to be fitted to validate the model. This validation is usually performed using the compressors' power consumption and mass flow rate. In addition, the pressure evolution with the orbiting angle, recorded only on the lab-scale prototype, can also be incorporated in the validation. The data flow chart of the model is presented in Figure 4.1. As in the experimental results, five operating variables are used to operate the compressor: they form the model's inputs. Those variables are the inlet pressure (p_{su}), the inlet vapor quality (Q_{su}), the outlet pressure (p_{ex}) or the pressure ratio, the compressor speed (N) and the oil circulation ratio (z_o). The parameters of the model are the geometrical parameters and the submodels' semi-empirical parameters. The model outputs include the exhaust enthalpy, mass flow rate, and shaft power consumption, as well as the temperatures, vapor quality, and pressure evolutions along the compression process, characterized by the orbiting angle.

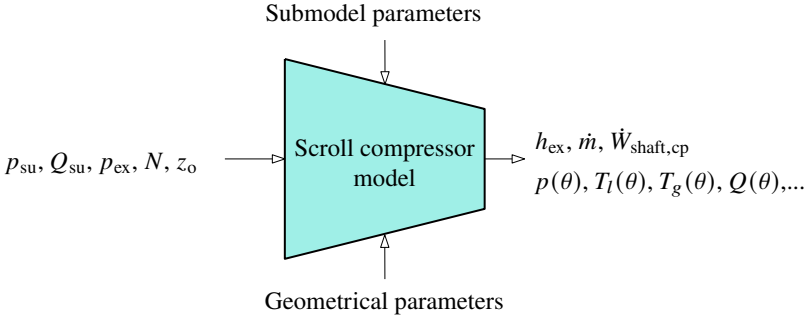

Figure 4.1: Inputs and outputs of the deterministic model.

Numerous deterministic models can be found in the literature, not only for scrolls but for displacement compressors (or expanders). One of the first models developed was intended to simulate a twin-screw compressor with oil injection (Fujiwara et al. 1995). In this model, air behaves as a perfect gas so that property (pressure, temperature, enthalpy) variation can easily be derived. Leakage and heat transfer are implemented in the model. Furthermore, the thermal non-equilibrium between the oil and the air is modeled, where the change of oil temperature depends on the heat transfer rate with the air and the mixing with the oil coming from upstream chambers by leakage. This model has been later improved by Seshaiah et al. (2007), and validated with experimental data. In the meantime, a deterministic model of rolling piston was developed by Liu et al. (1995). In this model, two-phase refrigerant compression is considered for liquid slugging, however, a thermal equilibrium is assumed. Therefore, any temperature difference between the two phases is instantly eliminated by heat and mass transfer. Similarly, Dutta et al. (2001) applies a homogeneous temperature model to a scroll compressor with liquid refrigerant injection. In this model, simple equations are used, enthalpies and densities are used as independent variables, while the pressure is directly deduced from the temperature due to the two-phase conditions. Nevertheless, not many details are provided regarding the geometrical, flow and heat transfer submodels as well as the solver employed. A year later, Chen et al. (2002a), proposed a thorough description of a scroll compressor, using analytical development for the geometry, and giving details on heat transfer, flow, leakage, discharge valve, solver and model closure to calculate the exhaust enthalpy and density. This model, however, does not model any liquid phase and is intended to be used with superheated fluids. Bell et al. (2012a) proposes a deterministic model for liquid-flooded scroll compressors. In this model, the liquid used to flood the compressor is of a different nature than the vapor, i.e., no phase change is considered. This model therefore includes equations for the liquid concentration in the compressor chambers, and considers a thermal equilibrium between the liquid and vapor phases. The same author took part in the development of the PDSim library (Bell et al. 2020), an open-source deterministic model for positive displacement compressors and expanders. This model aims to be versatile and easily modifiable for new applications or compressor types. However, the complexity of the code makes it difficult for less experienced users in Python and compressor modeling to use it efficiently. A two-phase deterministic model of scroll compressor developed in Python has already been developed by the author in Leclercq et al. (2022), however, this model was considering a thermal equilibrium and no heat transfer model was implemented. Moreover, lubricating oil was not considered in the model and no experimental validation was provided. The model introduced here is an improvement of the previous model and is also developed in Python. Therefore, it takes into account numerous phenomena, which can be listed as follows:

- The model takes into account the non-equilibrium between the vapor and liquid phases, considering the mass and heat exchanges between them. When such a fluid in a two-phase state undergoes a decrease in volume, with neither external nor internal heat transfer nor mass transfer, the density of the vapor phase is going to increase as well as its temperature, inducing a rise in pressure. Regarding the liquid phase, its change in temperature and in volume is negligible under the effect of the pressure only, creating a thermal non-equilibrium between the two phases, while the mechanical equilibrium is maintained throughout the compression. The liquid phase therefore becomes a subcooled liquid phase, due to the rise of pressure at constant temperature. This thermal non-equilibrium generates heat and mass transfer between the two phases, which are sources of irreversibilities and efficiency loss. This phenomenon will be detailed in the corresponding submodel section.
- The oil is included in the liquid phase. The liquid phase behaves differently when its composition is high in oil mass fraction (high vapor qualities) than when it is low (low vapor qualities). First, the difference in liquid phase viscosity influences the

leakage flows. Moreover, heating an oil liquid phase does not induce a phase change, whereas heating a refrigerant liquid phase can, depending on the pressure conditions. The assumption of split state, presented in Section 2.4.1 of the second chapter, is employed. The solubility of the mixture is therefore neglected in the compression process, the vapor quality is therefore independent of the liquid phase composition, and its evolution along the compression depends on phase change induced by heat transfers and leakages. Moreover, this assumption allows to link the pressure of the system with the vapor temperature, if the vapor is in a saturated state. The oil can therefore be seen as a heat sink, absorbing the heat of the two-phase pure refrigerant. Details regarding this effect are given in the corresponding submodel. The liquid phase temperature is assumed to be uniform, i.e., the oil and the refrigerant have the same temperature.

- Two-phase flow models are used for the suction and discharge flows, as well as in the mixing of the compression chamber with the discharge chamber.
- Advanced leakage models are used, where the composition of liquid and vapor of the leakage is a function of the liquid content of the chamber. For instance, when a high quantity of liquid is found in a chamber, the leakages are mostly (or only) liquid, while if almost no liquid is present, the leakages are mostly (or only) vapor. Different flow models are used for the two phases: a viscous flow model is used for the liquid phase, while a compressible nozzle flow is used for the vapor.
- Heat transfer is considered at the suction and discharge process, but also inside the chamber. The liquid and vapor phases independently exchange heat with the surrounding chamber walls. Moreover, they also exchange heat with each other.
- The inlet flow pattern is taken into account in the heat transfer and in the leakage. For instance, in a purely separated flow, the liquid remains at the bottom of the chamber without droplets traveling in the vapor. As a result, the heat exchange area decreases, and leakage is most likely liquid. Conversely, an annular flow provides a higher heat exchange area between the two-phase and a thinner liquid layer, allowing vapor leakages.
- The reed valve (discharge valve) is modeled. It helps reduce undercompression losses by preventing backflow, which limits the pressure rise and limits the work consumed by the discharge chamber over one compressor revolution. Moreover, secondary discharge ports along with intermediate discharge valves, are also modeled. They reduce overcompression losses by opening the compression chamber to the discharge when the pressure exceeds the discharge pressure.
- Finally, advanced mechanical losses are investigated. These losses, mainly studied in liquid-flooded screw compressors, can be of two kinds: frictional and momentum losses. Frictional losses come from the viscous shear met when the scroll passes over the liquid surface, whereas momentum losses are caused by the periodic accelerations experienced by the liquid that loses its speed due to turbulence.

The resolution process of the model is illustrated in Figure 4.2. First, the geometrical model takes parameters as inputs and provides the perimeter and volume variation with the orbiting angle, as well as the volume derivatives. For each chamber, control volumes (CVs) evolving along the compression have been defined. The model inputs are then recalculated using the desolubilization process defined in Section 2.4.1 and used to initialize the CVs at a shaft angle $\theta = 0$, defined as the angle corresponding to zero suction chamber volume. To proceed, the suction chambers are assumed to be at the inlet conditions, while the compression chambers' states are calculated using their initial volumes, allowing deduction of their initial densities. Assuming an isentropic efficiency of 65%, their states can be calculated using the procedure described in Section 2.4.4, with the density as an input. The discharge chamber state can simply be calculated with the outlet pressure, using the same procedure, with the pressure as an input. The initial volumes, masses and temperatures of each component (oil, liquid or vapor refrigerant) are therefore known. These guess values assume a thermal equilibrium,

thus, the temperature is uniform in each initialized chamber. The model inputs are also used to figure out the flow pattern at the compressor inlet, employed in the flow and heat transfer models. From the initial state of each chamber (temperatures, masses and volumes of each phase), other properties such as the pressure, calculated from the vapor phase state, as well as enthalpies, entropies and transport properties from each phase can be calculated. Then, the flow and heat transfer models allow to figure out the suction/discharge or leakage mass flow rates of each component $\dot{m}^k_{\phi,i}$ as well as the heat transfers to or from the phases $\dot{Q}^k_{\phi,i}$. Mass and energy conservation equations, part of the core model, are then applied to determine the derivatives of temperature, mass and volumes of each component. The equations incorporate the volume derivative along with the heat and mass transfer rates associated with the CVs. Therefore, variations of volume are operated by increasing the shaft angle by an angle step τ. These volume increases imply changes in the CVs' state. Euler forward is used to determine this new state, and this process is repeated until the discharge or merging processes occur, or until a complete revolution is performed. When those events occur, a shift in the chamber index is performed. After a complete revolution, the lumped-mass model, considering a single temperature of the compressor casing, determines the heat exchange between this casing and the suction, discharge, compression as well as the ambient air. Moreover, the mechanical losses model is applied, heat generation from the friction losses coming from the orbiting mechanism is transferred to the casing, while heat generation coming from fluid friction and momentum losses is transferred to the fluid. Finally, the current state of each CV is compared with its state from the previous revolution. If the difference in density and temperature is within a given tolerance, the simulation is considered complete. If not, the CVs are re-initialized with the previous CVs' states obtained.

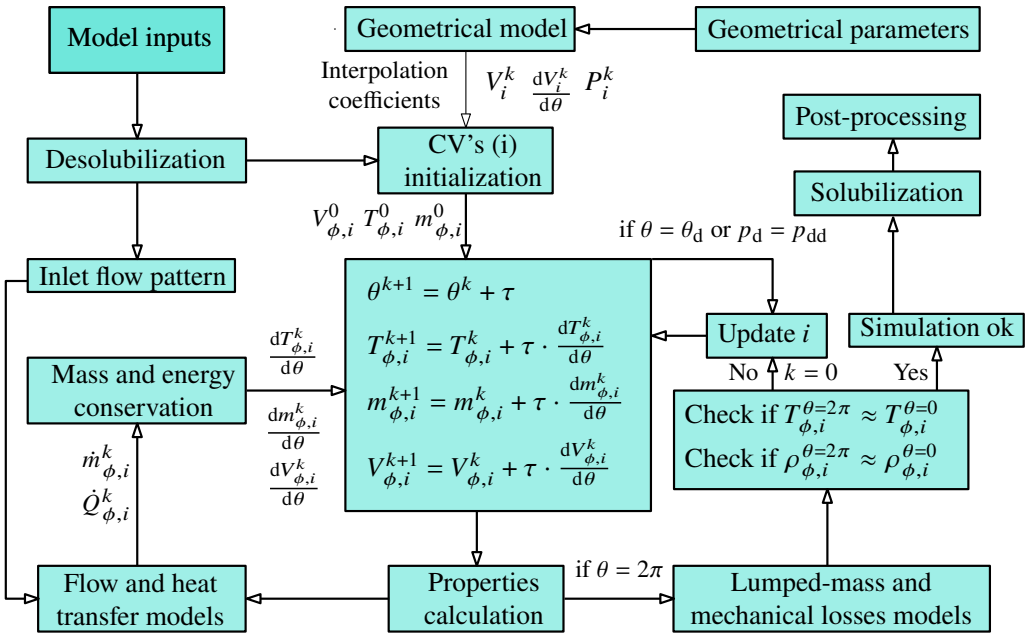

Figure 4.2: Flowchart of the deterministic model with k, the angle index, ϕ, the component index (oil, liquid or vapor refrigerant) and i, the chamber index.

4.3 Scroll geometrical model

The geometrical model constitutes the foundation of the deterministic model. It provides the variation of volumes and their derivatives along the suction, compression and discharge

processes, required to apply mass and energy conservation equations. The volumes defined by the scrolls' superposition can be identified by determining the contact points between the scrolls and using the analytical expressions of the curves composing them. In conventional scroll compressors, the shape of the curve is based on the form of an involute unwrapping from a circle. By knowing the radius of this circle, called the base circle, and of three angles (zero angle, starting angle and ending angle), it is possible to define an analytical expression of the scroll involute. Two scroll involutes are necessary to define a complete scroll with a thickness: the inner and the outer involutes. In total, six parameters allow to determine the geometry of the scrolls wraps without discharge (r_b, ϕ_{i0}, ϕ_{is}, ϕ_{ie}, ϕ_{o0}, ϕ_{os}). Moreover, two to six parameters are used to define the discharge geometry (r_0, r_1, r_2, ω, α and l). Those parameters allow to define the scrolls in two dimensions, and the constant scroll height h_s provides the third dimension. For the two scroll compressors tested in this thesis, the orbiting scroll has the same geometry as the fixed scroll. Several documents already cover how the analytical expressions of the curves defining the scrolls can be determined from these parameters. Ian Bell's thesis (Bell 2011) is recommended, as it provides clear explanations, for the scroll wraps as well as the discharge geometries. Moreover, other interesting geometrical parameters can be derived: the orbiting radius r_o, the scroll thickness t_s, the maximum number of coexisting compression chambers $N_{c,max}$ and the discharge angle θ_d, their calculations can be found in Appendix C.1.1. Regarding the discharge geometry of the retrofitted compressor, details can be found in Appendix C.1.2. Geometrical parameters allowing to define the two scrolls compressors investigated in the frame of the thesis can be found in Table 4.1. The resulting geometries can be found in Figure 4.3 and in Figure 4.4.

Parameter	Short description	Retrofitted compressor	Lab-scale prototype
ϕ_{i0}	Inner involute initial angle [deg]	80	81
ϕ_{is}	Inner involute starting angle [deg]	318	375
ϕ_{ie}	Inner involute ending angle [deg]	1052	1583
ϕ_{o0}	Outer involute initial angle [deg]	0	0
ϕ_{os}	Outer involute ending angle [deg]	145	195
r_b	Radius of base circle [mm]	3.15	3.2
h_s	Height of scroll [mm]	30.6	41
r_1	Radius of arc 1 [deg]	6.5	12.4
r_2	Radius of arc 2 [deg]	1	2
r_0	Radius of arc 0 [deg]	8.5	–
ω	Angle [deg] (see Appendix C.1.2)	24.17	–
α	Angle [deg] (see Appendix C.1.2)	45	–
l	Length [mm] (see Appendix C.1.2)	11.5	–
A_{dis}	Area of the discharge port [mm^2]	95	160
V_{disp}	Displacement volume [cm^3]	86	200
$r_{v,in}$	Built-in volume ratio [-]	2.3	3.0
r_o	Orbiting radius [mm] (see Appendix C.1.1)	5.28	5.53
t_s	Scroll thickness [mm]	4.62	4.52
$N_{c,max}$	Max. number of compression chambers [-]	2	3
θ_d	Discharge angle [deg]	7	116

Table 4.1: Compressors' geometrical parameters

The development of the geometrical model requires the knowledge of the geometry (shape) of each chamber created by the scrolls' superposition. The shapes formed by this superposition depend on the crank angle (or orbiting angle). Analytical developments of the volume can then be deduced from those chambers' shapes. As a matter of fact, analytical expressions of the volumes are required for computational efficiency, since numerically evaluating the volumes at each angular step would result in excessive computational time. Analytic developments for the volumes of such complex geometries were first proposed by B. Wang et al. (2005), later

Figure 4.3: Geometry of the retrofitted compressor.

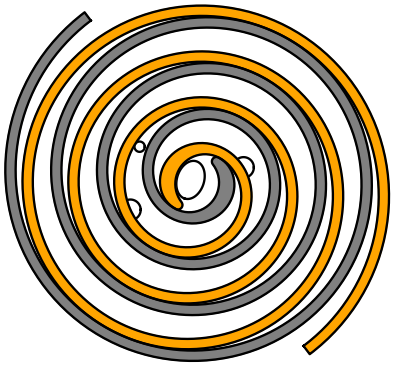

Figure 4.4: Geometry of the lab-scale prototype.

improved by Bell (2011). However, the need to simulate different discharge geometries than the conventional arc-arc or arc-line-arc (an arc-arc-line-arc in this case, see Appendix C.1.2) has driven the use of analytical developments through polynomial interpolations. Thereby, by knowing the scroll involutes equations as well as the coordinates of the contact points created by the scrolls' superposition, it is possible to define polygons accurately fitting the shape of the different chambers. The volumes of these polygons can be computed using the following equation:

$$V = \frac{1}{2} h_s \sum_{i=1}^{n-1} (x_i y_{i+1} - x_{i+1} y_i) \tag{4.1}$$

where x_i and y_i are the coordinates of the n points constituting the polygon that must be closed, meaning that $(x_0,\ y_0) = (x_n,\ y_n)$. Hence, the first step of the geometrical model is to compute those volumes for each chamber with an angle step of 1° for a whole rotation, 360 values will thereby be obtained for each chamber, and a 5th-order polynomial is used to interpolate those values. Thus, the equations can be written as

$$V(\theta) = c_6\theta^5 + c_5\theta^4 + c_4\theta^3 + c_3\theta^2 + c_2\theta + c_1. \tag{4.2}$$

Moreover, the derivative can easily be obtained using

$$\frac{\mathrm{d}V(\theta)}{\mathrm{d}\theta} = 5c_6\theta^4 + 4c_5\theta^3 + 3c_4\theta^2 + 2c_3\theta + c_2. \tag{4.3}$$

This technique allows, for a given geometry, to have relative errors between the volume given by the polygon area calculation and the interpolation of 0.8% for the maximum error and of 0.1% on average over a whole rotation. With a sufficiently high number of polygon points (> 300), the polygon approximation error is negligible compared to the interpolation error. When using this interpolation technique, a numerical issue can be encountered in the suction chamber for angles close to zero. The orbiting angle is here defined when the suction chamber starts to open, i.e., $V_s = 0$ when $\theta = 0$, however, there is an absolute error that can make the volume of the chamber slightly different than zero and even negative at the beginning of the rotation, which can create too large variations and non-physical values of density and lead to convergence instabilities. A solution to this issue was to add an offset equal to 1% of the displacement volume to all chamber volumes, which was the minimum value required to ensure model stability. It induces a non-zero (and positive) volume of the suction chamber and adds stability when this chamber starts to fill. Furthermore, it does not impact the results much as only 1% of the displacement volume is added. The representation of chambers'

volume evolutions of both the retrofitted compressor and the lab-scale prototype can be found in Figures 4.5 and 4.6.

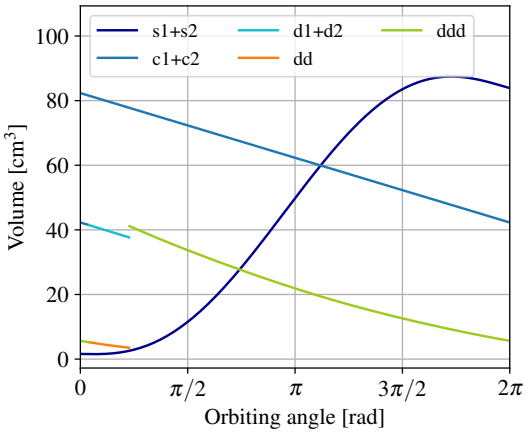

Figure 4.5: Volume evolutions in each chamber of the retrofitted compressor.

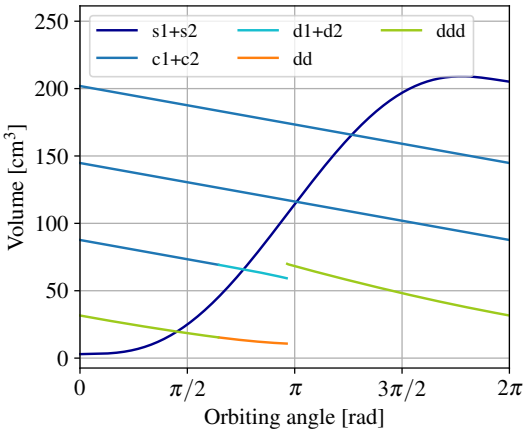

Figure 4.6: Volume evolutions in each chamber of the lab-scale prototype.

The scroll compressor concept relies on the fact that, during the relative orbiting movement between the two scrolls, the volumes of the closed chambers formed by their superposition decrease with the evolution of the orbiting angle. To simplify further analysis, names can be attributed to each chamber, following the evolutions shown in Figures 4.5 and 4.6. These chambers are represented in Figure 4.7 and 4.8 for the retrofitted compressor:

- Suction chambers s1 and s2: chambers starting theoretically with a zero volume at an orbiting angle $\theta = 0$ and reaching the displacement volume of the machine at the end of the rotation ($\theta = 2\pi$). At the next rotation, they become compression chambers c1 and c2. As can be understood, two different compression paths occur in parallel in the compressor. The maximum volume of the suction chamber is not reached at the end of the revolution, therefore, it is possible to obtain volumetric efficiencies greater than 1, at ideal conditions. This phenomenon was experienced by Nieter (1988).
- Compression chambers c1 and c2: chambers starting at the displacement volume of the machine and finishing when the orbiting angle becomes the discharge angle. They can be longer than a full revolution, i.e., several compression chambers can coexist in parallel, as can be seen in Figure 4.7. The discharge angle (θ_d) is defined as the angle at which the tip of one scroll nose starts detaching from the other scroll. The compression chambers enter therefore in direct communication with the discharge port and become the discharge chambers d1 and d2.
- Discharge chambers d1 and d2: chamber in communication with the discharge port but having different pressures than the chamber in direct contact with the discharge port (dd chamber). A merging process is thus occurring between chambers d1, d2 and dd starting from the discharge angle, where a flow appears between the chambers, as can be observed in Figure 4.8. When undercompression occurs, the pressure in d1 and d2 is lower than that in dd, whereas during overcompression, the reverse effect occurs. When an equilibrium of pressure is established, the merged chamber is called ddd.
- Discharge chamber dd: chamber which starts at the discharge angle and finishes when a pressure equilibrium with chambers d1 and d2 is reached.
- Discharge chamber ddd: chamber connected to the discharge ports, which becomes chamber dd during the merging process.
- A last chamber can be defined, not visible in the volume evolution figures: the suction-admission chamber (sa). This chamber represents the volume taken by the fluid after entering the scroll shell (or inlet port) and before entering the suction chambers s1 and

s2. This chamber volume variation is very low, however, it must be considered for the primary flow and leakage models. As a matter of fact, this chamber acts as a buffer to avoid flow oscillations generated by the suction chambers, compensating for density (and pressure) variations of its high volume, physically and numerically. By summing up the volumes of each defined co-existing chamber (including the sa chamber), the result should be constant and independent of the orbiting angle.

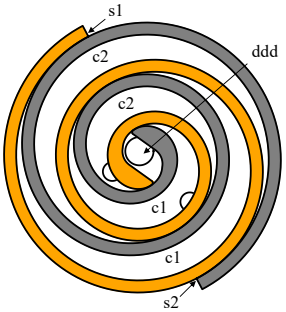

Figure 4.7: Chamber definition at $\theta = \theta_d$.

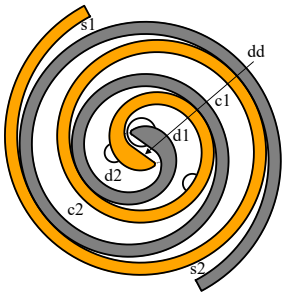

Figure 4.8: Chamber definition at $\theta = \theta_d + 90°$.

A similar procedure to that applied to the volume is used to obtain analytical expressions of the chamber perimeter, which are then used in the heat transfer and leakage calculations. The numerical expression of the perimeter of a polygon is given by

$$P = \sum_{i=1}^{n} \sqrt{(x_{i+1} - x_i)^2 + (y_{i+1} - y_i)^2} \tag{4.4}$$

Once again, the geometrical model calculates the perimeter of each chamber at each angle defined by the angle step at the beginning of the simulation, and provides coefficients derived from the interpolation of those perimeters varying with the orbiting angle.

Polygon descriptions of the main discharge port, intermediate discharge ports and pressure sensor ports were also required to determine their coverage by the orbiting scroll. The functional area resulting from this coverage has been computed using the Python library shapely (Gillies et al. 2022). Regarding the suction area (opening of s1 and s2 chambers) and the area of the opening of d1, d2 chambers to dd chamber, their calculations are based on analytical expressions provided by Bell (2011). Those areas varying with the orbiting angle can be found in Appendix C.1.3.

4.4 Core model

When a two-phase mixture or pure fluid undergoes a reduction of volume, the volume of the vapor phase is going to follow closely the total reduction of volume, while the liquid phase volume variation is negligible in comparison to this total reduction (in absolute variation). This variation of vapor volume induces a rise in temperature, creating a thermal disequilibrium between the two phases, whereas the mechanical equilibrium (uniform pressure) is maintained. Heat transfer, condensation and evaporation are thereby going to occur between the two phases, leading to variations in pressure that are difficult to predict.

Among the two-phase deterministic models found in the literature, several authors assume a thermal equilibrium between the two phases for simplicity (Bell et al. 2012a; Gudjonsdottir et al. 2019; Liu et al. 1995; Lin et al. 2020; Leclercq et al. 2022; M. Yang et al. 2022). In Lin et al. (2020), the two phases are modeled separately, but the evaporation rate is analytically determined to always reach the thermal equilibrium. As a pure fluid (R290) is being used, no concentration equation is applied. The thermodynamic variables used are the density and

the temperature, but no information is provided regarding the equation of state. The authors of Bell et al. (2012a) and Gudjonsdottir et al. (2019) model a two-phase compression using mixtures (oil-refrigerant or ammonia-water), inducing the use of a concentration equation. Moreover, in both papers, the use of pressure, temperature and concentration as independent thermodynamic variables allows the calculation of the remaining properties. Finally, in Liu et al. (1995) and Leclercq et al. (2022), a homogeneous phase is modeled using a pure fluid. Liu et al. (1995) provide an analytical formula for the calculation of the variation rate of vapor quality with the shaft angle ($\mathrm{d}Q/\mathrm{d}\theta$). Thereby, it seems that the vapor quality and the temperature are used as thermodynamic variables to determine the state of the fluid. In M. Yang et al. (2022), the enthalpy and the density are used as independent variables to determine the state of the two-phase refrigerant. In this article, the partial derivatives of the properties are analytically calculated based on saturation properties using the Clapeyron equation, as proposed by Thorade et al. (2013).

On the other hand, several authors (Ziviani 2017; Zaytsev 2003) propose a thermal non-equilibrium modeling. A deterministic model applied to an oil refrigerant-mixture expansion using a single-screw expander is developed in Ziviani (2017). This model uses a concentration equation for the oil content and uses the density and the temperature as independent thermodynamic variables for both liquid and vapor phases. Although it does not show how the condensation/evaporation effect of the refrigerant can be figured out, it constitutes a base for the mathematical developments shown in this thesis. In Zaytsev (2003), the author developed a two-phase compression model for a twin-screw compressor used in compression-resorption heat pumps, using the pressure, temperature and sorbent concentration as independent thermodynamic variables with the Ziegler-Trepp equation of state.

In this thesis, a model similar to the expansion model of Ziviani (2017) is developed. This model is an improved version of the mathematical model proposed in Leclercq et al. (2024c): the oil is now included in the two-phase compression equations. When the oil mass fraction is set to zero in the model, the results remain consistent with those reported in the article. The equations are solved to calculate the specific volume and temperature variation rates of both phases with the shaft angle of the displacement compressor. The model takes into account the non-equilibrium between the two phases, considering the mass and heat exchanges between them. Moreover, the interactions between the two phases are thoroughly described. The oil is included in the equations considering a split state (see Section 2.4.1), i.e., the solubility does not impact the resulting pressure of the compression. The equations are applied to a simple piston-cylinder setup filled with the oil-refrigerant mixture studied in this thesis (Emkarate RL32 - R1233zd(E)) to illustrate a simple application. The volume contained in the piston-cylinder setup is decreased at a fixed rate, until reaching a constant value where the system can rest until the thermal equilibrium is re-established. The evolution of pressure inside the cylinder is tracked, as well as the temperatures and masses of the liquid and vapor phases. The external heat transfer and leakages are taken into account in the equations, however, they will be neglected in the piston-cylinder application. This model therefore constitutes the core of the deterministic model, as it incorporates inputs from most of the submodels and applies the energy and mass balance equations. Moreover, it defines the property evolution of both phases during compression, enabling identification of the mixture state at each angular step of the compressor.

The core model is split into 3 parts: the interface interactions, the mass conservation equations and the energy conservation equations. Subsections are also dedicated to the calculation of derivatives and to the results of the model applications. The objective is to obtain the variation of pressure, under a variation of volume in which the two-phase fluid is initially at rest, in thermal and mechanical equilibrium. For the sake of simplicity, since the model is intended for use as a compressor deterministic model, the derivatives will be

expressed in terms of shaft angle variation (θ), and the speed of the compressor is given by the variable ω (in rad/s). As already stated, the two independent thermodynamic variables used to define the properties of both phases are the temperature and the density. Those variables are used along with the Helmholtz equation of state to determine other thermophysical properties such as the pressure, enthalpy and entropy. The variation of volume of the liquid phase with regard to the pressure being negligible, the pressure of the control volume is going to be set based on the vapor phase properties. To decrease the computational time of the model, the abstract state module of CoolProp 6.4.3 (Bell et al. 2014) has been used to compute the thermophysical properties.

4.4.1 Interface interactions

A representation of the studied control volume can be found in Figure 4.9. The control volume is subject to a volume variation rate $\mathrm{d}V_{\mathrm{CV}}/\mathrm{d}\theta$ distributed into volume variations of the vapor and liquid refrigerant and the oil, $\mathrm{d}V_{\mathrm{r,g}}/\mathrm{d}\theta$, $\mathrm{d}V_{\mathrm{r,l}}/\mathrm{d}\theta$ and $\mathrm{d}V_{\mathrm{o}}/\mathrm{d}\theta$, respectively. The kinetic and potential energies of the fluids within this control volume are neglected. The computations of the temperature and specific volume of both phases along the variation of volume with the shaft angle are computed using the forward Euler method, where the specific volume is converted into the density for the equation of state afterward. The choice of this method over a higher-order method (e.g., fourth-order Runge-Kutta) is justified by the stability obtained without excessively reducing the time step, allowing to conveniently build the model. Nevertheless, adopting a more advanced solver could now be considered, as the model is fully developed and operational. The equations are therefore given by

$$T_\phi^k(\theta) = T_\phi^{k-1}(\theta) + \frac{\mathrm{d}T_\phi}{\mathrm{d}\theta}\mathrm{d}\theta \tag{4.5}$$

$$v_\phi^k(\theta) = v_\phi^{k-1}(\theta) + \frac{\mathrm{d}v_\phi}{\mathrm{d}\theta}\mathrm{d}\theta \tag{4.6}$$

where ϕ stands for the component of the control volume to which the equations are applied, and $\mathrm{d}\theta$ is the shaft angle step used. Thus, the component ϕ can stand for liquid refrigerant (r,l), vapor refrigerant (r,g) or oil (o), although the temperature derivatives of the oil and the liquid refrigerant are the same. The mass and energy conservation equations will thereby help in determining $\mathrm{d}T_\phi/\mathrm{d}\theta$ and $\mathrm{d}v_\phi/\mathrm{d}\theta$, for the liquid and vapor refrigerant as well as the oil.

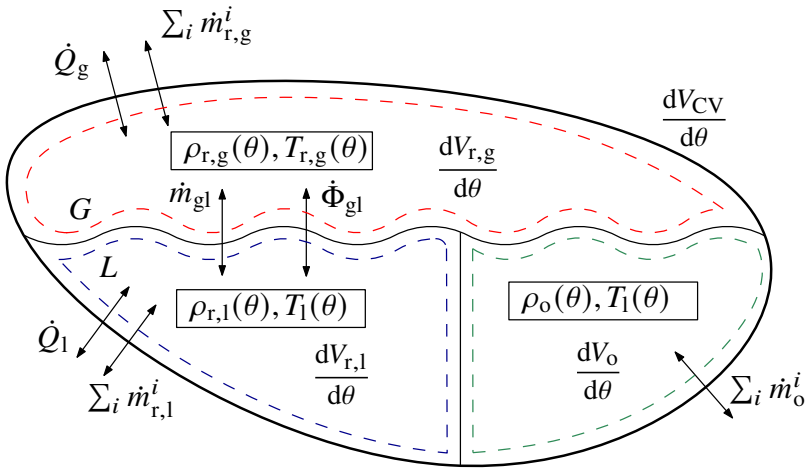

Figure 4.9: Definition of the control volume and the interactions with its environment (refrigerant vapor in red, refrigerant liquid in blue and oil in green).

When a two-phase mixture undergoes a decrease in volume, with neither external nor internal heat transfer or mass transfer, the density of the vapor phase is going to increase as well as its temperature, inducing a rise in pressure. Regarding the liquid phase, its change in temperature and in volume is negligible under the effect of the pressure only, creating a thermal non-equilibrium between the two phases, while the mechanical equilibrium is maintained through the compression. The liquid phase therefore becomes a subcooled liquid phase, due to the rise of pressure at constant temperature. Depending on the shape of the vapor saturation curve, increasing the pressure of the saturated vapor phase may or may not create condensation. Most refrigerants used are dry fluids, the rise in pressure of the saturated vapor phase is going to create a new pure refrigerant liquid phase, at the vapor phase temperature, as illustrated in Figure 4.11. If the mass and heat transfer are considered between the two phases, the new liquid phase is going to mix with the original liquid phase, thereby increasing its temperature. The difference in temperature between the vapor and liquid phase is also resulting in condensation/evaporation between the two phases, thereby inducing a mass transfer. Therefore, when one of the phases is saturated, temperature changes induced by heat transfer lead to mass transfer in the form of condensation or evaporation. These two effects have a role in the change of volume and mass of both liquid and vapor phases, having a significant impact on the resulting pressure. Naturally, if no refrigerant but only oil is present in the liquid phase, i.e., if the vapor phase is superheated, no mass transfer can occur between the two phases. This phenomenon can occur, as the split state defined in Section 2.4.1 of the second chapter is employed. The difficulties encountered in the modeling of those effects have been described in Öhman et al. (2013), where the two-phase expansion of pure refrigerant R134a in a Lysholm turbine is investigated. Several authors have modeled the interaction between the two phases in thermal non-equilibrium under some assumptions. The condensation resulting from the compression of the vapor phase can be considered instantaneous, which simplifies the equations. However, in saturated liquid expansion, the resulting evaporation cannot be considered instantaneous according to the literature. For instance, in the modeling of two-phase expansion developed by van Heule et al. (2023), a homogeneous relaxation model is implemented, thus, the flashing is not instantaneous and the thermal non-equilibrium is considered. Regarding compression, in both Guo et al. (2024) and Revellin et al. (2012), the energy transfer rates from the vapor phase to the liquid phase (either by heat transfer or mass transfer) $\dot{\Phi}_{gl}$ and from the liquid phase to the vapor phase $\dot{\Phi}_{lg}$ are defined as

$$\dot{\Phi}_{gl} = \dot{Q}_{gl} + \dot{m}_{gl} h_{r,g} \tag{4.7}$$

$$\dot{\Phi}_{lg} = \dot{Q}_{lg} + \dot{m}_{lg} h_{r,l} \tag{4.8}$$

where $\dot{Q}_{lg}$, $\dot{Q}_{gl}$ are the heat transfer rates and $\dot{m}_{gl}$, $\dot{m}_{lg}$, the mass transfer rates.

The interface between the vapor phase (G) and the liquid phase (L) can thereby be defined and the interactions (with only the pure refrigerant) are represented in Figure 4.10. This interface can be seen as an infinitely thin boundary between the two extended control volumes represented by the vapor and liquid phases. Therefore, the gradient of temperature that can appear between the two phases is not embedded inside the interface but in the extended control volumes boundaries, allowing to respect the temperature continuity through the control volumes boundaries and the interface.

From the mass and energy conservation equations at the interface, which can neither contain any mass nor energy, the following equalities can be deduced:

$$\dot{m}_{gl} + \dot{m}_{lg} = 0 \tag{4.9}$$

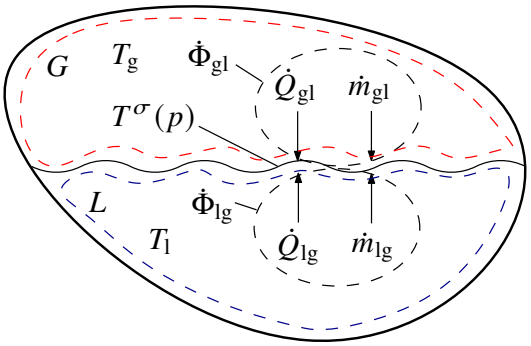

Figure 4.10: Refrigerant interface interactions.

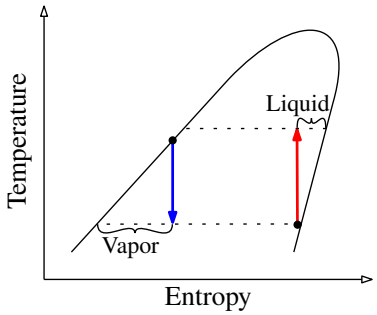

Figure 4.11: Saturated vapor isentropic compression in red, saturated liquid isentropic expansion in blue.

$$\dot{\Phi}_{gl} + \dot{\Phi}_{lg} = 0 \tag{4.10}$$

The heat transfer rates toward the interface can be defined considering an interface at the saturation temperature from the pressure p, they can be written as[1]

$$\dot{Q}_{gl} = AU_l \left(T_g - T^\sigma(p)\right) \tag{4.11}$$

$$\dot{Q}_{lg} = AU_g \left(T_l - T^\sigma(p)\right) \tag{4.12}$$

where AU_l, AU_g are the heat transfer conductances in W/K from the interface to the liquid phase and vapor phase, respectively. These two variables can be assumed to be equal to each other. Isolating the mass flow rate from the vapor phase to the liquid phase $\dot{m}_{gl}$ from equations 4.7, 4.8, 4.9 and 4.10 gives

$$\dot{m}_{gl} = -\frac{\left(\dot{Q}_{gl} + \dot{Q}_{lg}\right)}{\left(h_g - h_l\right)} = -\frac{\left(\dot{Q}_{gl} + \dot{Q}_{lg}\right)}{\Delta h^{SH} + \Delta h^\sigma + \Delta h^{SC}} \tag{4.13}$$

where Δh^{SH} is the sensible heat of superheating (from the saturated vapor state reference), Δh^{SC} is the sensible heat of subcooling and Δh^σ is the latent heat. In the case where the vapor phase is superheated and the liquid phase subcooled ($T_g > T^\sigma(p) > T_l$), two situations can be encountered: if the superheat equals the subcooling, the heat transfers from the two phases to the interface are equal, resulting in no mass transfer; if the superheat is higher, the heat transfer from the vapor phase to the interface is greater, resulting in a compensating mass flow from the liquid phase to the vapor phase (evaporation). In the case where the subcooling is higher than the superheat, the heat transfer from the liquid phase to the vapor phase is the highest, and a compensating condensation mass flow rate appears. In the situation where the vapor phase is at saturation (the most common case), the heat transfer from the vapor phase to the interface is zero; the heat transfer from the subcooled liquid phase to the saturated vapor is therefore entirely converted into a condensation mass flow rate.

The problem identified with the definition of the mass flow rate is the fact that it does not take into account the partial evaporation (also called flash)/partial condensation coming from the compression of the saturated vapor phase/expansion of the saturated liquid phase as illustrated in the Figure 4.11. As previously explained, the compression of the saturated vapor present in the two-phase mixture results in the creation of a liquid phase at the temperature of the vapor phase, which is going to mix with the liquid phase and thereby change its

[1]The notations AU_l and AU_g, to the author's perspective, could be switched in both equations. However, the adopted notation appears in this form in the literature.

temperature, resulting in a change of volume of the liquid phase. Depending on the initial vapor quality of the compression, this effect can be negligible, especially for low vapor qualities where the amount of liquid coming from the saturated vapor compression would be too small to significantly affect the liquid phase temperature. Nevertheless, these mass flow rates can be added to the definition provided in Equation 4.13 to take them into account, resulting in the total condensing mass flow rate defined in Equation 4.18. The mass transfer generated by the partial condensation and evaporation can be calculated from the deviation of the specific volume of the vapor and liquid phases from the saturated specific volumes. More specifically, it allows to know which quantity of vapor/liquid has been converted to saturated liquid/vapor from the mass of the vapor phase m_g or liquid phase m_l, respectively. The mass transfer from the vapor phase to the liquid phase m_{gl}^{σ} and the mass transfer from the liquid phase to the vapor phase m_{lg}^{σ} can simply be defined as follows:

$$m_{gl}^{\sigma} = m_g \cdot \max\left(0, \frac{v_g^{\sigma}(p) - v_g}{v_g^{\sigma}(p) - v_l^{\sigma}(p)}\right) \tag{4.14}$$

$$m_{lg}^{\sigma} = m_l \cdot \max\left(0, \frac{v_l - v_l^{\sigma}(p)}{v_g^{\sigma}(p) - v_l^{\sigma}(p)}\right) \tag{4.15}$$

This conversion can also be interpreted as a recalculation of the vapor quality of the vapor and liquid phases, which were initially equal to 1 and 0, respectively. After compression or expansion, the resulting condensing or evaporating masses can be deduced from the new vapor qualities.

Finally, the corresponding energy transfer from one phase to the other can be defined as follows, where the enthalpy of vaporization is considered inherently of the compression/expansion of the saturated phase:

$$\Phi_{gl}^{\sigma} = m_{gl}^{\sigma} \cdot h_l^{\sigma}(p) \tag{4.16}$$

$$\Phi_{lg}^{\sigma} = m_{lg}^{\sigma} \cdot h_g^{\sigma}(p) \tag{4.17}$$

The enthalpy of the mass transferred to the liquid phase (gl) is the saturated liquid enthalpy h_l^{σ}, as the condensation already occurred, while the enthalpy of the mass transferred to the vapor phase (lg) is the saturated vapor enthalpy h_g^{σ}.

4.4.2 Mass conservation equations

The total mass transfer rate condensed from the vapor phase to the liquid phase is defined as

$$\frac{\mathrm{d}m_{cond}}{\mathrm{d}\theta} = \frac{1}{\omega}\dot{m}_{gl} + \frac{1}{\mathrm{d}\theta}\left(m_{gl}^{\sigma} - m_{lg}^{\sigma}\right) \tag{4.18}$$

The mass conservation equations can simply be written considering the mass flow rates entering/leaving the control volume (three interactions represented in Figure 4.9) and the interaction between the vapor and the liquid phase (condensation rate) that is represented by Equation 4.18. Thus, mass conservation equations are written separately for the vapor refrigerant, the liquid refrigerant, and the oil:

$$\frac{\mathrm{d}m_{r,g}}{\mathrm{d}\theta} = \frac{1}{\omega}\left(\sum_i \dot{m}_{r,g}^{i} - \frac{\mathrm{d}m_{cond}}{\mathrm{d}\theta}\right) \tag{4.19}$$

$$\frac{\mathrm{d}m_{\mathrm{r,l}}}{\mathrm{d}\theta} = \frac{1}{\omega}\left(\sum_i \dot{m}^i_{\mathrm{r,l}} + \frac{\mathrm{d}m_{\mathrm{cond}}}{\mathrm{d}\theta}\right) \tag{4.20}$$

$$\frac{\mathrm{d}m_{\mathrm{o}}}{\mathrm{d}\theta} = \frac{1}{\omega}\sum_i \dot{m}^i_{\mathrm{o}} \tag{4.21}$$

The specific volume variation rates can then be defined as a function of the mass and volume variation rates, with the following definition for the component ϕ of the control volume:

$$\frac{\mathrm{d}v_\phi}{\mathrm{d}\theta} = \frac{1}{m_\phi}\frac{\mathrm{d}V_\phi}{\mathrm{d}\theta} - \frac{V_\phi}{m_\phi^2}\frac{\mathrm{d}m_\phi}{\mathrm{d}\theta} \tag{4.22}$$

The volume variation rates of the three components can then be linked together with the control volume variation rate. The vapor phase variation rate is isolated on the left-hand side, as it is defined in this direction: the vapor volume is much more sensitive to pressure variations than the liquid volume. Therefore, if the liquid volume varies, due, for instance, to an increase in temperature, the vapor volume is going to adapt to this volume variation. Conversely, the vapor volume variations barely have an impact on the liquid volume, as the resulting pressure variations are low and the liquid can be considered incompressible. The vapor phase volume variation rate is therefore defined as

$$\frac{\mathrm{d}V_{\mathrm{r,g}}}{\mathrm{d}\theta} = \frac{\mathrm{d}V_{\mathrm{CV}}}{\mathrm{d}\theta} - \frac{\mathrm{d}V_{\mathrm{r,l}}}{\mathrm{d}\theta} - \frac{\mathrm{d}V_{\mathrm{o}}}{\mathrm{d}\theta} \tag{4.23}$$

Thus, to determine the vapor volume variation rate, the variation rates of the oil and liquid refrigerant volumes must first be determined. Moreover, the volume variation rate of the whole CV is an input of the system. The derivatives of the refrigerant liquid volume $\mathrm{d}V_{\mathrm{r,l}}/\mathrm{d}\theta$ and of the oil volume $\mathrm{d}V_{\mathrm{r,l}}/\mathrm{d}\theta$ can be conveniently expanded to make explicit the dependency from the liquid phase temperature T_{l}, while neglecting the effect of pressure:

$$\begin{aligned}\frac{\mathrm{d}V_{\mathrm{r,l}}}{\mathrm{d}\theta} &= v_{\mathrm{r,l}}\frac{\mathrm{d}m_{\mathrm{r,l}}}{\mathrm{d}\theta} + m_{\mathrm{r,l}}\frac{\mathrm{d}v_{\mathrm{r,l}}}{\mathrm{d}\theta} \\ &= v_{\mathrm{r,l}}\frac{\mathrm{d}m_{\mathrm{r,l}}}{\mathrm{d}\theta} + m_{\mathrm{r,l}}\left(\frac{\partial v_{\mathrm{r,l}}}{\partial T}\right)_p \frac{\mathrm{d}T_{\mathrm{l}}}{\mathrm{d}\theta}\end{aligned} \tag{4.24}$$

$$\frac{\mathrm{d}V_{\mathrm{o}}}{\mathrm{d}\theta} = v_{\mathrm{o}}\frac{\mathrm{d}m_{\mathrm{o}}}{\mathrm{d}\theta} + m_{\mathrm{o}}\left(\frac{\partial v_{\mathrm{o}}}{\partial T}\right)_p \frac{\mathrm{d}T_{\mathrm{l}}}{\mathrm{d}\theta} \tag{4.25}$$

The current system of equations to be solved is therefore dependent on the variation rate of the liquid phase temperature, which is going to be computed from the energy conservation equations.

4.4.3 Energy conservation equations

The conservation of energy is applied in the same way for both phases, with derivatives expressed relative to time first:

$$\frac{\mathrm{d}U_\gamma}{\mathrm{d}t} = \sum_i \dot{m}^i_\gamma\, h^i_\gamma + \dot{W}_\gamma + \dot{Q}_\gamma \pm \dot{\Phi}_{\mathrm{cond}} \tag{4.26}$$

where γ stands for the phase: l for liquid and g for vapor, in contrast to ϕ that is standing for the component (refrigerant liquid, or vapor, or oil). U_γ is the internal energy of the phase represented by γ. The boundary work rate exchanged with the corresponding phase can be rewritten as

$$\dot{W}_\gamma = -p \frac{\mathrm{d}V_\gamma}{\mathrm{d}t} \tag{4.27}$$

Regarding the condensation energy transferred rate, it comes from interface interactions and can be defined as

$$\begin{aligned} \dot{\Phi}_{\mathrm{cond}} &= \dot{\Phi}_{\mathrm{gl}} + \frac{\omega}{\mathrm{d}\theta}\left[\Phi^\sigma_{\mathrm{gl}}(p) - \Phi^\sigma_{\mathrm{lg}}(p)\right] \\ &= \dot{\Phi}_{\mathrm{gl}} + \frac{\omega}{\mathrm{d}\theta}\left[m^\sigma_{\mathrm{gl}}\, h^\sigma_{\mathrm{l}}(p) - m^\sigma_{\mathrm{lg}}\, h^\sigma_{\mathrm{g}}(p)\right] \end{aligned} \tag{4.28}$$

where $\Phi^\sigma_{\mathrm{gl}}$ and $\Phi^\sigma_{\mathrm{lg}}$ have been taken from Equations 4.16 and 4.17. This term is taken with a negative sign for the vapor phase and with a positive sign for the liquid phase, in the energy conservation equation. Equation 4.26 can be rewritten with derivatives relative to the shaft angle θ:

$$\frac{\mathrm{d}U_\gamma}{\mathrm{d}\theta} = \frac{1}{\omega}\sum_i \dot{m}^i_\gamma\, h^i_\gamma - p\frac{\mathrm{d}V_\gamma}{\mathrm{d}\theta} + \frac{1}{\omega}\dot{Q}_\gamma \pm \frac{1}{\omega}\dot{\Phi}_{\mathrm{cond}} \tag{4.29}$$

For the liquid phase, the left-hand term of Equation 4.29 can be reformulated using the mass and the specific internal energies of the liquid refrigerant and the oil:

$$\begin{aligned} \frac{\mathrm{d}U_{\mathrm{l}}}{\mathrm{d}\theta} &= \frac{\mathrm{d}}{\mathrm{d}\theta}\left(m_{\mathrm{r,l}}u_{\mathrm{r,l}} + m_{\mathrm{o}}u_{\mathrm{o}}\right) \\ &= u_{\mathrm{r,l}}\frac{\mathrm{d}m_{\mathrm{r,l}}}{\mathrm{d}\theta} + u_{\mathrm{o}}\frac{\mathrm{d}m_{\mathrm{o}}}{\mathrm{d}\theta} + m_{\mathrm{r,l}}\frac{\mathrm{d}u_{\mathrm{r,l}}}{\mathrm{d}\theta} + m_{\mathrm{o}}\frac{\mathrm{d}u_{\mathrm{o}}}{\mathrm{d}\theta} \end{aligned} \tag{4.30}$$

Moreover, knowing that, derived from the Maxwell equations:

$$\left(\frac{\partial u_\phi}{\partial v}\right)_T = \left[T_\phi\left(\frac{\partial p}{\partial T}\right)_v - p\right] \tag{4.31}$$

The derivative $\mathrm{d}u_{\mathrm{r,l}}/\mathrm{d}\theta$ of Equation 4.30 can be expressed as follows

$$\frac{\mathrm{d}u_{\mathrm{r,l}}}{\mathrm{d}\theta} = \left(\frac{\partial u_{r,l}}{\partial T}\right)_v \frac{\mathrm{d}T_{\mathrm{l}}}{\mathrm{d}\theta} + \left[T_{\mathrm{l}}\left(\frac{\partial p}{\partial T}\right)_v - p\right]\frac{\mathrm{d}v_{\mathrm{r,l}}}{\mathrm{d}\theta} \tag{4.32}$$

where the derivative $(\partial p/\partial T)_v$ is here computed for the liquid phase with the methodology provided in the next subsection.

As shown in Appendix A.2, the internal energy of the oil can be considered independent from the pressure or from the specific volume, therefore, the derivative $\mathrm{d}u_{\mathrm{o}}/\mathrm{d}\theta$ from Equation 4.30 can be expressed with

$$\frac{\mathrm{d}u_{\mathrm{o}}}{\mathrm{d}\theta} = \left(\frac{\partial u_{\mathrm{o}}}{\partial T}\right)_p \frac{\mathrm{d}T_{\mathrm{l}}}{\mathrm{d}\theta} \tag{4.33}$$

Eventually, by substituting the expression of $\mathrm{d}v_{\mathrm{r,l}}/\mathrm{d}\theta$ from Equation 4.22 and using Equations 4.32 and 4.33, Equation 4.30 can be rewritten as

$$\frac{\mathrm{d}U_\mathrm{l}}{\mathrm{d}\theta} = u_{\mathrm{r,l}}\frac{\mathrm{d}m_{\mathrm{r,l}}}{\mathrm{d}\theta} + u_\mathrm{o}\frac{\mathrm{d}m_\mathrm{o}}{\mathrm{d}\theta} + m_\mathrm{o}\left(\frac{\partial u_\mathrm{o}}{\partial T}\right)_v\frac{\mathrm{d}T_\mathrm{l}}{\mathrm{d}\theta} + m_{\mathrm{r,l}}\left(\frac{\partial u_{\mathrm{r,l}}}{\partial T}\right)_v\frac{\mathrm{d}T_\mathrm{l}}{\mathrm{d}\theta} + m_{\mathrm{r,l}}T_\mathrm{l}\left(\frac{\partial p}{\partial T}\right)_v\left(\frac{\partial v_{\mathrm{r,l}}}{\partial T}\right)_p\frac{\mathrm{d}T_\mathrm{l}}{\mathrm{d}\theta} - p\frac{\mathrm{d}V_{\mathrm{r,l}}}{\mathrm{d}\theta} + pv_{\mathrm{r,l}}\frac{\mathrm{d}m_{\mathrm{r,l}}}{\mathrm{d}\theta} \tag{4.34}$$

Furthermore, the right-hand term of Equation 4.29 can be rewritten for the liquid phase as

$$\begin{aligned}\frac{\mathrm{d}U_\mathrm{l}}{\mathrm{d}\theta} &= \frac{1}{\omega}\sum_i \dot{m}^i_{\mathrm{r,l}}\,h^i_{\mathrm{r,l}} + \frac{1}{\omega}\sum_i \dot{m}^i_\mathrm{o}\,h^i_\mathrm{o} + \frac{1}{\omega}\dot{Q}_\mathrm{l} + \frac{1}{\omega}\dot{\Phi}_\mathrm{cond} - p\frac{\mathrm{d}V_{\mathrm{r,l}}}{\mathrm{d}\theta} - p\frac{\mathrm{d}V_\mathrm{o}}{\mathrm{d}\theta} \\ &= \frac{1}{\omega}\sum_i \dot{m}^i_{\mathrm{r,l}}\,h^i_{\mathrm{r,l}} + \frac{1}{\omega}\sum_i \dot{m}^i_\mathrm{o}\,h^i_\mathrm{o} + \frac{1}{\omega}\dot{Q}_\mathrm{l} + \frac{1}{\omega}\dot{\Phi}_\mathrm{cond} - p\frac{\mathrm{d}V_{\mathrm{r,l}}}{\mathrm{d}\theta} \\ &\quad - pv_\mathrm{o}\frac{\mathrm{d}m_\mathrm{o}}{\mathrm{d}\theta} - pm_\mathrm{o}\left(\frac{\partial v_\mathrm{o}}{\partial T}\right)_p\frac{\mathrm{d}T_\mathrm{l}}{\mathrm{d}\theta}\end{aligned} \tag{4.35}$$

Finally, given the fact that $u_\phi + pv_\phi = h_\phi$ for both the oil and the liquid refrigerant and simplifying the term $-p\mathrm{d}V_{\mathrm{r,l}}/\mathrm{d}\theta$ in both Equations 4.34 and 4.35, the terms in $\mathrm{d}T_\mathrm{l}/\mathrm{d}\theta$ can be isolated, giving

$$\begin{aligned}&\left[m_{\mathrm{r,l}}\left(\frac{\partial u_{\mathrm{r,l}}}{\partial T}\right)_v + m_{\mathrm{r,l}}T_\mathrm{l}\left(\frac{\partial p}{\partial T}\right)_v\left(\frac{\partial v_{\mathrm{r,l}}}{\partial T}\right)_p + m_\mathrm{o}\left(\frac{\partial h_\mathrm{o}}{\partial T}\right)_p\right]\frac{\mathrm{d}T_\mathrm{l}}{\mathrm{d}\theta} \\ &= -h_{\mathrm{r,l}}\frac{\mathrm{d}m_{\mathrm{r,l}}}{\mathrm{d}\theta} - h_\mathrm{o}\frac{\mathrm{d}m_\mathrm{o}}{\mathrm{d}\theta} + \frac{1}{\omega}\sum_i \dot{m}^i_{\mathrm{r,l}}\,h^i_{\mathrm{r,l}} + \frac{1}{\omega}\sum_i \dot{m}^i_\mathrm{o}\,h^i_\mathrm{o} + \frac{1}{\omega}\dot{Q}_\mathrm{l} + \frac{1}{\omega}\dot{\Phi}_\mathrm{cond}\end{aligned} \tag{4.36}$$

This equation translates the energy balance applied to the liquid phase. The derivative of the liquid phase temperature $\mathrm{d}T_\mathrm{l}/\mathrm{d}\theta$ can therefore be calculated only based on the interface interactions, the external heat transfer and mass flow rates, and does not depend on the total volume reduction. The right-hand side of the equation constitutes the internal energy change of the CV: the first two terms represent the energy variations due to changes in the refrigerant and oil masses within the CV; the next two terms correspond to the energy variations caused by refrigerant and oil flow; and the last two terms represent the variations due to heat transfer and vapor-phase condensation. Regarding the left-hand side, it constitutes the "inertia" of the control volume and defines how the temperature varies with changes in internal energy. Its first term is simply the constant-volume specific heat capacity of the refrigerant; the second accounts for the work induced by the specific-volume variation and is therefore negative but very small; and the last term represents the enthalpy variation of the oil. This last term could have been split into the exact same two terms of the refrigerant (heat capacity + work of specific volume variation), however, as can be seen in Equation 4.33, the internal energy variation with the pressure has been neglected.

For the vapor phase, the left-hand term of Equation 4.29 can be reformulated using Equations 4.22 and 4.32 (applied to the vapor phase):

$$\begin{aligned}\frac{\mathrm{d}U_\mathrm{g}}{\mathrm{d}\theta} &= u_\mathrm{r,g}\frac{\mathrm{d}m_\mathrm{r,g}}{\mathrm{d}\theta} + m_\mathrm{r,g}\frac{\mathrm{d}u_\mathrm{r,g}}{\mathrm{d}\theta} \\ &= u_\mathrm{r,g}\frac{\mathrm{d}m_\mathrm{r,g}}{\mathrm{d}\theta} + m_\mathrm{r,g}\left(\frac{\partial u_\mathrm{r,g}}{\partial T}\right)_v\frac{\mathrm{d}T_\mathrm{g}}{\mathrm{d}\theta} + T_\mathrm{g}\left(\frac{\partial p}{\partial T}\right)_v\frac{\mathrm{d}V_\mathrm{r,g}}{\mathrm{d}\theta} \\ &\quad - T_\mathrm{g}\left(\frac{\partial p}{\partial T}\right)_v v_\mathrm{r,g}\frac{\mathrm{d}m_\mathrm{r,g}}{\mathrm{d}\theta} - p\frac{\mathrm{d}V_\mathrm{r,g}}{\mathrm{d}\theta} + pv_\mathrm{r,g}\frac{\mathrm{d}m_\mathrm{r,g}}{\mathrm{d}\theta}\end{aligned} \tag{4.37}$$

Again, equaling Equations 4.37 and 4.29 applied to the vapor phase, considering that $u_\phi + pv_\phi = h_\phi$ and simplifying the term $-p\mathrm{d}V_\mathrm{r,g}/\mathrm{d}\theta$ in both sides, the term in $\mathrm{d}T_\mathrm{g}/\mathrm{d}\theta$ can be isolated, giving

$$\begin{aligned}m_\mathrm{r,g}\frac{\mathrm{d}T_\mathrm{g}}{\mathrm{d}\theta}\left(\frac{\partial u_\mathrm{r,g}}{\partial T}\right)_v &= \frac{1}{\omega}\sum_i \dot{m}^i_\mathrm{r,g}h^i_\mathrm{r,g} + \frac{1}{\omega}\dot{Q}_\mathrm{g} - \frac{1}{\omega}\dot{\Phi}_\mathrm{cond} \\ &\quad - h_\mathrm{r,g}\frac{\mathrm{d}m_\mathrm{r,g}}{\mathrm{d}\theta} - T_\mathrm{g}\left(\frac{\partial p}{\partial T}\right)_v\left(\frac{\mathrm{d}V_\mathrm{r,g}}{\mathrm{d}\theta} - v_\mathrm{r,g}\frac{\mathrm{d}m_\mathrm{r,g}}{\mathrm{d}\theta}\right)\end{aligned} \tag{4.38}$$

Here, the derivative $(\partial p/\partial T)_v$ is computed for the vapor phase, again, with the methodology provided in the next subsection. Thus, the derivative of the vapor phase temperature depends on the mass and heat transfers as well as the variation of its volume. Similarly to the liquid phase, the vapor phase first three right-hand side terms are the CV's internal energy variation due to mass transfer, heat transfer and condensation (or evaporation), respectively. The fourth term is the CV's mass variation contribution while the last term is the internal energy variation due to a change in specific volume. This time, the last term is not a function of the temperature variation but an external output influencing the temperature variation. Regarding the left-hand side term, the only contribution influencing the thermal inertia of the vapor phase is its constant-volume specific heat capacity.

Eventually, the system of equations can be solved explicitly step by step to obtain the five derivatives required to obtain the updated state after an angle step. As a reminder, those five derivatives are $\mathrm{d}v_\mathrm{r,g}/\mathrm{d}\theta$, $\mathrm{d}v_\mathrm{r,l}/\mathrm{d}\theta$, $\mathrm{d}v_\mathrm{o}/\mathrm{d}\theta$, $\mathrm{d}T_\mathrm{g}/\mathrm{d}\theta$ and $\mathrm{d}T_\mathrm{l}/\mathrm{d}\theta$. First, the interface interactions should be defined, using the heat transfer coefficients from the interface to the liquid phase AU_l and to the vapor phase AU_l in order to obtain the condensation mass flow rate $\mathrm{d}m_\mathrm{cond}/\mathrm{d}\theta$ and condensation energy transfer rate $\mathrm{d}\dot{\Phi}_\mathrm{cond}/\mathrm{d}\theta$, from Equations 4.18 and 4.28. Those two heat transfer coefficients can be assumed equal, although they are defined distinctly in the literature. Then, the mass derivatives of the three components can be calculated using the mass conservation Equations 4.19, 4.20 and 4.21. Afterward, using the mass flow rate and heat transfer rate of the liquid phase (as the pressure effect is neglected), $\mathrm{d}T_\mathrm{l}/\mathrm{d}\theta$ can be calculated, using Equation 4.36. The latter term allows to define the variation of volume of the vapor phase $\mathrm{d}V_\mathrm{r,g}/\mathrm{d}\theta$ via Equations 4.25, 4.24 and 4.23 and, thus, the derivatives $\mathrm{d}v_\mathrm{r,g}/\mathrm{d}\theta$, $\mathrm{d}v_\mathrm{r,l}/\mathrm{d}\theta$ and $\mathrm{d}v_\mathrm{o}/\mathrm{d}\theta$ using Equation 4.22. Finally, Equation 4.38 can be used to obtain $\mathrm{d}T_\mathrm{g}/\mathrm{d}\theta$ and the forward Euler method of Equations 4.5 and 4.6 can be used to obtain the next temperatures of the two phase and specific volumes of the three components. The pressure of the CV can be computed using the vapor phase specific volume and temperature. Although the system is solved, some derivatives need to be calculated using finite difference methods. This is done in the next subsection.

4.4.4 Derivatives calculations

Equations 4.36 and 4.38 require the calculation of several derivatives, for instance, the derivative $\left(\partial u_\phi/\partial T\right)_v$ can not always be replaced by the specific heat capacity at constant

volume, as sometimes, two-phase conditions can occur in one of the phase, leading to more internal energy balancing the phase change. These derivatives are therefore going to be directly calculated when those two-phase conditions are met, using a backward difference for the vapor phase and a forward difference for the liquid phase, to ensure the no-crossing of the saturation curves with $\mathrm{d}T = 0.1$ K:

$$\left(\frac{\partial u_{\mathrm{r,g}}}{\partial T}\right)_v = \frac{u(v_{\mathrm{r,g}}, T_{\mathrm{g}}) - u(v_{\mathrm{r,g}}, T_{\mathrm{g}} - \mathrm{d}T)}{\mathrm{d}T} \tag{4.39}$$

$$\left(\frac{\partial u_{\mathrm{r,l}}}{\partial T}\right)_v = \frac{u(v_{\mathrm{r,l}}, T_{\mathrm{l}} + \mathrm{d}T) - u(v_{\mathrm{r,l}}, T_{\mathrm{l}})}{\mathrm{d}T} \tag{4.40}$$

When single-phase conditions are met, the derivatives can simply be replaced by the specific heat capacity at constant volume provided by CoolProp. Regarding the term $\left(\partial v_{\mathrm{r,l}}/\partial T\right)_p$, it must be computed as a function of the pressure and the temperature, i.e., subcooled conditions close to saturation must be ensured. To avoid property calculation error, a temperature shift $\Delta T = 1$ [K] is introduced, which does not significantly change the results of the derivative. This temperature shift ensures that the property calculation is performed in either the superheated or subcooled region. The derivative is thereby calculated as

$$\left(\frac{\partial v_{\mathrm{r,l}}}{\partial T}\right)_p = \frac{v(p, T_{\mathrm{l}} - \Delta T + \mathrm{d}T) - v(p, T_{\mathrm{l}} - \Delta T - \mathrm{d}T)}{2\mathrm{d}T} \tag{4.41}$$

Moreover, the derivative $(\partial p/\partial T)_v$ is calculated differently for a subcooled, a superheated or a two-phase state, where a shift is again introduced to ensure being in the single-phase region. For the derivative in superheated vapor, the shift introduced is an increase in temperature, which gives

$$\left(\frac{\partial p}{\partial T}\right)_v = \frac{p(\rho_{\mathrm{r,g}}, T_{\mathrm{g}} + \Delta T + \mathrm{d}T) - p(\rho_{\mathrm{r,g}}, T_{\mathrm{g}} + \Delta T - \mathrm{d}T)}{2\mathrm{d}T} \tag{4.42}$$

For the derivative in subcooled liquid, the shift introduced is an increase in the density:

$$\left(\frac{\partial p}{\partial T}\right)_v = \frac{p(\rho_{\mathrm{r,l}} + \Delta\rho, T_{\mathrm{l}} + \mathrm{d}T) - p(\rho_{\mathrm{r,l}} + \Delta\rho, T_{\mathrm{l}} - \mathrm{d}T)}{2\mathrm{d}T} \tag{4.43}$$

Then, the Clapeyron equation is used to calculate the derivative in the two-phase region:

$$\left(\frac{\partial p}{\partial T}\right)_v = \frac{h^{\sigma}_{\mathrm{r,g}}(p) - h^{\sigma}_{\mathrm{r,l}}(p)}{T_\gamma \left(v^{\sigma}_{\mathrm{r,g}}(p) - v^{\sigma}_{\mathrm{r,l}}(p)\right)} \tag{4.44}$$

Finally, the derivative of the oil enthalpy with the temperature can be obtained by differentiating the expression provided in Appendix A.2:

$$\left(\frac{\partial h_{\mathrm{o}}}{\partial T}\right)_p = c_{p,\mathrm{o}}(T) - (p - p_{\mathrm{ref}}) \cdot \frac{a_{\rho,2} + 2a_{\rho,3}T}{\rho_{\mathrm{o}}^2} \tag{4.45}$$

where the first term simply corresponds to the specific heat capacity at constant pressure while the second term is the term in pressure involving the derivative of the specific volume with respect to the temperature.

4.4.5 Results and discussion

Case study

To better understand the previously defined core model, the derived equations can be applied to a simple piston-cylinder system presented in Figure 4.12. In this cylinder can be found a two-phase pure-refrigerant fluid (R1233zd(E)) at the initial conditions given in Table 4.2. Q_i stands for the initial vapor quality in mass fraction while α_i is the volume fraction or so-called void fraction. Therefore, even when the vapor quality is low, the majority of the volume is occupied by vapor. Neither external heat transfer nor leakage/flow is considered in this application. Moreover, the piston movement does not generate any friction, the work applied to the piston is therefore fully transmitted to the fluid.

V_i [cm^3]	Q_i [-]	α_i [-]	p_i [Pa]	T_i [K]	ρ_i [kg/m^3]
80	0.4	0.9889	$1.5{\cdot}10^5$	302.2	20.45

Table 4.2: Initial state before the simulated compression.

The volume defined by the piston-cylinder setup is going to be decreased linearly with a rate similar to what can be observed in a scroll compressor running at a speed of 2000 RPM, with a volume ratio of 5 reached after approximately 0.01 seconds. Then the system is going to be left at rest until the thermal equilibrium is reached again. The volume evolution can be found in Figure 4.13. Point 1 corresponds to the initial state, point 2 to the state right after volume reduction and point 2″ after the resting period, after which the thermal equilibrium is reached again. In this simulation, heat transfer conductances from the phases to the interface AU_ϕ have been randomly fixed at 120 W/K and the area A is simply taken as being the cylinder cross-section area (17.13 cm^2).

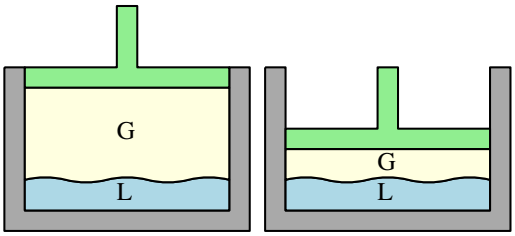

Figure 4.12: Piston-cylinder setup to simulate a two-phase compression, initial state on the left and final state on the right.

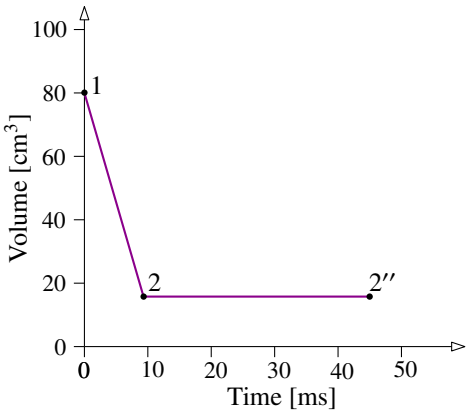

Figure 4.13: Simulated volume evolution of the piston-cylinder setup.

The variation of the temperatures of both phases as well as the pressure ratio over time can be found in Figure 4.14. The pressure ratio reaches its maximum just after the reduction of volume and the same holds for the vapor phase temperature. Regarding the liquid phase temperature, due to the high heat transfer coefficients used, it follows closely the vapor phase temperature, allowing to re-establish the equilibrium after a resting period of less than 0.05 seconds. During this resting period, the pressure decreases due to condensation decreasing the vapor phase density, generating an expansion with an increasing volume but a decreasing mass, inducing a reduction in the vapor phase density. Eventually, after the resting period, the vapor and liquid temperatures converge towards the saturation temperature. The use of a

split state presented in Section 2.4.1 of the second chapter justifies the convergence towards the saturation temperature, even when oil is used.

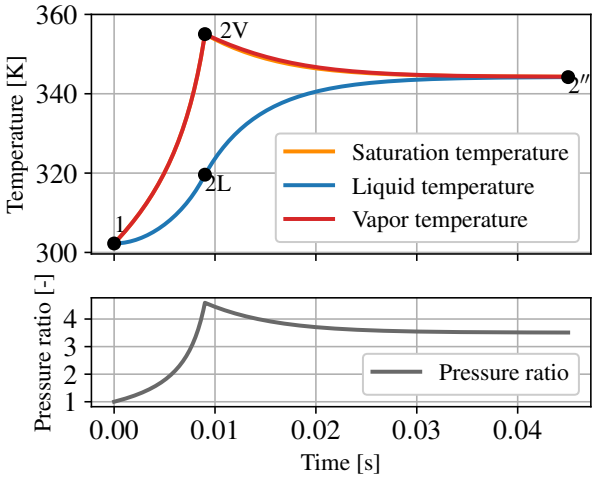

Figure 4.14: Evolution of the temperatures of both phases and evolution of the pressure ratio with time.

The pressure-enthalpy and temperature-entropy diagrams of the transformation can be found in Figure 4.15 and Figure 4.16. The observation of those two diagrams allows a deep understanding of what is occurring along the compression in both phases. The first observation that can be made is the fact that the vapor phase follows the vapor saturation line during the compression, while the liquid phase becomes subcooled due to the rise of pressure. During the resting period, the saturated vapor becomes superheated due to the expansion (decrease in density) generated by the condensation between the two phases. As can be observed in Figure 4.14, the saturation line stands between the two phases' temperatures. Therefore, a pseudo-state, where a superheated phase is mixed with a subcooled phase is observed during the resting phase, until the equilibrium is re-established, allowing two saturated phases to be reached at the same temperature. The vapor phase decrease in temperature during the resting period can be explained by the decrease in pressure coming from the decrease in density, indirectly created by the heat transfer. The heat transfer therefore creates condensation, generating this change of density: the vapor (high volume, small mass) becomes liquid (low volume, same mass). Conversely, the liquid phase temperature rise is mostly due to direct heat transfer generated by the condensation. The orange curve represents a pseudo-state where the liquid and vapor phases are mixed: it only serves to display the overall property variations of the fluid. A slight increase in entropy is observed in Figure 4.16, which means that the compression performed, despite being adiabatic, is not isentropic.

The energy consumption of the compression can be calculated in two different ways, calculating both terms of the energy conservation equation applied to the studied case (no heat exchange considered):

$$\Delta U = W_{\text{cp}} \tag{4.46}$$

Calculating the results from both sides of the equation allows checking the consistency of the model. The right-hand side of the equation gives

$$\Delta U = \frac{m_{\text{g}}}{m_{\text{cv}}} u_{\text{g}}(\rho_{\text{g}}, T_{\text{g}}) + \frac{m_{\text{l}}}{m_{\text{cv}}} u_{\text{l}}(\rho_{\text{l}}, T_{\text{l}}) - m_{\text{cv}} u(Q_i, T_i) = 18.63 \text{ [J]} \tag{4.47}$$

The left-hand side of the equation gives

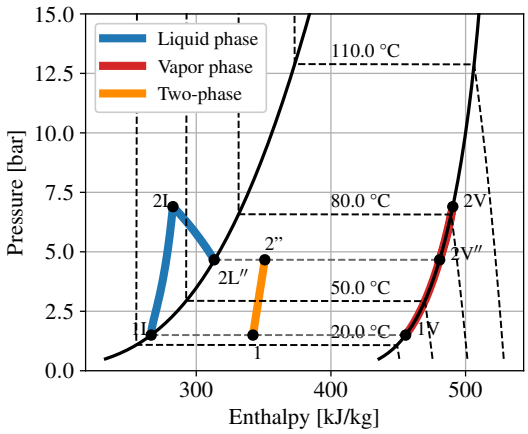

Figure 4.15: Pressure-enthalpy diagram of the two-phase compression without oil.

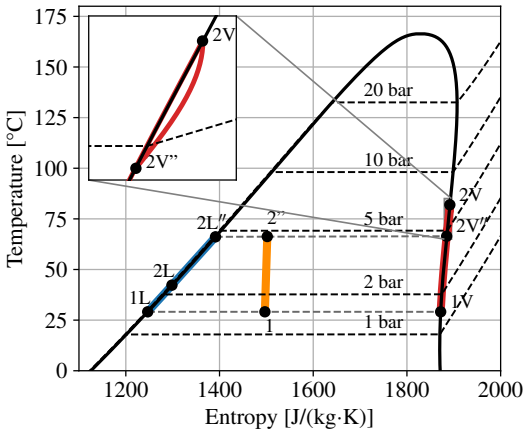

Figure 4.16: Temperature-entropy diagram of the two-phase compression without oil.

$$W_{\text{cp}} = -\int_{V_i}^{V_f} p \, \mathrm{d}V = 18.81 \text{ [J]} \tag{4.48}$$

The difference between the two values can be explained by the numerical errors introduced by the Euler forward method and the derivatives calculation. This equality does not need to reach the thermal equilibrium to be respected: the energy is transferred to the system during the compression. While at rest, no further work is introduced into the system, even if heat transfer and mass transfer occur between the liquid and the vapor phases. Nevertheless, the entropy of the system is still increasing while heat transfer occurs. The internal energy and entropy variations of the system are displayed in Appendix C.2.1. Finally, the isentropic efficiency of the process can be calculated, using the following definition:

$$\varepsilon_{\text{is}} = \frac{m_{\text{cv}} \, \Delta u_{\text{is}}}{\Delta U} = 83.82 \text{ [\%]} \tag{4.49}$$

This isentropic efficiency being inferior to one means that, even without external heat transfer, leakage, or friction introduced, a two-phase compression creates irreversibilities due to the heat transfer between the two phases. If the heat transfer coefficients AU_ϕ were higher, the difference between the phases' temperatures would be lower, resulting in a higher isentropic efficiency.

Impact of the oil

The case of a two-phase compression of a pure refrigerant has been studied with a simple application and conclusions could be drawn. The exact same application setup can be used to run multiple simulations, varying the initial vapor quality and using different oil mass fractions. The oil mass fraction has, in this case, been included using a split state: no apparent superheat is necessary to have a two-phase mixture, and the solubility does not have any contribution to the results. The impact of the oil on the two-phase compression core model can be studied throughout the final pressure ratio obtained with the setup, as well as with the isentropic efficiency obtained from the compression. Therefore, the variation of the final pressure ratio with the initial vapor quality is presented in Figure 4.17, while the isentropic efficiency can be found in Figure 4.18. The impact of the oil is clear: both the final pressure ratio (after the resting period) and the isentropic efficiency decrease when the oil mass fraction is increased. Nevertheless, this decrease is not significant. As the vapor quality displayed is the global vapor quality, the maximum x-value reached by each curve is

limited by the oil mass fraction represented by the curve. The previously defined application conditions stand on the two graphs at a vapor quality of 0.4 without any oil. As already stated and analyzed in Section 2.4.2 of the Chapter 2 and Section 3.4.1 of the Chapter 3, the pressure ratio reached by a two-phase compression decreases with the initial vapor quality. Again, this trend can clearly be observed in Figure 4.17. This trend is justified by the higher amount of condensation observed when more liquid is present: the liquid phase is heated up by the condensation of the vapor, resulting in a lower vapor density and thereby a lower final pressure. Furthermore, the decrease in vapor quality seems to induce a decrease in isentropic efficiency. This phenomenon was already observed in the previous application (which is part of the graph). Without a liquid phase (oil mass fraction of zero, with the maximum in vapor quality), the isentropic efficiency reaches a value of one, or, equivalently, an isentropic compression is performed. If a liquid phase is present, the higher the mass of liquid, the lower the efficiency, which can be explained by the inertia of the liquid phase taking more time to rise in temperature, thereby creating a higher temperature difference between the vapor and liquid phase during the compression. The impact of the oil resides in the higher heat capacity than the liquid refrigerant. Common values of specific heat capacity of the oil stand around 1800-2200 J/kg·K, while the liquid refrigerant heat capacity stands between 1000 and 1300 J/kg·K. Therefore, for the same mass of liquid, more energy can be stored in the liquid phase when a higher oil mass fraction is present. This phenomenon is equivalent to having a higher liquid mass: the difference in temperature between the liquid and vapor phase is more important when higher oil mass fractions are used. Thus, increasing the oil mass fraction is equivalent to shifting the zero-oil curve towards the right and lower isentropic efficiencies are observed for higher oil mass fractions. For the same reason, the final pressure ratio is lower for higher oil mass fractions: more internal energy is stored in the liquid phase, resulting in more condensation of the vapor phase, inducing a drop in final pressure. Therefore, if oil is present in the mixture, even at the highest possible vapor quality (or superheat), the isentropic efficiency is already impacted and can never approach 1.

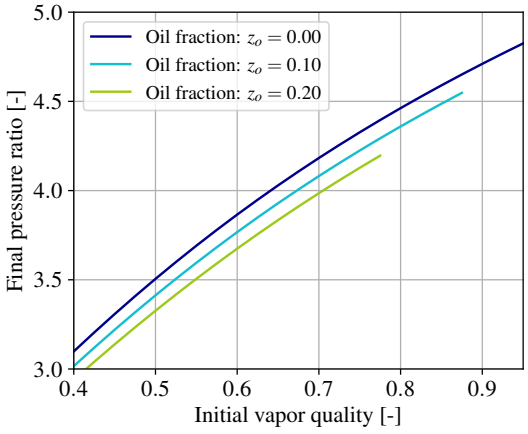

Figure 4.17: Final pressure ratio as a function of the initial vapor quality for several oil mass fractions.

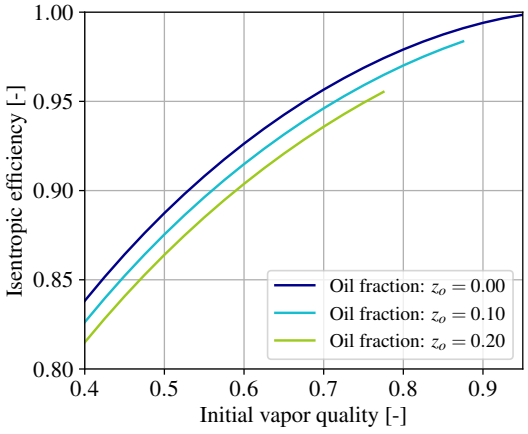

Figure 4.18: Isentropic efficiency as a function of the initial vapor quality for several oil mass fractions.

Impact of the heat transfer between the two phases

The heat transfers between the two phases depend on the heat exchange area between the vapor and the liquid A, as well as the heat transfer coefficient U_ϕ. In the previous applications, the heat transfer conductance AU_ϕ has been roughly estimated to be 120 W/K in the cylinder, although it strongly depends on the configuration of the flow, itself depending on

the speed and shape of the piston inside the cylinder. In order to investigate the influence of this conductance on the resulting final pressure and compression isentropic efficiency, three different conductances are going to be used in the previous application. A zero-conductance allows to simulate the case without heat transfer at all, a 300 W/K conductance allows to investigate the results of moderately high heat transfer without thermal equilibrium, and, finally, a 24000 W/K conductance allows to investigate the case of two-phase compression at thermal equilibrium (instantaneous condensation). The final pressure ratio varying with the initial vapor quality is presented in Figure 4.19 while the resulting isentropic efficiency can be found in Figure 4.20. The oil ratio has been fixed at 0.05 for this simulation. Once again, the presented pressure ratios are taken after the resting period. However, this equilibrium can never be reached without heat transfer between the two phases, i.e., the blue curve (no heat exchange) is the curve representing the maximum pressure achievable throughout a two-phase compression. In this curve, the vapor phase mass slightly decreases due to the phenomenon of partial condensation explained in Figure 4.11. This condensation only has an impact at high vapor quality, as the liquid phase temperature increases with this phenomenon due to the low liquid mass. However, at low vapor quality, the liquid phase is not impacted by the compression (the pressure influence is neglected) and the vapor phase condensation is not sufficient to decrease the vapor density and therefore the final pressure obtained. Hence, the pressure ratio increases when the initial vapor quality decreases, due to the lower volume available to compress the vapor. Finally, only a slight difference is observed between the thermal equilibrium and the non-equilibrium curves. This means that, despite the heat transfer being different, the final pressures obtained are close to each other. If even slight heat transfers were to be added to the no-heat-transfer curve, the final pressure ratio obtained would probably reach similar values. Regarding the isentropic efficiency, the trends observed were expected: less heat transfer implies a higher temperature difference between the two phases, inducing more irreversibilities. The thermal equilibrium exhibits very high heat transfers leading to a uniform temperature. Therefore, the isentropic efficiency reaches a value of one. The isentropic efficiencies obtained from a thermal non-equilibrium are lower, which also explains why the resulting pressure ratio of this curve is a bit higher. As a matter of fact, a lower isentropic efficiency means a higher final temperature, vapor quality and pressure. To conclude with the observed trends, the only way to improve the efficiency of an ideal two-phase compression at low vapor quality is to increase the heat transfer coefficient between the two phases, however, this improvement is associated with a decrease in pressure ratio. Increasing the turbulence of a two-phase flow during compression is a possible way to increase this heat transfer coefficient, for instance by increasing the speed of the volume reduction, provided that pressure losses are kept as low as possible.

4.5 Flow models

The core model previously defined predicts the evolution of the mixture properties under a volume reduction. In the application proposed to understand the model, a two-phase pure refrigerant/mixture undergoes a volume reduction, the pressure ratio and phase temperatures are tracked, and the resulting isentropic efficiency is computed. This application assumes an adiabatic process (no heat transfer with the environment) and no external mass transfer. In real applications, such heat and mass transfer processes can occur. Returning to the case of the scroll compressor, the multiple chambers defined in the geometrical model (Section 4.3) undergo well-defined volume reductions, while exchanging mass with each other and with their surroundings. For instance, the suction-admission chamber exchanges mass with the inlet port (flow entering the scroll shell) and with the suction chambers (flow through the detachment of the scrolls). The compression chambers exchange mass primarily in the form

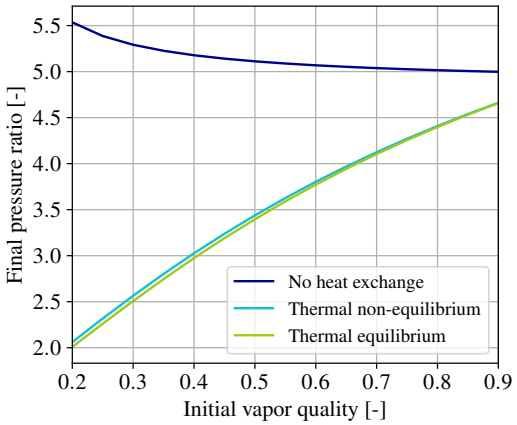

Figure 4.19: Final pressure ratio as a function of the initial vapor quality for three heat exchange conditions.

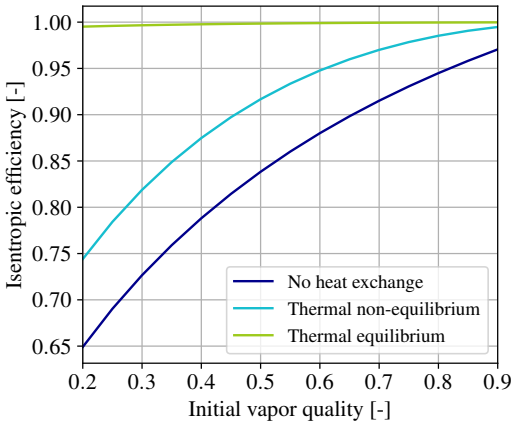

Figure 4.20: Isentropic efficiency as a function of the initial vapor quality for three heat exchange conditions.

of leakage, or throughout the intermediate discharge ports in case of overcompression. Those flows contributions are taken into account in the core model, under the name $\dot{m}^i_{\mathrm{r,g}}$ for the vapor refrigerant, $\dot{m}^i_{\mathrm{r,l}}$ for the liquid refrigerant and $\dot{m}^i_{\mathrm{o}}$ for the oil. The importance of the flow models resides in the accurate predictions of those flows: they strongly influence the performance of the machine. The model must accurately predict not only the total mass flow rate, but also the proportions of vapor refrigerant, liquid refrigerant, and oil. Multiple flow models can be found in the literature, depending on the flow geometry and the kind of flow. Geometry can, for instance, correspond to a nozzle shape, an orifice, a contraction or an enlargement, while the different kinds of flow include: incompressible, frictional, compressible, isentropic or isothermal.

4.5.1 Two-phase flow models

Chisholm (1983) proposes multiple two-phase flow models, validated with experimental data for defined geometries: incompressible flow, compressible isentropic flow without phase change and compressible isentropic flow with phase change. The incompressible two-phase mass flux is obtained from a force balance on the flowing mixture, considering a constant specific volume:

$$G^2 = -\frac{2}{k v_{\mathrm{l}}} \cdot \Delta p_{\mathrm{lo}} \tag{4.50}$$

where Δp_{lo} (negative number) expresses the pressure losses as if the flow were liquid only and k is a pressure loss coefficient, depending on the contraction ratio and the ratio between the downstream area and the upstream area. In the case of a nozzle, an approximation of $k = 10$ can be used (throat area equals half of the upstream area). The liquid-only pressure losses can be linked with the real pressure losses using a two-phase multiplier ϕ^2_{lo}. Multiple models are proposed in the literature to estimate this two-phase multiplier (Alimonti et al. 2010). Here, only the model of Chisholm (1983) will be used, it is defined as

$$\Delta p = \Delta p_{\mathrm{lo}} \cdot \phi^2_{\mathrm{lo}} \tag{4.51}$$

The two-phase multiplier is expressed as

$$\phi^2_{\mathrm{lo}} = 1 + \left(\frac{v_{\mathrm{g}}}{v_{\mathrm{l}}} - 1\right) \cdot \left(\frac{1}{K} \cdot Q(1-Q) + Q^2\right) \tag{4.52}$$

where K is the effective entrainment slip ratio, the expression of which depends on the Lockhart-Martinelli parameter, a dimensionless number that characterizes the relative pressure drops of liquid and gas phases in two-phase flow:

$$X = \left(\frac{\Delta p_\mathrm{l}}{\Delta p_\mathrm{g}}\right)^{1/2} = \frac{1-Q}{Q}\left(\frac{v_\mathrm{l}}{v_\mathrm{g}}\right)^{1/2} \tag{4.53}$$

When $X > 1$ the entrainment slip ratio K_0 is defined as

$$K_0 = \left[1 + Q\left(\frac{v_\mathrm{g}}{v_\mathrm{l}} - 1\right)\right]^{1/2} \tag{4.54}$$

while when $X < 1$, it is given by

$$K_0 = \left(\frac{v_\mathrm{g}}{v_\mathrm{l}}\right)^{1/4} \tag{4.55}$$

For a flow crossing a Nozzle, the effective entrainment slip ratio K can be expressed as a function of the entrainment slip ratio K_0 as

$$K = K_0^{0.4} \tag{4.56}$$

By substituting K into Equation 4.52, the two-phase multiplier can be computed as well as the liquid-only pressure losses from Equation 4.51 and the mass flux can be derived from it.

A compressible flow without phase change is also proposed by Chisholm (1983), in this case, considering the variation of the effective specific volume along the pressure evolution, the force balance on the flowing mixture (or linear momentum conservation) gives

$$G^2 = -2\,\frac{\displaystyle\int_{p_\mathrm{down}}^{p_\mathrm{up}} v_\mathrm{e}\,\mathrm{d}p}{v_\mathrm{e,down}^2 - \sigma^2 v_\mathrm{e,up}^2} \tag{4.57}$$

where σ is the ratio between the throat and the upstream areas. In the context of this work, since this ratio is small and squared, the term in σ is neglected, thereby minimizing the resulting mass flux.

The effective specific volume v_e is expressed as

$$v_e = \left[Q v_g + K(1-Q)v_l\right]\left[Q + \frac{1-Q}{K}\right] \tag{4.58}$$

with K calculated similarly as for an incompressible flow, i.e., using Equation 4.55. In the case where no phase change is considered, the vapor quality is kept constant at the upstream value. The values of the vapor and liquid specific volumes, for their part, vary with the pressure.

Finally, when considering phase changes, an isentropic flow can be assumed. In this case, the vapor quality used to calculate the effective specific volume (in Equation 4.58) is calculated considering the vapor quality variations. The values of the vapor and liquid specific volumes are still function of the pressure only and does not vary even though the flow is considered isentropic. If the Lockhart-Martinelli parameter (Equation 4.53) is smaller than one, thermal equilibrium is assumed in the nozzle, therefore, the vapor quality simply is the isentropic vapor quality ($Q = Q_\mathrm{is}$). When this parameter is greater than one, thermal non-equilibrium occurs, and the vapor quality is therefore given by

$$Q = Q_\mathrm{up} + \left(\frac{Q_\mathrm{is} - Q_\mathrm{up}}{Q_\mathrm{t} - Q_\mathrm{up}}\right)^2 (Q_\mathrm{is} - Q_\mathrm{up}) \tag{4.59}$$

where Q_t is defined as

$$Q_t = \frac{1}{1 - (v_g/v_l)^{1/2}} \tag{4.60}$$

Other compressible two-phase flow models can be found in the literature. One can cite the model proposed by Morris (1991), where no integration is required and the calculation of a discharge coefficient, depending on the nozzle geometry, is introduced. In the frame of this work, only the two-phase models from Chisholm will be employed. The mass flow rate coming from incompressible, compressible with and without phase change nozzle models of Chisholm are compared for a varying pressure ratio. The results can be found in Figure 4.21. As can be seen, not considering the compressibility of the flow gives the lower flow rate prediction, while the isentropic flow (with phase change) gives the highest. Moreover, the higher the pressure ratio, the larger the difference between the mass flow rate coming from a compressible flow with and without phase change, which can be explained by the difference between the upstream and downstream vapor quality increasing with the pressure ratio when considering phase change: higher pressure ratios mean more phase change.

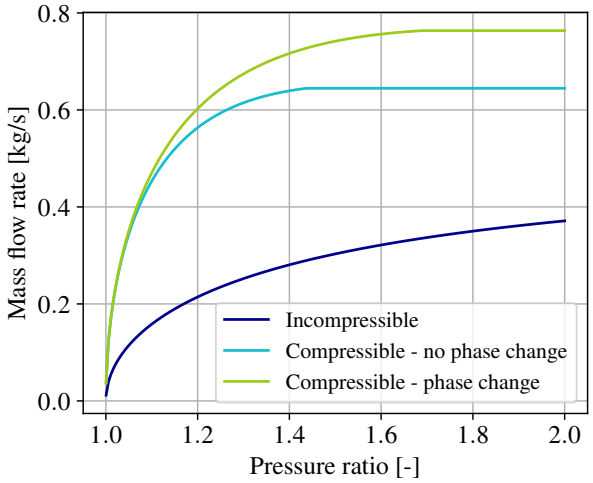

Figure 4.21: Evolution of the nozzle mass flow rate as a function of the pressure ratio for three two-phase models. Upstream pressure of 2 bar, upstream and throat cross-section areas of 4 and 2 cm^2.

Compressible models need to take into account choked conditions when they are met, i.e., to determine the pressure ratio at which supersonic conditions are reached. This can be seen for both compressible flow models employed in Figure 4.21, with the transition from a curve to a flat line. This ratio, called critical pressure ratio, can easily be computed for a two-phase flow using the model of Petrovic et al. (2016). In this model, a mean value of the isentropic expansion coefficient between the upstream cross-section and the location of the choked flow is calculated with

$$\kappa = \frac{c^2}{p/\rho} \tag{4.61}$$

where c is the two-phase speed of sound. Using this isentropic expansion coefficient allows to directly calculate the critical pressure ratio with the following definition:

$$r_{p,c} = \left(1 + \frac{\kappa - 1}{2}\right)^{\frac{\kappa}{\kappa - 1}} \tag{4.62}$$

When this ratio is exceeded, the flow is choked and the value of the mass flow rate stays constant despite the downstream conditions changing.

The two-phase speed of sound is given by:

$$c = \left[\frac{\alpha\rho}{\rho_g c_g^2} + \frac{(1-\alpha)\rho}{\rho_l c_l^2} \right]^{-1/2} \tag{4.63}$$

with ρ defined as the inverse of the effective specific volume v_e from Equation 4.58, calculated at the location of the choked flow. The speeds of sound in the liquid and vapor phases must also be calculated at the location of the choked flow. Moreover, α is the void fraction considering the slip between the two phases, it is defined as

$$\alpha = \frac{1}{1 + \frac{1-Q}{Q} K \frac{\rho_g}{\rho_l}} \tag{4.64}$$

Here, K is the effective entrainment slip ratio from Equation 4.56.

4.5.2 Primary flows

Two-phase flow models have therefore been defined to link the mass flow rate with a pressure difference between two control volumes. Those predictions strongly depend on the geometry of the flow, which does not always have the shape of a nozzle. For instance, the discharge port constitutes an abrupt change of section, sometimes even without a circular shape, which is far from a nozzle configuration. Therefore, geometry correction coefficients can be introduced to correct the predicted mass flow rates, but they require experimental validation. Eventually, only the isentropic flow considering phase change is used to predict the mass flow rate, the other models have been implemented for illustrative purposes only. Flow models are required to estimate the mass flow rate in the primary flow of the model, as well as for the leakage. Primary flows include the following flows:

- The flow from the supply pipe entering the casing of the compressor. This flow enters the suction-admission (sa) chamber defined in Section 4.3.
- The flows from the sa chamber to the suction (s1 and s2) chambers, which are created by the scrolls' relative positioning. This flow is periodic as the volumes of the suction chambers start from zero and evolve until the s1 and s2 chambers close when reaching the displacement volume.
- The flows appearing when the compression chambers (c1 and c2) open to the discharge chamber (ddd). During this merging phase, a flow is created until the pressure balance is reached, defining a new discharge chamber.
- The flow coming from the discharge chamber through the discharge port. This flow is also crossing the main discharge valve.
- The flows coming from the compression chambers through the intermediate discharge valves. Those flows only appear in the case of overcompression.

The modeling of the discharge valves (main and intermediate) is done using a simple quasi-static model not considering the valve dynamics. According to Pereira et al. (2010), implementing the valve dynamics in scroll compressors does not show advantages over the simple quasi-static model, even for high operation speed. The model employed originates from Chen et al. (2002a). This model considers an opening of the valve proportional to the difference in pressure between the outlet and the discharge chamber. A zero-opening is set when the inlet pressure does not exceed the outlet pressure. A maximum opening is set by the stopper of the valve. The vertical opening y of the discharge valve is given by the following equation, along with the maximum constraint:

$$y = \pi \frac{d^2}{4} \frac{1}{C_{\text{valve}}} \min(0, p - p_{\text{ex}})$$
$$y \leq y_{\text{stopper}} \tag{4.65}$$

which represents the force generated by the pressure difference, multiplied by the inverse of the spring constant. In this equation, d represents the diameter of the discharge port, p, the pressure inside the discharge chamber, p_{ex}, the exhaust pressure and C_{valve}, the spring constant. The maximum position of the valve (y_{stopper}) had been measured to be approximately 5 mm for the retrofitted compressor and designed similarly for the prototype, while the spring constant is set at 2000 N/m. The final throat area of the discharge port is given by the minimum between the discharge port area, which can be covered by the orbiting scroll, and the opening created by the valve, such as

$$A_{\text{dis}} = \min(A_{\text{dis,p}}, A_{\text{dis,v}}) \tag{4.66}$$

where $A_{\text{dis,p}}$ is the discharge port area defined in Section 4.3 and $A_{\text{dis,v}} = y\pi d$ is the area coming from the opening of valve. This model allowed to simulate the behavior of two kinds of discharge valve: the intermediate discharge valves intended to avoid overcompression and the main discharge valve, also called reed valve, reducing undercompression effects by preventing backflow.

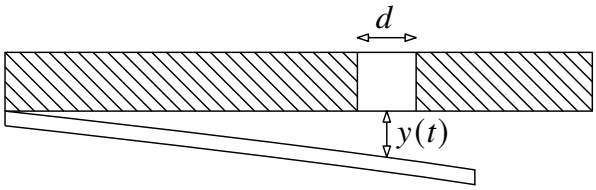

Figure 4.22: Schematic of the discharge valve model.

The flow simulated at the suction and the exhaust of the compressor can be found, in Figures 4.23 and 4.24, respectively. Two suction flows can be found in Figure 4.23, the flow entering the "suction-admission" chamber and the flow entering the suction chambers. The suction flow is initiated by the increasing volume of the suction chambers, therefore inducing a decrease in density in the suction-admission chamber. This decrease in density results in a decrease in pressure, generating a flow from the inlet of the compressor to the suction-admission chamber. Thus, even if the flow entering the suction chambers is periodic, a damping effect coming from the large volume and compressibility of the fluid in the suction-admission chamber stabilizes the inlet flow. In Figure 4.24, the discharge mass flow rate is distributed into two curves: a normal phase where the discharge chamber exchanges mass uniquely through the discharge port (or by leakage) and the merging phase where it exchanges not only mass through the discharge port but also with the previous compression chambers. The undercompression trend mentioned in the caption in Figure 4.24 denotes a pressure lower than the exhaust pressure in the compression chamber. Therefore, when this merging phase occurs, the flow rate quickly drops to zero as the pressure equilibrium resulting from this merging decreases the pressure. Without the reed valve, the discharge mass flow rate could become negative, resulting in backflow. After the merging process, the decrease in the discharge chamber volume leads to an increase in pressure, regenerating a discharge flow.

4.5.3 Flow pattern

The flow pattern of the two-phase mixture at the inlet of the compressor plays a critical role in determining the machine's performance. The distribution of liquid significantly influences

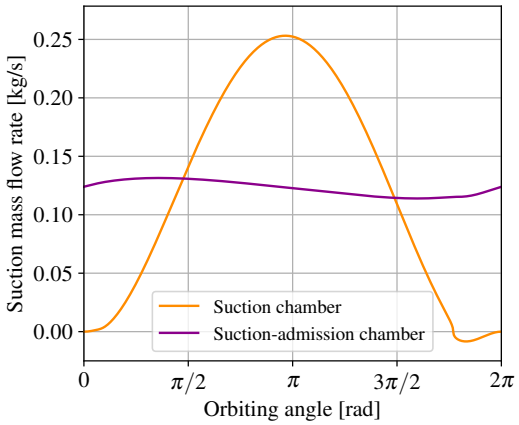

Figure 4.23: Suction mass flow rate simulated.

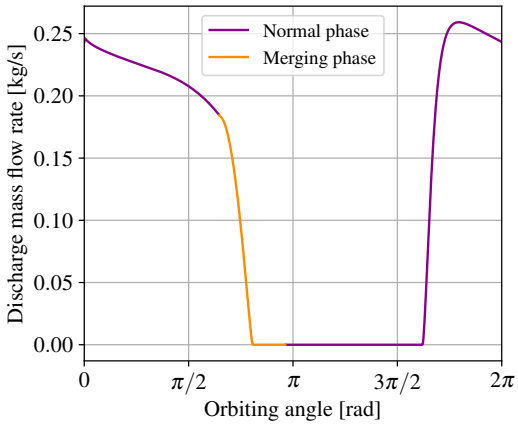

Figure 4.24: Discharge mass flow rate simulated with an undercompression trend.

heat transfer between the two phases and between the phases and the scrolls, but also the leakages between the chambers. Different flow regimes, such as annular, stratified, slug, intermittent or wavy flow, determine the distribution of the liquid phase, therefore influencing the heat exchange area between the two phases, but also the quantity of liquid covering the leakage gaps. For instance, a purely stratified flow provides a low heat exchange area between the two phases, while an annular flow with liquid droplets traveling within the vapor phase increases considerably this heat exchange area. Similarly, a stratified flow should provide a better sealing effect than an annular flow with a significant amount of droplets. Accurate characterization of the inlet flow pattern is thus essential to determine its influence on the compressor's performance.

The determination of the two-phase flow pattern map of the refrigerant R1233zd(E) and the two employed oils defined in Chapter 2 is based on the work of Wojtan et al. (2005). This work proposes some correlations defining the transition lines between the flow regimes, as a function of the mixture properties, as well as the void fraction for a horizontal tube. The map is represented with the vapor quality (Q) on the x-axis and the mass flux (G) on the y-axis.

The drift flux model, allowing to determine the void fraction, is given by Thome (n.d.):

$$\alpha = \frac{Q}{\rho_g}\left[(1+0.12(1-Q))\left(\frac{Q}{\rho_g}+\frac{1-Q}{\rho_l}\right)+\frac{1.18(1-Q)\left[g\sigma(\rho_l-\rho_g)\right]^{0.25}}{G\rho_l^{0.5}}\right]^{-1} \tag{4.67}$$

where the properties denoted by the subscript 'l' are the liquid-phase properties defined in Chapter 2, g is the gravitational acceleration equal to 9.81 m/s^2 and σ is the two-phase surface tension defined in Section 2.3.5 of the same chapter. From the sectional area of the tube A, dimensionless vapor and liquid cross-sectional areas can be defined, with D, the tube diameter:

$$A_{lD} = \frac{A(1-\alpha)}{D^2} \tag{4.68}$$

$$A_{gD} = \frac{A\alpha}{D^2} \tag{4.69}$$

An illustration of a stratified flow cross-section can be found in Figure 4.25. The wet angle θ_w can be calculated as a function of the void fraction with the approximation of Biberg (1999):

$$\theta_w = 2\pi - 2\left\{\pi(1-\alpha) + \left(\frac{3\pi}{2}\right)^{1/3}\left[1-2(1-\alpha)+(1-\alpha)^{1/3}-\alpha^{1/3}\right]\right.$$
$$\left. - \frac{1}{200}(1-\alpha)\alpha[1-2(1-\alpha)]\left[1+4\left((1-\alpha)^2+\alpha^2\right)\right]\right\} \tag{4.70}$$

This angle allows to derive of the liquid perimeter in contact with the tube P_l, the vapor perimeter P_g as well as the interface length P_{gl} and the liquid height h_l. The dimensionless liquid height h_{lD} and the dimensionless interface length P_{glD} can be expressed as a function of stratified angle θ_w:

$$h_{lD} = 0.5\left(1-\cos\left(\frac{2\pi-\theta_w}{2}\right)\right) \tag{4.71}$$

$$P_{glD} = \sin\left(\frac{2\pi-\theta_w}{2}\right) \tag{4.72}$$

The four dimensionless variables previously defined allow to obtain the transition lines between the flow regimes for a varying vapor quality. Three transition lines are required to obtain the flow pattern maps without heat transfer (which would impact the flow pattern): the intermittent/annular (I-A) constant vapor quality line, the slug/intermittent (Slug-I) or stratified-wavy/annular (SW-A) mass flux line and the stratified/stratified-wavy (S-SW) mass flux line. These transition lines are defined in Appendix C.3.1, as a function of A_{lD}, A_{gD}, h_{lD} and P_{glD}. The contribution of the oil mass fraction to these transition lines lies in the variation of the liquid-phase density and viscosity. Moreover, the pressure also plays a role, as it influences the vapor phase density. Finally, a flow pattern map can be generated from this methodology, at an oil circulation ratio, pressure and tube diameter as can be seen in Figure 4.26. The experimental points recorded from Chapter 3 can also be displayed on this graph, to give an idea of the inlet flow regime of each point. However, their display serves only as an indicative example, as the pressure and the OCR differ from one experimental point to another. Nevertheless, the selected pipe diameter corresponds to the real application, for both experimental campaigns (retrofitted compressor and lab-scale prototype). Overall, the majority of the recorded points stands in the stratified-wavy (SW) zone, although some points are showing annular (A) flow. A few points lie on the border between the stratified (S) and the stratified-wavy zones. In general, the experimental points recorded on the lab-scale prototype stand higher in mass flux than those of the retrofitted compressor: this can be explained by the higher displacement volume of this machine (200 cm^3 for the prototype versus 80 cm^3 for the retrofitted compressor). Illustrative representations of the flows can be found in Figure 4.27. These pictures have been taken from a sight glass placed upstream of the compressor. In the purely stratified flow, the phases are simply separated by gravity and no liquid droplet travels in the vapor phase. In the stratified-wavy regime, the phase separation becomes less distinct, and liquid droplets begin to travel within the vapor phase. In the annular flow regime, the tube walls are completely covered with liquid, making it more difficult to distinguish between the liquid and vapor phases. It is important to note that these images were used solely for flow visualization and illustrative purposes; no quantitative data could be extracted from them through image post-processing.

From the flow pattern, it is possible to define the entrainment ratio ψ, defined as the proportion of liquid traveling in the vapor phase at the vapor speed. This portion of liquid is carried by the vapor phase in the form of droplets. The maximum entrainment ratio ψ_{max} is given by Chisholm (1983) and is equal to 0.4. In the stratified flow regime, the entrainment

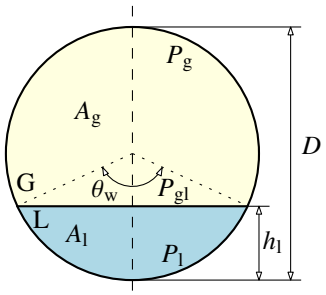

Figure 4.25: Stratified two-phase flow cross-section

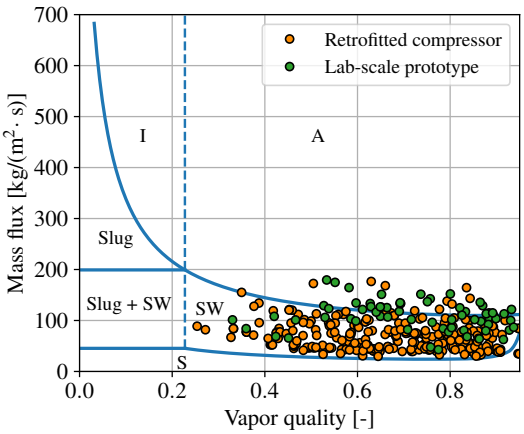

Figure 4.26: Flow pattern diagram for an OCR of 5%, a pressure of 1 bar and a tube diameter of 23 mm with experimental points displayed.

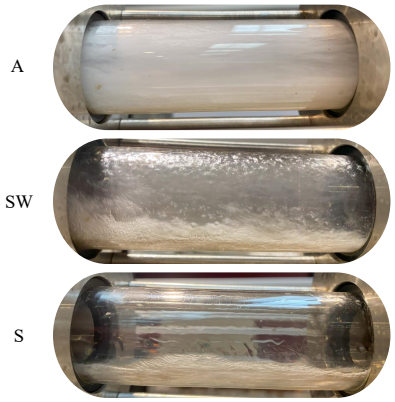

Figure 4.27: Experimental pictures of the sight glass for an annular flow (A), a stratified-wavy flow (SW) and a stratified flow (S).

ratio is assumed to be zero; in the annular flow regime, it is taken as its maximum value, ψ_{max}; and in the stratified-wavy regime, it is calculated as proportional to the difference between the mass fluxes defined at the boundaries. The calculation of ψ is thus following this law:

$$\psi(G,Q) = \begin{cases} 0 & \text{if } G < G_{strat} \text{ (stratified)} \\ \psi_{max} \cdot \dfrac{G - G_{strat}}{G_{wavy} - G_{strat}} & \text{if } G_{strat} \leq G \leq G_{wavy} \text{ (stratified-wavy)} \\ \psi_{max} & \text{if } G > G_{wavy} \text{ (annular)} \end{cases} \tag{4.73}$$

with G_{strat} and G_{wavy} defined in Appendix C.3.1.

The diameter of the droplets traveling in the vapor phase is of paramount importance to calculate the heat transfer between the two phases. As a matter of fact, it strongly influences the heat exchange area between the phases. The calculation of this diameter is based on the work from Lee et al. (2019), where the droplet diameters follow an upper limit log-normal (ULLN) distribution defined by two parameters α and β. The maximum diameter of this distribution can be calculated using the critical Weber number We_{crit}, assumed equal to 12. The Weber number is a dimensionless number that expresses the ratio of inertial forces to surface tension forces in a fluid flow. It is given by

$$We = \frac{G^2 D}{\rho_l \sigma} \tag{4.74}$$

The maximum diameter is therefore expressed by

$$D_{\max} = \frac{\sigma \mathrm{We}_{\mathrm{crit}}}{\rho_{\mathrm{g}} u_{\mathrm{g}}^2} \tag{4.75}$$

where u_{g} is the superficial vapor phase velocity, i.e., the velocity the vapor phase would have if it alone flowed through the entire cross-sectional area of the pipe:

$$u_{\mathrm{g}} = \frac{Q \cdot G}{\rho_{\mathrm{g}}} \tag{4.76}$$

Now that the maximum diameter has been defined, the mean droplet diameter of the ULLN distribution, also called the Sauter mean diameter D_{32}, can be computed from

$$\frac{D_{32}}{D_{\max}} = \frac{1}{\left(1 + a e^{1/4\beta^2}\right)} \tag{4.77}$$

where $\alpha = 1.9$ and $\beta = 0.72$ define the ULLN distribution. In this work, the Sauter mean diameter is assumed to be the diameter of all the liquid droplets traveling in the vapor phase. The flow pattern at the inlet of the compressor could therefore be defined based on the fluid properties, the mass flow rate, the pipe diameter and vapor quality. Moreover, from this flow pattern, the mass fraction of liquid traveling in the vapor phase in the form of droplets, i.e., the entrainment ratio, could be determined. Therefore, the liquid phase is separated into a film, traveling at the liquid phase speed and the droplets, traveling at the vapor phase speed. Finally, the mean diameter of these liquid droplets could be figured out based on a ULLN distribution, using the superficial speed and the density of the vapor. All those values could be determined from the inlet conditions of the compressor. During the compression, the vapor quality is changing due to the condensation of the vapor phase, as already explained in Section 4.4.5. This condensation would normally be distributed between the droplets and the film of the liquid phase, inducing an increase in droplet diameter (droplet growth), or the creation of new droplets (nucleation). However, such models are complex, especially when thermal non-equilibrium is involved. Moreover, the area defined by the supply pipe diameter is similar to the maximum cross-sectional area defined by the scroll superposition. The supply pipe sectional area is given by $A_{\mathrm{su,c}} = \pi D^2/4 = 4.15$ cm^2, while the maximum cross-sectional area of any chamber is given by

$$A_{\mathrm{c,max}} = 2 r_{\mathrm{o}} h_{\mathrm{s}} \tag{4.78}$$

with the orbiting radius r_{o} defined in Appendix C.1.1. For the retrofitted compressor, this cross-sectional area is given by $A_{\mathrm{c,max,r}} = 3.23$ cm^2 while, for the prototype, it is equal to $A_{\mathrm{c,max,r}} = 4.53$ cm^2. For both compressors, similar orders of magnitude are therefore obtained for the cross-sectional areas of the chambers and the supply pipe. Therefore, despite the cross-section shape being rectangular and the flow path being curved, the condensation occurring, the determined mean droplet diameter and entrainment ratio are assumed to be constant throughout the suction, compression and discharge processes.

4.5.4 Leakage flows

The compression process introduced in the core model (Section 4.4.5) considered an adiabatic compression of a given volume without mass transfer. In reality, when compressing superheated vapor or a two-phase mixture, the mechanism involved to reduce the volume of the control volume are not perfect: they are not perfectly sealed. Therefore, numerous mass transfers occur between the chambers of a scroll compressor. Generally, two types of leakage can be distinguished in a scroll compressor: radial and flank leakages. As presented in Figure 4.28, the radial leakage occurs along the radius, usually passing over the tip seal, while the

flank leakage occurs at the "contact" points between the fixed and the orbiting scrolls, along the flanks. The leakage paths definition of a scroll chamber can be seen in Figure 4.29. In total, six leakage paths can be defined: two for the flank leakages (fl_1 and fl_2) and four for the radial leakages (r_1, r_2, r_3 and r_4). The two flank leakage paths occur at the two contact points defining the chamber, while the four leakage paths account for the possibility to exchange mass with several upstream or downstream chambers at the same time. All leakages leaving the control volume are considered negative, and vice versa. Leakage can be generated by a pressure difference between two chambers, but also by the relative movement of the scrolls, even in the absence of a pressure difference. For instance, the relative movement between the tip of one scroll and the bottom of the other scroll generates a Couette flow, which could induce fluid transfer from one chamber to the other without any pressure difference. Nevertheless, this type of leakage is neglected in the present work. Two important model parameters can be introduced to model the leakage: the flank and the radial leakage gaps (δ_{fl} and δ_r, respectively). Those two parameters can be seen as average values of the gaps between the fixed and orbiting scrolls, influenced by the compliance mechanism, the thermal deformation and the vibrations. Thereby, the flank and radial leakage areas can be deduced from these gaps. The flank area A_{fl} is simply given, for each chamber, by the flank gap multiplied by the scroll height, while the radial leakage area A_r is the radial length defined by the contact points multiplied by the radial gap. Thereby, the latter is a function of the orbiting angle. The definition of the possible exchanges between the chambers, function of the orbiting angle and the maximum number of the compression chamber, will not be detailed in this work. Further details on this modeling can be found in Bell (2011).

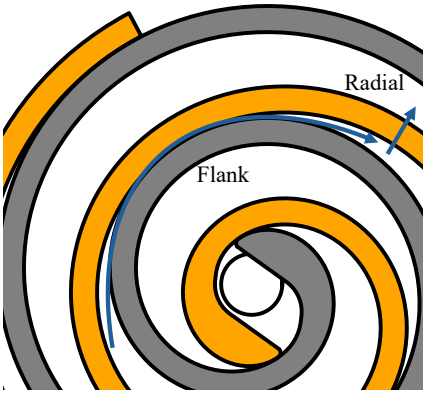

Figure 4.28: Definition of the flank and radial leakages.

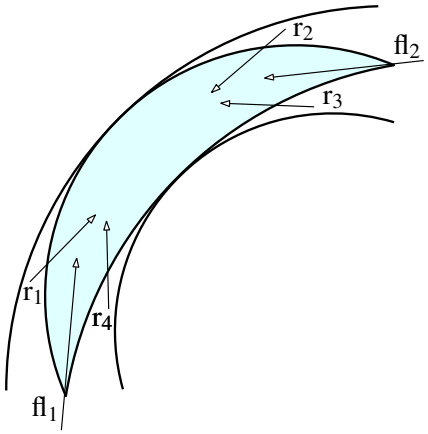

Figure 4.29: Definition of leakages for a control volume with several radial leakage paths.

In liquid-flooded compressors, leakage modeling can be complex for the following reasons:

- The liquid, depending on its position in the chamber, can cover the leakage gaps and act as a sealant. The sealing effect must be taken into account in the modeling.
- The leakage gaps, due to the presence of liquid, can vary due to deformation, compliance mechanisms, movement of the tip seal and vibrations. Assuming fixed leakage gaps would certainly be incorrect.
- The proportion of liquid and vapor leakage mass flow rate is strongly influenced by the leakage gaps, the sealing effect and the liquid viscosity.
- The proportion of liquid and vapor mass flow rates leaving a chamber is not necessarily equal to that entering the downstream chamber, as a pressure reduction generally induces evaporation.

– The liquid entering the downstream chamber does not necessarily mix with the existing liquid, and the same applies to the vapor. Moreover, vapor entering a colder liquid phase may condense instantaneously, whereas it would remain in the vapor phase if mixed directly with vapor.

Therefore, the modeling of the two-phase leakages requires several assumptions, and the introduction of a new parameter that needs to be validated with experimental data. The modeling is based on the liquid distribution within the chamber, where a liquid film of constant thickness is assumed to adhere to the wall and bottom surfaces. A visual representation of the chamber configuration can be found in Figure 4.30. The liquid volume of the film within the chamber can be defined using the previously defined entrainment ratio ψ:

$$V_{\mathrm{l,f}} = (1 - \psi) \cdot (V_{\mathrm{r,l}} + V_{\mathrm{o}}) \tag{4.79}$$

Moreover, the liquid-wall contact surface area is given by the sum of the surrounding surface area and the bottom surface area:

$$A_{\mathrm{wl}} = P^k(\theta) \cdot h_{\mathrm{s}} + \frac{V^k(\theta)}{h_{\mathrm{s}}} \tag{4.80}$$

where $P^k(\theta)$ and $V^k(\theta)$ are, respectively, the bottom perimeter and the volume of chamber k, defined in Section 4.3. The liquid-film thickness t_{l} is assumed to be very small, so that the vapor-liquid contact surface area can be assumed equal to the liquid-wall contact surface area. Therefore, from these liquid-film volume and contact area previously defined, it is possible to calculate the liquid-film thickness:

$$t_{\mathrm{l}} = \frac{V_{\mathrm{l,f}}}{A_{\mathrm{wl}}} \tag{4.81}$$

The liquid-film thickness can be compared with the radial leakage gap to determine whether a sealing effect exists. To do so, a coefficient multiplying the liquid-film thickness must be calibrated to account for centrifugal effects as well as the fluid motion generated by the orbiting movement. This multiplying liquid-thickness correction coefficient k_{l} can be introduced as follows: if $k_{\mathrm{l}} \cdot t_{\mathrm{l}} > \delta_{\mathrm{r}}$, leakages are liquid-only, if $k_{\mathrm{l}} \cdot t_{\mathrm{l}} < \delta_{\mathrm{r}}$, leakages are two-phase and if $k_{\mathrm{l}} \cdot t_{\mathrm{l}} = 0$, leakages are gaseous-only. The liquid height ratio r_{h} can therefore be introduced as

$$r_{\mathrm{h}} = \min(1, \frac{k_{\mathrm{l}} \cdot t_{\mathrm{l}}}{\delta_r}) \tag{4.82}$$

The leakage cross-sectional areas of the liquid and vapor leakages can be expressed as a function of this liquid height ratio and the total radial leakage area A_{r}:

$$A_{\mathrm{r,l}} = A_{\mathrm{r}} \cdot r_{\mathrm{h}} \tag{4.83}$$

$$A_{\mathrm{r,g}} = A_{\mathrm{r}} \cdot (1 - r_{\mathrm{h}}) \tag{4.84}$$

Defining distinguished leakage areas requires the use of independent flow models for the liquid and vapor leakages instead of a two-phase flow model. The vapor mass flow rate is based on a compressible flow as the Mach number usually exceeds 0.3 in leakage paths. The liquid mass flow rate is calculated by taking the minimum mass flow rate between a non-frictional incompressible flow and a frictional incompressible flow, such as

$$\dot{m}_{\mathrm{l}} = \min(\dot{m}_{\mathrm{l,fric}}, \dot{m}_{\mathrm{l,non-fric}}) \tag{4.85}$$

By doing so, when the liquid phase is composed mainly of oil, the high viscosity limits leakage in the channel by friction, whereas if the liquid phase consists primarily of refrigerant, viscosity

is not the limiting factor, but the pressure loss due to the sudden change of cross-sectional area. The definitions of the single-phase mass flow rates are given in Appendix C.3.2.

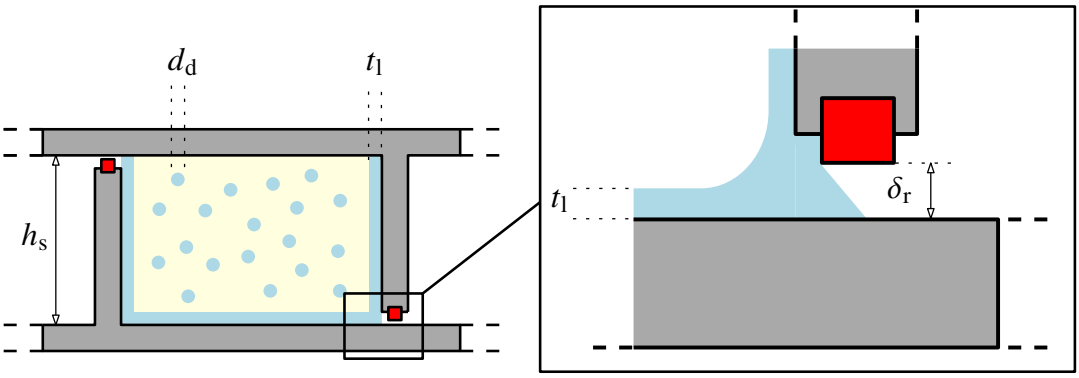

Figure 4.30: Liquid distribution within a scroll chamber and zoom on the radial leakage.

To further simplify the leakage calculation, the same approach is applied to both flank and radial leakages; therefore, only a single leakage gap needs to be calibrated: $\delta = \delta_r = \delta_{fl}$.

Now that both liquid and vapor leakage mass flow rates leaving the chamber have been defined, the vapor and liquid mass flow rates entering the new chambers can be calculated. Gasche et al. (2000) investigated the leakage mass flow rate in a rolling-piston compressor. The working fluid was a superheated R22-mineral oil mixture. The leakages were assumed to be purely liquid, and despite the superheat, the refrigerant was present in the liquid phase. Therefore, the continuous pressure decrease along the leakage path induced gasification (flashing) of the liquid refrigerant. In the given example, the leakages across the contact point of the rolling piston, caused by a pressure drop of 7.5 bar (from 14 bar to 6.5 bar), imply the void fraction of the flow to increase from 0 to 0.75, thereby significantly impacting the volumetric efficiency. Nevertheless, this model considers the temperature of the oil and the vapor refrigerant to be the same, i.e., thermal equilibrium is assumed. If the liquid phase is at a lower temperature, the gasification effect of the liquid refrigerant would be reduced, and the resulting downstream void fraction would be lower. Considering that the leakages in a scroll compressor are generated by pressure differences lower than 2 to 3 bar, and that the liquid and vapor phases may not be in thermal equilibrium (the liquid phase is likely to be subcooled), the vapor quality of the leakage leaving a chamber is assumed to be the same as the vapor quality of the leakage entering the downstream chamber. Therefore, the enthalpies of the components (oil, liquid refrigerant, and vapor) are assumed to remain constant throughout the leakage paths. Afjei et al. (1992) also investigated this flashing phenomenon in a two-phase scroll compressor and concluded that flashing may account for the decrease in volumetric efficiency, although it could also result from an increase in the leakage gap. Finally, the last simplifying assumption concerns the mixing of the leakage in the downstream chamber: the liquid is assumed to mix with the liquid phase, and the vapor with the vapor phase, without phase change through the leakage path. Moreover, the distribution between droplets and the liquid film is kept constant, as the entrainment ratio does not change in the chamber.

4.6 Heat transfer

Heat transfer in a scroll compressor takes place throughout several stages of the oil-refrigerant mixture: the supply, the suction, the compression, the discharge and the exhaust. These stages are influenced by frictional power losses, ambient heat transfer and the temperature distribution of the scroll compressor's components. These heat transfers to the mixture

influence its state by changing its temperature and/or its vapor quality. The heat transfer model can be divided into two time domains: the instantaneous heat transfer occurring inside the compressor chambers, which depends on the shaft angle, and the periodical average heat transfer, which is considered only after each rotation (Tanveer et al. 2022). First, the periodical average heat transfer model is described, showing how the scroll components interact throughout the passage of the oil-refrigerant mixture. Then, details are given about certain parts of this periodical average heat transfer model. For instance, describing the heat transfer within the chamber is important, particularly between the two phases, as it affects thermal non-equilibrium, itself affecting the chambers' pressures. Moreover, the exhaust heat transfer also requires detailed explanations, as it balances the temperature difference induced by the thermal non-equilibrium resulting from the two-phase compression. Therefore, even though heat transfers are usually considered to have a limited impact on compressor performance, they are regarded here as being equally important as other contributions, since two-phase compression is much more sensitive to heat transfer effects.

4.6.1 Periodical average heat transfer model

To simplify the analysis of the heat exchanges, all components of the compressor, apart from the scroll wraps, are treated as a single lumped mass, and an overall energy balance is applied to it. This lumped mass is considered at a constant temperature, and is updated at each iteration (full revolution) of the model. Figure 4.31 illustrates the thermal interactions between the refrigerant and this equivalent mass within the compressor. These interactions can be listed in what follows.

Supply heat transfer

It constitutes the first interaction between the scroll compressor and the oil-refrigerant mixture entering it. It starts at the supply pipe, passes through the suction-admission chamber defined by the scroll casing, and ends when entering the suction chambers defined by the scrolls. The lumped mass of the scroll compressor is usually at a higher temperature than the supplied mixture. Therefore, evaporation occurs during this first interaction. The supply heat transfer rate is usually calculated based on the assumption of an isothermal boundary condition, as the temperature of the lumped stays constant along the heat transfer. However, in the case of two-phase compression, even with a high OCR, heat transfer induces a phase change rather than a temperature change. Therefore, the process can also be regarded as isothermal from the mixture's perspective. Eventually, the heat transfer rate is given by

$$\dot{Q}_{su} = h_{su} A_{su} (T_{su} - T_{lump}) \tag{4.86}$$

The supply heat transfer can be regarded as internal pipe flow heat transfer, and more specifically, as saturated flow boiling in channels. Therefore, h_{su} represents the convective boiling heat transfer coefficient, which is calculated using Shah's correlation (Shah 2021). Further details about the calculation of the heat transfer coefficient can be found in Appendix C.4. The assumed supply pipe heat exchange area A_{su} is calculated based on the inlet pipe diameter and considering a length of 10 cm.

Chambers heat transfers

It accounts for the heat transfer between the mixture and the scroll wraps during the suction, compression and discharge phases. Chamber heat transfer models the interaction between the liquid and vapor phases with the scroll wraps (called the wall) and between the two phases. Its calculation is updated at each angle step, however, its periodical average interaction with the

scroll wraps is updated at each iteration. A fixed temperature distribution is assumed for the scroll wraps as a function of their length, and the residual from the energy balance between the scroll wraps and the chambers $\dot{Q}_{ch}$ is dissipated or absorbed by the lumped mass. More details are given in the subsequent section.

Exhaust heat transfer

In contrast to the supply heat transfer, it represents the final interaction between the compressor and the mixture. It begins when the flow exits the discharge ports and ends as it leaves the exhaust pipe. The difficulty in modeling the heat transfer lies in the temperature difference between the liquid and the vapor phases. Most of the time, the vapor phase is hotter than the lumped mass, whereas the liquid phase is cooler. More details to calculate the exhaust heat transfer rate $\dot{Q}_{ex}$ are also given in its own subsection.

Mechanical losses

They are generated by friction occurring at the moving contact between metallic components, taking place in the bearings and the orbiting mechanism. The power of these mechanical frictions directly contributes to the heating of the lumped mass. Another part of these mechanical losses, occurring within the mixture, does not heat the lumped mass but instead directly increases the temperature and/or changes the state of the mixture within the chamber. The calculation of the mechanical power losses $\dot{W}_{ML}$ is presented in Section 4.7.

Ambient losses

These are the heat losses to the surrounding air resulting from the temperature difference between the hotter lumped mass and the ambient air. The compressor is treated as a vertically oriented cylinder, and natural convection of the surrounding air is considered to calculate the heat transfer coefficient between the lumped mass and the air. Similar to the supply heat transfer, the calculation of the ambient heat transfer rate assumes an isothermal heat exchange and is expressed as follows

$$\dot{Q}_{amb} = h_{amb} A_{amb} (T_{amb} - T_{lump}) \tag{4.87}$$

where h_{amb} is the natural convection heat transfer coefficient calculated in Appendix C.4 with the correlation of Popiel et al. (2007) and A_{amb} is the external surface area of the cylinder approximating the compressor. The upper and bottom surfaces of the cylinder have been added to this ambient surface area. The ambient temperature T_{amb} is assumed to be at 20° C, corresponding to the ambient conditions in the laboratory where the compressors were tested. The temperature of the surface does not exceed 60° C for any operating point, therefore, radiation can be neglected as it is very low ($\approx$ 0.3 W/(m^{2}K)) compared to the natural convection ($\approx 5 - 10$ W/(m^{2}K)).

Resolution process

At each model iteration (complete revolution of the orbiting angle), every heat transfer as well as the mechanical losses can be evaluated using the lump temperature of the previous iteration. The residual heat transfer rate arising from the energy balance is given by

$$\dot{Q}_{res}(T_{lump}^{k-1}) = \dot{Q}_{su} + \dot{Q}_{ch} + \dot{Q}_{ex} + \dot{W}_{ML} + \dot{Q}_{amb} \tag{4.88}$$

where all heat exchange rates are considered positive when they tend to increase the temperature of the lump mass. If this residual is greater than 3 W, then a new lump temperature must

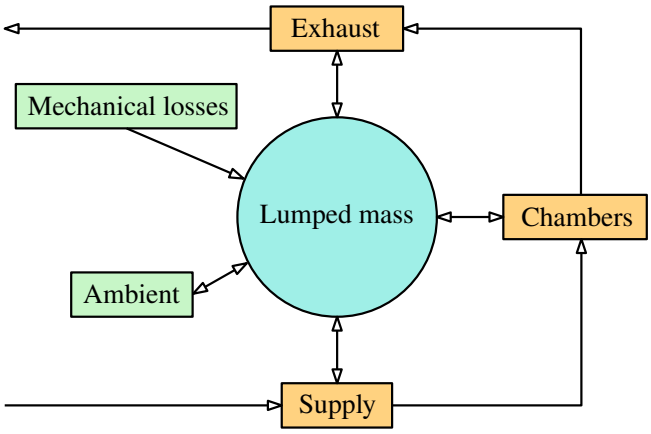

Figure 4.31: Lumped mass heat transfer interactions.

be calculated, while setting the residual $\dot{Q}_{\text{res}}$ to zero. In calculating the new lump temperature, only the suction and ambient heat transfer rates depend on this updated temperature. The mechanical losses are independent of the lump temperature, while the chamber and exhaust losses are evaluated using the lump temperature from the previous iteration to avoid unnecessary complexity. Re-evaluating the lump temperature only when a certain residual threshold is exceeded accelerates the convergence process and significantly reduces unnecessary iterations of the deterministic model, whose convergence criteria are described in a subsequent section.

Impact of the oil

According to Shao et al. (1995), the impact of the oil on condensation comes from two sources: the change in flow regime caused by the change of viscosity of the liquid phase and the change in saturation properties due to the oil presence (through solubility effects). Two methodologies can be applied to compute the appropriate heat transfer coefficient. On the one hand, the mixture heat transfer coefficient can be determined from the pure refrigerant heat transfer coefficient, using a correction factor depending on the liquid phase oil concentration (x_{o}). On the other hand, the liquid phase properties can be calculated based on the oil-refrigerant solution properties. As a matter of fact, the flow regime will ultimately be impacted if mixture properties are used. Shah (2021) reports similar trends for evaporation correlation, and advises the use of oil-refrigerant properties in the correlation. Therefore, the liquid properties used in the subsequent heat transfer coefficient calculations are those of the oil-refrigerant mixture. These properties have been defined in Chapter 2.

4.6.2 Chamber heat transfer

Within a chamber, heat exchange occurs between the vapor and liquid phases, as well as between the phases and the surrounding walls (scroll wraps). A visual representation showing the triangular approach between the vapor phase at a temperature T_{g}, the liquid phase at the temperature T_{l} and the wall at a temperature T_{w} can be found in Figure 4.32. To define the three heat transfer rates occurring within a chamber, three heat exchange areas and heat transfer coefficients must be defined.

Vapor-liquid heat exchange

The vapor-liquid heat exchange takes place between the liquid film and the vapor, as well as between the liquid droplets and the vapor phase, as can be observed in Figure 4.33. The

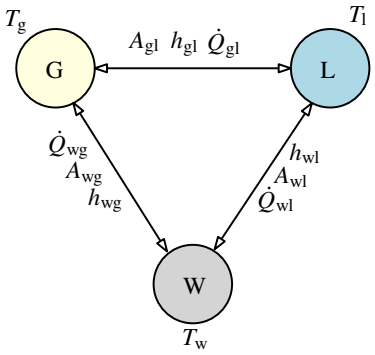

Figure 4.32: Chamber heat transfer triangle approach.

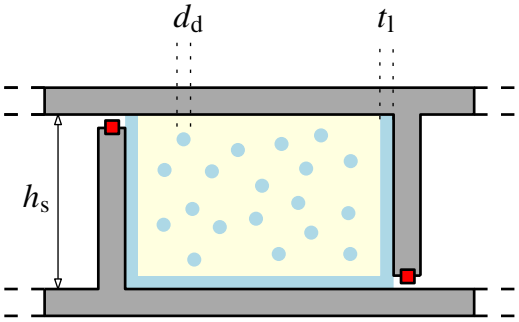

Figure 4.33: Liquid distribution within a scroll chamber.

calculation of the liquid droplet diameter $d_d = D_{32}$ and the liquid-film thickness t_l were already detailed in Equations 4.77 and 4.81, respectively. The total vapor-liquid heat exchange area can be expressed as the sum of the vapor-liquid film and the vapor-liquid droplets exchange areas:

$$A_{gl} = A_{gl,f} + A_{gl,d} = P^k(\theta) \cdot h_s + \frac{V^k(\theta)}{h_s} + 6\frac{V_{l,d}}{d_d} \tag{4.89}$$

where $P^k(\theta)$ and $V^k(\theta)$ are the chamber's perimeter and volume defined in Section 4.3. Moreover, $V_{l,d}$ is the total liquid volume of the droplets, expressed as a function of the entrainment ratio ψ (defined in Equation 4.73) as

$$V_{l,d} = \psi \cdot (V_{r,l} + V_o) \tag{4.90}$$

The vapor-liquid droplet heat exchange area ($A_{gl,d}$) is defined based on the volume of a spherical droplet, which can be related to its surface area through its diameter. This expression is independent of the number of droplets, which can be calculated from the total volume and the volume of a single droplet based on the droplet diameter d_d. Overall, the smaller the droplet diameter d_d, the larger the vapor-liquid droplet heat exchange area, even if the area of a single droplet decreases.

According to Dutta et al. (1996), accurate characterization of the liquid–vapor heat transfer area is crucial, as it strongly influences the pressure evolution within the chambers. The smaller the droplet diameter, the larger the total heat exchange area for a given volume. At certain points, the heat exchange area between the liquid droplets and the vapor phase becomes so large that the interfacial heat exchange area between the liquid film and the vapor phase becomes negligible. The heat exchange between the vapor phase and the liquid droplets can be calculated using the Ranz-Marshall correlations as done between oil droplets and vapor refrigerant in oil-injected twin-screw compressors by Stosic et al. (1992) and Huagen et al. (2004). The Nusselt number is given by

$$\mathrm{Nu} = 2 + 0.6 \cdot \mathrm{Re_g}^{1/2} \cdot \mathrm{Pr_g}^{1/3} \tag{4.91}$$

where the Reynolds and Prandtl numbers are calculated according to the vapor phase. The Reynolds number calculation is based on the speed of the chamber flow, defined in Section 4.7 and the characteristic length is the droplet diameter d_d. The heat transfer coefficient $h_{gl,d}$ also uses the same characteristic length.

The heat exchange between the vapor phase and the liquid film can be calculated using the Blasius solution of the laminar flow on the plate (Incropera et al. 2007). The Nusselt number

is this time given by

$$\mathrm{Nu} = 0.664 \cdot \mathrm{Re_g}^{1/2} \cdot \mathrm{Pr_g}^{1/3} \tag{4.92}$$

where the Reynolds number calculation is based on the same speed as for the droplet and the characteristic length is the scroll height h_s. The characteristic length for the heat transfer coefficient $h_{gl,f}$ is defined as the curved distance between the contact points that delimit the chamber. To avoid calculating it at each angle step, it can be approximated as half of the chamber perimeter.

Two heat transfer coefficients are employed for the vapor-liquid phase interactions. However, this phase is assumed to be at a single temperature T_l, i.e., the liquid droplet and liquid film temperatures should evolve at the same rate. Hence, a global vapor-liquid heat transfer coefficient must be used:

$$h_{gl} = \frac{h_{gl,f} \cdot A_{gl,f} + h_{gl,d} \cdot A_{gl,d}}{A_{gl}} \tag{4.93}$$

This heat exchange coefficient h_{gl}, along with the heat exchange surface area A_{gl} allows to define the heat transfer conductance between the liquid and the vapor in the core model (Equations 4.11 and 4.12), such that

$$AU_l = AU_g = A_{gl} \cdot h_{gl} \tag{4.94}$$

The heat conductance between the two phases resulting from the deterministic model simulations range between 10 W/K for the retrofitted compressor at 1000 RPM to 10000 W/K for the prototype at 5000 RPM. In comparison, the heat conductance values used in the core model simulations (Section 4.4.5), were 0 W/K (no heat exchange), 120 W/K, 300 W/K and 24000 W/K (thermal equilibrium).

Mixture-wall heat exchange

To define the heat exchange between the mixture and its metallic surroundings, the wall temperature T_w should first be defined. Jang et al. (2006) experimentally measured the temperature distribution of the fixed scroll in a scroll compressor tested under various controlled and uncontrolled conditions. They found that the temperature varies linearly along the scroll wraps from the initial angle to the final angle of the curve involute. Moreover, the slope of temperature variation is proportional to the outlet-inlet pressure difference, itself proportional to the outlet-inlet temperature difference.

Therefore, the temperature distribution along a scroll involute (inner or outer) is given by a function of the involute angle ϕ:

$$T(\phi) = T_{lump} + (\phi - \phi_m)\frac{T_{ex}^{\sigma}(p_{ex}) - T_{su}}{\phi_{is} - \phi_{ie}} \tag{4.95}$$

where the mean involute angle ϕ_m is defined as $\phi_m = 0.5\phi_{is} + 0.5\phi_{ie}$. The temperature distribution of a scroll involute can therefore be determined based on geometrical parameters, inputs of the deterministic model and the lump temperature T_{lump}. Finally, the wall temperature of a chamber at an orbiting angle θ is determined by an average of the temperatures defined by the four involute angles delimiting the chamber (two per contact point for the fixed and the orbiting scrolls):

$$T_w = \frac{T(\phi_{f,1}) + T(\phi_{f,2}) + T(\phi_{o,1}) + T(\phi_{o,2})}{4} \tag{4.96}$$

The liquid-film surface area in contact with the wall has the same value as the vapor-liquid film contact surface area ($A_{wl} = A_{gl,f}$), while the vapor-wall contact surface area is simply the area of the upper surface, i.e., the total volume divided by the scroll height:

$$A_{wg} = \frac{V^k(\theta)}{h_s} \tag{4.97}$$

Eventually, the vapor-wall and liquid-wall heat exchange coefficient can be determined also using the Blasius solution on a plate. The vapor-wall heat transfer coefficient is identical to the vapor-liquid film heat transfer coefficient ($h_{wg} = h_{gl,f}$). The liquid-wall heat transfer coefficient h_{wl} is calculated similarly, but using the liquid properties instead of the vapor properties.

In conventional approaches for modeling the heat transfer coefficient in scroll compressor chambers, the spiral motion of the flow and the orbiting motion of the scroll are usually taken into account through correction factors applied to the calculated heat transfer coefficient (B. Peng et al. 2017). This conventional approach applies to pure vapor compression, which uses the Dittus-Boelter equation to calculate the heat transfer coefficient (pipe internal flow). In the context of two-phase compression, the complexity and uncertainty associated with modeling these heat transfers are already high; therefore, such correction factors are not considered.

The heat exchange rates obtained between the oil-refrigerant mixture and the wall, calculated at each angle step, can be expressed as follows:

$$\dot{Q}_{wg}(\theta) = h_{wg} A_{wg} (T_g - T_w) \tag{4.98}$$

$$\dot{Q}_{wl}(\theta) = h_{wl} A_{wl} (T_l - T_w) \tag{4.99}$$

Finally, the heat exchange rate from the scrolls to the lumped mass is given by the sum of the contributions coming from the liquid and vapor phases:

$$\dot{Q}_{ch} = \frac{1}{2\pi} \int_0^{2\pi} \left(\dot{Q}_{wg}(\theta) + \dot{Q}_{wl}(\theta) \right) \mathrm{d}\theta \tag{4.100}$$

4.6.3 Exhaust heat transfer

The exhaust heat transfer is calculated using an approach similar to that of the supply heat transfer: it is assumed to occur within a pipe of given length (10 cm) and of the exhaust pipe diameter. Nevertheless, a simple condensation correlation cannot be applied, since at the beginning of the pipe the liquid and vapor phases have different temperatures. The same methodology applied to the heat transfer within the chamber is therefore going to be applied: the triangular methodology of Figure 4.32 is used between the vapor phase, the liquid phase and the pipe at the lump temperature. However, unlike the chamber heat transfer, the exhaust heat transfer calculation is only calculated after a complete iteration. Thus, to apply the same methodology, the pipe must be discretized in $N = 100$ parts, as illustrated in Figure 4.35. A cross-sectional view of a pipe part can be seen in Figure 4.34. The difference in the methodology applied within a chamber lies in the heat transfer surface area. The three heat transfer surface areas can here be expressed as a function of the wet angle θ_w defined in Equation 4.70:

$$A_{gl}^i = \frac{1}{N} D_{ex} \sin\left(\frac{2\pi - \theta_w}{2} \right) L_{ex} + \frac{6}{N} \frac{V_{l,d}}{\pi \cdot d_d} \tag{4.101}$$

$$A_{\mathrm{wg}}^{i} = \frac{1}{N}(2\pi - \theta_{\mathrm{w}}) D_{\mathrm{ex}} L_{\mathrm{ex}} \tag{4.102}$$

$$A_{\mathrm{wl}}^{i} = \frac{1}{N}\theta_{\mathrm{w}} D_{\mathrm{ex}} L_{\mathrm{ex}} \tag{4.103}$$

The heat transfer coefficients and heat transfer rates are obtained using the same correlations as the chamber heat transfer. To calculate the Reynolds numbers of the different flows, the phase velocities must be determined. They are expressed as a function of the void fraction α (Yao et al. 2023):

$$u_{\mathrm{g}} = \frac{Q\dot{m}}{\rho_{\mathrm{g}} \alpha A_{\mathrm{c,ex}}} \tag{4.104}$$

$$u_{\mathrm{l}} = \frac{Q\dot{m}}{\rho_{\mathrm{l}} (\alpha - 1) A_{\mathrm{c,ex}}} \tag{4.105}$$

The relative velocity between the vapor and liquid phases is simply given by $u_{\mathrm{g}} - u_{\mathrm{l}}$.

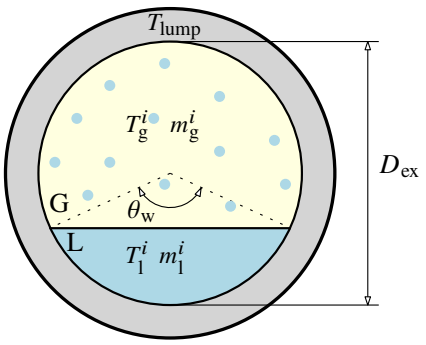

Figure 4.34: Cross-section area of the exhaust pipe.

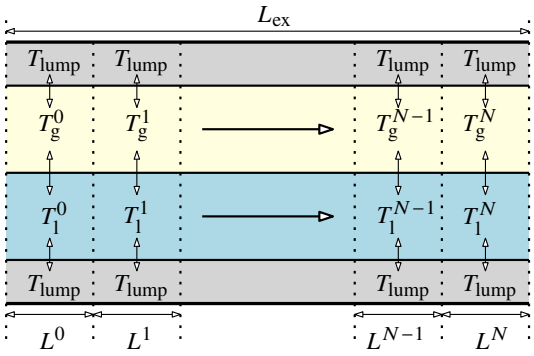

Figure 4.35: Finite-volume representation of the exhaust pipe.

At each length step of the pipe, the enthalpies of the phases are updated:

$$h_{\mathrm{g}}^{i} = h_{\mathrm{g}}^{i-1} + \frac{\dot{Q}_{\mathrm{wg}}^{i-1} - \dot{Q}_{\mathrm{gl}}^{i-1}}{\dot{m}_{\mathrm{g}}^{i-1}} \tag{4.106}$$

$$h_{\mathrm{l}}^{i} = h_{\mathrm{l}}^{i-1} + \frac{\dot{Q}_{\mathrm{wl}}^{i-1} + \dot{Q}_{\mathrm{gl}}^{i-1}}{\dot{m}_{\mathrm{l}}^{i-1}} \tag{4.107}$$

From these enthalpies, a procedure similar to that used for the split-state application heat transfer, presented in Section 2.4.3, can be applied. This procedure allows to determine the temperature of both phases as well as the mass transferred by condensation or evaporation. Nevertheless, thermal equilibrium is not assumed in this case: both phases' enthalpies should thus be compared with the phases' saturation enthalpies at the exhaust pressure. If the phase enthalpies differ from the saturation enthalpies, mass transfer can be deduced from these differences. An iterative process is then required to obtain the correct liquid and vapor temperatures, as well as the new vapor and liquid mass flow rates crossing the pipe. The final exhaust-lumped mass heat transfer rate can be obtained with

$$\dot{Q}_{\mathrm{ex}} = \sum_{i=0}^{N} \left(\dot{Q}_{\mathrm{wg}}^{i} + \dot{Q}_{\mathrm{wl}}^{i} \right) \tag{4.108}$$

To conclude with the heat transfer modeling, an example illustrating the application of the model is shown in Figure 4.36. In this figure, the heat exchange rates with the lumped mass are presented, together with the phase temperatures and the vapor quality evolution of the oil–refrigerant mixture. A first observation is that, overall, only the mechanical losses and the supply heat transfer are significant, while the other heat transfer rates are relatively low in comparison. Despite the high supply heat transfer rate, only the vapor quality is affected; this can be justified by the use of the split state. Regarding the exhaust heat transfer, the heat exchange rate may be low, however, the variations in vapor quality and in the vapor and liquid phase temperatures are quite significant during this stage.

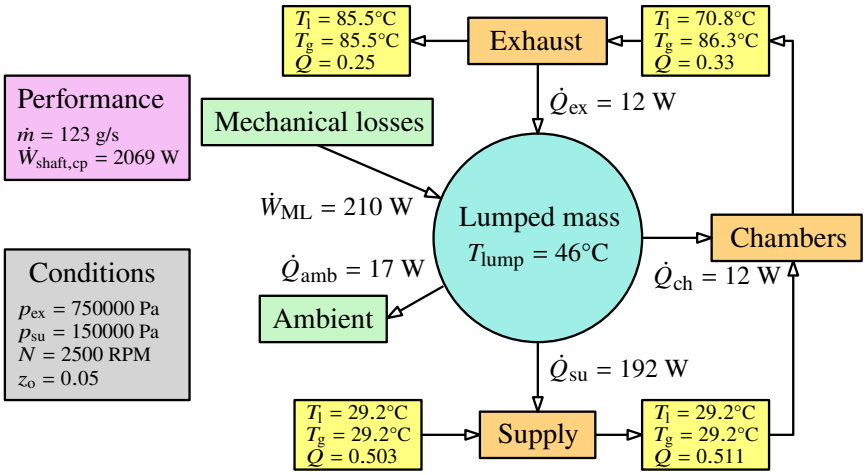

Figure 4.36: Heat transfer simulation example (lab-scale prototype).

4.7 Mechanical losses

The previously introduced mechanical losses W_{ML} account for the friction occurring within the scroll compressor, including viscous friction in the bearings and contact friction between moving components. These friction losses can be modeled by taking into account the dynamic interaction between the diverse components within the scroll compressor, this modeling approach is proposed by Chen et al. (2002b). A simpler modeling approach can be found in the semi-empirical model from Winandy et al. (2002), considering two parameter: a constant friction power losses $\dot{W}_{ML,0}$ and a proportionality coefficient α, multiplying the indicated power $\dot{W}_{in}$ of the compressor. In this modeling approach, the mechanical losses are given by

$$\dot{W}_{ML} = \dot{W}_{ML,0} + \alpha \cdot \dot{W}_{in} \tag{4.109}$$

Another simpler modeling approach was adopted by Bell (2011) and Lemort (2008) and many other authors: to consider mechanical friction directly proportional to the compressor speed. The friction torque τ_f is therefore introduced, such that

$$\dot{W}_{ML} = \tau_f \cdot \omega \tag{4.110}$$

This even simpler approach therefore assumes no friction at zero speed, which was experimentally validated by Cuevas et al. (2012) on an open-drive scroll compressor. As this thesis also focuses on the modeling of an open-drive compressor, the latter approach is adopted for simplicity. Nevertheless, the former approach may provide greater accuracy.

These mechanical losses contribute only to the heating up of the lumped mass. When considering two-phase compression, the liquid phase could also generate mechanical losses.

These liquid mechanical losses would in this case be dissipated directly within the oil-refrigerant mixture, and not in the lumped mass. These hydraulic losses are mainly investigated in screw compressors and expanders, where liquid flooding is used to seal the tip clearance and provide a cooling effect, thereby reducing thermal deformation. Zaytsev et al. (2000) studied the rotor tip friction of a screw compressor using an ammonia-water mixture, concluding that the torque loss is only significant when the liquid phase has a high viscosity, e.g., when oil is used. Vasuthevan et al. (2018) and Vasuthevan et al. (2022) investigated experimentally the tip friction torque using a turning plate inside a circular housing using different liquid volume ratios and running at different speeds. They found that, at low liquid mass fractions, the power loss increases linearly with tip speed but at a very low rate, whereas at high liquid mass fractions, the appearance of liquid sludge increases significantly the slope of the power loss variation. Nikolov et al. (2018) studied the impact of the clearance and of the tip speed in water-flooded air expanders. At high rotor tip-speeds, the internal leakage is negligible while the hydraulic losses are significant. The liquid flow is more likely to be a boundary-driven (Couette) flow. At low tip rotor tip-speeds, the internal leakage becomes significant while the hydraulic losses are reduced. In this case, the pressure-driven (Poiseuille) liquid flow predominates. To model those hydraulic losses, Heselmann et al. (2024) distinguish three types of hydraulic losses:

- The acceleration of the liquid flow when the injection is performed.
- The fluid friction due to the viscous aspect of the flow that can be boundary-driven (Couette flow), pressure-driven (Poiseuille flow) or both.
- The momentum power losses due to the liquid film being periodically accelerated.

In liquid-flooded scroll compressors, similar losses are to be expected. In the frame of two-phase compression, the liquid phase is not injected and already has momentum before entering the scroll; hence, the acceleration losses can be neglected. To determine the friction and momentum losses in a scroll compressor, it is first necessary to define two speeds: the tip speed and the flow speed. The tip speed in a scroll compressor is constant throughout the length of the scroll wraps due to the orbiting movement, thus, it is only a function of the compressor rotating speed and is defined as

$$U_{\text{tip}} = \frac{2\pi r_{\text{o}} N}{60} \tag{4.111}$$

The flow speed can be calculated by multiplying the average radius of the points limiting the chamber by the rotating speed (Pereira et al. 2017):

$$U_{\text{flow}} = \frac{N}{60} \cdot 2\pi r_{\text{b}} (2\pi N_{\text{c,max}} + \pi - \theta^{\star}) \tag{4.112}$$

Here, $\theta^{\star}$ is the cumulated orbiting angle which equals 2π in the suction chambers and r_{b} and $N_{\text{c,max}}$ are geometrical parameters defined in Section 4.3. Taking, for example, the lab-scale prototype running at 5000 RPM would give the speeds represented in Figure 4.37. For the same conditions, the tip speed would be 2.9 m/s.

In scroll compressors, due to the relatively low axial clearance, the friction losses can be assumed to only be the contribution of a Couette flow, and are therefore given by

$$\dot{W}_{\text{fric}} = w_{\text{c}} \cdot l_{\text{c}} \cdot \mu_{\text{l}} \cdot \frac{U^2}{h_{\text{c}}} \tag{4.113}$$

where w_{c}, l_{c} and h_{c} are the characteristic width, length and height of the flow, while μ_{l} is the liquid phase dynamic viscosity. Furthermore, the momentum power losses can be determined by

$$\dot{W}_{\text{mom}} = \frac{1}{6} \cdot \rho_{\text{l}} \cdot h_{\text{c}} \cdot w_{\text{c}} \cdot U^3 \tag{4.114}$$

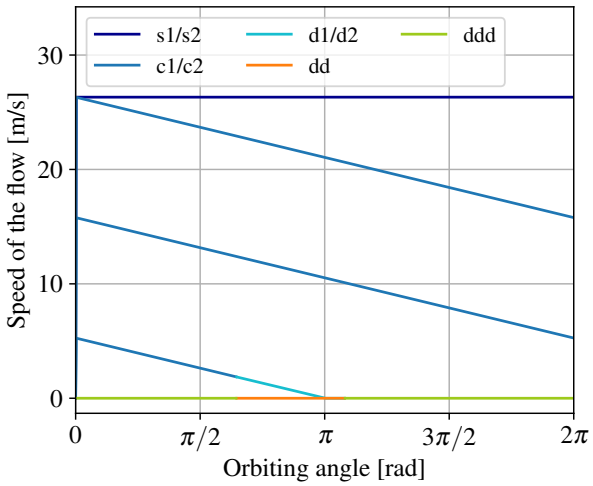

Figure 4.37: Evolution of the speed of the flow within the compressor (lab-scale prototype).

The motion of the scroll can be divided into two components: radial and tangential. As indicated by their names, the radial component drives the liquid along the radius, whereas the tangential component drives it tangentially. The radial contribution of the friction losses and momentum losses of chamber i at the orbiting angle θ is based on the tip speed U_{tip} and is expressed as

$$\dot{W}^{r}_{\text{fric},i}(\theta) = \frac{P_{\text{i}}(\theta)}{2} \cdot t_{\text{s}} \cdot \mu_{\text{l}} \cdot \frac{U^2_{\text{tip}}}{\delta} \tag{4.115}$$

$$\dot{W}^{r}_{\text{mom},i}(\theta) = \frac{1}{6} \cdot \rho_{\text{l}} \cdot t_{\text{l},i} \cdot \frac{P_{\text{i}}(\theta)}{2} \cdot U^3_{\text{tip}} \tag{4.116}$$

The tangential contribution of the friction and momentum losses is based on the flow speed U_{flow} and is defined by

$$\dot{W}^{t}_{\text{fric},i}(\theta) = h_{\text{s}} \cdot e_{\text{f}} \cdot \mu_{\text{l}} \cdot \frac{U^2_{\text{flow}}}{\delta} \tag{4.117}$$

$$\dot{W}^{t}_{\text{mom},i}(\theta) = \frac{1}{6} \cdot \rho_{\text{l}} \cdot \bar{A}_{\text{c,l},i} \cdot U^3_{\text{flow}} = \frac{1}{6} \cdot \dot{m}_{\text{l}} \cdot U^2_{\text{flow}} \tag{4.118}$$

where $e_{\text{f}} = 2.1$ mm is the characteristic length of the flank leakage defined by Bell et al. (2012a) and $\bar{A}_{\text{c,l},i}$ is the average cross-sectional area of the liquid phase in chamber i, allowing the liquid mass flow rate $\dot{m}_{\text{l}}$ to appear in the equation. It is important to highlight that the momentum losses represent an extreme-case scenario in which the liquid phase must be continuously accelerated, however, in reality, it does not lose its momentum so rapidly. Results of the total hydraulic friction and momentum power losses were obtained for a speed of 5000 RPM, an inlet vapor quality of 0.5 and a 5% OCR. They are displayed in Figure 4.38 and 4.39, respectively. As can be observed, the losses are the highest in the suction and compression chambers because of the higher flow speed. The highest total hydraulic losses can be found at an orbiting angle of zero and its value is 70 W. This value already accounts for the symmetric compression occurring, i.e., the single value of each chamber was doubled. Overall, given the fact that this simulation is an extreme-case scenario (highest speed and full momentum losses), and that the total hydraulic losses account for only 1.7% of the total power consumption (70 W out of 4100 W), those investigated losses could be neglected.

Therefore, it seems that the lower speeds ($\leq$ 25 m/s) involved in scroll compressors render these hydraulic losses negligible, whereas in screw compressors the higher tip length and higher tip speeds (up to 100 m/s) make their investigation important.

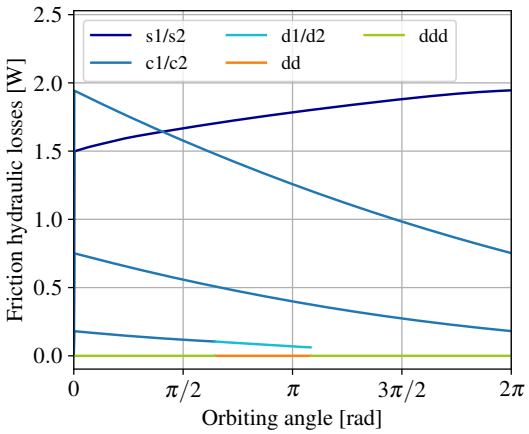

Figure 4.38: Friction hydraulic power losses of the lab-scale prototype at a speed of 5000 PM, an inlet vapor quality of 0.5 and an OCR of 5%.

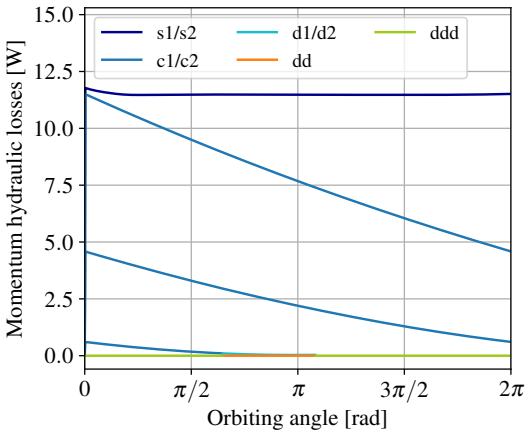

Figure 4.39: Momentum hydraulic power losses of the lab-scale prototype at a speed of 5000 PM, an inlet vapor quality of 0.5 and an OCR of 5%.

4.8 Model closure

The numerous submodels involved in the deterministic model interact with each other throughout the resolution process. Overall, the model is sequential; hence, the contribution of each submodels cannot be evaluated simultaneously, and a priority order must be defined. The flowchart of the deterministic model was presented in Figure 4.2, where the priority can already be observed, nevertheless, further details are provided in this section. Moreover, two resolution time scales (or angle scales) overlap, and some of the submodels may operate on both. Details of these two scales are thus provided. Finally, the stopping criteria are presented and some important aspects of the post-processing employed to obtain the performance of the compressor are given.

First and foremost, the geometrical submodel is executed to obtain the volume, volume derivative, and perimeter evolution of each chamber defined by the scrolls' superposition. Then, the model inputs are used to calculate the ideal mass flow rate, corresponding to a 100% volumetric efficiency. These inputs are passed through the desolubilization process presented in Section 2.4.1, in order to obtain the new inlet temperature, pressure and vapor quality. From that point, each chamber is initialized at an orbiting angle of zero, corresponding to a zero volume in the suction chambers. This initialization starts from a displacement volume filled with the inlet conditions, the state of the downstream chambers (compression, discharge) is determined using either the compression model with a density input (compression chamber) or a pressure input (discharge chamber) presented in Section 2.4.4, considering an isentropic efficiency of 65%.

A global view of each control volume of the deterministic model is represented in Figure 4.40. The su1 control volume simply represents the inlet state, after desobilization. The su2 control volume represents the state of su1 after supply heat transfer. The state of su2 is constant throughout the rotation, and only changes after a complete revolution is performed, due to changes in the mean mass flow rate and in the lump temperature. The sa chamber is the first control volume to vary with the orbiting angle, as it is influenced by the instantaneous mass flow rate variations and its own volume variation. After the chamber compression

process could be performed, the mass flow rates going through the main and intermediate discharge ports reach the ex1 control volume, whose state is calculated after a full revolution. Finally, the state of control volume ex2 is simply that of ex1 after the exhaust heat transfer.

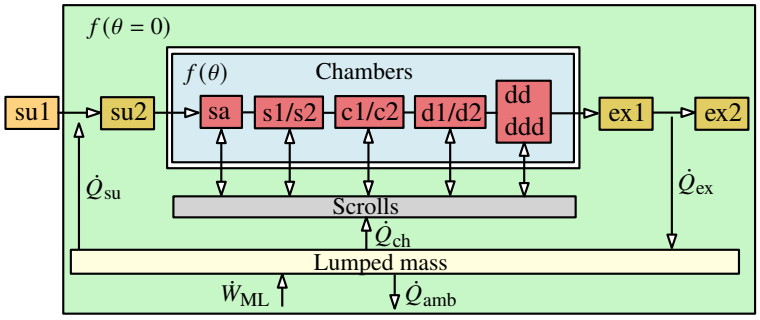

Figure 4.40: Representation of the control volumes, their interactions, and their angular resolution scale.

The control volumes shown in Figure 4.40 are now initialized, where CV su1, su2, sa and s1/s2 are at the supply state, while d1/d2, dd, ddd, ex1 and ex2 are at the exhaust state. From there, the lumped mass heat transfer model can already be run to calculate each heat transfer coefficient allowing to determine the transition between su1 and su2 and from ex1 to ex2, using the ideal mean mass flow rate calculated based on a 100% volumetric efficiency. After a complete revolution, where the flow model, the instantaneous heat transfer model and the core model have been working in coordination, the state evolution of the blue zone of Figure 4.40 can be calculated. The final states are then replacing the initial state of the following control volumes. For instance, the final state obtained at the end of the suction chamber (s1/s2) revolution becomes the initial state for compression chamber (c1/c2) of the following revolution. The state of ex1 can be determined by integrating the enthalpy fluxes leaving the discharge ports, followed by a recalculation of the state. These enthalpy fluxes come from the dd or ddd chamber when crossing the main discharge port, whereas they come from c1/c2 or d1/d2 chambers when crossing the intermediate discharge valves. The resulting average enthalpies of the refrigerant vapor, liquid, and oil can then be calculated as follows

$$h_{\mathrm{rg,ex1}} = \frac{\int (\dot{m}_{\mathrm{r,g,main}} h_{\mathrm{r,g,main}} + \dot{m}_{\mathrm{r,g,int}} h_{\mathrm{r,g,int}}) \mathrm{d}\theta}{\int (\dot{m}_{\mathrm{r,g,main}} + \dot{m}_{\mathrm{r,g,int}}) \mathrm{d}\theta} \tag{4.119}$$

$$h_{\mathrm{rl,ex1}} = \frac{\int (\dot{m}_{\mathrm{r,l,main}} h_{\mathrm{r,l,main}} + \dot{m}_{\mathrm{r,l,int}} h_{\mathrm{r,l,int}}) \mathrm{d}\theta}{\int (\dot{m}_{\mathrm{r,l,main}} + \dot{m}_{\mathrm{r,l,int}}) \mathrm{d}\theta} \tag{4.120}$$

$$h_{\mathrm{o,ex1}} = \frac{\int (\dot{m}_{\mathrm{o,main}} h_{\mathrm{o,main}} + \dot{m}_{\mathrm{o,int}} h_{o,int}) \mathrm{d}\theta}{\int (\dot{m}_{\mathrm{o,main}} + \dot{m}_{\mathrm{o,int}}) \mathrm{d}\theta} \tag{4.121}$$

Those obtained enthalpies would define the state of ex1 chamber if no pressure losses were experienced through the discharge port, i.e., the pressure upstream to the discharge valves would be the given exhaust pressure (model input). However, the discharge usually occurs with a pressure difference, varying throughout the angle progression. Therefore, condensation/evaporation usually occurs when crossing the discharge ports, which changes the enthalpies and the vapor quality of the flow. Naturally, the total mixture specific enthalpy is conserved, which allows the new vapor quality and the temperature of the phases to be calculated. The ex1 chamber vapor quality is given by

$$Q_{\text{ex1}} = \frac{\int (\dot{m}_{\text{r,g,main}} + \dot{m}_{\text{r,g,int}}) \mathrm{d}\theta}{\int (\dot{m}_{\text{main}} + \dot{m}_{\text{int}}) \mathrm{d}\theta} \tag{4.122}$$

In a similar way to the exhaust heat transfer (Section 4.6.3), the enthalpies are compared with saturation enthalpies at the exhaust pressure to determine if evaporation/condensation occured. The new vapor quality is updated accordingly and the liquid and vapor phase temperatures can be determined from the updated enthalpies.

After each revolution, the stopping criteria are evaluated to assess convergence. The following inequality must be satisfied for the simulation to stop:

$$\frac{X_{\phi,i}^{\theta=0} - X_{\phi,i}^{\theta=2\pi}}{X_{\phi,i}^{\theta=2\pi}} \leq \text{tol} \tag{4.123}$$

where X stands either for the temperature or the density. The index ϕ refers to the phase (liquid or vapor) and the index i to the chamber. This converging criterion must therefore be respected for each chamber and each phase.

Finally, the provided mass flow rate as well as the mechanical power consumption can be calculated. The mean mass flow rate can be determined by integrating the instantaneous mass flow rate from the su2 chamber to the sa chamber, or by integrating the instantaneous mass flow rate crossing the discharge port, over one full rotation. The calculation is expressed as follows

$$\dot{m} = \frac{1}{2\pi} \int_0^{2\pi} \dot{m}_{\text{su1}\rightarrow\text{sa}} \mathrm{d}\theta \tag{4.124}$$

The power at the shaft can be obtained by applying an overall energy balance to the model:

$$\dot{W}_{\text{shaft,cp}} = \dot{m}(h_{\text{ex2}} - h_{\text{su1}}) - \dot{Q}_{\text{amb}} \tag{4.125}$$

The isentropic and volumetric efficiencies can be obtained by using the procedure detailed in Section 3.3.3 (experimental performance indicator). The isentropic enthalpy of compression can be determined using either the split or the mixed state (see Section 2.4.1); as previously shown, this choice does not affect the results.

Eventually, the model requires three parameters as inputs. They are included in the updated compressor model diagram shown in Figure 4.41. These three parameters are summarized as follows:

- δ: leakage gap defining both the radial and flank leakages. It can be seen as an average value of the gaps between the fixed and orbiting scrolls, influenced by the compliance mechanism, the thermal deformation, vibration and displacement of the tip seal. This single value represents the gap for all chambers and may vary as a function of the model inputs.
- k_{l}: liquid-thickness correction coefficient allowing to determine whether a sealing effect exists. To do so, it multiplies the liquid-film thickness to account for centrifugal effects as well as the fluid motion generated by the orbiting movement. This parameter is also be a function of the model inputs.
- τ_{f}: friction torque multiplying the rotation speed to determine the mechanical power loss. This parameter should be a fixed value for a given compressor.

The simulation results provided by the deterministic model are strongly sensitive to these three parameters; their accurate calibration is therefore required for the model to perform well.

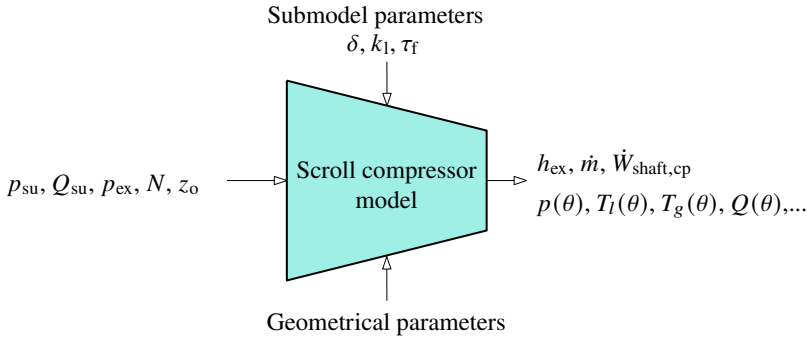

Figure 4.41: Inputs, outputs, and parameters of the deterministic model.

4.9 Summary and conclusions

This chapter presents the numerical modeling of the two-phase scroll compressors, with the objective of providing clearer analyses of the trends obtained in the experimental investigations (Chapter 3). To this aim, a deterministic model was developed, attempting to model as accurately as possible the physical phenomena involved within scroll compressors working under a two-phase regime. This model takes the same inputs as the post-processing methodology developed in Chapter 3: the compressor speed, the OCR, the exhaust pressure and the supply vapor quality and pressure. The model outputs are the mechanical power consumption, the provided mass flow rate but also the evolution of the mixture properties, e.g., the pressure and the temperatures, throughout the compression process. This deterministic model is divided into several submodels, working in coordination to provide the machine performance output. These submodels include a geometrical model that calculates the chamber volumes; a core model describing the two-phase compression behavior; mass and heat transfer models that represent the interactions within and between the chambers; and a mechanical loss model accounting for friction in the associated mechanisms. Eventually, this model relies on three semi-empirical parameters with clear physical meaning: the leakage gap δ, the liquid-thickness correction coefficient k_l, and the friction torque τ_f, required in the flow and mechanical loss submodels.

To the author's knowledge, the numerous physical effects accounted for in the deterministic model make it novel in the literature.

The main outcomes of this chapter can be summarized as follows:

- A deterministic model allowing the simulation of scroll compressors working with two-phase oil-refrigerant flows was presented. This model investigates the numerous physical phenomena involved in two-phase compression: phase change, thermal non-equilibrium, flow pattern, sealing effect, hydraulic power losses, two-phase heat transfer.
- The two-phase core model allowed to explain the trend of two-phase compression without considering the leakage or external heat transfer. Therefore, this model is simulating a purely adiabatic process. The results have shown that despite the process being adiabatic, it is not reversible and therefore not isentropic due to the temperature difference appearing between the two phases throughout the compression. Moreover, the final pressure ratio achieved during the compression of a two-phase mixture decreases as the initial vapor quality decreases; this can be explained by the greater condensation occurring during compression reducing the vapor phase density.
- The impact of the oil has also been investigated using the core model, and simulation results have shown that the higher specific heat capacity of the oil implies even more condensation to reach thermal equilibrium, increasing even more the irreversibilities and decreasing the final pressure ratio achievable.

- The oil-refrigerant mixture flow pattern map, depending on the mass flux and the inlet vapor quality has been derived to account for the distribution of the liquid phase at the inlet but also within the compressor. Significant deviations can, for instance, arise from a stratified flow, where the liquid and vapor phases do not mix, and an annular flow, where an important mass fraction of liquid travels at the vapor-phase velocity in the form of droplets.
- The liquid distribution within a chamber defined by the scrolls' superposition is addressed by assuming the presence of a liquid film on the wall and bottom surfaces of the chamber, while the remaining liquid is considered to exist in the form of droplets. The liquid film thickness is compared with the leakage gap to determine the vapor-liquid distribution of the leakages leaving the chamber.
- Heat transfer was assessed by assuming a isothermal lumped mass. Heat transfer occurs on two scales within the model: at the averaged level over one rotation, where heat transfer rates with the lumped mass are determined, and during the compression process involving the two-phase mixture and the scroll walls.
- The mechanical losses are twofold: friction losses and hydraulic losses. Friction losses are modeled using conventional techniques found in the literature. The investigation of hydraulic losses is inspired by studies on screw compressors, but is negligible in scroll compressors.

In practice, the development of the model was carried out in parallel with its validation; this was the case for both the leakage and heat transfer models. Before proposing the chamber heat transfer and leakage modeling strategies presented in this chapter, other approaches were attempted but proved unsuccessful. This trial-and-error process allows convergence toward a solution that is most representative of reality. Most of the physical phenomena involved in the model do not rely on any parameters; however, this does not imply that they are perfectly represented. This is the case, for instance, of heat transfer, whose modeling relies on assumptions and correlations developed within a slightly different framework from that for which they were originally intended. Therefore, even if the model is able to predict the performance of the machine within a given deviation range, this does not imply that the internal processes leading to the predicted performance correspond to the actual one, i.e., the fitting of parameters could compensate for deviations in submodels that do not rely on these parameters. Nevertheless, the validation of the model performed in the next chapter does not simply rely on the mechanical power and mass flow rate: the pressure evolution is also recorded on a portion of the compression and discharge processes. This pressure evolution can be predicted by mean of the deterministic model, enabling a more rigorous validation and thus, a more accurate representation of the physical phenomena involved. This validation is part of the next chapter.

References

Bell, Ian H. (2011). "Theoretical and Experimental Analysis of Liquid Flooded Compression in Scroll Compressors". PhD thesis. Purdue University.

Leclercq, Nicolas and Lemort, Vincent (2022). "Modeling and Simulation of a Two-Phase Scroll Compressor". In: *International Compressor Engineering Conference*. Purdue University.

Zaytsev, D. and Ferreira, C. A. Infante (2000). "Aspects of Two-Phase Flow Screw Compressor Modelling Part I: Leakage Flow and Rotor Tip Friction". In: *Proceeding of the International Compressor Engineering Conference*. Purdue University.

Liu, Zheji and Soedel, Werner (1995). "A Mathematical Model for Simulating Liquid and Vapor Two-Phase Compression Processes and Investigating Slugging Problems in Compressors". In: *HVAC and R Research* 1.2, pp. 99–109. ISSN: 10789669. DOI: 10.1080/10789669.1995.10391312.

Guo, Nini, Lin, Jie, and Wu, Jianhua (Dec. 2024). "Simulation on Two-Phase Refrigerant Compression in the Cylinder of Rotary Compressors Using CFD Method". In: *Scientific Reports* 14.1. ISSN: 20452322. DOI: 10.1038/s41598-024-56856-y.

Bell, Ian H. et al. (Nov. 2012a). "Liquid Flooded Compression and Expansion in Scroll Machines - Part II: Experimental Testing and Model Validation". In: *International Journal of Refrigeration* 35.7, pp. 1890–1900. ISSN: 01407007. DOI: 10.1016/j.ijrefrig.2012.07.008.

Afjei, Th., Suter, P., and Favrat, D. (1992). "Experimental Analysis of an Inverter-Driven Scroll Compressor with Liquid Injection". In: *International Compressor Engineering Conference*. Purdue University.

Dutta, Asit K., Yanagisawa, Tadashi, and Fukuta, Mitsuhiro (Sept. 2001). "An Investigation of the Performance of a Scroll Compressor under Liquid Refrigerant Injection". In: *International Journal of Refrigeration* 24.6, pp. 577–587. ISSN: 01407007. DOI: 10.1016/S0140-7007(00)00041-4. (Visited on 09/09/2025).

Gudjonsdottir, V., Ferreira, C. A. Infante, and Goethals, A. (Feb. 2019). "Wet Compression Model for Entropy Production Minimization". In: *Applied Thermal Engineering* 149, pp. 439–447. ISSN: 13594311. DOI: 10.1016/j.applthermaleng.2018.12.065.

Shah, Mizra Mohammad (Feb. 2021). *Two-Phase Heat Transfer*. 1st ed. Wiley. ISBN: 978-1-119-61865-2. DOI: 10.1002/9781119618652. (Visited on 09/10/2025).

Bell, Ian H. et al. (Feb. 2014). "Pure and Pseudo-Pure Fluid Thermophysical Property Evaluation and the Open-Source Thermophysical Property Library Coolprop". In: *Industrial and Engineering Chemistry Research* 53.6, pp. 2498–2508. ISSN: 08885885. DOI: 10.1021/ie4033999.

Leclercq, Nicolas and Lemort, Vincent (2024c). "A Mathematical Model for the Simulation of Two-phase Compression in Thermal Non-equilibrium". In: *1st Belgian Symposium of Thermodynamics*. Vol. Paper ID: 68. Liège.

Winandy, Eric, O, Claudio Saavedra, and Lebrun, Jean (Feb. 2002). "Experimental Analysis and Simplified Modelling of a Hermetic Scroll Refrigeration Compressor". In: *Applied Thermal Engineering* 22.2, pp. 107–120. ISSN: 13594311. DOI: 10.1016/S1359-4311(01)00083-7. (Visited on 09/11/2025).

Cuevas, Cristian, Fonseca, Nestor, and Lemort, Vincent (June 2012). "Automotive Electric Scroll Compressor: Testing and Modeling". In: *International Journal of Refrigeration* 35.4, pp. 841–849. ISSN: 01407007. DOI: 10.1016/j.ijrefrig.2011.11.019. (Visited on 09/11/2025).

Fujiwara, M and Osada, Y (May 1995). "Performance Analysis of an Oil-Injected Screw Compressor and Its Application". In: *International Journal of Refrigeration* 18.4, pp. 220–227. ISSN: 01407007. DOI: 10.1016/0140-7007(95)00008-Y. (Visited on 09/10/2025).

Seshaiah, N. et al. (Jan. 2007). "Mathematical Modeling of the Working Cycle of Oil Injected Rotary Twin Screw Compressor". In: *Applied Thermal Engineering* 27.1, pp. 145–155. ISSN: 13594311. DOI: 10.1016/j.applthermaleng.2006.05.007. (Visited on 09/10/2025).

Chen, Yu et al. (Sept. 2002a). "Mathematical Modeling of Scroll Compressors—Part I: Compression Process Modeling". In: *International Journal of Refrigeration* 25.6, pp. 731–750. ISSN: 01407007. DOI: 10.1016/S0140-7007(01)00071-8. (Visited on 09/10/2025).

Bell, Ian H. et al. (Feb. 2020). "PDSim: A General Quasi-Steady Modeling Approach for Positive Displacement Compressors and Expanders". In: *International Journal of Refrigeration* 110, pp. 310–322. ISSN: 01407007. DOI: 10.1016/j.ijrefrig.2019.09.002. (Visited on 09/11/2025).

Wang, Baolong, Li, Xianting, and Shi, Wenxing (Sept. 2005). "A General Geometrical Model of Scroll Compressors Based on Discretional Initial Angles of Involute". In: *International Journal of Refrigeration* 28.6, pp. 958–966. ISSN: 01407007. DOI: 10.1016/j.ijrefrig.2005.01.015. (Visited on 09/11/2025).

Nieter, Jeff J (1988). "Dynamics of Scroll Suction Process". In: *International Compressor Engineering Conference*. Purdue University.

Gillies, Sean et al. (Dec. 2022). *Shapely*. Zenodo. DOI: 10.5281/ZENODO.7428463. (Visited on 09/14/2025).

Lin, Jie, Lian, Yongsheng, and Wu, Jianhua (Apr. 2020). "Numerical Investigation on Vapor-Liquid Two-Phase Compression in the Cylinder of Rotary Compressors". In: *Applied Thermal Engineering* 170, p. 115022. ISSN: 13594311. DOI: 10.1016/j.applthermaleng.2020.115022. (Visited on 09/11/2025).

Yang, Minghong et al. (June 2022). "A Computationally Efficient Scroll Compressor Model for Both Single-Phase and Two-Phase Compression Considering Scroll Wrap Temperature Distribution". In: *International Journal of Refrigeration* 138, pp. 159–168. ISSN: 01407007. DOI: 10.1016/j.ijrefrig.2022.03.008. (Visited on 09/09/2025).

Thorade, Matthis and Saadat, Ali (Dec. 2013). "Partial Derivatives of Thermodynamic State Properties for Dynamic Simulation". In: *Environmental Earth Sciences* 70.8, pp. 3497–3503. ISSN: 1866-6280, 1866-6299. DOI: 10.1007/s12665-013-2394-z. (Visited on 09/26/2025).

Ziviani, Davide (2017). "Theoretical and Experimental Characterization of Single-Screw Expanders for ORC Applications". PhD thesis. Universiteit Gent. ISBN: ISBN978-94-6355-047-5.

Zaytsev, D. (2003). "Development of Wet Compressor for Application in Compression-Resorption Heat Pumps". PhD thesis. Technische Universiteit Delft.

Öhman, Henrik and Lundqvist, Per (2013). "Experimental Investigation of a Lysholm Turbine Operating with Superheated, Saturated and 2-Phase Inlet Conditions". In: *Applied Thermal Engineering*. Vol. 50, pp. 1211–1218. DOI: 10.1016/j.applthermaleng.2012.08.035.

van Heule, Xander et al. (Jan. 2023). "Modelling of Two-Phase Expansion in a Reciprocating Expander". In: *Applied Thermal Engineering* 218, p. 119224. ISSN: 13594311. DOI: 10.1016/j.applthermaleng.2022.119224. (Visited on 09/16/2025).

Revellin, Rémi et al. (June 2012). "A Comprehensive Non-Equilibrium Thermodynamic Analysis Applied to a Vapor-Liquid Two-Phase Flow of a Pure Fluid". In: *International Journal of Multiphase Flow* 42, pp. 184–193. ISSN: 03019322. DOI: 10.1016/j.ijmultiphaseflow.2012.02.008.

Chisholm, D. (1983). *Two-Phase Flow in Pipelines and Heat Exchangers*. London ; New York: G. Godwin in association with Institution of Chemical Engineers. ISBN: 978-0-7114-5748-5.

Alimonti, Claudio, Falcone, Gioia, and Bello, Oladele (Nov. 2010). "Two-Phase Flow Characteristics in Multiple Orifice Valves". In: *Experimental Thermal and Fluid Science* 34.8, pp. 1324–1333. ISSN: 08941777. DOI: 10.1016/j.expthermflusci.2010.06.004. (Visited on 09/10/2025).

Morris, S.D. (July 1991). "Compressible Gas-Liquid Flow through Pipeline Restrictions". In: *Chemical Engineering and Processing: Process Intensification* 30.1, pp. 39–44. ISSN: 02552701. DOI: 10.1016/0255-2701(91)80007-C. (Visited on 09/10/2025).

Petrovic, Milan and Stevanovic, Vladimir (2016). "Two-Component Two-Phase Critical Flow". In: *FME Transaction* 44.2, pp. 109–114. ISSN: 1451-2092. DOI: 10.5937/fmet1602109P. (Visited on 09/10/2025).

Pereira, Evandro L.L. and Deschamps, Cesar J (2010). "A Lumped Thermodynamic Model for Scroll Compressors with Special Attention to the Geometric Characterization during the Discharge Process". In: *International Compressor Engineering Conference*. Purdue University.

Wojtan, Leszek, Ursenbacher, Thierry, and Thome, John R. (July 2005). "Investigation of Flow Boiling in Horizontal Tubes: Part I—A New Diabatic Two-Phase Flow Pattern Map". In: *International Journal of Heat and Mass Transfer* 48.14, pp. 2955–2969. ISSN: 00179310. DOI: 10.1016/j.ijheatmasstransfer.2004.12.012. (Visited on 09/10/2025).

Thome, John R. (n.d.). "Chapter 17: Void Fractions in Two-Phase Flows". In: *Engineering Data Book III*.

Biberg, Dag (Dec. 1999). "An Explicit Approximation for the Wetted Angle in two-Phase Stratified Pipe Flow". In: *The Canadian Journal of Chemical Engineering* 77.6, pp. 1221–1224. ISSN: 0008-4034, 1939-019X. DOI: 10.1002/cjce.5450770619. (Visited on 10/06/2025).

Lee, Sang Won and No, Hee Cheon (Aug. 2019). "Droplet Size Prediction Model Based on the Upper Limit Log-Normal Distribution Function in Venturi Scrubber". In: *Nuclear Engineering and Technology* 51.5, pp. 1261–1271. ISSN: 17385733. DOI: 10.1016/j.net.2019.03.014. (Visited on 09/10/2025).

Gasche, José Luiz, Ferreira, R T S, and Prata, A T (2000). "Two-Phase Flow of Oil-Refrigerant Mixture Through the Radial Clearance in Rolling Piston Compressors". In: *Proceedings of the International Compressor Engineering Conference*. Purdue University.

Tanveer, M. Mohsin et al. (Oct. 2022). "Mechanistic Chamber Models: A Review of Geometry, Mass Flow, Valve, and Heat Transfer Sub-Models". In: *International Journal of Refrigeration* 142, pp. 111–126. ISSN: 01407007. DOI: 10.1016/j.ijrefrig.2022.06.016. (Visited on 09/09/2025).

Popiel, C.O., Wojtkowiak, J., and Bober, K. (Nov. 2007). "Laminar Free Convective Heat Transfer from Isothermal Vertical Slender Cylinder". In: *Experimental Thermal and Fluid Science* 32.2, pp. 607–613. ISSN: 08941777. DOI: 10.1016/j.expthermflusci.2007.07.003. (Visited on 10/12/2025).

Shao, D.W and Granryd, E (Jan. 1995). "Heat Transfer and Pressure Drop of HFC134a-oil Mixtures in a Horizontal Condensing Tube". In: *International Journal of Refrigeration* 18.8, pp. 524–533. ISSN: 01407007. DOI: 10.1016/0140-7007(96)81779-8. (Visited on 09/09/2025).

Dutta, Asit K., Yanagisawa, Tadashi, and Fukuta, M (1996). "A Study on Compression Characteristic of Wet Vapor Refrigerant". In: *Proceeding of the International Compressor Engineering Conference*. Purdue University.

Stosic, N. et al. (Jan. 1992). "Investigation of the Influence of Oil Injection upon the Screw Compressor Working Process". In: *International Journal of Refrigeration* 15.4, pp. 206–220. ISSN: 01407007. DOI: 10.1016/0140-7007(92)90051-U. (Visited on 09/10/2025).

Huagen, Wu, Ziwen, Xing, and Pengcheng, Shu (June 2004). "Theoretical and Experimental Study on Indicator Diagram of Twin Screw Refrigeration Compressor". In: *International Journal of Refrigeration* 27.4, pp. 331–338. ISSN: 01407007. DOI: 10.1016/j.ijrefrig.2004.01.004. (Visited on 09/09/2025).

Incropera, Frank P. et al., eds. (2007). *Fundamentals of Heat and Mass Transfer*. 6. ed. Hoboken, NJ: Wiley. ISBN: 978-0-471-45728-2.

Jang, Kitae and Jeong, Sangkwon (Aug. 2006). "Experimental Investigation on Convective Heat Transfer Mechanism in a Scroll Compressor". In: *International Journal of Refrigeration* 29.5, pp. 744–753. ISSN: 01407007. DOI: 10.1016/j.ijrefrig.2005.12.002. (Visited on 09/10/2025).

Peng, Bin, Zhao, Shengxian, and Li, Yaohong (Oct. 2017). "Thermodynamic Model and Experimental Study of Oil-free Scroll Compressor". In: *Journal of Physics: Conference Series* 916, p. 012048. ISSN: 1742-6588, 1742-6596. DOI: 10.1088/1742-6596/916/1/012048. (Visited on 09/10/2025).

Yao, Yufang and Hrnjak, Pega (Oct. 2023). "Measurement and Modeling of Void Fraction for Developing Two-Phase Flow of R134a in a Horizontal Tube after an Expansion Valve". In: *International Journal of Refrigeration* 154, pp. 125–137. ISSN: 01407007. DOI: 10.1016/j.ijrefrig.2023.07.009. (Visited on 09/10/2025).

Chen, Yu et al. (Sept. 2002b). "Mathematical Modeling of Scroll Compressors — Part II: Overall Scroll Compressor Modeling". In: *International Journal of Refrigeration* 25.6, pp. 751–764. ISSN: 01407007. DOI: 10.1016/S0140-7007(01)00072-X. (Visited on 09/10/2025).

Lemort, Vincent (2008). "Contribution to the Characterization of Scroll Machines in Compressor and Expander Modes". PhD thesis. University of Liège.

Vasuthevan, Hanushan and Brümmer, Andreas (Nov. 2018). "Multiphase-Flow Simulation of a Rotating Rectangular Profile within a Cylinder in Terms of Hydraulic Loss Mechanisms". In: *IOP Conference Series: Materials Science and Engineering* 425, p. 012002. ISSN: 1757-899X. DOI: 10.1088/1757-899X/425/1/012002. (Visited on 09/10/2025).

— (2022). "Generic Experimental Investigation of Hydraulic Losses within Twin-Screw Machines". In: *The 9th International Conference on Compressor and Refrigeration*. Purdue University.

Nikolov, Alexander and Brümmer, Andreas (Nov. 2018). "Impact of Different Clearance Heights on the Operation of a Water-Flooded Twin-Screw Expander—Experimental Investigations Based on Indicator Diagrams". In: *IOP Conference Series: Materials Science and Engineering* 425, p. 012008. ISSN: 1757-899X. DOI: 10.1088/1757-899X/425/1/012008. (Visited on 09/10/2025).

Heselmann, Matthias, Dämgen, Ulrich, and Brümmer, Andreas (2024). "Experimental Investigation of the Distribution of Two-Phase Flow in Oil-Injected Twin-Screw Compressors". In: *13th International Conference on Compressors and Their Systems*. Ed. by Matthew Read et al. Cham: Springer Nature Switzerland, pp. 61–76. DOI: 10.1007/978-3-031-42663-6_6. (Visited on 09/10/2025).

Pereira, Evandro L.L. and Deschamps, Cesar J. (Oct. 2017). "A Heat Transfer Correlation for the Suction and Compression Chambers of Scroll Compressors". In: *International Journal of Refrigeration* 82, pp. 325–334. ISSN: 01407007. DOI: 10.1016/j.ijrefrig.2017.05.033. (Visited on 09/09/2025).

Chapter 5

Two-phase Compression: Model Validation and Performance Analysis

Chapter Abstract

In this chapter, the approach used to validate the numerical model presented in Chapter 4 is described. The model validation is based on data coming from the experimental investigations presented in Chapter 3. Validation results of both tested machines are presented and analyzed. On the one hand, the lab-scale prototype model validation is based on three predicted outputs: the mass flow rate, the mechanical power consumption and the average pressure measured by the dynamic pressure sensor (Kulite). On the other hand, the validation of the retrofitted compressor is only based on the power consumption and mass flow rate. The validation shows good agreement, with average relative deviations of 2.11%, 3.41%, and 2.51% for the predicted power consumption, mass flow rate, and mean internal pressure, respectively, for the lab-scale prototype, and 2.17% and 4.45% for the predicted power consumption and mass flow rate, respectively, for the retrofitted compressor. Performance analysis of the two compressors is then carried out, using variations of variables (pressure, temperatures, vapor quality) throughout the compression, pressure-volume diagrams, individual points comparison and a sensitivity analysis of the model. The analysis performed on the validated pressure-volume diagrams allows the definition of several factors contributing to the isentropic efficiency values, such as the indicated efficiency. In the sensitivity analysis performed on the calibrated model, the different sources of efficiency losses are quantified for varying inlet vapor qualities. In general, the results are in agreement with the already observed experimental trends. Moreover, the four presented analyses allow a complete understanding of two-phase compression behavior. Therefore, this final chapter allows both a qualitative and quantitative understanding of the impact of two-phase flow on scroll compressor performance, thereby addressing the questions raised in the thesis introduction. The results presented in this chapter were not published at the time of writing; it is not based on any already existing publication.

5.1 Introduction

The deterministic model presented in Chapter 4 aimed at providing the best performance predictions based on the multiple physical phenomena involved in two-phase compression and scroll compressors in general. Nevertheless, despite its globally deterministic aspects, submodels rely on semi-empirical parameters, which require fitting for the model to be calibrated. To perform this model calibration, the data resulting from the experimental investigations presented in Chapter 3 are used. The model can thereby be calibrated on the two tested machines and validated afterwards. Therefore, this final chapter constitutes the missing link to understand the behavior of two-phase compression in scroll machines: it uses

the experimental data presented in Chapter 3 to calibrate the deterministic model described in Chapter 4, which itself relies on the mixture properties and concepts introduced in Chapter 2. The first modeling results of the deterministic model can then be finally presented, with a typical operating point of the lab-scale prototype. Validated pressure–volume diagrams are then analyzed to further enhance the understanding of two-phase compression, followed by individual operating point comparisons investigating the origin and impact of leakages resulting from variations in speed, vapor quality, pressure ratio, and oil circulation ratio (OCR). A sensitivity analysis is then used to quantify the source of isentropic and volumetric efficiency losses experienced by the machine when exposed to two-phase flows. The deterministic model allows certain submodels to be pushed to their limits; for instance, the leakage, heat transfer, and mechanical loss submodels can be deactivated. Deactivating each submodel individually enables to assess the efficiency gain or loss associated with the phenomena represented by the deactivated submodel. The analysis of the trends outlined in the experimental results can thus be confirmed, and the model limitations can be understood.

5.2 Calibration methodology

The calibration of the model requires the fitting of three parameters, previously defined in Chapter 4. These parameters include:

- The leakage gap δ, defining both the radial and flank leakages in one single value. It can be seen as an average value of the gaps between the fixed and orbiting scrolls, influenced by the compliance mechanism, the thermal deformation, vibration and displacement of the tip seal. This parameter vary as a function of the model inputs, and is not constant for a compressor model.
- The liquid-thickness correction coefficient k_l, influencing the proportion between liquid and vapor leakage. To do so, it multiplies the liquid-film thickness to account for centrifugal effects as well as the fluid motion generated by the orbiting movement. This parameter is also be a function of the model inputs.
- The friction torque τ_f multiplying the rotation speed to determine the mechanical power loss. This parameter is a fixed value for a given compressor.

Among these three parameters, two are dependent on the input conditions: the leakage gap and the liquid-thickness correction coefficient. The friction torque can be considered constant for a given compressor. The dependence of the leakage gap on the inlet conditions comes from the deformation of the scrolls and the movement of the tip seals, varying with the speed, the liquid-phase thickness and viscosity. Moreover, the dependence of the liquid-thickness correction coefficient on the inlet conditions comes from the liquid phase viscosity, quantity and distribution within the chamber (speed-dependent). Furthermore, it also depends on the leakage gap through the effect of surface tension. The fitting of these three parameters is based on three model outputs, which are:

- The compressor mass flow rate $\dot{m}$, influenced by the leakage and the variation of mixture density between the supply pipe and the suction chambers.
- The compression mechanical power consumption $\dot{W}_{\mathrm{shaft,cp}}$, influenced by the pressure level within the chambers, and the mechanical losses.
- The mean pressure at the sensor level $\bar{p}$, corresponds to an angle-averaged pressure measurable by the dynamic pressure sensor presented in Chapter 3. This pressure measurement is only usable to fit the parameters of the lab-scale prototype. Influenced by the leakage and the heat transfer within the chambers.

Two of the model outputs are strongly correlated: the mean pressure and the mechanical power consumption. As a matter of fact, the higher the pressure within a chamber, the larger the area under the pressure–volume diagram, representing the indicated work of one compressor

revolution. Therefore, validating the mean pressure prediction automatically validates the indicated power of the machine, which is a component of the shaft power consumption. The fact that the number of outputs equals the number of parameters facilitates the development of a dedicated calibration algorithm, at least for the lab-scale prototype, which benefits from internal pressure measurements. Therefore, three distinct experimental variables are used for the calibration of the lab-scale prototype, allowing an robust validation of the model. The calibration methodology applied is similar to that used by Bell et al. (2012a). First, the input-dependent parameters are individually fitted to perfectly match the prediction of the model with each experimental point recorded. In the case of Bell et al. (2012a), the methodology was applied to the flank leakage gap. Therefore, in this case, two parameters need to be individually fitted. A pair of (δ, k_l) is therefore obtained for each data point by minimizing the relative deviation between the model predictions and the measurement. Afterwards, these parameters are predicted as a function of the model inputs. An interpolation or probabilistic regression model can thus be applied to the set of parameters obtained from the individual, or "perfect" calibration. The objective of this submodel is to predict the value of the parameters for given input conditions. Hence, this validated submodel is integrated into the deterministic model, allowing the model to be run with predicted parameters for each tested point. Moreover, this parameter prediction submodel also allows verification of the impact of the various inputs on the parameters. The methodology employed to predict the parameter is a Gaussian Process (GP) regression model, similar to GPExp (Quoilin et al. 2016), used to analyze the experimental results in Chapter 3. This GP prediction model is therefore integrated into the deterministic model, after training on the parameters obtained from the individual fitting, as represented in Figure 5.1.

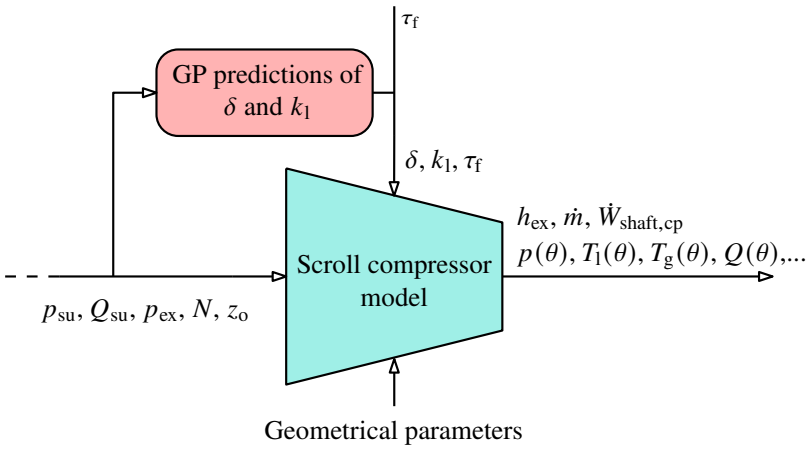

Figure 5.1: GP parameter prediction model embedded within the deterministic model.

5.2.1 Influence of the parameters

To fit the GP prediction model, pairs of parameters (δ, k_l) must be obtained for each data point. Nevertheless, the three model parameters influence the three outputs of the model, i.e., no output depends solely on a single parameter value. The influence of an increase in the parameter value on each output can be found in Table 5.1.

First, an increase of k_l results in an increase of the mass flow rate. The cause of this increase is the decrease in the vapor/liquid leakage proportion. Liquid leakage going into the suction chambers takes less volume than the vapor leakage, resulting in a better volumetric suction capacity of these suction chambers. Moreover, a reduction in vapor leakage leads to an overall decrease in pressure within the chambers. Decreased vapor leakage introduces a lower

Output variable	Increase in k_1	δ	τ_f
$\dot{m}$	↗	↘	↘
$\dot{W}_{shaft,cp}$	⤭	⤭	↗
$\bar{p}$	↘	↗	↗

Table 5.1: Influence of the model parameters on the output variables.

vapor mass into the compression chambers, resulting in lower density and, consequently, lower pressure. This decrease in pressure also affects the internal work of the machine by decreasing it. However, the increase in mass flow rate also affects the final power consumption, therefore, the increase in k_1 can either result in an increase or a decrease in the power consumption. Second, an increase in the leakage gap δ reduces the machine's mass flow rate due to the greater leakage into the suction chambers. Again, these leakages decrease the volumetric suction capacity of these chambers. These increased leakages also increase the mean pressure, tending to increase the power consumption. Nevertheless, once again, the decrease in mass flow rate tends to decrease the final power consumption, thus, the behavior of the power consumption depends on the operating conditions. Finally, the friction torque τ_f also influences the three outputs. The higher the friction torque, the higher the lumped-mass temperature, resulting in increased evaporation at the inlet, which increases the vapor quality before the suction chamber, which decreases the mass flow rate. Moreover, this higher temperature increases the mean pressure, and, consequently, the indicated power. The final influence on the power consumption is therefore twofold: the friction torque increases both the mechanical power losses and the indicated power consumption. To quantify the sensitivity of the outputs to the parameters, sensitivity coefficients can be defined. The sensitivity coefficient of output y to parameter p is given by the relative change in output per relative change in parameters:

$$S_{p\to y} = \frac{\Delta y/y_0}{\Delta p/p_0} \tag{5.1}$$

The parameter sensitivity coefficients of the validated models for both tested compressors are presented in Tables 5.2 and 5.3. These coefficients are computed from variation in parameters of -10% and +10%, and therefore calculated using a central difference. These coefficients are condition-dependent, i.e., they vary from one operating point to another. Nevertheless, such coefficients allow comparison of the influence magnitudes of the three parameters. As expected, the influences of the first two parameters on the mass flow rate and pressure are significant, while that of the third parameter is mainly observed in the power consumption output due to increased mechanical losses, counteracting the mass flow rate reduction.

Output variable	Increase of 100% in k_1	δ	τ_f
$\dot{m}$	9.96%	-17.04%	-5.23%
$\dot{W}_{shaft,cp}$	3.49%	5.05%	33.5%
$\bar{p}$	-4.98%	4.17%	1%

Table 5.2: Parameter sensitivity coefficients for the lab-scale prototype model.

Output variable	Increase of 100% in k_1	δ	τ_f
$\dot{m}$	7.13%	-22.62%	-3.5%
$\dot{W}_{shaft,cp}$	-1.36%	0.8%	27.03%
$\bar{p}$	-3.55%	4.97%	0.49%

Table 5.3: Parameter sensitivity coefficients for the retrofitted compressor model.

5.2.2 Individual fitting of the lab-scale prototype model

No optimization algorithm from the SciPy Python library (Virtanen et al. 2020) performed adequately in identifying the parameter pair that minimizes the error, therefore, a simple in-house algorithm was developed for this calibration. This algorithm consists of a bisection loop nested within another bisection loop, as can be seen in Figure 5.4. The stability of this method relies on the quasi-monotonic behavior of the average relative deviation of the mass flow rate prediction with respect to the leakage gap, and of the average relative deviation of the mean pressure with respect to the liquid-thickness correction coefficient, as represented in Figures 5.2 and 5.3, respectively.

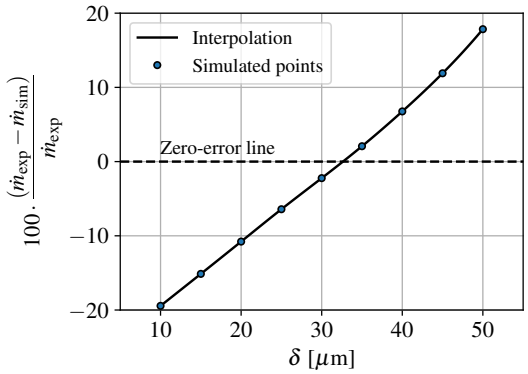

Figure 5.2: Variation of the mass flow rate relative deviation as a function of the leakage gap δ in the lab-scale prototype model.

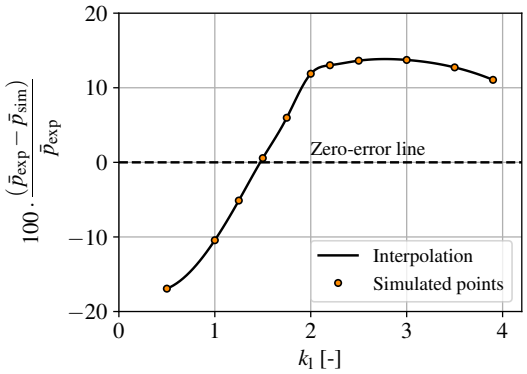

Figure 5.3: Variation of the mean pressure relative deviation as a function of the liquid-thickness correction coefficient k_l in the lab-scale prototype model.

Due to the multiple cross-influences between the parameters and the outputs, individually fitting each pair of (δ, k_l) requires knowledge of the friction torque, which is assumed constant for a given compressor. Therefore, a guess value for the friction torque is used. Then the "perfect" calibration of (δ, k_l) using the double-bisection process is performed, and the friction torque value is adjusted to minimize the average relative deviation of the power consumption for the whole dataset afterwards. As previously explained, the friction torque value is directly proportional to the mechanical power losses, but not to the total power consumption, as it also influences the indicated power consumption via decreased mass flow rate or mean pressure increase. Therefore, the friction torque value cannot simply be linearly adjusted with the average absolute deviation of the shaft power consumption.

The idea behind the double bisection process is, for each tested value of k_l, to find the leakage gap value δ minimizing the mass flow rate relative deviation. Hence, for each simulated point shown in Figure 5.3, the relative deviation of the mass flow rate is minimized through a bisection on the parameter δ, whose trend is illustrated in Figure 5.2. Another bisection can therefore be applied on k_l to find the minimum in the relative deviation of the mean pressure. As can be seen in Figure 5.3, at a certain value of k_l, the monotonic behavior of the pressure relative deviation ceases; these points correspond to the transition from two-phase leakage to fully liquid leakage.

Finally, the flowchart of the individual parameters fitting is presented in Figure 5.4. The first step of this calibration is to find a friction loss guess value. Then, ranges and initial values must be set on k_l and δ to initiate the bisection loops. Then, inputs and outputs from the experimental data set are retrieved for each experimental point k. The first bisection loop on δ is then executed. When the relative deviation of the mass flow rate ($RD_{\dot{m}}$) falls below the tolerance $\text{tol}_{\dot{m}}$, the relative deviation of the mean pressure is evaluated, and the value of

k_l is adjusted accordingly, constituting the second bisection loop. The characteristics of the two bisection loops are the following:

- The delta fitting loop starts with a range $[\delta_{min}, \delta_{max}] = [5, 80]$ μm at the average value $\delta = 42.5$ μm. The convergence tolerance is given by $tol_{\dot{m}} = 0.5\%$. When the relative deviation $RD_{\dot{m}}$ is positive, the mass flow rate should be increased. Therefore, the leakage should be decreased and the leakage gap should decrease. In this case, the higher bound of the range becomes the previous gap, and the new tested gap can be taken as the average value. Conversely, if the deviation is negative, the gap is increased and the lower bound updated. Convergence problems can occur when too high leakage gaps are simulated, as it can lead to negative mass flow rate and instability, in which case the gap is automatically decreased.
- The liquid-thickness correction coefficient loop starts with a range $[k_{l\min}, k_{l,\max}] = [0.2, 8]$ at the average value of 4.1. It has the same convergence tolerance as the leakage gap, i.e., $tol_{\bar{p}} = 0.5\%$. When the mean pressure relative deviation is negative, i.e., when the mean simulated pressure is too high, liquid leakage must be increased, therefore, the value of k_l is increased. The lower bound takes the previous values of k_l, and the new average is calculated. Conversely, if the deviation is positive, the higher bound is changed with the previous value, k_l is thereby reduced.

Once both tolerance criteria are satisfied, the final values of k_l and δ are stored, and the individual fitting procedure is applied to the next experimental point. The default angle step used to run the model is 0.008 rad.

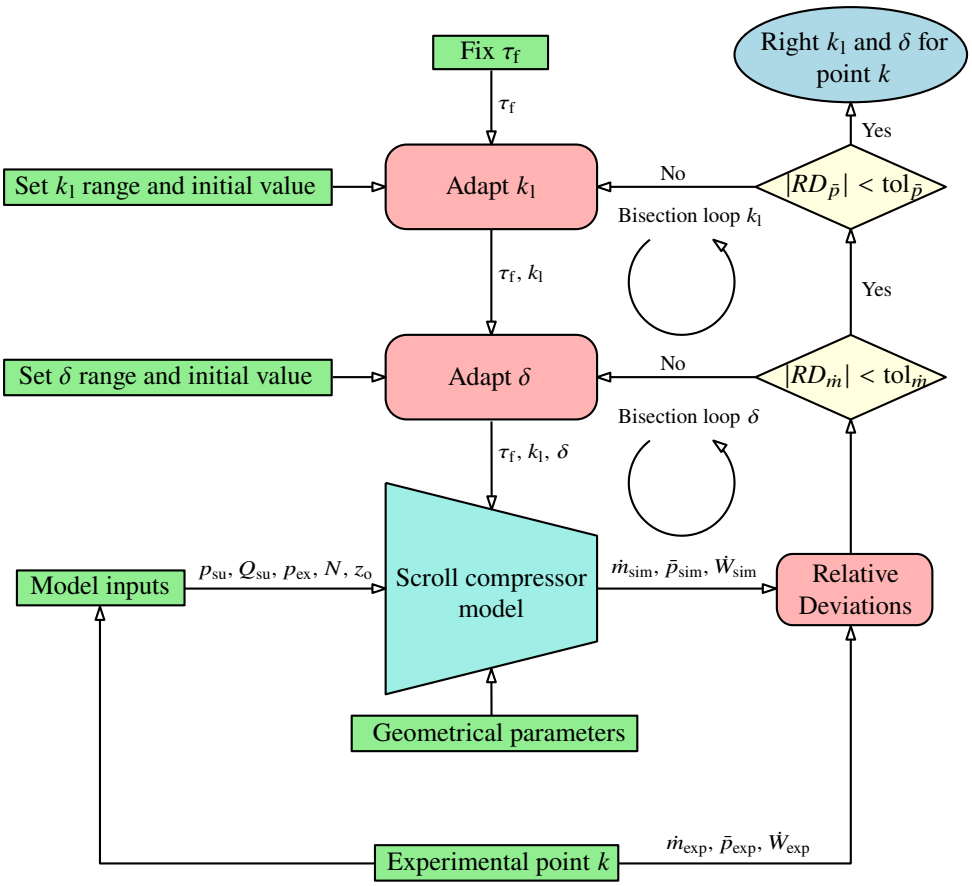

Figure 5.4: Flowchart of the parameter fitting procedure applied to each experimental data point from the lab-scale prototype.

As already stated in the presentation of the deterministic model (Chapter 4), the development of the model was carried out in parallel with its validation; that is, different model features were tested, and if the calibration failed, these features were modified. This trial-and-error procedure allowed convergence toward the current version of the deterministic model. The tested features include only the leakage submodel and can be found in Table 5.4. As can be seen, five calibrations were necessary to reach the final model version of the deterministic model and the final individual fitting. Changes between the calibrations primarily include testing different leakage submodels, but also the change of parameter numbers or modification of the individual calibration algorithm. The addition of a second liquid-thickness correction parameter is intended to test the model with an independent parameter for the suction chambers, as the suction of the two-phase fluid may not directly generate a sealing effect due to centrifugal forces that modify the liquid distribution within the suction chamber. By doing so, the leakage into the suction chamber depends only on this new parameter and not on that of the compression chamber, which eliminates the cross-dependence between these parameters and the outputs, i.e., the liquid-thickness correction coefficient of the compression chamber does not influence the mass flow rate anymore. Eventually, the model appears to calibrate well without this feature, which does not imply that the latter assumption is incorrect. The success rate of an individual calibration is calculated as the ratio of points that could be calibrated within the given tolerances for both the leakage gap and correction parameter fitting. Moreover, the successful sets were analyzed using the GP prediction to determine whether a correlation truly exists between the model inputs and the predicted parameters. The ideal calibration (Calibration 5) exhibits both an excellent convergence rate (with almost all points within the given tolerances) and good GP prediction accuracy, as will be shown in a subsequent section, thereby concluding the individual calibration procedure for the lab-scale prototype.

	Model feature	Results (% of calibrated points)
Calibration 1	Single two-phase leakage model with correction factor	Bad convergence (< 50%)
Calibration 2	Independent leakage flow model with parameter k_l	Decent convergence (> 50%)
Calibration 3	Independent leakage flow model with 2 parameters: - fixed $k_{l,s}$ for the suction chambers; - variable $k_{l,c}$ for the other chambers	Acceptable convergence (> 75%) Bad GP predictions
Calibration 4	Independent leakage flow model with parameter k_l and correction factors on the vapor mass flow rate	Acceptable convergence (> 75%) Bad GP predictions
Calibration 5	Independent leakage flow model with parameter k_l and enhanced calibrator	Excellent convergence (> 95%) Good GP predictions

Table 5.4: Tested calibration features on the lab-scale prototype model.

The individual calibration procedure is a long process: each individually fitted point requires an average of six iterations for each leakage gap tuning loop and four iterations for each liquid-thickness correction parameter loop, i.e., 24 iterations per point. A run of the deterministic model takes on average five minutes, therefore, two hours are needed to individually calibrate one point. Fortunately, these individual calibration processes can be parallelized by running several Python instances simultaneously. Yet, at least one or two days are required for the individual calibration of the lab-scale prototype dataset (68 points).

Moreover, the different friction torque values tested are not included in Table 5.4, making the process even longer. The calibration procedure is complex, as certain tested parameter sets may cause the model to crash for various reasons. The encountered problems linked to parameter fitting are the following:

- Testing excessively high liquid-thickness correction parameters resulted in a large leakage gap required to fit the mass flow rate, with vapor leakage occurring into the suction chambers. These tested parameter sets generated strong instabilities, leading to model crashes. A solution to avoid this issue is to divide the angle step by two each time the model generates a specific instability, with a maximum division factor of eight (corresponding to a minimum angle step of 0.001 rad).
- Too high leakage gaps at low correction parameters, resulting in negative mass flow rates of the compressor; a simple reduction of the gap could solve this issue.
- No convergence due to the full-liquid leakage negative slope of the pressure deviation with the liquid-thickness correction parameters, which can be observed in Figure 5.3. The calibration algorithm had to be improved to detect this zone and reduce the correction parameter accordingly.

Finally, the GP prediction results obtained from the individual fitting of each parameter are presented in the next section, along with the cross-validation for each data point. These parameter predictions are then used to validate the model of the lab-scale prototype.

5.2.3 Individual fitting of the retrofitted compressor model

The dynamic pressure measurements of the lab-scale prototype, along with the power consumption and mass flow rate measurements, enabled the calibration of the three parameters of its deterministic model. Nevertheless, such a sensor could not be installed on the retrofitted compressor, resulting in three parameters that can only be fitted using two outputs. Initially, predictions of liquid-thickness correction parameters coming from the lab-scale prototype GP submodel were intended to be used, however, not enough experimental data could be used for the GP to be well calibrated, as will be shown in the subsequent section. Using k_1 predictions could have allowed to use the mass flow rate output to fit the leakage gap, and the power consumption output to fit the friction loss coefficient. Hence, this methodology did not work as expected, as high power consumptions (up to 100% of relative deviation) were obtained. Therefore, a similar methodology to that used to calibrate the lab-scale prototype model is employed. A bisection loop fitting the leakage gap with the mass flow rate is nested within a bisection loop fitting the liquid-thickness correction parameter with the power consumption. Then the question of how to fix the friction torque value arises. In fact, using the bisection loop to fit k_1 does not allow the power consumption relative deviation to remain within the same tolerance as for the individual fitting of the lab-scale prototype. Therefore, the main bisection loop was used to minimize the absolute value of each power consumption relative deviation. This minimization process allows to obtain values of the k_l. The liquid-thickness correction parameter is thus obtained individually for each data point by minimizing the individual point relative deviation of the power consumption, while the friction torque value is determined by minimizing the average relative deviation of the power consumption for the whole dataset. Once again, the variation of the mass flow rate relative deviation with the leakage gap can be found in Figure 5.5, whereas the variation of the power consumption relative deviation can be found in Figure 5.6. In the illustrated example of the first bisection loop, it is possible to find a value of k_1 minimizing the power consumption relative deviation. The sensitivity of the mass flow rate relative deviation to the leakage gap is similar to that of the lab-scale prototype (see Figure 5.2). Nevertheless, the sensitivity of the power consumption relative deviation to the liquid-thickness correction parameter is smaller than the sensitivity to the mean pressure of the lab-scale prototype (Figure 5.3). It should be noted that this sensitivity is not captured

by the coefficients presented in Table 5.3, because in this case, the leakage gap is adjusted simultaneously to maintain a constant mass flow rate. The low sensitivity of the power consumption to k_1 can be explained by the small number of coexisting compression chambers in this compressor, which prevents leakage from significantly increasing the pressure throughout compression. Thus, the influence of the parameter k_1 on the power consumption results is minimal, however, it strongly influences the final value of the leakage gap.

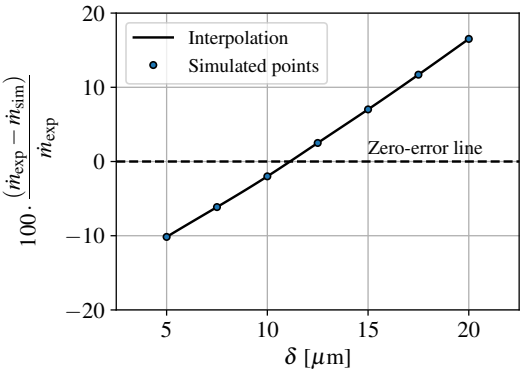

Figure 5.5: Variation of the mass flow rate relative deviation as a function of the leakage gap δ in the retrofitted compressor model.

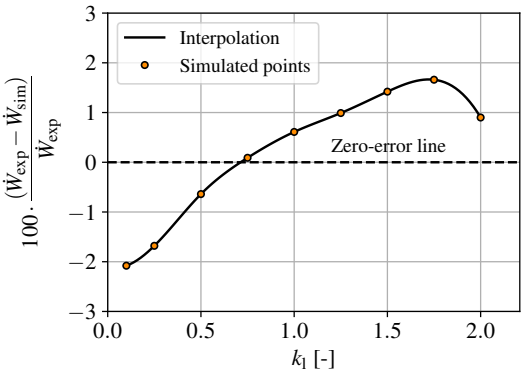

Figure 5.6: Variation of the power consumption relative deviation as a function of the liquid-thickness correction coefficient k_1 in the retrofitted compressor model.

Finally, the flowchart of the individual parameters fitting of the retrofitted compressor is presented in Figure 5.4. The individual calibration procedure of the retrofitted compressor is similar to that used for the lab-scale prototype model. Again, the first step of this calibration procedure is to find a friction loss guess value. Then, ranges and initial values must be set on k_1 and δ to initiate the bisection loops. Then, inputs and outputs from the experimental data set are retrieved for each experimental point k. The first bisection loop on δ is then executed. When the relative deviation of the mass flow rate ($RD_{\dot{m}}$) falls within the given tolerance $\text{tol}_{\dot{m}}$, the relative deviation of the power consumption is evaluated, and the value of k_1 is adjusted accordingly to minimize the absolute value of the relative deviation. This constitutes the second bisection loop. This individual fitting of parameters is run several times on the whole dataset, adjusting the friction torque value (constant for all points) at each iteration, to minimize the average relative deviation on the power consumption. In total, 269 points are individually calibrated under the same simulation conditions of the lab-scale prototype. Fortunately, running the model for this compressor is two times faster than for the lab-scale prototype due to the lower number of coexisting compression chambers. An individual calibration procedure can take up to three days of computational time.

5.3 Model validation

The models of both the lab-scale prototype and the retrofitted compressor are calibrated using the procedures mentioned in the previous section. First, the individual calibration procedures were conducted to find pairs of parameters (δ, k_1) respecting the converging criteria for both machines. Then, the friction torque values were adjusted to minimize the total relative deviation of the compressor consumption. These pairs of parameters are used to train the parameter prediction submodel embedded within the deterministic model. This submodel is a GP algorithm that predicts the parameter values as a function of the model inputs. Moreover, the submodel uses the output of the leakage-gap predicting GP as an additional input to

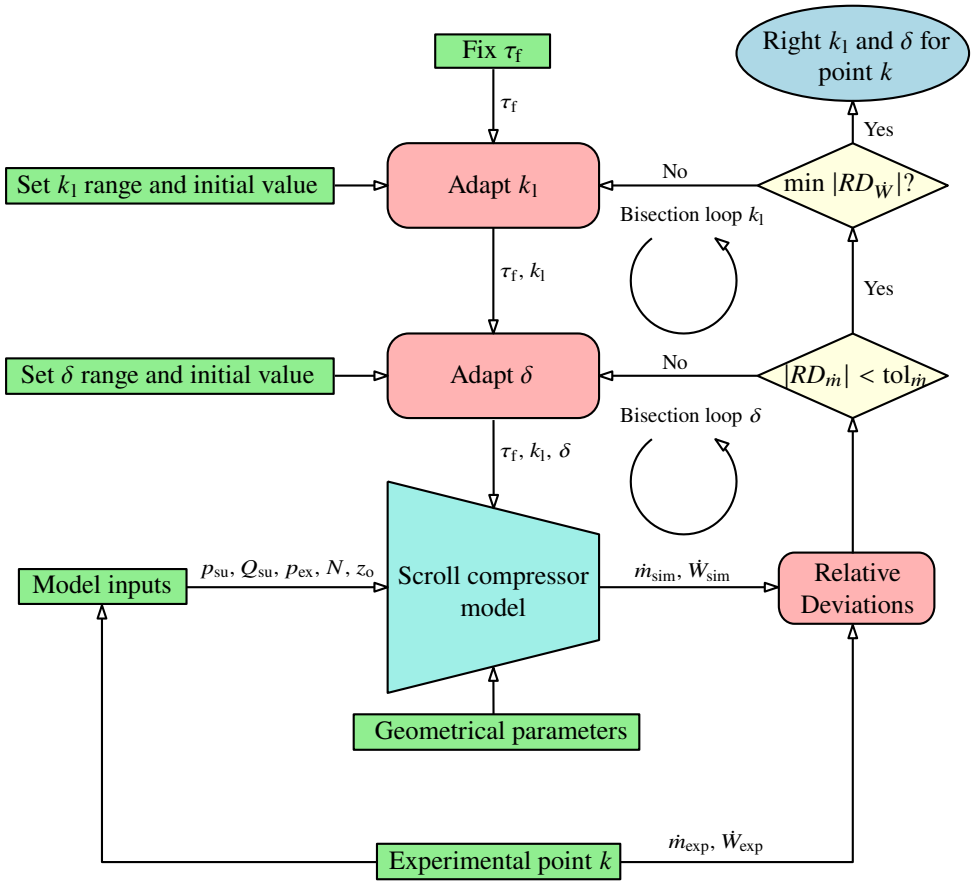

Figure 5.7: Flowchart of the parameter fitting procedure applied to each experimental data point from the retrofitted compressor.

predict the liquid-thickness correction coefficient k_l. Therefore, the following relations can be written:

$$\delta = f(p_{su}, Q_{su}, p_{ex}, N, z_o) \tag{5.2}$$

$$k_l = f(p_{su}, Q_{su}, p_{ex}, N, z_o, \delta) \tag{5.3}$$

The results from these parameter predictions are analyzed in the following subsections. Subsequently, the calibrated models are run using the input conditions derived from the experimental data sets for the two tested compressors. The good validation of the models is finally verified.

5.3.1 Lab-scale prototype

The predicted leakage gaps for the 68 points of the lab-scale experimental data set are presented in Figure 5.8. The x-axis represents the values obtained from the individual calibration procedure, whereas the y-axis shows the direct or cross-validated predicted values from the GP model. Overall, a significant Average Relative Deviation (ARD) of 8.54% is found for the direct prediction, while the ARD is 14.11% for the cross-validation. These deviations may seem high, but according to the sensitivity coefficients calculated in Table 5.2, a 20% increase in the leakage gap would result in a decrease of only 3.04% in the mass flow rate. Moreover, based on the ratio between the prediction and cross-validation relative deviations (which should be comprised between 1 and 2), the algorithm does not exhibit

either overfitting or underfitting. The fitted leakage gaps vary between 6 μm to 78 μm, with an average value of 30.22μm, showing that strong variations in the leakage gap are generated when the input values are varied. Similarly, the prediction of the liquid-thickness correction coefficients can be found in Figure 5.9. Relative deviations of the k_l predictions are way higher than those of the δ predictions, with 23.1% of ARD for the prediction and 54.57% for the cross-validation. According to the sensitivity coefficients calculated in Table 5.2, an increase of 50% in k_l results in a decrease in the mean pressure of 2.49% and an increase in the power consumption of 1.75%, which seems pretty low. Moreover, negative values are predicted, which do not have any physical meaning. Therefore, negatively predicted values are set to zero. The high relative deviations can be explained by values close to zero; for a constant absolute deviation, this results in high numerators (the absolute deviation) divided by low denominators (the close-to-zero value). For these reasons, the Average Absolute Deviation (AAD) is also provided, allowing comparison with the calibration performed on the retrofitted compressor in the subsequent subsection. High deviations in the k_l predictions can also be partially explained by their dependence on the prediction of the leakage gap. Therefore, if deviations already occurred when predicting the leakage gap, the k_l predictions would necessarily be affected. Values of k_l are distributed between 0.1 and 7.9, with an average value of 2.38. As a reminder, the liquid-thickness correction coefficient allows for correcting the liquid-film thickness calculated from the liquid distribution assumptions within the chambers (cfr Section 4.5.4 of Chapter 4). Therefore, a value close to unity indicates that the liquid distribution and leakage modeling assumptions, among other assumptions, are likely close to reality. Nevertheless, a value higher than unity indicates a strong sealing effect, reducing the vapor leakage, while a value lower than unity indicates that the liquid does not exhibit any sealing effect and that high vapor leakage occurs. The issue resulting from the dependence between k_l and δ lies in the fact that, under some conditions, the sealing effect could hide in a low leakage gap instead of a high liquid-thickness correction parameter.

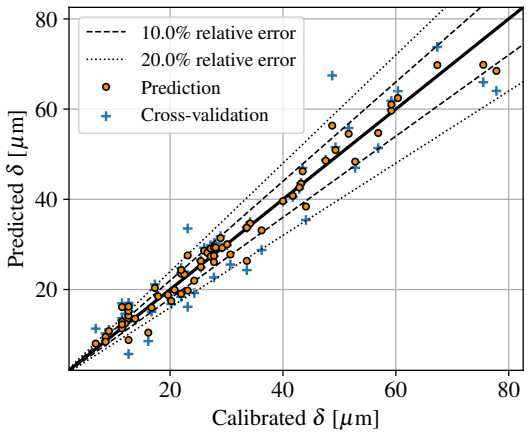

Figure 5.8: GP prediction of the leakage gap δ in the lab-scale prototype. ARD = 8.54% , AAD = 2.09 μm on the prediction and ARD = 14.11%, AAD = 3.45 μm on the cross-validation.

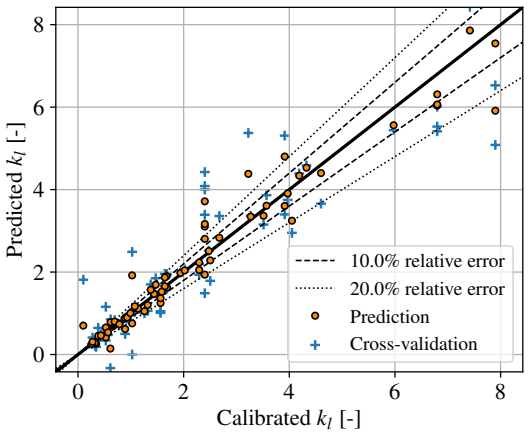

Figure 5.9: GP prediction of liquid-thickness correction coefficient k_l in the lab-scale prototype. ARD = 23.10%, AAD = 0.29 [-] on the prediction and ARD = 54.57%, AAD = 0.57 [-] on the cross-validation.

The results of the lab-scale prototype model validation can be found in Figure 5.10. Overall, despite the limited accuracy of the parameter predictions, the results look promising, with ARD of 2.11% for the mass flow rate, 3.41% for the power consumption and 2.51% for the pressure prediction. It is also worth noting that the fitted friction torque, adjusted by canceling the average deviation of the power consumption, was found to be 1.6 Nm. In comparison, when using three constant parameters, namely the average values of the leakage

gap and liquid-thickness correction factor, together with a fixed friction torque of 1.6 Nm, the ARD increases to 24.73% for the mass flow rate, 13.27% for the power consumption, and 5.08% for the isentropic efficiency. This justifies the need for varying parameters.

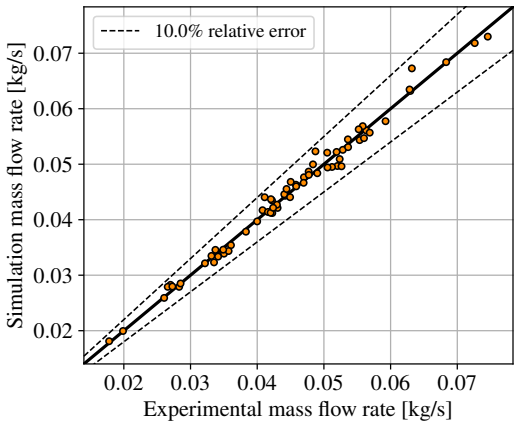

(a) Mass flow rate $\dot{m}$ (ARD = 2.11%).

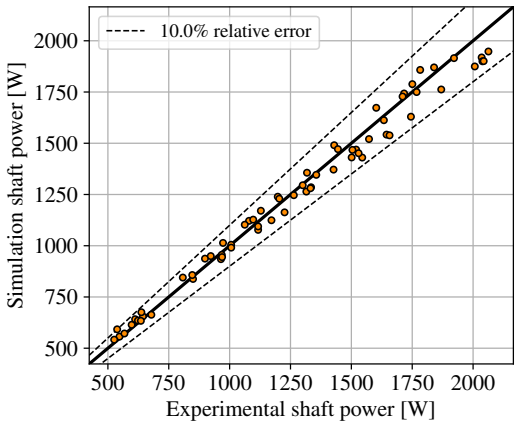

(b) Power consumption $\dot{W}_{\text{shaft,cp}}$ (ARD = 3.41%).

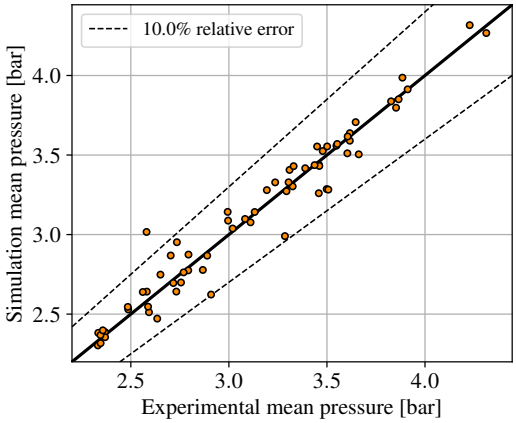

(c) Mean pressure $\bar{p}$ (ARD = 2.51%).

Figure 5.10: Validation results of the lab-scale prototype.

5.3.2 Retrofitted compressor

The predicted leakage gaps for the 269 points of the retrofitted compressor experimental data set are presented in Figure 5.8. Overall, although the graph may appear cluttered because of the high number of points, the predictions are better than those of the lab-scale prototype, with an ARD of 6.85% for the prediction and 9.98% for the cross-validation. The sensitivity coefficient of δ for the retrofitted compressor on the mass flow rate is of the same order of magnitude as that of the lab-scale prototype, therefore, the resulting mass flow rate deviation should be minimal. For this compressor, the fitting leakage gaps range from 4 μm to 38 μm, with an average value of 18.31μm, indicating that the retrofitted compressor may overall have lower gaps than the lab-scale prototype that has gaps going up to 78 μm. In fact, the axial clearance of the prototype was intentionally increased to ensure the safe operation of the machine, which can explain the observed trend. The predicted liquid-thickness correction parameters can be found in Figure 5.12, with important deviation both on the predicted value (ARD of 59.77%) and on the cross-validation (ARD of 116.73%). Again, these significant deviations, already observed in the prototype results, can be explained by the proximity to zero, which induces high relative deviations for a constant absolute deviation trend. By

comparison, the AAD values for the predictions and cross-validation are 0.11 and 0.19, respectively, which are approximately three times lower than the AAD observed in the lab-scale prototype k_l predictions. Once again, the non-physical negative values predicted are set to zero. In general, lower values of k_l are predicted for the retrofitted compressor, with an average value of 0.53, which may be a consequence of the lower δ values. Moreover, only a few values of k_l are higher than 2. The individual fitting of the k_l values is directly based on the power consumption rather than on the pressure evolution. As shown in Figure 5.6, the sensitivity of the power consumption at constant mass flow rate to k_l is quite low. This low sensitivity results from the smaller number of coexisting compression chambers: the pressure increase due to leakage remains limited, as they occur over only through 1.2 rotations of the machine, whereas 2.4 rotations are necessary to realize the compression within the prototype. Furthermore, the radial leakage from the discharge chamber to the compression chambers is not modeled, which is equivalent to having a very high k_l for these leakages. Therefore, lower k_l values are required to allow more vapor leakage, thereby increasing the pressure.

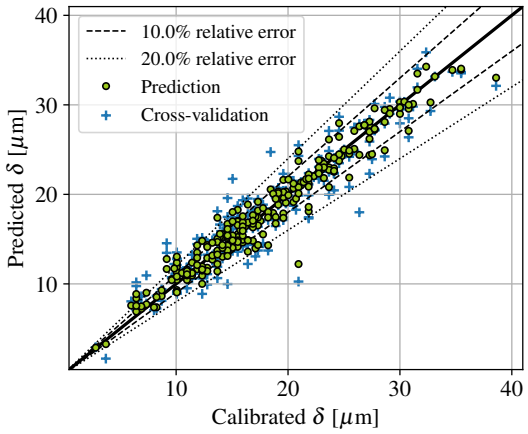

Figure 5.11: GP prediction of the leakage gap δ in the retrofitted compressor. ARD = 6.85%, AAD = 1.09 μm on the prediction and ARD = 9.98%, AAD = 1.55 μm on the cross-validation.

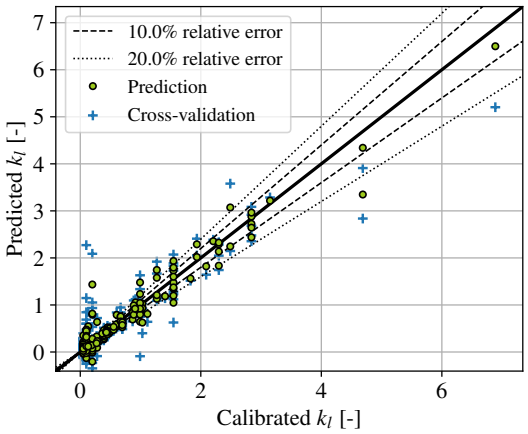

Figure 5.12: GP prediction of liquid-thickness correction coefficient k_l in the retrofitted compressor. ARD = 59.77%, AAD = 0.11 [-] on the prediction and ARD = 116.73%, AAD = 0.19 [-] on the cross-validation.

The results of the retrofitted compressor model validation can be found in Figure 5.10. Overall, despite the limited accuracy of the parameter predictions, the results look promising, with ARD of 2.17% for the mass flow rate and 4.45% for the power consumption. Despite the overall good validation, four mass flow rate points appear to be non-negligibly overpredicted by the model, without any repercussion on the power consumption. These points are most likely the result of model imperfections. In addition, the power consumption seems to be slightly overpredicted at low power and underpredicted at high power, which is again a limitation of the model. It should be noted that no pressure measurements could be performed on this compressor. Eventually, the fitted friction torque, adjusted by canceling the average deviation of the power consumption, was found to be 0.42 Nm, which is non-negligibly lower than the value obtained for the prototype (1.6 Nm). This suggests that the orbiting mechanism is significantly less efficient than that of the retrofitted compressor. Moreover, this difference can also be explained by the larger size of the prototype. As a reminder, the displacement volume of the prototype is 200 cm^3, whereas that of the retrofitted compressor is 86 cm^3. Despite the significant difference in displacement volume, the mass flow rates and power consumptions of the two compressors fall within similar ranges. This can be explained by the experimental testing conditions: the retrofitted compressor could be tested up to 5000 RPM, whereas the prototype could only be tested up to 3250 RPM.

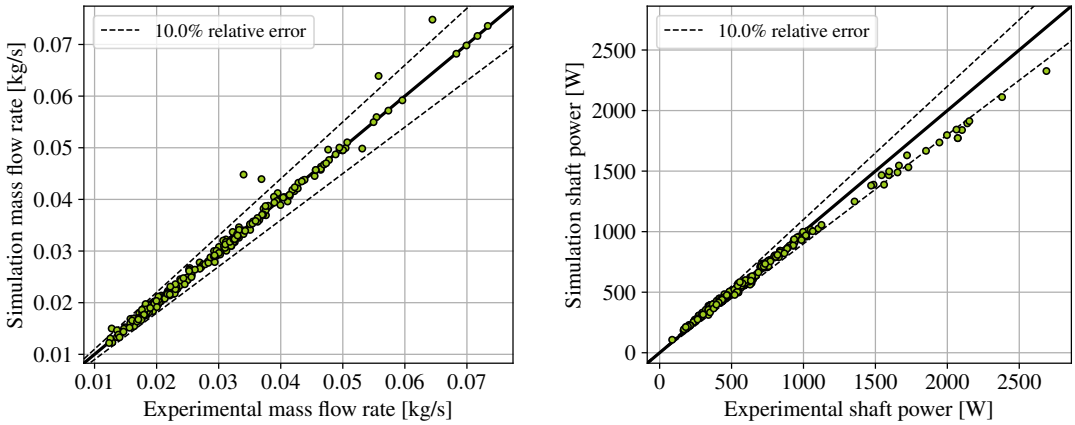

(a) Mass flow rate $\dot{m}$ (ARD = 2.17%). (b) Power consumption $\dot{W}_{\text{shaft,cp}}$ (ARD = 4.45%).

Figure 5.13: Validation results of the retrofitted compressor.

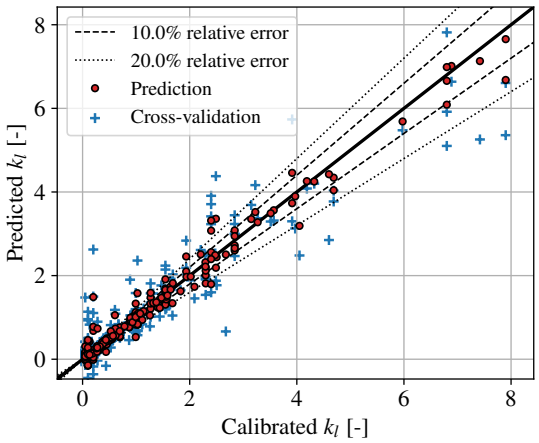

Figure 5.14: GP prediction of liquid-thickness correction coefficient k_1 in both tested machine. ARD = 37.13%, AAD = 0.10 [-] on the prediction and ARD = 105.93%, AAD = 0.27 [-] on the cross-validation.

Finally, the initial idea of obtaining common predictions of the liquid-thickness correction parameter for both machines is implemented using individual calibration data. In fact, unlike the leakage gap, which is strongly machine-dependent, the liquid-thickness correction parameter is based exclusively on the physical principle of the sealing effect produced by the liquid phase. Therefore, if the modeling approach is correct, this parameter should be predicted similarly for both machines. GP predictions of k_1 for both compressors can be found in Figure 5.14. Overall, the relative deviation results lie between those of the compressors taken individually, with an ARD of 37.13% on the prediction and 105.93% on the cross-validation. Nevertheless, the AAD of the prediction is the lowest with a value of 0.1. Validation results using this GP prediction can be found in Appendix C.5. Overall, the validation results from this GP prediction are slightly enhanced, as can be observed in Table 5.5. More specifically, the ARD of the lab-scale prototype predictions is improved for all three output predictions, whereas the validation results of the retrofitted compressor change only marginally. In conclusion, in addition to providing complementary information and confirming observed trends, testing two compressors also enhances the accuracy of the validated model through the numerous experimental points used for calibration.

	Prototype		Retrofitted	
k_1 prediction from	Prototype	Both	Retrofitted	Both
ARD of $\dot{W}_{\text{shaft,cp}}$	3.41%	3.19%	4.45%	4.43%
ARD of $\dot{m}$	2.11%	1.84%	2.17%	2.17%
ARD of $\bar{p}$	2.51%	1.92%		

Table 5.5: ARD of different quantities for k_1 prediction.

5.4 Analysis of the compressor performance

Using the validated deterministic models, the compressor performance can finally be analyzed in depth. The trends observed in the experimental result analyses (Chapter 3), although already partially explained, are further confirmed in this section. First, the overall results from a typical operating point using the lab-scale prototype are analyzed. Then, pressure-angle and pressure-volume diagrams, compared with experimental data, are used to analyze the efficiency losses at these operating points, providing a different perspective on the origin of these losses. Next, individual points allow comparison of the factors influencing leakage, such as speed, vapor quality, pressure ratio and OCR, thereby revealing the mechanisms involved in the efficiency variation and the key difference between the two investigated compressors. Finally, a sensitivity analysis of both models is performed for varying pressure ratios and vapor qualities. Sources of losses, such as mechanical losses, thermal non-equilibrium, leakage, and heat transfer, are progressively added to assess their impact on the isentropic and volumetric efficiencies.

5.4.1 Overall results

The usefulness of a deterministic model in understanding the phenomena involved in two-phase compression lies in its ability to predict the variations in pressure, temperature, and vapor quality in every chamber of the scroll compressor over a full revolution. The experimental data analysis helped identify trends and provide plausible explanations. The individual presentation of the deterministic model's submodels also offered insights into expected behaviors, and the validated deterministic model can now be used to complete the understanding of two-phase compression. First, a typical operating point characteristic of the prototype was simulated to gain insight into the processes occurring within the compressor. The prototype model was simulated with an inlet pressure of 1.5 bar, a pressure ratio of 4, an inlet vapor quality of 0.5, an oil circulation ratio of 0.05 and a speed of 2500 RPM, resulting in isentropic and volumetric efficiencies of 55% and 76%, respectively. The evolution of the pressure throughout the compression can be found in Figure 5.15. As can be seen, the inlet pressure losses are negligible, whereas the discharge pressure losses are significant (0.2 bar), despite the medium simulated speed. The slope of the pressure increase in the first compression chamber (c1/c2) is pretty low, certainly due to the condensation and the leakage occurring. Then, the slope increases slightly, however, despite the built-in volume ratio of 3, a final compression pressure of 3.5 bar could only be achieved at the discharge angle, resulting in a compression ratio of 2.33. The pressure at the discharge angle (3.5 bar) is therefore much lower than the exhaust pressure (6 bar), leading to significant undercompression losses. At the discharge angle, the compression chambers (c1/c2) become discharge chambers (d1/d2) in contact with the discharge ports and a merging phase between the (d1/d2) and dd chambers occurs, resulting in a decrease of the main discharge chamber pressure (dd). It is exactly during this merging phase that the undercompression losses occur: significant pressure drops take place, leading to irreversibilities. Therefore, despite the presence of the discharge valve

preventing backflow into the main discharge chamber, another backflow actually corresponds to the merging process between the d1/d2 and dd chambers. When pressure equilibrium is reached, the new discharge chamber (ddd), resulting from the merging phase, continues to decrease in volume until its pressure once again exceeds the discharge pressure. The vapor quality evolution can be found in Figure 5.16. The first interesting observation that can be made is the fact that, despite the initial vapor quality of 0.5, the vapor quality entering the suction chambers (s1/s2) varies between 0.53 and 0.59. The origin of this increase is twofold: (1) heat transfer at the inlet and within the admission chamber causes partial fluid evaporation, and (2) vapor leakage from the compression chamber raises the vapor quality while reducing the usable volume of the suction chambers. Then, in the first compression chamber, the vapor quality stays constant despite the compression. Again, the origin of this phenomenon is twofold: (1) vapor leakage from the subsequent compression chambers tends to increase the vapor mass within the chamber, and (2) condensation can only result from heat transfer between the liquid and vapor phases, which requires time to occur since the temperature difference is minimal. Then, the compression decreases the vapor quality until the discharge chamber. After the merging phase, despite the difference in vapor quality from the merging chambers (d1/d2 and dd), the resulting discharge chamber (ddd) is considered to have a uniform vapor quality. Finally, the vapor and liquid temperature evolutions can be found in Figures 5.17 and 5.18. Naturally, the vapor temperature closely follows the same trend as the pressure. Nevertheless, the liquid temperature, which is actually subcooled throughout the compression, is not influenced by the pressure. Its temperature is influenced by three phenomena, already described in Section 4.4: (1) partial condensation of saturated vapor during compression, (2) condensation caused by heat transfer, resulting in liquid mass transfer at higher temperature, and (3) heating due to the same heat transfer that initiated condensation. Nevertheless, the temperature difference between the vapor and liquid phases remains relatively small throughout the compression, with only a 10 K difference observed in the discharge chamber.

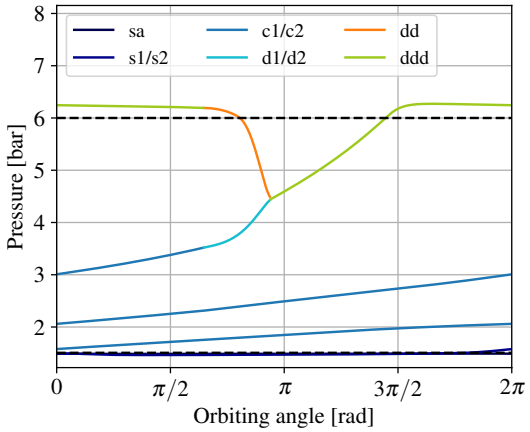

Figure 5.15: Evolution of the pressure in each chamber of the lab-scale prototype (simulation results).

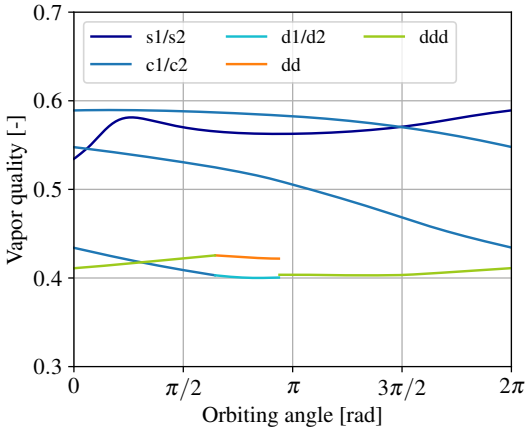

Figure 5.16: Evolution of the vapor quality in each chamber of the lab-scale prototype (simulation results).

5.4.2 Pressure-volume diagrams analysis

The pressure-volume ($p-V$) diagram of a positive-displacement compressor provides detailed insight into its thermodynamic performance. By representing the evolution of pressure with respect to the displaced volume during a full compression cycle, it allows identification of key processes such as suction, compression, discharge, and re-expansion (undercompression

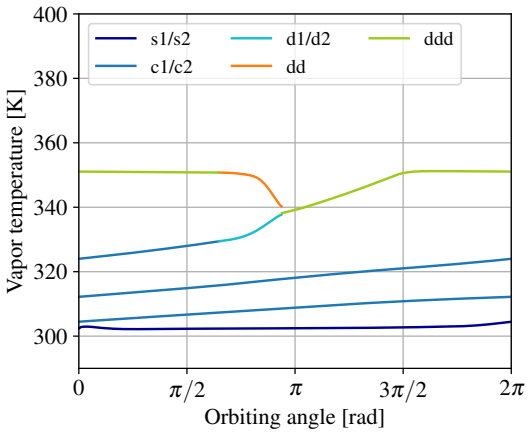

Figure 5.17: Evolution of the vapor temperature in each chamber of the lab-scale prototype (simulation results).

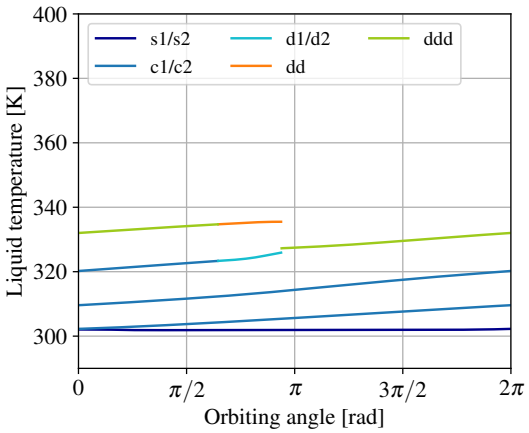

Figure 5.18: Evolution of the liquid temperature in each chamber of the lab-scale prototype (simulation results).

case). The enclosed area of the $p - V$ loop corresponds to the indicated work, from which the indicated power and indicated efficiency can be derived. Deviations of the measured or simulated curve from the ideal theoretical shape reveal the presence of loss mechanisms such as pressure drops, heat transfer, leakage and imperfect compression losses. Consequently, the $p - V$ diagram is a powerful diagnostic and analytical tool for assessing the energetic performance of positive-displacement compressors. To use them effectively, advanced definitions of the volumetric end isentropic efficiencies must first be established based on the work of Lemort et al. (2023). These definitions allow some performance loss mechanisms to be assessed individually by factoring the isentropic and volumetric efficiencies, already defined in Chapter 3 with Equations 3.11 and 3.9, respectively.

Volumetric efficiency

The volumetric efficiency of the scroll compressor can be decomposed into two contributions: pressure and heat transfer losses, and leakage losses. Therefore, the volumetric efficiency can be defined as

$$\varepsilon_{\mathrm{v}} = \frac{\dot{m}}{\dot{m}_{\mathrm{th}}} = \frac{\dot{m}}{\dot{m}_{\mathrm{in}}} \cdot \frac{\dot{m}_{\mathrm{in}}}{\dot{m}_{\mathrm{th}}} = \varepsilon_{\mathrm{v,lk}} \cdot \varepsilon_{\mathrm{v,PT}} \tag{5.4}$$

where $\dot{m}_{\mathrm{th}}$ is the theoretical mass flow rate, defined as the product of the volumetric flow rate and the supply density, and $\dot{m}_{\mathrm{in}}$ is the internal mass flow rate, representing the flow that would enter if leakages were eliminated. Consequently, the volumetric efficiency can be decomposed into two factors: the leakage-related volumetric efficiency, $\varepsilon_{\mathrm{v,lk}}$, and the pressure drop- and heat transfer-related volumetric efficiency, $\varepsilon_{\mathrm{v,PT}}$. The first factor, as indicated by its name, assesses the impact of the leakage on the compressor mass flow rate, whereas the second factor accounts for the mass flow rate reduction induced by heat transfer and pressure drop. The internal flow rate $\dot{m}_{\mathrm{in}}$ can be calculated by adding the actual mass flow rate to the leakage mass flow rate:

$$\dot{m}_{\mathrm{in}} = \dot{m} + \dot{m}_{\mathrm{lk}} \tag{5.5}$$

The leakage mass flow rate, in contrast to what is considered in semi-empirical modeling, refers only to the leakage associated with the suction chambers. Suction-related leakages are the only leakages impacting the mass flow rate of the machine. They can easily be calculated by integrating the instantaneous leakage at each angle step as determined by the deterministic

model. Nonetheless, an important problem has been identified with this definition: it assumes that the density of the leakage entering the suction chambers is the same as the density of the ingested mass. For instance, let us imagine that the leakage consists only of vapor and that the suction mass is predominantly liquid. This would result in a negligible mass contribution from the leakage, although it could occupy a large portion of the volume, leading to a low apparent contribution from leakage and a high one from pressure losses and heat transfer, i.e., an incorrect interpretation. Therefore, in the deterministic model, the internal flow rate can be calculated using the average density in the suction-admission chamber $\bar{\rho}_{sa}$ (downstream of the heat transfer and pressure losses) with the following formula:

$$\dot{m}_{in} = N V_{disp} \bar{\rho}_{sa} \tag{5.6}$$

The leakage-loss mass flow rate can be defined as

$$\dot{m}_{loss,lk} = \dot{m}_{in} - \dot{m} \tag{5.7}$$

It is important to note that the leakage-loss mass flow rate $\dot{m}_{lk,loss}$ is not equivalent to the leakage mass flow rate entering the suction chamber $\dot{m}_{lk}$, but rather to the leakage volumetric mass flow rate entering the suction chamber ($N \cdot V_{disp}$) multiplied by the density of the ingested flow. For instance, liquid leakage occupies a negligible volume in the suction chambers, resulting in a negligible leakage-loss mass flow rate despite the high leakage mass flow rate entering the suction chambers. Conversely, vapor leakage results in a high leakage-loss mass flow rate despite a low leakage mass flow rate.

Isentropic efficiency

Similarly, the isentropic efficiency of the scroll compressor can be decomposed into several factors accounting for different loss mechanisms. Before delving into the decomposition, some work rates that have significant contributions to the machine's performance should first be defined. First, the theoretical power of the machine corresponds to the power it would consume if compressing the theoretical mass flow rate and operating under isentropic specific work conditions. It can be defined as:

$$\dot{W}_{th} = \dot{m}_{th} \cdot (h_{ex,is} - h_{su}) \tag{5.8}$$

It can also be calculated by multiplying the ideal compression work and the rotation speed of the compressor (in RPS), such that

$$\dot{W}_{th} = N \cdot W_{ideal} \tag{5.9}$$

The ideal compression work W_{ideal} can be obtained by integrating the ideal compression curve (isentropic) on the $p - V$ diagram. For instance, it corresponds to the gray curve on Figure 5.19b and the value written as "W_{ideal}". Another important power can be defined within the scroll compressor: the indicated power. Once again, this power can not easily be deduced from the mechanical losses and the power consumption of the machine as could be done in a semi-empirical model. The indicated power is influenced by the continuous heat transfer occurring throughout the compression. Using a deterministic model, it can easily be calculated by integrating the $p - V$ curve of the compressor and multiplying the resulting indicated work by its speed. An illustrating example of the indicated work can also be found in Figure 5.19b with its value written as "W_{real}". Therefore, the indicated power can be calculated as

$$\dot{W}_{in} = N \cdot W_{real} \tag{5.10}$$

Finally, the isentropic efficiency can be decomposed into the following factors:

$$\varepsilon_{is} = \frac{\dot{m}}{\dot{m}_{th}} \cdot \frac{\dot{W}_{in}}{\dot{W}_{shaft,cp}} \cdot \frac{\dot{W}_{th}}{\dot{W}_{in}} = \varepsilon_v \cdot \frac{\dot{W}_{in}}{\dot{W}_{shaft,cp}} \cdot \frac{W_{ideal}}{W_{real}} = \varepsilon_{v,lk} \cdot \varepsilon_{v,PT} \cdot \eta_m \cdot \varepsilon_{in} \tag{5.11}$$

where η_m is the mechanical efficiency and ε_{in} is the indicated efficiency. Four factors thereby contribute to the final isentropic efficiency: the leakage-related volumetric efficiency $\varepsilon_{v,lk}$, the pressure drop- and heat transfer-related volumetric efficiency $\varepsilon_{v,PT}$, mechanical efficiency η_m and the indicated efficiency ε_{in}. The latter can entirely be defined based on $p-V$ diagrams. Their contributions are going to be quantified in the next subsection.

Pressure-volume diagrams

To clarify the position of the dynamic pressure sensor and its role in the pressure-volume diagram, pressure-angle diagrams corresponding to various experimental operating points are presented alongside the respective $p-V$ diagrams. Therefore, the pressure-angle diagrams are plotted over the dynamic pressure measurement range, as already done in Section 3.5.2. The starting orbiting angle (at $\theta = 0$) no longer corresponds to the zero-volume suction chamber, but instead to the angle at which full pressure-sensor coverage is achieved, similarly to the approach adopted in Section 3.5.2. Moreover, the experimental dynamic pressure measurements are displayed on both the $p-\theta$ and $p-V$ diagrams, together with their corresponding ARD values compared to the simulation curves. Similarly to what was done in the experimental investigations (Section 3.5.2), various operating points have been selected for analysis: high, medium and low inlet vapor quality points with high, medium and low pressure ratios (9 points in total). The necessity of plotting diagrams for the nine operating points lies in the visual information that can only be observed in these diagrams, such as pressure losses, leakage, and under-, over-, or ideal-compression trends. To help with the analysis, values of the four contributions to the isentropic efficiency can be found in Table 5.6. Moreover, high-, medium-, and low-vapor-quality $p-V$ diagrams can be found in Figures 5.19, 5.20 and 5.21, respectively. They are inspired by the experimental work from B. Peng et al. (2017). The areas under the ideal curves and the real curves are calculated and displayed on each diagram, allowing a visual representation of the indicated efficiency.

Point	Figure	Vapor quality	Pressure ratio	$\varepsilon_{v,lk}$	$\varepsilon_{v,PT}$	η_m	ε_{in}	ε_{is}	ε_v
1	5.19a	High	High	89.18%	96.66%	79.88%	95.02%	**65.34%**	**86.2%**
2	5.19c	High	Medium	89.96%	95.4%	75.00%	99.49%	**63.95%**	**85.82%**
3	5.19e	High	Low	90.82%	96.13%	76.72%	91.65%	**61.31%**	**87.3%**
4	5.20a	Medium	High	74.07%	93.56%	81.63%	80.87%	**45.69%**	**69.3%**
5	5.20c	Medium	Medium	82.53%	95.06%	74.31%	95.41%	**55.55%**	**78.46%**
6	5.20e	Medium	Low	84.18%	95.53%	72.28%	94.31%	**54.74%**	**80.42%**
7	5.21a	Low	High	66.16%	88.53%	75.61%	82.28%	**36.39%**	**58.57%**
8	5.21c	Low	Medium	65.65%	86.8%	72.70%	79.1%	**32.74%**	**56.98%**
9	5.21e	Low	Low	68.17%	87.96%	70.82%	90.67%	**38.46%**	**59.96%**

Table 5.6: Contribution to the isentropic and volumetric efficiencies for 9 experimental operating points.

Naturally, the points represented in Table 5.6 are experimental points, numerically simulated with the validated deterministic model of the lab-scale prototype. Thus, all the results presented in the table are simulated with the inputs taken from tested experimental conditions. These results allow a deeper understanding of the performance by analyzing the factors contributing to the isentropic and volumetric efficiencies.

As a first observation, the isentropic and volumetric efficiencies drop when the vapor quality decreases; this result was already observed in the experimental investigations. Moreover, the analysis also confirms that the influence of the leakage on the volumetric efficiency is more important than the influence of the pressure losses and heat transfer, for all the points. As a matter of fact, the influence from the leakage becomes critical at low vapor quality: it is the main contribution to the poorest isentropic efficiency encountered. In general, the highest leakage-related volumetric efficiencies are observed at low pressure ratios, which is consistent with expectations. Interestingly, the pressure drop- and heat transfer-related volumetric efficiency also decreases with decreasing vapor quality, which can be attributed to flow evaporation and higher pressure encountered upstream of the suction process. The mechanical losses appear relatively high, as indicated by the relatively low mechanical efficiency, nevertheless, they remain of the same order of magnitude regardless of the vapor quality or pressure ratio. The observed slight decrease in mechanical efficiency can be attributed to the growing dominance of mechanical losses, due to the slightly lower power consumption when decreasing the vapor quality. The last contribution to the isentropic efficiency is the indicated efficiency. This efficiency gathers the contribution of the thermal non-equilibrium, leakage not related to the suction chambers and non-ideal compression. Overall, the indicated efficiencies are unexpectedly high, even at low vapor qualities, where the simulated pressure curve appears somewhat close to and parallel with the ideal pressure curve. From the observation of Figure 5.19d, it appears that, in the absence of discharge pressure drops, the indicated efficiency could exceed unity. An explanation for this phenomenon could be leakage from the compression chambers to the suction chamber, leading to a lower density in the compression chamber than in the ideal case, and resulting in a lower pressure evolution. Overall, a higher indicated efficiency is traded for a lower leakage-related volumetric efficiency at a high vapor quality. Conversely, if a volumetric efficiency higher than one could be achieved, it would probably result in a reduction in indicated efficiency due to a higher density than the ideal-case density in the compression chamber. At high vapor quality, the indicated efficiency is fully consistent: approximately equal to 1 for perfect compression, slightly lower for undercompression (95.02%), and even lower for overcompression (91.65%). Nevertheless, this trend is not respected anymore at lower vapor qualities. For medium vapor qualities, it appears that undercompression leads to high losses; however, these losses are not directly attributed to undercompression itself, but rather to leakage or heat transfer that increases the pressure before discharge, as represented in Figure 5.20b. The impact of the reed valve is clearly observable in the case of undercompression: after the discharge angle θ_d, a sudden pressure rise occurs until pressure equilibrium is reached, and volumetric compression continues thereafter, almost isentropically, as already reported by Huang (2012). The impact of undercompression can be represented by the small additional area defined by this sudden pressure rise, which remains relatively low compared with the total area under the curve. Without a reed valve, this pressure rise would have reached the exhaust pressure, generating a non-negligible area that represents a consequent amount of extra work over one compressor revolution. Finally, at low vapor qualities, all three points exhibit undercompression trends, resulting in lower indicated efficiency. In general, undercompression losses do not appear as vertical lines, as is often depicted when defining undercompression. It therefore seems, when observing undercompression, that the losses are not generated by the undercompression itself, with the extra work it would bring after the discharge, but rather by an increase in pressure, which could be the result of leakage or thermal non-equilibrium. Undercompression is thus detrimental for two-phase compression, but not through the expected mechanism. Leakages seem to be generated between the discharge chamber and the compression chambers, resulting in a higher pressure in the compression chambers. Moreover, thermal non-equilibrium could also be emphasized at higher pressure ratios. In conclusion, the proposed methodology enables the identification of the main causes of the low isentropic efficiency at low vapor

qualities: reduced volumetric efficiency, primarily due to high volumetric leakage entering the suction chambers, along with a slight reduction in indicated efficiency due to undercompression, leakages throughout the compression and thermal non-equilibrium. The important drop in leakage-related volumetric efficiency with the decrease in vapor quality implies high leakage-loss mass flow rate $\dot{m}_{\mathrm{lk}}$, defined in Equation 5.7. Therefore, increasing the liquid mass fraction appears to increase the leakage-loss mass flow rate, which is represented in the deterministic model by an increase in the leakage gap. This increase in leakage gap may be caused by the appearance of a vertical force on the compressor tip seals due to liquid flashing into vapor during radial leakage flows or simply by the tip seal becoming stuck due to the significant presence of liquid. Besides, the contribution of mechanical efficiency is also significant, and the indicated efficiency is not as low as might have been expected, but still decreases when observing undercompression.

Regarding the validation of the pressure curves, as indicated by the low ARD calculated within the validity window of the $p - \theta$ diagrams, the agreement is quite good. However, the unexpected behavior of the experimental pressure curves outside the validity window at low vapor qualities remains unexplained.

5.4.3 Individual points comparison

The previous analysis revealed that leakage has a detrimental impact on compressor performance, especially at low vapor quality and low speed, for the experimental data analyzed. The same trend was observed when analyzing the experimental results of Chapter 3, Section 3.4.1 via the volumetric efficiency. The previous analysis is, however, lacking data at high speeds and low vapor quality due to test bench limitations during the campaign carried out on the lab-scale prototype. The analysis of the experimental data presented in Chapter 3 enabled the application of an interpolation algorithm to analyze the effect of an increase in speed on the volumetric efficiency, indicating a major improvement (Section 3.4.2). Nevertheless, it is still unclear what causes this improvement, as it could occur from a reduction in leakage or from leakage becoming relatively less significant compared to the total mass flow rate, especially at low vapor quality and high speed. Moreover, another misunderstood phenomenon is the reduction in leakage due to the reduced residence time of the fluid within the machine at higher speeds.

Therefore, based on the decomposition of the volumetric efficiency, it is possible to deepen the analysis and determine the consequences of an increase in speed on leakage. First, the effects of the leakage, heat transfer and pressure losses on the mass flow rate delivered by the machine must be recalled. The mass flow rate is impacted by heat transfer and pressure losses, since the density of the fluid entering the suction chambers is lower than the supply density, resulting in a decreased volumetric capacity. Moreover, the leakages fill a part of the suction chamber volume, also reducing the volumetric capacity. Two variables can therefore be defined: the pressure drop- and heat transfer-related loss mass flow rate $\dot{m}_{\mathrm{loss,PT}}$, and the already defined leakage-related loss mass flow rate $\dot{m}_{\mathrm{loss,lk}}$. They are linked to the delivered and theoretical mass flow rates through the following equation:

$$\dot{m} = \dot{m}_{\mathrm{th}} - \dot{m}_{\mathrm{loss,PT}} - \dot{m}_{\mathrm{loss,lk}} \tag{5.12}$$

To calculate those mass flow rates, the following definitions can be used, based on the internal mass flow rate $\dot{m}_{\mathrm{in}}$ defined in Equation 5.6:

$$\dot{m}_{\mathrm{loss,PT}} = \dot{m}_{\mathrm{th}} - \dot{m}_{\mathrm{in}} \tag{5.13}$$

$$\dot{m}_{\mathrm{loss,lk}} = \dot{m}_{\mathrm{in}} - \dot{m} \tag{5.14}$$

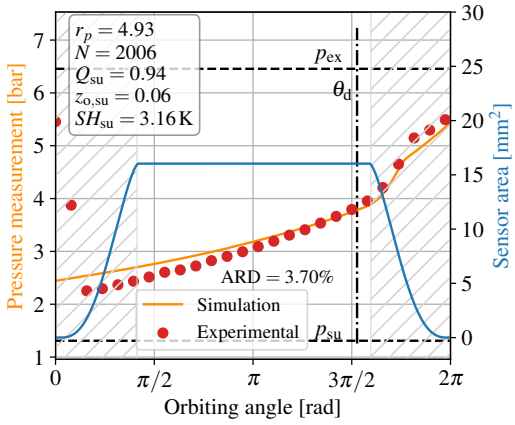

(a) $p - \theta$ at a high pressure ratio.

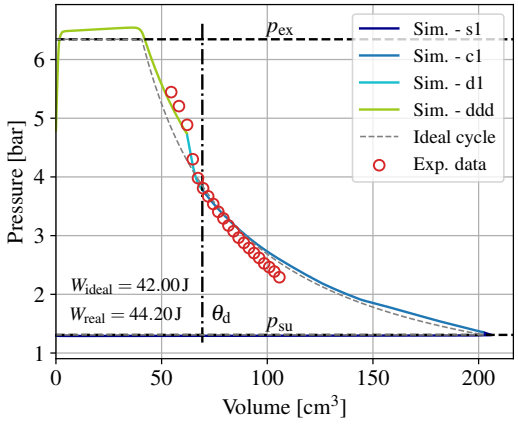

(b) $p - V$ at a high pressure ratio.

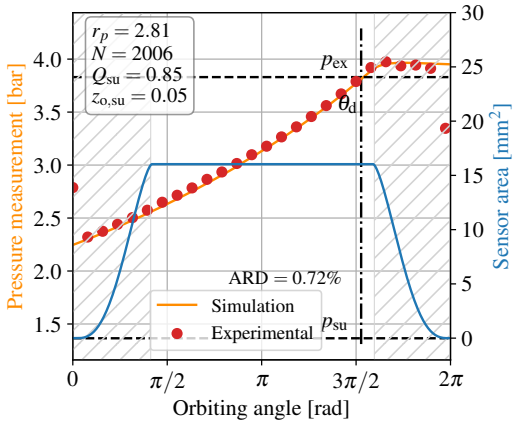

(c) $p - \theta$ at a medium pressure ratio.

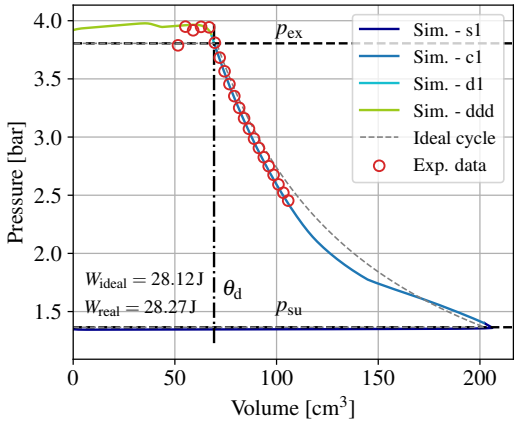

(d) $p - V$ at a medium pressure ratio.

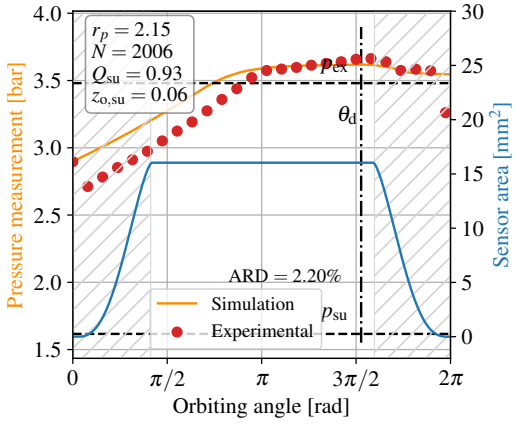

(e) $p - \theta$ at a low pressure ratio.

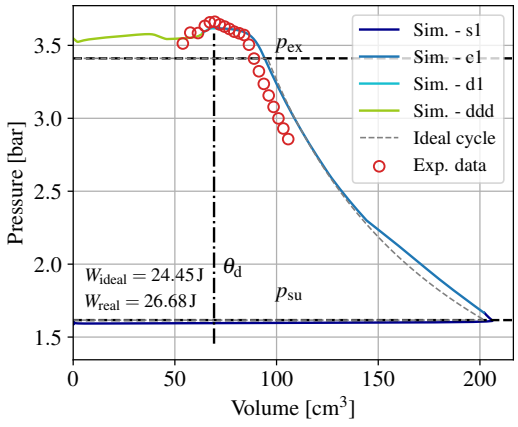

(f) $p - V$ at a low pressure ratio.

Figure 5.19: Pressure-angle and corresponding pressure-volume diagrams at high vapor quality experimental points for low, medium, and high pressure ratios.

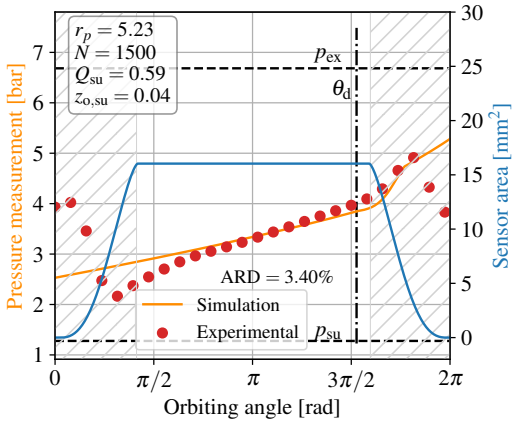

(a) $p - \theta$ at a high pressure ratio.

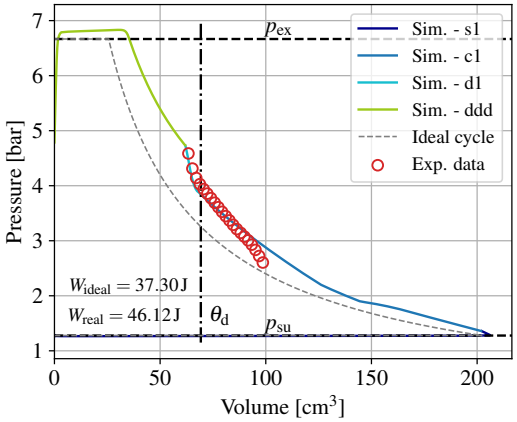

(b) $p - V$ at a high pressure ratio.

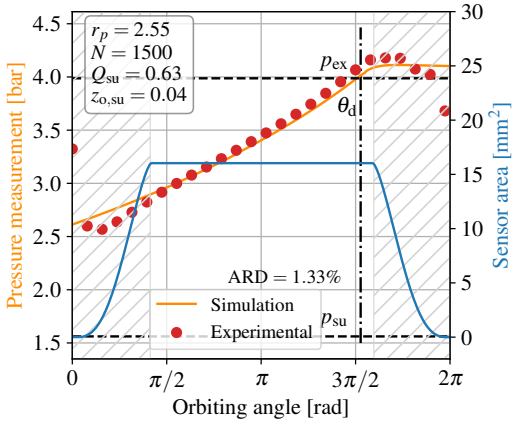

(c) $p - \theta$ at a medium pressure ratio.

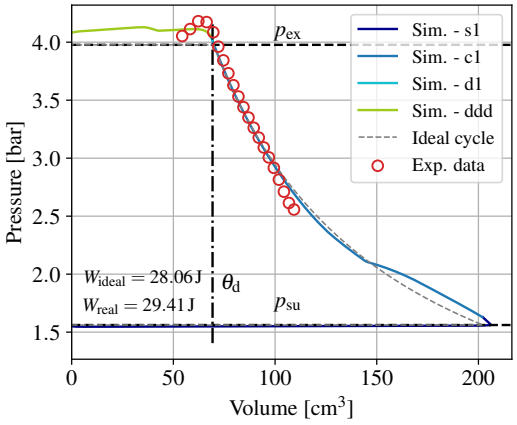

(d) $p - V$ at a medium pressure ratio.

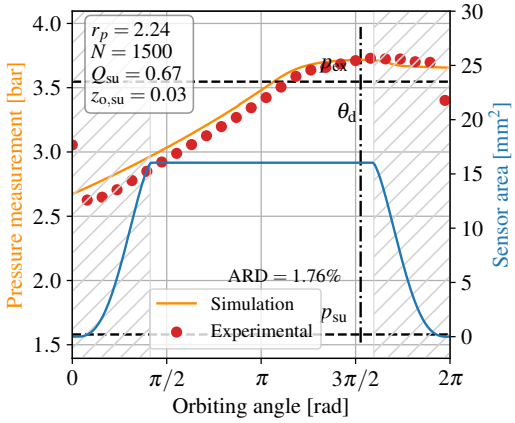

(e) $p - \theta$ at a low pressure ratio.

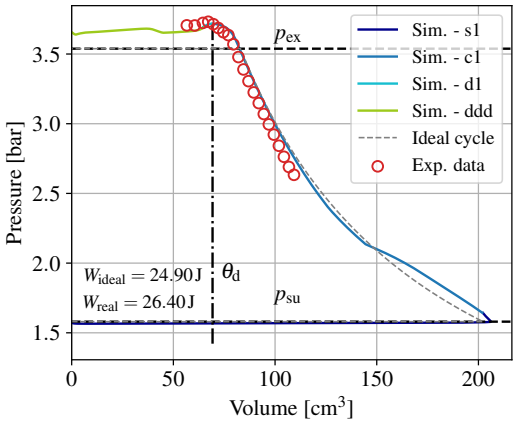

(f) $p - V$ at a low pressure ratio.

Figure 5.20: Pressure-angle and corresponding pressure-volume diagrams at medium vapor quality experimental points for low, medium, and high pressure ratios.

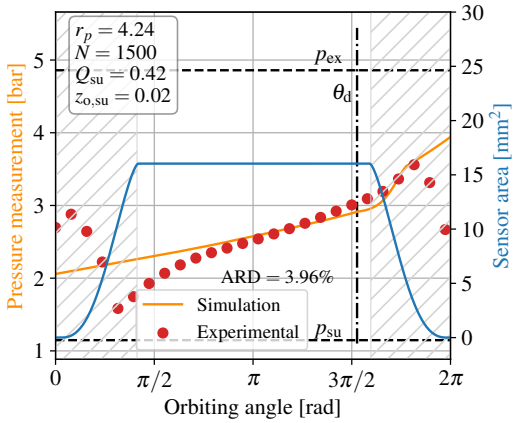

(a) $p - \theta$ at a high pressure ratio.

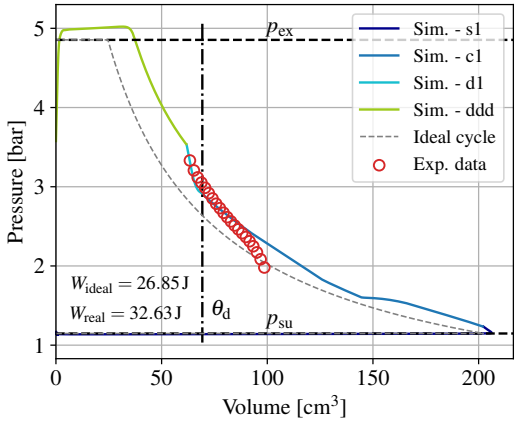

(b) $p - V$ at a high pressure ratio.

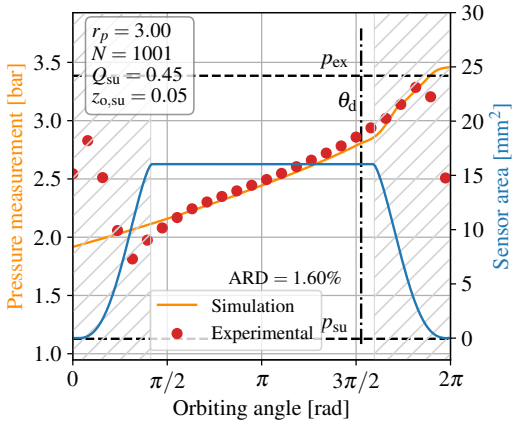

(c) $p - \theta$ at a medium pressure ratio.

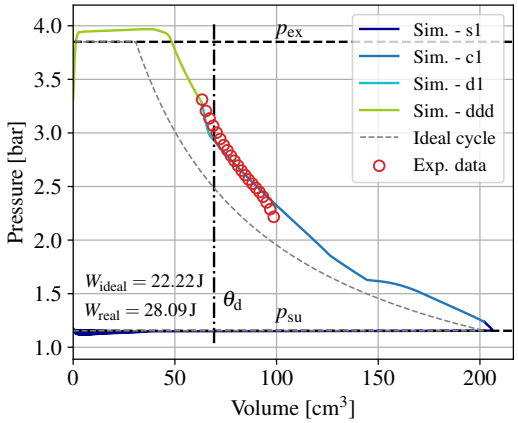

(d) $p - V$ at a medium pressure ratio.

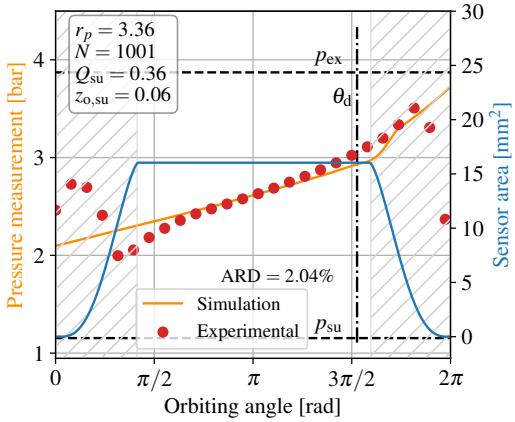

(e) $p - \theta$ at a low pressure ratio.

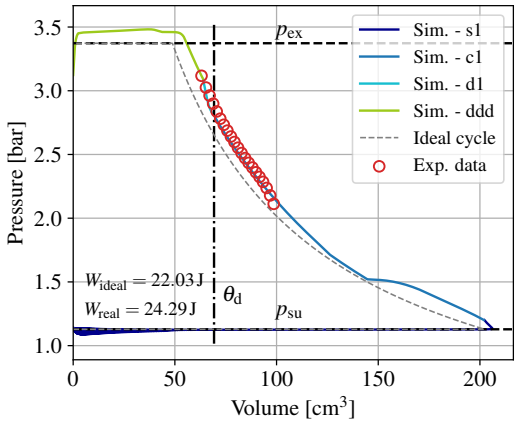

(f) $p - V$ at a low pressure ratio.

Figure 5.21: Pressure-angle and corresponding pressure-volume diagrams at low vapor quality experimental points for low, medium, and high pressure ratios.

Particular attention must be paid to the leakage-related loss mass flow rate $\dot{m}_{\text{loss,lk}}$, which does not represent the mass flow rate leaking to the suction chamber, but rather the suction mass flow rate that cannot enter the suction chamber due to volume pre-filled by leakage.

In addition to the influence of speed, the impact of a decrease in vapor quality can also be investigated using the same methodology. Finally, the influence of the pressure ratio on both the retrofitted compressor and the lab-scale prototype can also be investigated.

The simulated point of Section 5.4.1, i.e., an inlet vapor quality of 0.5, a pressure ratio of 4 with an OCR of 0.05 and an inlet pressure of 1.5 bar, is here simulated at two different speeds: 1000 RPM and 4000 RPM to check the impact on the volumetric efficiency. Moreover, another point, representing the use of 4 compressors placed in parallel and running at 1000 RPM, enables a comparison of the mass flow rates with a single machine running at 4000 RPM. The results can be found in Table 5.7. The results, along with the leakage gaps calculated by the model, are presented in Table 5.7. The results confirm a non-negligible increase in volumetric efficiency when increasing the speed, which was already observed in the experimental results. Nevertheless, the leakages associated with the speed of 4000 RPM, are consequently higher than the leakage at 1000 RPM, which can be explained by the higher leakage gap calculated by the Gaussian prediction of the parameters. Therefore, despite the largest leakages at 4000 RPM, the volumetric efficiency is higher. Moreover, the pressure drop- and heat transfer-related loss mass flow rate is also higher at 4000 RPM. These observations lead to the following conclusion: the volumetric efficiency improvement at higher speed and low vapor quality is only the consequence of the relatively lower importance of the mass flow rate loss compared to the theoretical mass flow rate. The expected "sealing effect" does not exist at the analyzed operating conditions, and the leakage is even increased due to a larger gap area. As already stated, an explanation for this increase in gap area could be the tip seal becoming stuck due to the significant presence of liquid within the compressor or being lifted upward due to flashing liquid refrigerant during leakages.

Regarding the reduced residence time of the fluid at higher speed, its importance depends on how the problem is considered:

- When speaking in mass flow rate, the unit depends on the time, thus, the residence time implicitly considered is always 1 second, regardless of the machine speed. In this case, a higher mass flow rate is obtained at higher speed, while the sum of the leakage-related mass flow rate and the pressure drop- and heat transfer-related mass flow rate becomes proportionally lower, increasing the volumetric efficiency.
- When looking at the problem over one compressor revolution, the theoretical mass entering the suction chambers is the same regardless of the speed, while the residence time is lower at a higher speed, resulting in a better filling of the suction chamber over one revolution, which also leads to an increase in volumetric efficiency.

Number of compressors	Speed [RPM]	Leakage gap [μm]	$\dot{m}_{\text{th}}$ [g/s]	$\dot{m}_{\text{loss,PT}}$ [g/s]	$\dot{m}_{\text{loss,lk}}$ [g/s]	$\dot{m}$ [g/s]	$\varepsilon_{\text{v,PT}}$ [-]	$\varepsilon_{\text{v,lk}}$ [-]	ε_{v} [-]
1	1000	21.25	55.06	3.59	11.26	40.21	93.47%	78.13%	73.03%
4	1000	21.25	220.24	14.36	45.04	160.84	93.47%	78.13%	73.03%
1	4000	41.92	220.24	15.55	26.25	178.44	92.94%	87%	81.06%

Table 5.7: Impact of an increase in compressor speed on the volumetric efficiency of the lab-scale prototype.

The impact of a decrease in vapor quality on leakage can be evaluated by comparing the nominal operating point at a speed of 4000 RPM and a vapor quality of 80% with the same operating point at a vapor quality of 50% (i.e., the same point as in Table 5.7). The results can be found in Table 5.8. The first row corresponds to the operating point at a vapor quality of 80%, and the second row corresponds to the same point with an inlet quality of 0.5. The

impact of the decrease in vapor quality can clearly be seen in both pressure drop- and heat transfer-related loss mass flow rate $\dot{m}_{\text{loss,PT}}$ and leakage-related loss mass flow rate $\dot{m}_{\text{loss,lk}}$, which increase consequently. Despite the increase in mass flow rate losses, the resulting volumetric efficiency only slightly decreases from 83.69% to 81.06%, limited by the relative increase of the theoretical mass flow rate at low vapor quality.

Number of compressors	Vapor quality [-]	Leakage gap [μm]	$\dot{m}_{\text{th}}$ [g/s]	$\dot{m}_{\text{loss,PT}}$ [g/s]	$\dot{m}_{\text{loss,lk}}$ [g/s]	$\dot{m}$ [g/s]	$\varepsilon_{\text{v,PT}}$ [-]	$\varepsilon_{\text{v,lk}}$ [-]	ε_{v} [-]
1	0.8	35.59	137.44	8.16	14.25	115.03	94.06%	88.98%	83.69%
1	0.5	41.92	220.24	15.55	26.25	178.44	92.94%	87.00%	81.06%

Table 5.8: Impact of a decrease in vapor quality on the volumetric efficiency of the lab-scale prototype.

The impact of the pressure ratio is examined for both machines in Table 5.9. As already observed in the experimental investigations presented in Chapter 3, the volumetric efficiency of the retrofitted compressor is much more affected by variations in pressure ratio than that of the lab-scale prototype. The leakage-related mass flow rate is increased significantly, due to the proximity between the suction chambers and the discharge chamber, working at higher pressures. For the lab-scale prototype, the larger number of compression chambers (i.e., larger scroll involute angles) prevents any direct leakage between the discharge chamber and the suction chambers; therefore, the pressure ratio does not affect the leakage. A higher pressure ratio could nonetheless affect the compressor's work with more leakages within the compression chambers.

Type of compressors	Pressure ratio [-]	Leakage gap [μm]	$\dot{m}_{\text{th}}$ [g/s]	$\dot{m}_{\text{loss,PT}}$ [g/s]	$\dot{m}_{\text{loss,lk}}$ [g/s]	$\dot{m}$ [g/s]	$\varepsilon_{\text{v,PT}}$ [-]	$\varepsilon_{\text{v,lk}}$ [-]	ε_{v} [-]
Retrofitted	2	33.07	89.68	3.52	12.00	74.13	96.07%	86.03%	82.66%
Retrofitted	4	33.07	89.68	3.99	17.3	68.40	95.55%	79.80%	76.25%
Prototype	2	41.92	220.24	15.55	25.2	179.49	93.68%	87.00%	81.50%
Prototype	4	41.92	220.24	15.55	26.25	178.44	92.94%	87.00%	81.06%

Table 5.9: Impact of an increase in pressure ratio on the volumetric efficiency for both investigated compressors.

The impact of the OCR on the volumetric and isentropic efficiencies has been experimentally observed in Chapter 3, Section 3.4.3, showing an overall increase in both efficiencies for an increase in OCR at high vapor quality but a decrease at low vapor quality. The possible reason for this increase at low vapor quality is the increase in leakage due to a change in flow pattern, as a higher liquid thickness would be present at the bottom of the pockets. Conversely, the highest viscosity obtained at high vapor quality seems to decrease the leakage. These two effects are further analyzed numerically in Table 5.10, where a comparison between two operating points at different OCR, for low and high vapor quality is presented. As can be seen, the obtained numerical results are in agreement with the experimental results obtained, i.e., when the OCR is increased, the volumetric efficiency decreases at low vapor quality, while it increases at high vapor quality. The apparent reason for the variation in leakage is the change in leakage gaps associated with the change in OCR. These variations in leakage gaps may encapsulate submodel inaccuracies or other effects that are not taken into account in the model. For instance, the increase in leakage gap at a low vapor quality may include flashing from the liquid refrigerant in the oil, while the decrease at a low vapor quality may be the result of a sealing effect. For the four investigated points, the parameter k_1 is predicted to be zero by the model, which does not help explaining the origin of the leakage variation.

Vapor quality [-]	OCR [-]	Refrigerant-only vapor quality [-]	Leakage gap [μm]	$\dot{m}$ [g/s]	$\dot{m}_{\text{loss,lk}}$ [g/s]	$\varepsilon_{\text{v,PT}}$ [-]	$\varepsilon_{\text{v,lk}}$ [-]	ε_{v} [-]	ε_{in} [-]	ε_{is} [-]
0.4	5%	0.42	22.38	49.83	15.55	93.56%	76.22%	71.31%	65.05%	42.46%
0.4	10%	0.45	24.34	47.31	17.25	92.80%	73.28%	67.00%	64.32%	40.12%
0.8	5%	0.84	16.30	28.00	5.73	96.65%	83.00%	80.22%	83.21%	59.88%
0.8	10%	0.89	11.30	29.7	3.43	97.30%	89.65%	87.23%	84.72%	66.66%

Table 5.10: Impact of an increase in the OCR on the volumetric and isentropic efficiencies at low and high vapor quality for the retrofitted compressor (speed of 2500 RPM, pressure ratio of 4).

5.4.4 Sensitivity analysis

The $p - V$ diagram analysis is only based on real experimental data, simulated using the validated deterministic model. Therefore, it only shows the trends of experimental points that have been tested on the test bench, using the lab-scale prototype. The deterministic model can also be used to extend the analysis to operating points that could not be tested on the test bench due to limitations. Furthermore, the comparison of individual points allows comparison of variations in vapor quality, speed, pressure ratio, and OCR in detail; however, it provides only limited information on general trends due to the limited amount of data presented by tables. In addition, information is missing on the contributions to the efficiency losses within the indicated efficiency and the distribution of heat transfer and pressure losses on the volumetric efficiency. Therefore, a deeper analysis is required to determine these contributions and further improve the understanding of certain trends.

To better understand the impact of different loss mechanisms on the compressors' performance, a sensitivity analysis of the efficiencies is carried out. The analysis considers how, successive non-ideal effects such as mechanical losses, thermal non-equilibrium, leakages and heat transfer affect the isentropic and volumetric efficiencies as a function of the pressure ratio and the vapor quality. The successive curve starts with the near-ideal curve, where only the non-ideal compression, i.e., undercompression and overcompression losses, and the pressure losses are taken into account. Then, each curve adds the contribution of a given loss source, thereby illustrating its relative influence on the compressor's behavior. With this different approach, the contribution of the thermal non-equilibrium appears clearer. Furthermore, the heat transfer influence can be isolated from the pressure loss influence. In addition, the already observed influence of the mechanical loss and leakage will be confirmed. The pressure losses could not be isolated from the non-ideal compression losses, as the flow models implemented in the deterministic model require a pressure difference to perform. The contributions of each submodel are added sequentially in an order chosen to minimize interactions between them. For instance, mechanical losses play an important role in heating the lumped mass, and the impact of heat transfer would be different if they were added first.

The first comparison is done on the lab-scale prototype comparing two speeds: 4000 RPM and 1500 RPM, at a constant vapor quality of 0.5. The inlet pressure is fixed at 1.5 bar and the OCR at 0.05 for all the results presented in this subsection. As can be seen in Figures 5.22 and 5.23, a high speed is detrimental to the discharge pressure losses. The most ideal curve is more than 10% point below the maximum efficiency of 1 at the speed of 4000 RPM, while it is only 2% point below the maximum at 1500 RPM. The shape of the curve is a typical curve for a pressure ratio variation. Surprisingly, when adding the mechanical losses to the plot, the impact (difference between the two curves) is more important at a lower speed. The value of the mechanical loss is undoubtedly higher for a higher speed, but relatively lower when compared to the total power consumption. The effect of the thermal non-equilibrium is more important at a low speed, indicating that turbulence effects enhance the heat transfer at high speed. The impact of the leakage is considerable and, as previously observed, it is a

function of the pressure ratio. Finally, the impact of the heat transfer is non-negligible but does not seem to be impacted by the pressure ratio. Overall, similar results are observed for the all-combined-effects curves, in terms of shape and value, regardless of the speed.

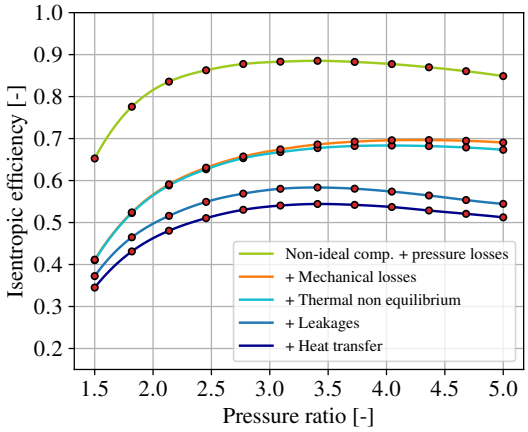

Figure 5.22: Sensitivity analysis of the isentropic efficiency as a function of pressure ratio at a vapor quality of 0.5 and a speed of 4000 RPM for the lab-scale prototype.

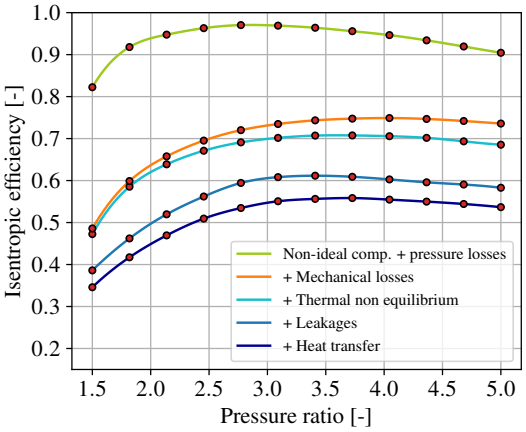

Figure 5.23: Sensitivity analysis of the isentropic efficiency as a function of pressure ratio at a vapor quality of 0.5 and a speed of 1500 RPM for the lab-scale prototype.

Volumetric efficiencies for the same comparison can be found in Figures 5.24 and 5.25. The near-ideal curve is a constant value at both speeds. The maximum value reached at the speed of 4000 RPM is 0.95 due to the high suction pressure losses, while an efficiency higher than one is observed at the lower speed. A volumetric efficiency higher than one is a well-known phenomenon resulting from the maximum suction volume not coinciding with the end of the revolution. Then, adding the mechanical losses to the near-ideal curve does not impact the volumetric efficiency, and neither does adding the thermal equilibrium. These two submodels, without suction heat transfer, do not play any role in the suction process. The leakage, however, seems to have a stronger impact at low speed, which can be explained by the relatively higher leakage compared to the lower theoretical mass flow rate, thereby decreasing the volumetric efficiency. Moreover, the leakage gaps are usually smaller at low speeds, which confirms this explanation. Finally, including heat transfer in the volumetric efficiency analysis leads to the same conclusion as for the isentropic efficiency: its impact is not dominant and remains similar at both speeds, and does not evolve with the pressure ratio.

The second analysis compares the isentropic efficiencies of the lab-scale prototype and the retrofitted compressor at the same speed of 4000 RPM. Overall, higher efficiency could be achieved with the lab-scale prototype at this speed. The impact of pressure losses is more pronounced on the lab-scale prototype, as demonstrated by the lower maximum of the near-ideal curve, likely due to the higher mass flow rate. Naturally, a larger discharge port area was designed to avoid these pressure losses; nonetheless, they still have a significant impact. Mechanical losses are lower for the retrofitted compressor, which can be supported by the 4 times lower friction torque value obtained throughout the model calibrations. The lab-scale prototype, due to its hand-made Oldham-ring-based orbiting mechanism and radial compliance, seems to generate much more friction than the ball mechanism of the retrofitted compressor without compliance. Finally, the impact of the thermal non-equilibrium is significant on the retrofitted compressor. Once again, it may be the result of lower turbulence due to the lower displacement volume of this compressor.

The comparison between the two compressors continues with the volumetric efficiency, which can be found in Figures 5.28 and 5.29. Once again, the suction pressure losses seem very low for the retrofitted compressor, as indicated by the value higher than 1, while a maximum

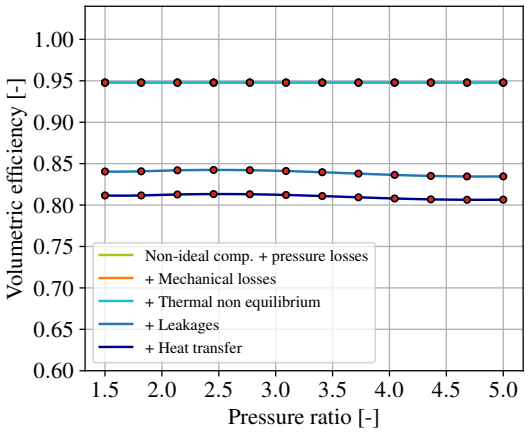

Figure 5.24: Sensitivity analysis of the volumetric efficiency as a function of pressure ratio at a vapor quality of 0.5 and a speed of 4000 RPM for the lab-scale prototype.

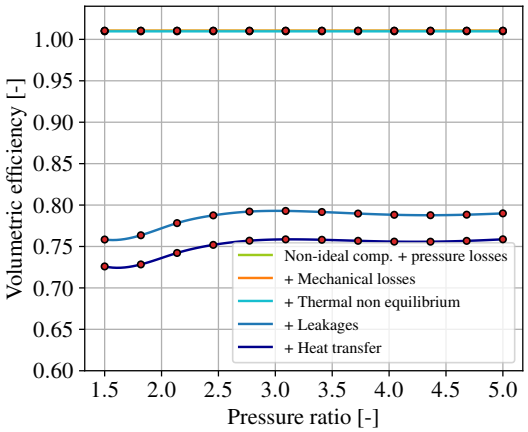

Figure 5.25: Sensitivity analysis of the volumetric efficiency as a function of pressure ratio at a vapor quality of 0.5 and a speed of 1500 RPM for the lab-scale prototype.

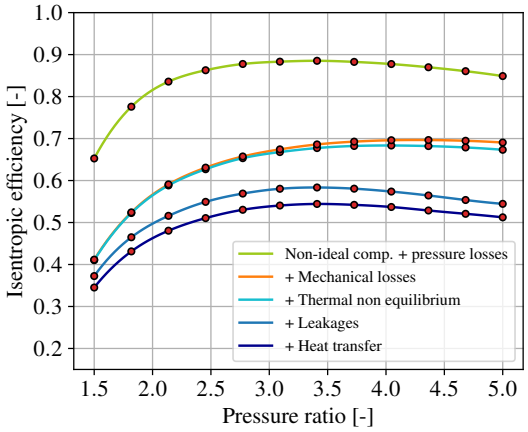

Figure 5.26: Sensitivity analysis of the isentropic efficiency as a function of pressure ratio at a vapor quality of 0.5 and a speed of 4000 RPM for the lab-scale prototype.

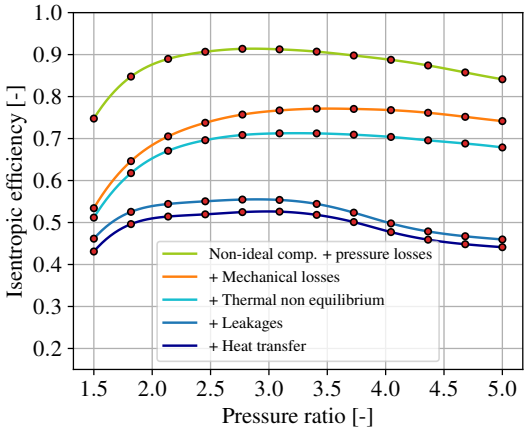

Figure 5.27: Sensitivity analysis of the isentropic efficiency as a function of pressure ratio at a vapor quality of 0.5 and a speed of 4000 RPM for the retrofitted compressor.

of 0.95 is achieved by the lab-scale prototype. In contrast, for the retrofitted compressor, the impact of leakage is significant and strongly pressure-ratio dependent. This dependence on the pressure ratio can be explained by the lower number of coexisting compression chambers for this compressor, which increases the impact of the discharge pressure on the suction chambers leakage. Conversely, for the lab-scale prototype, no direct leakage area can be found between the discharge chamber and the suction chamber; therefore, the pressure ratio does not impact the leakage. No explanation could be found for the wavy behavior of the curves.

The third analysis compares the isentropic efficiency of the retrofitted compressor for a variation in speed. A similar analysis is already proposed for the prototype in Figures 5.22 and 5.23; however, the different behaviors observed experimentally between the two machines make this comparison interesting to see how the speed differently (and similarly) impacts the two machines. The comparison can be found in Figures 5.30 and 5.31. For this machine, particularly at low speed, the impact of mechanical losses strongly depends on the pressure ratio, as the lower power consumption makes these losses relatively more significant. Similarly, the impact of thermal non-equilibrium is also important under the same conditions,

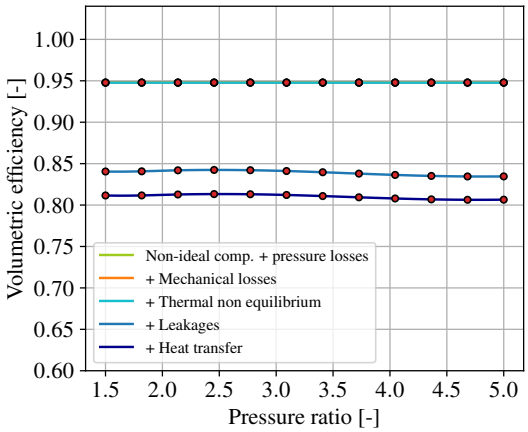

Figure 5.28: Sensitivity analysis of the volumetric efficiency as a function of pressure ratio at a vapor quality of 0.5 and a speed of 4000 RPM for the lab-scale prototype.

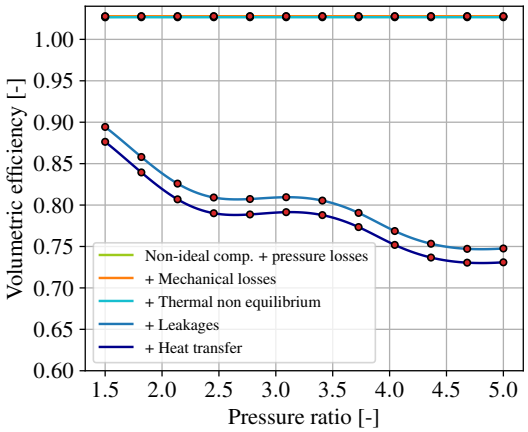

Figure 5.29: Sensitivity analysis of the volumetric efficiency as a function of pressure ratio at a vapor quality of 0.5 and a speed of 4000 RPM for the retrofitted compressor.

which could be due to its relatively high impact, but also to the quasi-separated flow at the compressor inlet, limiting heat transfer between the two phases. The pressure losses are also strongly impacted by the increase in speed, as evidenced by the maximum in isentropic efficiency, reaching a value of 97% at 1500 RPM and 92% at 4000 RPM. Eventually, the pressure losses negatively impact the highest speed, however, the mechanical losses and thermal non-equilibrium effects, which are more significant at lower speeds, compensate for the pressure losses, resulting in a similar isentropic efficiency curve in terms of magnitude. Nevertheless, a difference can be observed in the shape of the curves. The maxima of the curves are shifted towards higher pressure ratios when increasing the speed. This effect, already observed experimentally, is the result of the reduction of undercompression losses at high speed, due to a less sharp increase of pressure when the compression chambers open to the discharge chamber (mixing phase). This trend can be analyzed more deeply using $p-V$ diagrams, representing the near-ideal case at 1500 and 4000 RPM, in undercompression. These diagrams can be found in Figure 5.32. First, they allow to clearly observe the additional pressure losses generated by the increase in speed, considerably increasing the area under the curve, resulting in a lower indicated efficiency. Moreover, despite the ideality of the curve, the ideal cycle still lies below the real curve. This phenomenon has already been described in Section 5.4.2: a volumetric efficiency higher than 1 can theoretically be achieved, at the expense of an indicated efficiency lower than 1, due to the additional compression work. A final observation is the decrease of the undercompression losses at higher speed, explained by the smoother rise of pressure of the merging phase at the opening of the compression chambers. This effect can more specifically be observed in Figures 5.32c and 5.32d, where, for the same conditions, the compression work at 1500 RPM is clearly higher than at 4000 RPM.

In addition to the varying-pressure-ratio analysis, the impact of the vapor quality will be directly investigated by using the same methodology, using a variation of the vapor quality instead of the pressure ratio (in the x-axis). For this analysis, the pressure ratio has been fixed at a value of 4. Isentropic efficiency comparison between the lab-scale prototype and the retrofitted compressor can be found in Figures 5.33 and 5.34. For the lab-scale prototype, it seems that, when adding the losses one by one, the near-ideal curve is just shifted towards lower values. The lower efficiency at low vapor quality can therefore be explained by increased undercompression or increased discharge pressure losses. Overall, the same trends can be observed for both compressors, except for the thermal non-equilibrium

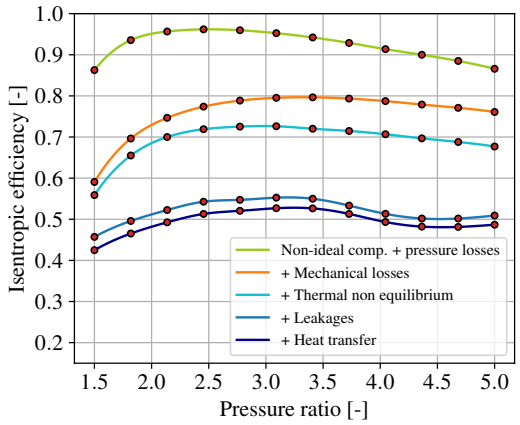

Figure 5.30: Sensitivity analysis of the isentropic efficiency as a function of pressure ratio at a vapor quality of 0.5 and a speed of 1500 RPM for the retrofitted compressor.

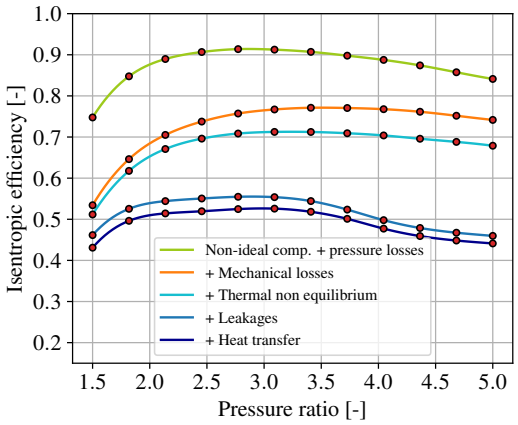

Figure 5.31: Sensitivity analysis of the isentropic efficiency as a function of pressure ratio at a vapor quality of 0.5 and a speed of 4000 RPM for the retrofitted compressor.

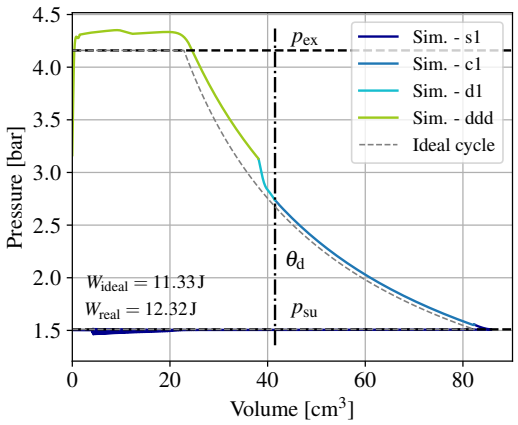

(a) $p - V$ diagram at 1500 RPM.

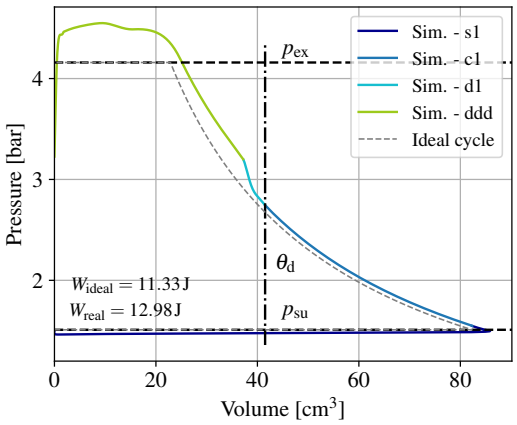

(b) $p - V$ diagram at 4000 RPM.

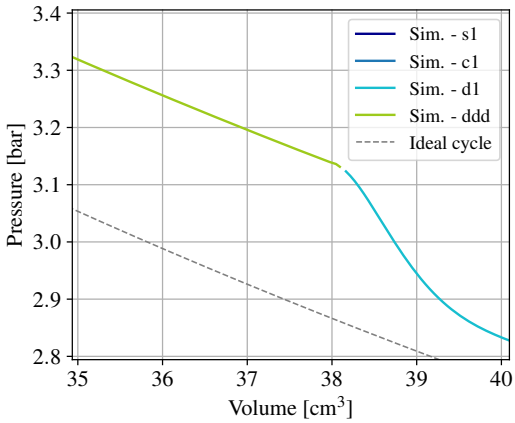

(c) Zoom of the $p - V$ diagram at 1500 RPM.

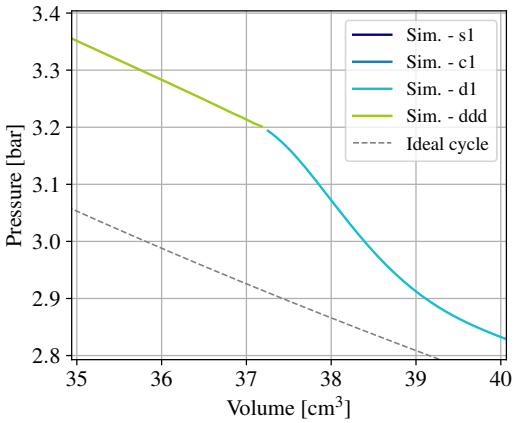

(d) Zoom of the $p - V$ diagram at 4000 RPM.

Figure 5.32: Pressure–volume diagrams and zoom of the merging phase for the retrofitted compressors in the near-ideal case at 1500 RPM and 4000 RPM in undercompression conditions.

contribution that seems more consequent for the retrofitted compressor. At this pressure ratio and speed, when decreasing the vapor quality, the leakage impact remains constant

for the lab-scale prototype, while it increases for the retrofitted compressor. This constant impact for the lab-scale prototype was not highlighted in the previous p–V diagram analysis, where the leakage impact seemed more pronounced. Nevertheless, high speed could not be experimentally tested on the lab-scale prototype, especially at low vapor quality, due to test-bench limitations. The analyses are thus compatible.

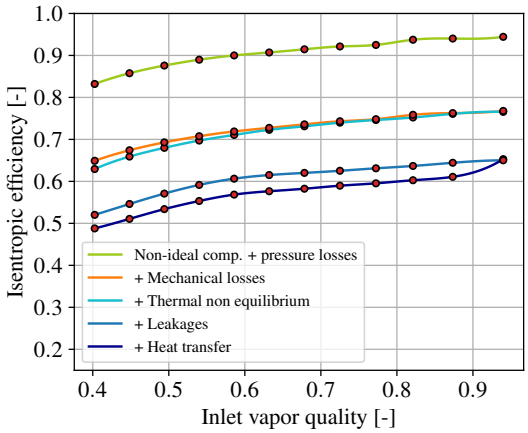

Figure 5.33: Sensitivity analysis of the isentropic efficiency as a function of the vapor quality at a pressure ratio of 4 and a speed of 4000 RPM for the lab-scale prototype.

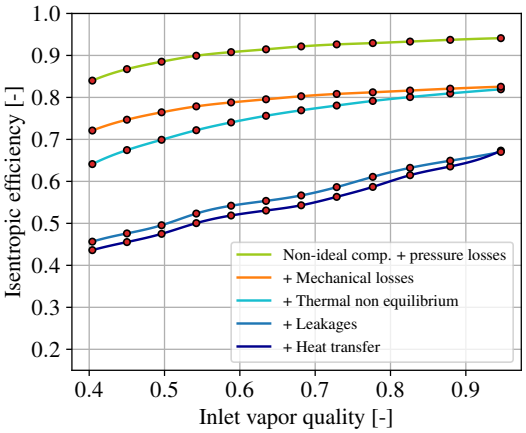

Figure 5.34: Sensitivity analysis of the isentropic efficiency as a function of the vapor quality at a pressure ratio of 4 and a speed of 4000 RPM for the retrofitted compressor.

Finally, the last results to be analyzed are the volumetric efficiency comparison for both compressors, with a varying inlet vapor quality. This comparison can be found in Figure 5.35 and 5.36. In general, volumetric efficiencies are also negatively impacted by the decrease in vapor quality. Once again, the first curve seems to be shifted when adding the losses for the lab-scale prototype. Therefore, the near-ideal curve is already impacted, and lower vapor qualities seem to increase the suction pressure losses. In contrast, the near-ideal curve of the retrofitted compressor is not impacted by the decrease in vapor quality. Again, the impact of leakage is significant for both machines, especially for the retrofitted compressor at low vapor quality. Two explanations can be given for this trend: first, the direct contact between the discharge chamber and the suction chamber in the retrofitted compressor, and second, the relative importance of the leakage mass flow rate compared to the theoretical mass flow rate as vapor quality varies. Therefore, despite its lower leakage gaps, the retrofitted compressor is more sensitive to leakage. This conclusion is consistent with the findings of the experimental investigation.

5.5 Summary and conclusions

This chapter constitutes the pillar of any modeling work: the model calibration and validation using experimental data retrieved from Chapter 3. Hence, the deterministic models introduced in Chapter 4 from the two experimentally investigated compressors are validated. The calibration targeted three parameters with clear physical meaning: the leakage gap δ, the liquid-thickness correction coefficient k_l, and the friction torque τ_f. Three or two outputs could be used for this calibration: the mass flow rate $\dot{m}$, the shaft power consumption $\dot{W}_{\text{shaft,cp}}$, and the mean pressure $\bar{p}$ (only for the lab-scale prototype). The embedded GP submodels, trained on individually fitted parameter pairs, enabled prediction of the input-dependent parameters: δ and k_l. The resulting validation exhibits good agreement: for the lab-scale prototype, ARD values of 1.84% ($\dot{m}$), 3.19% ($\dot{W}_{\text{shaft,cp}}$), and 1.92% ($\bar{p}$) were obtained; for the retrofitted compressor, ARD values of 2.17% ($\dot{m}$) and 4.45% ($\dot{W}_{\text{shaft,cp}}$) were achieved.

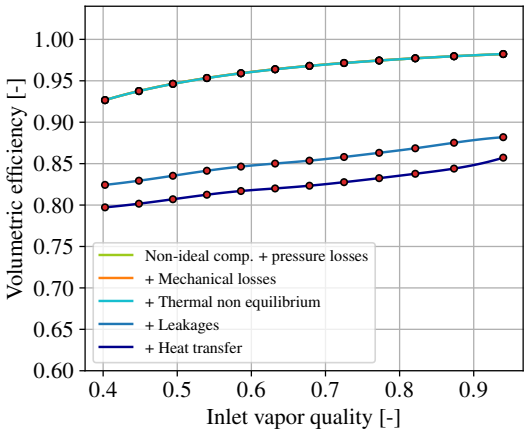

Figure 5.35: Sensitivity analysis of the volumetric efficiency as a function of the vapor quality at a pressure ratio of 4 and a speed of 4000 RPM for the lab-scale prototype.

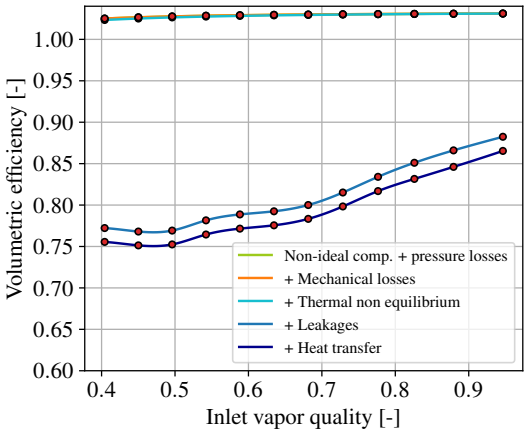

Figure 5.36: Sensitivity analysis of the volumetric efficiency as a function of the vapor quality at a pressure ratio of 4 and a speed of 4000 RPM for the retrofitted compressor.

The analysis of the results is organized into four complementary parts. First, the variations with the shaft angle of the main model variables, such as the pressure, the vapor quality and the two phases temperatures, are analyzed in order to first identify diverse phenomena occurring within the compressor, such as the thermal non-equilibrium, pressure losses and the importance of vapor leakage. Second, the validated $p - V$ diagrams are analyzed to provide a mechanistic understanding of the compression process and to identify the main sources of deviation from ideal behavior under different operating conditions. To this aim, the isentropic efficiency is decomposed into four contributing factors: the leakage-related and pressure loss/heat transfer-related volumetric efficiencies, and the mechanical and indicated efficiency. The pressure-volume diagram-derived indicated efficiency makes it possible to understand the contributions of non-ideal compression losses and thermal non-equilibrium. Next, individual points are compared in tables to investigate the impacts of variations in vapor quality, speed, pressure ratio, and OCR on the compressor performance. The impact of leakage is clarified in these tables, and the key difference between the two machines is highlighted. Finally, a sensitivity study of the isentropic and volumetric efficiencies is performed to quantify the respective influence of the various loss mechanisms, mechanical friction, leakage, heat transfer, and thermal non-equilibrium, on the overall performance of the compressor. This final analysis allows to decouple the effects of the non-ideal compression and thermal non-equilibrium losses influencing the indicated efficiency. Moreover, it also allows to decouple the volumetric efficiency contribution of the pressure losses and heat transfer.

The main outcomes of this chapter can be summarized as follows:

- Inputs-dependent parameters could be individually calibrated for the lab-scale prototype using a double-bisection process, minimizing the relative deviation on the mass flow rate and on the mean pressure. The friction torque value was then adjusted to minimize the average relative deviation of the power consumption (3 fitted parameters for 3 outputs).
- A similar procedure is applied to the retrofitted compressor, with the first bisection loop used to minimize the power consumption relative deviation of each point. Again, the friction torque was obtained by minimizing the average relative deviation of the whole dataset (3 fitted parameters for 2 outputs).
- Values of the leakage gaps were found to be higher for the lab-scale prototype (up to 80 μm vs 38 μm) and values of the liquid-thickness correction parameters were found to be generally lower for the retrofitted compressor. The higher leakage gaps can be

explained by the higher axial clearance of the prototype. Nevertheless, the smaller value of k_l may be a limitation of the model, over-correcting the sealing effect for a potentially-wrong initial assumption. Moreover, the friction torque of the prototype is four times higher than that of the retrofitted compressor (1.6 Nm vs. 0.42 Nm).

- The analysis of the lab-scale prototype simulated point at low vapor quality indicates that vapor leakage in the suction chambers is significant, as well as exhaust pressure losses.
- The analysis of the validated pressure-volume diagram indicates the strong influence of the leakage on the isentropic efficiency at low vapor quality for the low tested speeds. This analysis highlights the importance of volumetric (rather than mass) leakage entering the suction chamber, as it pre-fills the space and reduces the compressor capacity. The influence of the mechanical losses is also considerable for the prototype, as illustrated by its high friction torque value. Finally, although undercompression is clearly observed as evidenced by the indicated efficiencies, the most detrimental impact arises from leakage, especially at low speed, where the proportion of leakage relative to the theoretical mass flow rate is high. Unfortunately, the analysis of the impact of the lowest vapor qualities, performed on simulated experimental points, is limited to low speeds due to test bench limitations.
- Then, individual point analyses underline in detail the impacts of variations in vapor quality, speed, pressure ratio, and OCR on volumetric and isentropic efficiency. As already observed experimentally, a decrease in vapor quality considerably increases leakage, thereby reducing volumetric efficiency. Nevertheless, despite the increase in leakage with increasing speed, the relative contribution of leakage-related mass flow rate compared to the increasing theoretical mass flow rate results in an overall improvement in volumetric efficiency. Moreover, the key difference between the two investigated compressors resides in the impact of the pressure ratio, which significantly influences the volumetric efficiency of the retrofitted compressor, while it does not affect that of the lab-scale prototype. This behavior is explained by the direct contact between the discharge chamber and the suction chambers, allowing suction-related leakage to vary with the pressure ratio in the retrofitted compressor. The larger size of the lab-scale prototype allows to avoid this unwanted effect.
- Finally, the results of the sensitivity analysis indicate that leakages and the pressure losses are the primary source of both volumetric and isentropic efficiency decrease at low vapor quality for both machines. It was also observed that the lab-scale prototype manages the leakage and the thermal non-equilibrium better than the retrofitted compressor, certainly due to higher turbulence. Nevertheless, high mechanical losses were observed in the prototype due to the higher friction torque value, a consequence of its prototype design.

Therefore, this chapter provides both a qualitative and quantitative understanding of the impact of two-phase flow on scroll compressor performance, thereby addressing the primary research question raised in the introduction. This complete analysis of the compressor performance under two-phase conditions motivates the design-oriented recommendations presented in the conclusion chapter of this thesis. The overall trends observed from the experimental and simulation results are also summarized in the conclusion as well as the perspectives of the work.

References

Virtanen, Pauli et al. (Mar. 2020). "SciPy 1.0: Fundamental Algorithms for Scientific Computing in Python". In: *Nature Methods* 17.3, pp. 261–272. ISSN: 1548-7091, 1548-7105. DOI: 10.1038/s41592-019-0686-2. (Visited on 11/03/2025).

Bell, Ian H. et al. (Nov. 2012a). "Liquid Flooded Compression and Expansion in Scroll Machines - Part II: Experimental Testing and Model Validation". In: *International Journal of Refrigeration* 35.7, pp. 1890–1900. ISSN: 01407007. DOI: 10.1016/j.ijrefrig.2012.07.008.

Quoilin, Sylvain and Schrouff, Jessica (May 2016). "Assessing Steady-State, Multivariate Experimental Data Using Gaussian Processes: The Gpexp Open-Source Library". In: *Energies* 9.6, p. 423. ISSN: 1996-1073. DOI: 10.3390/en9060423.

Peng, Bin, Zhao, Shengxian, and Li, Yaohong (Oct. 2017). "Thermodynamic Model and Experimental Study of Oil-free Scroll Compressor". In: *Journal of Physics: Conference Series* 916, p. 012048. ISSN: 1742-6588, 1742-6596. DOI: 10.1088/1742-6596/916/1/012048. (Visited on 09/10/2025).

Lemort, Vincent, Olivier, Gérard, and De Pelsemaker, Christophe (2023). *Thermal Energy Management in Vehicles*. Automotive Series. Hoboken, NJ: John Wiley and Sons, Inc.

Huang, Paul Xiubao (2012). "Under-Compression (Over-Expansion) – An Isochoric Or Adiabatic Process?" In: *Proceedings of the International Compressor Engineering Conference*. Ray W. Herrick Laboratories, Purdue University.

Chapter 6

Conclusions and Perspectives

6.1 Toward a deeper understanding of two-phase compression

Two-phase compression, from both machine and thermodynamic cycle performance perspectives, has been investigated numerically since the 1990s and experimentally since the 2000s. However, the lack of understanding of performance sensitivity to two-phase conditions requires a deeper study of scroll compressors operating with two-phase refrigerant flow.

Therefore, this PhD thesis, entitled "*Contribution to the improvement of scroll compressors operating under two-phase conditions*", aims to answer the following key question introduced in the introduction chapter: how can two-phase compression be made efficient enough to be of practical interest? Elements of answer to this question, applied to scroll compressors, are provided following a well-known investigation pathway: experimental testing, numerical modeling, model validation, and results analysis. Thereby, the answer is progressively developed throughout the thesis manuscript. This investigation procedure may primarily appear as a series of steps required to fully understand a topic, as presented in this manuscript; however, it is far from being that simple. When starting these investigations, the author had no clue where to begin, on either the experimental or numerical side, given the limited literature available on the topic. Therefore, the numerical and experimental investigations were conducted in parallel: numerical findings guided the experimental investigations, while experimental findings clarified the direction of the numerical investigations. Ultimately, this journey toward a deeper understanding of two-phase compression did not follow any predefined structure, and was just guided by problem-solving, opening the way to new problems to be solved. Many discussions, readings, reflections, questioning, observations, explorations, and overthinking, have guided this research work, to eventually find appropriate answers and to reach the point where a conclusion can be drawn. This iterative procedure progressively opened the way to all investigated fields addressed in the thesis. Besides, they helped define the boundaries of the research fields, allowing to find the right trade-off between depth of the investigations and time constraints. Beyond those boundaries can be found further research options, also known as "perspectives". Throughout this journey, the author was often asked to give shape to the investigations and the results obtained through conference papers, journal articles, presentations and deliverables. They allowed this research to be restructured and shaped in order to communicate it to other researchers potentially interested in it. This PhD manuscript represents the final form of this research and is structured to facilitate the understanding of its investigations and findings, following a clear guiding thread.

This concluding chapter presents a summary of the contributions of this PhD thesis. The main contributions of each chapter are therefore outlined to highlight their key outcomes and findings. It is followed by an overview of the principal experimental observations, their physical interpretation and corresponding numerical validation. Possible answers to the key question "How can two-phase compression be made efficient enough to be of practical interest?" are then presented before concluding with the perspectives of this research work.

6.2 Contributions of the PhD thesis

The contributions and outcomes of this PhD thesis have already been presented in the conclusions of each chapter. Nevertheless, a summary of the important outcomes and contributions is presented hereunder:

- **Chapter 1. Introduction**
  This chapter introduces the motivations behind this research by providing a state-of-the-art on the use of two-phase flow in positive-displacement compressors, both in terms of machine performance and thermodynamic cycle performance. A practical application is proposed where a heat pump cycle, using two-phase compression with varying vapor qualities at the compressor inlet is investigated. The obtained results are strongly dependent on the compressor performance, showing that higher heat pump coefficients of performance can be achieved if a decent compressor isentropic efficiency is maintained at low vapor quality. This leads to the following question: how can two-phase compression be made efficient enough to be of practical interest?

- **Chapter 2. Oil-Refrigerant Mixture Modeling**
  The role of oil–refrigerant mixtures in this research work became so significant that it ultimately obtained a dedicated chapter. This chapter introduces the modeling of oil-refrigerant mixture starting with a new approach where the two-phase mixture is distributed in four parts (two components and two phases), leading to the basic equations defining the mixtures. The properties of two oil-refrigerant mixtures are then modeled and validated using experimental data obtained from setups of the Schaufler Chair of Refrigeration, Cryogenics and Compressor Technology of the Technische Universität Dresden. Two-phase mixture properties, such as the enthalpy and entropy, could be derived from there. Finally, applications based on two-phase mixture properties, used in the subsequent numerical modeling of this thesis (e.g., heat transfer and compression), are presented. They highlight the need for a simplifying modeling assumption, conceptualized as the "desolubilization" of the oil-refrigerant mixture.

- **Chapter 3. Two-phase Compression: Experimental Investigations**
  This chapter presents the experimental investigations conducted on two scroll compressors, using a test bench that allows control of the inlet pressure, pressure ratio, inlet vapor quality, oil circulation ratio and the compressor speed. The objective of this test bench is to record the compressor performance, namely the delivered mass flow rate and power consumption, which are then translated into volumetric and isentropic efficiencies. A retrofitted compressor withstood two-phase conditions for more than 200 hours of operation without any signs of damage. Moreover, a third-version lab-scale prototype was tested for at least 70 hours of operation, with minor damage observed. A detailed analysis of the performance is provided, examining how volumetric and isentropic efficiencies vary with the five control variables. The main findings from this analysis are gathered below, and physical interpretations are also provided. The lab-scale prototype is equipped with a dynamic pressure sensor, allowing partial measurement of the compression and discharge chambers' pressure. The pressure evolution over one revolution confirms the analyses derived from the performance results. Moreover, it constitutes an additional variable for validating the deterministic model developed in the following chapter.

- **Chapter 4. Two-phase Compression: Numerical Modeling**
  This chapter presents the full development of a deterministic model of a scroll compressor, operating in two-phase conditions. This model investigates the numerous physical

phenomena involved in two-phase compression, including phase change, thermal non-equilibrium, flow patterns, sealing effects, hydraulic power losses, and two-phase heat transfer, to reproduce as accurately as possible the experimentally observed trends. It takes as inputs the operating variables of the experimental investigations, and gives as outputs the delivered mass flow rate, the power consumption and the evolution of the mixture properties throughout the compression. Most of the physical phenomena involved in the model do not rely on any parameters; however, this does not imply that they are perfectly represented. Eventually, the deterministic model is based on three parameters with clear physical meaning: the leakage gap δ, the liquid-thickness correction coefficient k_l, and the friction torque τ_f. This model development objective is to represent as accurately as possible physical phenomena occuring within the compressor, allowing identification and quantification of the source of losses. The validation of this deterministic model for the two experimentally investigated compressors is presented in the following chapters, followed by an analysis of the performance results.

– **Chapter 5. Two-phase Compression: Model Validation**
This chapter presents, in a first part, the calibration of the deterministic model for the two experimentally investigated compressors and, in a second part, the compressors' performance analysis based on the validated models. The calibration methodologies, which differ for the two compressors, are detailed. They are based on double-bisection processes: for the lab-scale prototype, on the mass flow rate and the mean pressure over one revolution; and for the retrofitted compressor, on the mass flow rate and power consumption. Therefore, three distinct experimental variables are used for the calibration of the lab-scale prototype, allowing an robust validation of the model. The analysis of the performance results is organized into four complementary parts: a properties evolution analysis within the compressor; a pressure–volume diagram analysis, helping to understand the distribution of volumetric and isentropic efficiencies into factors targeting specific losses; a point-by-point analysis examining the impact of changes in vapor quality, speed, pressure ratio, and oil circulation ratio using tables; and finally, a sensitivity analysis of the deterministic model, starting from a near-ideal variation of the efficiencies with pressure ratio or vapor quality and progressively adding the different sources of losses to this near-ideal curve. The findings of these analyses are summarized below, where the main experimental observations are gathered, the assumed physical interpretations are proposed, and the numerical validations of these interpretations are provided.

Overall, quantitative results are generated only in Chapter 3, through the analysis of the experimental results, and in Chapter 5, through the performance analysis of the results generated by the validated deterministic models for both compressors. Some of the quantitative results of these chapters can be found in their respective conclusions (Sections 3.6 and 5.5). The introduction (Chapter 1) sets the foundation of this research, while Chapters 2 and 4 establish the modeling framework required to generate the results presented in the other chapters. Table 6.1 summarizes the main experimental observations and indicates the section(s) and figure(s) where they are presented. For each observation, the corresponding physical interpretation is retrieved. A numerical validation of this interpretation is also provided, referencing the relevant section(s), figure(s) and/or table(s) where the supporting evidence can be found. The first observations concern the testing of the retrofitted compressor. Trends regarding the volumetric and isentropic efficiency, related to the inlet vapor quality, the pressure ratio, the speed and the oil circulation ratio are summarized and analyzed. Then, trends for the lab-scale prototype, differing from those of the retrofitted compressor, are also provided and analyzed, highlighting the differences between the two compressors.

Experimental observations	Physical interpretation	Numerical validation
Volumetric efficiency decreases as vapor quality decreases (retrofitted compressor, Section 3.4.1, Figure 3.18).	More volumetric leakage in the suction chamber.	Interpretation confirmed in Section 5.4.2, Table 5.6 with the decrease in leakage-related volumetric efficiency but also in Table 5.8 examining directly the value of the leakage-related mass flow rate and in Section 5.4.4, Figure 5.36 with the increasing gap between the near-ideal curve and the leakage contribution curve as the vapor quality decreases.
Isentropic efficiency decreases as vapor quality decreases (retrofitted compressor, Section 3.4.1, Figure 3.17).	Contribution of the decrease in volumetric efficiency and thermal non-equilibrium between liquid and vapor phases through the compression.	Interpretation confirmed with the link made between volumetric and isentropic efficiencies in Section 5.4.2, Table 5.6 and with the increasing contribution of the thermal non-equilibrium in 5.4.4, Figure 5.34, while other contributions do not vary as the vapor quality decreases.
Shift of the ideal pressure ratio towards lower values as the vapor quality decreases (retrofitted compressor, Section 3.4.1, Figure 3.17).	Decreasing vapor quality reduces the pressure achieved for a given built-in volume ratio.	Interpretation confirmed numerically in Section 1.2.2, Table 1.1, in Section 2.4.1, Figure 2.33, in Section 4.4.5, Figure 4.17 and in Section 5.4.4, Figure 5.33, but also confirmed experimentally with the dynamic pressure sensor in Section 3.5.2, Figure 3.45b.
Volumetric efficiency increases as speed increases (retrofitted compressor, Section 3.4.2, Figure 3.20).	Can be due to a decrease in volumetric leakage into the suction chambers or by the leakage becoming relatively lower compared to the delivered mass flow rate.	Interpretation numerically confirmed in Section 5.4.3, Table 5.7. The leakage-related mass flow rate increases with the speed (no sealing effect), but the volumetric efficiency increases.
Isentropic efficiency decreases as speed increases at high vapor quality, but increases with speed at low vapor quality (retrofitted compressor, Section 3.4.2, Figure 3.19).	Combined effect of increased mechanical losses (reducing isentropic efficiency) and increased volumetric efficiency (improving it).	Interpretation not numerically investigated but physically consistent.
Isentropic efficiency increases at high pressure ratio and low vapor quality as speed increases (retrofitted compressor, Section 3.4.2, Figure 3.19).	Reduction of the undercompression losses at high speed.	Effect numerically observed in Section 5.4.4, with the shift of the maximum in isentropic efficiency at high speed towards a higher pressure ratio (Figures 5.30 and 5.31) and more specifically investigated with the rise of pressure from the merging phase (undercompression) in Figures 5.32c and 5.32d.

Volumetric efficiency increases as OCR increases at high vapor quality, but decreases with OCR at low vapor quality (retrofitted compressor, Section 3.4.3, Figure 3.24).	Increased leakage at low vapor quality and sealing effect at high vapor quality due to higher liquid-phase viscosity.	Interpretation partially confirmed in Section 5.4.3, Table 5.10, showing the effect of an increase of OCR at both low- and high-vapor qualities on the isentropic and volumetric efficiencies. These effects are implicitly included through the variation of the leakage gaps, which may account for unmodeled phenomena.
Shift of the ideal pressure ratio towards lower values as the OCR increases (retrofitted compressor, Section 3.4.3, Figures 3.23) and 3.25.	Higher heat capacity of the oil reaches lower pressure ratios when compressed, decreasing the overcompression effect and intensifying the undercompression effect.	Interpretation numerically investigated in Section 4.4.5, Figure 4.17 where the final pressure ratio is decreased when the OCR is increased for a given initial vapor quality.
Higher volumetric efficiency of the lab-scale prototype compared to the retrofitted compressor (Section 3.5.1, Figure 3.28).	Higher displacement volume reduces the relative impact of leakage compared to the delivered mass flow rate in the lab-scale prototype.	Interpretation confirmed in Section 5.4.3, Table 5.9, where the two machines are compared at a pressure ratio of 4. Despite the higher leakage-related mass flow rate and heat-transfer- and pressure-loss-related mass flow rate, the volumetric efficiency of the lab-scale prototype is higher. The comparison of the volumetric efficiency loss distribution is presented in Section 5.4.4, Figures 5.28 and 5.29.
Higher isentropic efficiency of the lab-scale prototype at high compression ratios, but lower efficiency at low compression ratios (Section 3.5.1, Figure 3.27).	Higher built-in volume ratio of the lab-scale prototype (3 vs. 2.3), shifting the optimal pressure ratio, and stronger impact of mechanical losses, despite the positive effect of improved volumetric efficiency.	Interpretation confirmed in Section 5.4.4, Figures 5.26 and 5.27, where the efficiency maxima shift toward higher pressure ratios for the lab-scale prototype and mechanical losses have a stronger impact. Additionally, greater thermal non-equilibrium losses are observed for the retrofitted compressor.
Independence of the mass flow rate from the pressure ratio for the lab-scale prototype (Section 3.5.1, Figure 3.30)	Higher number of compression chambers working in parallel (larger scroll involute angle) avoiding direct leakage between the suction chamber and the discharge chamber	Interpretation confirmed in Section 5.4.3, Table 5.9, where two operating points at different pressure ratios are compared, showing no variation in leakage-related mass flow rate and constant volumetric efficiency. Same results observed in Section 5.4.4, Figures 5.28 and 5.29, where the leakage impact does not vary with the pressure ratio for the lab-scale prototype.

Increase of the lab-scale prototype power consumption as the vapor quality decreases (Section 3.5.1, Figure 3.29)	Larger pressure losses for the lab-scale prototype, impacting the volumetric efficiency.	Interpretation confirmed in Section 5.4.4, Figure 5.35, showing a dependence of near-ideal volumetric efficiency on inlet vapor quality due to suction pressure losses.

Table 6.1: Summary of the experimentally observed trends, their physical interpretation and their numerical validation.

In addition to these observed and validated experimental trends, the following important observations have been made in the model results analysis:

- A decomposition of the isentropic efficiency into factors, which are the volumetric efficiency, the indicated efficiency and the mechanical efficiency demonstrated that any decrease in volumetric efficiency propagates to the isentropic efficiency. As a matter of fact, leakages, inlet heat transfer, and pressure losses, which influence the volumetric efficiency, generate irreversibilities, thereby affecting the isentropic efficiency as well. This decomposition into factors can be found in Section 5.4.2.
- For the retrofitted compressor, leakages are the most important source of losses and are detrimental to both isentropic and volumetric efficiencies. More specifically, volumetric leakages (rather than mass leakages) going into the suction chambers, limit the volume that can be sucked by the compressor, thereby impacting the volumetric as well as the isentropic efficiency. These volumetric leakages consist mainly of vapor, as the liquid leakage volume is negligible compared with the vapor volume. It has been shown that these volumetric leakages are increased when the vapor quality increases, but also when the speed increases. In these two cases, the relative impact of the decrease is limited in comparison with the increase in delivered mass flow rate, originating from the increase in speed or the decrease in vapor quality. Nevertheless, the pressure ratio also strongly influences the leakage mass flow rate of the retrofitted compressor, and the delivered mass flow rate is not increased in this case, resulting in a strong decrease in both volumetric and isentropic efficiencies when the pressure ratio increases. More information about these results can be found in Section 5.4.3 and 5.4.4, Figures 5.29 and 5.27.
- The lab-scale prototype behaves differently from the retrofitted compressor due to its larger size for two reasons. First, its larger size allows the source of losses to be relatively smaller compared to its mass flow rate/power consumption. Second, the larger scroll involute angle implies the existence of several compression chambers working in parallel (up to three); therefore, no direct leakage path exists between the discharge chamber and the suction chambers. As a consequence, the pressure ratio does not influence the leakages as much as in the retrofitted compressor, allowing better potential isentropic and volumetric efficiencies at high pressure ratios. Nevertheless, high mechanical losses are observed in this compressor, due to its prototype nature, as indicated by the friction torque parameter being three times higher than that of the retrofitted compressor. More information about these impacts can be found in Section 5.4.4, Figures 5.28 and 5.22.
- For both machines, the numerical results indicated that leakages play an important role in decreasing both the volumetric and isentropic efficiencies. Moreover, for the retrofitted compressor, its impact is pressure-ratio-dependent. On the one hand, it has been shown that increasing the speed reduces the impact of leakages, despite the increase in leakage-related mass flow rate loss induced by the increase in speed. On the other hand, increasing the inlet vapor quality, increases the impact of leakage, as demonstrated by the decrease in volumetric efficiency, despite the increase in the total mass flow rate. Therefore, the leakage-related mass flow rate loss increases when the vapor quality decreases. In both speed-increase and vapor-quality-decrease cases, the leakage-related mass flow rate loss increases, reflecting the increase in leakage gap predicted by the models. The interpretation of this increase in leakage gap is the displacement of the tip seal due to the presence of a liquid layer on the scroll surfaces or due to liquid refrigerant flashing; however, this hypothesis has not been proven.
- When comparing the results of the two investigated compressors, it has been demonstrated that the results are strongly size-related. In other words, the defined volumetric and isentropic efficiencies depend on the machine size, as they account for losses by comparing non-ideal performance with the corresponding ideal case. If the ideal case performance is high, losses

in the compressor could have a relatively lower impact. The lab-scale prototype, with a displacement volume 2.5 times larger, has a higher theoretical mass flow rate and isentropic power. If the magnitude of the loss mechanisms (leakage, friction, pressure losses, heat transfer) has a lower relative impact than the relative increase in size (displacement volume), this results in higher isentropic and volumetric efficiencies.

6.3 Compressor optimization strategies

Finally, potential compressor design improvements for two-phase compression are proposed based on the various analyses and conclusions. An optimized compressor can be virtually created based on these strategies. This machine can then be simulated using the deterministic model to evaluate its performance. From the previous summary of experimental and numerical observations, the following guidelines can be deduced, to optimize the design of a new two-phase compressor achieving higher volumetric and isentropic efficiencies:

- The compressor size can be increased to make the power-related and mass-flow-rate-related losses relatively lower compared to the ideal power consumption and mass flow rate. For this purpose, the scroll involute ending angle can be increased by one additional revolution, allowing a supplementary compression chamber to coexist. At the same time, the other parameters of the lab-scale prototype are kept constant to maintain the same scroll thickness and orbiting radius. Nevertheless, the scroll height has been decreased from 41 mm to 35 mm to allow the increase in scroll diameter without increasing the centrifugal force. The feasibility of this increase has not been verified using a real scroll compressor force model. As a consequence of these changes, the built-in volume ratio of the machine is increased from 3 to 3.7, and the displacement volume from 200 cm^3 to 220 cm^3.
- The discharge port size can be increased to minimize exhaust pressure losses. Keeping the same oval shape as the lab-scale prototype discharge port, the area can be increased from 160 mm^2 to 262.5 mm^2 without spatial restrictions.
- The leakages can be minimized using a better sealing technology. Tip seals activated by the high pressure, although it has not been proven, seem not work properly in the presence of high liquid quantity. A mechanically-activated tip seal may help in reducing the leakage gap. A leakage gap of 20 μm is assumed to be achievable using an alternative sealing technique. At the same time, no sealing effect has is assumed in the following simulations: the liquid-layer correction coefficient has been set at 0.
- In the same line of reasoning, the mechanical friction of the compressor could be reduced by employing a more optimized orbiting mechanism. The Oldham ring, along with the radial compliance mechanism used in the prototype generate consequent friction losses, as demonstrated by the high friction torque value of 1.6 Nm obtained from the model calibration procedure. Conversely, the retrofitted compressor had a friction torque of 0.42 Nm. As a reasonable trade-off, a value of 0.8 Nm is assumed to be achievable with an optimized orbiting mechanism similar to that of the retrofitted compressor.

Finally, the geometry of the optimized compressor is presented in Figure 6.3. It can be compared with the geometry of the lab-scale prototype shown in Figure 6.2. As can be seen, the geometries of both machines are similar; they have the same overall shape, discharge geometry and intermediate discharge ports. The only observable differences are the larger area of the main discharge port and the additional revolution of the scrolls in the optimized design. A comparison of the characteristics of the three compressors, i.e., the retrofitted, the prototype and the optimized compressors, can be found in Table 6.2.

The sensitivity analysis results of the optimized compressor simulations can be found in Figures 6.4 and 6.5, for the volumetric and isentropic efficiency, respectively. Once again, the pressure ratio is used on the x-axis, while the vapor quality is fixed at 0.5. Moreover, the oil circulation ratio is set at 5% and the inlet pressure at 1.5 bar. Important pressure losses are observed at the inlet of the compressor via the near-ideal volumetric efficiency curve but also certainly through the compressor discharge port. These pressure losses can be explained by the higher displacement volume of the optimized compressor. The near-ideal isentropic efficiency curve is therefore similar to that of the lab-scale prototype, with the exception that its maximum is shifted due to the larger built-in volume ratio of the optimized compressor. The impact of thermal non-equilibrium on the isentropic efficiency completely

Figure 6.1: Retrofitted compressor geometry.

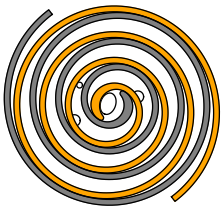

Figure 6.2: Lab-scale prototype geometry.

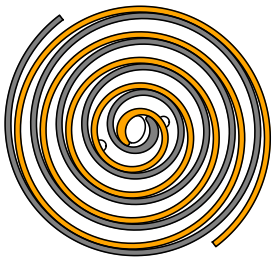

Figure 6.3: Optimized compressor geometry.

Characteristics	Retrofitted compressor	Lab-scale prototype	Optimized design
Involute ending angle [deg]	1052	1583	1943
Scroll height [mm]	30.6	41	35
Displacement volume [cm^3]	86	200	220
Built-in volume ratio [-]	2.3	3.0	3.75
Max. number of compression chamber [-]	2	3	4
Area of the discharge port [mm^2]	95	160	262.5
Leakage gap [μm]	[4-38]	[6-78]	20
Liquid-thickness correction coefficient [-]	[0.1-6.8]	[0.1-7.9]	0
Friction torque [Nm]	0.42	1.6	0.8

Table 6.2: Comparison of the characteristics of the three simulated compressors.

disappears due to the turbulence generated by the high rotational speed and the larger displacement volume. Further increasing the speed of the machine or the built-in volume ratio without modifying the geometry would only lead to additional pressure losses, without improving thermal equilibrium, which is already saturated. Finally, the impacts of mechanical losses and leakage are significantly reduced due to the fixed model parameters. Overall, when taking into account all sources of losses, an isentropic efficiency of 69% can be reached at a pressure ratio of 3.5. Furthermore, decent isentropic efficiencies can be achieved at even further pressure ratios, as the impact of undercompression is limited due to the high speed. In conclusion, under certain feasible geometrical optimization assumptions, a satisfactory isentropic efficiency (up to 69%) can be achieved even at low vapor qualities and high pressure ratios, which constitutes a promising result for further investigation of two-phase compression in scroll compressors.

6.4 Perspectives

The experimental and numerical investigations carried out to achieve the present findings opened the way to perspectives, i.e., interesting investigation paths that could be explored to improve the results or to continue the research on two-phase compression. These perspectives could not be explored in the present work due to time constraints, which limited the scope of the research and the depth of certain aspects. These improvements and follow-up research topics are summarized below:

– In the introduction, thermodynamic cycles that could benefit from two-phase compression are presented, based on the literature and on a practical heat pump application. These examples were used to introduce the need for deeper research in two-phase compression. On the one hand, more examples of practical applications providing quantitative results could be explored to highlight a stronger need for two-phase compression. On the other hand, a more accurate numerical model could have been used to enhance the prediction of the performance improvements brought by two-phase compression, thereby further motivating research in this field. To push the analysis

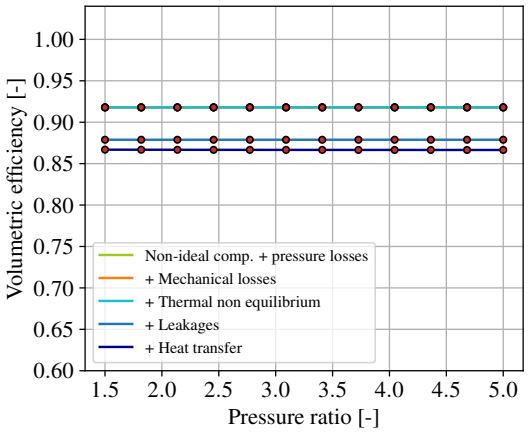

Figure 6.4: Sensitivity analysis of the volumetric efficiency as a function of pressure ratio at a vapor quality of 0.5 and a speed of 4000 RPM for the optimized compressor design.

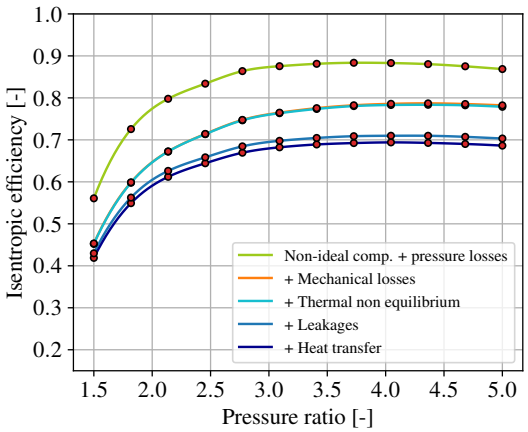

Figure 6.5: Sensitivity analysis of the isentropic efficiency as a function of pressure ratio at a vapor quality of 0.5 and a speed of 4000 RPM for the optimized compressor design.

even further, experimental investigations could be carried out on a thermodynamic cycle using two-phase compression.

– The impact of the oil has been numerically and experimentally investigated in terms of performance by changing the oil circulation ratios. Nevertheless, other aspects such as machine lifetime, impact on thermodynamic cycles, and chemical instability have not been studied, despite their importance. The oil is essential in a positive-displacement compressor to ensure cooling and lubrication of the machine. The cooling effect of the oil can be ensured by the liquid refrigerant. Nevertheless, the use of a two-phase fluid in compressors greatly reduces the liquid-phase viscosity, which could limit the machine's lifetime due to increased surface friction. Studying this aspect would be useful, particularly in the design of an oil-free scroll compressor.
– The present investigations could be extended to hermetic compressors, which would better address industrial applications. In this case, an additional testing campaign would be required using a hermetic compressor. On the modeling side, only minor changes to the heat transfer and mechanical loss submodels would be necessary.
– The test bench could have been equipped with additional sensors, for instance, a two-phase capacitance-based density sensor to directly evaluate the vapor quality at the compressor inlet, allowing a comparison with the value derived from the energy balance. Furthermore, a measurement of the outlet vapor quality would provide another variable that can be used for model validation. The outlet pipe could also be equipped with localized temperature sensors to measure if a thermal non-equilibrium between the two phases is observed at the compressor outlet. The outlet pipe could also be equipped with a localized temperature sensor to determine whether thermal non-equilibrium between the two phases is observed at the compressor outlet. To achieve even greater accuracy in the compressor performance data, the compressor could be installed inside an isothermal enclosure in order to quantify the heat losses to the ambient environment. In addition, changing the needle of the control valve during the testing campaigns would have allowed further testing under different conditions, thereby enabling the acquisition of additional data points and avoiding a dependence between the tested speed range and the tested vapor quality and pressure ratio ranges. Finally, in the same order of ideas, a higher-capacity torquemeter would have enabled testing of the prototype at higher speeds and allowed further analysis.
– Additional pressure sensors on the lab-scale prototype itself could have been useful to get more information about the pressure-volume diagram of the compressor at different testing conditions. For instance, a better characterization of the pressure evolution from the beginning of the compression process and during discharge could be achieved. With these additional data, greater accuracy could be obtained regarding leakage and thermal non-equilibrium, using the deterministic model. In addition, the unclear potential "sealing effect", of the liquid refrigerant

could be better assessed using these data.

- A better mixing between the liquid and the vapor has proven to improve the compressors' performance. A solution to enhance this mixing is the horizontal placement of the compressor instead of vertical. This horizontal placement would allow the liquid phase not to stay at the bottom of the fixed scroll by gravity effect, but to be forced to move horizontally. New experimental campaigns on the same machines, placed vertically would allow understanding of the impact of machine orientation. Moreover, the assumption regarding liquid distribution within the chambers could be revised accordingly.
- The aforementioned experimental investigation perspectives could enhance the calibration of the deterministic model. Nevertheless, some of the modeling assumptions could be improved to further increase the accuracy, provided that new experimental data are available for validation. For instance, the very simple mechanical losses model could be upgraded to a two-parameter model, or even more complex model. Moreover, a higher-order solver (e.g., the fourth-order Runge–Kutta method) could be implemented to improve the accuracy and reduce the computational time of the model.
- Finally, the methodology used to vary the submodel parameters (leakage gap and liquid-thickness correction factor) with the operating conditions should be further developed in order to better understand the influence of each input on these parameters. Such an analysis would help assess the extent of the impact of each varying input and improve the understanding of how a specific compressor design may influence the overall machine performance.

Ultimately, these perspectives highlight the remaining challenges and opportunities that must be addressed to fully assess the potential of two-phase compression using scroll compressors.

Appendix A

Oil-refrigerant mixture modeling

A.1 Cubic equations of state

The generalized three-parameter cubic equation of state (EoS) is given by

$$p = \frac{RT}{v - b_{\mathrm{m}}} - \frac{a_{\mathrm{m}}}{v^2 + (b_{\mathrm{m}} + c_{\mathrm{m}})v - b_{\mathrm{m}}c_{\mathrm{m}}} \tag{A.1}$$

with the mixing parameters given by the following equations, using the van der Waals mixing rule (Equation A.3):

$$a_{\mathrm{m}} = \sum_i \sum_j x_i x_j a_{ij} \tag{A.2}$$

$$a_{ij} = (1 - k_{ij})\sqrt{a_i a_j} \tag{A.3}$$

$$b_{\mathrm{m}} = \sum_i x_i b_i \tag{A.4}$$

$$c_{\mathrm{m}} = \sum_i x_i c_i \tag{A.5}$$

The pure fluid parameters a_i, b_i and c_i are given by

$$a_i = \alpha(T_{r,i}, \omega) \cdot \Omega_{a,i} \cdot \frac{R^2 T_{c,i}^2}{p_{c,i}} \tag{A.6}$$

$$b_i = \Omega_{b,i} \cdot \frac{RT_{c,i}}{p_{c,i}} \tag{A.7}$$

$$c_i = \Omega_{c,i} \cdot \frac{RT_{c,i}}{p_{c,i}} \tag{A.8}$$

where $p_{c,i}$ and $T_{c,i}$ are, respectively, the critical pressure and temperature of component i, while $T_{r,i} = T/T_{c,i}$ is the reduced temperature of component i. The expressions of Ω_a, Ω_b and Ω_c as well as $\alpha(T)$ for the equations of state from Peng-Robinson(PR), Soave-Redlich-Kwong (SRK) and Patel-Teja-Valderrama (PTV) can be found in Table A.2. Z_c is the compressibility factor at the critical point.

Now deriving the expression for the cubic polynomial in terms of compressibility factor Z:

$$Z^3 + a_2 \cdot Z^2 + a_1 \cdot Z + a_0 = 0 \tag{A.9}$$

Let's define some coefficients A, B and C such as:

$$A = \frac{a_m p}{(RT)^2}, \quad B = \frac{b_m p}{RT}, \quad C = \frac{c_m p}{RT} \tag{A.10}$$

The coefficients of Equation A.9 can be found in Table A.1.

EoS	Ω_a	Ω_b	Ω_c	α and m functions
PR	0.45724	0.07779	0.07779	$\alpha = \left(1 + m(1 - \sqrt{T_r})\right)^2$ $m = 0.37464 + 1.54226\omega - 0.26992\omega^2 \quad (\omega \leq 0.49)$ $m = 0.37964 + 1.48503\omega - 0.164423\omega^2 + 0.016666\omega^3 \quad (\omega > 0.49)$
SRK	0.42748	0.08664	0	$\alpha = \left(1 + m(1 - \sqrt{T_r})\right)^2$ $m = 0.48508 + 1.55171\omega - 0.15613\omega^2$
PTV	0.66121 - $0.761057 \cdot Z_c$	0.02207 - $0.20868 \cdot Z_c$	0.57765 - $1.87080 \cdot Z_c$	$\alpha = \left(1 + m(1 - \sqrt{T_r})\right)^2$ $m = 0.46283 + 3.58230\omega Z_c + 8.19417(\omega Z_c)^2$

Table A.1: Model-specific constants (rounded) and α-function formulations for PR, SRK, and PTV equations of state. From D.-Y. Peng et al. (1976), Soave (1972), Valderrama (1990), and Valderrama (2003).

EoS	a_2	a_1	a_0
PR	$-(1 - B)$	$A - 3B^2 - 2B$	$-AB + B^2 + B^3$
SRK	-1	$A - B - B^2$	$-AB$
PTV	$C - 1$	$A - B^2 - 2BC - B - C$	$B^2C + BC - AB$

Table A.2: Cubic equation coefficients a_2, a_1, and a_0 in $Z^3 + a_2Z^2 + a_1Z + a_0 = 0$ for PR, SRK, and PTV equations of state. From D.-Y. Peng et al. (1976), Soave (1972), Valderrama (1990), and Valderrama (2003).

Let's define some constants:

$$Q_m = v_m + \frac{b_m + c_m}{2}, \quad d_m = \sqrt{b_m c_m + \left(\frac{b_m + c_m}{2}\right)^2} \tag{A.11}$$

$$q_m = d_m + \frac{b_m + c_m}{2}, \quad m_m = -d_m + \frac{b_m + c_m}{2} \tag{A.12}$$

The residual entropy is then given by:

$$s^R = R \ln\left(\frac{v - b_m}{v}\right) - \frac{1}{2d_m}\frac{da_m}{dT} \ln\left(\frac{v + m_m}{v + q_m}\right) \tag{A.13}$$

Finally, the fugacity coefficients can be derived as follows.

Peng-Robinson

$$\ln \phi_i = \frac{b_i}{b}(Z - 1) - \ln(Z - B) + \frac{A}{2\sqrt{2}B}\left[\frac{2}{a}\sum_j x_j a_{ij} - \frac{b_i}{b_m}\right] \ln\left(\frac{Z + (1 + \sqrt{2})B}{Z + (1 - \sqrt{2})B}\right) \tag{A.14}$$

Soave-Redlich-Kwong

$$\ln \phi_i = \frac{b_i}{b_m}(Z - 1) - \ln(Z - B) - \frac{A}{B}\left[\frac{2}{a}\sum_j x_j a_{ij} - \frac{b_i}{b_m}\right] \ln(1 + B/Z) \tag{A.15}$$

Patel-Teja-Valderrama

$$\begin{aligned} RT \ln \phi_i = &-RT \ln(Z - B) + RT\left(\frac{b_i}{v - b_m}\right) \\ &- \sum_j x_j a_{ij} \cdot \frac{1}{d_m} \cdot \ln\left(\frac{Q_m + d_m}{Q_m - d_m}\right) \\ &+ \frac{a_m(b_i + c_i)}{2(Q^2 - d_m^2)} \\ &+ \frac{a_m}{8d_m^3}\left[c_i(3b_m + c_m) + b_i(3c_m + b_m)\right] \\ &\times \left[\ln\left(\frac{Q_m + d_m}{Q_m - d_m}\right) - \frac{2Q_m d_m}{Q_m^2 - d_m^2}\right] \end{aligned} \tag{A.16}$$

A.2 Oil properties

Density and viscosity

The density and the viscosity of the oils are not used alone; they are always treated with the liquid phase properties, i.e., in combination with the refrigerant. They can, however, be computed using the Henderson equations defined in Equations 2.22 and 2.25 with a refrigerant liquid composition $x_r = 0$, which would give

$$\rho_o(T) = a_{\rho,1} + a_{\rho,2}T + a_{\rho,3}T^2 \tag{A.17}$$

$$\log(\log(\mu_o(T) + 0.7)) = a_{\mu,1} + a_{\mu,2}\log(T) + a_{\mu,3}\log^2(T) \tag{A.18}$$

with T expressed in K and μ_o in mPa·s. The parameters can be found in Table A.3.

k	$a_{\rho,k}$	$a_{\mu,k}$
1	$1.25 \cdot 10^{3}$	$-2.51 \cdot 10$
2	$-9.70 \cdot 10^{-1}$	$2.37 \cdot 10$
3	$3.07 \cdot 10^{-4}$	-5.45

Table A.3: Empirical parameters of the Henderson equation for pure oil, for both density and viscosity.

Specific heat capacity

Thome (1995) recommends the following equation to calculate the liquid specific heat capacity of an oil:

$$c_{p,\mathrm{o}} = 4.186 \left(\frac{0.388 + 0.00045(1.8T + 32)}{\sqrt{s}} \right) \tag{A.19}$$

where the specific heat capacity is expressed in kJ/(kg·K), the temperature in °C and the specific gravity s is defined as the ratio of the density of the oil to the density of water at 288.56 K (60°F) ($s = \rho_{\mathrm{o}}(288.56\,\mathrm{K})/\rho_{\mathrm{w}}(288.56\,\mathrm{K})$). From this formula, the oil specific heat capacity can be reformulated as follows:

$$c_{p,\mathrm{o}} = a_{\mathrm{cp},0} + a_{\mathrm{cp},1} T \tag{A.20}$$

with $a_{\mathrm{cp},0} = 758.3/\sqrt{s}$ and $a_{\mathrm{cp},1} = 3.4/\sqrt{s}$. In this formula, the temperature is expressed in K and the specific heat capacity in J/(kg·K). The density of water ρ_{w} at 288.56 K is equal to 998.5 kg/m^3. Regarding the density of the oils employed, they are given by $\rho_{\mathrm{po}} = 989.95$ and $\rho_{\mathrm{om}} = 969.18$ kg/m^3.

Enthalpy

The enthalpy of the oil is calculated by integrating the expression of dh with the temperature and the pressure:

$$\mathrm{d}h = c_p \,\mathrm{d}T + \left[v - T \left(\frac{\partial v}{\partial T} \right)_p \right] \mathrm{d}p \tag{A.21}$$

$$h_{\mathrm{o}}(T,p) = h_{\mathrm{ref}} + \int_{T_{\mathrm{ref}}}^{T} c^{L}_{p,\mathrm{o}}(T)\,\mathrm{d}T + \int_{p_{\mathrm{ref}}}^{p} \left[v_{\mathrm{o}}(T,p) - T \left(\frac{\partial v_{\mathrm{o}}}{\partial T} \right)_p \right] \mathrm{d}p \tag{A.22}$$

where the specific volume of the oil is given by $v_{\mathrm{o}}(T) = 1/\rho_{\mathrm{o}}(T)$. Assuming a zero reference enthalpy and developing the first and second terms gives

$$\begin{aligned} h_{\mathrm{o}}(T,p) &= a_{\mathrm{cp},0}(T - T_{\mathrm{ref}}) + \frac{a_{\mathrm{cp},1}}{2}\left(T^2 - T_{\mathrm{ref}}^2\right) + (p - p_{\mathrm{ref}}) \cdot \frac{\rho_o + a_{\rho,2}T + 2a_{\rho,3}T^2}{\rho_o^2(T)} \\ &\approx a_{\mathrm{cp},0}(T - T_{\mathrm{ref}}) + \frac{a_{\mathrm{cp},1}}{2}\left(T^2 - T_{\mathrm{ref}}^2\right) + (p - p_{\mathrm{ref}}) \cdot \frac{1}{\rho_o(T)} \end{aligned} \tag{A.23}$$

with the reference temperature T_{ref} chosen equal to 273.15 K and the reference pressure equal to 101325 Pa. When combining property models from different sources, reference-state consistency is required to obtain a valid mixture property model. In the case where only energy balance are applied, the reference state consistency does not matter, even when the composition of the mixture changes.

Entropy

The entropy of the oil is calculated in the same way as the enthalpy, i.e., an integration of ds is performed with the temperature and the pressure:

$$\mathrm{d}s = c_p \frac{\mathrm{d}T}{T} - \left(\frac{\partial v}{\partial T}\right)_p \mathrm{d}p \tag{A.24}$$

$$s_\mathrm{o}(T,p) = s_\mathrm{ref} + \int_{T_\mathrm{ref}}^{T} \frac{c^L_{p,\mathrm{o}}(T)}{T}\mathrm{d}T - \int_{p_\mathrm{ref}}^{p}\left(\frac{\partial v_\mathrm{o}}{\partial T}\right)_p \mathrm{d}p \tag{A.25}$$

Assuming a zero reference enthalpy and developing the first and second terms gives

$$s_\mathrm{o}(T,p) = a_{\mathrm{cp},0}\ln\left(\frac{T}{T_\mathrm{ref}}\right) + a_{\mathrm{cp},1}(T - T_\mathrm{ref}) + (p - p_\mathrm{ref})\frac{a_{\rho,2} + 2a_{\rho,3}T}{\rho_o^2(T)} \tag{A.26}$$

Internal energy

The internal energy of the oil is given by

$$\begin{aligned} u_\mathrm{o}(T,p) &= h_\mathrm{o}(T) - (p - p_\mathrm{ref})\cdot v_\mathrm{o}(T) \\ &= a_{\mathrm{cp},0}(T - T_\mathrm{ref}) + \frac{a_{\mathrm{cp},1}}{2}\left(T^2 - T_\mathrm{ref}^2\right) \end{aligned} \tag{A.27}$$

making the internal energy of the oil independent of the pressure.

Thermal conductivity

The thermal conductivity of the oil is assumed to vary linearly with the temperature. The linear law has been calibrated using experimental data. Only three points have been recorded, at 300 K, 350 K and 400 K. Eventually, the oil thermal conductivity, expressed in W/(mK), is given by

$$\lambda_\mathrm{o}(T) = a_{\lambda,0} + a_{\lambda,1}T \tag{A.28}$$

with $a_{\lambda,0} = 0.204$ and $a_{\lambda,1} = -0.00016$ for both oil tested.

Surface tension

The following definition of the surface tension, expressed in N/m is proposed by Hanna et al. (2017) with the temperature in °C:

$$\sigma_\mathrm{o}(T) = 0.03742 - 0.0001253(T + 273.15) \tag{A.29}$$

A.3 Refrigerant properties not found in CoolProp

Thermal conductivity

The thermal conductivity of the refrigerant HCFO R1233zd(E) is not available in CoolProp 6.4.3. Knowing the low level of vapor phase superheat and liquid phase subcooling, the thermal conductivity of in vapor and liquid is assumed to be that of saturated phases. Alam et al. (2018) proposes two correlations for the saturated thermal conductivity of R1233zd(E), for the liquid and vapor phases, respectively, in W/(mK):

$$\lambda_{\mathrm{r}}^{\sigma,L}(T^{\sigma}) = (-0.2614T^{\sigma} + 159.19) \cdot 10^{-3} \tag{A.30}$$

$$\lambda_{\mathrm{r}}^{\sigma,G}(T^{\sigma}) = (0.09513T^{\sigma} - 17.963) \cdot 10^{-3} \tag{A.31}$$

Surface tension

The surface tension of R1233zd(E) in N/m is given by Kondou et al. (2015). It is written as

$$\sigma_{\mathrm{r}}(T) = \sigma_0 \cdot \left(1 - \frac{T}{T_c}\right)^n \tag{A.32}$$

where $\sigma_0 = 0.06195$ and $n = 1.277$. When the temperature exceeds the critical temperature T_c, the surface tension is set to zero.

A.4 Residual entropy scaling

The procedure to calculate the viscosity of a mixture using the residual entropy scaling technique is provided by X. Yang et al. (2021). The liquid viscosity of a mixture is expressed as

$$\mu^L = \mu_{\rho\to 0} + \mu^R \tag{A.33}$$

where $\mu_{\rho\to 0}$ is the dilute gas viscosity of the mixture and μ^R its residual viscosity. The dilute gas viscosity can be evaluated using Wilke's approximation:

$$\mu_{\rho\to 0} = \sum_{i=1}^{N} \frac{\tilde{x}_i \mu_{\rho\to 0,i}}{\sum_{j=1}^{N} \tilde{x}_j \phi_{ij}} \tag{A.34}$$

where ϕ_{ij} is given by

$$\phi_{ij} = \frac{\left[1 + \left(\frac{\mu_{\rho\to 0,i}}{\mu_{\rho\to 0,j}}\right)^{1/2} \left(\frac{m_j}{m_i}\right)^{1/4}\right]^2}{\sqrt{8(1 + m_i/m_j)}} \tag{A.35}$$

with m_i, the molecular mass of component i.

The dilute gas viscosity of the pure component can be calculated with the following equation:

$$\mu_{\rho\to 0,i} = \frac{5}{16}\sqrt{\frac{m_i k_B T}{\pi}} \cdot \frac{1}{\sigma_i^2 \Omega_i^{(2,2)*}} \tag{A.36}$$

where $k_B = 1.380649 \cdot 10^{-23}$ J/mol is the Boltzmann constant, σ_i is the collision diameter of a Lennard-Jones (L-J) 12-6 particle, and $\Omega_i^{(2,2)*}$ is the reduced collision integral obtained with an empirical correlation:

$$\Omega_i^{(2,2)*} = 1.16145 \cdot (T_i^*)^{-0.14874} + 0.52487 \cdot e^{-0.77320T_i^*} + 2.16178 \cdot e^{-2.43787T_i^*} \tag{A.37}$$

where $T_i^* = k_B T/\varepsilon_i$ is the dimensionless temperature and ε_i/k_B is the reduced L-J pair-potential energy. Thereby, σ_i and ε_i are both fluid-specific values. For R1233zd(E), ε/k_B is equal to 349.08 K and σ is equal to 0.524 nm.

The average molecular mass of the mixture is defined as a molar fraction weighted sum of the molecular masses of the mixture's components:

$$m = \sum_i \tilde{x}_i m_i \tag{A.38}$$

The residual viscosity contribution of the mixture μ^R can be calculated using the following equations:

$$\mu^R = \frac{\mu^{R+} \rho_N^{2/3} \sqrt{m k_B T}}{(s^+)^{2/3}} \tag{A.39}$$

$$\ln(\mu^{R+} + 1) = n_{\mu,1} s^+ + n_{\mu,2} (s^+)^{1.5} + n_{\mu,3} (s^+)^2 + n_{\mu,4} (s^+)^{2.5} \tag{A.40}$$

$$s^+ = -s^R / R \tag{A.41}$$

where $R = 8.3145$ J/(mol·K) is the universal gas constant, ρ_N is the number density in 1/m^3 defined as the Avogadro number divided the specific volume, i.e., $\rho_N = N_A/\tilde{v}$ and s^R is the residual entropy of the mixture, previously defined in Equation A.13. The four parameters $n_{\mu,k}$ ($k = 1, 2, 3, 4$) are mole-fraction-weighted averages of the pure-component coefficients (already fitted for each pure component):

$$n_{\mu,k} = \sum_i x_i n_{\mu,k,i} \quad \text{for } k = 1, 2, 3, 4 \tag{A.42}$$

A.5 Other oil characteristics

The other oil studied in the frame of the thesis is actually a mixture between the pure oil Emkarate RL32 and Petronas POE40, with 39% and 61% mass fractions, respectively. Nonetheless, for this oil-refrigerant mixture, less experimental data could be collected, therefore, only the solubility data will be presented, providing a calibrated Cavestri equation. The other properties of this mixture are assumed to be those of the first oil-refrigerant mixture studied. The data from the second oil-refrigerant mixture, along with the calibrated Cavestri equation, can be found in Figure A.2, and for the sake of comparison, the plot of the first oil-refrigerant mixture has also been added in Figure A.1. Despite the very close liquid solution viscosity measurements obtained, the shape of the $p - x - T$ diagrams are slightly different: the second tested oil exhibits less solubility with the refrigerant.

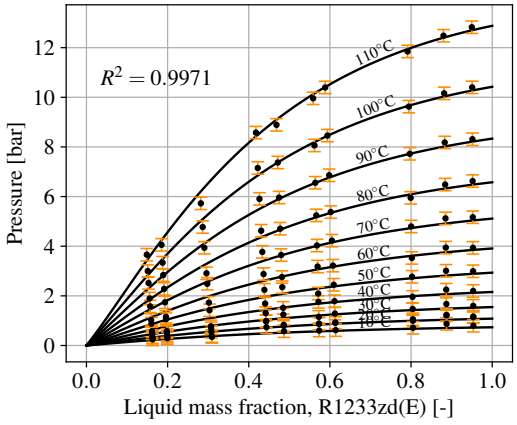

Figure A.1: Vapor pressure predicted by Cavestri's equation and experimental data with uncertainties (orange bars) for the first oil-refrigerant mixture.

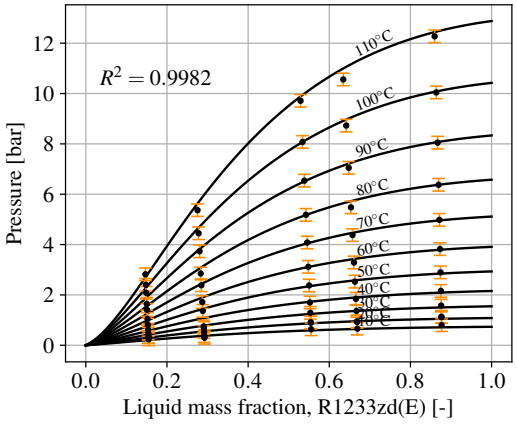

Figure A.2: Vapor pressure predicted by Cavestri's equation and experimental data with uncertainties (orange bars) for the second oil-refrigerant mixture.

The parameters of the Cavestri equations (Equation 2.19) for both oils can be found in Table A.4. The molar mass is assumed to be 300 g/mol for both oils.

	Cavestri First oil	Cavestri Second oil
a_1	$-4.81 \cdot 10^{-12}$	$1.05 \cdot 10^{-5}$
a_2	$-3.36 \cdot 10^{-9}$	$1.07 \cdot 10^{-3}$
a_3	$-2.04 \cdot 10^{-6}$	$-7.92 \cdot 10^{-6}$
a_4	$4.18 \cdot 10^{-11}$	$1.05 \cdot 10^{-5}$
a_5	$1.42 \cdot 10^{-8}$	$2.14 \cdot 10^{-3}$
a_6	$4.74 \cdot 10^{-6}$	$3.69 \cdot 10^{-6}$

Table A.4: Empirical parameters of the Cavestri equation for both oil-refrigerant mixtures studied.

Appendix B

Experimental investigations

B.1 Test bench images

B.1.1 General images

Face and rear pictures of the test bench can be found in Figures B.1 and B.2. Those pictures are for illustrative purposes only. The test bench dimensions are 2.4×2×1 m.

Figure B.1: Face picture of the test bench.

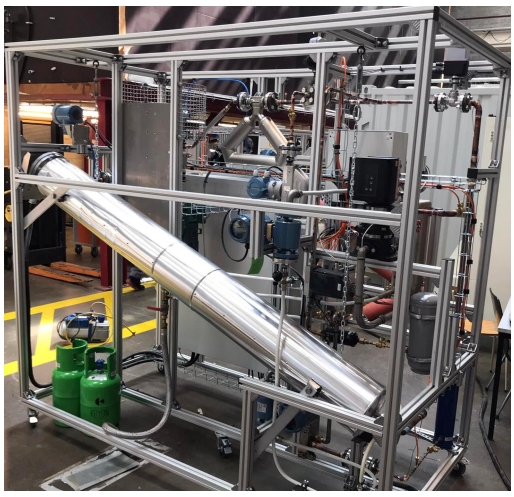

Figure B.2: Rear picture of the test bench.

B.1.2 Compressors images

Pictures of the SANDEN machine retrofitted compressor can be found in Figures B.3 and B.4. The compressor has been opened after the three testing campaigns conducted, including one without oil circulating. No evident damage could be found after more than 200 hours of operation (including 20 hours without oil). The ball mechanism is an orbiting mechanism without compliance.

A 3D representation of the lab-scale prototype can be found in B.5. It allows to see the inlet (upper pipe) and the outlet placed vertically (bottom pipe). It has an external diameter of 25 cm, against 17 cm for the retrofitted compressor. A picture of the fixed scroll can be found in Figure B.6. A significant difference in the number of turns can be found compared with the retrofitted machine, explaining the difference in built-in volume ratio (3 for the prototype vs 2.3 for the retrofitted compressor).

Figure B.3: Orbiting scroll of the retrofitted compressor.

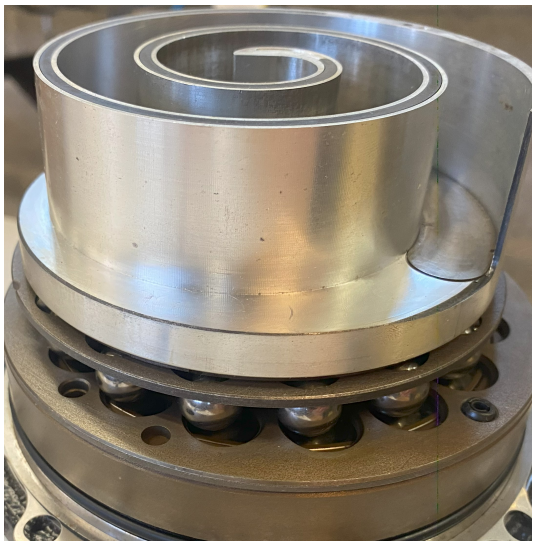

Figure B.4: Orbiting ball mechanism of the retrofitted compressor.

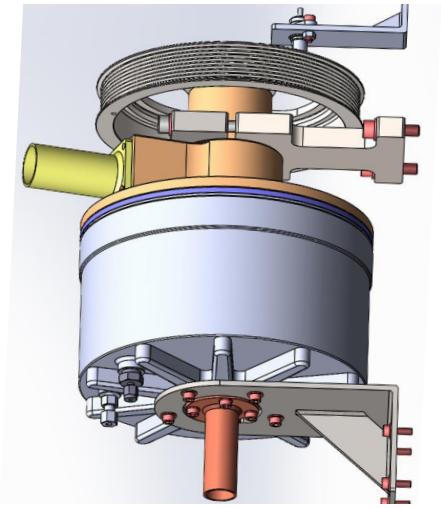

Figure B.5: Lab-scale prototype 3D representation.

Figure B.6: Fixed scroll of the lab-scale prototype.

B.1.3 Sealing joint wear

Pictures of the sealing joints can be found in Figures B.7 and Figure B.8. After one year of use, significant wear of the Viton joint was observed, despite its "supposed" compatibility with the refrigerant R1233zd(E).

B.2 Data post-processing

B.2.1 Test bench operating point example

A temperature-entropy along with a pressure-enthalpy diagram of a real operating point can be found in Figures B.9 and B.10. Only the refrigerant state is represented on this diagram, as the oil is only circulating in a restricted part of the test bench. The corresponding test bench diagram with values of pressures, temperatures, mass flow rates and compressor conditions can be found in Figure B.11. As can be seen, the isentropic efficiency is pretty low (52%) while

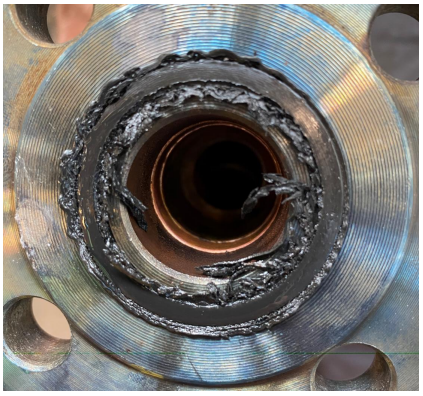

Figure B.7: Picture of the sealing joint (Viton) in the flanges after one year of use.

Figure B.8: Picture of the new sealing joint at the top and worn sealing joints at the bottom.

the entropy seems to be constant along the compression (see Figure B.9). This phenomenon can be explained by the cooling effect of the oil, resulting in a transfer of entropy from the refrigerant to the oil, which can not be visualized on the diagram. The pressure and heat losses can also be observed in the figures.

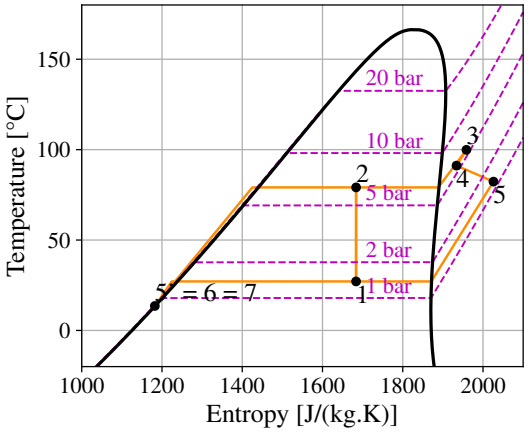

Figure B.9: Temperature-entropy diagram of a test bench operating point.

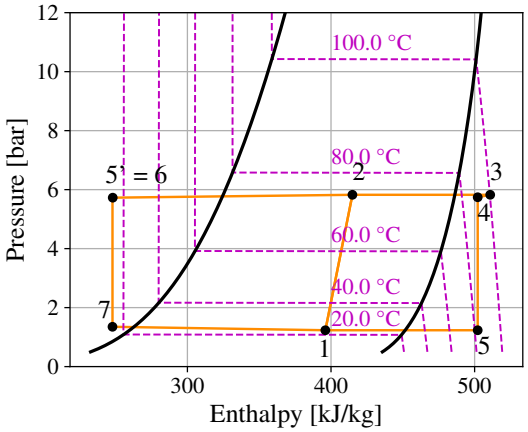

Figure B.10: Pressure-enthalpy diagram of a test bench operating point.

B.2.2 Pulley-belt system efficiency

The power friction linear law from the pulley-belt system of the retrofitted compressor is given by

$$\dot{W}_{\text{f,belt}} = a_1 N_{\text{cp}} + a_2 \tag{B.1}$$

where $a_1 = 0.0737$ and $a_2 = -10.06$, calibrated between 200 and 5000 RPM. This law therefore assumes the friction losses to be a function of the speed only, while the torque usually has an impact too.

Regarding the lab-scale prototype, such a law could not be calibrated and an efficiency of 95% has been assumed.

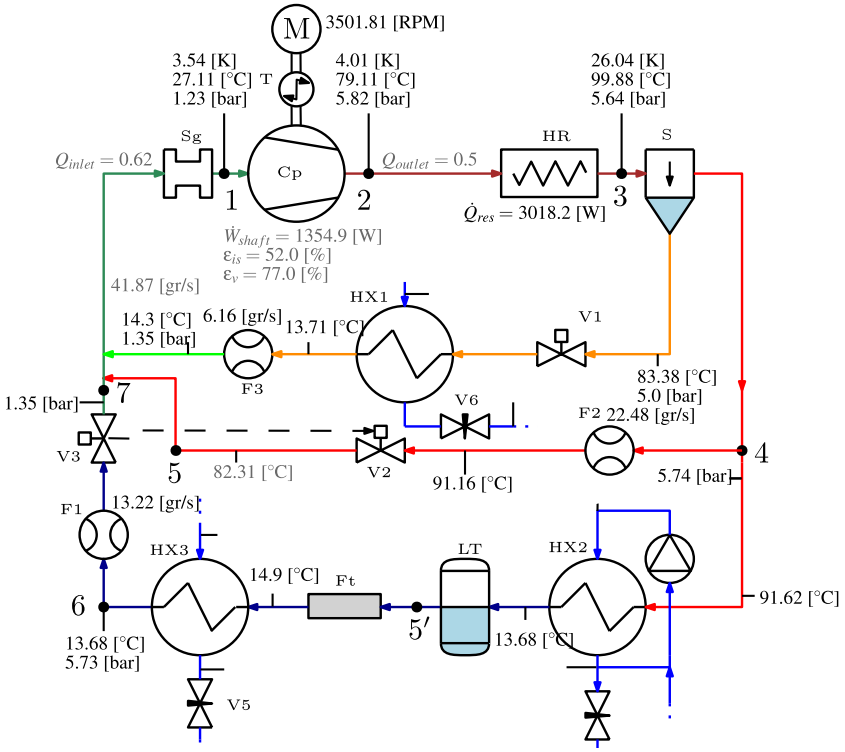

Figure B.11: Test bench diagram with values of an operating point (measured values in black, calculated in gray).

B.3 Retrofitted compressor results post-processing

B.3.1 Isentropic and volumetric efficiency 3D maps

The isentropic and volumetric efficiency 3D maps have been displayed to help better understand the shape of the 2D color maps; they can be found in Figures B.12 and B.13. They are complementary: 3D maps provide clearer visualization of the shape, whereas 2D color maps offer greater accuracy in the displayed values.

B.3.2 Mass flow rate and power consumption results

The GPExp algorithm has also been applied to the compressor power and mass flow rate. The predictions of direct performance versus performance indicators are expected to be more accurate, as fewer uncertainties are involved. However, the results are predictions of mass flow rate and power consumption, which do not reflect the internal losses within the compressor; hence, it is less straightforward to determine whether the performance is good or not. Nevertheless, the trends can still be analyzed. The predictions of mass flow rate and power consumption of both machines can be found in Figures B.14 and B.15 and the corresponding relative deviations in Table B.1. As expected, the deviations are much lower when predicting direct performance, since the mass flow rate can be trusted within a 1% relative uncertainty and the power consumption within a 0.5% relative uncertainty.

The power consumption and mass flow rate of the retrofitted compressor are plotted with similar conditions to those of the reference plots of the isentropic and volumetric efficiencies, i.e., an inlet pressure of 1.5 bar, an OCR of 5% and a compressor speed of 2500 RPM. They can respectively be found in Figures B.16 and B.17. Interestingly, the compressor power does not vary with the inlet vapor quality, as could have been expected as the compression of liquid requires less work than that of vapor. The shaft power consumption expression can be

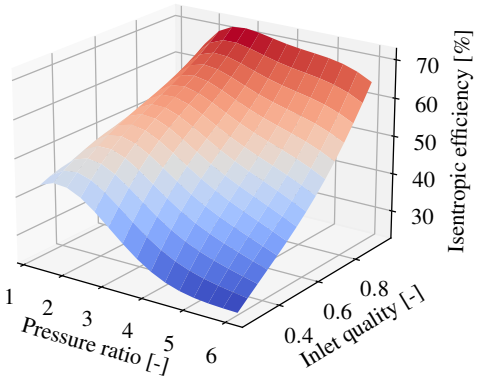

Figure B.12: 3D evolution of the isentropic efficiency for the retrofitted compressor, with an inlet pressure of 1.5 bar, an OCR of 5% and a compressor speed of 2500 RPM (reference case).

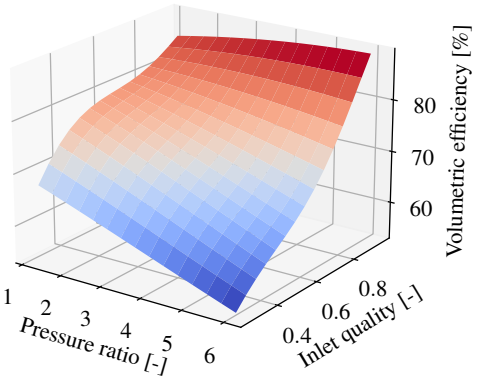

Figure B.13: 3D evolution of the volumetric efficiency for the retrofitted compressor, with an inlet pressure of 1.5 bar, an OCR of 5% and a compressor speed of 2500 RPM (reference case).

	Predictions		Cross-validation	
	$\dot{m}_{tot}$	$\dot{W}_{shaft}$	$\dot{m}_{tot}$	$\dot{W}_{shaft}$
Retrofitted compressor ($comp_r$)	0.61%	0.16%	0.95%	0.24%
Lab-scale prototype ($comp_p$)	0.78%	0.36%	1.67%	0.58%

Table B.1: Average relative deviation (ARD) of the prediction and the cross-validation of the mass flow rate and consumed power for both tested machines.

rewritten as follows:

$$\dot{W}_{shaft} = \dot{Q}_{amb} + \dot{m}_{tot}\Delta h = \dot{Q}_{amb} + \dot{m}_{r,v}(h^{ex}_{r,v} - h^{su}_{r,v}) + \dot{m}_{l}(h^{ex}_{l} - h^{su}_{l}) \tag{B.2}$$

The influence of a decrease in inlet quality on the power consumption could come from two different sources: the increasing mass flow rate of liquid, which decreases the mass flow rate of vapor, and the thermal non-equilibrium or the leakages increasing the compression work as higher pressures are reached inside the compression chamber. The distribution of the inlet mass flow rate between vapor and liquid can respectively be found in Figures B.18 and B.19. As predicted, a slight decrease in vapor mass flow rate is observed as the vapor quality decreases. Despite this decrease, power consumption remains constant across vapor quality; thus, the compensation is either due to the power required to compress the liquid or to an increase in the work needed to compress the vapor, or a combination of both effects. Only an accurate compressor model would be able to clarify this. Regarding the influence of the pressure ratio, the explanation is fairly straightforward. The lower the pressure ratio, the lower the power consumption, despite the reduction in isentropic efficiency once the optimal value has been reached. It can be explained by the isentropic work that is decreasing even faster when low pressure ratios are reached. If a pressure ratio of 1 could have been tested, the isentropic work would be zero, unlike the power consumption, therefore reaching a 0% isentropic efficiency. The decrease of mass flow rate with the increasing pressure ratio can simply be justified by leakages and supply heat transfer, as higher temperatures are reached at higher pressure ratios.

Ideal compression work and theoretical mass flow rate are also provided in Figures B.20 and B.21. The ideal compression work simply is the difference between the isentropic

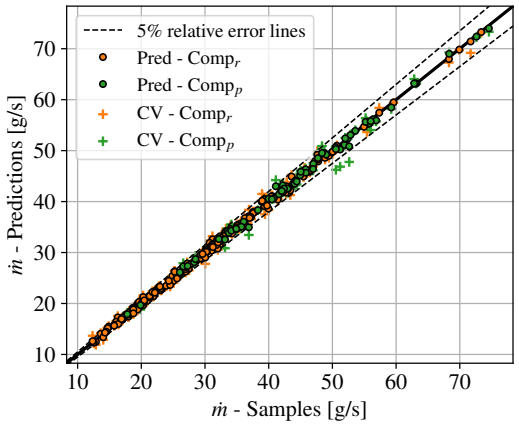

Figure B.14: Datasets versus predictions (Pred) and cross-validation (CV) for the mass flow rate.

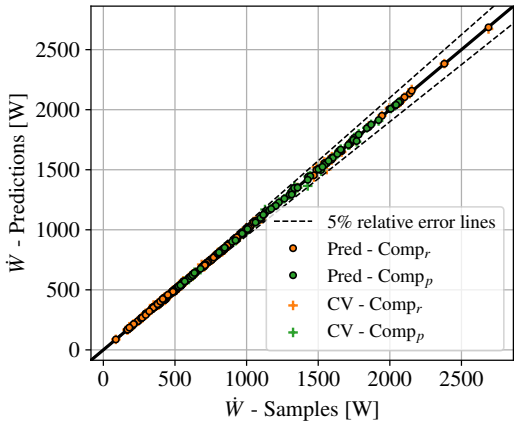

Figure B.15: Datasets versus predictions (Pred) and cross-validation (CV) for the power consumption.

enthalpy at the exhaust pressure and the suction enthalpy. As expected, this compression work is decreasing with a decrease in vapor quality, as the compression of liquid requires less work than the compression of vapor. At the same time, the ideal mass flow rate increases with vapor quality, making the ideal compression power (i.e., the product of both) less sensitive to vapor quality. As expected, the ideal mass flow rate is totally independent of the outlet pressure, as it is calculated based on compressor upstream conditions only. Regarding the ideal work, it naturally increases with the pressure ratio, as the isentropic exhaust enthalpy would be higher.

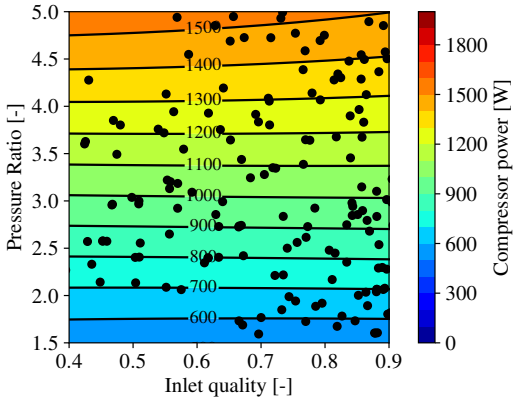

Figure B.16: Evolution of the power consumption for the retrofitted compressor, with an inlet pressure of 1.5 bar, an OCR of 5% and a compressor speed of 2500 RPM (reference case).

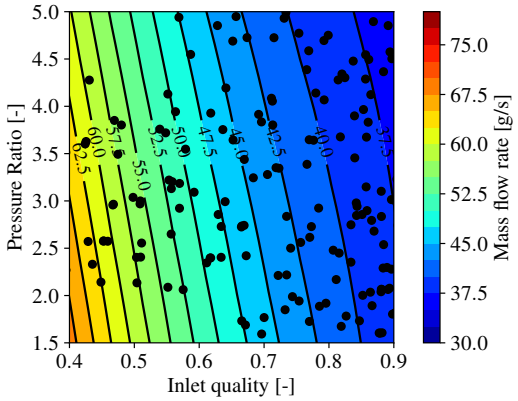

Figure B.17: Evolution of the mass flow rate for the retrofitted compressor, with an inlet pressure of 1.5 bar, an OCR of 5% and a compressor speed of 2500 RPM (reference case).

B.3.3 Effect of the inlet pressure

A change in the inlet pressure does not significantly change the isentropic and volumetric efficiencies, as observed in Figures B.22 and B.23. Up to 5% of absolute deviation is observed in some areas of the 2D maps, which can certainly be explained by the significant modification of mass flow rate, as the vapor density is strongly influenced by the pressure. Internal leakage and flows are also influenced by these changes in density, resulting in these slight deviations from the reference case.

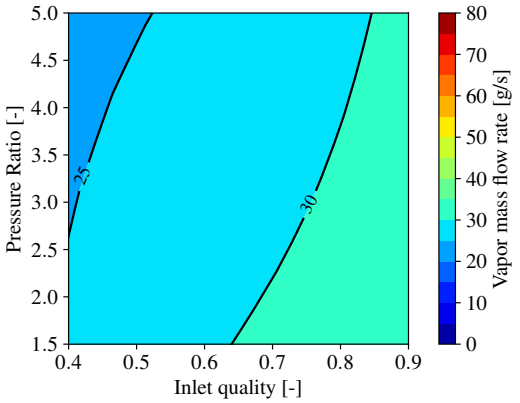

Figure B.18: Evolution of the vapor mass flow rate for the retrofitted compressor, with an inlet pressure of 1.5 bar, an OCR of 5% and a compressor speed of 2500 RPM (reference case).

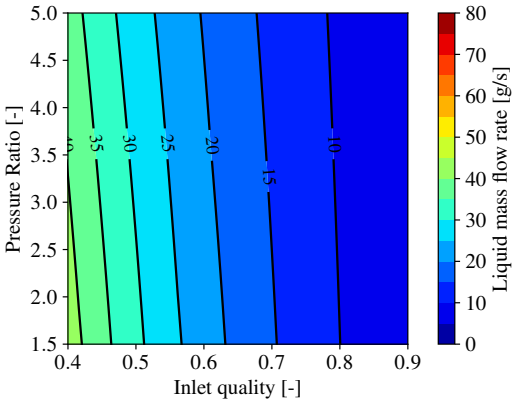

Figure B.19: Evolution of the liquid mass flow rate for the retrofitted compressor, with an inlet pressure of 1.5 bar, an OCR of 5% and a compressor speed of 2500 RPM (reference case).

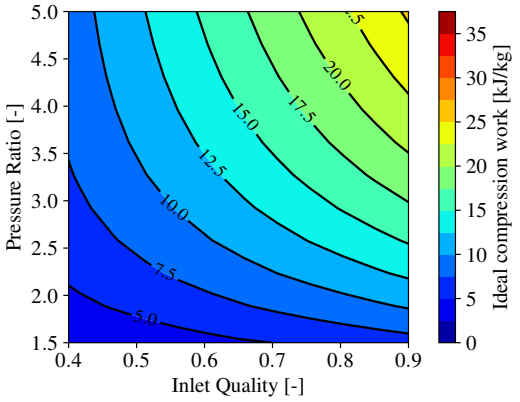

Figure B.20: Evolution of the ideal work of compression for the retrofitted compressor, with an inlet pressure of 1.5 bar, an OCR of 5% and a compressor speed of 2500 RPM (reference case).

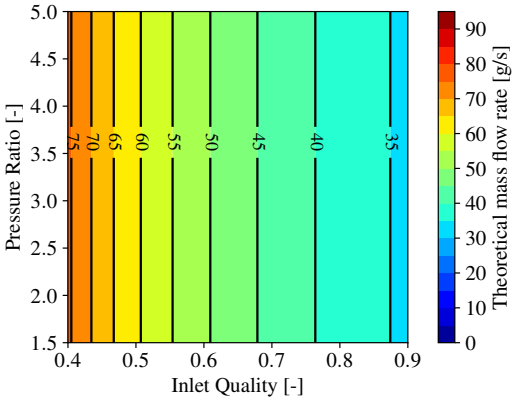

Figure B.21: Evolution of the theoretical mass flow rate for the retrofitted compressor, with an inlet pressure of 1.5 bar, an OCR of 5% and a compressor speed of 2500 RPM (reference case).

B.4 Lab-scale prototype results post-processing

B.4.1 Isentropic and volumetric efficiency maps

The isentropic and volumetric efficiency maps (both 2D and 3D) of the lab-scale prototype have been displayed to help better understand the difference maps provided in Section 3.5.1. They can be found in Figures B.24 and B.25 for the 3D maps, and in Figures B.26 and B.27 for the 2D maps. An interesting observation can be made: higher isentropic and volumetric efficiencies are obtained at high pressure ratios for this machine. Indeed, the volumetric efficiency does not decrease with increasing pressure ratio, which could be explained by the higher number of coexisting compression chambers, preventing direct leakage from the discharge chambers to the suction chambers. This constant volumetric efficiency cannot be observed when displaying the efficiency difference between the two compressors.

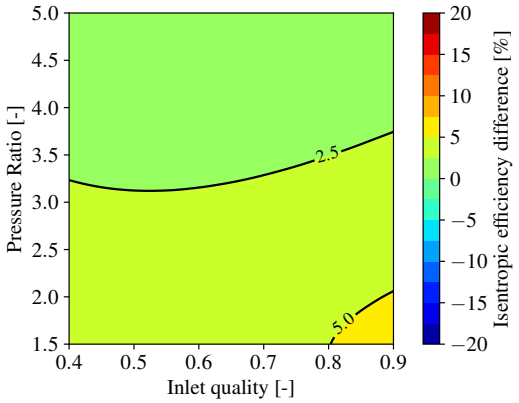

Figure B.22: Difference in isentropic efficiency from the reference case inlet pressure of 1.5 bar to 2 bar.

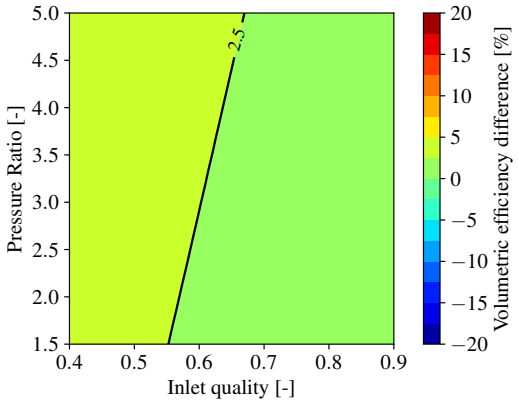

Figure B.23: Difference in volumetric efficiency from the reference case inlet pressure of 1.5 bar to 2 bar.

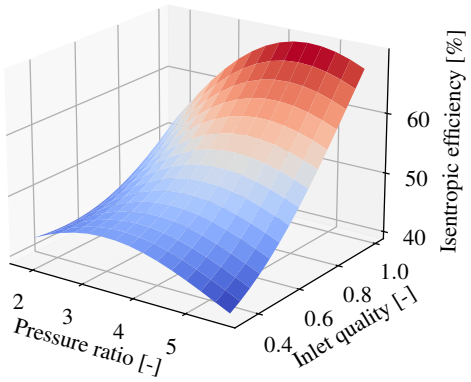

Figure B.24: 3D evolution of the isentropic efficiency for the lab-scale prototype, with an inlet pressure of 1.5 bar, an OCR of 5% and a compressor speed of 2500 RPM (reference case).

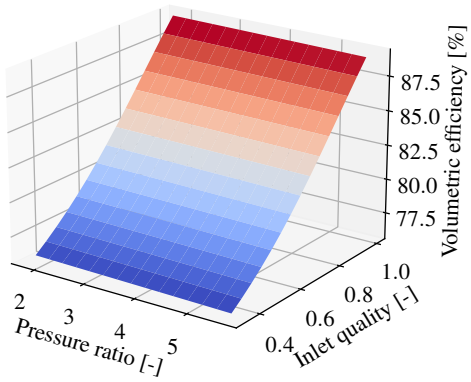

Figure B.25: 3D evolution of the volumetric efficiency for the lab-scale prototype, with an inlet pressure of 1.5 bar, an OCR of 5% and a compressor speed of 2500 RPM (reference case).

B.4.2 Compressor real speed measurement

An inductive sensor was used to achieve the highest possible accuracy in speed measurement. The specific model, Uprox+ Ni15U-EM18WD-AP6X, is a normally open sensor, meaning it outputs the input voltage when no change in the magnetic field is detected. When a change in the magnetic field is detected, the sensor outputs a new voltage, typically between 0 and 1 V. Magnets were attached to the pulley, and the sensor was positioned directly above the, as shown in Figure B.28.

An example signal from the sensor is displayed in Figure B.29, where the distance between two down peaks represents the revolution period T_{rev}. The rotational speed in RPM can then be calculated from it using the following formula:

$$N = \frac{60}{T_{\text{rev}}}. \tag{B.3}$$

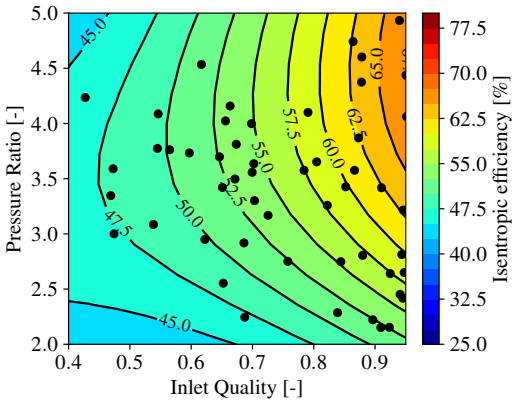

Figure B.26: Evolution of the isentropic efficiency for the lab-scale prototype, with an inlet pressure of 1.5 bar, an OCR of 5% and a compressor speed of 2500 RPM (reference case).

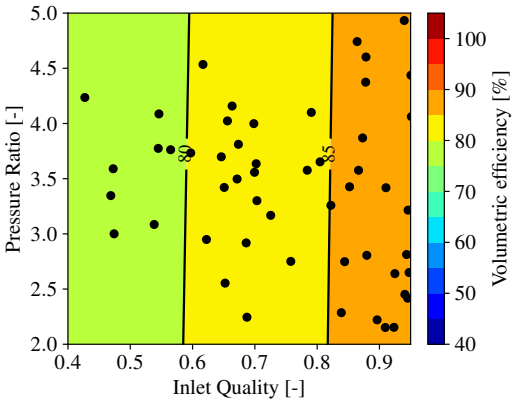

Figure B.27: Evolution of the volumetric efficiency for the lab-scale prototype, with an inlet pressure of 1.5 bar, an OCR of 5% and a compressor speed of 2500 RPM (reference case).

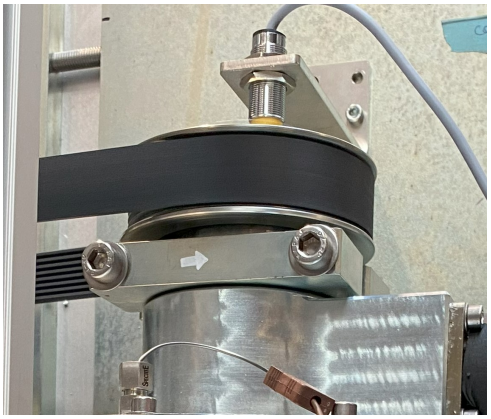

Figure B.28: Placement of the inductive sensor.

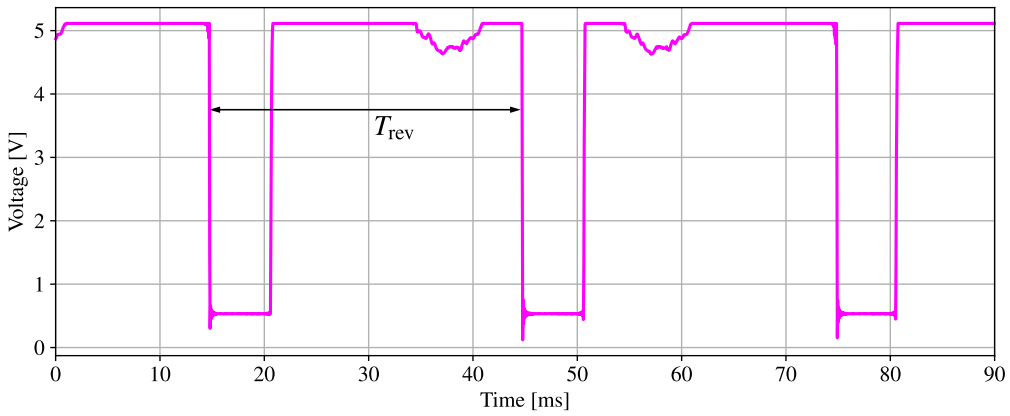

Figure B.29: Voltage signal from the inductive sensor.

Appendix C

Numerical investigations

C.1 Geometrical model

C.1.1 Geometrical parameters derived

The geometrical parameters defined in Section 4.3 allows the derivation of other interesting geometrical parameters. First, the orbiting radius imposed by the scroll geometry is given by

$$r_o = r_b \left(\pi - \phi_{i0} + \phi_{o0}\right) \tag{C.1}$$

Then, the scroll thickness t_s can be expressed by:

$$t_s = r_b \left(\phi_{i0} - \phi_{o0}\right) \tag{C.2}$$

The number of coexisting compression chambers at the orbiting angle θ is formulated as:

$$N_c = \text{floor}\left(\frac{\phi_{ie} - \theta - \phi_{os} - \pi}{2\pi}\right) \tag{C.3}$$

The maximum number of coexisting compression chambers is the number of compression chamber at the orbiting angle $\theta = 0$, it is therefore defined as:

$$N_{c,max} = \text{floor}\left(\frac{\phi_{ie} - \phi_{os} - \pi}{2\pi}\right) \tag{C.4}$$

Finally, from this maximum number of compression chambers, it is possible to derive the discharge angle θ_d, from which the last compression chambers open to the discharge chamber:

$$\theta_d = \phi_{ie} - \phi_{os} - 2\pi N_{c,max} - \pi \tag{C.5}$$

The values of these derived parameters for the retrofitted and lab-scale prototypes are included in Table 4.1.

C.1.2 Retrofitted compressor discharge geometry

The off-the-shelf machine discharge geometry is not a usual one like the arc-arc, or the arc-line-arc geometries. Indeed, the retrofitting of the compressor showed that the geometry is an arc-arc-line-arc with the two first arcs not tangential. A diagram of this discharge geometry can be found in Figure C.1.

With all the parameters presented in Figure C.1, the complete geometry will be figured out step by step in order to determine every coordinates of the polygon representing chambers dd and ddd. Starting by the bottom of the diagram, knowing the position of point (x_{is}, y_{is}) as being the first point of the inner scroll involute, the point (x_0, y_0) that is the centre of arc 0 can be easily figured out by the tangential constraint found in the link between the inner scroll

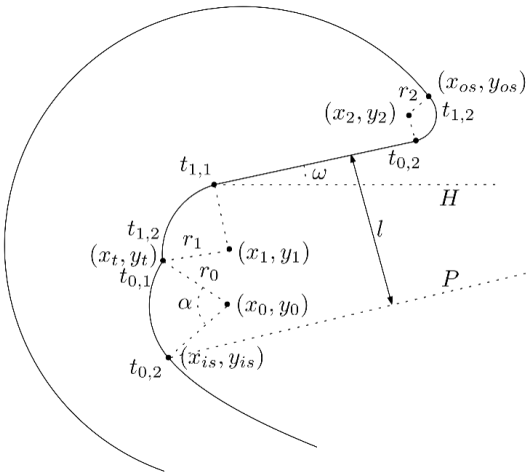

Figure C.1: Diagram of the retrofitted compressor discharge geometry.

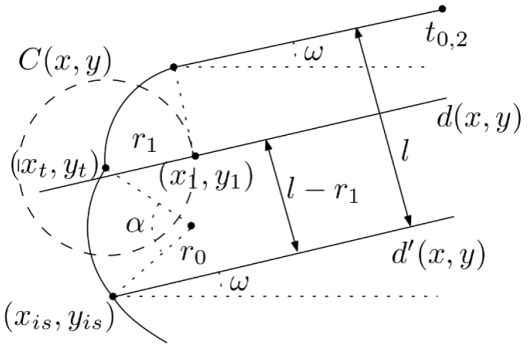

Figure C.2: Detailed diagram of the retrofitted compressor discharge geometry.

involute and the arc. A tangential constraint at a point implies that both normal vector of the linked curves is the same, one can thus write

$$(x_0, y_0) = \big(x_{\text{is}} - r_0 \sin \phi_{\text{is}},\ y_{\text{is}} + r_0 \cos \phi_{\text{is}}\big). \tag{C.6}$$

The angle $t_{0,2}$ with regard to point $(x_0,\, y_0)$ is simply the four-quadrant arctangent angle, which is the anti-clockwise angle in the four-quadrant datum plane. Its value can be determined with

$$t_{0,2} = \text{atan2}\big(y_{\text{is}} - y_0,\ x_{\text{is}} - x_0\big). \tag{C.7}$$

The angle $t_{1,2}$ can now easily be found with the following equation:

$$t_{0,1} = t_{0,2} - \alpha. \tag{C.8}$$

By knowing this angle and the position of the arc 0 centre, it is possible to determine the position of point $(x_t,\, y_t)$:

$$(x_t, y_t) = \big(x_0 + r_0 \cos t_{0,1},\ y_0 + r_0 \sin t_{0,1}\big). \tag{C.9}$$

Starting from the upper side of the diagram from Figure C.1, the centre of arc 2 can easily be determined in the same way of arc 0's one:

$$(x_2, y_2) = \big(x_{\text{os}} - r_2 \sin \phi_{\text{os}},\ y_{\text{os}} + r_2 \cos \phi_{\text{os}}\big). \tag{C.10}$$

The only crucial remaining parameters to figure out in order to have a complete definition of the discharge geometry is the centre of arc 1, which will not be easily computable as being not tangential to the arc 0 and as the length of the line is not known. From Figure C.1, some implicit relation can be derived as can be seen in Figure C.2. To compute the coordinates of arc 1's centre, a circle of radius r_1 can be drawn from point $(x_t,\, y_t)$, the equation of this circle is therefore given by

$$C(x, y) \equiv (x - x_t)^2 + (y - y_t)^2 = r_1^2. \tag{C.11}$$

Afterwards, a line called $d(x, y)$ can be drawn passing by the centre of arc 1, indeed, knowing the angle ω and point $(x_{\text{is}},\, y_{\text{is}})$ allows to compute the equation of the $d'(x, y)$ line

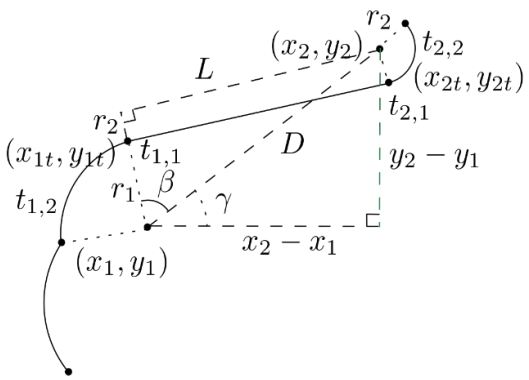

Figure C.3: Arc-line-arc discharge geometric parameters.

$$\tan\gamma = \frac{y_2 - y_1}{x_2 - x_1} \tag{C.14}$$

$$\cos\beta = \frac{r_1 + r_2}{D} \tag{C.15}$$

$$D = \sqrt{(x_2 - x_1)^2 + (y_2 - y_1)^2} \tag{C.16}$$

$$x_{1t} = x_1 + r_1\cos(\gamma + \alpha) \tag{C.17}$$

$$y_{1t} = y_1 + r_1\sin(\gamma + \alpha) \tag{C.18}$$

$$L = \sqrt{D^2 - (r_1 + r_2)^2} \tag{C.19}$$

$$x_{2t} = x_{1t} + L\sin(\gamma + \alpha) \tag{C.20}$$

$$y_{2t} = y_{1t} - L\cos(\gamma + \alpha) \tag{C.21}$$

and also knowing that the distance between the two lines d and d' is given by $l - r_1$, one thus has

$$d(x, y) \equiv y = (x - x_{\text{is}})\tan\omega + y_{\text{is}} + \frac{l - r_1}{\cos\omega}. \tag{C.12}$$

The crossing point between circle $C(x, y)$ and line $d(x, y)$ gives the coordinates of (x_1, y_1), as equaling y in these equations gives, after some developments:

$$\begin{aligned}(-1 - \tan^2\omega)x^2 + \left(2x_t + 2x_{\text{is}}\tan^2\omega - 2\tan\omega\left(y_{\text{is}} + \tfrac{l-r_1}{\cos\omega} - y_t\right)\right)x \\ + r_1^2 - x_t^2 - x_{\text{is}}^2\tan^2\omega - \left(y_{\text{is}} + \tfrac{l-r_1}{\cos\omega} - y_t\right)^2 \\ + 2x_{\text{is}}\tan\omega\left(y_{\text{is}} + \tfrac{l-r_1}{\cos\omega} - y_t\right) = 0.\end{aligned} \tag{C.13}$$

which is a second-degree equation in x that can be easily solved to obtain the coordinate x_1 of arc 1 centre, moreover substituting x_1 in the equation of $d(x, y)$ allows to get y_1.

Now that the centre of arc 1 has been found, the rest of the geometry can be determined like a simple arc-line-arc discharge geometry. This is what is made in Figure C.3 with the series of trivial trigonometry-based equations. Finally, the points on the line can be found using a line equation with points (x_{1t}, y_{1t}) and (x_{2t}, y_{2t}) and the point on arc 1 and arc 2 only needs to know their limit angles in the four-quadrant datum like done in Equation C.22. Regarding the discharge port its centre coincides with the position of point (x_1,y_1).

$$\begin{aligned}t_{1,1} &= \gamma + \alpha \\ t_{1,2} &= \text{atan2}\left(y_{\text{is}} - y_1,\ x_{\text{is}} - x_1\right) \\ t_{2,1} &= \text{atan2}\left(y_{1t} - y_2,\ x_{1t} - x_2\right) \\ t_{2,2} &= \text{atan2}\left(y_{\text{os}} - y_2,\ x_{\text{os}} - x_2\right)\end{aligned} \tag{C.22}$$

The discharge geometry of the retrofitted machine is finally totally figured out. The parameters used to fully describe this geometry can be found in Table 4.1.

C.1.3 Area variations

Examples of area variations within the scroll compressors can be found in Figures C.4, C.5, C.6, C.7, C.8, C.9.

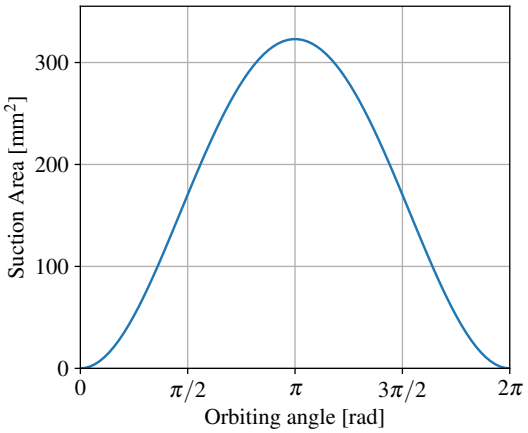

Figure C.4: Suction area of the retrofitted compressor.

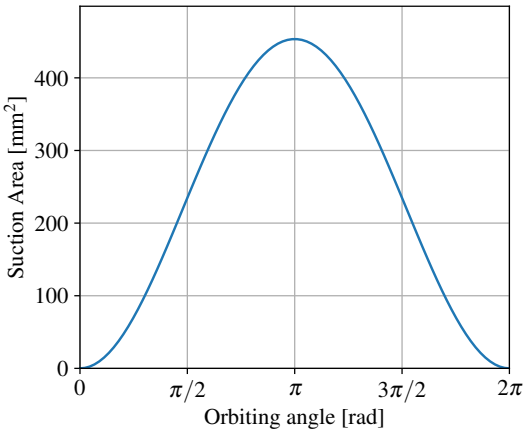

Figure C.5: Suction area of the lab-scale prototype.

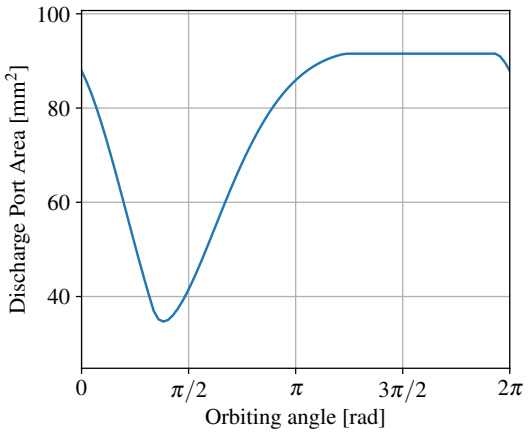

Figure C.6: Discharge area of the retrofitted compressor.

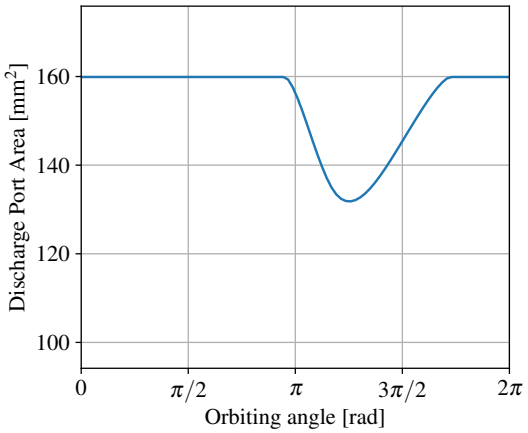

Figure C.7: Discharge area of the lab-scale prototype.

C.2 Core model

C.2.1 Case study

The internal energy variation of the case study presented in Section 4.4.5 can be found in Figure C.10 as well as the volume ratio. The internal energy only varies when the volume changes, as without volume variation no work can be transferred to the system. Nevertheless, the entropy continues to vary, even when the system is at rest, this can be seen in Figure C.11. Moreover, the temperature difference between the vapor and liquid phases can also be found on the plot. A clear trend can be observed: the temperature difference seems to behave like the derivative of the entropy evolution. The entropy variation is low when the temperature difference is low, then, the slope reaches a maximum when the temperature difference is maximal, and starts to decrease when the temperature difference decreases. This phenomenon was expected since the higher the heat transfer, the higher the irreversibility creation, reflected by the entropy generation of the system.

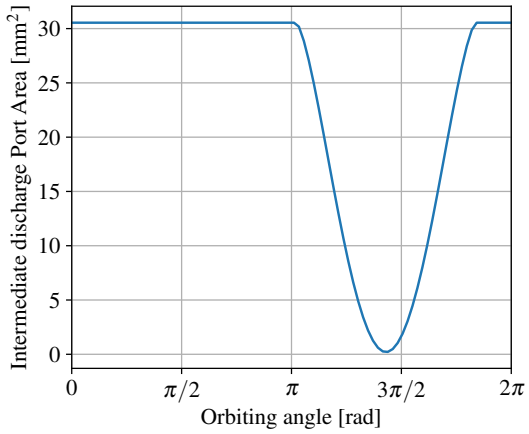

Figure C.8: Intermediate discharge ports area of the lab-scale prototype.

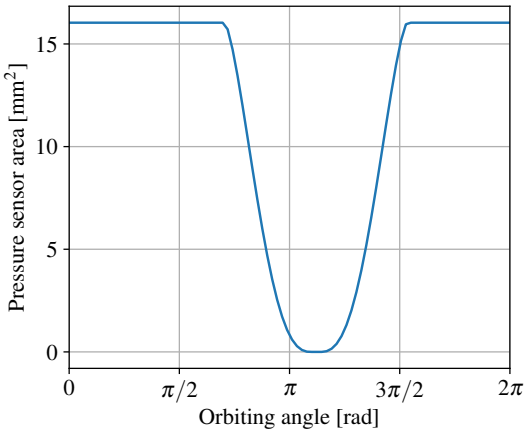

Figure C.9: Pressure sensor area

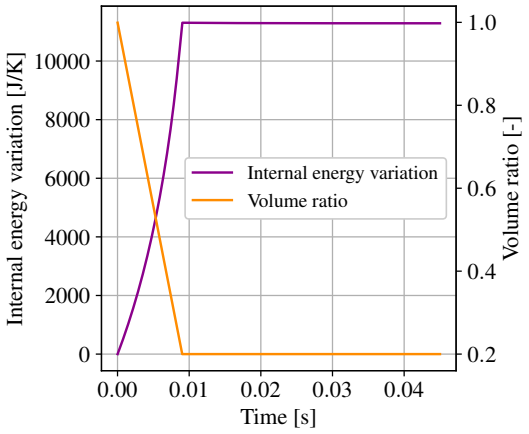

Figure C.10: Internal energy variation of the system and volume ratio varying with time.

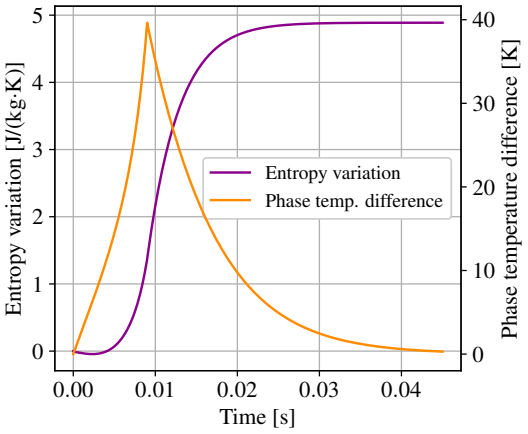

Figure C.11: Entropy variation of the system and temperature difference between the two phases varying with time.

C.3 Flow model

C.3.1 Flow pattern determination

The four dimensionless variables defined in Section 4.5.3 allow to obtain the transition lines between the flow regimes for a varying vapor quality. Those four dimensionless variables are the dimensionless cross-sectional areas of vapor (A_{gD}), of liquid (A_{lD}), the dimensionless liquid height h_{lD} and interface length P_{glD}. Three transition lines are required to obtain the flow pattern maps without heat transfer: the intermittent/annular (I-A) constant vapor quality line, the slug/intermittent (Slug-I) or stratified-wavy/annular (SW-A) mass flux line and the stratified/stratified-wavy (S-SW) mass flux line.

The first transition line is the intermittent/annular boundary, defined by the constant vapor quality Q_{IA}, it is given by

$$Q_{\mathrm{IA}} = \left\{ \left[0.34^{1/0.875} \left(\frac{\rho_{\mathrm{g}}}{\rho_{\mathrm{l}}} \right)^{-1/1.75} \left(\frac{\mu_{\mathrm{l}}}{\mu_{\mathrm{g}}} \right)^{-1/7} + 1 \right] \right\}^{-1} \tag{C.23}$$

The second transition line defines the boundary between a slug and intermittent flow (I) but also between a stratified-wavy and annular flow, it is given by the variation of the mass

flux G_{wavy} with the vapor quality:

$$G_{\text{wavy}} = \left\{ \frac{16 A_{\text{gD}}^3 g D \rho_{\text{l}} \rho_{\text{g}}}{Q^2 \pi^2 \left[1 - (2h_{\text{lD}} - 1)^2\right]^{0.5}} \left[\frac{\pi^2}{25 h_{\text{lD}}^2} \left(\frac{\text{We}}{\text{Fr}_{\text{l}}} \right)^{-1} + 1 \right]^{0.5} \right\} + 50 \tag{C.24}$$

where We and Fr_{l} are, respectively, the Weber and Froude number of the liquid phase, defined as

$$\text{Fr}_{\text{l}} = \frac{G^2 (1 - Q)}{\rho_{\text{l}}^2 \, g \, D} \tag{C.25}$$

$$\text{We} = \frac{G^2 D}{\rho_{\text{l}} \, \sigma} \tag{C.26}$$

The last transition line to be defined is the boundary between a stratified and stratified-wavy, it is given by the variation of the mass flux G_{strat} as a function of the vapor quality:

$$G_{\text{strat}} = \left\{ \frac{226.3^2 A_{\text{lD}} A_{\text{gD}}^2 \rho_{\text{g}} (\rho_{\text{l}} - \rho_{\text{g}}) \mu_{\text{l}} g}{Q^2 (1 - Q) \pi^3} \right\}^{1/3} \tag{C.27}$$

The following zones can therefore be defined:

- The stratified zone (S) and the bottom of the map, located below $G_{\text{strat}}(Q)$ when $Q > Q_{\text{IA}}$ and below $G_{\text{strat}}(Q_{\text{IA}})$ when $Q < Q_{\text{IA}}$.
- The slug + stratified wavy (Slug + SW) zone, located where $Q < Q_{\text{IA}}$ and $G_{\text{strat}}(Q_{\text{IA}}) < G < G_{\text{wavy}}(Q_{\text{IA}})$.
- The slug zone located where $Q < Q_{\text{IA}}$ and $G_{\text{wavy}}(Q) > G > G_{\text{wavy}}(Q_{\text{IA}})$.
- The intermittent zone (I) located where $Q < Q_{\text{IA}}$ and $G > G_{\text{wavy}}(Q)$.
- The stratified-wavy zone (SW) located where $Q > Q_{\text{IA}}$ and $G_{\text{strat}}(Q) < G < G_{\text{wavy}}(Q)$.
- the annular zone (A) located where $Q > Q_{\text{IA}}$ and $G > G_{\text{wavy}}(Q)$.

These different zones are represented in Figure 4.26.

C.3.2 Single-phase flow models

Single-phase flow models are used to compute the leakage. Three single-phase flow models are used: a frictional incompressible flow, a non-frictional incompressible flow, and a compressible flow (also non-frictional).

Frictional incompressible flow

A frictional flow refers to a flow regime in which the pressure drop or energy loss is primarily caused by frictional forces between the moving fluid and the walls of the channel. In the case of leakage, the liquid phase Reynolds number is given by

$$\text{Re}_{D_{\text{h}}} = \frac{G D_{\text{h}}}{\mu_{\text{l}}} \tag{C.28}$$

where the hydraulic diameter is defined as:

$$D_{\text{h}} = 2\delta \cdot r_{\text{h}} \tag{C.29}$$

with r_{h}, the liquid height ratio defined in Section 4.5.4.

The Darcy friction factor is different when the flow is laminar ($\text{Re}_{D_{\text{h}}} < 1038$) or turbulent ($\text{Re}_{D_{\text{h}}} \geq 1038$), it can be expressed as

$$f = \begin{cases} \dfrac{64}{\mathrm{Re}_{D_\mathrm{h}}} & \text{if } \mathrm{Re}_{D_\mathrm{h}} < 1038 \\ \dfrac{0.35}{\mathrm{Re}_{D_\mathrm{h}}^{0.25}} & \text{if } \mathrm{Re}_{D_\mathrm{h}} \geq 1038 \end{cases} \tag{C.30}$$

The corresponding pressure drop can be calculated with

$$\Delta p = \frac{f G^2 L}{2 \rho_\mathrm{l} D_\mathrm{h}} \tag{C.31}$$

where the length of the flow path is equal to the scroll thickness t_s for a radial leakage, whereas it can be set to $e_\mathrm{f} = 2.1$ mm for flank leakages according to Bell et al. (2012a). Finally, the mass flow rate can be calculated with the following expression:

$$\dot{m} = A \left(\frac{2 \rho \mu_\mathrm{l}^b \Delta p}{a D_\mathrm{h}^{b+1} L} \right)^{\frac{1}{b+2}} \tag{C.32}$$

where a and b are obtained from the following expression:

$$f = a \, \mathrm{Re}_{D_h}^b \tag{C.33}$$

Non-frictional incompressible flow

The non-frictional incompressible flow pressure drop resides in the change of section, not considered in the frictional incompressible flow. It is therefore simply based on a pressure drop coefficient linking the mass flow rate to the pressure drop. The mass flow rate is therefore given by

$$\dot{m} = C_\mathrm{d} \cdot A \cdot \sqrt{2 \, \rho_\mathrm{l} \, \Delta p} \tag{C.34}$$

where the discharge coefficient can be assumed to be $C_\mathrm{d} = 0.1$ for aspect ratio > 1000. The aspect ratio can be defined as the downstream cross-sectional area divided by the throat area, it is greater than 1000 for leakages.

Compressible flow

A compressible flow applies to the vapor phase leakages, as the Mach number of the flow is usually higher than 0.3 due to the low leakage areas. The mass flow rate of a compressible (isentropic) flow is defined as

$$\dot{m} = \begin{cases} A \sqrt{2 p_\mathrm{up} \rho_\mathrm{g} \frac{\kappa}{\kappa - 1} \left(r_p^{\frac{2}{\kappa}} - r_p^{\frac{\kappa+1}{\kappa}} \right)}, & \text{if } r_p > r_{p,\mathrm{c}} \\ A \sqrt{2 p_\mathrm{up} \rho_\mathrm{g} \frac{\kappa}{\kappa+1}} \left(\frac{2}{\kappa+1} \right)^{\frac{1}{\kappa-1}}, & \text{if } r_p \leq r_{p,\mathrm{c}} \end{cases} \tag{C.35}$$

where r_p is the pressure ratio. The critical pressure ratio $r_{p,\mathrm{c}}$ is given by:

$$r_{p,\mathrm{c}} = \left(\frac{2}{\kappa + 1} \right)^{\frac{\kappa}{\kappa-1}} \tag{C.36}$$

The isentropic expansion coefficient κ is simply defined as the ratio of specific heats:

$$\kappa = \frac{c_p}{c_v} \tag{C.37}$$

C.4 Heat transfer coefficients

C.4.1 Flow boiling in channels (Shah correlation)

The estimation of the heat transfer coefficient during evaporation in channels is based on Shah correlation (Shah 2021), which uses liquid-only flow properties and empirical correction factors. As recommended by Shah, accounting for the oil presence can simply be done by using the oil-refrigerant mixture properties of the liquid phase.

The single-phase heat-transfer coefficient for turbulent liquid flow is obtained from the Dittus-Boelter correlation:

$$h_{\mathrm{SP}} = \frac{\lambda}{D_h}\, 0.023\, \mathrm{Re}^{0.8}\, \mathrm{Pr}^{0.4} \tag{C.38}$$

The corresponding heat flux is expressed as:

$$q = 3\, h_{\mathrm{LT}}\, (T_{\mathrm{w}} - T_{\mathrm{su}}) \tag{C.39}$$

where h_{LT} is the heat-transfer coefficient for the liquid-only flow.

The Boiling number is defined by

$$\mathrm{Bo} = \frac{q}{G\, h_{\mathrm{fg}}} \tag{C.40}$$

with G the mass flux and h_{fg} the latent heat of vaporization.

The suppression factor proposed by Gungor and Winterton is given by

$$F = \begin{cases} 14.7\, \mathrm{Bo}^{0.5}, & \text{if Bo} \geq 0.0011 \\ 15.4\, \mathrm{Bo}^{0.5}, & \text{otherwise} \end{cases} \tag{C.41}$$

The Froude number for liquid-only flow is expressed as

$$\mathrm{Fr}_{\mathrm{lo}} = \frac{((1-Q)\, G)^2}{g\, D_h\, \rho_{\mathrm{l}}^2} \tag{C.42}$$

where Q is the vapor quality and ρ_{l} the liquid density.

The exponent n depends on the liquid-only Froude number:

$$n = \begin{cases} 0, & \text{if } \mathrm{Fr}_{lo} \geq 0.04 \\ 1, & \text{otherwise.} \end{cases} \tag{C.43}$$

The parameter A is defined as:

$$A = C_{\mathrm{v}}\, \left(0.38\, \mathrm{Fr}_{\mathrm{lo}}^{-0.3}\right)^n \tag{C.44}$$

where C_{v} is an empirical parameters given by

$$C_{\mathrm{v}} = \left(\frac{1-Q}{Q}\right)^{0.8} \left(\frac{\rho_g}{\rho_l}\right)^{0.5} \tag{C.45}$$

The heat transfer coefficients for different boiling regimes are calculated as follows

$$h_{\mathrm{TP1}} = 230\,\mathrm{Bo}^{0.5}\,h_{\mathrm{LT}} \tag{C.46}$$

$$h_{\mathrm{TP2}} = 1.8\,A^{-0.8}\,h_{\mathrm{LT}} \tag{C.47}$$

$$h_{\mathrm{TP3}} = F\,\exp\left(2.47\,A^{-0.15}\right) \tag{C.48}$$

$$h_{\mathrm{TP4}} = F\,\exp\left(2.74\,A^{-0.1}\right) \tag{C.49}$$

Finally, the overall two-phase heat-transfer coefficient is obtained by taking the maximum of the heat transfer coefficients from the different boiling regimes:

$$h_{\mathrm{TP}} = \max(h_{\mathrm{TP1}},\, h_{\mathrm{TP2}},\, h_{\mathrm{TP3}},\, h_{\mathrm{TP4}}) \tag{C.50}$$

C.4.2 Natural convection around a vertical cylinder

The convective heat transfer between a vertical cylinder of height H_{cp} and diameter D_{cp} (see Figure C.12) and the surrounding air under natural convection conditions can be estimated using the Grashof and Rayleigh numbers, followed by an empirical correlation for the Nusselt number (Popiel et al. 2007).

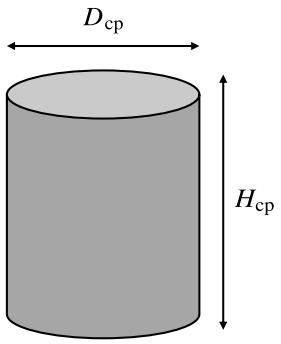

Figure C.12: Cylinder representation for ambient heat transfer calculation.

The Grashof and Rayleigh numbers are given by

$$\mathrm{Gr} = \frac{g\,\beta\,|T_{\mathrm{wall}} - T_{\mathrm{amb}}|\,H^3}{\nu^2} \tag{C.51}$$

$$\mathrm{Ra}_H = \mathrm{Pr}\,\mathrm{Gr} \tag{C.52}$$

where the gravitational acceleration is $g = 9.81$ m/s^2, $\beta = 1/T_{\mathrm{amb}}$ [1/K], the Prandtl number of ambient air can be set at $\mathrm{Pr} = 0.71$ while its kinematic viscosity ν can be assumed to be $\nu = 1.5 \cdot 10^{-5}$ m^2/s.

The geometric aspect ratio of the cylinder is defined as

$$\mathrm{HD}_{\mathrm{ratio}} = \frac{H_{\mathrm{cp}}}{D_{\mathrm{cp}}} \tag{C.53}$$

The coefficients of the Nusselt number correlation depend on the aspect ratio as

$$A = 0.519 + 0.03454\,\mathrm{HD}_{\mathrm{ratio}} + 0.0008772\,\mathrm{HD}_{\mathrm{ratio}}^2 + 8.855 \times 10^{-6}\,\mathrm{HD}_{\mathrm{ratio}}^3 \tag{C.54}$$

$$n = 0.25 - 0.00253\,\mathrm{HD}_{\mathrm{ratio}} + 1.152 \times 10^{-5}\,\mathrm{HD}_{\mathrm{ratio}}^2 \tag{C.55}$$

The height-based Nusselt number is then expressed as

$$\mathrm{Nu}_H = A\,\mathrm{Ra}_H^n \tag{C.56}$$

Finally, the convective heat transfer coefficient is obtained from

$$h = \frac{\mathrm{Nu}_H\,\lambda}{D} \tag{C.57}$$

where $\lambda = 0.026$ W/(mK) is the thermal conductivity of ambient air.

C.5 Validation

C.5.1 Lab-scale prototype

Validation results of the lab-scale prototype can be found in Figure C.13 using k_1 predictions coming from both compressors individual calibrations.

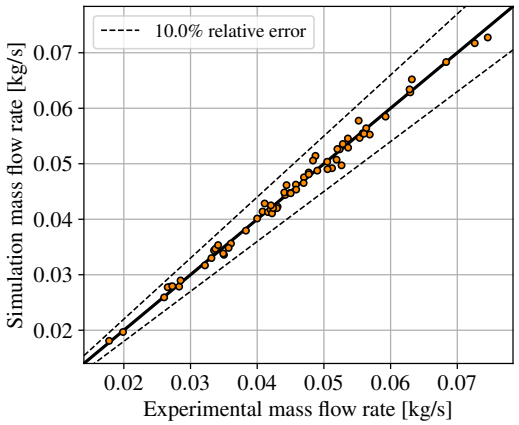

(a) Mass flow rate $\dot{m}$ (ARD = 1.84%).

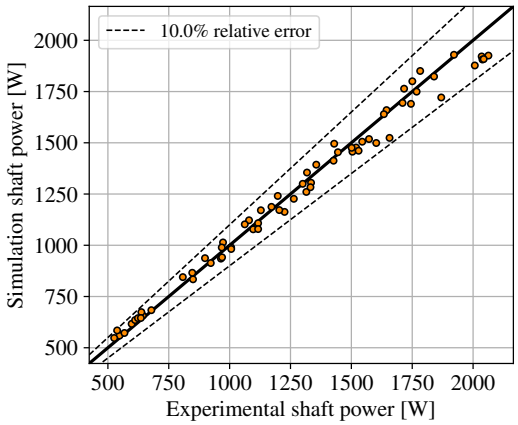

(b) Power consumption $\dot{W}_{\mathrm{shaft,cp}}$ (ARD = 3.19%).

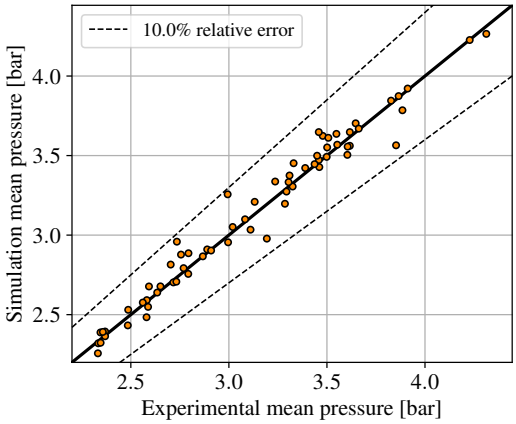

(c) Mean pressure $\bar{p}$ (ARD = 1.92%).

Figure C.13: Validation results of the lab-scale prototype with k_1 predictions coming from both compressors individual calibrations.

C.5.2 Retrofitted compressor

Validation results of the retrofitted compressor can be found in Figure C.13 using k_1 predictions coming from both compressors individual calibrations.

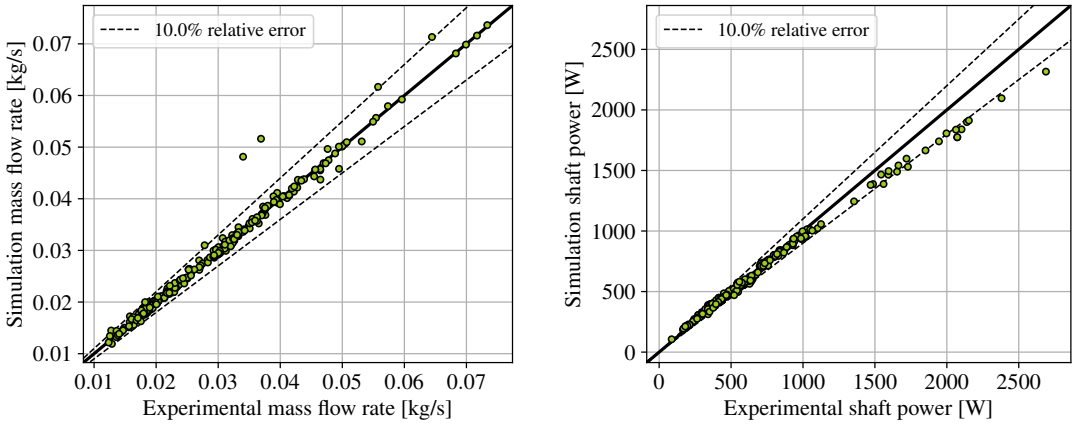

(a) Mass flow rate $\dot{m}$ (ARD = 2.17%).

(b) Power consumption $\dot{W}_{\text{shaft,cp}}$ (ARD = 4.43%).

Figure C.14: Validation results of the retrofitted compressor with k_1 predictions coming from both compressors individual calibrations.

Bibliography

Bell, Ian H. (2011). "Theoretical and Experimental Analysis of Liquid Flooded Compression in Scroll Compressors". PhD thesis. Purdue University.

Virtanen, Pauli et al. (Mar. 2020). "SciPy 1.0: Fundamental Algorithms for Scientific Computing in Python". In: *Nature Methods* 17.3, pp. 261–272. ISSN: 1548-7091, 1548-7105. DOI: 10.1038/s41592-019-0686-2. (Visited on 11/03/2025).

Leclercq, Nicolas, Vega, Javier, and Lemort, Vincent (2023). "Investigations on a Heat Pump Using Two-Phase Refrigerant Compressions". In: *36th International Conference on Efficiency, Cost, Optimization, Simulation and Environmental Impact of Energy Systems (ECOS 2023)*. ECOS 2023, pp. 804–814. ISBN: 978-1-7138-7492-8. DOI: 10.52202/069564-0073.

European Commission (2016). *An EU Strategy on Heating and Cooling*.

— (2022). *Clean Energy Technology Observatory, Heat Pumps in the European Union: Status Report on Technology Development, Trends, Value Chains and Markets : 2022*. (Visited on 11/27/2025).

International Energy Agency (2022). *Annual Report 2022: Heat Pumping Technologies*. Tech. rep.

Fleiter, Tobias, Steinbach, Jan, and Ragwitz, Mario (2017). *Mapping and Analyses of the Current and Future (2020 - 2030) Heating/Cooling Fuel Deployment (Fossil/Renewables)*. Tech. rep.

International Institute of Refrigeration (2024). *A Strong Global Compressor Market*.

Taft, G L (1972). "Selection and Application of Industrial Screw Compressors". In: International Compressor Engineering Conference.

Zimmern, B (1984). "From Water to Refrigerant: Twenty Years to Develop the Oil Injection-Free Single Screw Compressor". In: International Compressor Engineering Conference.

Nikolov, Alexander and Brümmer, Andreas (2014). "Influence of Water Injection on the Operating Behaviour of Screw Machines". In: 9th International Conference on Screw Machines.

Yusha, V L, Chernov, G I, and Fedorova, M A (Nov. 2018). "Mathematical Modeling of Working Processes of Variable Frequency Screw Compressor with Differentiated Oil Supply into the Working Chamber". In: *IOP Conference Series: Materials Science and Engineering* 425, p. 012003. ISSN: 1757-899X. DOI: 10.1088/1757-899X/425/1/012003. (Visited on 09/09/2025).

He, Zhilong et al. (May 2018). "Experimental Investigation into the Effect of Oil Injection on the Performance of a Variable Speed Twin-Screw Compressor". In: *Energies* 11.6, p. 1342. ISSN: 1996-1073. DOI: 10.3390/en11061342. (Visited on 09/10/2025).

Wang, Chuang et al. (Oct. 2018). "Development of an Oil Free Water-Lubricated Twin-Screw Air Compressor". In: *Applied Thermal Engineering* 143, pp. 396–402. ISSN: 13594311. DOI: 10.1016/j.applthermaleng.2018.07.119. (Visited on 09/10/2025).

Ferreira, C. A. Infante, Zaytsev, D., and Zamfirescu, C. (2006a). "Wet Compression of Pure Refrigerants". In: International Compressor Engineering Conference.

Li, H et al. (1992). "Research of Oil-Injected Scroll Compressor Working Process". In: *Proceedings of the International Compressor Engineering Conference*. Purdue University.

Leclercq, Nicolas and Lemort, Vincent (2022). "Modeling and Simulation of a Two-Phase Scroll Compressor". In: *International Compressor Engineering Conference*. Purdue University.

Zaytsev, D. and Ferreira, C. A. Infante (2000). "Aspects of Two-Phase Flow Screw Compressor Modelling Part I: Leakage Flow and Rotor Tip Friction". In: *Proceeding of the International Compressor Engineering Conference*. Purdue University.

Liu, Zheji and Soedel, Werner (1995). "A Mathematical Model for Simulating Liquid and Vapor Two-Phase Compression Processes and Investigating Slugging Problems in Compressors". In: *HVAC and R Research* 1.2, pp. 99–109. ISSN: 10789669. DOI: 10.1080/10789669.1995.10391312.

Prasad, B. G. Shiva (Sept. 2002). "Effect of Liquid on a Reciprocating Compressor". In: *Journal of Energy Resources Technology* 124.3, pp. 187–190. ISSN: 0195-0738, 1528-8994. DOI: 10.1115/1.1491981. (Visited on 10/23/2025).

Lin, Jie et al. (July 2022). "Simulation of Single and Two-Phase Refrigerant Compression in Rotary Compressors". In: *Applied Thermal Engineering* 211. ISSN: 13594311. DOI: 10.1016/j.applthermaleng.2022.118465.

Guo, Nini, Lin, Jie, and Wu, Jianhua (Dec. 2024). "Simulation on Two-Phase Refrigerant Compression in the Cylinder of Rotary Compressors Using CFD Method". In: *Scientific Reports* 14.1. ISSN: 20452322. DOI: 10.1038/s41598-024-56856-y.

Wang, Jun et al. (Dec. 2015). "Analysis and Numerical Simulation of a Novel Gas–Liquid Multiphase Scroll Pump". In: *International Journal of Heat and Mass Transfer* 91, pp. 27–36. ISSN: 00179310. DOI: 10.1016/j.ijheatmasstransfer.2015.07.086. (Visited on 09/09/2025).

Bush, James W and Elson, John P (1988). "Scroll Compressor Design Criteria for Residential Air Conditioning and Heat Pump Applications, Part I: Mechanics". In: International Compressor Engineering Conference.

Sakuda, A et al. (2001). "Performance Improvement of Scroll Compressor with New Sealing-Oil Supply Mechanism". In: International Conference on Compressors and their Systems. DOI: C591/019/2001.

Hiwata, A et al. (2002). "Performance Investigation with Oil-Injection to Compression Chambers on CO2-scroll Compressor". In: *International Compressor Engineering Conference*. Purdue University.

Bell, Ian H. et al. (Nov. 2012a). "Liquid Flooded Compression and Expansion in Scroll Machines - Part II: Experimental Testing and Model Validation". In: *International Journal of Refrigeration* 35.7, pp. 1890–1900. ISSN: 01407007. DOI: 10.1016/j.ijrefrig.2012.07.008.

Zhao, Yuanyang et al. (June 2005). "Theoretical and Experimental Studies of Water Injection Scroll Compressor in Automotive Fuel Cell Systems". In: *Energy Conversion and Management* 46.9-10, pp. 1379–1392. ISSN: 01968904. DOI: 10.1016/j.enconman.2004.08.006. (Visited on 11/05/2025).

Afjei, Th., Suter, P., and Favrat, D. (1992). "Experimental Analysis of an Inverter-Driven Scroll Compressor with Liquid Injection". In: *International Compressor Engineering Conference*. Purdue University.

Dutta, Asit K., Yanagisawa, Tadashi, and Fukuta, Mitsuhiro (Sept. 2001). "An Investigation of the Performance of a Scroll Compressor under Liquid Refrigerant Injection". In: *International Journal of Refrigeration* 24.6, pp. 577–587. ISSN: 01407007. DOI: 10.1016/S0140-7007(00)00041-4. (Visited on 09/09/2025).

Cho, Honghyun, Chung, Jin Taek, and Kim, Yongchan (Jan. 2003). "Influence of Liquid Refrigerant Injection on the Performance of an Inverter-Driven Scroll Compressor". In: *International Journal of Refrigeration* 26.1, pp. 87–94. ISSN: 01407007. DOI: 10.1016/S0140-7007(02)00017-8. (Visited on 10/23/2025).

Wang, Baolong et al. (Apr. 2008). "Numerical Research on the Scroll Compressor with Refrigeration Injection". In: *Applied Thermal Engineering* 28.5-6, pp. 440–449. ISSN: 13594311. DOI: 10.1016/j.applthermaleng.2007.05.012. (Visited on 09/10/2025).

Xu, Xing, Hwang, Yunho, and Radermacher, Reinhard (Mar. 2011). "Refrigerant Injection for Heat Pumping/Air Conditioning Systems: Literature Review and Challenges Discussions". In: *International Journal of Refrigeration* 34.2, pp. 402–415. ISSN: 01407007. DOI: 10.1016/j.ijrefrig.2010.09.015. (Visited on 09/09/2025).

Emhardt, Simon, Tian, Guohong, and Chew, John (Aug. 2018). "A Review of Scroll Expander Geometries and Their Performance". In: *Applied Thermal Engineering* 141, pp. 1020–1034. ISSN: 13594311. DOI: 10.1016/j.applthermaleng.2018.06.045. (Visited on 09/09/2025).

Smith, Ian, Stosic, Nikola, and Aldis, Colin (1995). "Trilateral Flash Cycle System: A High Effiency Power Plant For Liquid Resources". In: *Proceedings World Geothermal Congress*.

Itard, L.C.M (Sept. 1995). "Wet Compression versus Dry Compression in Heat Pumps Working with Pure Refrigerants or Non-Azeotropic Mixtures". In: *International Journal of Refrigeration* 18.7, pp. 495–504. ISSN: 01407007. DOI: 10.1016/0140-7007(95)93788-L. (Visited on 11/05/2025).

Vorster, P.P.J and Meyer, J.P (June 2000). "Wet Compression versus Dry Compression in Heat Pumps Working with Pure Refrigerants or Non-Azeotropic Binary Mixtures for Different Heating Applications". In: *International Journal of Refrigeration* 23.4, pp. 292–311. ISSN: 01407007. DOI: 10.1016/S0140-7007(99)00050-X.

Feng, Cao et al. (Oct. 2009). "Study on Performance of a Heat Pump Water Heater Using Suction Stream Liquid Injection". In: *Applied Thermal Engineering* 29.14-15, pp. 2942–2948. ISSN: 13594311. DOI: 10.1016/j.applthermaleng.2009.03.001. (Visited on 11/05/2025).

Yang, Minghong et al. (Nov. 2015). "Evaluation of Two-Phase Suction, Liquid Injection and Two-Phase Injection for Decreasing the Discharge Temperature of the R32 Scroll Compressor". In: *International Journal of Refrigeration* 59, pp. 269–280. ISSN: 01407007. DOI: 10.1016/j.ijrefrig.2015.08.004. (Visited on 11/05/2025).

Seong, Kyoungjin, Lee, Daehui, and Lee, Jinho (Mar. 2017). "The Effects of Wet Compression by the Electronic Expansion Valve Opening on the Performance of a Heat Pump System". In: *Applied Sciences* 7.3, p. 248. ISSN: 2076-3417. DOI: 10.3390/app7030248. (Visited on 10/22/2025).

Sun, Shuaihui et al. (Dec. 2021). "Influence of Two-Phase Suction Injection on Performances of the Scroll Refrigeration Compressor with a High-Temperature Shell". In: *Proceedings of the Institution of Mechanical Engineers, Part E: Journal of Process Mechanical Engineering* 235.6, pp. 2059–2072. ISSN: 0954-4089, 2041-3009. DOI: 10.1177/09544089211030216. (Visited on 10/22/2025).

Pan, Xi et al. (Dec. 2024). "Investigation on Saturated Vapor and Two-Phase Refrigerant Injection in the Rotary Compressor for the Extreme Hot and Cold Conditions". In: *Applied Thermal Engineering* 257, p. 124210. ISSN: 13594311. DOI: 10.1016/j.applthermaleng.2024.124210. (Visited on 11/05/2025).

Brunin, O, Feidt, M, and Hivet, B (Aug. 1997). "Comparison of the Working Domains of Some Compression Heat Pumps and a Compression-Absorption Heat Pump". In: *International Journal of Refrigeration* 20.5, pp. 308–318. ISSN: 01407007. DOI: 10.1016/S0140-7007(97)00025-X. (Visited on 11/07/2025).

Zamfirescu, Calin (Mar. 2009). "Modeling And Optimization of an Ammonia-Water Compression-Resorption Heat Pumps With Wet Compression". In: *Transactions of the Canadian Society for Mechanical Engineering* 33.1, pp. 75–88. ISSN: 0315-8977, 2816-5691. DOI: 10.1139/tcsme-2009-0008. (Visited on 10/23/2025).

Ferreira, C. A. Infante and Zaytsev, Dmytro (2002). "Experimental Compression - Resorption Heat Pump for Industrial Applications". In: International Compressor Engineering Conference.

Ferreira, C. A. Infante, Zamfirescu, C., and Zaytsev, D. (June 2006b). "Twin Screw Oil-Free Wet Compressor for Compression-Absorption Cycle". In: *International Journal of Refrigeration* 29.4, pp. 556–565. ISSN: 01407007. DOI: 10.1016/j.ijrefrig.2005.10.006.

van de Bor, D.M., Infante Ferreira, C.A., and Kiss, Anton A. (Sept. 2015). "Low Grade Waste Heat Recovery Using Heat Pumps and Power Cycles". In: *Energy* 89, pp. 864–873. ISSN: 03605442. DOI: 10.1016/j.energy.2015.06.030. (Visited on 11/07/2025).

Gudjonsdottir, V., Ferreira, C. A. Infante, and Goethals, A. (Feb. 2019). "Wet Compression Model for Entropy Production Minimization". In: *Applied Thermal Engineering* 149, pp. 439–447. ISSN: 13594311. DOI: 10.1016/j.applthermaleng.2018.12.065.

Briola, Stefano et al. (July 2021). "Thermo-Economic Analysis of a Novel Trigeneration Cycle Enabled by Two-Phase Machines". In: *Energy* 227. ISSN: 03605442. DOI: 10.1016/j.energy.2021.120453.

Bell, Ian H. et al. (Mar. 2015). "A Generalized Moving-Boundary Algorithm to Predict the Heat Transfer Rate of Counterflow Heat Exchangers for Any Phase Configuration". In: *Applied Thermal Engineering* 79, pp. 192–201. ISSN: 13594311. DOI: 10.1016/j.applthermaleng.2014.12.028. (Visited on 01/09/2026).

Han, Dong-Hyouck, Lee, Kyu-Jung, and Kim, Yoon-Ho (July 2003a). "Experiments on the Characteristics of Evaporation of R410A in Brazed Plate Heat Exchangers with Different Geometric Configurations". In: *Applied Thermal Engineering* 23.10, pp. 1209–1225. ISSN: 13594311. DOI: 10.1016/S1359-4311(03)00061-9. (Visited on 01/09/2026).

Han, Dong-Hyouck, Lee, K S, and Kim, Yoon-Ho (July 2003b). "The Characteristics of Condensation in Brazed Plate Heat Exchangers with Different Chevron Angles". In: *Journal of the Korean Physical Society*, pp. 66–73.

Shah, Mizra Mohammad (Feb. 2021). *Two-Phase Heat Transfer*. 1st ed. Wiley. ISBN: 978-1-119-61865-2. DOI: 10.1002/9781119618652. (Visited on 09/10/2025).

Byrne, Paul and Ghoubali, Redouane (Feb. 2019). "Exergy Analysis of Heat Pumps for Simultaneous Heating and Cooling". In: *Applied Thermal Engineering* 149, pp. 414–424. ISSN: 13594311. DOI: 10.1016/j.applthermaleng.2018.12.069. (Visited on 01/09/2026).

Kliem, Bernhard Paul (2005). "Grundlagen Des Zweiphasen-Schraubenmotors". PhD thesis. Universität Dortmund.

Bianchi, Giuseppe et al. (Dec. 2017). "Development and Analysis of a Packaged Trilateral Flash Cycle System for Low Grade Heat to Power Conversion Applications". In: *Thermal Science and Engineering Progress* 4, pp. 113–121. ISSN: 24519049. DOI: 10.1016/j.tsep.2017.09.009. (Visited on 10/23/2025).

van Heule, Xander et al. (Oct. 2025). "Sensitivity Study of a Partially Evaporating Organic Rankine Cycle Model with Non-Equilibrium Expansion". In: *Applied Thermal Engineering* 276, p. 126682. ISSN: 13594311. DOI: 10.1016/j.applthermaleng.2025.126682. (Visited on 11/05/2025).

Leclercq, Nicolas et al. (2024a). "Modeling and Experimental Validation of the Thermophysical Properties of a POE+R1233zd(E) Mixture". In: *Proceeding of the International Compressor Engineering Conference*. Purdue University.

Youbi-Idrissi, M. and Bonjour, Jocelyn (Mar. 2008). *The Effect of Oil in Refrigeration: Current Research Issues and Critical Review of Thermodynamic Aspects*. DOI: 10.1016/j.ijrefrig.2007.09.006.

Li, H. and Hrnjak, Predrag (2013). "Effect of Lubricant on Two-phase Refrigerant Distribution in Microchannel Evaporator". In: *International Journal of Materials and Manufacturing* 6.3, pp. 567–575. DOI: 10.2307/26268552. JSTOR: 10.2307/26268552.

Youbi-Idrissi, M. et al. (May 2004). "Oil Presence in an Evapoator: Experimental Validation of a Refrigerant/Oil Mixture Enthalpy Calculation Model". In: *International Journal of Refrigeration*. Vol. 27, pp. 215–224. DOI: 10.1016/j.ijrefrig.2003.11.001.

Barbosa, J.R. (2001). "Phase Change of Single Component Fluids and Mixtures in Annular Flow". PhD thesis. University of London & Imperial College of Science, Technology and Medicine.

Yang, Xiaoxian and Richter, Markus (2024). "Thermophysical Property Model of Lubricant Oils and Their Mixtures with Refrigerants". In: *Proceedings of the International Compressor Engineering Conference*. Ray W. Herrick Laboratories, Purdue University.

Neto, Moisés A. Marcelino and Barbosa, Jader R. (2011). "Modeling the Thermodynamic Properties of Refrigerant–Oil Mixtures and the Effect of the Oil Circulation Ratio on the Performance of Vapor Compression Systems". In: *Proceedings of the VI Congresso Brasileiro de Termodinâmica Aplicada*. CBTermo Organizing Committee.

Ossorio, Ruben et al. (2022). "Impact of Lubricant in the Evaporator as a Function of Oil Circulation Rate in Variable Speed Heat Pumps Working with R290". In: *Proceedings of the International Refrigeration and Air Conditioning Conference*. Purdue University.

de Hemptinne, Jean-Charles (2012). *Select Thermodynamic Models for Process Simulation : A Practical Guide Using a Three Steps Methodology*. Editions Technip. ISBN: 978-2-7108-0949-4.

Scialdone, John J., Miller, Michael K., and Montoya, Alex F. (1996). *Methods of Measuring Vapor Pressures of Lubricants With Their Additives Using TGA and/or Microbalances*. Tech. rep. NASA.

van Konynenburg, P. H. and Scott, R. L. (Dec. 1980). "Critical Lines and Phase Equilibria in Binary van Der Waals Mixtures". In: *Philosophical Transactions of the Royal Society of London. Series A, Mathematical and Physical Sciences* 298.1442, pp. 495–540. ISSN: 0080-4614. DOI: 10.1098/rsta.1980.0266.

Thome, John R. (1995). "Comprehensive Thermodynamic Approach to Modeling Refrigerant-Lubricating Oil Mixtures". In: *HVAC and R Research* 1.2, pp. 110–125. ISSN: 10789669. DOI: 10.1080/10789669.1995.10391313.

Dickes, Rémi (2019). "Charge-Sensitive Methods for the off-Design Performance Characterization of Organic Rankine Cycle (ORC) Power Systems". PhD thesis. University of Liège.

Ossorio, Ruben and Navarro-Peris, Emilio (Mar. 2021). "Study of Oil Circulation Rate in Variable Speed Scroll Compressor Working with Propane". In: *International Journal of Refrigeration* 123, pp. 63–71. ISSN: 01407007. DOI: 10.1016/j.ijrefrig.2020.12.002. (Visited on 09/09/2025).

Albatati, Faisal Ali S. (2015). "Investigation of Environmentally Friendly Power Generation Systems for Low-Grade Waste Heat Recovery". PhD thesis. University of Nottingham.

Bell, Ian H. et al. (Feb. 2014). "Pure and Pseudo-Pure Fluid Thermophysical Property Evaluation and the Open-Source Thermophysical Property Library Coolprop". In: *Industrial and Engineering Chemistry Research* 53.6, pp. 2498–2508. ISSN: 08885885. DOI: 10.1021/ie4033999.

Bruno, Thomas J et al. (Aug. 2019). *Thermophysical Properties of Polyol Ester Lubricants*. Tech. rep. NIST IR 8263. Gaithersburg, MD: National Institute of Standards and Technology, NIST IR 8263. DOI: 10.6028/NIST.IR.8263. (Visited on 09/24/2025).

Yang, Xiaoxian et al. (Nov. 2023). "Thermophysical Property Modeling of Lubricant Oils and Their Mixtures with Refrigerants Using a Minimal Set of Experimental Data". In:

Industrial and Engineering Chemistry Research 62.44, pp. 18736–18749. ISSN: 15205045. DOI: 10.1021/acs.iecr.3c02474.

Stöckel, Katharina et al. (Aug. 2023). "Measurement of Vapour Pressure, Miscibility and Thermal Conductivity for Binary and Ternary Refrigerant Lubricant Mixtures in the Context of Heat Pump Tumble Dryers". In: *International Journal of Refrigeration* 152, pp. 223–233. ISSN: 01407007. DOI: 10.1016/j.ijrefrig.2023.04.016.

Youbi-Idrissi, M. (2003). "Impact de l'huile de Lubrification Sur Les Performances Thermodynamiques Des Pompes à Chaleur Réversibles". PhD thesis. Conservatoire national des arts et métiers (CNAM).

Mermond, Y., Feidt, M., and Marvillet, C. (Nov. 1999). "Propriétés Thermodynamiques et Physiques Des Mélanges de Fluides Frigorigènes et d'huiles". In: *International Journal of Refrigeration* 22.7, pp. 569–579. ISSN: 01407007. DOI: 10.1016/S0140-7007(99)00015-8.

Han, Xiao Hong et al. (Sept. 2010). "Solubility and Miscibility for the Mixture of (Ethyl Fluoride + Polyol Ester Oil)". In: *Journal of Chemical and Engineering Data* 55.9, pp. 3200–3207. ISSN: 00219568. DOI: 10.1021/je1000507.

Martz, W. L. and Jacobi, A. M. (1994). *Refrigerant-Oil Mixtures and Local Composition Modeling*. Tech. rep. Air Conditioning and Refrigeration Center, University of Illinois.

Peng, Ding-Yu and Robinson, Donald B. (Feb. 1976). "A New Two-Constant Equation of State". In: *Industrial & Engineering Chemistry Fundamentals* 15.1, pp. 59–64. ISSN: 0196-4313. DOI: 10.1021/i160057a011.

Neto, Moisés A. Marcelino and Barbosa, Jader R. (May 2010). "Solubility, Density and Viscosity of Mixtures of Isobutane (R-600a) and a Linear Alkylbenzene Lubricant Oil". In: *Fluid Phase Equilibria* 292.1-2, pp. 7–12. ISSN: 03783812. DOI: 10.1016/j.fluid.2009.12.029.

Bock, Jessica (2015). "Vapor-Liquid Equilibria of a Low Gwp Refrigerant, R-1234ZE(E), Mixed with a POE Lubricant". PhD thesis. University of Illinois at Urbana-Champaign.

Wang, Xiaopo, Jia, Xiucan, and Wang, Dongbo (Apr. 2021). "Experimental Investigation on the Solubility of R290 in Two Mineral Oils". In: *International Journal of Refrigeration* 124, pp. 13–19. ISSN: 01407007. DOI: 10.1016/j.ijrefrig.2020.12.021.

Caramaschi, Matteo et al. (2023). "Experimental Investigations and Modeling of Propylene and DME Solubility in PAG Oil". In: *Proceedings of the International Congress of Refrigeration*. International Institute of Refrigeration. DOI: DOI:10.18462/iir.icr.2023.0412.

Jia, Xiucan et al. (June 2020). "Phase Equilibrium of R1234yf and R1234ze(E) with POE Lubricant and Thermodynamic Performance on the Evaporator". In: *Fluid Phase Equilibria* 514. ISSN: 03783812. DOI: 10.1016/j.fluid.2020.112562.

Soave, Giorgio (June 1972). "Equilibrium Constants from a Modified Redlich-Kwong Equation of State". In: *Chemical Engineering Science* 27.6, pp. 1197–1203. ISSN: 00092509. DOI: 10.1016/0009-2509(72)80096-4.

Patel, Navin C. and Teja, Amyn S. (1982). "A New Cubic Equation of State for Fluids and Fluid Mixtures". In: *Chemical Engineering Science* 37.3, pp. 463–473. ISSN: 00092509. DOI: 10.1016/0009-2509(82)80099-7.

Yokozeki, A. (Feb. 2007). "Solubility Correlation and Phase Behaviors of Carbon Dioxide and Lubricant Oil Mixtures". In: *Applied Energy* 84.2, pp. 159–175. ISSN: 0306-2619. DOI: 10.1016/j.apenergy.2006.05.003. (Visited on 07/22/2025).

Wilson, Grant M. (Jan. 1964). "Vapor-Liquid Equilibrium. XI. A New Expression for the Excess Free Energy of Mixing". In: *Journal of the American Chemical Society* 86.2, pp. 127–130. ISSN: 0002-7863. DOI: 10.1021/ja01056a002.

Renon, Henri and Prausnitz, J. M. (Jan. 1968). "Local Compositions in Thermodynamic Excess Functions for Liquid Mixtures". In: *AIChE Journal* 14.1, pp. 135–144. ISSN: 0001-1541. DOI: 10.1002/aic.690140124.

Neto, Moisés A. Marcelino and Barbosa, Jader R. (Jan. 2008). "Solubility, Density and Viscosity of a Mixture of R-600a and Polyol Ester Oil". In: *International Journal of Refrigeration* 31.1, pp. 34–44. ISSN: 01407007. DOI: 10.1016/j.ijrefrig.2007.08.004.

Heil, J. F. and Prausnitz, J. M. (July 1966). "Phase Equilibria in Polymer Solutions". In: *AIChE Journal* 12.4, pp. 678–685. ISSN: 0001-1541. DOI: 10.1002/aic.690120412.

Tesser, R. et al. (Oct. 1999). "Description of the Vapor–Liquid Equilibrium in Binary Refrigerant/Lubricating Oil Systems by Means of an Extended Flory–Huggins Model". In: *Journal of Fluorine Chemistry* 99.1, pp. 29–36. ISSN: 00221139. DOI: 10.1016/S0022-1139(99)00119-0.

Dawo, Fabian et al. (Apr. 2021). "R1224yd(Z), R1233zd(E) and R1336mzz(Z) as Replacements for R245fa: Experimental Performance, Interaction with Lubricants and Environmental Impact". In: *Applied Energy* 288. ISSN: 03062619. DOI: 10.1016/j.apenergy.2021.116661.

Zhelezny, V. P. et al. (Sept. 2007). "An Experimental Investigation and Modelling of the Solubility, Density and Surface Tension of 1,1,1,3,3-Pentafluoropropane (R-245fa)/Synthetic Polyolester Compressor Oil Solutions". In: *Journal of Fluorine Chemistry* 128.9, pp. 1029–1038. ISSN: 00221139. DOI: 10.1016/j.jfluchem.2007.05.011.

Brocus, Julien et al. (Feb. 2022). "Solubility Measurements of Refrigerants in Polyolesters Lubricants at Temperature from 323.K to 383.K". In: *International Journal of Refrigeration* 134, pp. 278–292. ISSN: 01407007. DOI: 10.1016/j.ijrefrig.2021.09.025.

Neto, Moisés A. Marcelino, França, Rafael M., and Barbosa, J.R. (2014). "Convection-Driven Absorption of R-1234yf in Lubricating Oil". In: *International Journal of Refrigeration* 44, pp. 151–160. ISSN: 01407007. DOI: 10.1016/j.ijrefrig.2014.05.008.

Cavestri, Richard C. (1995). *Measurement of Viscosity, Density, and Gas Solubility of Refrigerant Blends in Selected Synthetic Lubricants*. Tech. rep. Imagination Resources, Inc.

Valderrama, José O. (1990). "A Generalized Patel-Teja Equation of State for Polar and Nonpolar Fluids and Their Mixtures." In: *JOURNAL OF CHEMICAL ENGINEERING OF JAPAN* 23.1, pp. 87–91. ISSN: 0021-9592. DOI: 10.1252/jcej.23.87.

Yang, Xiaoxian et al. (Dec. 2022). "Linking Viscosity to Equations of State Using Residual Entropy Scaling Theory". In: *International Journal of Thermophysics* 43.12. ISSN: 15729567. DOI: 10.1007/s10765-022-03096-9.

Hughes, D. W., Mcmullan, J. T., and Morgan, R. (1982). "Determination of the Thermodynamic Properties of Refrigerant-Oil Mixtures". In: *Proceedings of the International Compressor Engineering Conference*. Ray W. Herrick Laboratories, Purdue University.

Wei, Wenjian et al. (June 2008). "Models of Thermodynamic and Transport Properties of POE VG68 and R410A/POE VG68 Mixture". In: *Frontiers of Energy and Power Engineering in China* 2.2, pp. 227–234. ISSN: 16737393. DOI: 10.1007/s11708-008-0020-7.

Conde, Manuel R. (Jan. 1996). "Estimation of Thermophysical Properties of Lubricating Oils and Their Solutions with Refrigerants: An Appraisal of Existing Methods". In: *Applied Thermal Engineering* 16.1, pp. 51–61. ISSN: 13594311. DOI: 10.1016/1359-4311(95)00011-2.

Medvedev, Oleg O., Zhelezny, Petr V., and Zhelezny, Vitaly P. (Jan. 2004). "Prediction of Phase Equilibria and Thermodynamic Properties of Refrigerant/Oil Solutions". In: *Fluid Phase Equilibria* 215.1, pp. 29–38. ISSN: 03783812. DOI: 10.1016/j.fluid.2003.06.006.

Barbosa, J.R., Lacerda, V.T., and Prata, A.T. (Mar. 2004). "Prediction of Pressure Drop in Refrigerant–Lubricant Oil Flows with High Contents of Oil and Refrigerant Outgassing

in Small Diameter Tubes". In: *International Journal of Refrigeration* 27.2, pp. 129–139. ISSN: 0140-7007. DOI: 10.1016/j.ijrefrig.2003.08.004. (Visited on 07/22/2025).

Henderson, David R. (1994). *Solubility, Viscosity and Density of Refrigerant/Lubricant Mixtures*. Tech. rep. Spauschus Associates.

Quiñones-Cisneros, S. E. et al. (Aug. 2005). "Phase and Viscosity Behaviour of Refrigerant-Lubricant Mixtures". In: *International Journal of Refrigeration* 28.5, pp. 714–724. ISSN: 01407007. DOI: 10.1016/j.ijrefrig.2004.12.004.

Youbi-Idrissi, M. et al. (May 2003). "Impact of Refrigerant–Oil Solubility on an Evaporator Performances Working with R-407C". In: *International Journal of Refrigeration* 26.3, pp. 284–292. ISSN: 01407007. DOI: 10.1016/S0140-7007(02)00129-9.

Leclercq, Nicolas, Bederna, Benedikt G., and Lemort, Vincent (2024b). "Experimental Testing of a Scroll Compressor with Two-Phase Refrigerant Flows". In: *13th International Conference on Compressors and Their Systems*. Springer, pp. 239–250. DOI: 10.1007/978-3-031-42663-6_19.

— (Sept. 2025). "Experimental Study of a Retrofitted Scroll Compressor for Operation with Two-Phase Refrigerant Flows". In: *International Journal of Refrigeration* 177, pp. 219–231. ISSN: 01407007. DOI: 10.1016/j.ijrefrig.2025.05.013. (Visited on 08/15/2025).

Honeywell International Inc. (2018). *A Better Environment with Next-Generation Solstice Zd Refrigerant*.

Sugimoto, Kazuo, Shimizu, Shigemi, and Terauchi, Kiyoshi (1985). "Rotation-Preventing Device for an Orbiting Piston-type Fluid Displacement". US Patent 4545746.

Carrier Corporation (2004). *High Efficiency Compression for Commercial and Industrial Applications*.

Tromp, Stéphane (2018). "Lubrication with a Refrigerant: An Industrial Challenge Investigated through Multiscale Modeling Based on Fluid/Surface Chemistry". PhD thesis. Université de Lyon (INSA).

Billiet, Marijn (2019). "Phase Distribution of a Refrigerant Two-Phase Flow over an Impacting t-Junction". PhD thesis. Universiteit Gent.

Danel, François (1978). "Mesure Locale Dans Les Écoulements Diphasiques: Développements Récents Des Sondes Optiques". In: *La Houille Blanche N°5*.

De Kerpel, Kathleen (2015). "Refrigerant Two-Phase Flow Behaviour and Pressure Drop up- and Downstream of a Sharp Return Bend". PhD thesis. Universiteit Gent.

Elstroem, Michael (2017). "New Refrigerant Quality Measurement and Demand Defrost Methods". In: *IIAR Natural Refrigeration Conference & Heavy Equipment Expo*.

Kaya, Alihan (2021). "Experimental Study of Nucleate and Convective Flow Boiling in a Large Diameter Horizontal Tube". PhD thesis. Universiteit Gent.

Pochet, Steven (2012). "Développement d'un Système Pour La Mesure Du Taux de Vide Dans Un Écoulement Diphasique Par Une Méthode Utilisant Des Micro-Ondes". PhD thesis. Ecole Polytechnique de Montréal.

Sakamoto, Yuki et al. (July 2019). "Investigation of the Void Fraction–Quality Correlations for Two-Phase Hydrogen Flow Based on the Capacitive Void Fraction Measurement". In: *International Journal of Hydrogen Energy* 44.33, pp. 18483–18495. ISSN: 03603199. DOI: 10.1016/j.ijhydene.2019.05.066.

Dorfman, Abram and Fridman, Ella (June 2006). "Vapor Quality Measurement by a Discharging Calorimeter". In: *Fluid Phase Equilibria* 244.1, pp. 46–51. ISSN: 03783812. DOI: 10.1016/j.fluid.2006.03.019.

Fukuta, Mitsuhiro et al. (2018). "Quality Measurement of Two Phase Flow with Plug Flow". In: *International Refrigeration and Air Conditioning Conference*. Purdue University.

Dutton, Robert E. and Mattar, Wade M. (2006). "Two-Phase Steam Measurement System". US Patent 2006/0123923 A1.

Delhaye, Jean-Marc (1968). *Mesure Du Taux de Vide Local En Écoulement Diphasique Eau-Air Par Un Anémomètre à Film Chaud*. Tech. rep. Centre d'Etudes Nucléaires.

Wojtan, Leszek, Ursenbacher, Thierry, and Thome, John R. (2004). "Interfacial Measurements in Stratified Types of Flow. Part II: Measurements for R-22 and r-410A". In: *International Journal of Multiphase Flow* 30.2, pp. 125–137. ISSN: 03019322. DOI: 10.1016/j.ijmultiphaseflow.2003.11.009.

Bell, Ian H. et al. (Nov. 2012b). "Liquid-Flooded Compression and Expansion in Scroll Machines - Part I: Model Development". In: *International Journal of Refrigeration* 35.7, pp. 1878–1889. ISSN: 01407007. DOI: 10.1016/j.ijrefrig.2012.07.010.

Ramaraj, Sugirdhalakshmi et al. (2014). "Experimental Analysis of Oil Flooded R410A Scroll Compressor". In: *International Journal of Refrigeration* 46, pp. 185–195. ISSN: 01407007. DOI: 10.1016/j.ijrefrig.2014.08.006.

Quoilin, Sylvain and Schrouff, Jessica (May 2016). "Assessing Steady-State, Multivariate Experimental Data Using Gaussian Processes: The Gpexp Open-Source Library". In: *Energies* 9.6, p. 423. ISSN: 1996-1073. DOI: 10.3390/en9060423.

Chang, Yu Choung et al. (2004). "Computer Simulation and Experimental Validation of Scroll Compressors". In: *International Compressor Engineering Conference*. Purdue University.

Mahfouz, Hamdy A Gouda (2004). "Analytical and Experimental Study on a Scroll Compressor". In: *International Compressor Engineering Conference*. Purdue University.

Picavet, Alain and Ginies, Pierre (2014). "Experimental Pressure-Volume Diagrams of Scroll Compressors". In: *International Compressor Engineering Conference*. Purdue University.

Wang, Baolong et al. (Jan. 2007). "Design of Experimental Bench and Internal Pressure Measurement of Scroll Compressor with Refrigerant Injection". In: *International Journal of Refrigeration* 30.1, pp. 179–186. ISSN: 01407007. DOI: 10.1016/j.ijrefrig.2006.04.007. (Visited on 10/22/2025).

Leclercq, Nicolas and Lemort, Vincent (2024c). "A Mathematical Model for the Simulation of Two-phase Compression in Thermal Non-equilibrium". In: *1st Belgian Symposium of Thermodynamics*. Vol. Paper ID: 68. Liège.

Winandy, Eric, O, Claudio Saavedra, and Lebrun, Jean (Feb. 2002). "Experimental Analysis and Simplified Modelling of a Hermetic Scroll Refrigeration Compressor". In: *Applied Thermal Engineering* 22.2, pp. 107–120. ISSN: 13594311. DOI: 10.1016/S1359-4311(01)00083-7. (Visited on 09/11/2025).

Cuevas, Cristian, Fonseca, Nestor, and Lemort, Vincent (June 2012). "Automotive Electric Scroll Compressor: Testing and Modeling". In: *International Journal of Refrigeration* 35.4, pp. 841–849. ISSN: 01407007. DOI: 10.1016/j.ijrefrig.2011.11.019. (Visited on 09/11/2025).

Fujiwara, M and Osada, Y (May 1995). "Performance Analysis of an Oil-Injected Screw Compressor and Its Application". In: *International Journal of Refrigeration* 18.4, pp. 220–227. ISSN: 01407007. DOI: 10.1016/0140-7007(95)00008-Y. (Visited on 09/10/2025).

Seshaiah, N. et al. (Jan. 2007). "Mathematical Modeling of the Working Cycle of Oil Injected Rotary Twin Screw Compressor". In: *Applied Thermal Engineering* 27.1, pp. 145–155. ISSN: 13594311. DOI: 10.1016/j.applthermaleng.2006.05.007. (Visited on 09/10/2025).

Chen, Yu et al. (Sept. 2002a). "Mathematical Modeling of Scroll Compressors—Part I: Compression Process Modeling". In: *International Journal of Refrigeration* 25.6, pp. 731–750. ISSN: 01407007. DOI: 10.1016/S0140-7007(01)00071-8. (Visited on 09/10/2025).

Bell, Ian H. et al. (Feb. 2020). "PDSim: A General Quasi-Steady Modeling Approach for Positive Displacement Compressors and Expanders". In: *International Journal of Refrigeration* 110, pp. 310–322. ISSN: 01407007. DOI: 10.1016/j.ijrefrig.2019.09.002. (Visited on 09/11/2025).

Wang, Baolong, Li, Xianting, and Shi, Wenxing (Sept. 2005). "A General Geometrical Model of Scroll Compressors Based on Discretional Initial Angles of Involute". In: *International Journal of Refrigeration* 28.6, pp. 958–966. ISSN: 01407007. DOI: 10.1016/j.ijrefrig.2005.01.015. (Visited on 09/11/2025).

Nieter, Jeff J (1988). "Dynamics of Scroll Suction Process". In: *International Compressor Engineering Conference*. Purdue University.

Gillies, Sean et al. (Dec. 2022). *Shapely*. Zenodo. DOI: 10.5281/ZENODO.7428463. (Visited on 09/14/2025).

Lin, Jie, Lian, Yongsheng, and Wu, Jianhua (Apr. 2020). "Numerical Investigation on Vapor-Liquid Two-Phase Compression in the Cylinder of Rotary Compressors". In: *Applied Thermal Engineering* 170, p. 115022. ISSN: 13594311. DOI: 10.1016/j.applthermaleng.2020.115022. (Visited on 09/11/2025).

Yang, Minghong et al. (June 2022). "A Computationally Efficient Scroll Compressor Model for Both Single-Phase and Two-Phase Compression Considering Scroll Wrap Temperature Distribution". In: *International Journal of Refrigeration* 138, pp. 159–168. ISSN: 01407007. DOI: 10.1016/j.ijrefrig.2022.03.008. (Visited on 09/09/2025).

Thorade, Matthis and Saadat, Ali (Dec. 2013). "Partial Derivatives of Thermodynamic State Properties for Dynamic Simulation". In: *Environmental Earth Sciences* 70.8, pp. 3497–3503. ISSN: 1866-6280, 1866-6299. DOI: 10.1007/s12665-013-2394-z. (Visited on 09/26/2025).

Ziviani, Davide (2017). "Theoretical and Experimental Characterization of Single-Screw Expanders for ORC Applications". PhD thesis. Universiteit Gent. ISBN: ISBN978-94-6355-047-5.

Zaytsev, D. (2003). "Development of Wet Compressor for Application in Compression-Resorption Heat Pumps". PhD thesis. Technische Universiteit Delft.

Öhman, Henrik and Lundqvist, Per (2013). "Experimental Investigation of a Lysholm Turbine Operating with Superheated, Saturated and 2-Phase Inlet Conditions". In: *Applied Thermal Engineering*. Vol. 50, pp. 1211–1218. DOI: 10.1016/j.applthermaleng.2012.08.035.

van Heule, Xander et al. (Jan. 2023). "Modelling of Two-Phase Expansion in a Reciprocating Expander". In: *Applied Thermal Engineering* 218, p. 119224. ISSN: 13594311. DOI: 10.1016/j.applthermaleng.2022.119224. (Visited on 09/16/2025).

Revellin, Rémi et al. (June 2012). "A Comprehensive Non-Equilibrium Thermodynamic Analysis Applied to a Vapor-Liquid Two-Phase Flow of a Pure Fluid". In: *International Journal of Multiphase Flow* 42, pp. 184–193. ISSN: 03019322. DOI: 10.1016/j.ijmultiphaseflow.2012.02.008.

Chisholm, D. (1983). *Two-Phase Flow in Pipelines and Heat Exchangers*. London ; New York: G. Godwin in association with Institution of Chemical Engineers. ISBN: 978-0-7114-5748-5.

Alimonti, Claudio, Falcone, Gioia, and Bello, Oladele (Nov. 2010). "Two-Phase Flow Characteristics in Multiple Orifice Valves". In: *Experimental Thermal and Fluid Science* 34.8, pp. 1324–1333. ISSN: 08941777. DOI: 10.1016/j.expthermflusci.2010.06.004. (Visited on 09/10/2025).

Morris, S.D. (July 1991). "Compressible Gas-Liquid Flow through Pipeline Restrictions". In: *Chemical Engineering and Processing: Process Intensification* 30.1, pp. 39–44. ISSN: 02552701. DOI: 10.1016/0255-2701(91)80007-C. (Visited on 09/10/2025).

Petrovic, Milan and Stevanovic, Vladimir (2016). "Two-Component Two-Phase Critical Flow". In: *FME Transaction* 44.2, pp. 109–114. ISSN: 1451-2092. DOI: 10.5937/fmet1602109P. (Visited on 09/10/2025).

Pereira, Evandro L.L. and Deschamps, Cesar J (2010). "A Lumped Thermodynamic Model for Scroll Compressors with Special Attention to the Geometric Characterization during

the Discharge Process". In: *International Compressor Engineering Conference*. Purdue University.

Wojtan, Leszek, Ursenbacher, Thierry, and Thome, John R. (July 2005). "Investigation of Flow Boiling in Horizontal Tubes: Part I—A New Diabatic Two-Phase Flow Pattern Map". In: *International Journal of Heat and Mass Transfer* 48.14, pp. 2955–2969. ISSN: 00179310. DOI: 10.1016/j.ijheatmasstransfer.2004.12.012. (Visited on 09/10/2025).

Thome, John R. (n.d.). "Chapter 17: Void Fractions in Two-Phase Flows". In: *Engineering Data Book III*.

Biberg, Dag (Dec. 1999). "An Explicit Approximation for the Wetted Angle in two-Phase Stratified Pipe Flow". In: *The Canadian Journal of Chemical Engineering* 77.6, pp. 1221–1224. ISSN: 0008-4034, 1939-019X. DOI: 10.1002/cjce.5450770619. (Visited on 10/06/2025).

Lee, Sang Won and No, Hee Cheon (Aug. 2019). "Droplet Size Prediction Model Based on the Upper Limit Log-Normal Distribution Function in Venturi Scrubber". In: *Nuclear Engineering and Technology* 51.5, pp. 1261–1271. ISSN: 17385733. DOI: 10.1016/j.net.2019.03.014. (Visited on 09/10/2025).

Gasche, José Luiz, Ferreira, R T S, and Prata, A T (2000). "Two-Phase Flow of Oil-Refrigerant Mixture Through the Radial Clearance in Rolling Piston Compressors". In: *Proceedings of the International Compressor Engineering Conference*. Purdue University.

Tanveer, M. Mohsin et al. (Oct. 2022). "Mechanistic Chamber Models: A Review of Geometry, Mass Flow, Valve, and Heat Transfer Sub-Models". In: *International Journal of Refrigeration* 142, pp. 111–126. ISSN: 01407007. DOI: 10.1016/j.ijrefrig.2022.06.016. (Visited on 09/09/2025).

Popiel, C.O., Wojtkowiak, J., and Bober, K. (Nov. 2007). "Laminar Free Convective Heat Transfer from Isothermal Vertical Slender Cylinder". In: *Experimental Thermal and Fluid Science* 32.2, pp. 607–613. ISSN: 08941777. DOI: 10.1016/j.expthermflusci.2007.07.003. (Visited on 10/12/2025).

Shao, D.W and Granryd, E (Jan. 1995). "Heat Transfer and Pressure Drop of HFC134a-oil Mixtures in a Horizontal Condensing Tube". In: *International Journal of Refrigeration* 18.8, pp. 524–533. ISSN: 01407007. DOI: 10.1016/0140-7007(96)81779-8. (Visited on 09/09/2025).

Dutta, Asit K., Yanagisawa, Tadashi, and Fukuta, M (1996). "A Study on Compression Characteristic of Wet Vapor Refrigerant". In: *Proceeding of the International Compressor Engineering Conference*. Purdue University.

Stosic, N. et al. (Jan. 1992). "Investigation of the Influence of Oil Injection upon the Screw Compressor Working Process". In: *International Journal of Refrigeration* 15.4, pp. 206–220. ISSN: 01407007. DOI: 10.1016/0140-7007(92)90051-U. (Visited on 09/10/2025).

Huagen, Wu, Ziwen, Xing, and Pengcheng, Shu (June 2004). "Theoretical and Experimental Study on Indicator Diagram of Twin Screw Refrigeration Compressor". In: *International Journal of Refrigeration* 27.4, pp. 331–338. ISSN: 01407007. DOI: 10.1016/j.ijrefrig.2004.01.004. (Visited on 09/09/2025).

Incropera, Frank P. et al., eds. (2007). *Fundamentals of Heat and Mass Transfer*. 6. ed. Hoboken, NJ: Wiley. ISBN: 978-0-471-45728-2.

Jang, Kitae and Jeong, Sangkwon (Aug. 2006). "Experimental Investigation on Convective Heat Transfer Mechanism in a Scroll Compressor". In: *International Journal of Refrigeration* 29.5, pp. 744–753. ISSN: 01407007. DOI: 10.1016/j.ijrefrig.2005.12.002. (Visited on 09/10/2025).

Peng, Bin, Zhao, Shengxian, and Li, Yaohong (Oct. 2017). "Thermodynamic Model and Experimental Study of Oil-free Scroll Compressor". In: *Journal of Physics: Conference Series* 916, p. 012048. ISSN: 1742-6588, 1742-6596. DOI: 10.1088/1742-6596/916/1/012048. (Visited on 09/10/2025).

Yao, Yufang and Hrnjak, Pega (Oct. 2023). "Measurement and Modeling of Void Fraction for Developing Two-Phase Flow of R134a in a Horizontal Tube after an Expansion Valve". In: *International Journal of Refrigeration* 154, pp. 125–137. ISSN: 01407007. DOI: 10.1016/j.ijrefrig.2023.07.009. (Visited on 09/10/2025).

Chen, Yu et al. (Sept. 2002b). "Mathematical Modeling of Scroll Compressors — Part II: Overall Scroll Compressor Modeling". In: *International Journal of Refrigeration* 25.6, pp. 751–764. ISSN: 01407007. DOI: 10.1016/S0140-7007(01)00072-X. (Visited on 09/10/2025).

Lemort, Vincent (2008). "Contribution to the Characterization of Scroll Machines in Compressor and Expander Modes". PhD thesis. University of Liège.

Vasuthevan, Hanushan and Brümmer, Andreas (Nov. 2018). "Multiphase-Flow Simulation of a Rotating Rectangular Profile within a Cylinder in Terms of Hydraulic Loss Mechanisms". In: *IOP Conference Series: Materials Science and Engineering* 425, p. 012002. ISSN: 1757-899X. DOI: 10.1088/1757-899X/425/1/012002. (Visited on 09/10/2025).

— (2022). "Generic Experimental Investigation of Hydraulic Losses within Twin-Screw Machines". In: *The 9th International Conference on Compressor and Refrigeration*. Purdue University.

Nikolov, Alexander and Brümmer, Andreas (Nov. 2018). "Impact of Different Clearance Heights on the Operation of a Water-Flooded Twin-Screw Expander—Experimental Investigations Based on Indicator Diagrams". In: *IOP Conference Series: Materials Science and Engineering* 425, p. 012008. ISSN: 1757-899X. DOI: 10.1088/1757-899X/425/1/012008. (Visited on 09/10/2025).

Heselmann, Matthias, Dämgen, Ulrich, and Brümmer, Andreas (2024). "Experimental Investigation of the Distribution of Two-Phase Flow in Oil-Injected Twin-Screw Compressors". In: *13th International Conference on Compressors and Their Systems*. Ed. by Matthew Read et al. Cham: Springer Nature Switzerland, pp. 61–76. DOI: 10.1007/978-3-031-42663-6_6. (Visited on 09/10/2025).

Pereira, Evandro L.L. and Deschamps, Cesar J. (Oct. 2017). "A Heat Transfer Correlation for the Suction and Compression Chambers of Scroll Compressors". In: *International Journal of Refrigeration* 82, pp. 325–334. ISSN: 01407007. DOI: 10.1016/j.ijrefrig.2017.05.033. (Visited on 09/09/2025).

Lemort, Vincent, Olivier, Gérard, and De Pelsemaker, Christophe (2023). *Thermal Energy Management in Vehicles*. Automotive Series. Hoboken, NJ: John Wiley and Sons, Inc.

Huang, Paul Xiubao (2012). "Under-Compression (Over-Expansion) – An Isochoric Or Adiabatic Process?" In: *Proceedings of the International Compressor Engineering Conference*. Ray W. Herrick Laboratories, Purdue University.

Valderrama, José O. (Apr. 2003). "The State of the Cubic Equations of State". In: *Industrial & Engineering Chemistry Research* 42.8, pp. 1603–1618. ISSN: 0888-5885, 1520-5045. DOI: 10.1021/ie020447b. (Visited on 07/22/2025).

Hanna, Rani and Zoughaib, Assaad (2017). "Atomization of High Viscosity Liquids through Hydraulic Atomizers Designed for Water Atomization". In: *Experimental Thermal and Fluid Science* 85, pp. 140–153. ISSN: 08941777. DOI: 10.1016/j.expthermflusci.2017.03.004.

Alam, Md. Jahangir et al. (June 2018). "Measurement of Thermal Conductivity and Correlations at Saturated State of Refrigerant Trans-1-chloro-3,3,3-Trifluoropropene (R-1233zd(E))". In: *International Journal of Refrigeration* 90, pp. 174–180. ISSN: 0140-7007. DOI: 10.1016/j.ijrefrig.2018.02.004. (Visited on 07/28/2025).

Kondou, Chieko et al. (May 2015). "Surface Tension of Low GWP Refrigerants R1243zf, R1234ze(Z), and R1233zd(E)". In: *International Journal of Refrigeration* 53, pp. 80–89. ISSN: 0140-7007. DOI: 10.1016/j.ijrefrig.2015.01.005. (Visited on 07/28/2025).

Yang, Xiaoxian et al. (Mar. 2021). “Entropy Scaling of Viscosity—III: Application to Refrigerants and Their Mixtures”. In: *Journal of Chemical & Engineering Data* 66.3, pp. 1385–1398. ISSN: 0021-9568, 1520-5134. DOI: 10.1021/acs.jced.0c01009. (Visited on 07/28/2025).